

**Final Report**

**BRAYTON-CYCLE HEAT EXCHANGER  
TECHNOLOGY PROGRAM**

by

**J.J. Killackey, M.G. Coombs, R.F. Graves, C.J. Morse**

**AIRESEARCH MANUFACTURING COMPANY OF CALIFORNIA  
Los Angeles, California**

**Prepared for**

**NATIONAL AERONAUTICS AND SPACE ADMINISTRATION**

**August 1976**

**NASA Lewis Research Center  
CONTRACT NO. NAS3-15347**

*W. L. ...  
...*

**Page**  
**Intentionally**  
**Left Blank**



## FOREWORD

The program described in this report was conducted by AiResearch Manufacturing Company of California, a division of The Garrett Corporation, under NASA contract NAS3-15347. The work was performed under the direction of Mr. Paul T. Kerwin, Project Manager, Power Generation and Storage, NASA-Lewis Research Center. The AiResearch Program Manager was Mr. James J. Killackey.

The valuable contributions of the following members of the AiResearch technical staff are acknowledged: James C. Gibson, development engineering; C. Morse, finned-tube heat transfer test; Murray G. Coombs and Landon Stratton, heat exchanger design and analysis; Richard F. Graves and Tekai Vishwanath, structural design and bellows analysis; Lynn Kindlimann, metallurgical evaluations; and Levon M. Minassian, transient temperature analysis.

Values for the physical quantities are given in both SI and U. S. Customary Units. The measurements and calculations were made in U.S. Customary Units.

**Page**  
**Intentionally**  
**Left Blank**

# CONTENTS

<u>Section</u>		<u>Page</u>
1	SUMMARY AND INTRODUCTION	1-1
	Summary	1-1
	Finned-Tube Heat Transfer	1-1
	Modularized Waste Heat Exchanger Development	1-1
	Recuperator Submodules	1-1
	1140°K (1600°F) Bellows Development	1-1
	Low-Cost High-Temperature Braze Alloy	1-2
	Introduction	1-2
2	Finned-Tube Heat Transfer Tests	2-1
	Test Core Description	2-1
	Test Setup and Procedure	2-6
	Results and Discussion	2-6
	Concluding Remarks	2-10
	References	2-11
3	Modularized Waste Heat Exchanger Development	3-1
	Header Bar Design	3-1
	Module Fabrication	3-5
	Concluding Remarks	3-8
4	Recuperator Submodules	4-1
	Thermal Design and Analysis	4-1
	Preliminary Design	4-1
	Transient Analysis	4-15/16
	Structural Design and Analysis	4-50
	Preliminary Design Criteria	4-50
	Core Structural Analysis	4-61
	Mounting Analysis	4-70
	Seal-Plate/Side-Plate Pressure Containment	4-76
	Tube Sheet/Header Bar Thermal Analysis	4-76
	Material Selection	4-80
	Hastelloy X Parent Metal Tests	4-87
	Quarter-size Modules	4-94
	Design	4-94
	Thermal Analysis of One-Quarter-Size Submodule	4-97
	Low-Cycle Fatigue Analysis	4-107
	Fabrication	4-108

## CONTENTS (Continued)

<u>Section</u>	<u>Page</u>
Performance Test	4-120
Thermal Cycle Test, SN1	4-126
Design Modifications for SN2 Submodule	4-155
Recommended Design Improvements	4-176
References	4-176
 5 Task 2H--1140°K (1600°F) Bellows Development	
Bellows Types	5-1
Formed Bellows	5-1
Welded Bellows	5-3
Machined Bellows	5-3
Design Data	5-4
Environment	5-4
Candidate Material Properties	5-4
Typical Mechanical Properties	5-4
Preliminary Design Criteria	5-4
Service Requirements	5-4
Stress Requirements	5-6
Bellows Parametric Design Studies	5-9
Conclusions	5-9
References	5-16
 6 Low-Cost, High-Temperature Braze Alloy Development	6-1
Candidate Materials	6-1
Preliminary Investigation	6-4
Braze Alloy Hardness	6-10
Oxidation Testing	6-12
Results and Discussion	6-12
Conclusions	6-16
Bend Tests	6-18
Brazing Alloy Diluent Studies	6-18
Noble Metal Diluents	6-18
Hastelloy X Diluent	6-24
Nickel-Base Alloy Diluents	6-25
Conclusions	6-29
Weld-Over-Braze Tests	6-29
Plate/Bar Test Specimen	6-29
Finned Test Specimen	6-31
Conclusions	6-33

## CONTENTS (Continued)

<u>Section</u>	<u>Page</u>
Creep-Rupture Testing	6-34
Specimen Design	6-34
Fabrication	6-37
Testing	6-37
Results and Discussion	6-39
Conclusions	6-46
Tensile Tests	6-46
Concluding Remarks	6-47
References	6-49
Appendix A	Cyclic Creep Relaxation A-1
B	Derivation of Shear Lag Formula B-1
C	Bellows Design C-1
D	Bellows Design Summaries D-1
E	Braze Joint Photomicrographs E-1

## ILLUSTRATIONS

<u>Figure</u>		<u>Page</u>
2-1	HXDA Heat-Source Heat Exchanger (Nak to Xe-He).	2-2
2-2	Finned Tubular Test Core.	2-3
2-3	Test Core Tube Inside Geometry.	2-5
2-4	Heat Transfer Test Setup.	2-7
2-5	Finned Tubular Core Test Results Using Gas Properties at Bulk Average Temperatures.	2-8
2-6	Finned Tubular Core Test Results Using Modified Reynolds Number Correlation.	2-9
3-1	Typical Single Liquid Module Assembly	3-2
3-2	Verification of Double Braze Seal	3-3
3-3	Candidate Header Bar Configurations	3-4
3-4	Header Bar Configuration	3-4
3-5	Pressure Bag/Test Panel Assembly for Atmosphere Furnace Brazing	3-6
3-6	Modularized Waste Heat Exchanger Double Containment Test Panel	3-7
3-7	Liquid Sandwich Module Pressure Bag Brazing Fixture	3-9
3-8	Double Containment Header Bar Brazing (Micro 28002)	3-10
3-9	Panel Internal Brazing Joints (Micro 28002)	3-11
4-1	Variation of Counterflow Section Weight with Pressure Drop for Selected Fin Sets	4-3
4-2	Recuperator Submodule	4-5
4-3	Recuperator Mass vs Effectiveness	4-6
4-4	Startup Flow Transient	4-8
4-5	Startup Temperature Transient	4-9
4-6	Recuperator Module Pressure Drops Versus Mass	4-10

# ILLUSTRATIONS (Continued)

<u>Figure</u>		<u>Page</u>
4-7	Selected Recuperator Counterflow Section	4-11
4-8	Recuperator Pressure Drop Summary	4-12
4-9	Manifold Design Criteria for Uniform Flow Distribution	4-13
4-10	Conventional Recuperator Submodule Design	4-19
4-11	Transient Thermal Model	4-21
4-12	Axial Transient Temperature Distribution Adjacent to the Solid Header on the Hot Side	4-23
4-13	Axial Transient Temperature Distribution Adjacent to the Solid Header Bar on the Cold Side	4-24
4-14	Hot-Side Thermal Transient Temperature Distribution Normal to the Flow (Using Solid Header Bar)	4-25
4-15	Cold-Side Thermal Transient Temperature Distribution Normal to the Flow (Using Solid Header Bar)	4-26
4-16	Transient Temperature Distribution Normal to the Flow Direction at a Station 0.38 cm (0.15 in.) in the Heat Transfer Fin	4-27
4-17	Transient Temperature Distribution Normal to the Flow Direction at a Station 1.27 cm (0.5 in.) in the Heat Transfer Fin	4-28
4-18	Transient Temperature Distribution Normal to the Flow at a Station 2.29 cm (0.9 in.) in the Heat Transfer Fin	4-29
4-19	Transient Temperature Distribution Normal to the Flow Direction at a Station 4.06 cm (1.6 in.) in the Heat Transfer Fin	4-30
4-20	Transient Temperature Distribution Normal to the Flow at a Station 7.24 (7.24 in.) in the Heat Transfer Fin	4-31
4-21	Transient Temperature Distribution Normal to the Flow at a Station 11.68 cm (4.6 in.) in the Heat Transfer Fin	4-32
4-22	End Section Thermal Transient Parallel to the Hot Gas Flow (Using Solid Header Bar)	4-33
4-23	End Section Thermal Transient Parallel to the Cold Gas Flow (Using Solid Header Bar)	4-34

# ILLUSTRATIONS (Continued)

<u>Figure</u>		<u>Page</u>
4-24	Fine-Grid Model for Conventional Header Bar (Three-Dimensional Thermal Gradient)	4-36
4-25	Fine-Grid Model for Formed U-Channel Header (Three-Dimensional Thermal Gradient)	4-37
4-26	Fine-Grid Thermal Transient, Solid Header Bar Model	4-38
4-27	Fine-Grid Thermal Transient, Hollow Header Bar Model	4-39
4-28	Fine-Grid Thermal Transient, U-Channel Header	4-40
4-29	Transient Temperature Distribution for U-Channel Header Bar With Seal Plate	4-41
4-30	Transient Temperature Distribution for Narrow Header Bar	4-42
4-31	Tube Plate Maximum Thermal Gradient as a Function of Tube Plate Thickness (Time = 105 sec.)	4-44
4-32	Tube Plate Maximum Thermal Gradient Factor as a Function of Tube Plate Thickness (Time = 105 sec.)	4-45
4-33	Tube Plate Temperature as a Function of Tube Plate Thickness (Time = 105 sec.)	4-46
4-34	Tube Plate Temperature Variation Using Buffer Fins	4-47
4-35	Tube Plate Temperature Variation Using Buffer Fins (No Header Bar Effect)	4-48
4-36	Tube Plate Temperature Variation Using Buffer Fins (No Header Bar Effect)	4-49
4-37	Transient Analyses of Hot Gas Inlet Manifold of Header Bar with Minimum Fluid Flow	4-51
4-38	Transient Analyses of Hot Gas Inlet Manifold of Header Bar with Maximum Fluid Flow	4-52
4-39	Transient Analyses of Cold Gas Outlet Manifold to Header Bar with Minimum Fluid Flow	4-53
4-40	Transient Analysis of Cold Gas Outlet Manifold of Header with Maximum Fluid Flow	4-54
4-41	Transient Analysis of Hot Gas Inlet Manifold to Header Bar 2.5 cm (1 in.) from Joint Interface	4-55



# ILLUSTRATIONS (Continued)

<u>Figure</u>		<u>Page</u>
4-42	Typical Stress-Strain Cycles Illustrating Creep Damage Conditions	4-60
4-43	Plate-Fin Recuperator with Triangular End Sections	4-64
4-44	Deflection Overshoot for Various Sheet Thicknesses	4-65
4-45	Deflection Shape for Several Plate Thicknesses	4-66
4-46	Model for Determining Deflection Shapes	4-67
4-47	Plate Thickness Transition Concept to Minimize Thermal Strains	4-71
4-48	Comparison of Recuperator Fin Pressures	4-72
4-49	Recuperator and Mount Orientation	4-77
4-50	Mounting Bracket Details	4-78
4-51	Finite Element Model for Seal Plate/Side Plate Interface Analysis	4-79
4-52	Recuperator Tube Sheet/Header Bar Thermal Stress Versus Number of Cycles to Failure for Various Levels of Stress by the Manson-Halford Equation	4-81
4-53	100-Hour Damage Integral for Relaxation of Initial Stress ( $\sigma_0$ ) Due to Secondary Creep Only	4-82
4-54	Finite Element Model for Analysis of Temperature Stresses	4-83
4-55	Triangular End Finite Element Model for Analysis of Temperature Stresses	4-84
4-56	Increase in Elastic Stress for a Nonrectangular Header Bar Based on the Shear Lag Approximation	4-85
4-57	Hastelloy X Material Specimens for Obtaining Stress-Strain Curve.	4-88
4-58	Hastelloy X Material Monotonic Stress-Strain Curve at 644°K (700°F).	4-89
4-59	Hastelloy X Material Monotonic Stress-Strain Curve at 1005°K (1350°F)	4-90

# ILLUSTRATIONS (Continued)

<u>Figure</u>		<u>Page</u>
4-60	Hastelloy X Material Cyclic Stress-Strain Curve at 644°K (700°F)	4-91
4-61	Hastelloy X Material Cyclic Stress-Strain Curve at 1005°K (1350°F)	4-92
4-62	Hastelloy X Material Pseudobrazing Cycle Pretest Thermal Treatment	4-93
4-63	Thermal Model of One-Quarter-Size Recuperator Module	4-98
4-64	Recuperator Submodule Thermal Transient	4-99
4-65	Temperature Gradients after Initiation of Transients	4-100
4-66	Detailed Thermal Model, One-Quarter-Size Module Critical Area	4-101
4-67	Critical Area Temperature Distribution at Station 3.16 cm	4-102
4-68	Critical Area Temperature Distribution 90 sec After Startup	4-103
4-69	Fast Transient	4-104
4-70	Critical Area Temperature Distribution, at Station 3.16 for Fast Transient	4-105
4-71	Critical Area Temperature Distribution 70 sec After Startup, Fast Transient	4-106
4-72	Test Conditions for Thermal Cycle Testing, 80-Cycle Life	4-108
4-73	Offset Heat Transfer Fins	4-110
4-74	Header Bar	4-111
4-75	Side Plate	4-112
4-76	Core Assembly Installed in Carbon Braze Fixture	4-113
4-77	Core Assembly After First Braze Operation	4-114
4-78	Machined Core Assembly	4-115
4-79	Manifold Splitter	4-116
4-80	Pan Attachment Flange	4-117

# ILLUSTRATIONS (Continued)

<u>Figure</u>		<u>Page</u>
4-81	Heat Exchanger Manifolds	4-118
4-82	Heat Exchanger Submodule	4-119
4-83	Performance Test Setup (One-Quarter-Size Module)	4-121
4-84	Pressure Drop, One-Quarter-Size Recuperator Submodule	4-122
4-85	Pressure Drop, One-Quarter-Size Recuperator Submodule	4-123
4-86	Test and Analytical Heat Transfer Performance.	4-124
4-87	Thermal Cycling Facility Schematic	4-127
4-88	Temperature Transients at Low-Pressure Gas Inlet	4-128
4-89	Leak Check Immersion Levels	4-130
4-90	Sectioned Segments of Core with Needles Used for Pressurizing Inserted	4-132
4-91	Location of Micros Taken from Section Including Low-Pressure Passes 11 through 13	4-133
4-92	Micro Sample 684-25X	4-134
4-93	Micro Sample 684-25X	4-135
4-94	Micro Sample 685-25X	4-136
4-95	Micro Sample 686 and 687-25X	4-137
4-96	Micro Sample 687 and 688-25X	4-138
4-97	Micro Sample 688 and 689-25X	4-139
4-98	Micro Sample 689 and 690-25X	4-140
4-99	Micro Sample 691 and 692-25X	4-141
4-100	Micro Sample 692 and 693-25X	4-142
4-101	Micro Sample 693-25X	4-143
4-102	Micro Sample 695-11X	4-144
4-103	Micro Sample 695 Unetched	4-145

# ILLUSTRATIONS (Continued)

<u>Figure</u>		<u>Page</u>
4-104	Micro Sample 696-22X	4-146
4-105	Micro Sample 752 Unetched-25X	4-148
4-106	Micro Sample 753 and 754 Unetched-25X	4-149
4-107	Micro Sample 755 Unetched	4-150
4-108	Cold End MBR Passes 1 through 12	4-151
4-109	Micro Sample 1001	4-152
4-110	Micro Sample 1021-70X Splitter-to-Core Joint	4-153
4-111	Air Pumping Mechanism	4-154
4-112	Completed Splitter, Recuperator Submodule No. 2	4-157
4-113	Leakage Flow Across Splitter (Hot End)	4-159
4-114	Test Damage after 100 Thermal Cycles, Second Recuperator Submodule	4-160
4-115	Test Damage Area Identification, Second Recuperator Submodule	4-161
4-116	Test Damage Repair	4-163
4-117	Splitter-Core Joint at Low-Pressure Inlet (After Test)	4-165
4-118	Core Face at Low-Pressure Inlet After Test	4-166
4-119	Micrograph Locations, Submodule SN2	4-167
4-120	Metallographic Examination Submodule, SN2, MR3519	4-168
4-121	Metallographic Examination Submodule, SN2, MR3520	4-170
4-122	Metallographic Examination Submodule, SN2, MR3516	4-171
4-123	Metallographic Examination Submodule, SN2, MR3522	4-172
4-124	Metallographic Examination Submodule, SN2, Splitter-Core Joint	4-173
4-125	Splitter-Core Joint Design	4-175

# ILLUSTRATIONS (Continued)

<u>Figure</u>		<u>Page</u>
5-1	Range of Convolution Shape Parameters and Materials Investigated.	5-10
5-2	Dimensional Description of Convolution Shapes Investigated.	5-11
5-3	Shell Analysis Model for Convolution parametric Parametric Studies.	5-12
5-4	Bellows Design Parameters as a Function of Pitch ( $h/r = 1/8$ )	5-13
5-5	Active Length and Stiffness vs Height	5-14
6-1	Tee-Section for Braze Alloy Screening	6-5
6-2	Plate-fin Specimen for Braze Alloy Evaluation and Oxidation Testing (Cut into 2.54 cm (1-in.) squares as shown).	6-13
6-3	Plate-Fin Oxidation Test Specimens	6-14
6-4	Bend Tests on Tee Sections.	6-19
6-5	Plate-Fin Specimen Brazed at 1433°K with a Mixture of NB210 and 10 Percent Palniro (Micro 26982, Oxalic Acid Etch 100X)	6-24
6-6	Plate-Header Bar Weld Test Sample	6-30
6-7	Plate-Header Bar Stack Brazed at 1422°K (2100°F) with Microbraz 30 (J-8100).	6-32
6-8	Creep-Rupture Test Specimen.	6-35
6-9	Exploded View of Creep-Rupture Test Panel.	6-36
6-10	Pressure Test System Schematic	6-38
6-11	Palniro 1 Creep-Rupture Testing.	6-41
6-12	Microbraz 30 Creep-Rupture Testing	6-42
6-13	Microbraz 210 (75 percent) - Microbraz 30 (25 percent) Creep-Rupture Testing	6-43
6-13	Summary of Brazing Alloy Creep-Rupture Testing	6-44
6-14	Larson-Miller Curves Showing Plate-Fin Creep-Rupture Testing Related to Mini Brayton-Cycle Recuperator Design Point	6-45

## TABLES

<u>Table</u>		<u>Page</u>
2-1	Heat Source Heat Exchanger and Test Core Geometries	2-4
4-1	Recuperator Submodule Design Conditions	4-2
4-2	Fin Geometries	4-2
4-3	Manifold Design for Uniform Flow Distribution	4-14
4-4	Variation of Tube Plate Thicknesses	4-43
4-5	Recuperator Design Criteria	4-57
4-6	Preliminary Inertia and Vibration Load Criteria	4-58
4-7	Candidate Materials Physical and Mechanical Properties	4-62
4-8	Material Allowable Design Stresses at 1000°K	4-63
4-9	Fin-Creep Stress Summary	4-69
4-10	Fin-Tensile Stress (Pressure Loaded)	4-70
4-11	Preliminary Inertia and Vibration Load Criteria	4-73
4-12	Preliminary Duct Loading Criteria Applied to Mounts	4-74
4-13	Preliminary Mount Design Loads	4-75
4-14	Test Data Analysis Summary One-Quarter-Size Test Submodule SK52160-1, SN-1	4-125
5-1	Bellows Convolutions and Characteristics	5-2
5-2	1140°K(1600°F) Material Properties (Sheet Metal)	5-5
5-3	Short Time Pressure Containment Design Stresses	5-6
5-4	Preliminary High-Temperature Bellows Design Stresses	5-8
6-1	Candidate Brazing Alloys	6-3
6-2	Results of Tee Section Screening of Candidate Braze Alloys	6-6

# TABLES (Continued)

<u>Table</u>		<u>Page</u>
6-3	Braze Alloys Selected for Additional Examination in a Plate-Fin Configuration	6-9
6-4	Hardness Tests on Brazements	6-11
6-5	Plate Fin Specimen Oxidation Data	6-15
6-6	Summary of Brazing Alloy Testing	6-17
6-7	Studies on Brazing Alloy Combinations	6-20
6-8	Results of Brazing Alloy Dilution Studies Utilizing Noble Metal Brazing Alloys	6-21
6-9	Effects of Noble Metal Brazing Alloy Additions of the Performance of Standard Brazing Alloys	6-23
6-10	Candidate Alloys for Brazing Hastelloy X Plate-Fin Heat Exchangers	6-26
6-11	Effects of Diluting Candidate Brazing Alloys with Hastelloy X Powder	6-27
6-12	Nicrobraz 210 and Nicrobraz 30 Combination Brazing Alloys	6-28
6-13	Creep Test Results for Brazing Alloy Evaluation	6-40
6-14	Tensile Data for Hastelloy X Material Brazed with 75 Percent Nicrobraz 210, Twenty-Five Percent Nicrobraz 30, and Palniro 1	6-46

## DRAWINGS

<u>Drawing No.</u>		<u>Page</u>
L198782	Recuperator HXDA (NASA/Lewis)	4-17/18
SK52160	Recuperator Assy, 1/4 Module Test Unit	4-95/96
SK52534	Splitter Pan, Recuperator	4-156



**SECTION 1**

**SUMMARY AND INTRODUCTION**

## SECTION 1

### SUMMARY AND INTRODUCTION

#### SUMMARY

A technology program was conducted to obtain design data, resolve critical design features, and advance manufacturing techniques for heat exchanger systems suitable for closed-loop Brayton-cycle power systems. Results are presented for five individual tasks.

#### Finned-Tube Heat Transfer

Heat transfer and pressure drop data are presented for a finned-tubular heat transfer matrix. Air was the test medium and the results are presented as friction factor,  $f$ , and Colburn modulus,  $j$ , versus Reynolds number. The matrix consisted of a staggered, triangular tube array with copper-stainless laminated strips helically wound on the tubes to form a disk-fin geometry.

#### Modularized Waste Heat Exchanger Development

The object was to develop a means to provide double containment of the organic heat transport fluid within the heat exchanger. Single-sandwich liquid modules were successfully brazed using H-shaped header bars that incorporated means to verify double containment.

#### Recuperator Submodules

The design, fabrication, and test of compact plate-fin heat exchangers representative of full-scale Brayton-cycle recuperators in terms of thermal and structural performance capabilities are presented. Specialized design techniques necessary to achieve a temperature effectiveness of 0.975 in the full-size unit were utilized. Low-cycle fatigue was identified as the most critical structural design problem. Heat transfer performance test results are presented. Thermal cycle testing was conducted at off-limit conditions to induce premature low-cycle fatigue cracking; two units were tested. Structurally weak areas were identified and design modifications were developed to improve the cyclic life.

#### 1140°K (1600°F) Bellows Development

The task objective was to design a bellows for operation at 1140°K (1600°F) and 1380 kN/m<sup>2</sup> (200 psia) operating pressure that would withstand 1000 operating cycles over a 50 000-hour lifetime. Both superalloy and refractory metals were candidate materials. Formed bellows were selected and a shell analysis program was used to determine the cyclic and creep life for various designs using the convolution shape, material thickness and number of plies as design parameters. Practical bellows designs were derived.

## Low-Cost High-Temperature Braze Alloy

The goal was to select a low-cost braze alloy to replace the gold-base alloys currently being used in the recuperator. The replacement alloys were to meet or exceed the gold-base alloy properties in terms of strength, ductility, oxidation resistance, and brazing characteristics of flow, penetration, and stability. The study was limited to existing braze alloys, but did include consideration of alloy combinations as well as alloys diluted with small fractions of either gold-base alloy or parent metal powders. Screening tests were conducted with 22 different alloys applied to Hastelloy X and Type 347 stainless steel parent metals. Microbraz 30 and a combination of Microbraz 210 and 30 braze alloys were determined to meet the task objectives.

### INTRODUCTION

This report presents a summary of a major portion of the work performed by AiResearch for the Lewis Research Center under Contract Number NAS3-15347 from June 1971 through October 1975. This program was a follow-on to the NASA study reported in NASA CR-72783 entitled "Conceptual Design Study of a Nuclear Brayton-Cycle Heat Exchanger and Duct Assembly (HXDA)" and NASA CR-72816 entitled "Preliminary Design Study of a Nuclear Brayton-Cycle Heat Exchanger and Duct Assembly (HXDA)". In June 1971, the development of the HXDA was initiated with a program to design, fabricate and test a heat exchanger and duct assembly suitable for a closed Brayton-cycle space power system in the 150-kwe class. The initial phase of this program was the preliminary system design and a series of small-scale tests directed toward obtaining data and demonstrating certain design techniques.

In January 1972, the HXDA program was reoriented from the development of a specific power system to a technology program for advanced Brayton-cycle heat exchangers and associated equipment. The detailed design and full-size heat exchanger fabrication efforts were terminated; however, the small-scale tests and several fabrication technology tasks were retained. This resulted in the formulation of some 10 work tasks that were completed during a 4-1/2 year period. Each work task had as its objective the development of design data and/or the resolution of some critical design feature for heat exchanger systems suitable for advanced closed-loop Brayton-cycle power systems.

In October 1972, a topical report entitled "Brayton-Cycle Heat Exchanger and Duct Assembly (HXDA) Preliminary Design and Technology Tests" (NASA CR-121011) was issued. This report presented the information developed on the tasks that had been completed as of June of that year. The tasks summarized in NASA CR-121011 were as follows:

- Reference preliminary design
- Brazing development tests
- Recuperator structural tests
- Heat-source heat exchanger structural tests
- Alternate low-temperature braze alloy development

The remaining tasks were as follows:

- Finned-tube heat transfer tests
- Modularized waste heat exchanger development
- Recuperator submodules
- 1140°K (1600°F) bellows development
- Low-cost, high-temperature braze alloy development

These last five tasks are reported here. Results of these studies will help to produce Brayton-cycle heat exchanger and interconnecting duct assemblies with improved cyclic life, greater reliability, and lower cost.

**SECTION 2**  
**FINNED-TUBE HEAT TRANSFER TESTS**

## SECTION 2

### FINNED-TUBE HEAT TRANSFER TESTS

The original HXDA system employed a liquid metal (NaK) heat transport loop to transfer the heat generated by a nuclear reactor to the Brayton-cycle working fluid. This transfer takes place in the heat-source heat exchanger with NaK on one side and the xenon-helium working fluid on the other. In the preliminary system design study (reported in NASA-CR-121011), an extensive parametric survey was made to determine the optimum heat transfer matrix for the heat-source heat exchanger. From these studies, the heat exchanger shown in fig. 2-1 was selected. This heat exchanger is a finned-tube matrix with NaK on the inside of the tubes and Xe-He on the outside. A summary description of the heat exchanger and the selected matrix is included in fig. 2-1. The fins for this matrix consist of strips of a copper-stainless steel laminate helically wound on the tubes to form a disc-fin tubular geometry. The copper-stainless steel laminate (0.00762 cm copper, 0.00508 cm stainless) provides both the high conductivity required for efficient heat transfer and the necessary strength at the heat source operating temperature.

The analysis leading to the selection of this fin-tube matrix was based on rather large extrapolations of available experimental data. Consequently, it was the intent of this task to experimentally confirm the predicted heat transfer and pressure drop characteristics of the selected matrix.

#### TEST CORE DESCRIPTION

A test core was designed and fabricated as shown in fig. 2-2. It is essentially a section of the HXDA heat-source heat exchanger core with minor differences in the core matrix due to fabrication effects. It consists of a bank of helically wound finned tubes arranged in an equilateral triangular pattern. The test core geometry and the full-size heat-source heat exchanger geometry are compared in table 2-1. The test unit has the same gas-side matrix geometry but smaller overall core dimensions compared to the full-size HSHX.

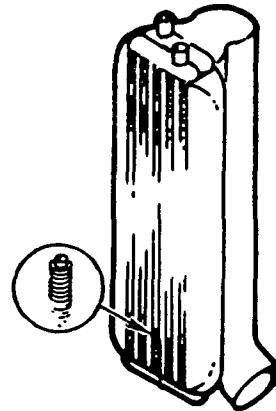
The test core consists of two active tube rows and three inactive tube rows, one inactive row being downstream (with reference to gas flow) and the other two upstream of the active section. The purpose of the inactive tubes is to establish the appropriate gas-side velocity profiles at the entrance and exit faces of the active core so that heat transfer measurements on the two-row section will reflect accurately the performance of a multi-tube row heat exchanger.

The test core fin pitch of 11.5 fins per cm (table 2-1) is based on measurement of several finned tubes after fabrication and brazing.

\*References enclosed at end of section

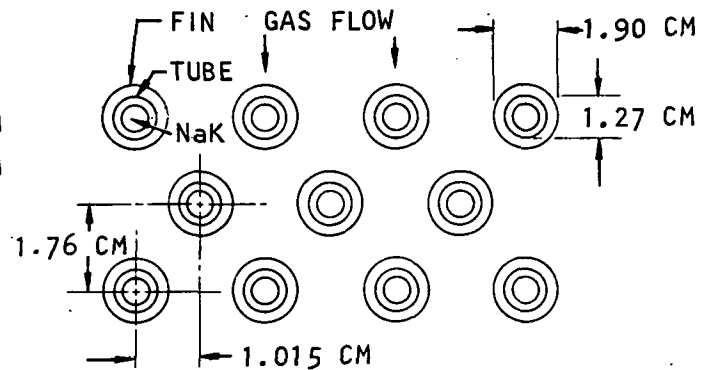
## CORE DESCRIPTION

GAS PRESSURE DROP	0.45 PERCENT
MASS (WET)	73 kg
LIQUID PRESSURE DROP	5.1 kN/M <sup>2</sup>
GAS-FLOW LENGTH	0.143 M
TUBE LENGTH (CORE)	1.06 M
NO-FLOW LENGTH (CORE)	0.243 M
NUMBER OF TUBES	92
NUMBER OF TUBE ROWS	8
NUMBER OF PASSES	2



## CORE MATRIX

TUBE OD	1.27 CM
FIN DIA	1.90 CM
FIN THICKNESS, COPPER	0.00762 CM
FIN THICKNESS, STAINLESS	0.00508 CM
FINS/CM	11.8
TRANSVERSE TUBE SPACING	2.03 CM
TUBE ROW SPACING	1.76 CM



S-7020

Figure 2-1.--HXDA Heat-Source Heat Exchanger  
(NaK to Xe-He).

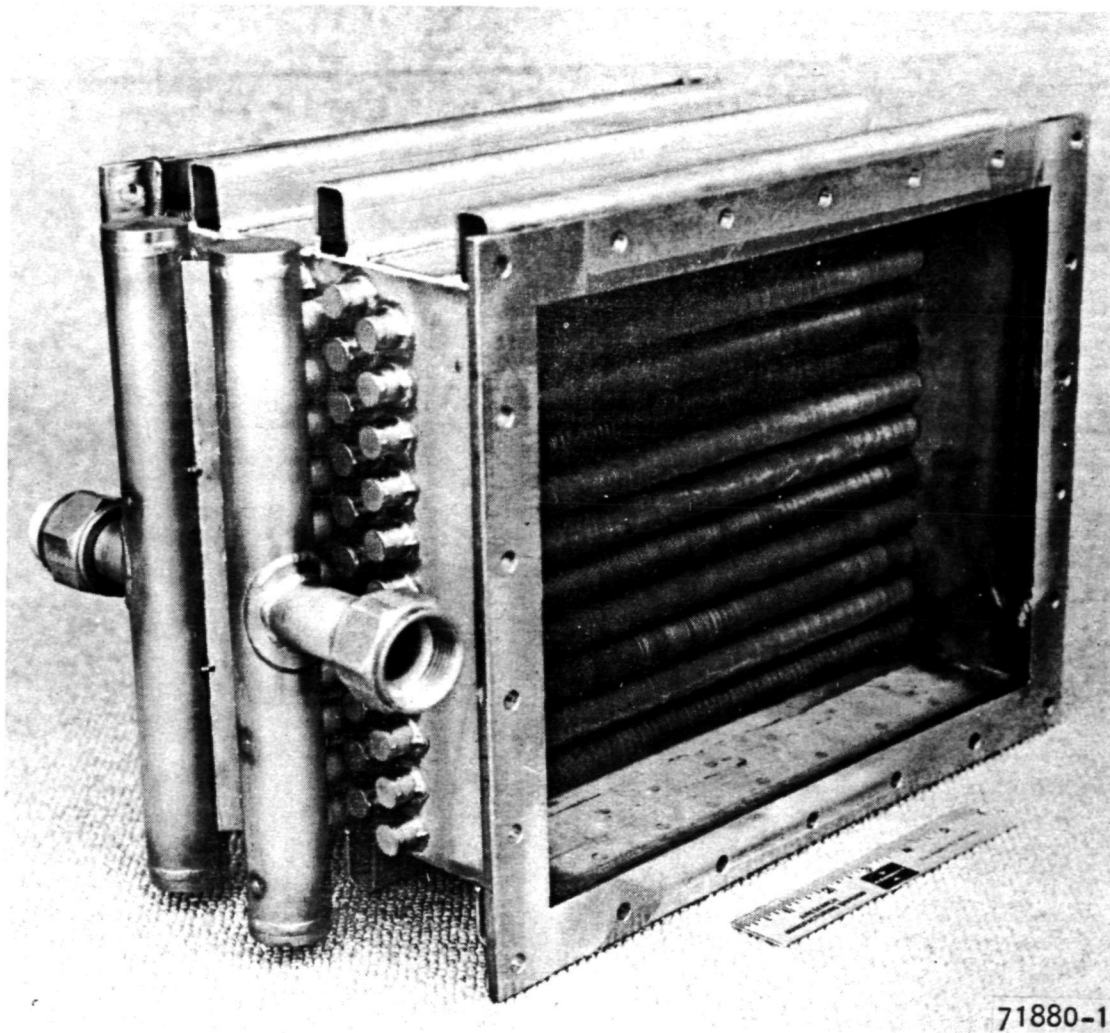


Figure 2-2.--Finned Tubular Test Core.



TABLE 2-1

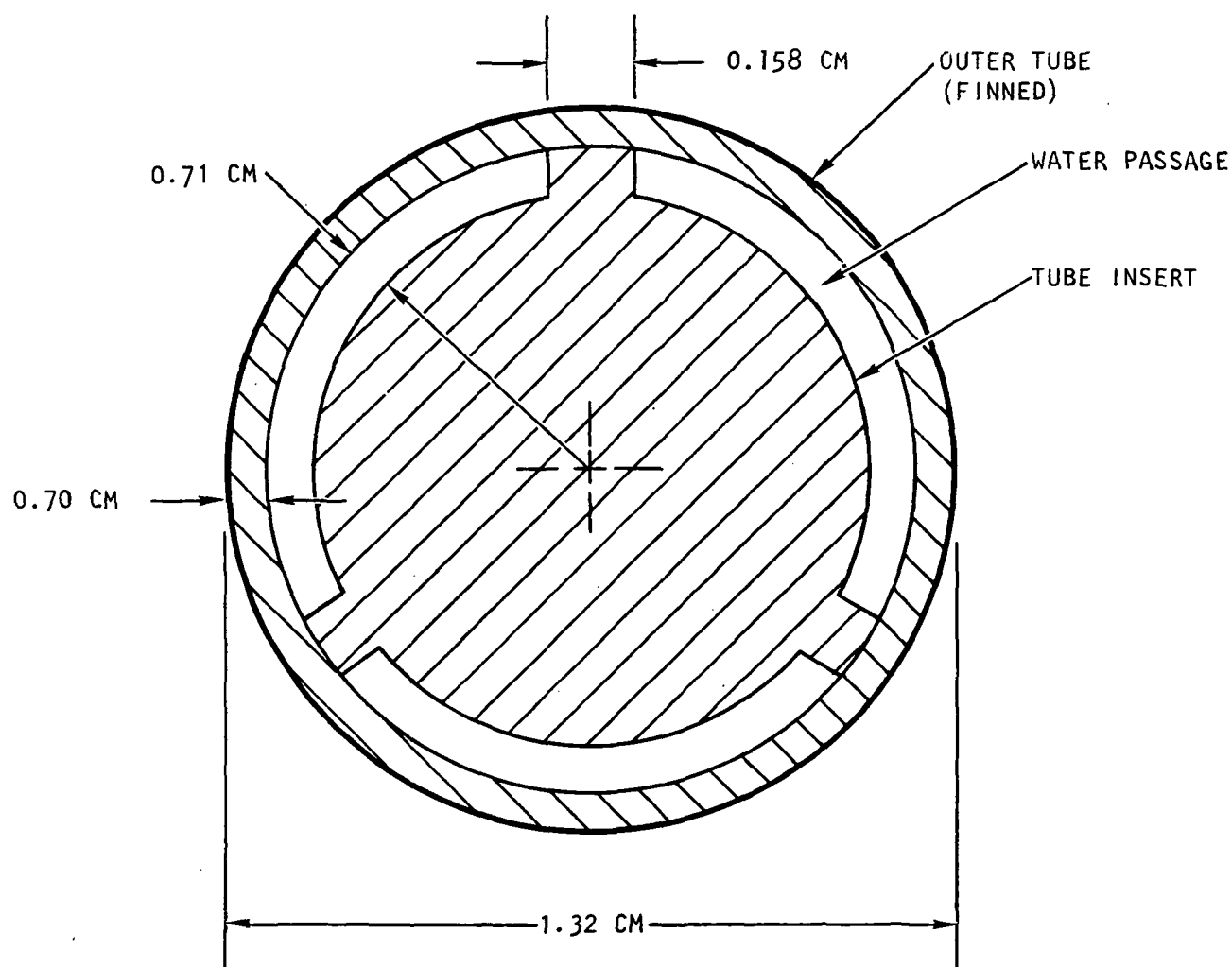
## HEAT-SOURCE HEAT EXCHANGER AND TEST CORE GEOMETRIES

Parameter	HSHX	Test Core
Tube outer diameter, cm	1.27	1.27
Fin diameter, cm	1.90	1.90
Fin thickness, cm (active tubes)	0.00762 (Cu) 0.00508 (S.S.)	0.00762 (Cu) 0.00711 (S.S.)
Fin thickness, cm (inactive tubes)	---	0.01524 (S.S.)*
Fin pitch, cm <sup>-1</sup>	11.8	11.5
Transverse tube spacing, cm	2.03	2.03
Tube row spacing, cm	1.76	1.76
Number of tubes per tube row	13.5	11
Number of tube rows	8	2 active 3 inactive
Number of liquid passes	2	2
Tube length, cm	112	30.5
No-flow length, cm	28.3	23.3
Gas-flow length, cm	14.3	3.67 (active) 8.96 (total)

\*Four (of a total of 33) of these inactive tubes had the bimetal (0.00762 cm Cu, 0.00711 cm S.S.) fins.

To reduce end effects, baffles are used in the spaces at the indented ends of all tube rows. The baffles used are partial cylindrical sections sized to give (approximately) an end path flow area equal to the average of the interior path flow area between tubes and one-half the interior path flow area between tubes. It is anticipated that baffles also will be used in the full-size heat-source heat exchanger to improve performance by reducing gas bypassing at the core ends. The effect could be significant because of the relatively few tubes per tube row in this unit.

The tube inside geometry for the test core is shown in fig. 2-3. A high inside (water) conductance is obtained by using only a small space between concentric tubes for the flow area. Selection of a water flow rate to give highly turbulent flow for all test points resulted in a high inside-to-outside conductance ratio. Thus, small errors in the prediction of the water-side (inside) heat transfer coefficient have a negligible effect on the calculation of the air-side (outside) coefficient.



S-74729

Figure 2-3.--Test Core Tube Inside Geometry.

## TEST SETUP AND PROCEDURE

The test setup and instrumentation are shown in fig. 2-4. The test core transfers heat from a controlled hot air supply to water at ambient temperature. In the air circuit, the test unit is located approximately one equivalent diameter downstream of a bellmouth entry, which produces uniform flow distribution and minimal boundary layer buildup at the core inlet face. Flow is measured using a standard orifice section upstream of the core. Inlet and outlet temperatures are obtained as averages for four thermocouple measurements upstream of the core (just prior to the bellmouth) and four measurements from a mixing box downstream of the core. In addition, 12-point thermocouple screens were located at the inlet and outlet core faces. Gas inlet pressure was measured with either a mercury or water manometer, depending on the pressure level, and gas pressure drop was measured with a water manometer.

On the water side, flow rate was measured with a turbine flowmeter. Unit inlet and outlet temperatures and the temperature difference were obtained from thermocouples located at inlet and outlet mixing tees. Inlet pressure and unit pressure drop were measured with gauges.

Testing consisted of a series of isothermal pressure drop tests using ambient air, followed by a series of heat transfer tests. For the heat transfer tests a constant water flow rate of 167 lb/min was used, yielding Reynolds numbers in the range of 8700 to about 10 000. Airflow rate was varied up to the maximum available from the facility. The air inlet temperature was set at 477°K (400°F) for the initial series of test points, and a second series of runs at an air inlet temperature of 590°K (610°F).

## RESULTS AND DISCUSSION

The data were reduced to obtain friction factor ( $f$ ) and Colburn Modulus ( $j$ ) curves for the finned tubular matrix over the range of test Reynolds numbers. The friction factor curves are based on the isothermal runs only because fluid property evaluation is straightforward for these runs. The heat transfer data were reduced first on the basis of gas properties evaluated at bulk average temperature (recommended by Kays and London, ref. 2-1, for all interrupted-boundary-layer surfaces) and then on the basis of a modified Reynolds number correlation used by the AiResearch tubular and finned-tubular heat exchanger programs. The latter correlation is described in ref. 2-2. The results for these two different methods of fluid property evaluation are shown in figs. 2-5 and 2-6. In both cases the data for the 477°K (400°F) and 590°K (610°F) air inlet temperatures form two distinct  $j$  curves, with the modified Reynolds number correlation reducing the spread between curves by only a minor amount. A third correlation using the temperature ratio method of correcting fluid properties, as recommended by Kays (ref. 2-3), shows a similar spread between the 477°K (400°F) and 590°K (610°F) data. For future design purposes, the correlation

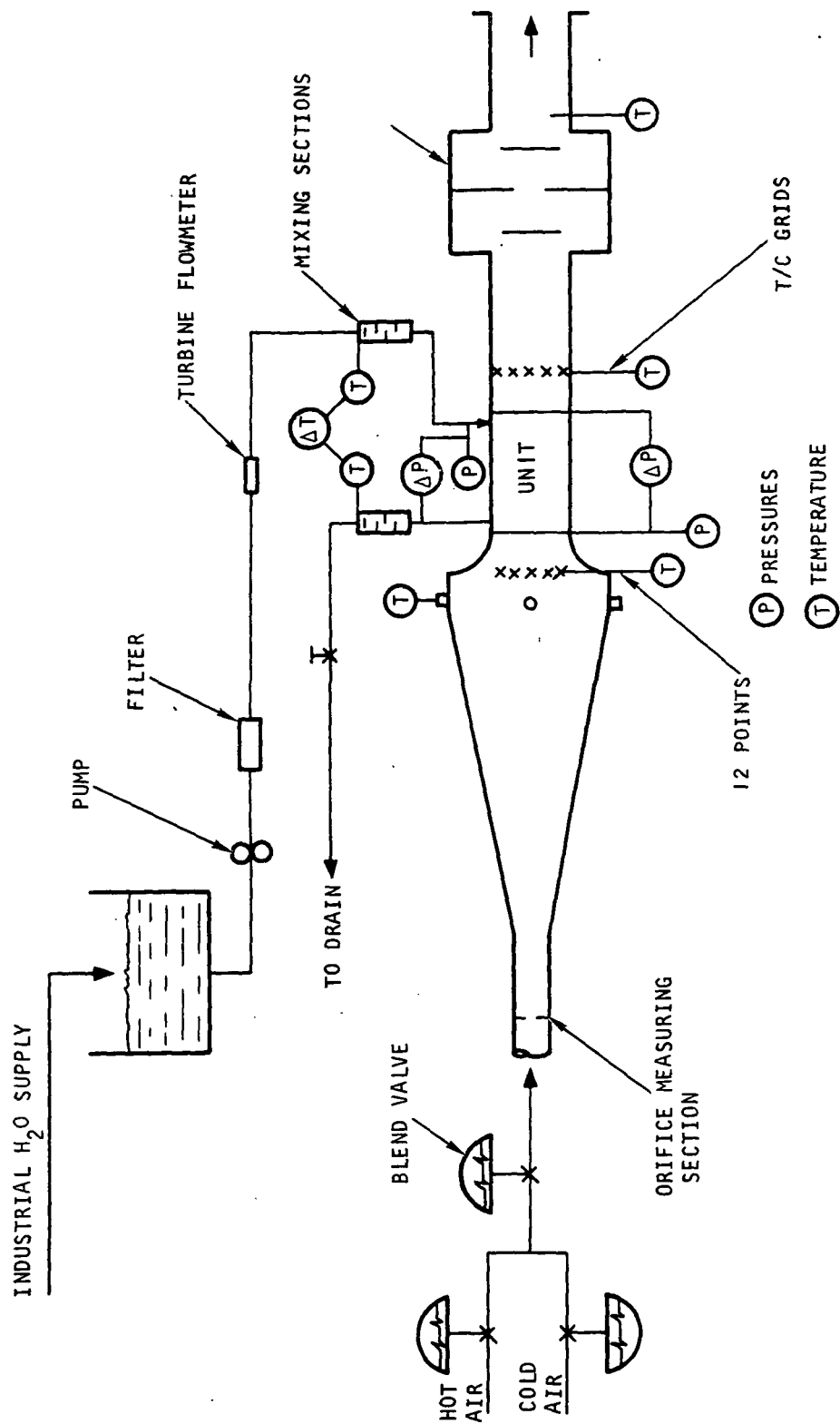


Figure 2-4.--Heat Transfer Test Setup.

S-74782

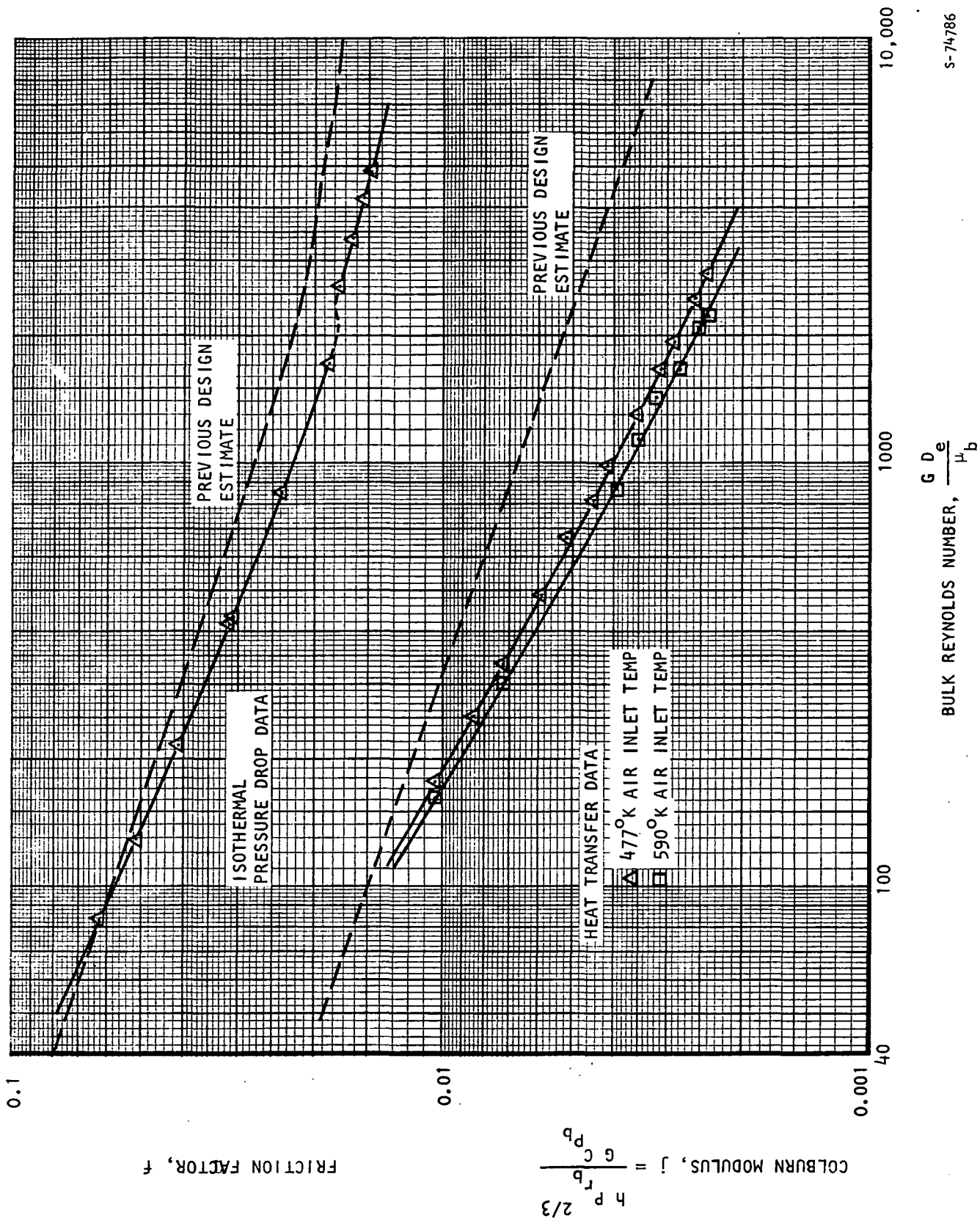


Figure 2-5.--Finned Tubular Core Test Results Using Gas Properties at Bulk Average Temperatures.

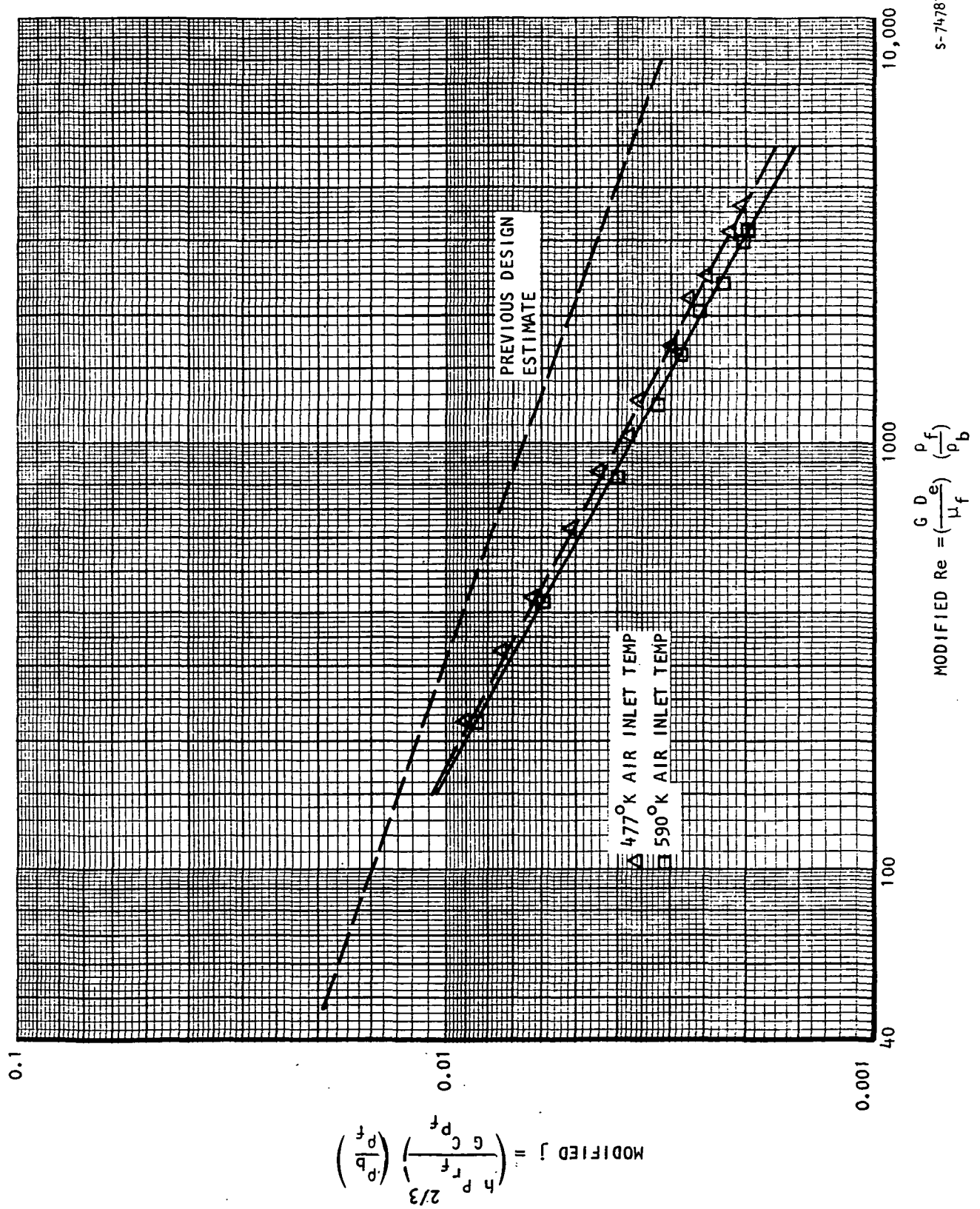


Figure 2-6.--Finned Tubular Core Test Results Using Modified Reynolds Number Correlation.

of fig. 2-6 is most appropriate because it is consistent with AiResearch design procedures. The results for a 477°K (400°F) air inlet temperature are believed to be more accurate because of the lower bulk-to-surface temperature differentials for these runs.

#### CONCLUDING REMARKS

Two factors are believed to be primarily responsible for the difference between measured and predicted performance for this test matrix. The first factor relates to a difference between ideal and as-fabricated fin geometry. During the fabrication process, in which strips of the stainless steel-copper laminate are spirally wound on the tubes, the fin tends to fold over at the outer diameter where the material is being stretched. The result is the formation of cup-shaped fins instead of the ideal flat fins assumed for the performance estimates. The cupping of the fins can be seen in Figure 2-7, a photograph of fin-tube sample. This geometry defect would tend to increase the flow resistance of the test matrix, resulting in an increase in the ratio of friction factor,  $f$ , to Colburn modulus,  $j$ . An increase in  $f/j$  is evident in the curves of Figure 2-5.

The second factor affecting test core performance relates to defects in the tube-fin joints. These defects were discovered after testing by external inspection of the first and last two rows of tubes, and by a borescope examination of the interior (hidden) tube row. It was determined that in these cases, the fin had retracted axially along the tube, leaving an area of bare tube adjacent to an area of bunched fins. Figure 2-8 is a schematic diagram of the two active tube rows, as viewed from the manifold end of the core. The locations of the three defective tubes and the approximate extent of the fin pullback for each case are marked on this diagram. This defect in the heat transfer matrix undoubtedly contributed to the reduction in measured heat transfer performance seen in Figure 2-5.

It is concluded that the measured performance of Figures 2-5 or 2-6 can be used conservatively in future heat exchanger design analysis. Improvements in fabrication procedures to reduce the fin geometry defects discussed above would improve the performance to yield somewhat higher  $j$  and lower  $f/j$  values than were obtained for the test core.

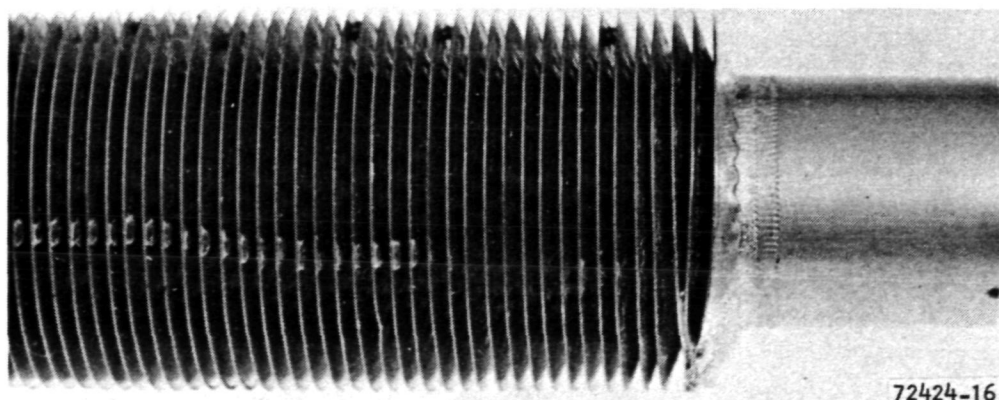


Figure 2-7. Closeup View of Finned Tube Sample

F-25140

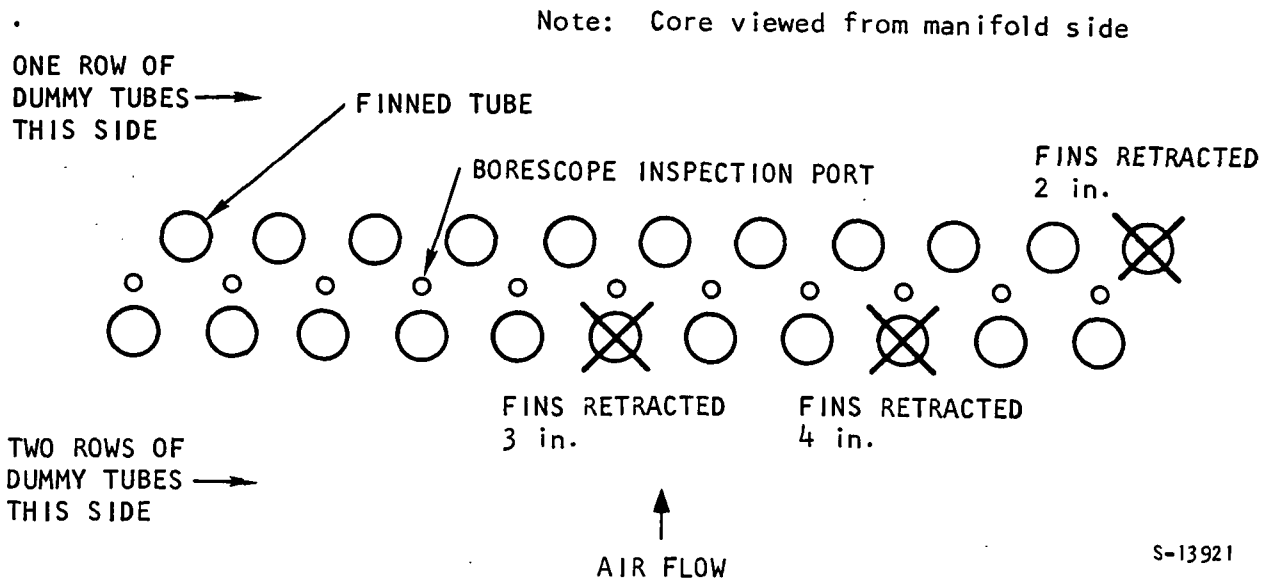


Figure 2-8. Borescope Inspection of Finned Tube Test Core

#### REFERENCES

- 2-1. Kays and London, Compact Heat Exchangers, 2nd edition, McGraw-Hill Book Company, New York, 1964.
- 2-2. Humble, L.V., W.H. Lowdermik, and L.G. Desmon, Measurements of Average Heat Transfer and Friction Coefficients for Subsonic Flow of Air in Smooth Tubes at High Surface and Fluid Temperatures, NACA-TR-1020, December, 1950.
- 2-3. Kays, W.M., Convection Heat and Mass Transfer, McGraw-Hill Book Company, New York, 1966.



### **SECTION 3**

## **MODULARIZED WASTE HEAT EXCHANGER DEVELOPMENT**

## SECTION 3

### MODULARIZED WASTE HEAT EXCHANGER DEVELOPMENT

An investigation was made of methods for providing verified double-braze joint containment of the organic fluid in the waste heat exchanger. The selected double-containment concept is illustrated in figs. 3-1 and 3-2. In this approach, each liquid passage is formed as a separate module. The fluid is contained by a continuous slotted header bar placed around the edge of each liquid module. A small tube is inserted partially through the header bar into the space formed by the slots. This tube is used to pressurize the header bar slot with helium to verify the double braze joint. The core is assembled by stacking these individually leak-checked modules with the gas-side fins and header bars and then brazing the complete assembly at a lower temperature than was used in brazing the liquid modules. This provides a means of verifying at least at one stage of assembly that there is double containment of the organic fluid and that each of the two containment braze joints is leak tight.

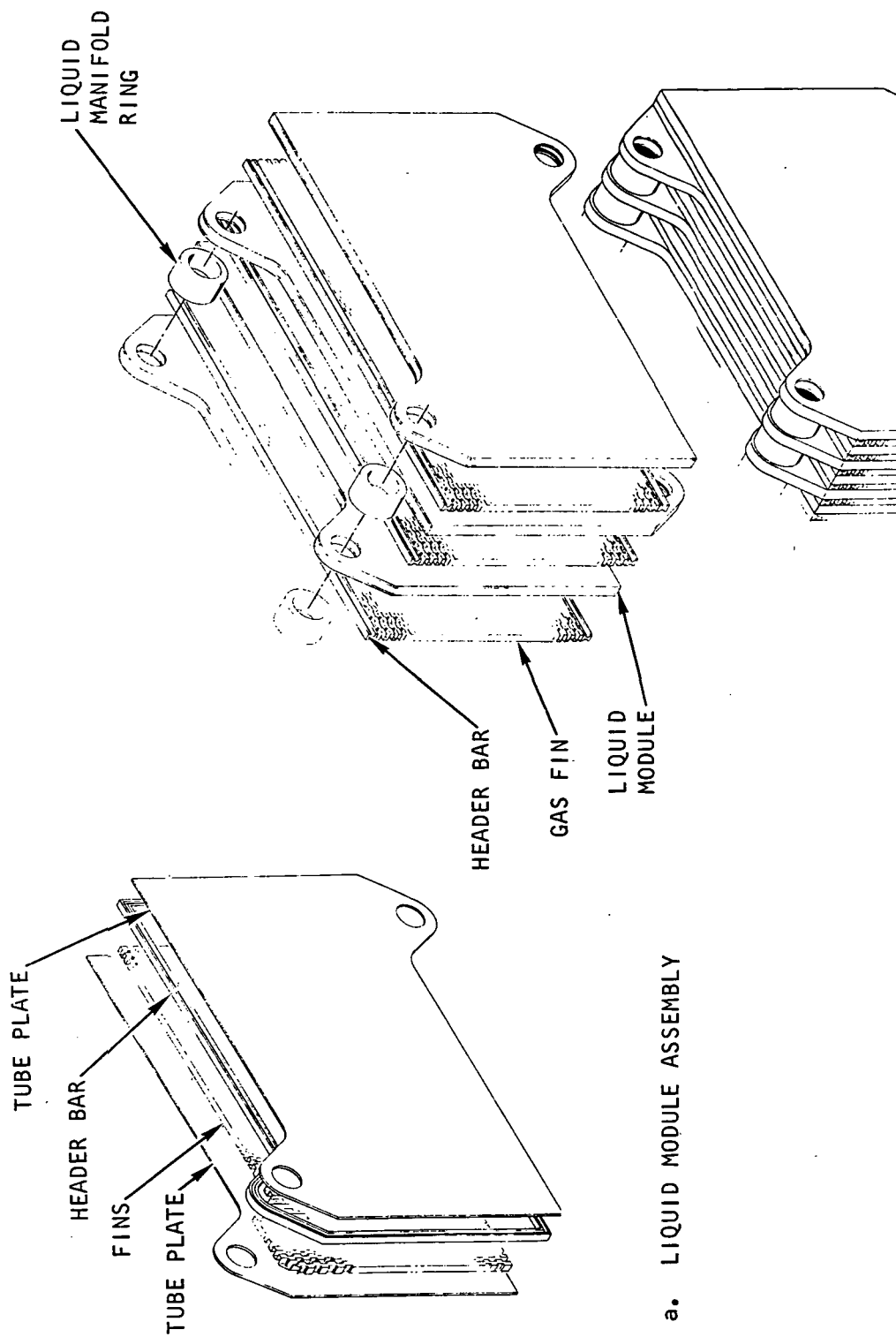
Development work for this task proceeded along two lines: (1) studies to identify the optimum header bar design and method of fabrication, and (2) fabrication and testing of individual liquid modules to develop brazing techniques.

#### HEADER BAR DESIGN

Several double-containment designs were reviewed, including the H, N, W, and K configurations shown in fig. 3-3 and two spaced single-header bars. The H cross-sectional configuration was most attractive from the standpoints of thermal response and fabrication. Thermal stresses generally are less severe when the H cross-sectional configuration is used (because of the inter-connecting conduction path) than when two separate header bars are used.

Two methods for forming the grooved header bars into the desired configuration were tried and discarded. The first method involved upsetting wire into the H cross-sectional configuration and subsequently bending the wire into the desired shape for heat exchanger construction. Attempts to bend the wire with the necessary minimum bend radius were unsuccessful. The process of chemically milling the groove into the header bar was investigated next. Chemical milling efforts proved unsuccessful due to insufficient control during masking of the surface area to be etched and also lack of control of the etching during chemical milling.

It was decided to machine the grooved header bars by profile milling. This process is suitable because of the limited number of header bars required for heat exchanger assembly. Profile milling can provide square corners and/or



S-80410

Figure 3-1.--Typical Single Liquid Module Assembly.

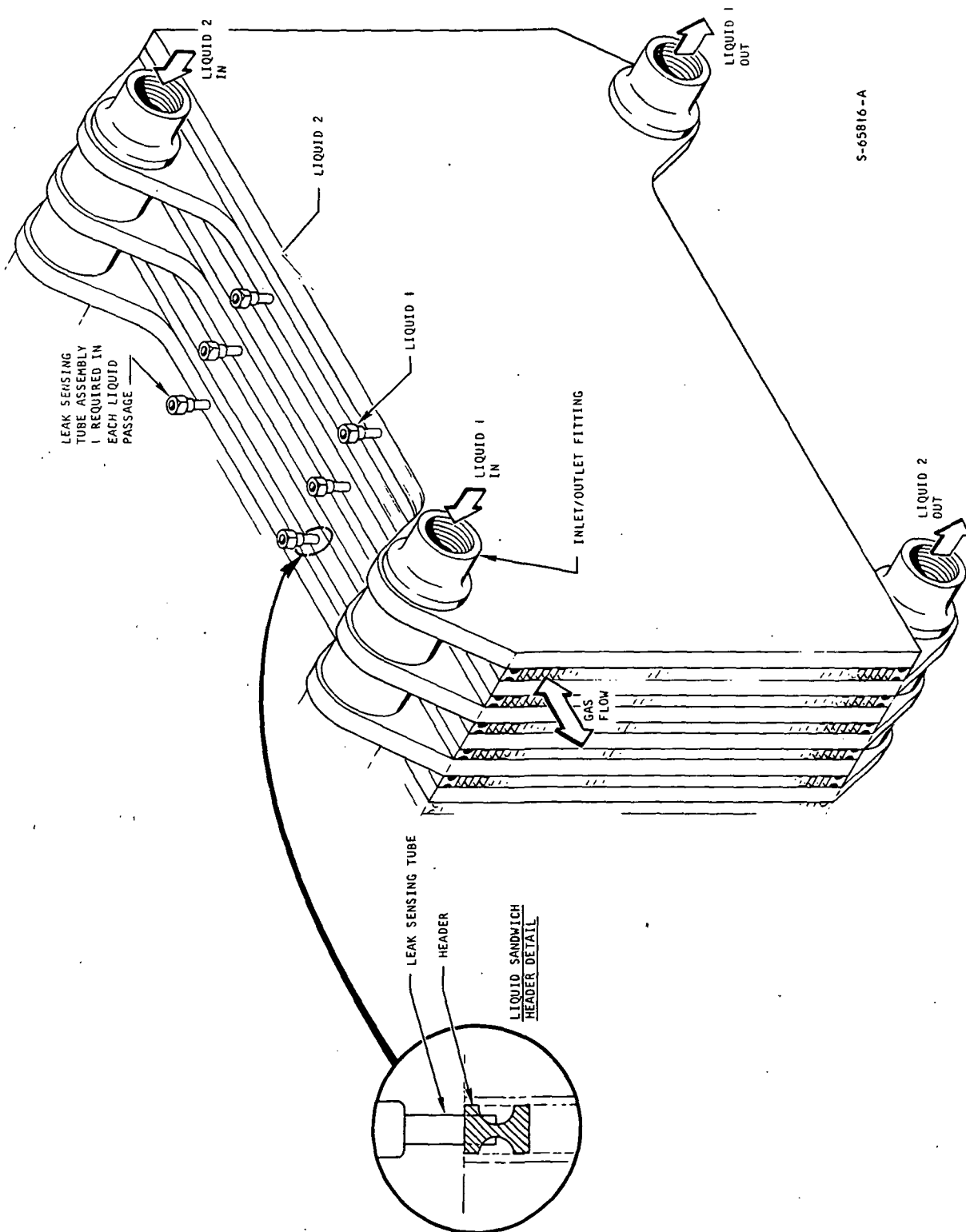


Figure 3-2.---Verification of Double Braze Seal.

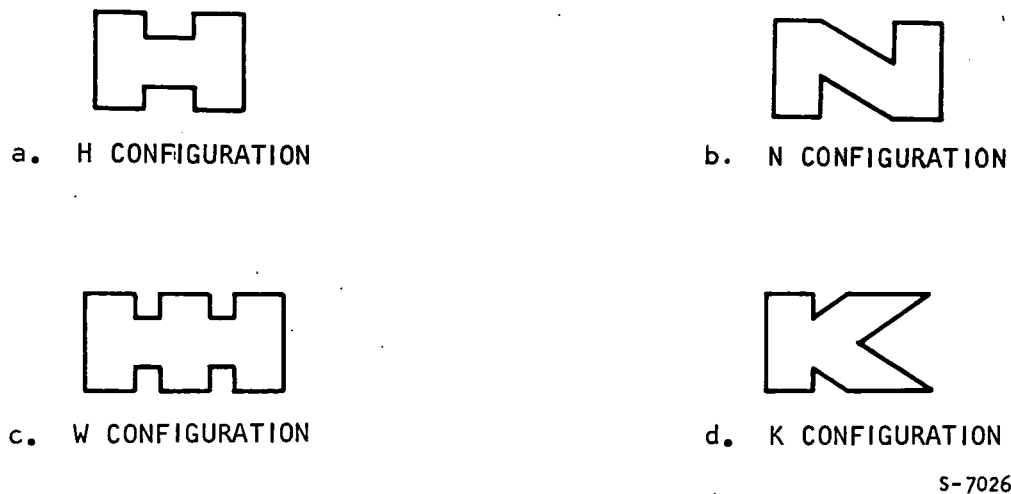


Figure 3-3.--Candidate Header Bar Configurations.

tabs as required for pan attachment to the core assembly. Test samples (6 in. long) of the header bar were machined as shown in fig. 3.4(a). The design later was updated to reflect welding experience on low-cycle fatigue test specimens (see Section 6 of NASA-CR-121011). The original H configuration was changed to incorporate an 0.100-in. land on the outside edge to allow any welding to be performed without weld-braze alloy cracking problems. The revised header bar design is shown in fig. 3-4(b).

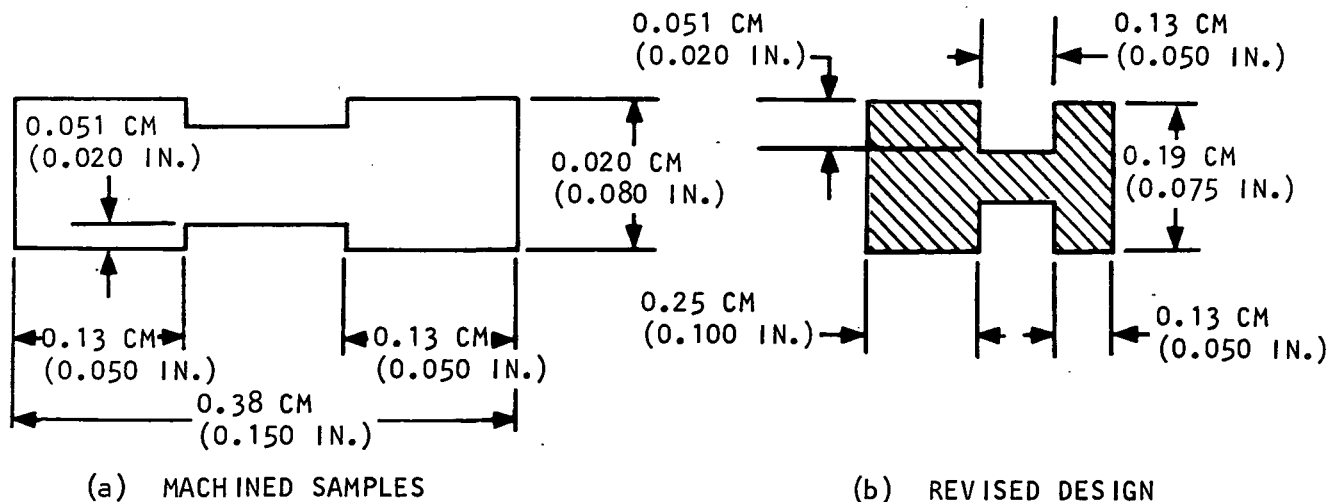


Figure 3-4.--Header Bar Configuration.

## MODULE FABRICATION

A five-sandwich waste heat exchanger test core consisting of three liquid modules and two gas-side fin passages was designed. The overall dimensions were 54.9 by 48.8 by 1.5 cm. The fabrication procedure consists of initially brazing the liquid modules with Palniro 1 (AMS 4784), a gold-base braze material, and then brazing the liquid modules and gas-side fins into an integral test core using Nicuman 23, the alternate braze alloy selected in Task 2F (see Section 6 of NASA-CR-121011). The present task was concerned with developing brazing techniques for the liquid modules.

Because of the large plan area of the test core (approximately 50 by 50 cm), special conformable pressure bags were designed and fabricated for use in brazing the liquid modules. The pressure bags were used to create a uniform pressure load over the face of the module as required for good brazing.

Test panels were assembled and brazed in a hydrogen atmosphere furnace to verify the pressure bag technique. The test panels used nickel fins.

The first test panel was alloyed with 0.005-cm-thick Nicuman 23 braze foil and brazed at 1250°K (1790°F) in the atmosphere furnace. After removal from the double pressure bag assembly (see fig. 3-5), visual inspection of the heat panel revealed that the graphite plates placed between the inner and outer bags to maintain flatness in the brazed assembly were cracked in several places, allowing the panel assembly to distort. The test panel flatness results were, therefore, inconclusive. The graphite plates had fractured because a defect in the inner pressure bag design allowed the inner bag skin to have wrinkles in the surface. These wrinkles caused high stress areas on the graphite plates during the brazing cycle, which resulted in the graphite plates fracturing.

Visual inspection of the part revealed that neither the plate fin area nor the Nicuman 23 brazing alloy was contaminated, indicating that the hydrogen gas had purged the entire 50- by 50-cm panel assembly. The Nicuman 23 braze alloy had started to melt in some areas but, in general, the brazing foil had not melted, indicating that the panel assembly did not reach the proper temperature.

A second pressure bag assembly was fabricated, and a new test panel (fig. 3-6) was assembled inside the inner bag for hydrogen atmosphere brazing. An additional thermocouple was attached to the test panel to monitor the panel temperature as well as the temperature of the outer bag during brazing. The test panel was assembled in the inner bag, which in turn was placed between the two 1-in. graphite plates. The graphite plates-inner bag assembly was sealed in the outer bag (fig. 3-5). The assembly was brazed in an atmosphere furnace at 1250°K (1790°F) with hydrogen purging the inner bag.

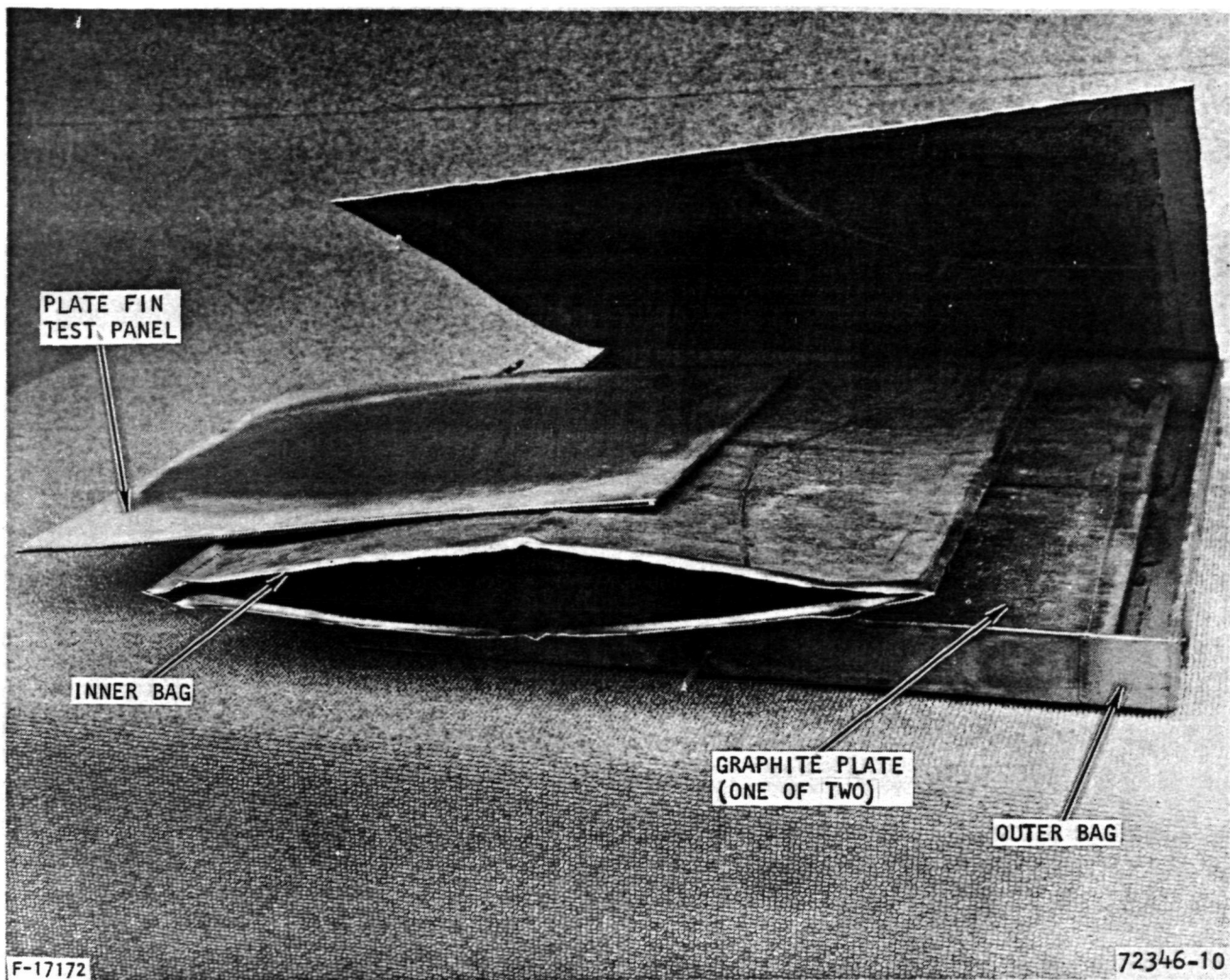
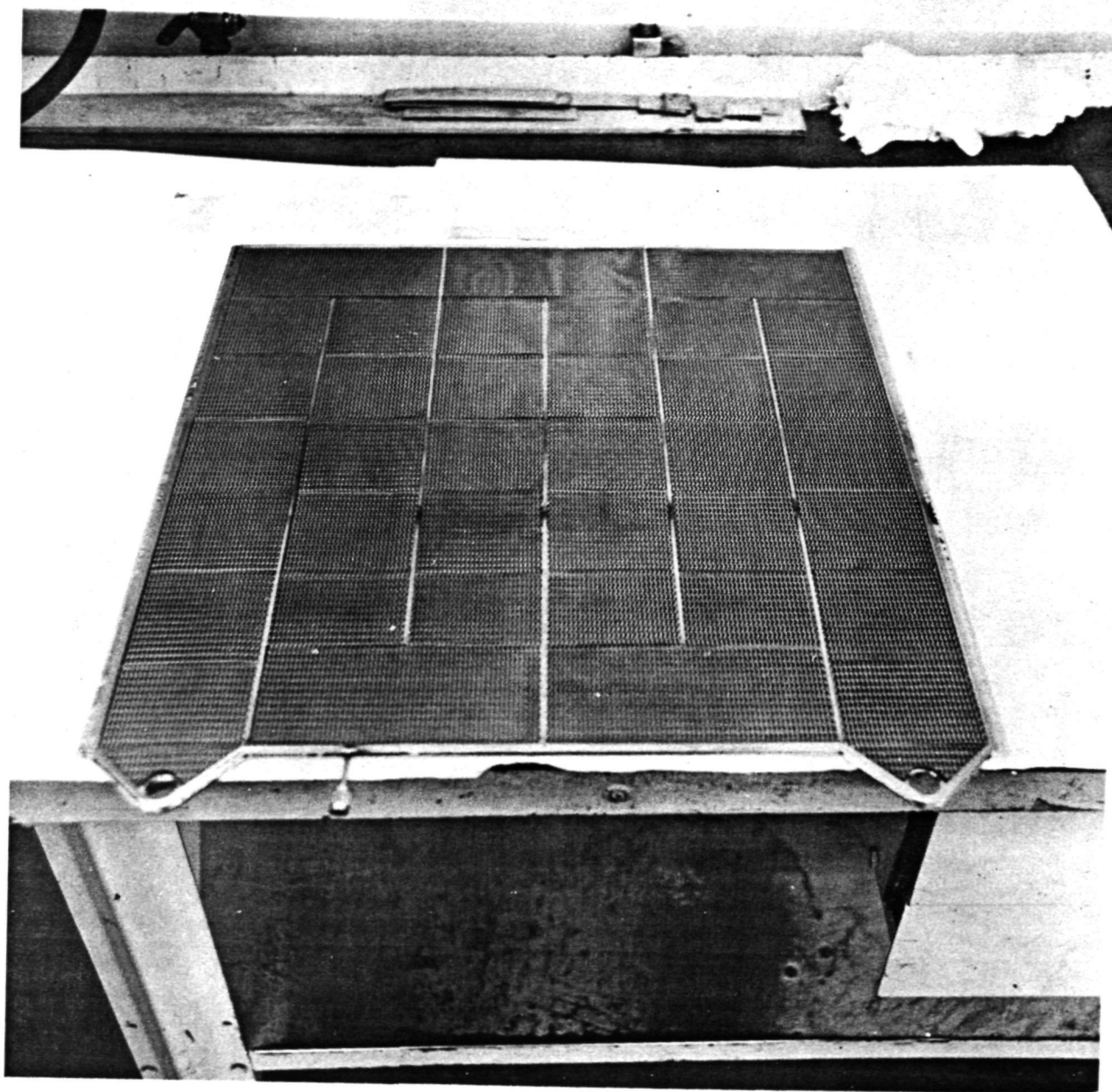


Figure 3-5.--Pressure Bag/Test Panel Assembly for Atmosphere Furnace Brazing.



14379

Figure 3-6.--Modularized Waste Heat Exchanger Double Containment Test Panel.



After brazing, examination of the second pressure bag assembly showed that the sides of the pressure bag were deflected inward and bearing on the inner bag containing the test panel. The pressure bag was redesigned using Inconel 600 material for the sides. Also, rods were installed to support the sides of the pressure bag at the midspans. A pressure tap was located in the side plate to measure the pressure within the pressure bag instead of in the vacuum line as was done on the first and second pressure bag assemblies.

The second test panel was evaluated for flatness and quality of brazing (Nicuman 23, 0.005 cm (.002-in.)-thick foil). The brazed panel assembly was 0.20 cm (0.080 in.) out of flat at the center of the panel. This convex shape was due to the sides of the pressure bag bearing on the test panel during the brazing cycle. The brazing of the fins to the tube sheets was satisfactory, verifying that the atmosphere within the test panel was adequate for brazing.

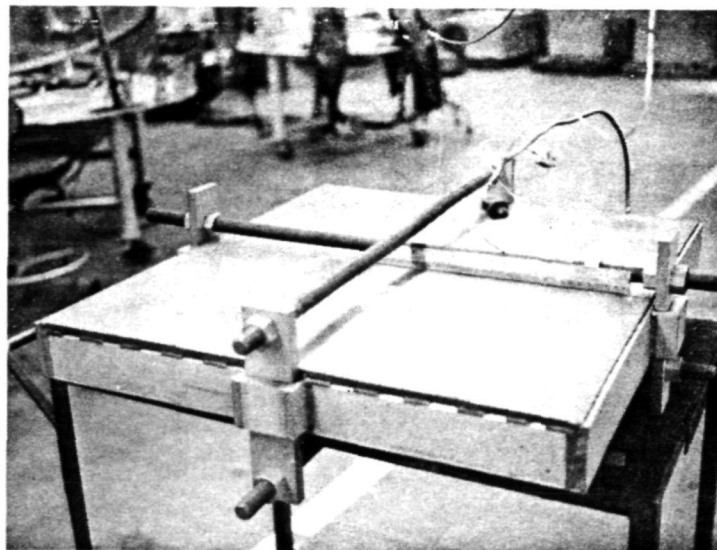
The first liquid sandwich with the Palniro 1 brazing foil was brazed next using the pressure bag brazing technique. The redesign of the pressure bag proved to be successful; however, bosses on the panel interfered with the graphite fixturing during the cooling portion of the brazing cycle and caused some curvature in the panel. The second liquid module with the Palniro 1 brazing foil was brazed without the inlet and outlet bosses on the panel (see fig. 3-7) to prevent the fixture/boss interference and maintain the high degree of flatness required for subsequent step brazing.

The second liquid sandwich module was evaluated after brazing. The panel brazing quality was good, with the helium leakage from the double containment header bar less than  $1 \times 10^{-8}$  scc/sec at one atmosphere pressure. This low leakage demonstrated double containment. The panel room temperature burst test was terminated at  $18.9 \times 10^3$  kN/m<sup>2</sup> gauge pressure without incurring a braze joint separation.

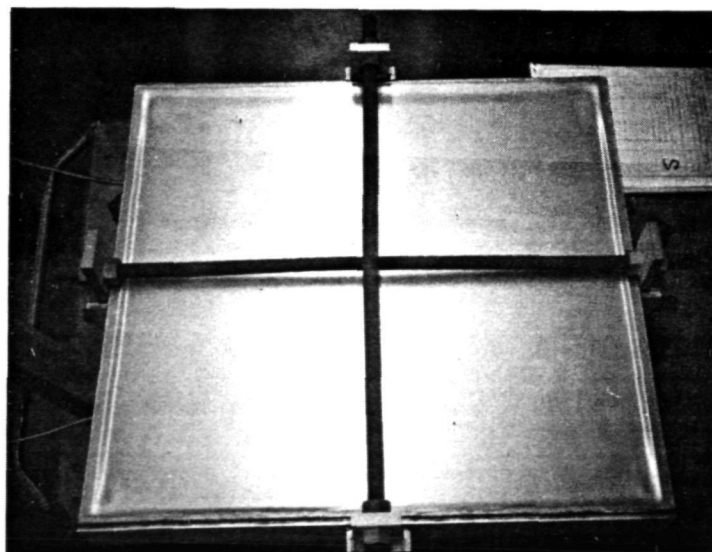
The plate-fin sandwich was sectioned, and a metallographic evaluation of the brazed joints was performed. Metallographic sections were taken from the double containment header bar, the reinforcing bar inside the panel, and a typical tube sheet-to-fin brazing joint. These photomicrographs are shown in figs. 3-8 and 3-9. As indicated by the metallographic examination, the brazing of the plate-fin sandwich was successful. The examination confirms the burst test and helium leakage test results.

#### CONCLUDING REMARKS

Brazing development tests indicate that large flat panels, about 50 by 50 cm, may be successfully brazed. The selected braze fixturing and technique will: (1) produce a panel that is sufficiently flat to permit assembly of the overall heat exchanger in a subsequent brazing operation, (2) prevent contamination by using the hydrogen brazing atmosphere and purging technique, and (3) produce uniform loading essential to obtaining complete braze joint integrity by use of the pressurized bag. Helium leak checks performed on the brazed panel confirm that it is possible to verify double containment at the header bar braze joints.



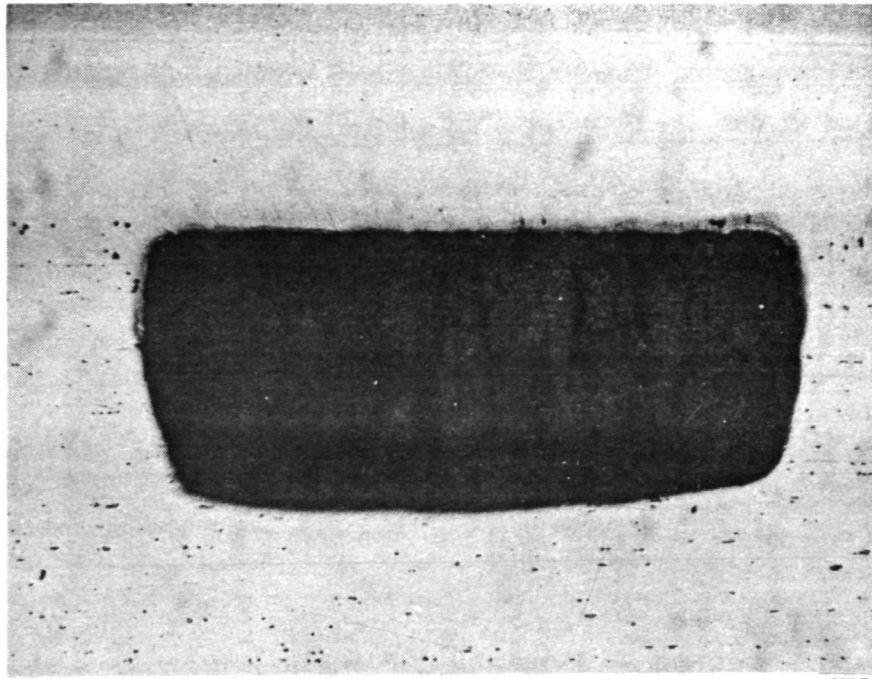
OVERALL VIEW



TOP VIEW SHOWING SKIN DEFORMATION

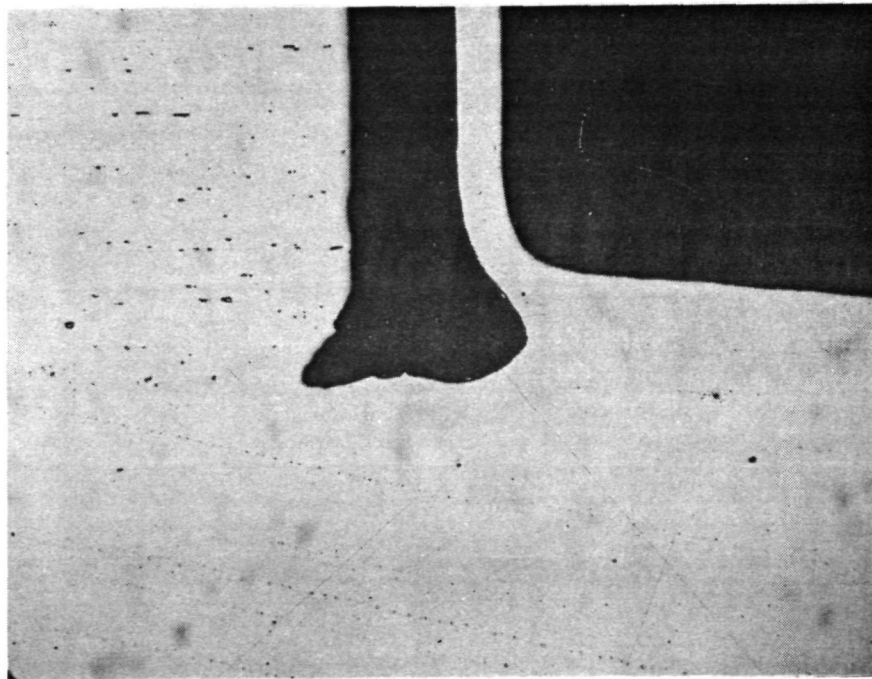
Figure 3-7.--Liquid Sandwich Module  
Pressure Bag Brazing Fixture.

F-18289



X75

a. CHANNEL BRAZING SHOWING DOUBLE CONTAINMENT BRAZING JOINTS

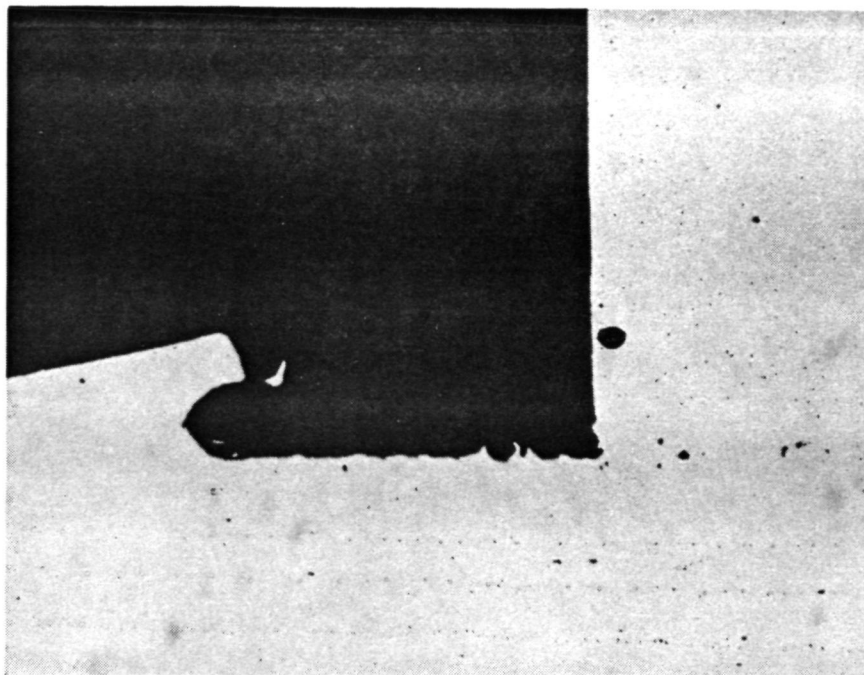


X75

b. DOUBLE CONTAINMENT HEADER BAR-TO-TUBE SHEET BRAZING JOINT

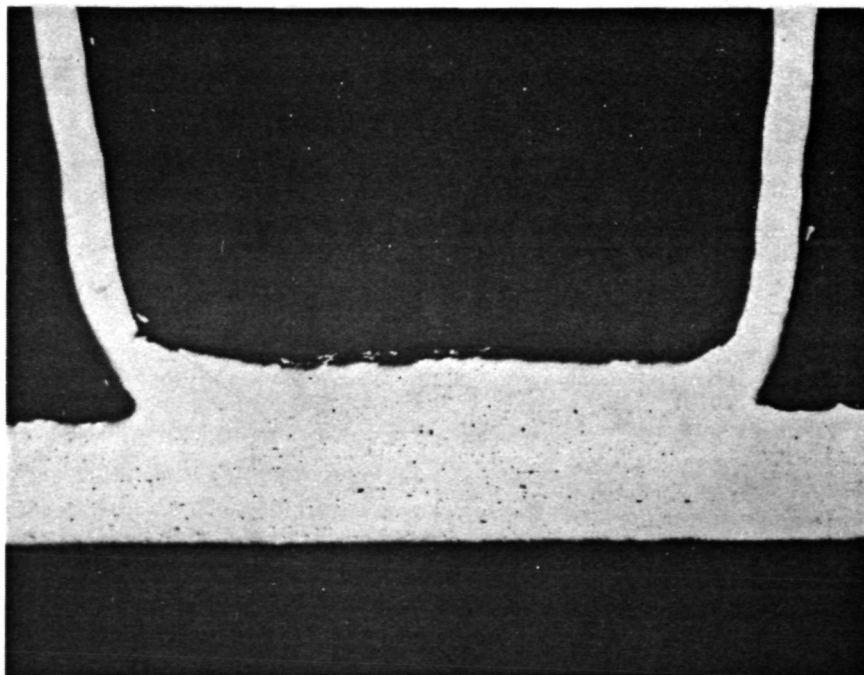
F-18428

Figure 3-8.--Double Containment Header Bar Brazing (Micro 28002).



X75

a. REINFORCING BAR-TO-TUBE SHEET BRAZING JOINT



X75

b. FIN-TO-TUBE SHEET BRAZING JOINT

F-18427

Figure 3-9.--Panel Internal Brazing Joints (Micro 28002).

**SECTION 4**  
**RECUPERATOR SUBMODULES**

## SECTION 4

### RECUPERATOR SUBMODULES

The objective of this task was to design, fabricate, and performance- and cycle-test recuperator submodules. These submodules are compact, plate-fin heat exchangers designed for operation in a closed Brayton-cycle power system. They are representative of full-scale units in terms of thermal and structural performance capabilities and construction techniques. Requirements included operation for a total of 100 000 hr at a maximum gas temperature of 995°K (1331°F) with 1000 startup and shutdown cycles and without performance deterioration or leakage of the cycle working fluid. To meet these stringent requirements with a high degree of confidence, several unique features were incorporated in the submodule designs.

Two one-quarter-size submodules were fabricated and tested. These units incorporate a counterflow section that is one-half the flow length and one-half the stack height of the full-size submodules.

Testing of the first one-quarter-size submodule included both performance testing to verify the thermal design and thermal cycle testing to establish the cyclic life of the unit. Testing of the second submodule involved only the thermal cycle tests. The primary purpose of these tests was to verify the unique structural design concepts that were incorporated to meet the specified life and leakage requirements. Verification testing was accomplished by subjecting the submodules to repeated thermal cycles at conditions calculated to cause failure in less than 1000 cycles. Survival time under the off-limit conditions of the tests was used to establish the required cyclic life under normal operating conditions.

### THERMAL DESIGN AND ANALYSIS

#### Preliminary Design

Initial Design Conditions.--The recuperator submodule was designed to meet the design conditions presented in table 4-1. Based on the levels of temperature and pressure shown in this table, which were assumed to define the structural as well as thermodynamic requirements for the recuperator, it was determined that a 0.010-cm (0.004-in.) fin thickness of Hastelloy X in conjunction with fin densities of 7.87 fins/cm (20 fins/in.) on the high-pressure side and 6.30 fins/cm (16 fins/in.) on the low-pressure side would provide the required cyclic and operating life.

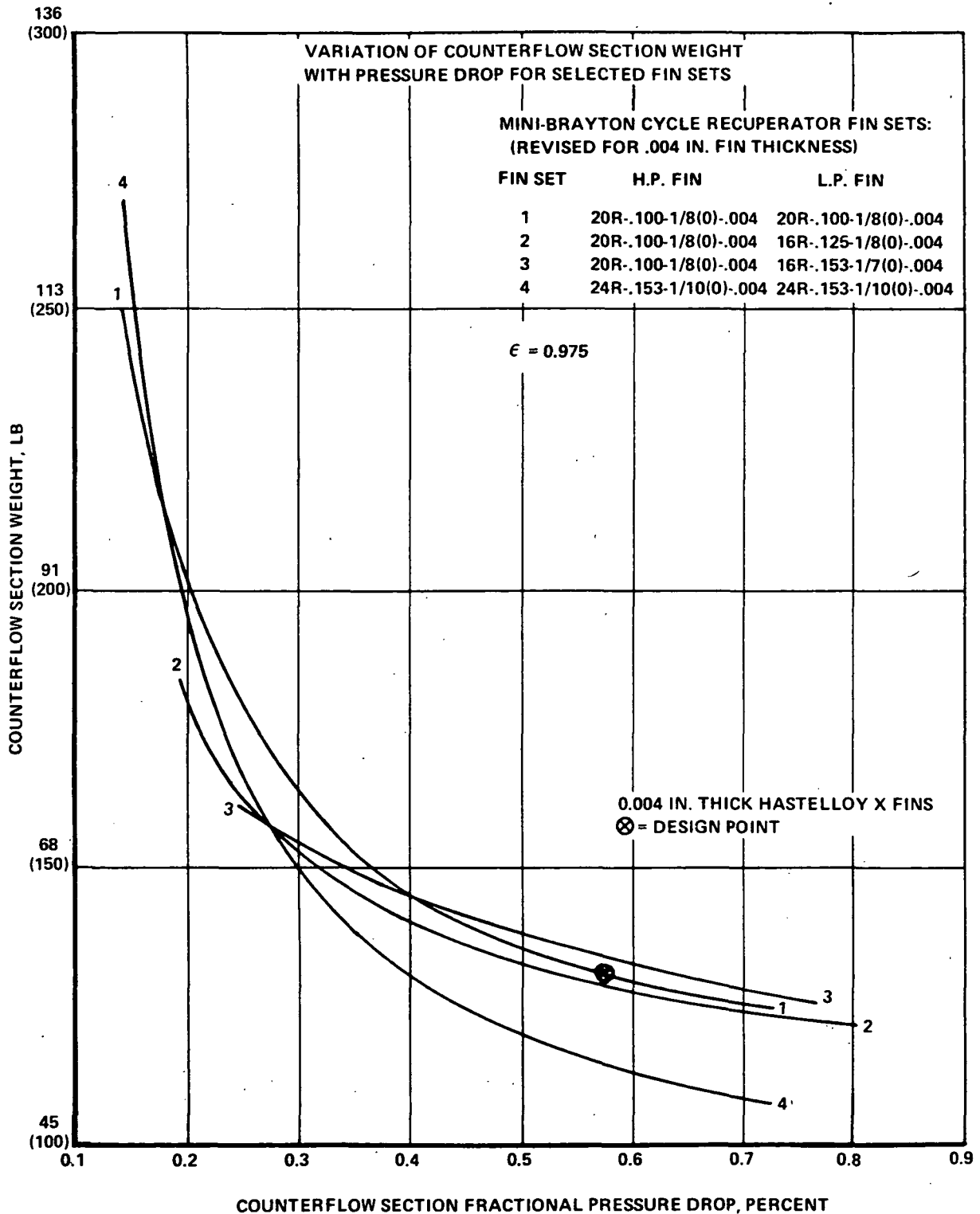
Preliminary structural analysis also indicated a required tube plate thickness of 0.015 cm (0.006 in.) for interior passages and 0.020 cm (0.008 in.) for passages located near the sides. Using these material thicknesses, parametric curves of counterflow section weight as a function of pressure drop were generated for a large number of high- and low-pressure fin geometry combinations. Weight curves for several of these combinations are shown in fig. 4-1 and the corresponding fin geometries are specified in table 4-2.

TABLE 4-1  
RECUPERATOR SUBMODULE DESIGN CONDITIONS  
(Initial problem statement.)

Working fluid	Xenon-Helium
Molecular weight	83.8
Mass flow rate	0.175 kg/sec (0.386 lb/sec)
Effectiveness	0.975
Total pressure loss ratio, P/P	0.00707
Hot-side inlet temperature	1010°K (1818°R)
Hot-side inlet pressure	533 kN/m <sup>2</sup> (77.3 psia)
Cold-side inlet temperature	378°K (679°R)
Cold-side inlet pressure	785 kN/m <sup>2</sup> (114.4 psia)
Operating life	10 yr
Cyclic life	1000 cycles

TABLE 4-2  
FIN GEOMETRIES

Fin Set	High-Pressure Side		Low-Pressure Side	
	Fin Ht, cm (in.)	Fins/cm (in.)	Fin Ht cm (in.)	Fins/cm (in.)
1	0.254 (0.100)	7.87 (20)	0.254 (0.100)	7.87 (20)
2	0.254 (0.100)	7.87 (20)	0.318 (0.125)	6.30 (16)
3	0.254 (0.100)	7.87 (20)	0.389 (0.153)	6.30 (16)
4	0.389 (0.153)	9.45 (24)	0.389 (0.153)	9.45 (24)



S-75663

Figure 4-1.--Variation of Counterflow Section Weight  
with Pressure Drop for Selected Fin Sets.



Based on fig. 4-1, fin set number 1, which consists of 7.87 rectangular fins/cm (20 rectangular fins/in.) at a plate spacing of 0.254 cm (0.100 in.) on both high- and low-pressure sides, was selected for the recuperator design. Fin set 1 was preferred over fin set 2 because it yields a core approximately 15 cm (6 in.) shorter for the same fractional pressure drop with a mass difference of only 1 kg (2 lb). It can be seen from fig. 4-1 that a higher fin density, such as 9.45 fins/cm (24 fins/in.) would produce a lighter recuperator design, but fabrication of Hastelloy X fins at densities greater than 7.87 fins/cm (20 fins/in.) cannot be achieved with existing tooling and may be impractical even with development due to difficulties inherent in forming the Hastelloy material. It may be noted in this respect that higher fin densities than 7.87 fins/cm (20 fins/in.) can be fabricated at reduced fin heights, but the larger number of tube plates required in a recuperator design utilizing lower fin heights represents a weight penalty that negates the advantage of higher fin density.

Based on the use of fin set 1, a counterflow section pressure drop of 0.58 percent was selected and end sections were designed. The overall recuperator design is shown in fig. 4-2. Total weight of this design is 63 kg (138 lb), including counterflow and end sections, but not including manifolds.

To obtain a tradeoff between weight and performance, recuperator designs also were generated for reduced recuperator effectivenesses. The resultant curve of weight versus effectiveness is shown in fig. 4-3. By reducing effectiveness from 0.975 to 0.965, a weight reduction of 21 kg (47 lb), or 38 percent of total recuperator mass, is achieved. A further reduction in effectiveness to 0.95 yields a total recuperator core weight of 27 kg (60 lb).

Final Design Conditions.--Based on the preliminary data presented above, a new design point condition for the recuperator submodules was established by NASA. The revised design point is shown below:

Effectiveness	0.975
Working fluid	Xe-He (molecular weight = 83.8)
Hot side (low pressure)	
Flow rate	0.162 kg/sec (0.357 lb/sec)
Inlet temperature	996°K (1792°R)
Inlet pressure	494 kN/m <sup>2</sup> abs (71.7 psia)
Cold side (high pressure)	
Flow rate	0.159 kg/sec (0.350 lb/sec)
Inlet temperature	380°K (685°R)
Inlet pressure	732 kN/m <sup>2</sup> abs (106.2 psia)
Pressure drop ratio	
$\Delta P/P$ total both sides	0.0070

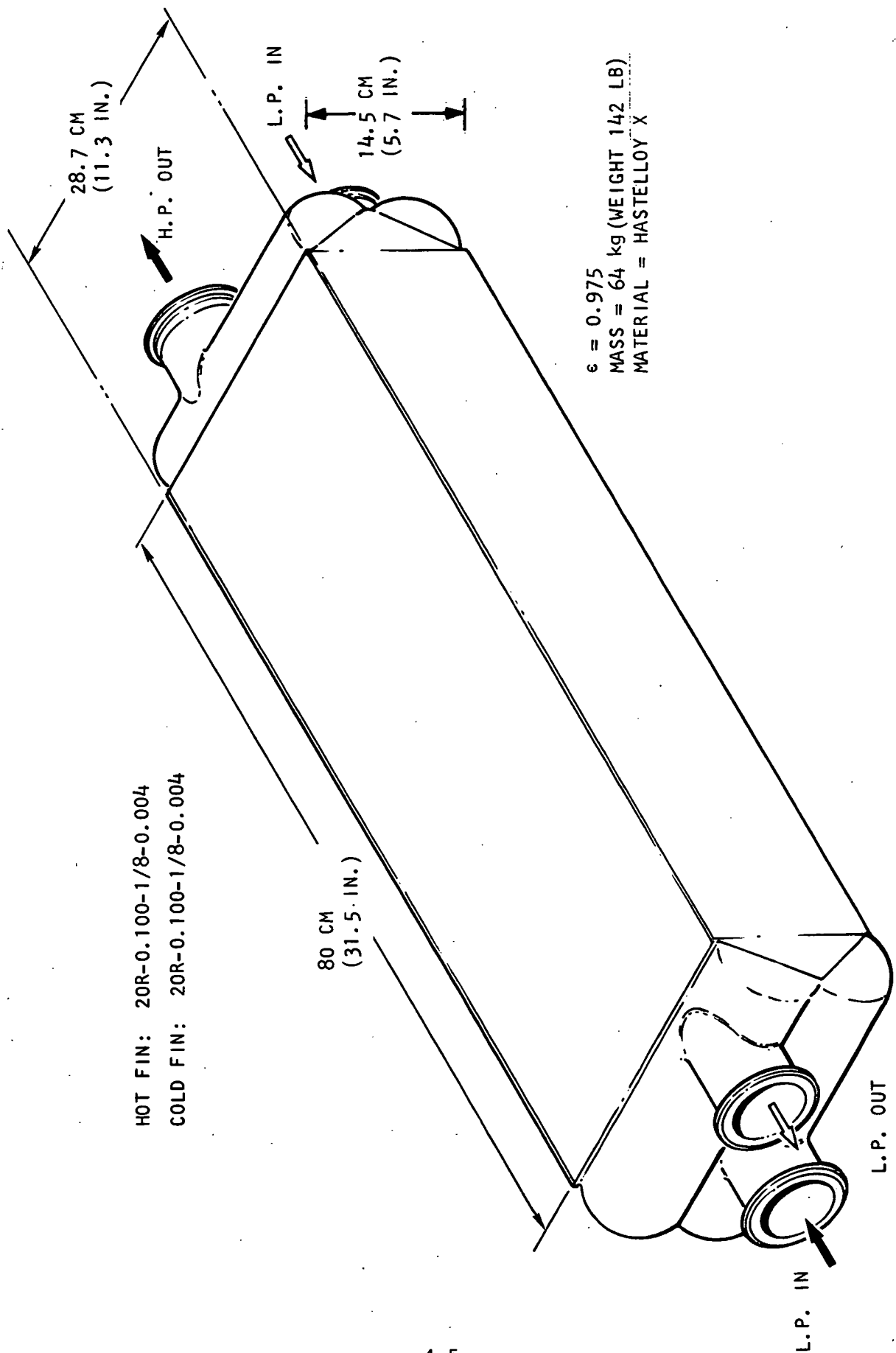
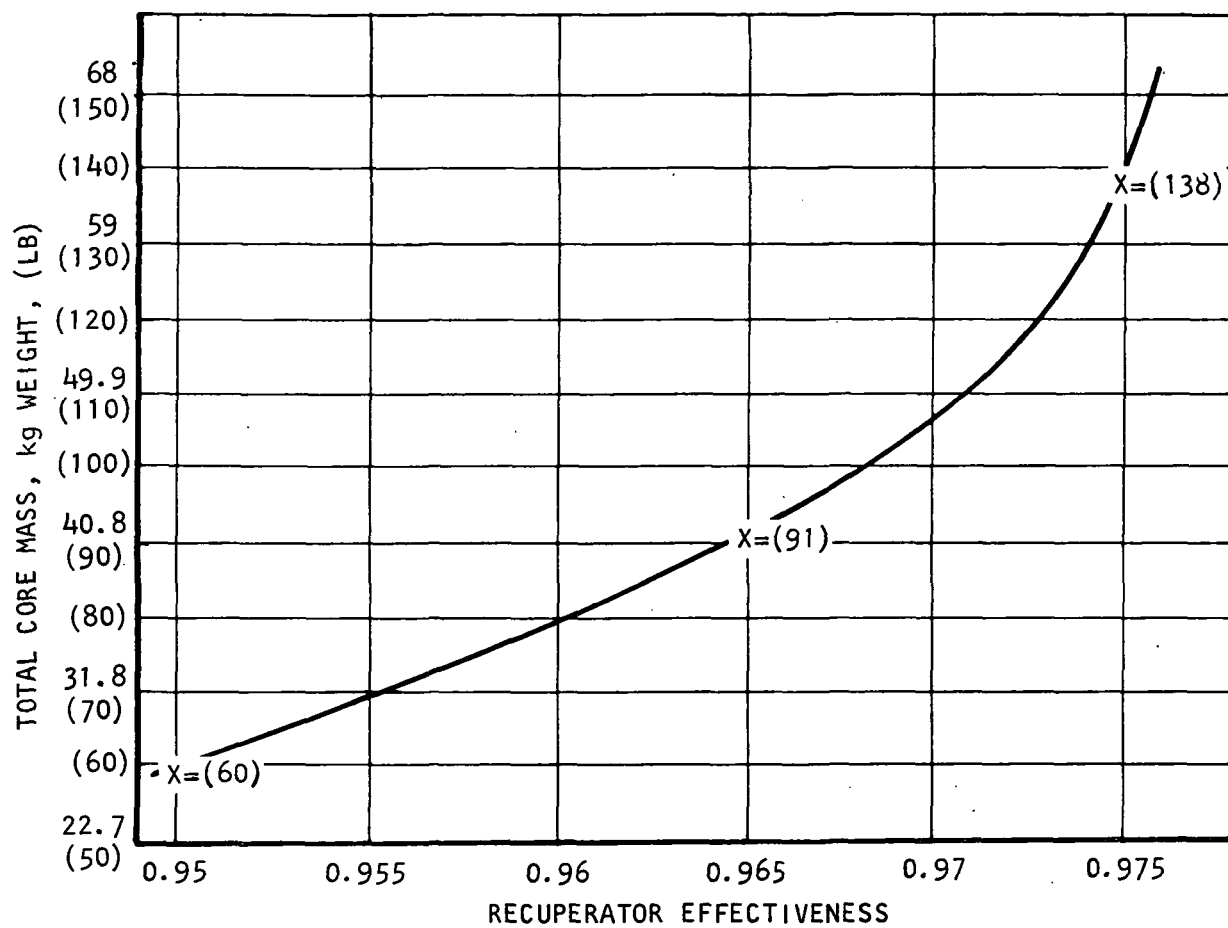


Figure 4-2.--Recuperator Submodule.



S-75662-A

Figure 4-3.--Recuperator Mass vs Effectiveness.

The startup transient used for preliminary design is presented in figs. 4-4 and 4-5. These figures give the gas flow and gas temperatures as a function of time for a typical Brayton system startup transient.

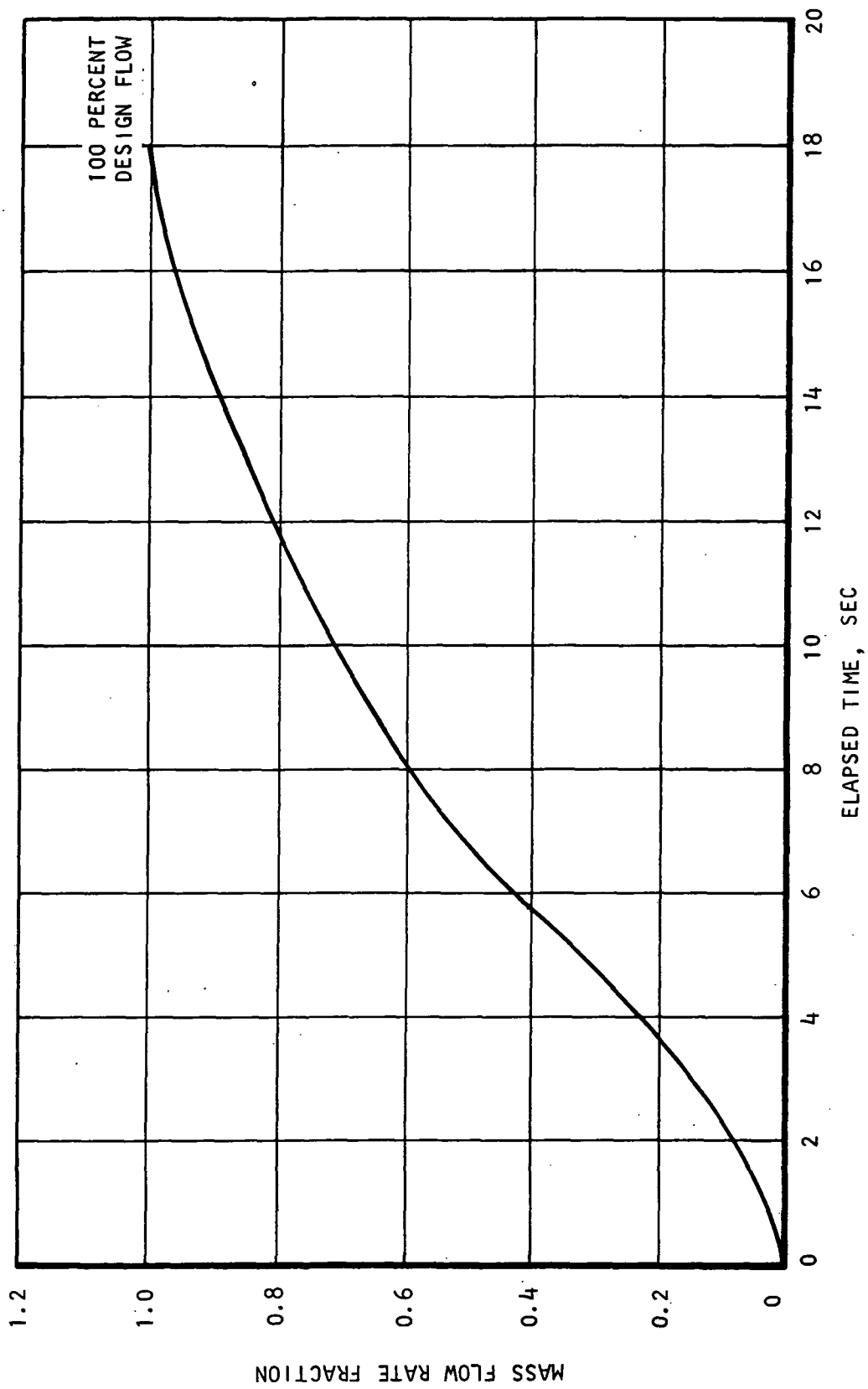
The recuperator submodules were designed using the above design requirements. Based on previous work, the best (i.e., minimum weight) fin sets for the recuperator submodules were found to be fin sets 1 and 2, which are:

<u>Fin Set</u>	<u>Cold Fin</u>	<u>Hot Fin</u>
1	7.87 fins/cm (20 fins/in.)	7.87 fin/cm (20 fins/in.)
	0.254 cm (0.100 in.) high,	0.254 cm (0.100 in.) high
	0.32 cm (1/8 in.) offset length	0.32 cm (1/8 in.) offset length
	0.010 cm (0.004 in.) thick	0.010 cm (0.004 in.) thick
2	7.87 fins/cm (20 fins/in.)	6.3 fins/cm (16 fins/in.)
	0.254 cm (0.100 in.) high	0.318 cm (0.125 in.) high
	0.32 cm (1/8 in.) offset length	0.32 cm (1/8 in.) offset length
	0.010 cm (0.004 in.) thick	0.010 cm (0.004 in.) thick

The variation in recuperator weight as a function of  $(\Delta P/P)_{\text{total}}$  is shown in fig. 4-6 for both fin sets 1 and 2. In the range of total pressure drops between 0.40 and 0.80 percent, there is little weight difference between the two fin sets, fin set 1 being the lightest. The core design selected was fin set 1 at a core  $(\Delta P/P)_{\text{total}} = 0.461$  percent. This allows a  $\Delta P/P = 0.239$  percent for the two end sections and entrance and exit manifold losses. The core dimensions are shown in fig. 4-7. The mass of the counterflow section of the core is 40 kg (88.5 lb). The addition of end sections and manifolds will bring the total mass up to approximately 45 kg (100 lb).

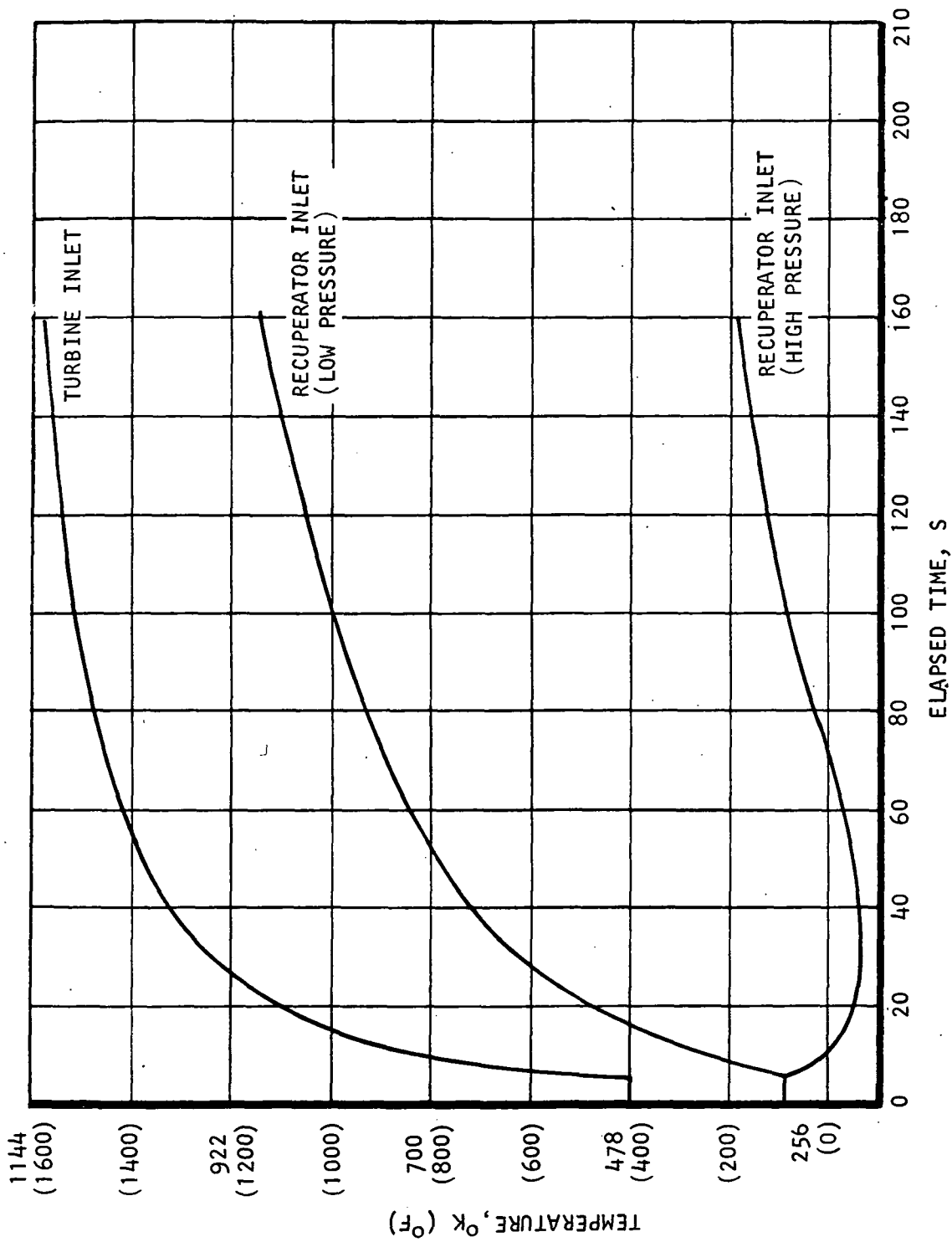
Triangular end sections were designed using plain fins of 6.3 fins/cm (16 fins/in.). The 5.08-cm (2.0 in.) rectangular end sections lead to a slight pressure drop imbalance that is still within acceptable limits. A summary of the pressure drops for the recuperator is shown in fig. 4-8.

The manifolds for the recuperator were designed to yield a uniform flow distribution. The criteria for uniform flow distribution is shown in fig. 4-9. Applying these criteria, the low-pressure inlet and outlet areas are approximately equal and were taken at 43.6 cm (6.76 in.), while the high-pressure outlet manifold is required to be 2.27 times the area of the high-pressure inlet manifold. These relationships and the estimated manifold pressure drops are given in table 4-3.



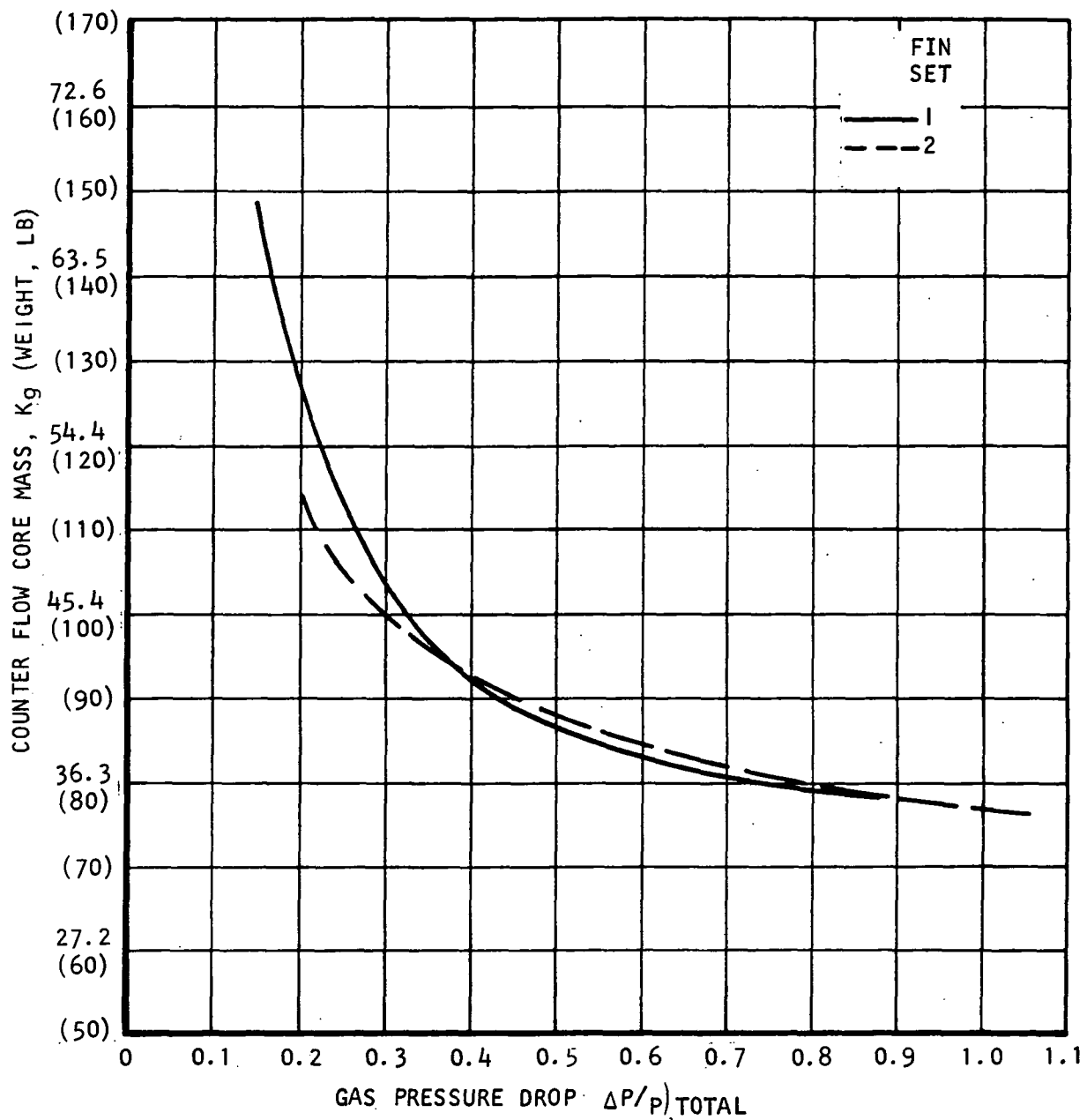
S-77090-A

Figure 4-4.--Startup Flow Transient.



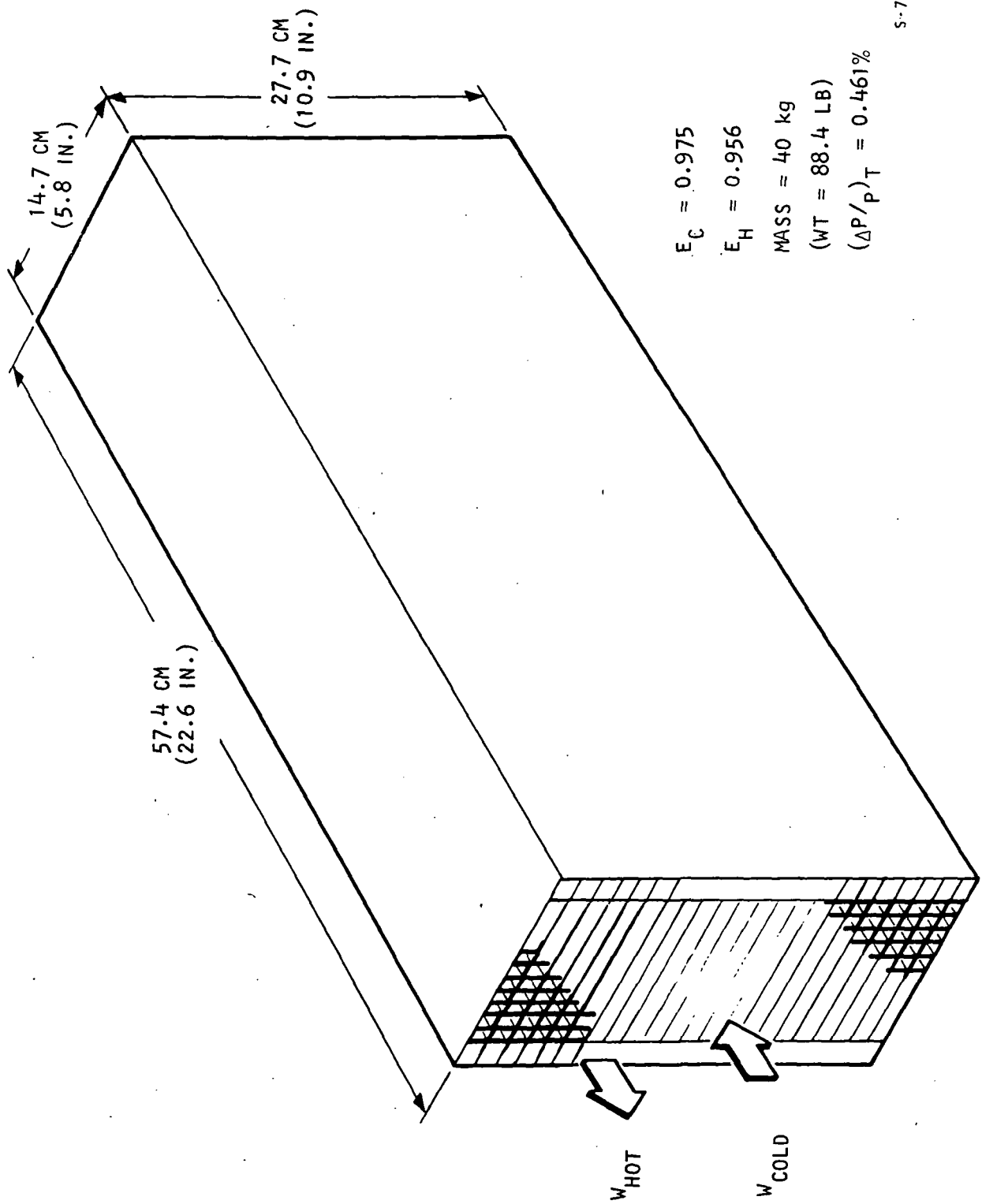
S-77086-A

Figure 4-5.---Startup Temperature Transient.



S-77088 -A

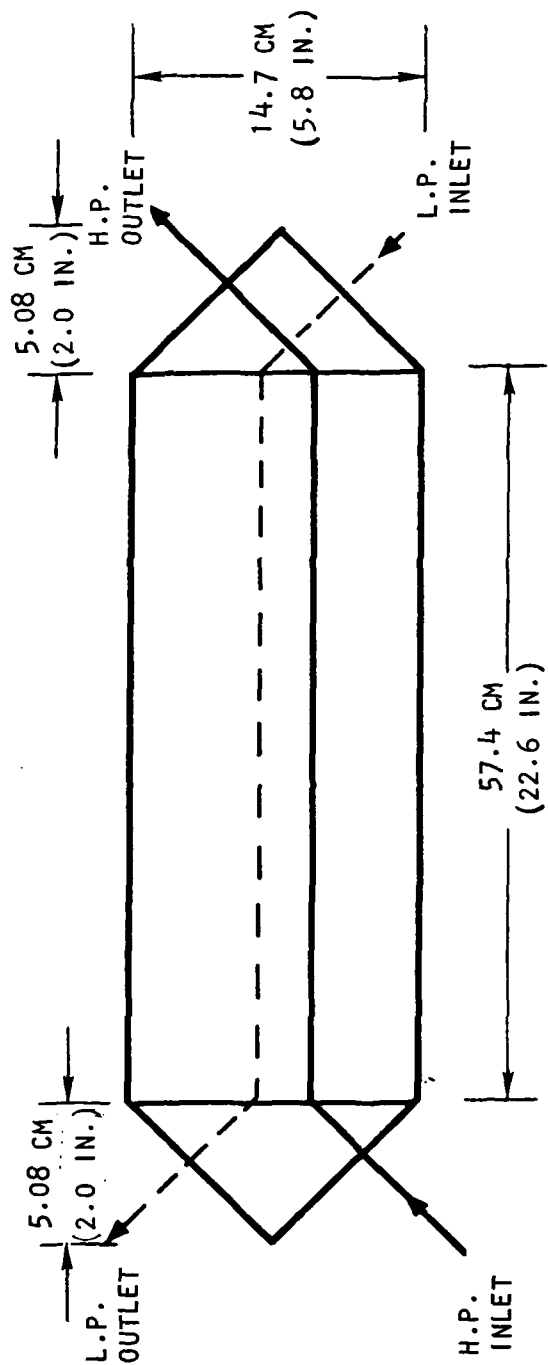
Figure 4-6.--Recuperator Module Pressure Drops Versus Mass.



S-7291

Figure 4-7.--Selected Recuperator Counterflow Section.



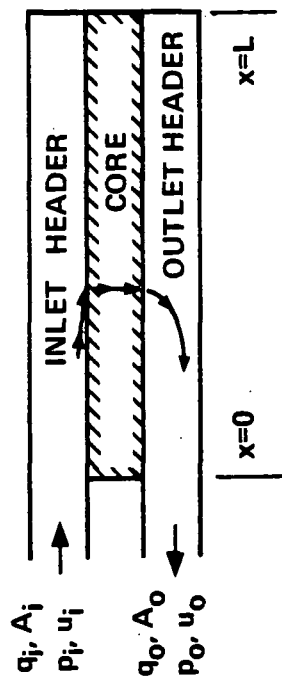


LOW PRES- SURE (HOT)	PRESSURE DROP (%)			END SECTION Δ P IMBALANCE
	END SECTIONS*	CORE	TOTAL	
INLET OUTLET	0.0181 0.0041	0.323	0.364	4.05%
HIGH PRES- SURE (COLD)				
INLET OUTLET	0.0017 0.0081	0.138	0.157	4.33%
TOTAL	0.0320	0.461	0.521	

\* FRICTIONAL LOSS ONLY

S-7288

Figure 4-8.--Recuperator Pressure Drop Summary.



## CONSTANT AREA HEADERS, "U" FLOW

### • INLET PRESSURE GRADIENT

$$P - P_i = q_i \left[ 1 - \left( 1 - \frac{x}{L} \right)^2 \right]$$

### • OUTLET PRESSURE GRADIENT

$$P - P_o = 2q_o \left[ 1 - \left( 1 - \frac{x}{L} \right)^2 \right]$$

### • FOR UNIFORM DISTRIBUTION

$$q_i = 2 \times q_o$$

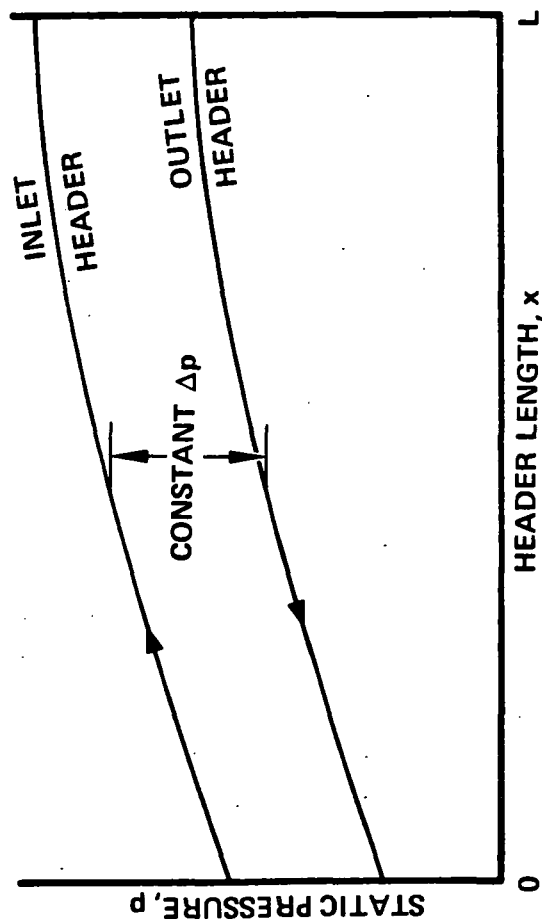


TABLE 4-3

MANIFOLD DESIGN FOR UNIFORM FLOW DISTRIBUTION

	FLOW AREA SQ CM (SQ IN.)	PRESSURE DROP (%)		
		MANI- FOLDS	CORE + END SECTION	TOTAL
HIGH PRESSURE (COLD) $\frac{A_o}{A_i} \cong 2.27$ INLET OUTLET	19.2 (2.98) 43.6 (6.76)	0.096	0.157	0.253
LOW PRESSURE (HOT) $\frac{A_o}{A_i} \cong 1.0$ INLET OUTLET	43.6 (6.76) 43.6 (6.76)	0.081	0.364	0.445
			TOTAL	0.698

$$\frac{q_i}{q_o} = 2.0 ; \frac{A_o}{A_i} = \sqrt{\frac{2\rho_i}{\rho_o}}$$

S-7290

The layout drawing of the first generation heat exchanger is shown in drawing L198782. This design incorporates several novel features designed to provide increased reliability and cyclic life. The plates, fins, and header bars are designed to be stacked and brazed in a conventional manner. After this operation, the braze joints along the sides are exposed; a defect in any of these joints could result in a leakage of working fluid and the eventual shutdown of the power system. To reduce the number of exposed joints and potential leak paths, seal plates are brazed to the core sides (see Section BB in drawing L198782). To obtain an adequate fit up for brazing, the exposed header bars are machined to obtain a flat surface. After brazing, the seal plate is welded to an extension of the side plate to provide a double containment seal. The development of this technique is fully described in refs. 4-1 and 4-2.

The high-pressure and low-pressure manifolds on each end of the core assembly are designed as a continuous hoop with a splitter plate used to separate the flow streams. The ends of the manifold hoop are designed to be welded to extensions of the seal plate (see Section AA in Drawing L198782). This design eliminates welding the manifolds directly along the core braze joints as is the case in typical plate-fin heat exchanger design. Previous experience with other Brayton-cycle recuperators (NASA Engine "B" program) indicated that the weld joint was in a highly stressed area and the cracks would develop after only 15 to 30 cycles of operation.

The manifold splitter plate is designed to be first brazed to the apex of the triangular end sections. The plate is dished to better withstand the pressure differential between the two streams.

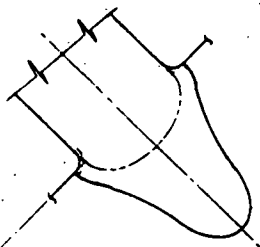
In a third and final braze operation, the mounts are joined to the seal plate surface. Material is removed from the base of the mount to reduce the thermal lag of the mount relative to the heat exchanger core. An overall view of the heat exchanger is shown on Figure 4-10.

#### Transient Analysis

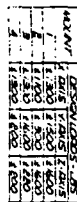
During the system startup transient, the temperature response varies in the fins, plates, header bars, and manifolds. Large temperature differences can be produced in adjacent structures due to the difference in their mass and in the local heat transfer coefficient. This results in high thermal stresses that can produce plastic deformation in local areas. Damage produced by plasticity and creep during each operating cycle accumulates, and after a sufficient number of cycles a low-cycle fatigue crack develops; this crack can propagate through the parent metal, weld, or braze joint. Cracking can result in internal bypassing of the working fluid (loss in system power output) or in loss of working fluid to space (system shutdown). Low-cycle fatigue was identified as the failure mechanism on the NASA Engine B recuperator. In this test, cracks were observed to develop in the header bar-to-tube plate joints after 15 to 30 cycles of operation.

System operating requirements now specify that the units shall survive 1000 operating cycles. A major portion of the recuperator analytical design effort was, therefore, invested in predicting the transient temperature behavior of the

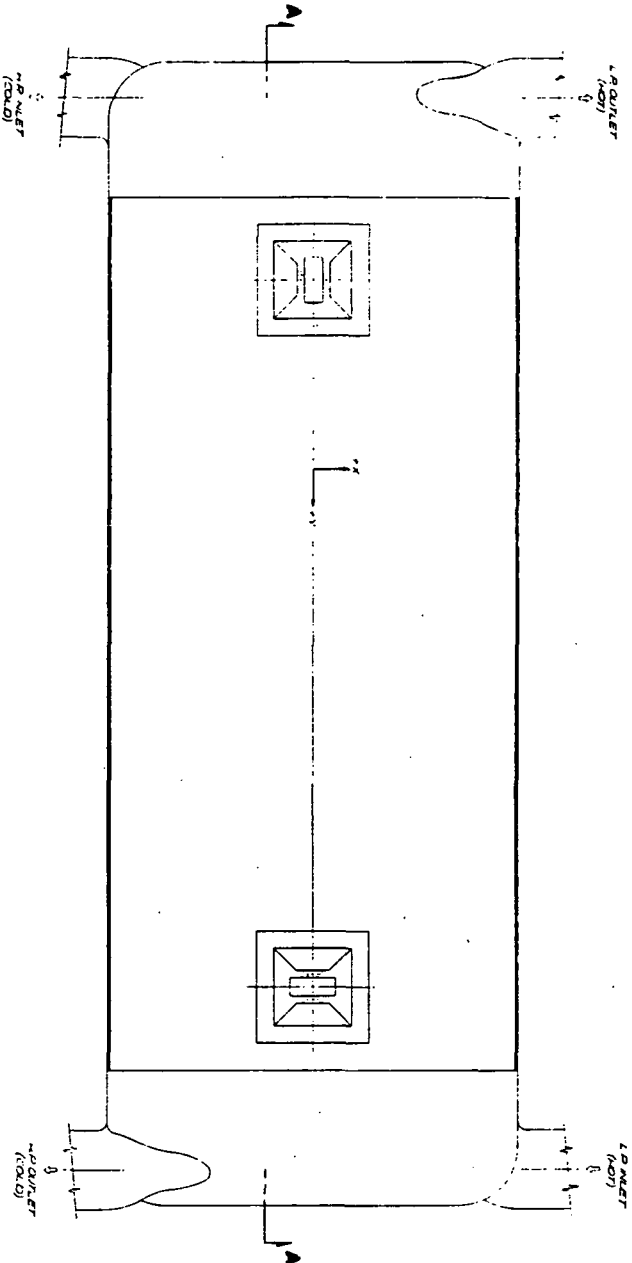
MOUNT	DESIGN LOADS - LBS		
	X-AXIS	Y-AXIS	Z-AXIS
1	±1300	±1500	±1600
2	±1100	±300	±1600
3	±1300	±1600	±800
4	±1300	±800	±800



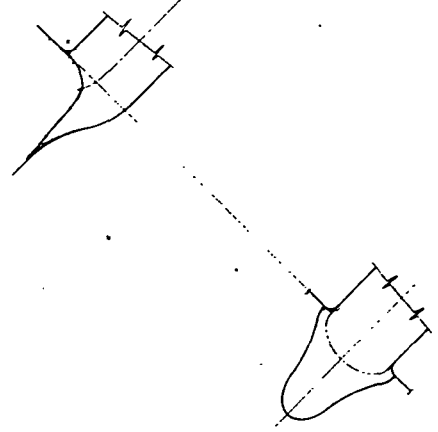
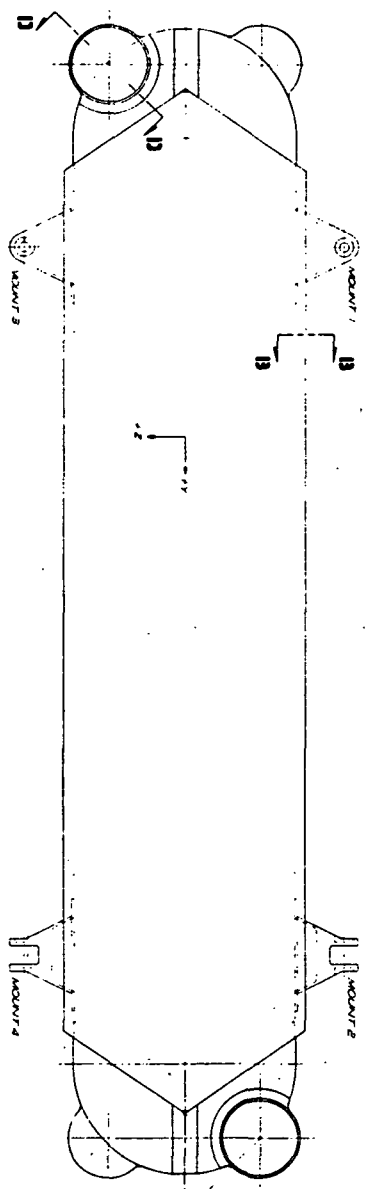
<small>THIS LAYOUT DRAWING IS A PROPERTY OF THE COMPANY AND IS NOT TO BE REPRODUCED OR USED IN ANY MANNER WITHOUT THE WRITTEN PERMISSION OF THE COMPANY. IT IS THE RESPONSIBILITY OF THE USER TO OBTAIN THE NECESSARY PERMISSIONS FROM THE COMPANY BEFORE REPRODUCING OR USING THIS DRAWING IN ANY MANNER.</small>				<small>AMERICAN MANUFACTURING COMPANY</small> <small>A DIVISION OF THE AMERICAN MANUFACTURING COMPANY</small>	
LAYOUT					
<b>RECUPERATOR</b> <b>HXDR (NASA/LEWIS)</b>				<b>70210 L 198782</b>	
<small>CONVENTIONAL HEADER BDR</small>				<small>SCALE 1/1</small>	



4-17/18  
FORWARDED TO ADAM ✓

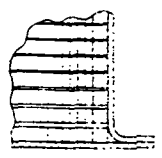


VIEW	DESCRIPTION	DATE
1	1.0 INCH (25.4)	1.0 INCH (25.4)
2	1.0 INCH (25.4)	1.0 INCH (25.4)
3	1.0 INCH (25.4)	1.0 INCH (25.4)
4	1.0 INCH (25.4)	1.0 INCH (25.4)
5	1.0 INCH (25.4)	1.0 INCH (25.4)
6	1.0 INCH (25.4)	1.0 INCH (25.4)
7	1.0 INCH (25.4)	1.0 INCH (25.4)
8	1.0 INCH (25.4)	1.0 INCH (25.4)
9	1.0 INCH (25.4)	1.0 INCH (25.4)
10	1.0 INCH (25.4)	1.0 INCH (25.4)
11	1.0 INCH (25.4)	1.0 INCH (25.4)
12	1.0 INCH (25.4)	1.0 INCH (25.4)
13	1.0 INCH (25.4)	1.0 INCH (25.4)
14	1.0 INCH (25.4)	1.0 INCH (25.4)
15	1.0 INCH (25.4)	1.0 INCH (25.4)
16	1.0 INCH (25.4)	1.0 INCH (25.4)
17	1.0 INCH (25.4)	1.0 INCH (25.4)
18	1.0 INCH (25.4)	1.0 INCH (25.4)
19	1.0 INCH (25.4)	1.0 INCH (25.4)
20	1.0 INCH (25.4)	1.0 INCH (25.4)

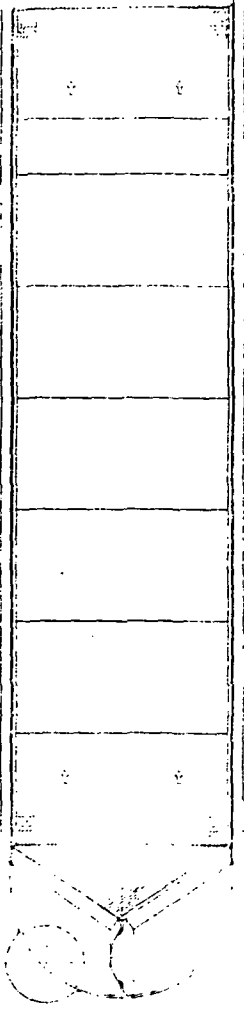




SECTION D-D



SECTION B-B  
SCALE 2/1



SECTION A-A  
2 R 10055 (HOT)  
24 TENSILE STRENGTH & SWEAT  
EFFECT 200 THERM

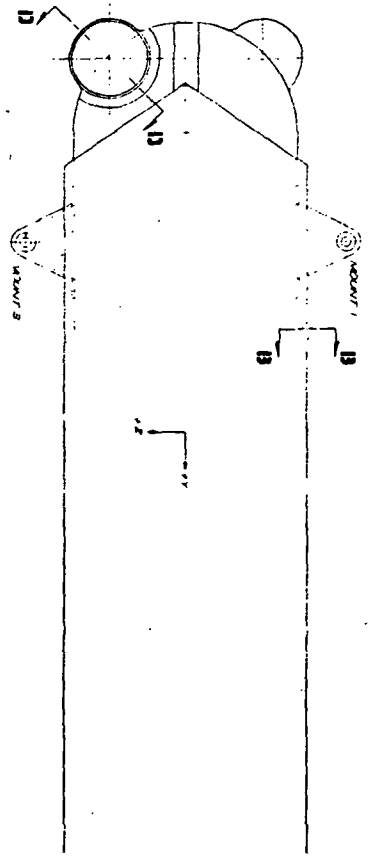
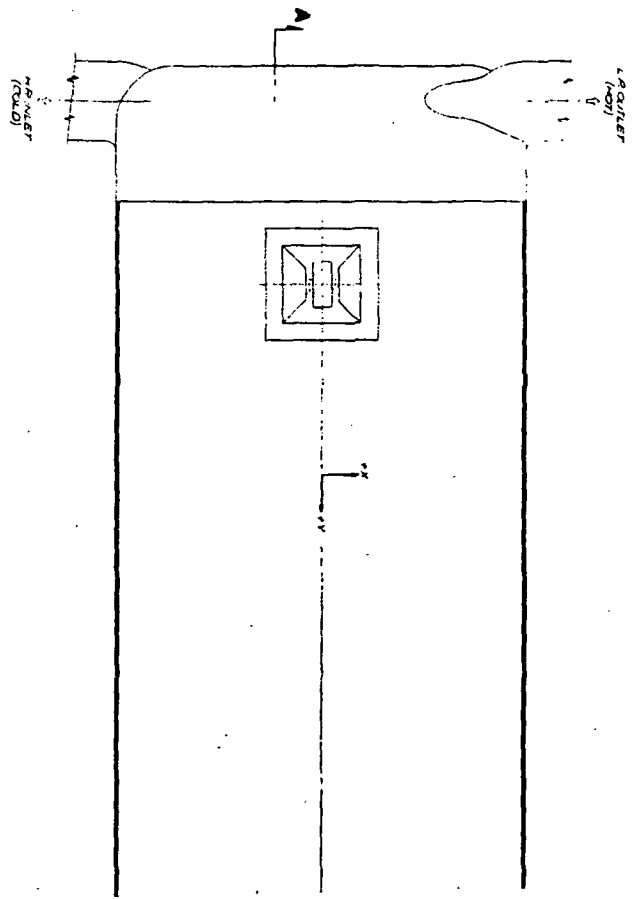
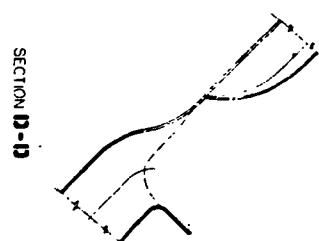


FIGURE FRAME 2

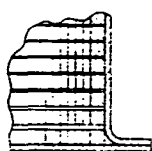
FIGURE FRAME 3



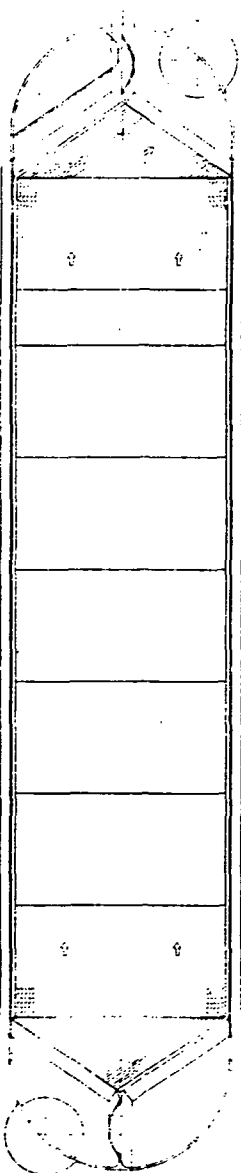
ORIGINAL PAGE IS  
OF POOR QUALITY



SECTION D-D



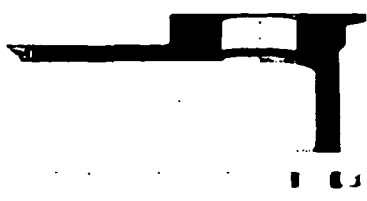
SECTION B-B  
SCALE 4/1



SECTION A-A  
L.P. CROSS (H.O.T.)  
1/4" TYPICAL (1/2" MAXIMUM) SPACING  
EXCEPT 1/2" MAXIMUM

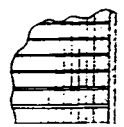
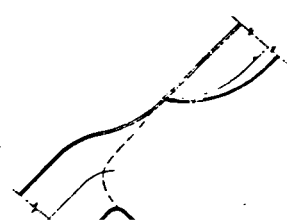
FOLDOUT FRAME 1

FOLDOUT FRAME 2

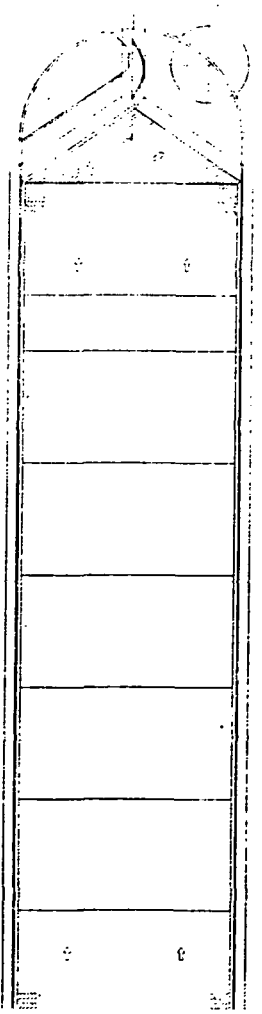


ORIGINAL PAGE IS  
OF POOR QUALITY

SECTION D-D



SECTION B-B  
SCALE 4/1



SECTION A-A  
L.R. CROSS (NOT)  
IN TERMINATE IN A RICH (D) FRAMES'S SHALLOO,  
ENTERED IN INVENTION

FOLDOUT FRAME /

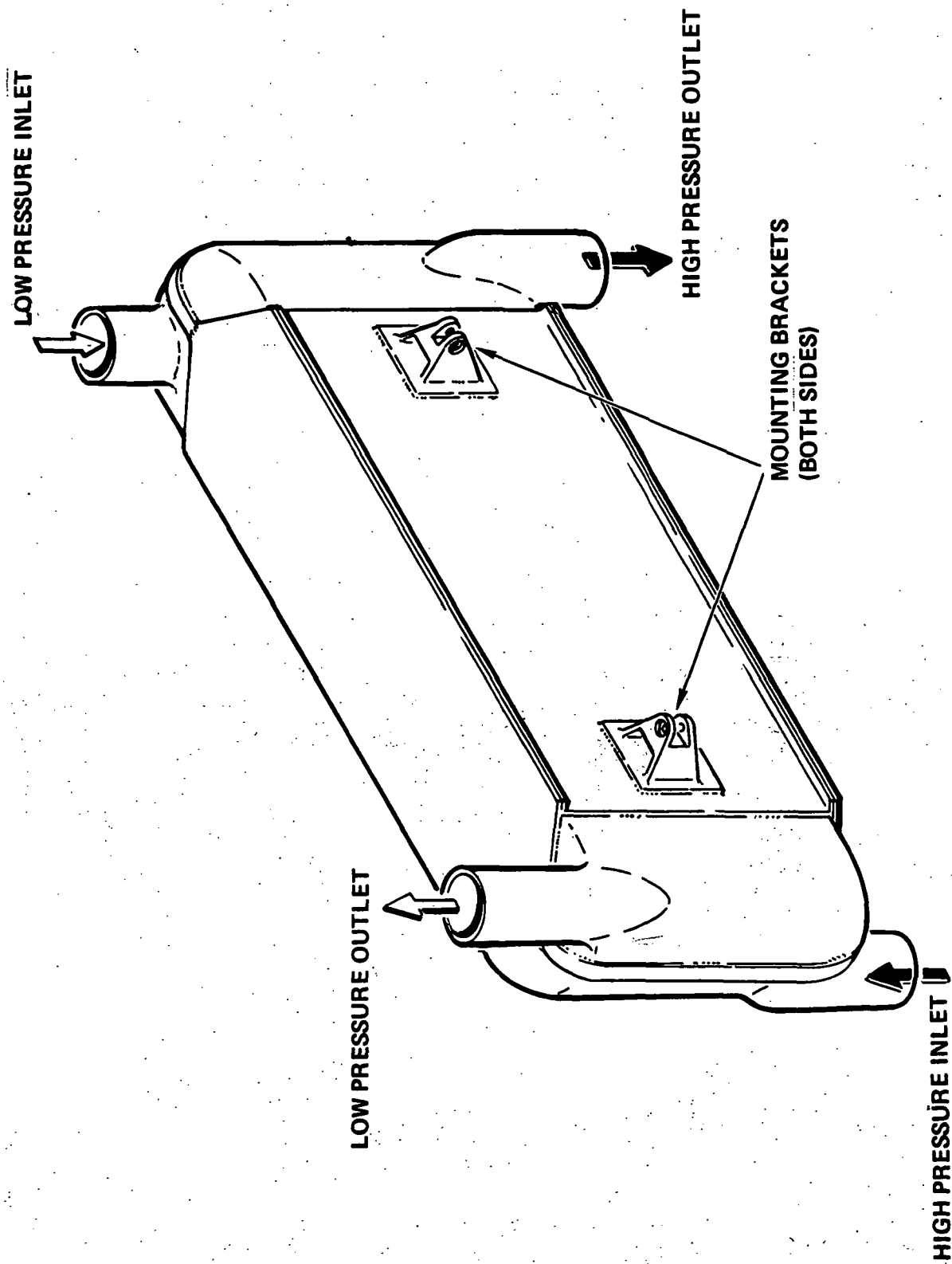


Figure 4-10.--Recuperator Submodule Design.

submodule. These analyses serve to identify the critical areas, i.e., areas where large temperature gradients exist, and to study the behavior of alternate structural designs. Moreover, the transient temperature data are used as the basis for the low-cycle fatigue analysis described in the following section.

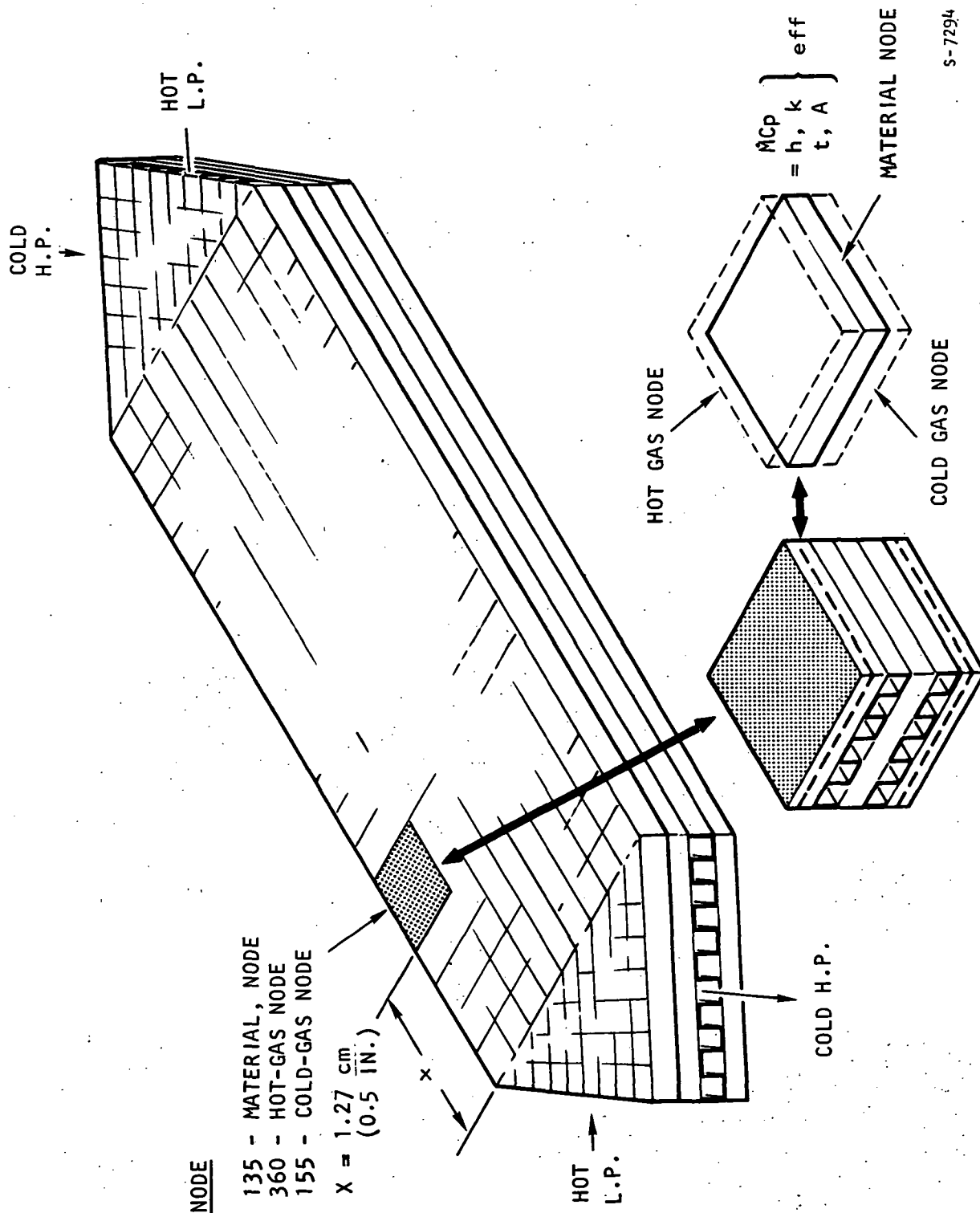
Overall Heat Exchanger Thermal Analysis.--A transient analysis was performed to determine the thermal lag that occurs during system startup between the header bars and tube sheets of the heat exchanger assembly. The startup system transients for this analysis are shown in figs. 4-4 and 4-5.

The thermal model of the overall heat exchanger was divided into a thermal nodal network with many small nodes at the hot-gas inlet end and progressively fewer nodes toward and cold-gas inlet end of the heat exchanger. The development of this nodal network model was guided by previous experience gained with the BHXU-Engine B system tests at NASA. Trouble spots (i.e., high-temperature gradients) were expected to be at the hot end (hot-gas inlet and cold-gas outlet) of the heat exchanger.

The conventional heat exchanger design as shown in drawing L198782 was the design for which the thermal model was made. In this effort, the idea was first to establish a simple but representative model, and later to add (as required) more detailed features. Thus, no internal radiation was considered and the radiation to the surroundings from the seal plate and manifolds was ignored.

To eliminate top and bottom end effects, only the middle sandwich was considered. The analytical model consisted of one hot-gas side fin layer, one cold-gas side fin layer, and two tube plates, as shown schematically in fig. 4-11. Thus, the system boundary will be adiabatic. In this model, all four (hot- and cold-gas, inlet and outlet) manifolds were accounted for as well as the triangular end sections. Two gas nodes were associated with every metal node, -- one for the hot gas and another for the cold gas. The thermal model ultimately contained about 600 nodes -- approximately 200 metal nodes, 200 hot-gas nodes, and 200 cold-gas nodes. The fluid streams were divided into eight hot-gas fluid streams and correspondingly, eight cold-gas fluid streams. For the hot- and cold-gas fins (rectangular offset type), test data were used for heat transfer and pressure drop (friction) analysis. Simple, standard correlations of flow through rectangular ducts were used for the analyses of the end turning section fins (plain, rectangular) and the hollow header bars. For the manifolds, a circular tube correlation was used. Only the hot- and cold-gas heat transfer fins in the counterflow section of the core have high heat transfer performance and consequently have the primary effect on the temperature distribution. The other fins produce only secondary effects.

Hot- and cold-gas inlet temperatures, hot- and cold-gas flow, all were considered as functions of time in the transient temperature analyses. Hot- and cold-gas properties for Xe-He were considered as functions of time. The thermal conductivity of the Hastelloy-X material also was taken as a function of temperature. The heat conduction in all three directions was considered, and for the rectangular offset fins, a special conformal mapping method was used for heat conduction in the longitudinal direction. The contact resistance



S-7294

Figure 4-11.--Transient Thermal Model.

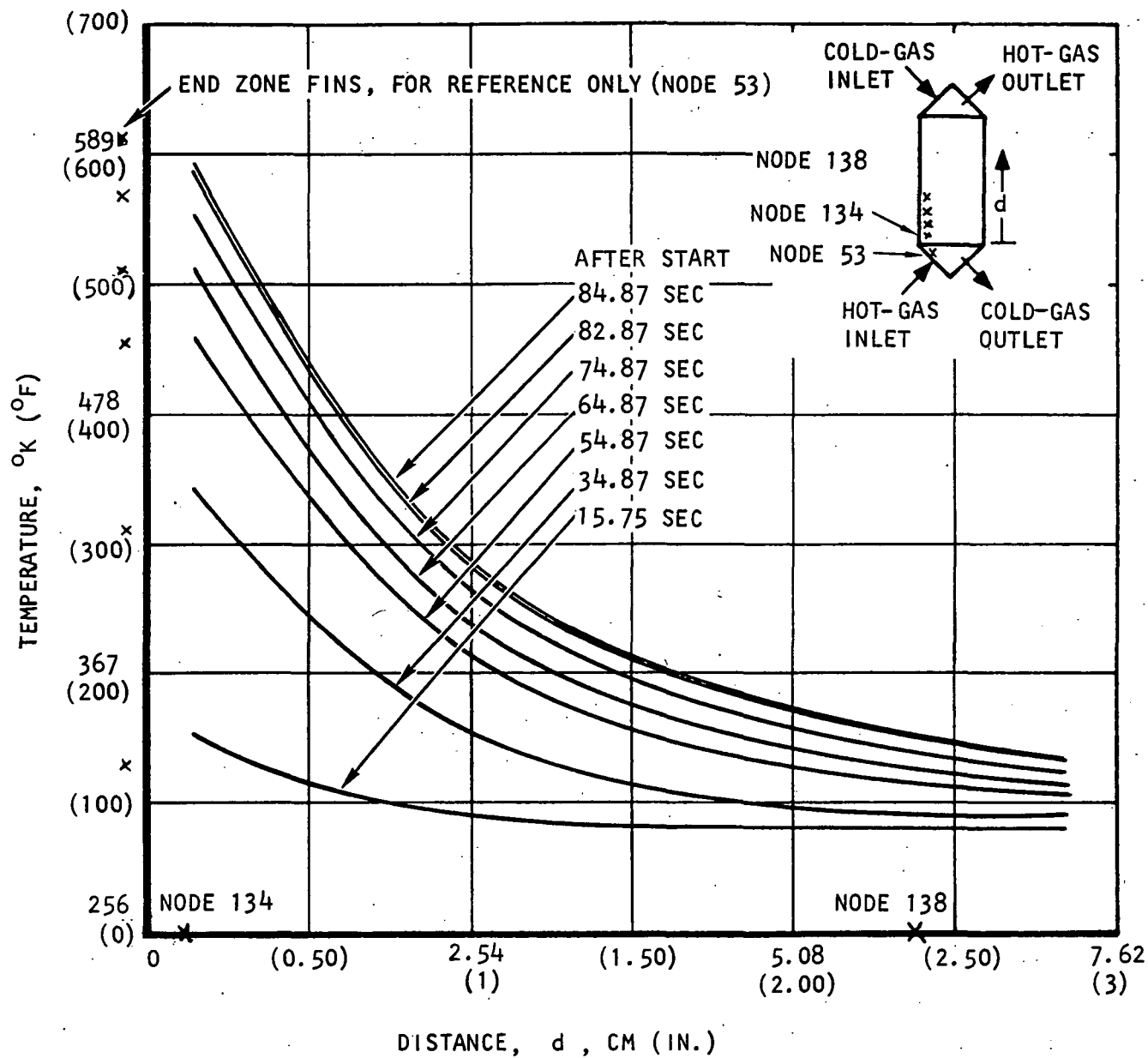
at the interface of the header bars and the seal plate (brazed joint) was considered (resistance =  $200 \text{ hr-m}^2\text{-}^\circ\text{K/kg cal}$  ( $0.001 \text{ hr ft}^2 \text{ }^\circ\text{F/Btu}$ ) in the calculations. Flow distribution in the hot- and cold-gas fluid streams was assumed to be in proportion to the flow area in the heat transfer section. This was assumed because the total end zone lengths are the same for all gas streams and the main flow resistance is offered by the compact, high-efficiency fins in the counterflow section of the heat exchanger. Pressure losses at the manifold entrance, manifold exit, turning fin entrance, turning fin exit, 90-degree turns and mitered bends, as well as contraction and expansion at the heat transfer section entrances and exits, were considered.

The conventional recuperator was analyzed with the following three header bar configurations: (a) solid header bars, (b) hollow header bars without any flow inside, and (c) hollow header bars having hot- and cold-gas flow inside. For all three cases, a 0.063-cm- (0.025-in.) thick seal plate was included on both sides of the recuperator. The tube plate thickness was 0.0152 cm (0.006 in.) and the brazing material thickness was taken as 0.00254 cm (0.001 in.) on each side of the tube sheet. This gives an equivalent tube plate thickness of 0.0203 cm (0.008 in.). Hot- and cold-gas fin, tube plate, seal plate, manifolds, and header bar material were Hastelloy-X. The effect of brazing material on the thermal conductivity of the tube plate was ignored in this model because a gold-based brazing alloy was used.

The transient analysis was run until the thermal gradients became equal to or less than the previous gradient (i.e., beyond the time of maximum thermal gradient). Curves showing temperature as a function of distance, with time as a parameter, were plotted in the fluid flow direction (parallel to the fins) as well as perpendicular to the fluid flow direction (normal to the fins). Sets of curves were plotted for each of the three header bar configurations. However, no difference in the thermal transient response of the unit was observed between the three header bar configurations. Figs. 4-12 and 4-13 show the axial temperature gradients along the two sides of the unit adjacent to the header bar. The axial temperature gradient is more severe on the side with the smaller turning fin flow length. The turning fins, therefore, act as a buffer and reduce the thermal gradients in the tube sheet.

The thermal transients normal to the fluid flow direction were taken in the area that exhibited the severest axial thermal gradients. This area was located at the hot-gas inlet end at the corner of the heat exchanger where the turning fin flow length was shortest. The thermal profiles normal to the fluid flow direction on each side of the heat exchanger are shown in figs. 4-14 and 4-15. Transverse temperature profiles across the total core are also shown in figs. 4-16 through 4-21 at various locations along the fluid flow direction. These profiles were generated at 45 and 80 sec after startup.

The thermal transients along the outside surfaces of the turning sections were less severe than the core corner area mentioned above. The end section thermal transient parallel to the hot-gas flow is presented in fig. 4-22 and the end section thermal transient parallel to the cold-gas flow is presented in fig. 4-23.



S-78259-A

Figure 4-12.--Axial Transient Temperature Distribution Adjacent to the Solid Header on the Hot Side.

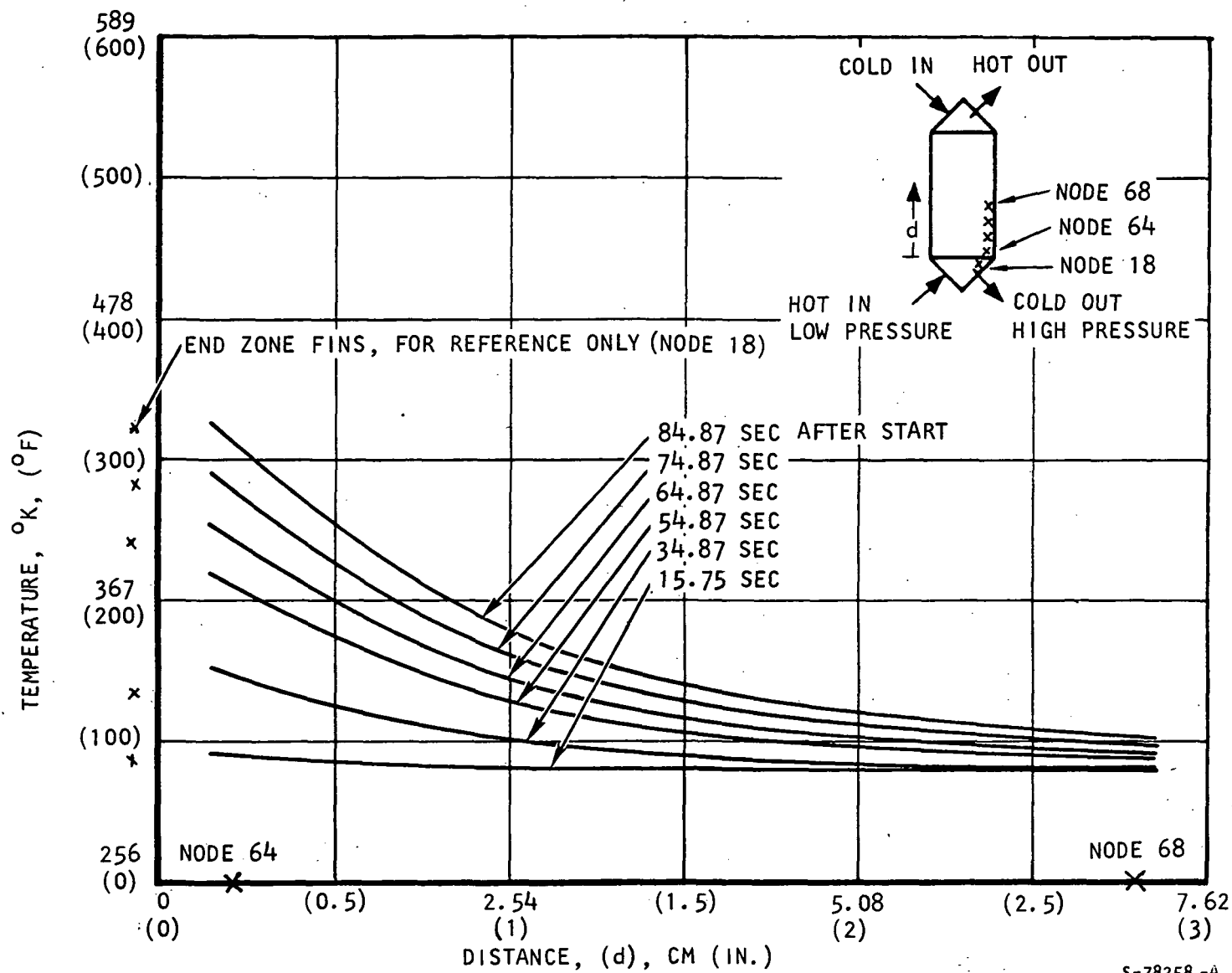
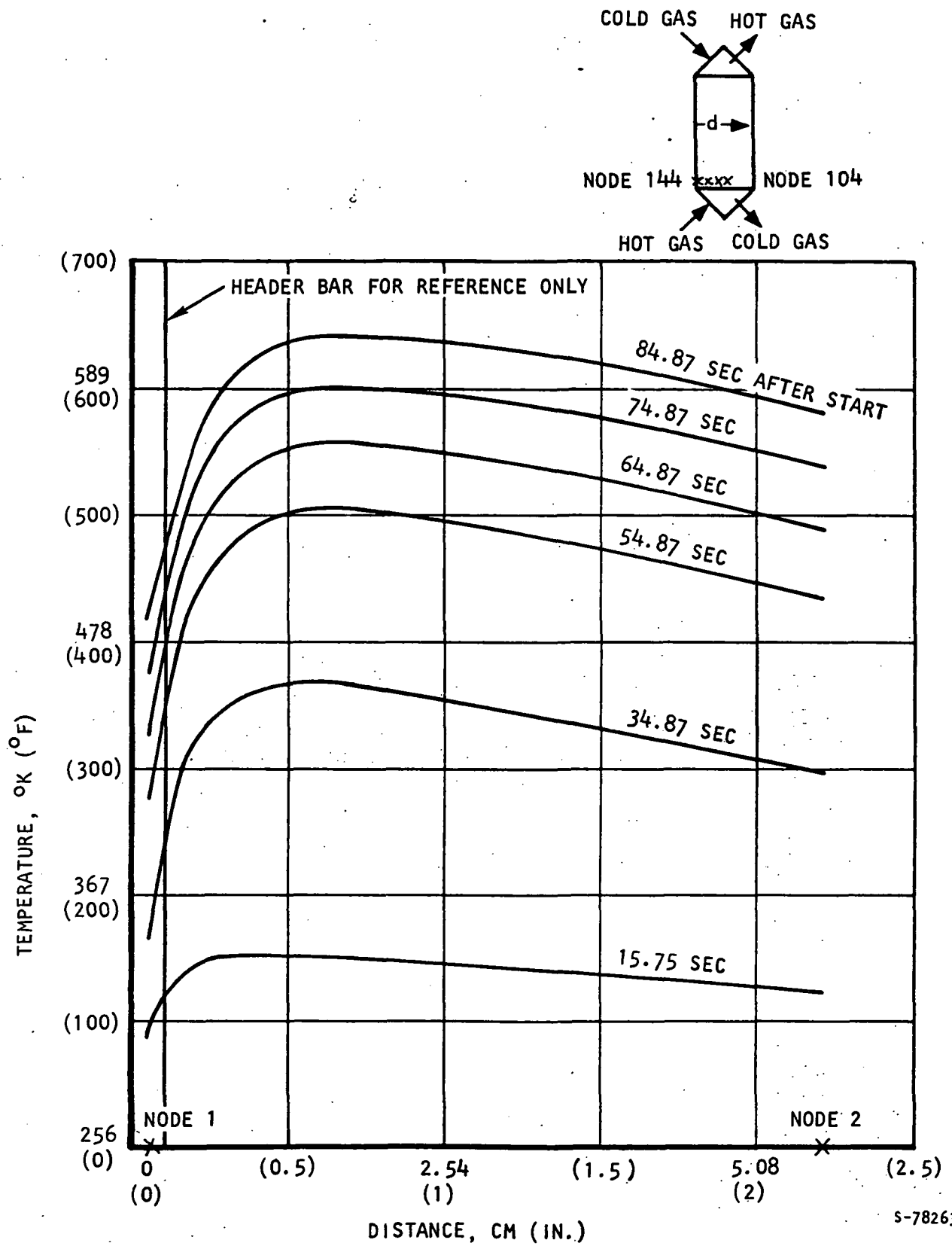


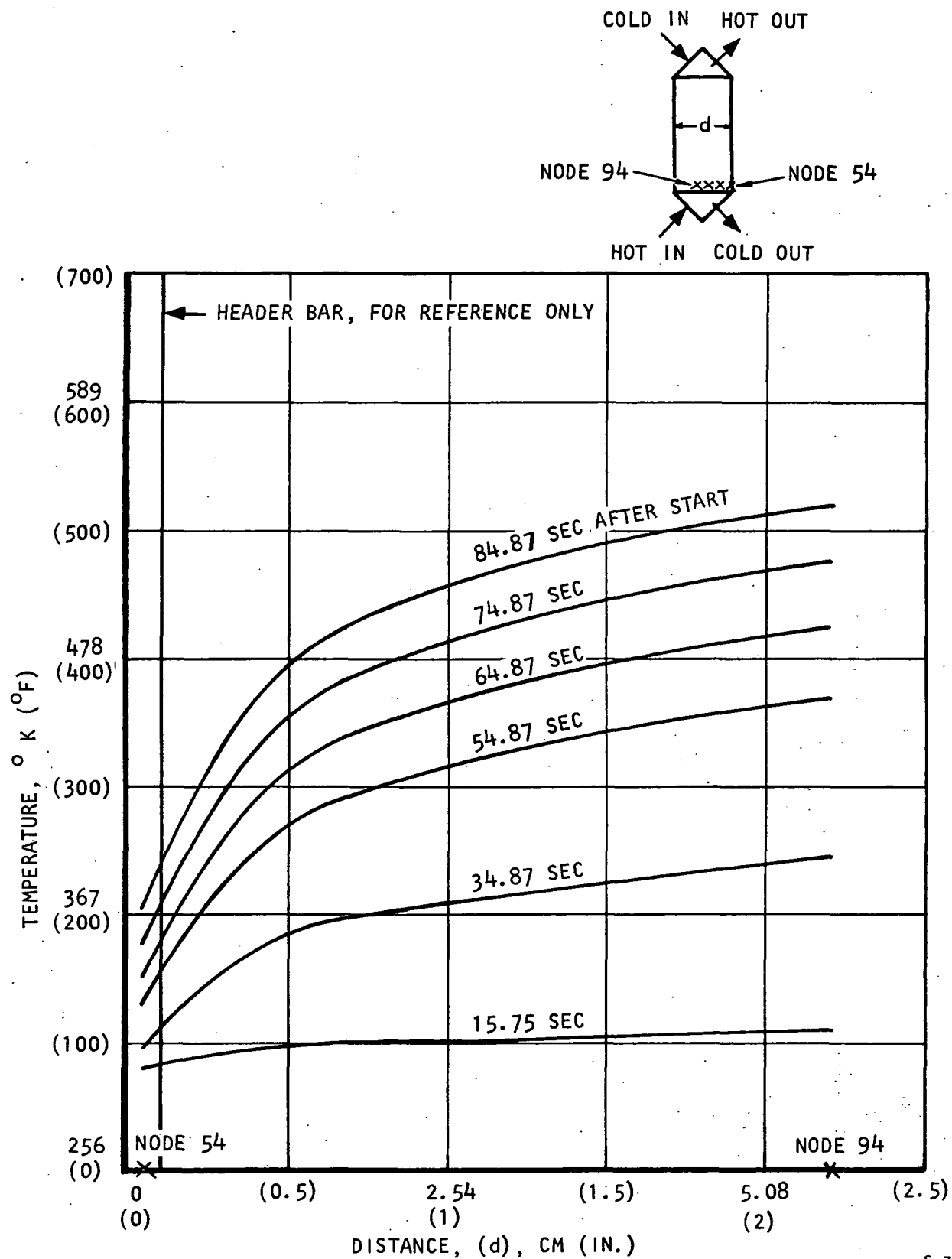
Figure 4-13.--Axial Transient Temperature Distribution Adjacent to the Solid Header Bar on the Cold Side.





S-78263 -A

Figure 4-14.--Hot-Side Thermal Transient Temperature Distribution Normal to the Flow (Using Solid Header Bar).



S-78257-A

Figure 4-15.--Cold-Side Thermal Transient Temperature Distribution Normal to the Flow (Using Solid Header Bar).

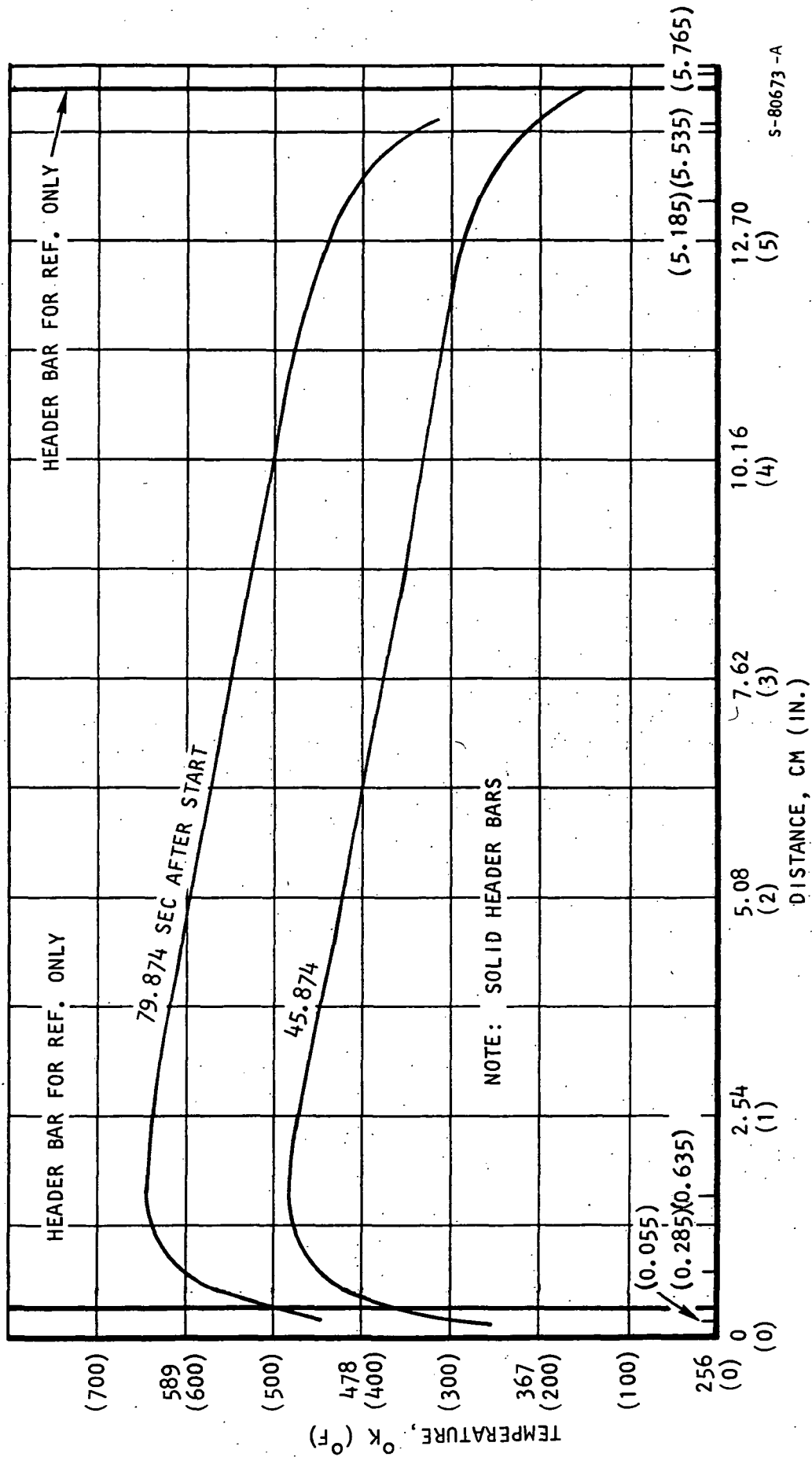


Figure 4-16.--Transient Temperature Distribution Normal to the Flow Direction at a Station 0.38 cm (0.15 in.) in the Heat Transfer Fin.

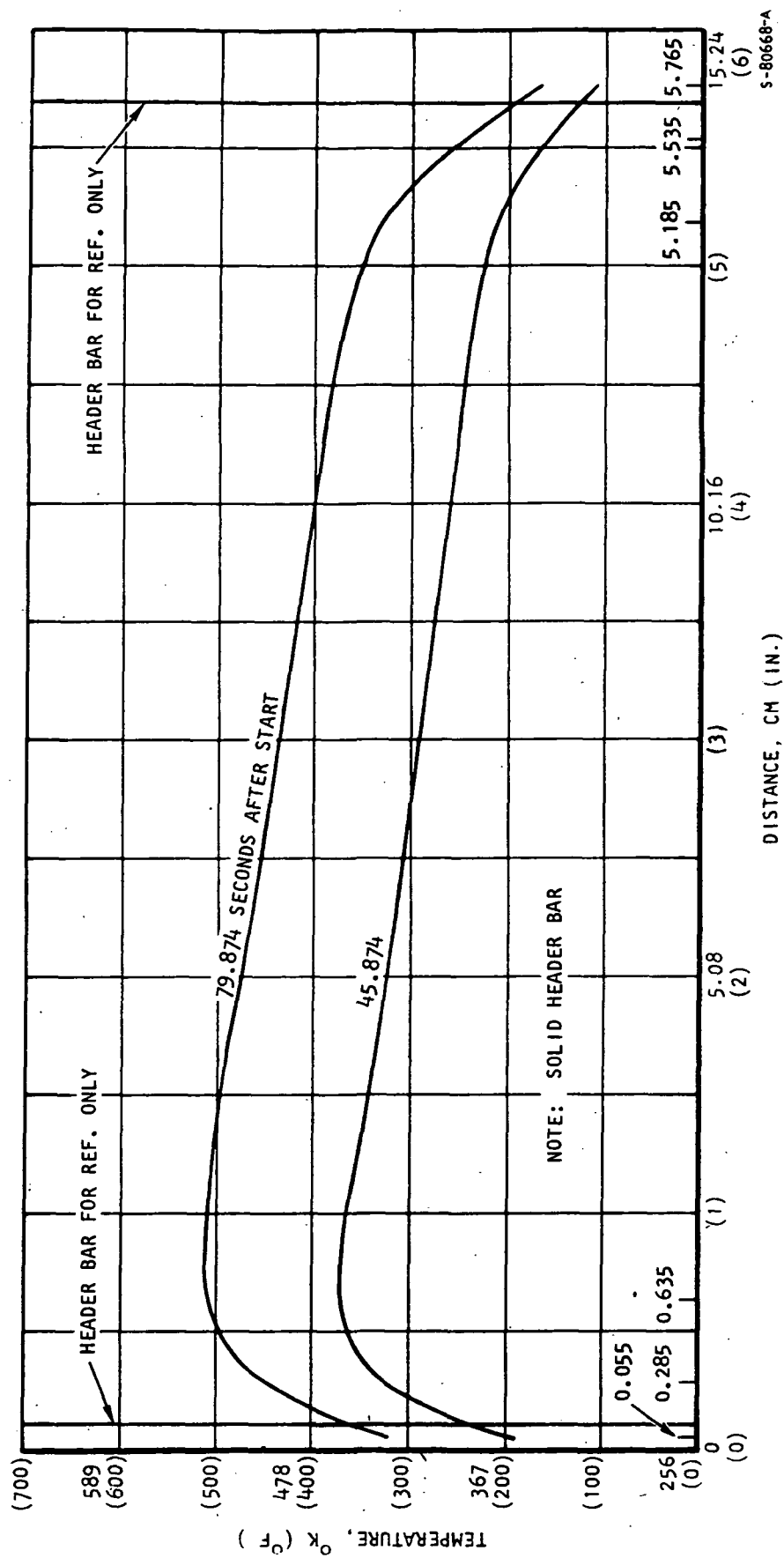
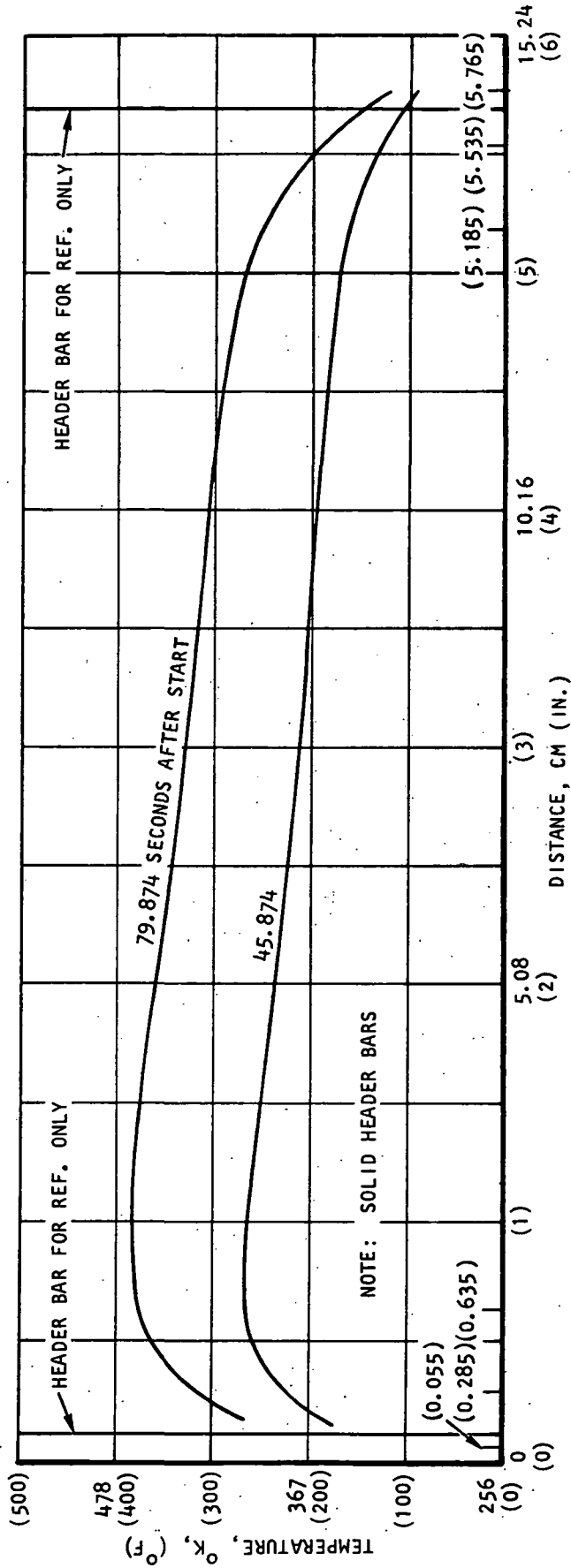
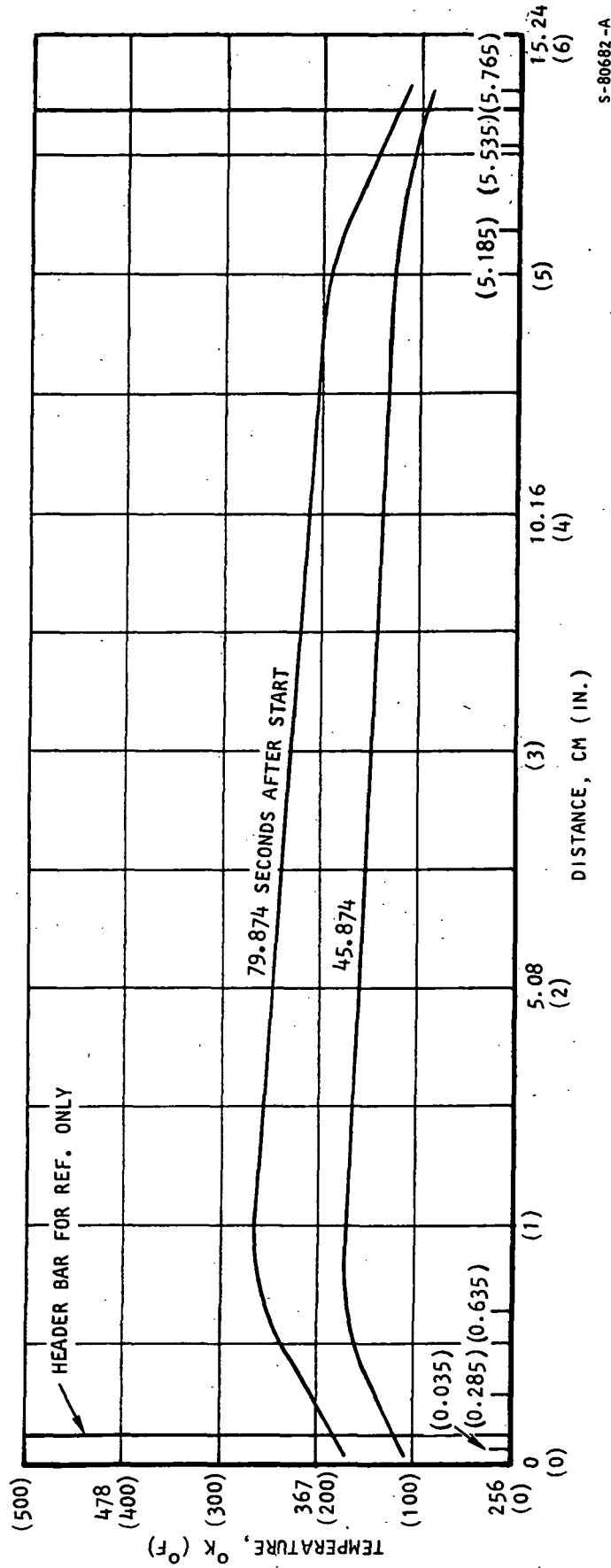


Figure 4-17.--Transient Temperature Distribution Normal to the Flow Direction at a Station 1.27 cm (0.5 in.) in the Heat Transfer Fin.



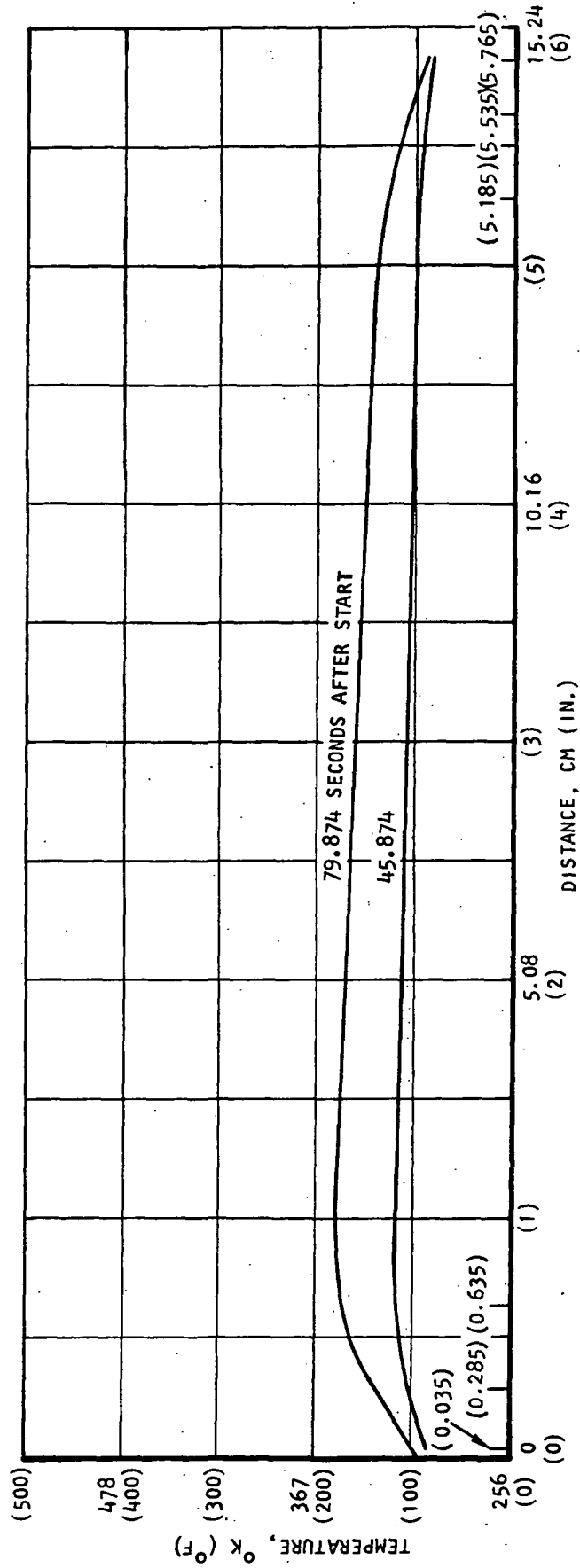
S-80676-A

Figure 4-18.--Transient Temperature Distribution Normal to the Flow at a Station 2.29 cm (0.9 in.) in the Heat Transfer Fin.



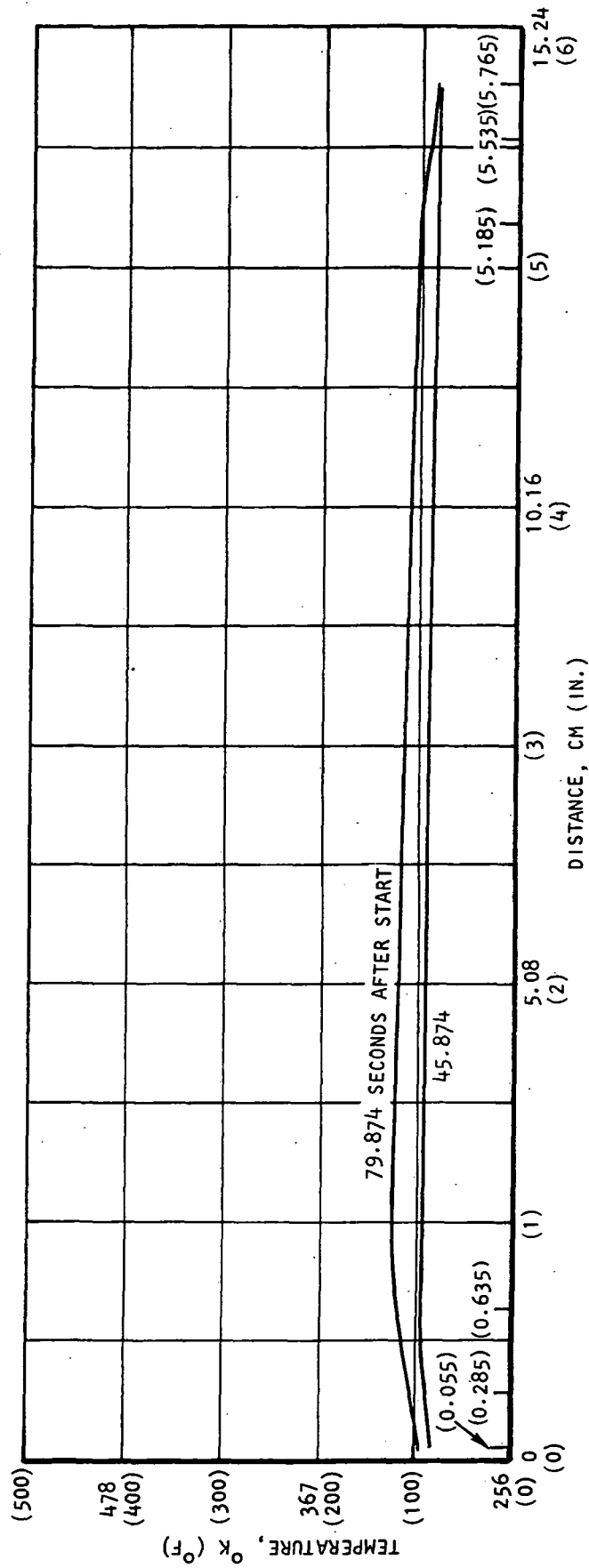
S-80682-A

Figure 4-19.---Transient Temperature Distribution Normal to the Flow Direction at a Station 4.06 cm (1.6 in.) in the Heat Transfer Fin.



S-80683 -A

Figure 4-20.---Transient Temperature Distribution Normal to the Flow  
at a Station 7.24 (7.24 in.) in the Heat Transfer Fin.

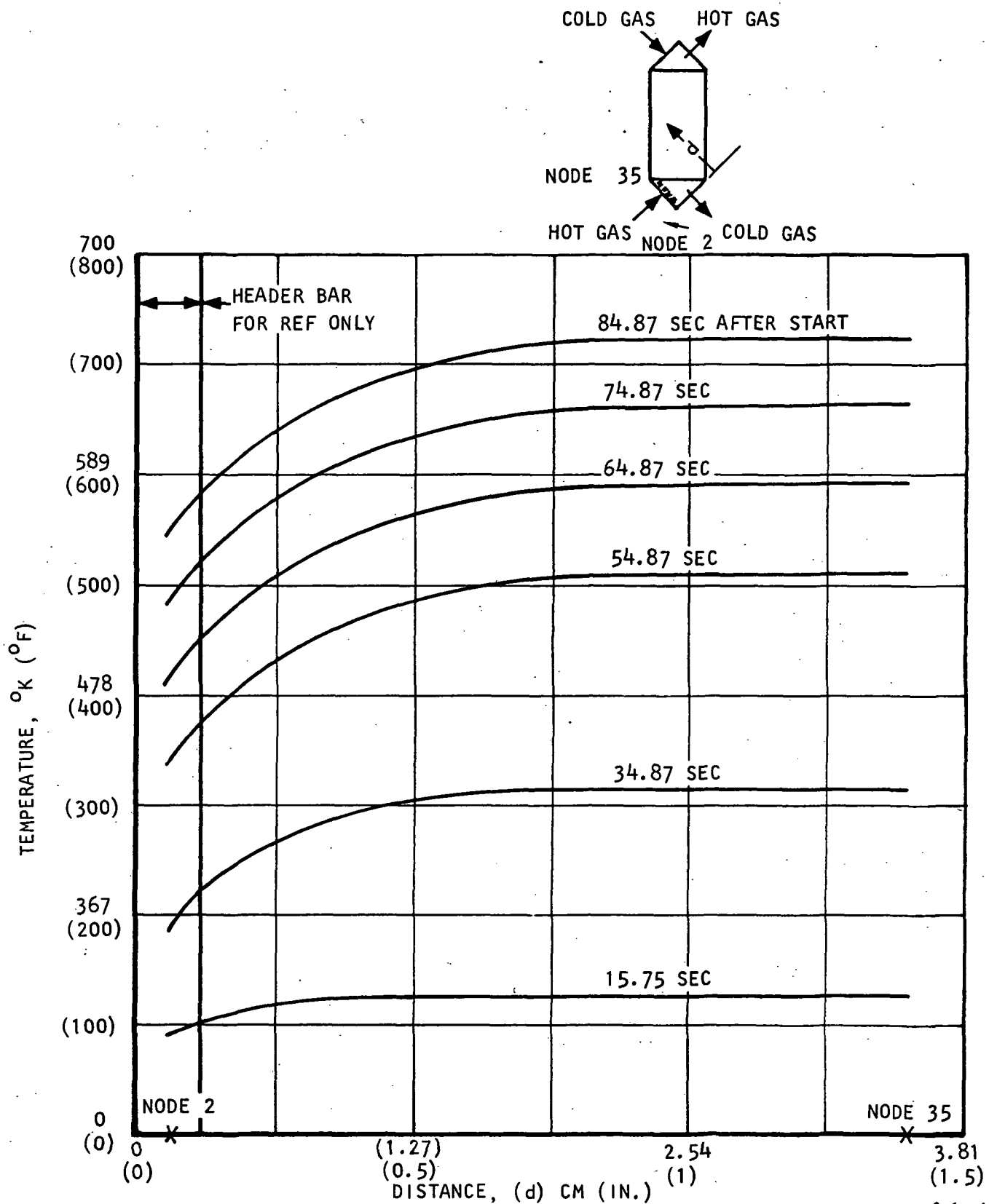


S-80681 -A

Figure 4-21.---Transient Temperature Distribution Normal to the Flow  
at a Station 11.68 cm (4.6 in.) in the Heat Transfer Fin.







S-78261-A

Figure 4-23.--End Section Thermal Transient Parallel to the Cold Gas Flow (Using Solid Header Bar).

The preceding analysis was reviewed and a smaller, more detailed model was considered necessary to obtain the thermal transient conditions of the tube sheet relative to the header bar. The detailed model of the tube sheet/header bar zone at one point in the unit was investigated using the thermal boundary conditions from the larger model.

Fine-grid Thermal Analysis.--For the standard header bar and U-channel header bar, the fine-grid, three-dimensional models are shown in figs. 4-24 and 4-25, respectively. The fine-grid model was required to obtain the thermal gradients adjacent to the header bar and also to minimize the computer time required for the thermal analysis.

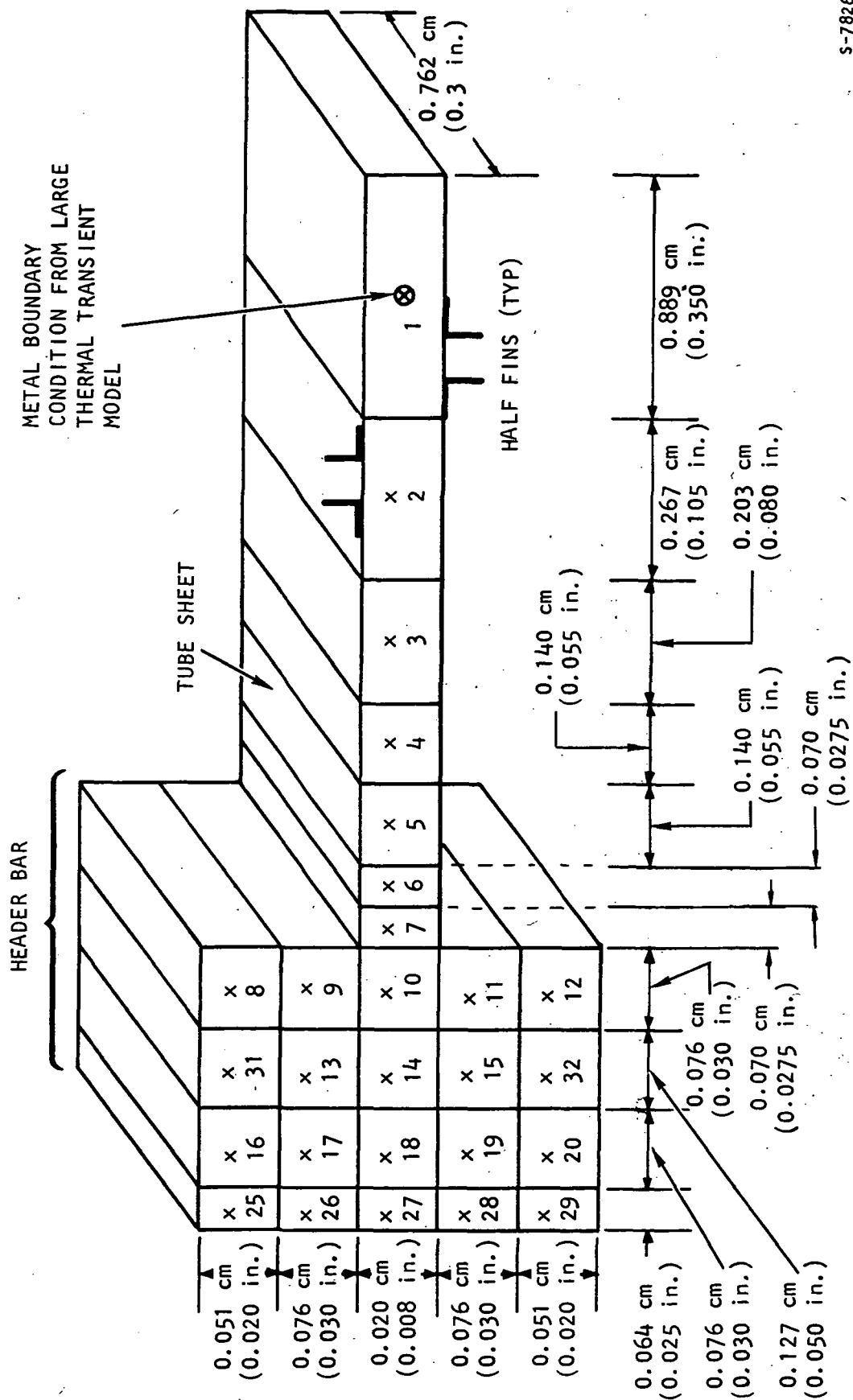
Three transient thermal analyses were made with the fine-grid thermal model (45 thermal nodes) using the solid header bar, hollow header bar, and U-channel header. The solid and hollow header bar configurations incorporated a 0.064-cm-thick (0.025-in.-thick) seal plate brazed to the header bar.

With temperature as a function of distance and with time as a parameter, curves were plotted for the three header conditions to obtain the thermal gradient normal to the fluid flow direction. The thermal transients for the solid header bar, hollow header bar, and U-channel header are presented in figs. 4-26, 4-27, and 4-28, respectively. As shown, smaller thermal gradients are produced when the header bar mass is smaller in relation to the tube sheet mass.

The longitudinal temperature gradients across the solid and hollow header bars appear to be negligible, since the header bar mass and heat capacity are quite large compared to the fins and tube plates. The hollow header bar has 84 percent of the mass of the solid header bar and shows a negligible change in the thermal transient temperatures. However, the U-channel, which has 25 percent the mass of the solid header bar, does affect the transient thermal gradients substantially.

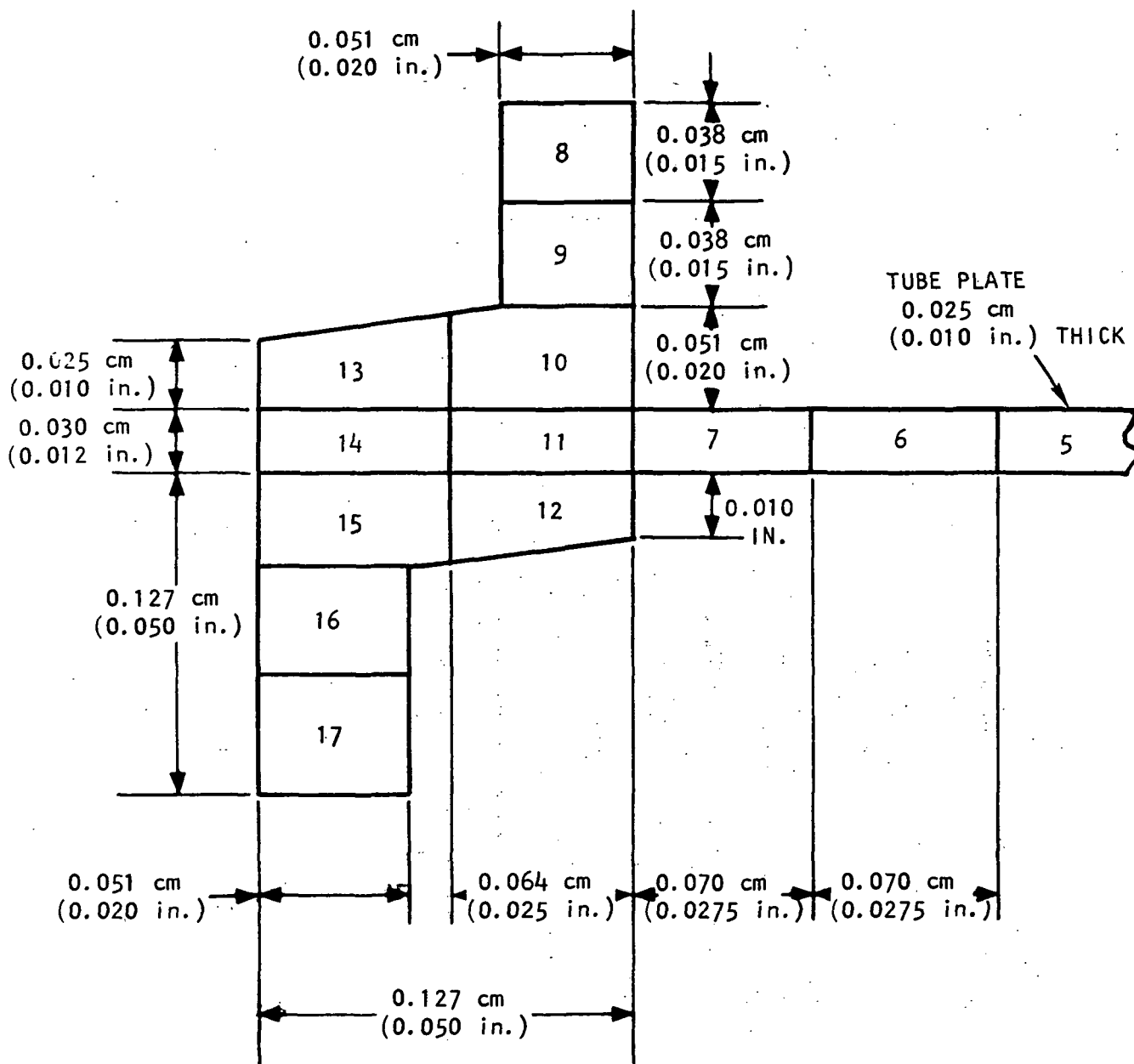
Two additional header bar/seal plate cores that were analyzed are the U-channel header bar (with seal plate) and the narrow header bar. The data generated for each of these cases are shown in figs. 4-29 and 4-30. These figures show similar thermal gradients, but the U-channel header bar appears more attractive for structural reasons.

Tube Plate Thickness Thermal Effects.--To satisfy structural integrity, the core module was designed with tube plates that increase in thickness toward the side plates of the brazed assembly. Since there is a different mass on each side of the fin in a sandwich that has two different thicknesses of tube plates, there will be a thermal stress imposed on the fin during startup (and shutdown) thermal transients. Tube plate thicknesses were varied from 0.015 cm (0.006 in.) at the center of the core to 0.102 cm (0.040 in.) at the side plate. The intermediate tube plate thicknesses and side plate thicknesses are tabulated in table 4-4.



S-78265 -B

Figure 4-24.---Fine-Grid Model for Conventional Header Bar  
(Three-Dimensional Thermal Gradient).



S-78264 -A

Figure 4-25.--Fine-Grid Model for Formed U-Channel Header  
(Three-Dimensional Thermal Gradient).

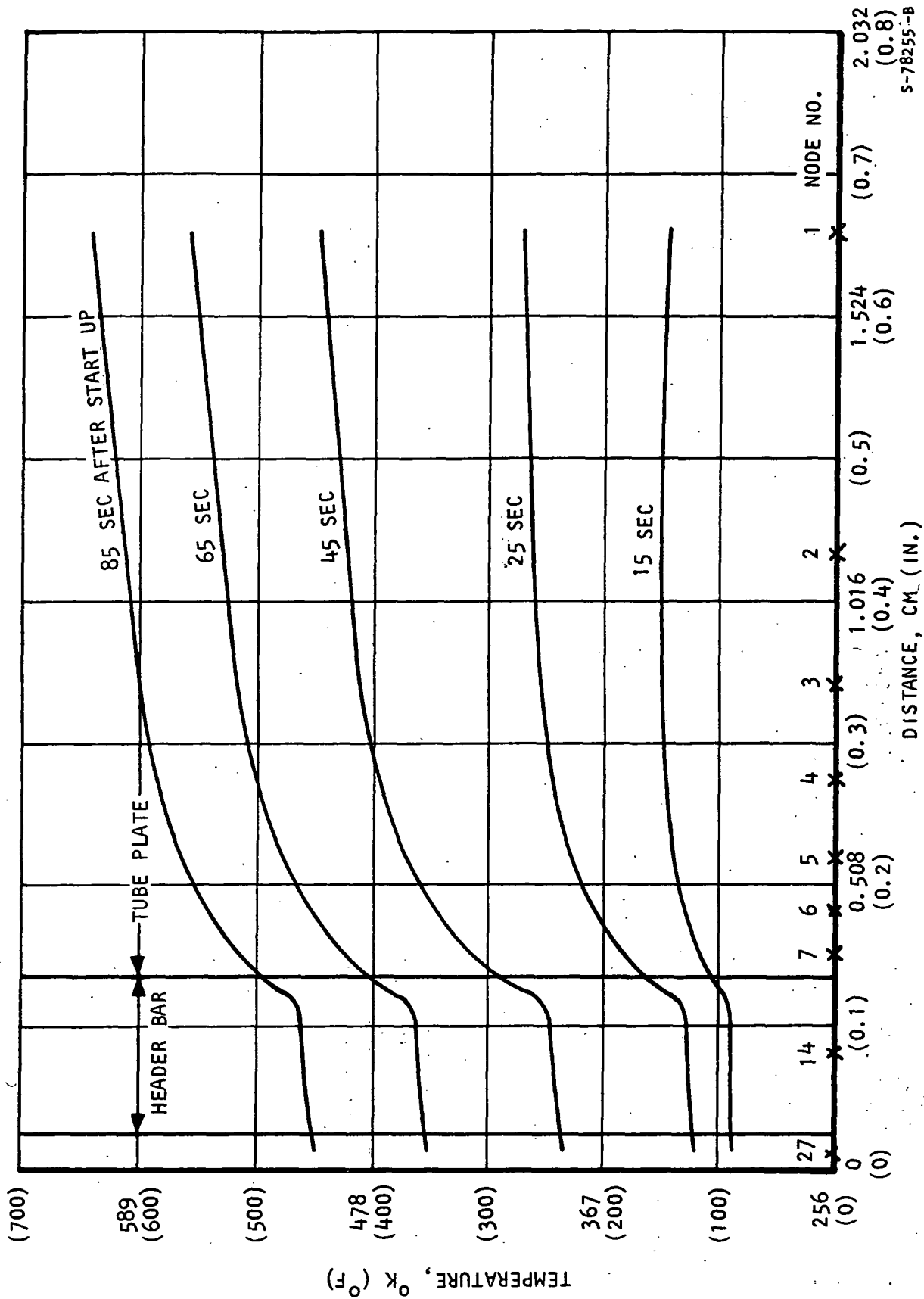
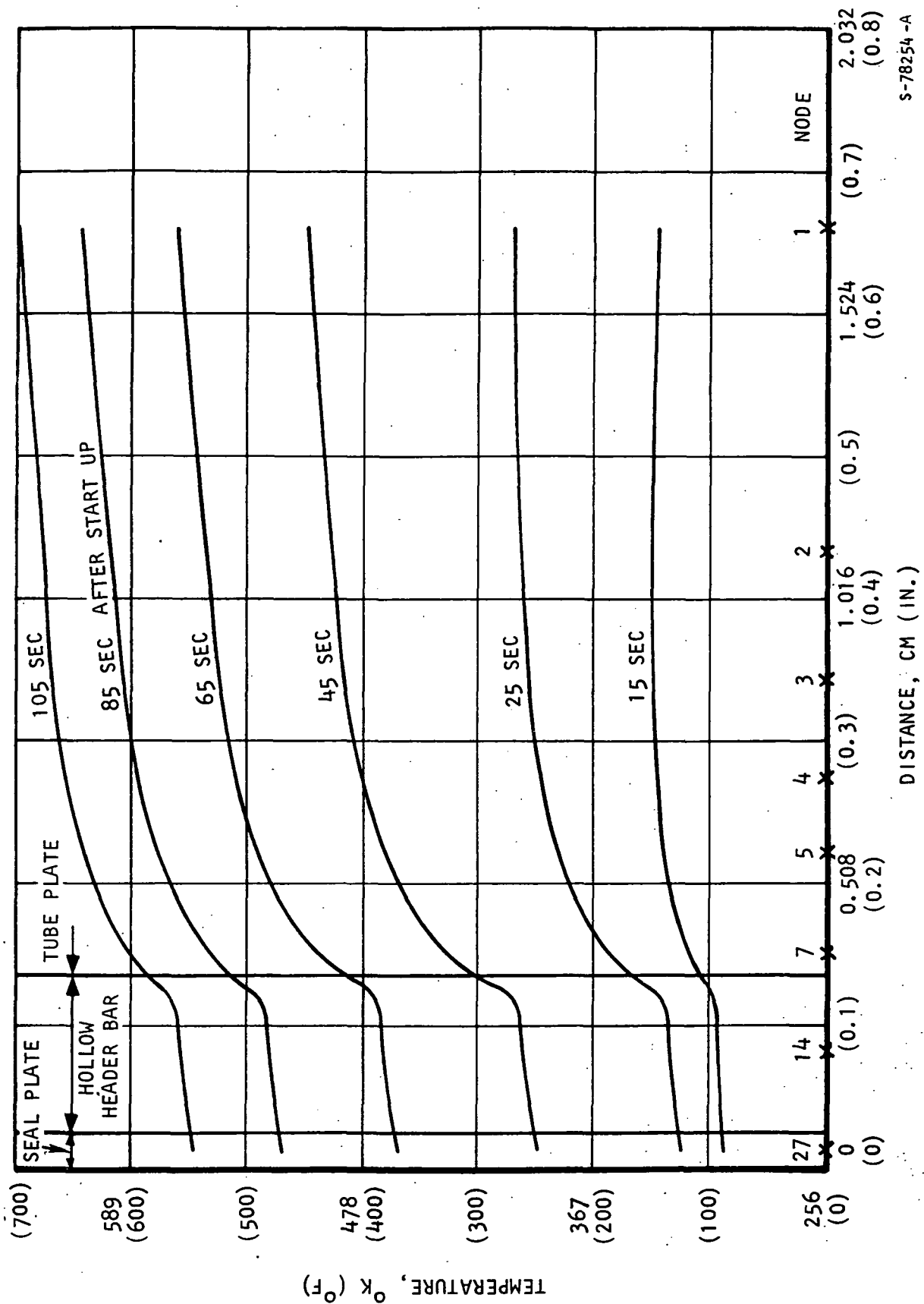


Figure 4-26.--Fine-Grid Thermal Transient, Solid Header Bar Model.



S-78254 -A

Figure 4-27.--Fine-Grid Thermal Transient, Hollow Header Bar Model.

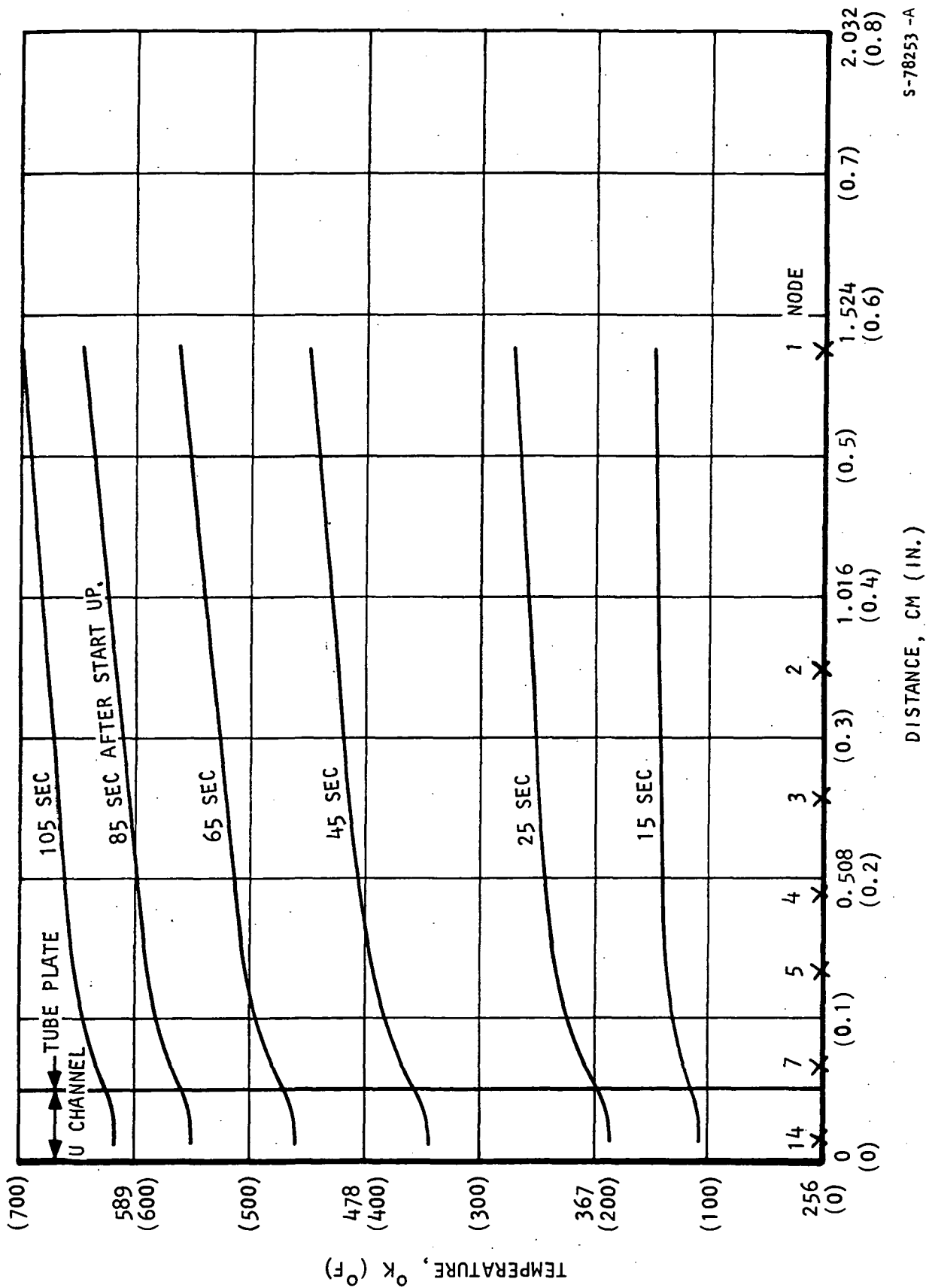


Figure 4-28.--Fine-Grid Thermal Transient, U-Channel Header.



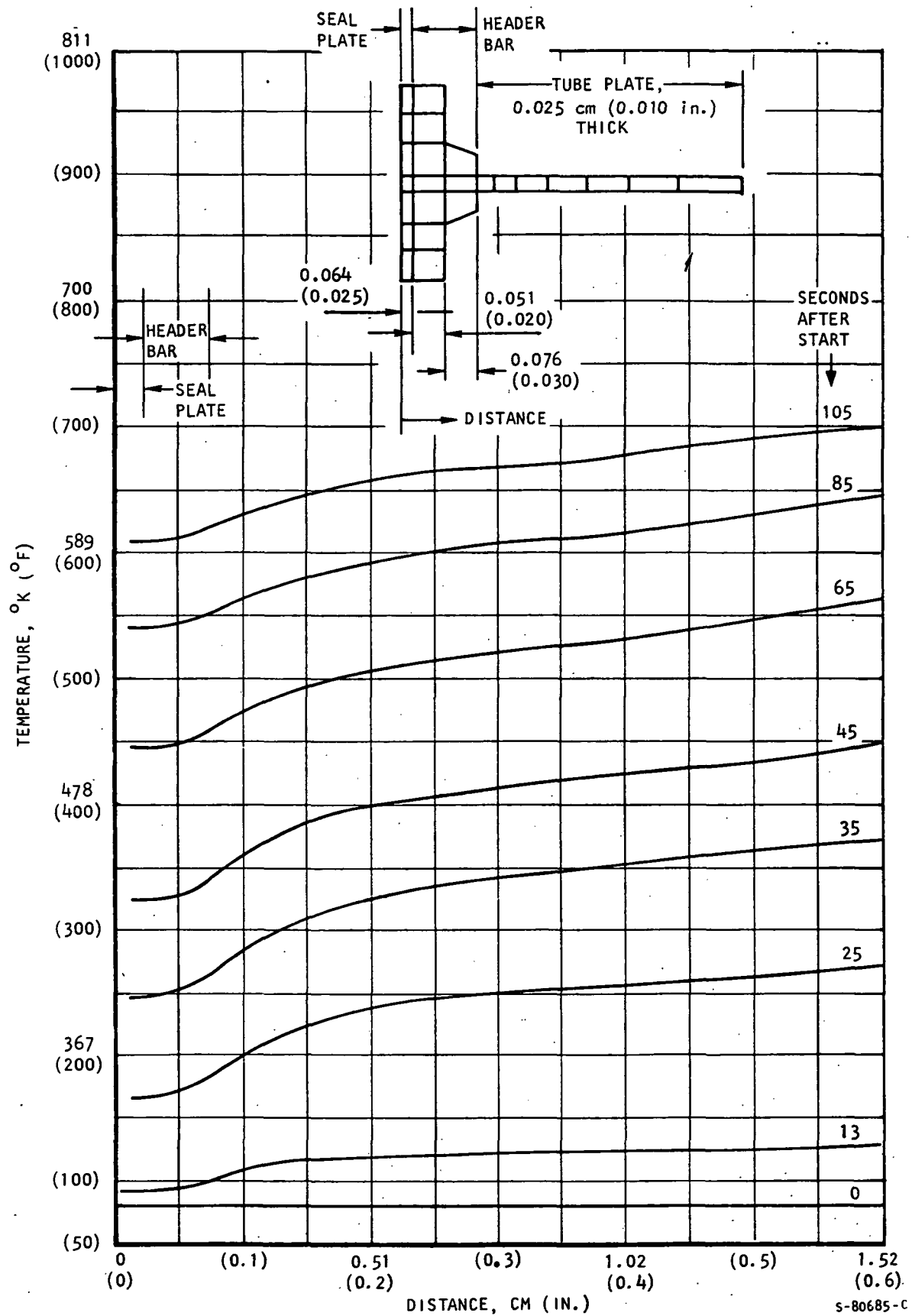
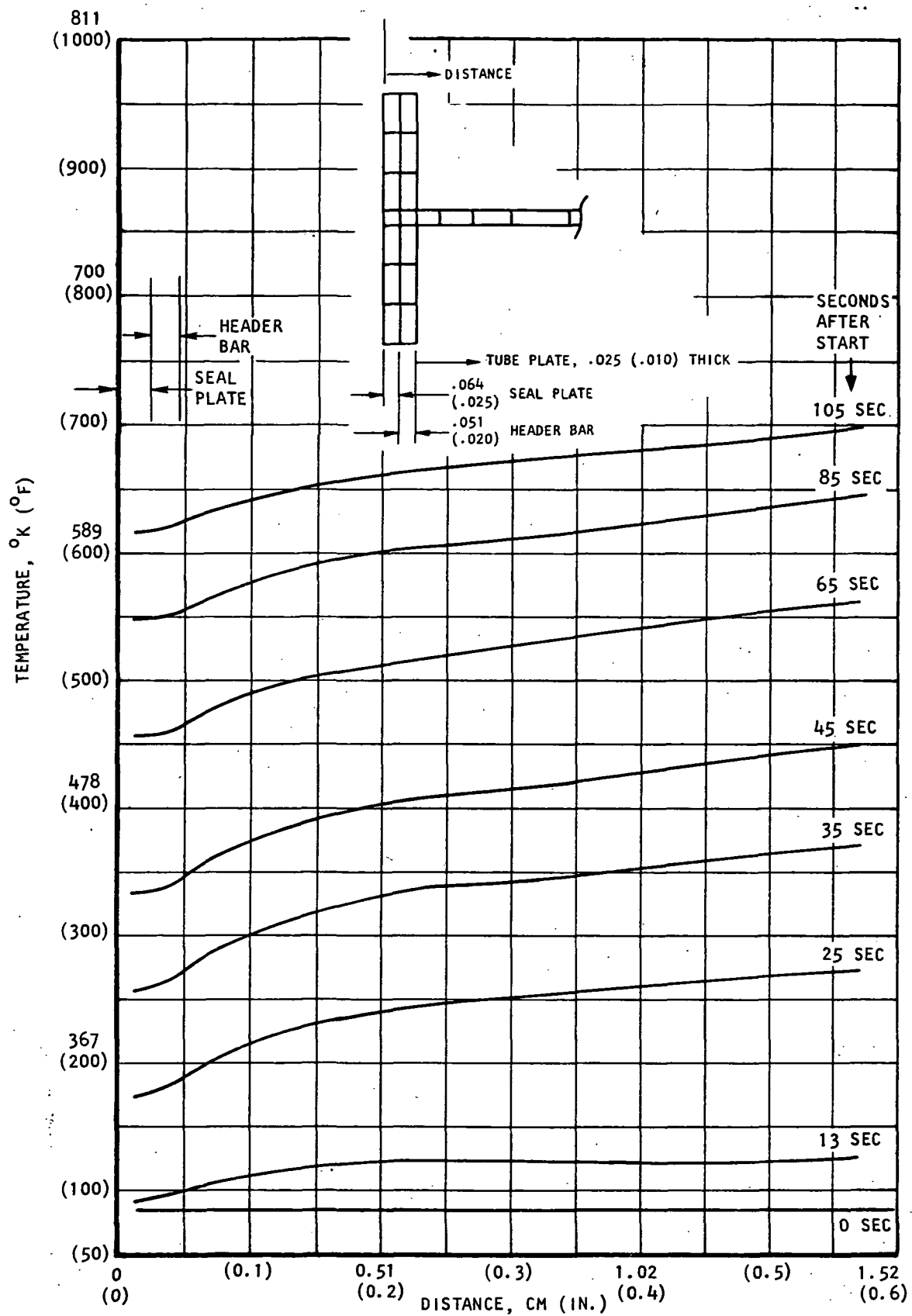


Figure 4-29.--Transient Temperature Distribution for U-Channel Header Bar With Seal Plate.



S-7285-A

Figure 4-30.--Transient Temperature Distribution for Narrow Header Bar.

TABLE 4-4

## VARIATION OF TUBE PLATE THICKNESSES

Tube Plate Location	Tube Plate Thicknesses	
	cm	in.
At center	0.015 0.020 0.031	0.006 0.008 0.012
Various locations between center and side plate	0.041 0.020 0.081	0.016 0.020 0.032
At side plate	0.102	0.040

A simplified computer program was used to perform this transient analysis in lieu of the more complex transient analysis program (H0910). The advantage of the simplified computer program is that it is a less complex two-dimensional program and takes much less computer time. The simplified program, however, cannot account for the header bar mass effect and is limited to analyzing heat exchanger cores in the areas not influenced by the header bar mass during a thermal transient.

The seven cases of tube plate thickness are presented in figs. 4-31 to 4-33 as maximum  $\Delta T/\Delta X$ , maximum  $(\Delta T/\Delta X)\Delta T$ , and maximum temperature as a function of tube plate thickness at 105 sec in the startup transient. It can be seen that as the tubeplate thickness increases, the maximum temperature gradient  $(\Delta T/\Delta X)$  increases, but the maximum temperature of the tube plate at a given time decreases.

Thermal Buffer (Transition) Fins.--A thermal buffer fin was investigated because of the difference in fin efficiency between the high-efficiency heat transfer fins and the low-efficiency turning fins. This thermal efficiency difference causes discontinuity and high temperature gradients at the interface between the two fins.

A thermal buffer or transition fin was selected for analysis on the basis of having a thermal efficiency between the heat transfer fin and the turning fin. The two fin geometries selected for the analysis were: (1) 41 fins/cm (16 fins/in.), 0.015 cm (0.006 in.) thick; and (2) 51 fins/cm (20 fins/in.), 0.010 cm (0.004 in.) thick. The two axial flow lengths selected for the buffer fin were 1.3 cm (0.5 in.) and 7.6 cm (3.0 in.). These lengths were selected to see the effect on the tube sheet temperature during the transient. Fig. 4-34 shows the effect of the 1.3 cm (0.5 in.) and 7.6 cm (3.0 in.) buffer fin. Figs. 4-35 and 4-36 show the effect of a 5.1-cm (2.0-in.) long buffer fin.

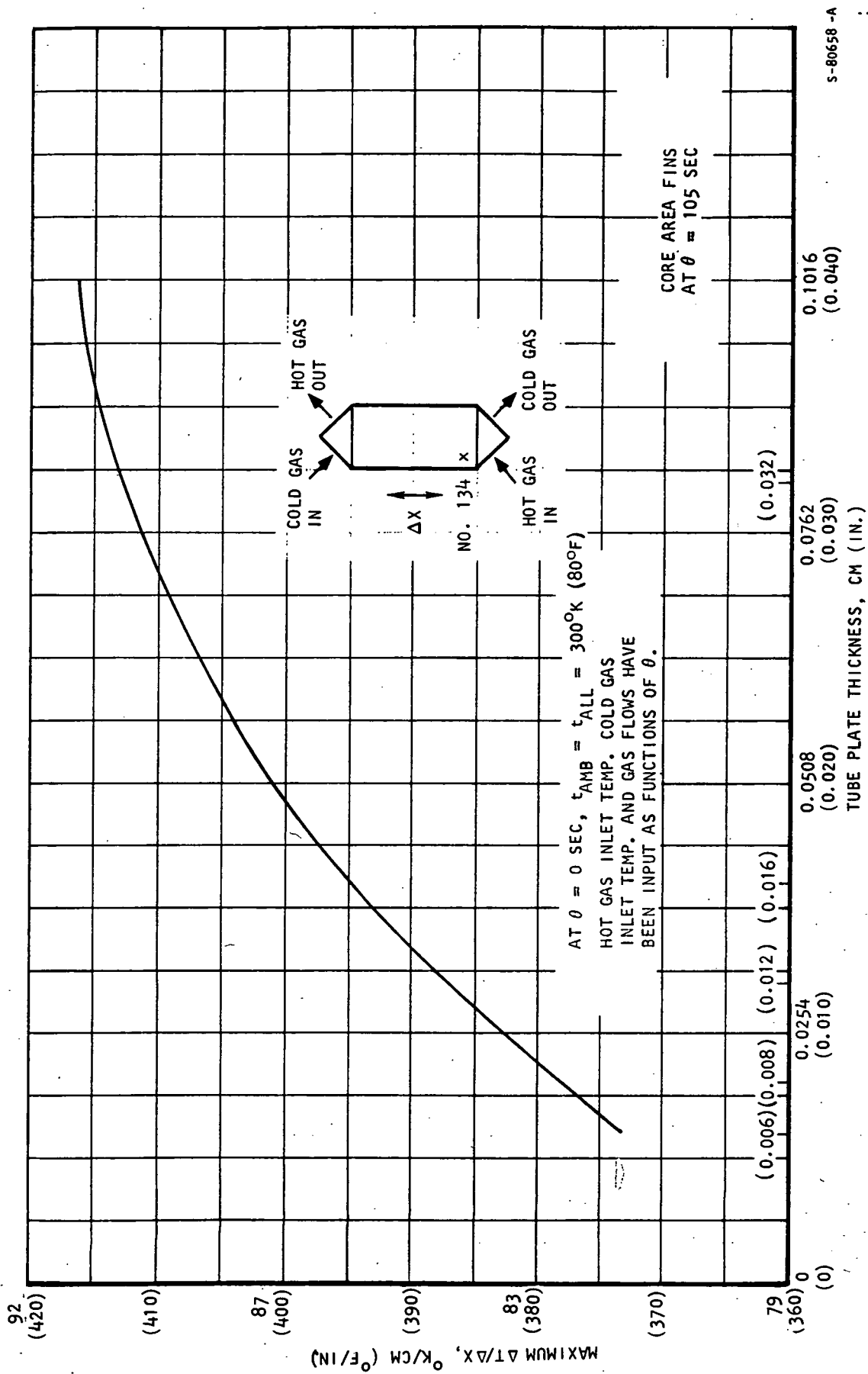
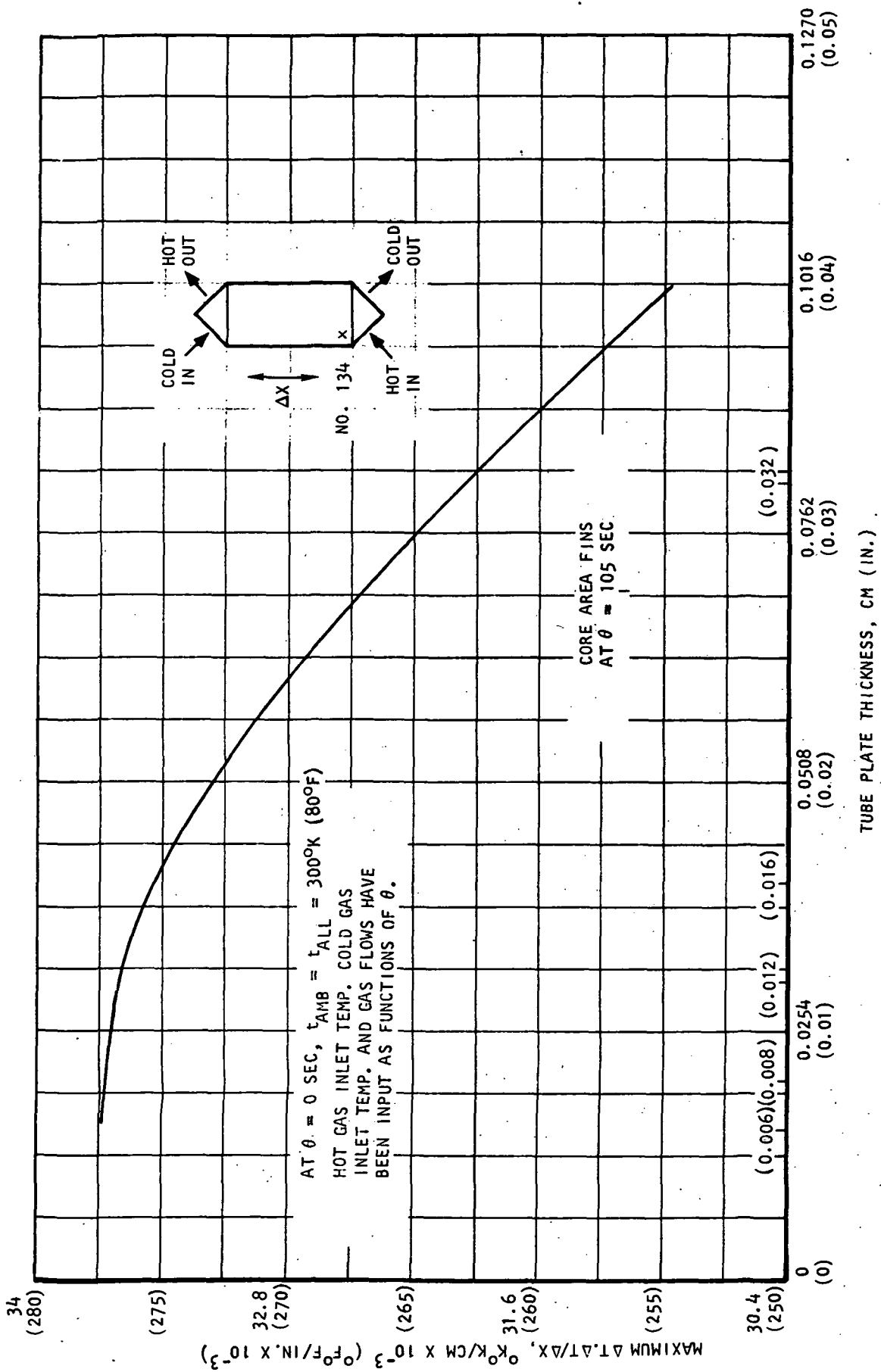


Figure 4-31.--Tube Plate Maximum Thermal Gradient as a Function of Tube Plate Thickness (Time = 105 sec.).



S-80657-A

Figure 4-32.---Tube Plate Maximum Thermal Gradient Factor as a Function of Tube Plate Thickness (Time - 105 sec.).

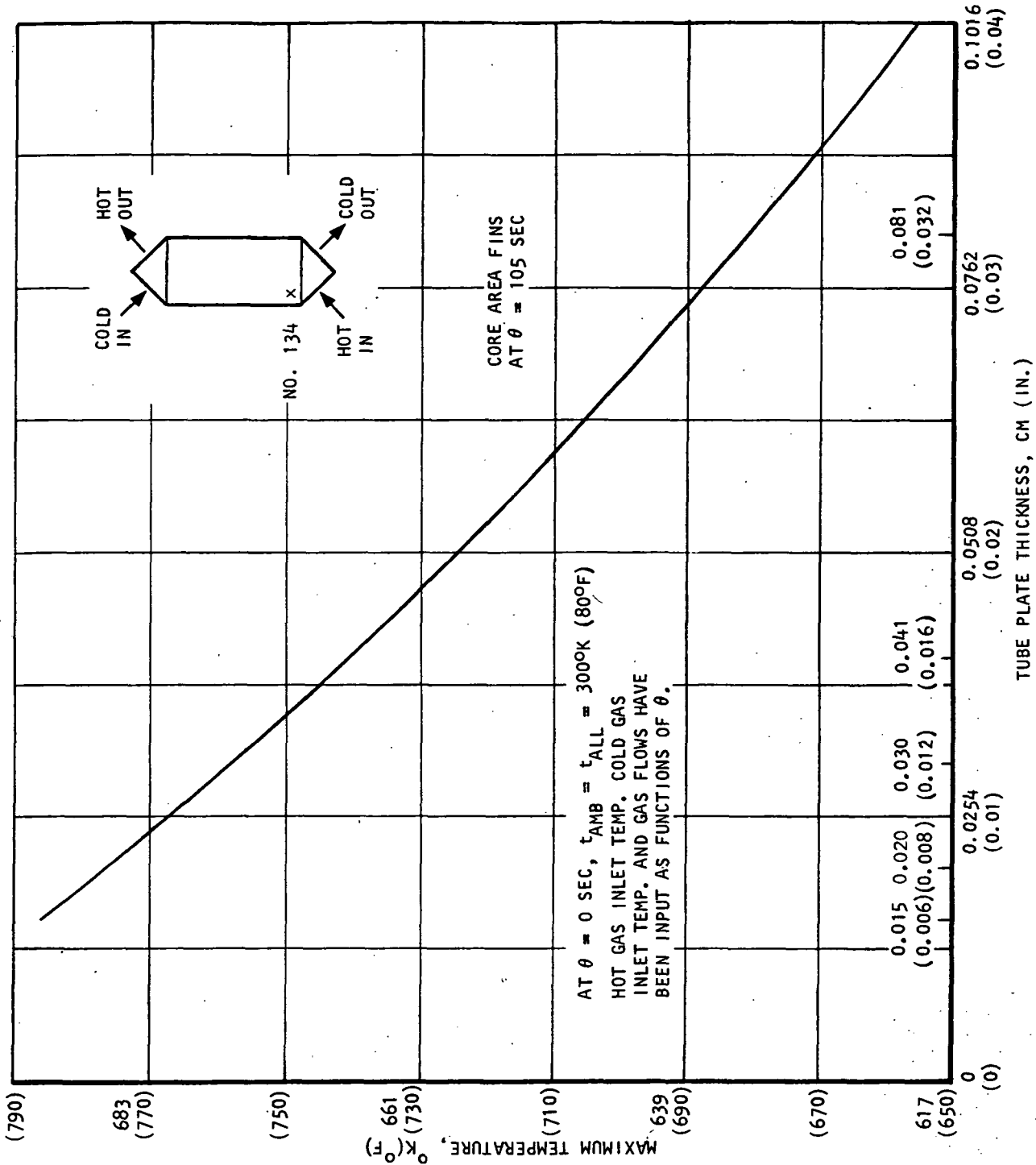
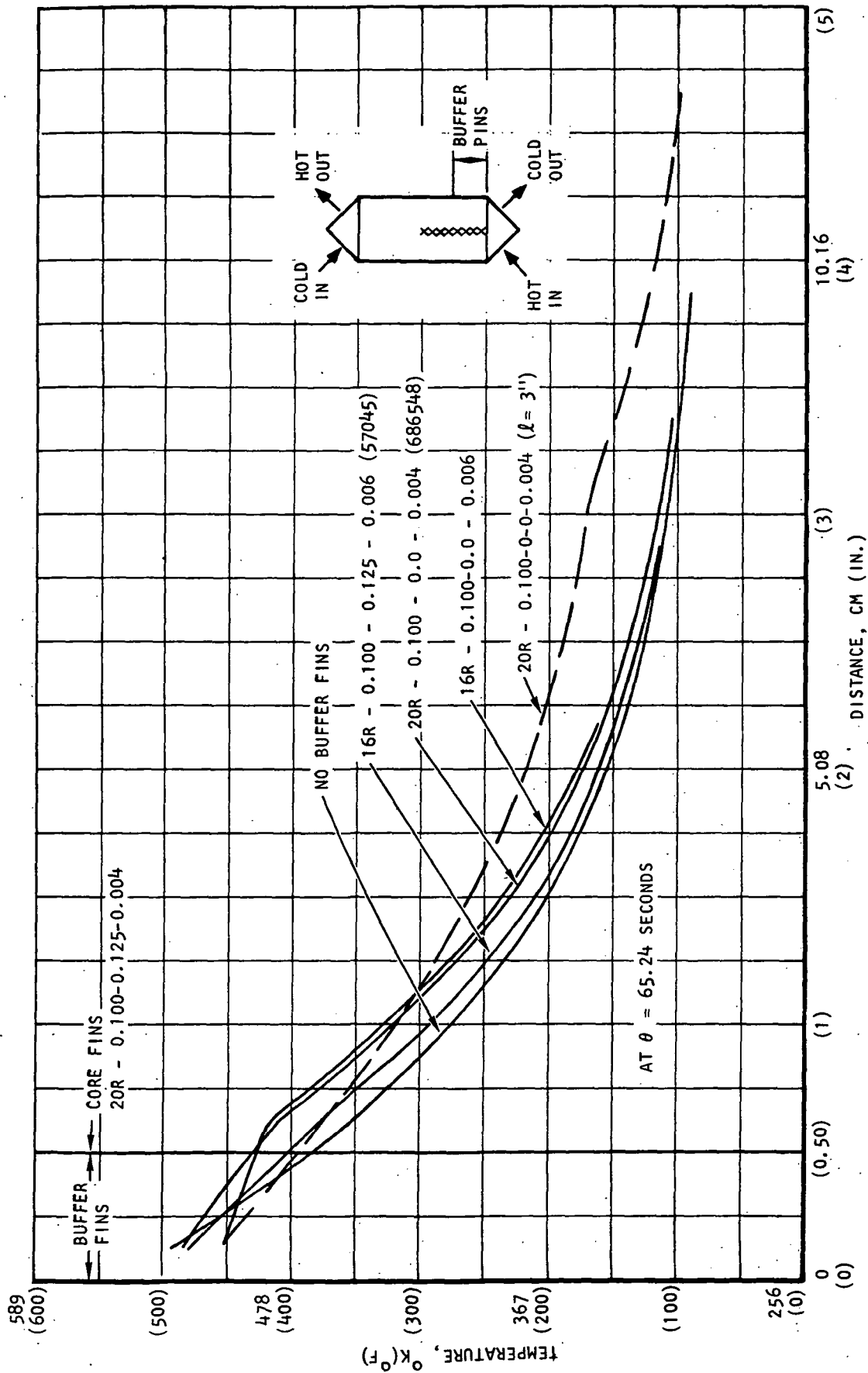
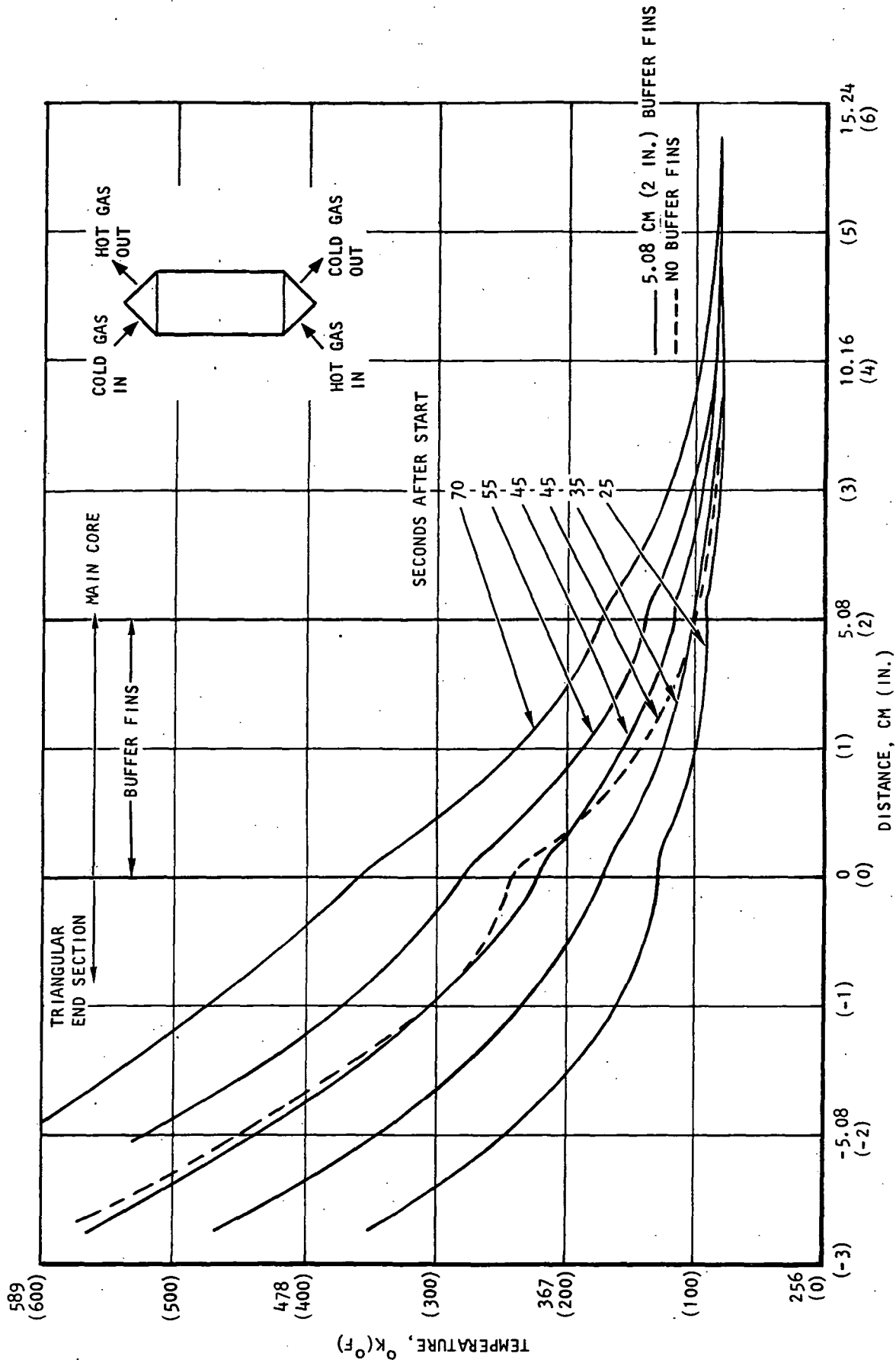


Figure 4-33.--Tube Plate Temperature as a Function of  
Tube Plate Thickness (Time = 105 sec.).



S-80654-A

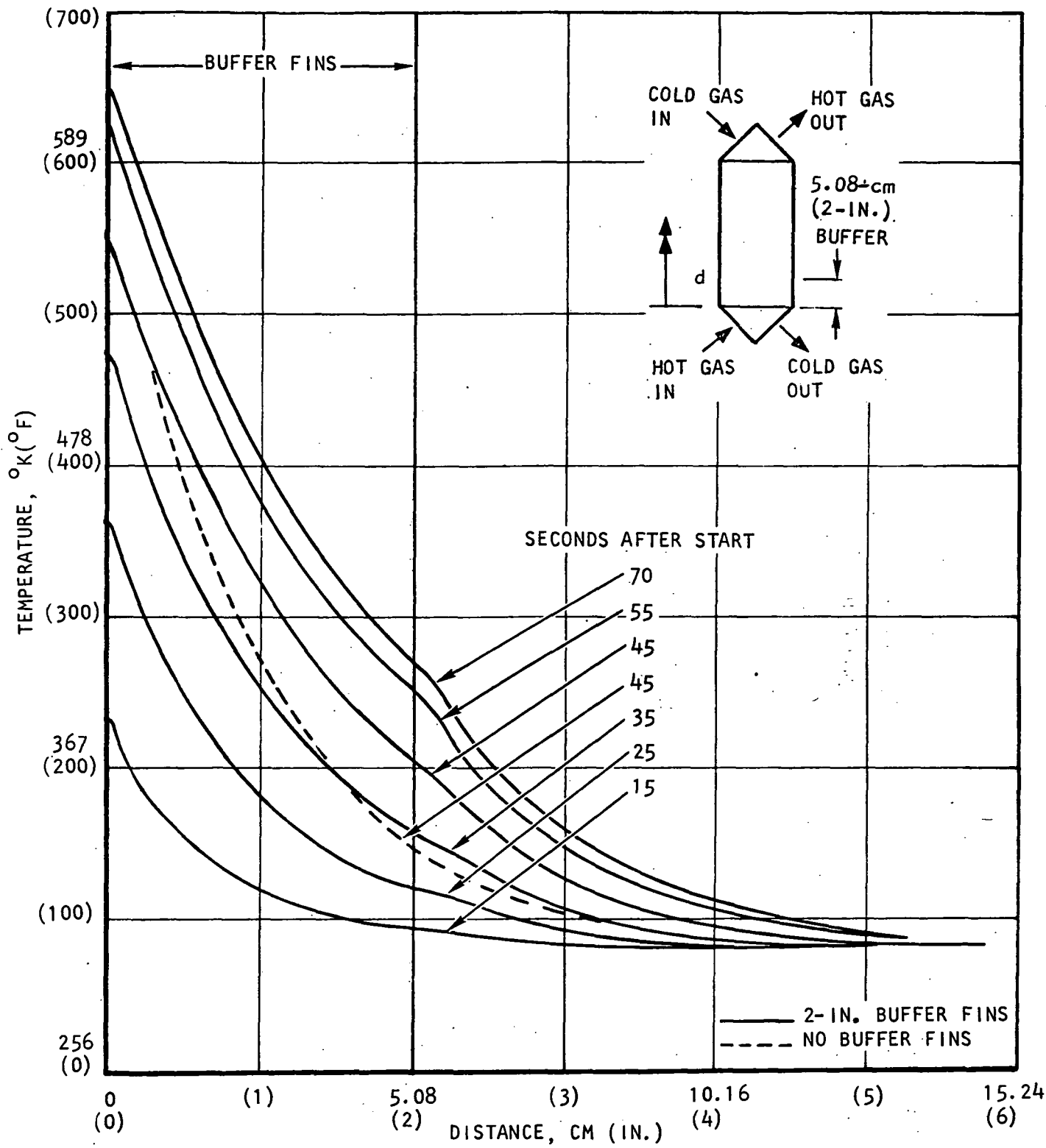
Figure 4-34.--Tube Plate Temperature Variation Using Buffer Fins.



S-80677 -A

Figure 4-35.--Tube Plate Temperature Variation Using Buffer Fins (No Header Bar Effect).





S-80678 -A

Figure 4-36.--Tube Plate Temperature Variation Using Buffer Fins (No Header Bar Effect).

The transient thermal response of the tube plate with the buffer fin did decrease the thermal gradient, but its benefit was negligible in view of the tube plate to header bar thermal response differential and the overall thermal gradient along the axial (flow length) of the tube plate.

Manifold to Header Bar Thermal Analysis.--The manifold to solid header bar thermal response differential was investigated for the purpose of documenting the thermal differential between these two heat exchanger components.

The cases considered are for the manifold flow at the maximum and minimum flow rates which correspond to the ends of the manifold nearest to and furthest from the duct, respectively. These figures are presented in figs. 4-37 through 4-40. The worst thermal response differential between the manifold and the solid header bar occurs for the minimum flow near the hot-gas inlet. For comparison to BHXU-Engine B test data, the nodal point temperatures, fig. 4-41, were plotted approximately 2.5 cm (1.0 in.) away from the interface between the manifold and the header bar, to correspond to thermocouple locations on the Engine B recuperator. A comparison between the two cases was made with the conclusion that the computer transient analysis is in reasonable agreement with the test data. This comparative evaluation can be made since the recuperator submodule starting thermal transient is more severe than the Engine B startup thermal transient.

## STRUCTURAL DESIGN AND ANALYSIS

### Preliminary Design Criteria

This section treats the various structural aspects related to the recuperator preliminary design. The preliminary design of the recuperator establishes basic material selections and the core heat exchanger fin geometry required to satisfy life requirements at the specified operating conditions.

Design Life Criteria.--The operating requirements for the recuperator include a maximum operating temperature 1000°K (1330°F) in the recuperator for a design life of 100 000 hr (approximately 10 yr). For sustained operation at this temperature, the design allowable stress is based upon one-percent creep deformation in 100 000 hr, with the maximum fluid pressure levels specified for the system design point.

The potential short time overpressure condition and fabrication reliability is assured by providing proof and burst pressure test requirements of 150 percent and 250 percent, respectively.

Life requirements further specify that the recuperator must endure 1000 operating cycles without failure. A typical operating cycle is defined as startup of the unit, followed by sustained steady-state operation at the design temperatures and pressure levels and finally, shutdown of the unit until ambient conditions are attained. This requirement serves to define the most severe thermal loads due to transient temperature differences in the recuperator structures. In general, thermal stresses exceeding the

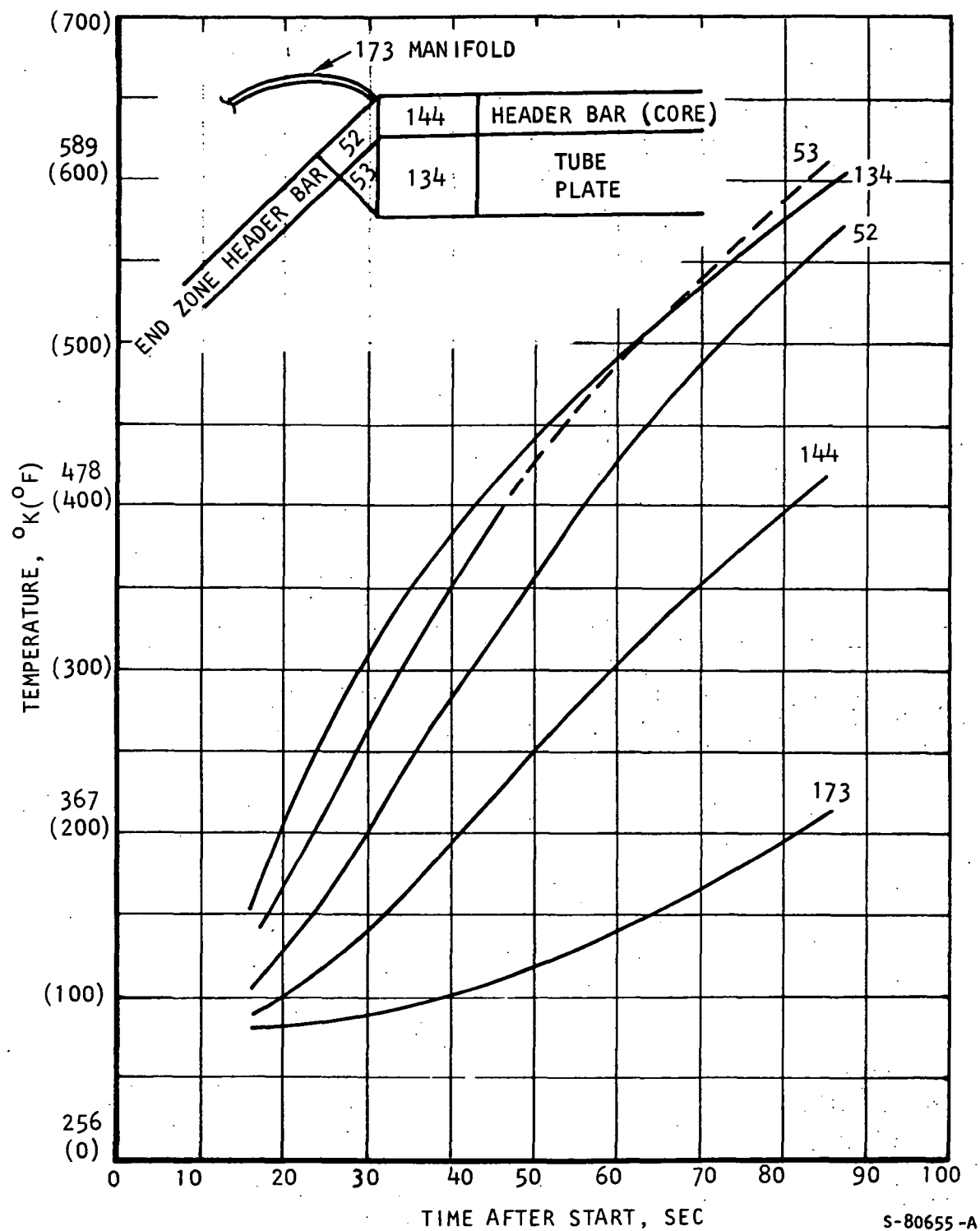


Figure 4-37.--Transient Analyses of Hot Gas Inlet Manifold of Header Bar with Minimum Fluid Flow.

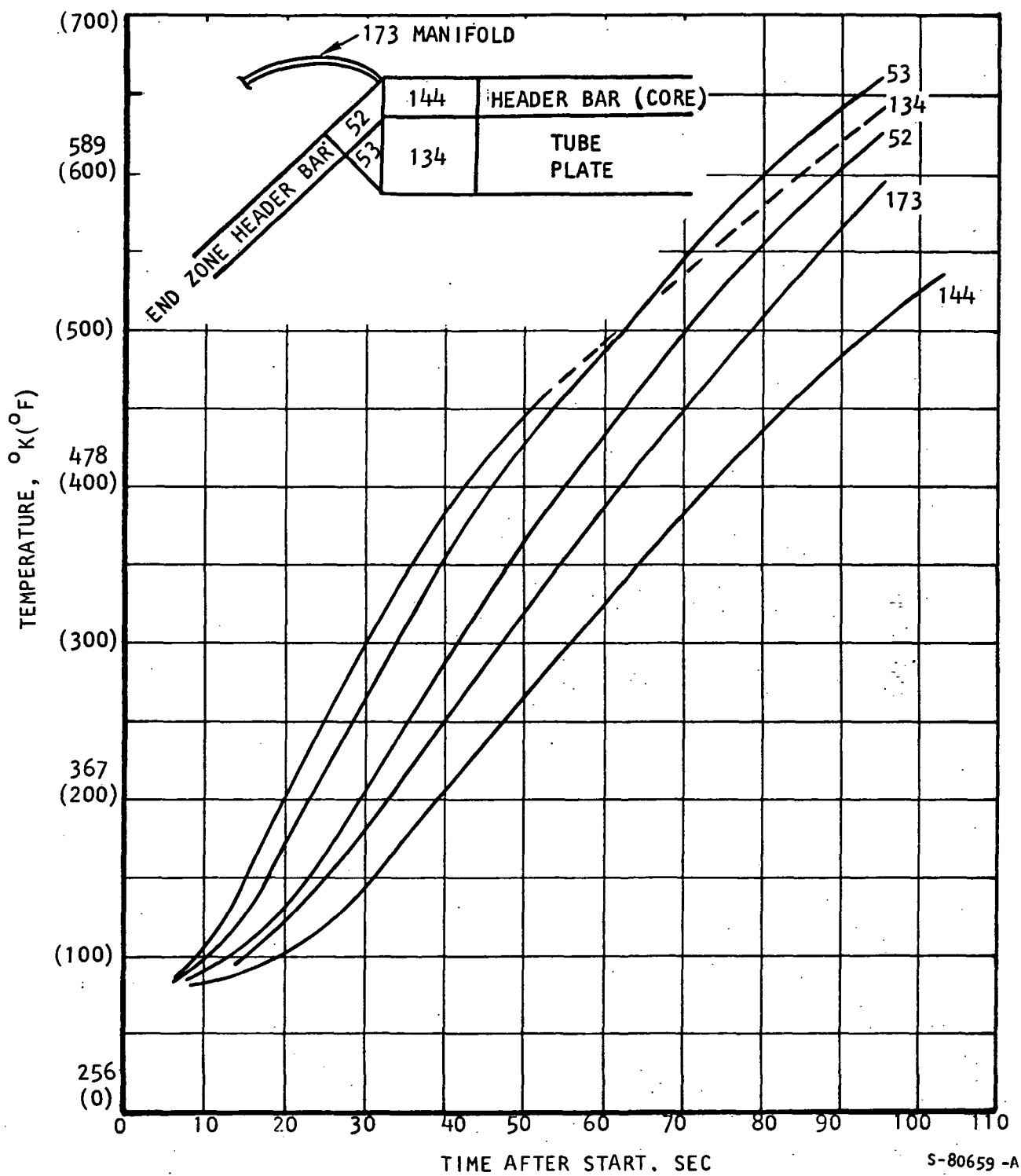


Figure 4-38.--Transient Analyses of Hot Gas Inlet Manifold of Header Bar with Maximum Fluid Flow.

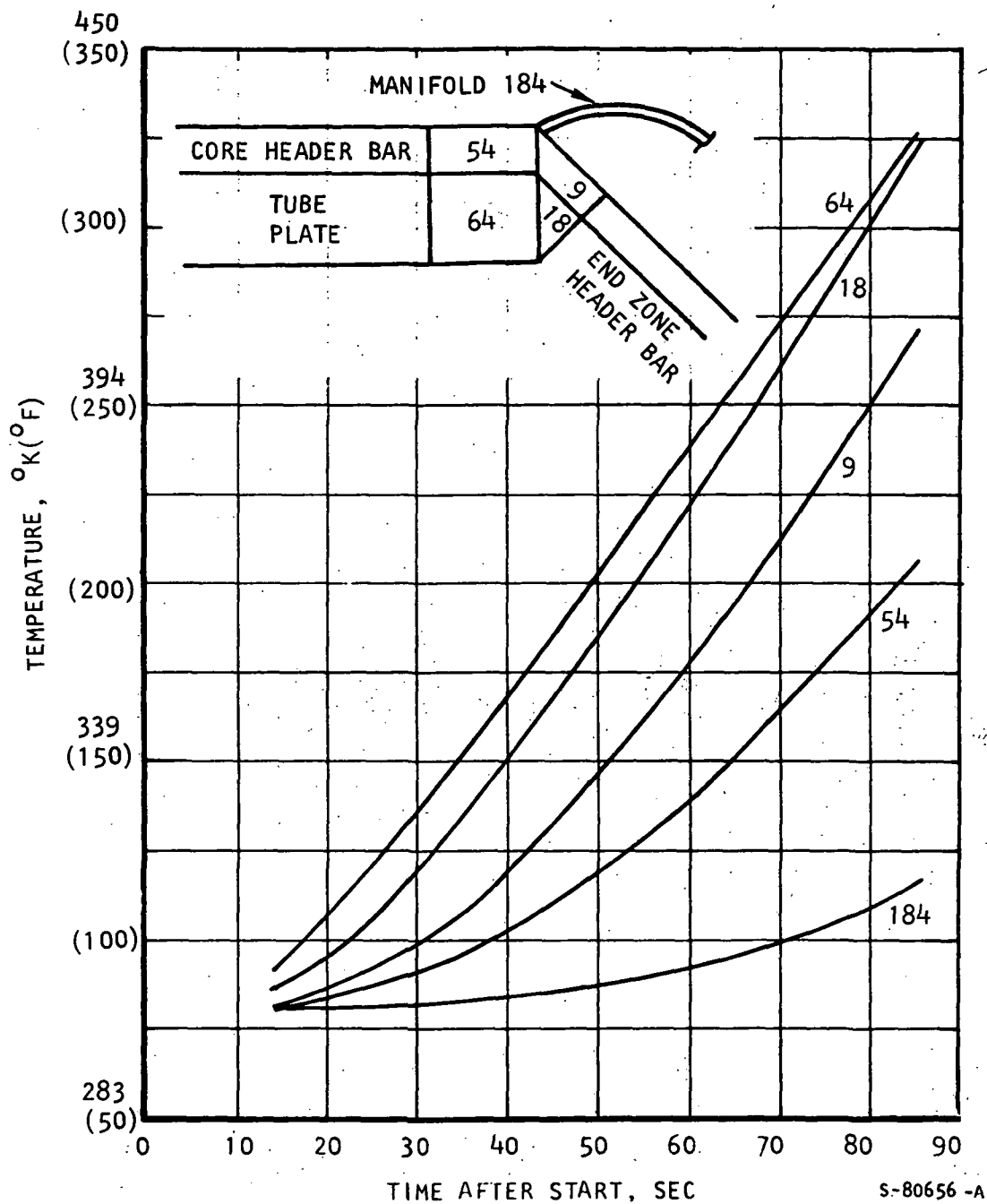


Figure 4-39.--Transient Analyses of Cold Gas Outlet Manifold to Header Bar with Minimum Fluid Flow.

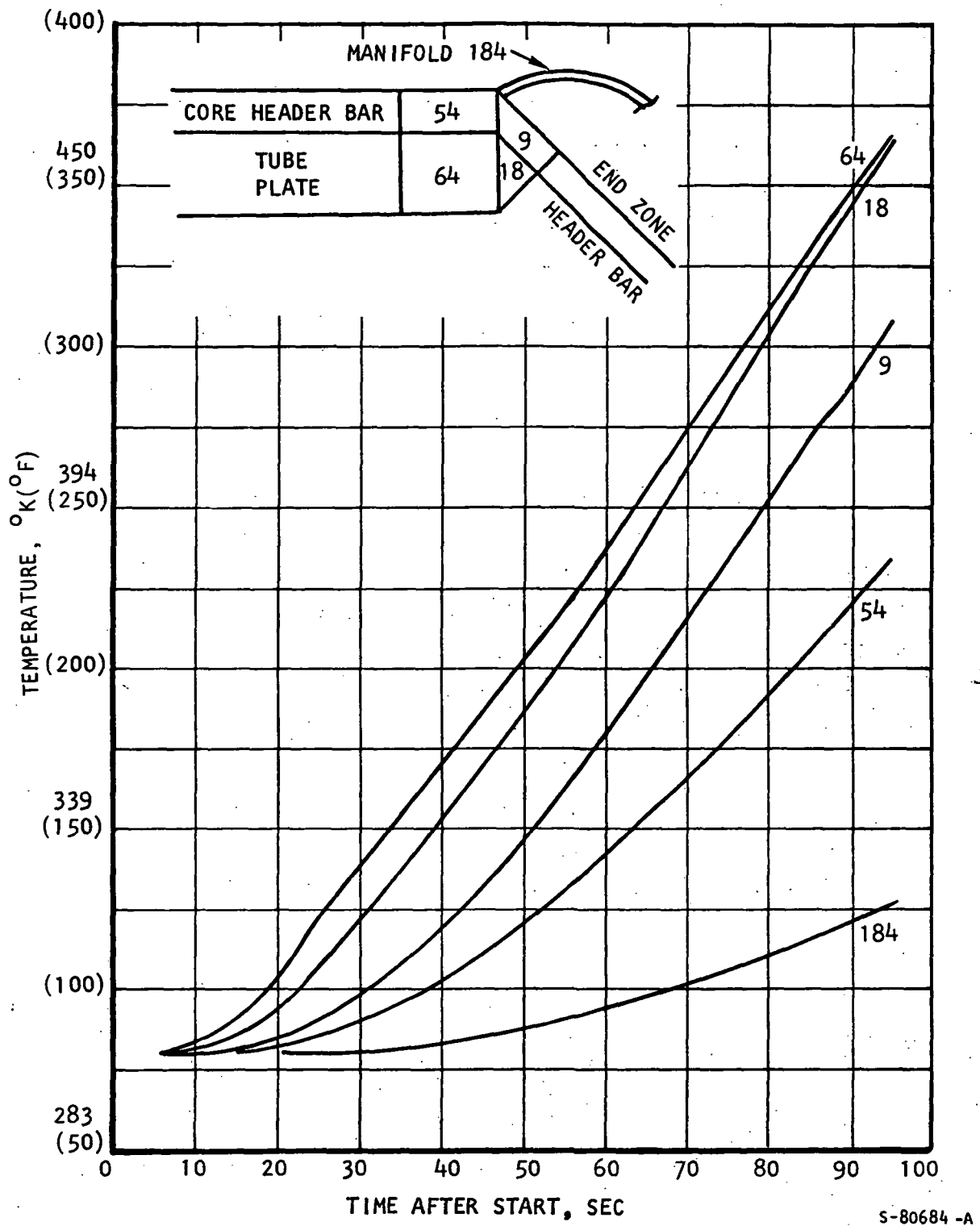


Figure 4-40.--Transient Analysis of Cold Gas Outlet Manifold to Header with Maximum Fluid Flow.

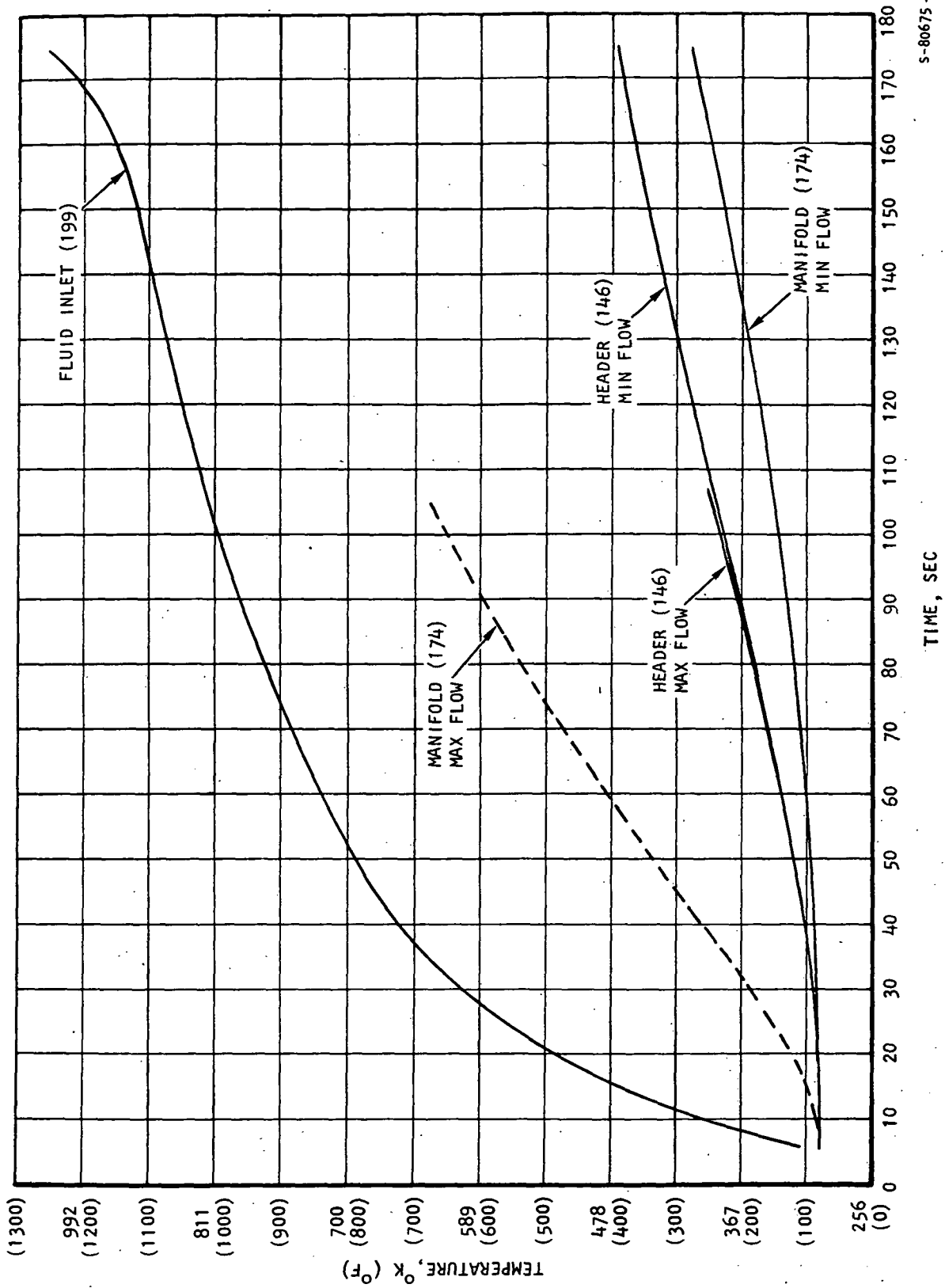


Figure 4-41.---Transient Analysis of Hot Gas Inlet Manifold to Header Bar 2.5 cm (1 in.) from Joint Interface.

S-80675 -A

material yield strength cannot be completely avoided due to the required startup and shutdown conditions. Preliminary cyclic fatigue life is estimated by considering the relation between the accumulated plastic strain per cycle and critical plastic strain necessary to cause initiation of a crack in the recuperator structures.

Inertia loads may be experienced during any phase of the operating cycle. The mounting brackets must, therefore, be designed to endure the required inertia loads at the elevated temperature design condition. The maximum inertia loads occur for a relatively short time duration, such as vehicle launch and, therefore, short time material properties are used for this requirement.

A summary of the design life criteria and the specified operating conditions for the recuperator design point is shown in table 4-5.

Allowable Stresses for Internal Pressure Design.--The standard design practice employed by AiResearch is to design the pressure carrying structure for proof pressures of 1.5 times the working pressures and for burst pressures of 2.5 times the working pressures. The structure must not yield at proof pressure or rupture at burst pressure. This implies that the proof pressure is the governing design condition if the ratio of yield stress to ultimate stress is less than 0.6 and that the burst pressure will govern if the ratio is greater than 0.6. The allowable stress at working pressure is, therefore, the lesser of the following:

$$\sigma_{all} = (f_{tu})/2.5 \quad (4-1a)$$

$$\sigma_{all} = (f_{ty})/1.5 \quad (4-1b)$$

When the limiting stress is due to bending, a small amount of yielding can be allowed in the outermost fibers, which leads to a modified stress distribution through the thickness. The ideal plastic bending moment is 1.5 times the computed elastic bending moment for the same peak stress. Accordingly, the allowable indicated elastic stress due to bending loads is taken to be 1.5 times the allowable values in equation (4-1a).

Inertia and Vibratory Load Criteria.--The recuperator is designed for inertia and vibratory loads as specified for the NASA environmental specification for the HXDA system. However, since the recuperator mounting studies were not completed at the time of the preliminary design analysis, the inertia loading shown in table 4-6 was assumed for the heat exchanger internal structures. The design allowable stresses for inertia loads are determined from the short time material properties using equation (4-1a).



TABLE 4-5

## RECUPERATOR PRELIMINARY DESIGN CRITERIA

## (a) Design Life Criteria

Life Requirements	Condition	Stress Criteria
100 000 hr (10 yr)	Maximum temperature and pressure	Total distortion does not exceed 1 percent creep
1000 cycles	Transient startup and shutdown cycle	Accumulated plastic strain is less than critical failure strain
Proof pressure test	150 percent over-pressure for short time	Stresses must be less than material yield strength
Burst pressure test	250 percent over-pressure for short time	Stresses must be less than material ultimate strength
Inertia loading	150 percent load factor for short time	Stresses must be less than material yield strength

## (b) Operating Conditions at Design Point

Fluid Circuit	Conditions	Design Point
Low-pressure side	Inlet temperature	1000°K (1332°F)
	Inlet pressure	494 kN/m <sup>2</sup> (71.7 psi)
High-pressure side	Inlet temperature	380°K (225°F)
	Inlet pressure	732 kN/m <sup>2</sup> (106.2 psi)

TABLE 4-6  
PRELIMINARY INERTIA AND VIBRATION LOAD CRITERIA

Direction	Type	Load Factor	Combined Load Factor
Longitudinal	Vibration	8g	24g
	Shock	10g	
	Acceleration	6g	
Lateral	Vibration	8g	20g
	Shock	10g	
	Acceleration	2g	

Allowable Thermal Fatigue Stresses.--The magnitude of thermal stress due to temperature developed during the rapid heat-up cycle of the system results in plastic deformations in various components, particularly in the hot operating regions. The minimum operating life requirement of the unit is 1000 thermal cycles. A minimum design life of 4000 cycles is used to ensure that the 1000-cycle life is achieved. The design analyses are based on the accumulated plastic strain approach for estimating fatigue life.

At temperatures where creep is not a factor, the allowable strain is based on the Manson method (ref. 4-3) for computing fatigue life based on the accumulated plastic strain. The cycle life,  $N$ , is related to the plastic strain range,  $\epsilon_p$ , by

$$N = (C/\epsilon_p)^{1.67} \quad (4-2)$$

where  $C$ , the ductility constant, is based on material reduction-in-area properties,  $RA$ , by the relation

$$C = \left\{ \ln \left[ 100 / (100 - RA) \right] \right\}^{0.6}$$

The fatigue damage per cycle for a single strain level is therefore

$$\Delta\Phi_F = (\epsilon_p/C)^{1.67} \quad (4-3)$$

The allowable strain for a given life can be obtained directly from this equation when  $C$  is known.

Cumulative effects for different load cycles during the material life are handled by a fatigue damage rule similar to Miner's rule. In addition, since both creep and fatigue are occurring simultaneously, the effects of the two material damage phenomena are important.

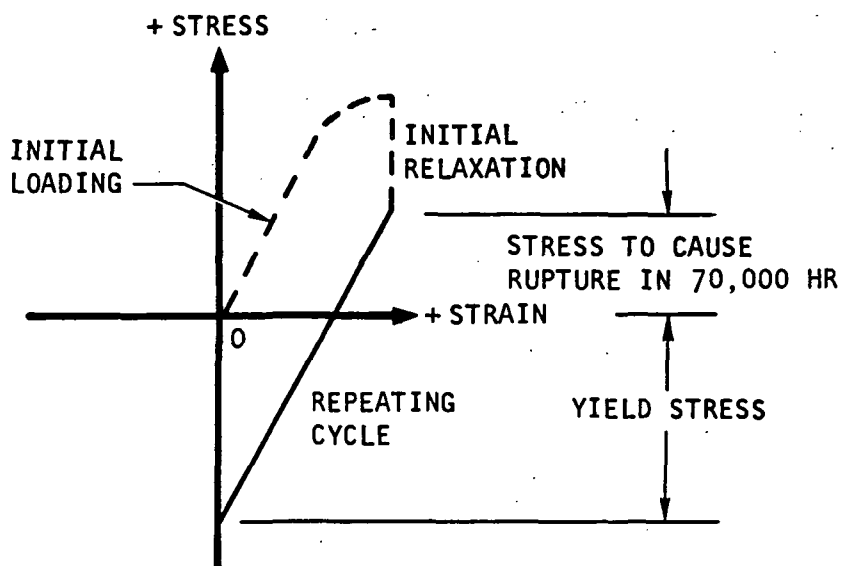
Accumulated creep damage can be divided into two types: (1) creep during a cycle characterized by continuously varying stresses and strains, and (2) repetitive creep relaxation during extended times at constant applied strain. Of the two types, the accumulated damage due to repetitive creep relaxation is the most serious since the accumulated time under the applied constant strain may be nearly equal to the service life of the unit. Therefore, even though the stress steadily decreases during each interval of relaxation, the integrated damage cannot exceed that due to the acceptable constant stress applied for the 100 000-hr service life. Since the amount of relaxation becomes relatively small as the acceptable steady stress is reached, the allowable maximum repeating stress is approximately equal to this acceptable steady stress level. A repeating cycle that avoids this repetitive relaxation damage can be achieved by limiting the applied total strain, or applied apparent elastic stress, to the sum of the yield stress (strain) and the acceptable stress (strain) for 1-percent elongation in 100 000 hr. The allowable total strain is then

$$\epsilon_{all} = (\sigma_y + \sigma_{1\% \text{ in } 100\,000 \text{ hr}})/E \quad (4-4)$$

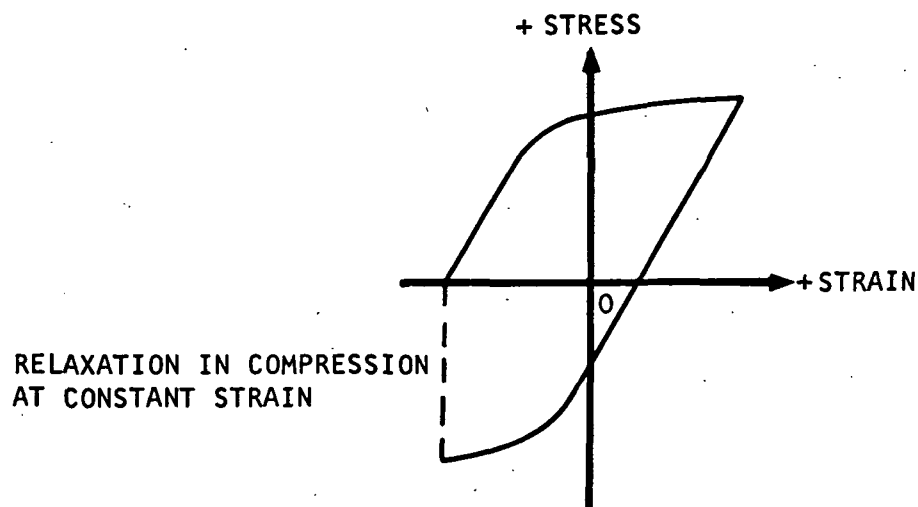
where  $E$  is the material elastic modulus. The acceptable cycle, shown in fig. 4-42, is preceded by an initial loading and stress relaxation at constant (maximum) strain. In subsequent cycles the material stress-strain history follows the elastic line from the yield stress at shutdown (cold) to the stress for 1 percent creep deformation (hot). The safety factor achieved by using this criteria will generally not be calculated; however, use of minimum yield values, stress to 1 percent elongation rather than rupture, and ignoring the small tolerable amount of relaxation at stresses above the acceptable steady-state level represent an acceptable margin of safety.

The above approach applies for either tensile or compressive sustained holds at elevated temperatures. However, recent work by Cooper (ref. 4-4) and Halford (ref. 4-5) indicates that compressive stresses are not damaging during constant strain or constant stress applications. This suggests that a second criterion be used when sustained tensile stresses are not present (bending loads are therefore excluded). The allowable repetitive strain can then be considerably greater than that given by equation (4-4), but noticeably lower than the fatigue estimate due to the presence of accumulated creep damage. The damage can be estimated for a stress-strain cycle such as shown in fig. 4-42b where no damage is attributed to a compressive relaxation if it exists. Good agreement of tests and estimates based on available engineering creep data have been obtained by Spera (refs. 4-6 and 4-7) and also from recent work at AIRESEARCH for NASA Langley (ref. 4-8). For a single stress-strain loop the following expression was evaluated to analytically determine the cycle damage fraction (overtemperature capability was again included)

$$\Delta\Phi_c = \int_0^t \frac{dt}{t_r} \quad (4-5)$$



- a. REPEATING CYCLE (SOLID LINE) TO AVOID REPETITIVE RELAXATION DAMAGE IN TENSION



- b. STABILIZED STRAIN LOOP WITH RELAXATION IN COMPRESSION (DAMAGE CALCULATED DURING CYCLE SHOWN BY SOLID LINE)

S-65000 -A

Figure 4-42.--Typical Stress-Strain Cycles Illustrating Creep Damage Conditions.

Material Properties.--Physical and mechanical properties of the two candidate materials considered, Hastelloy X and Type 347 stainless steel, are shown in table 4-7. The allowable design stresses for the candidate materials were obtained by use of the design life criteria and are shown in table 4-8.

### Core Structural Analysis

A preliminary structural analysis was performed to establish the basic plate-fin heat exchanger structural integrity in conjunction with optimum heat transfer performance. By use of the structural design criteria, fin density, fin thicknesses, and tube plate thicknesses were established to satisfy the design point fluid conditions for the required operational life. The plate-fin recuperator with triangular end sections is shown schematically in fig. 4-43.

Pressure Containment Analysis.--When an internal pressure is applied to a plate-fin structure such as that shown in fig. 4-43, it will behave in a manner similar to a clamped edge beam on an elastic foundation. The deformed surface shows that the maximum deflection is greater than the load per fin ( $q$ ) divided by the fin spring rate ( $k$ ). The percentage fin overload due to the elastic foundation was constant for the range of thickness analyzed and was found to be 4.2 percent of the deflection predicted by equation (4-6a) (see fig. 4-44). The location of the maximum deflection changes for different sheet thicknesses and moves toward the center of the span for sheets of increasing thickness (see fig. 4-45). It is possible that the thickness could be increased to such an extent that the fin overload phenomena would not develop.

A discrete model analysis of the continuous system was used to determine the deflection shape. The model is shown in fig. 4-46 and the formulas used to determine various quantities are shown below.

Central fin deflection (fully developed)

$$y_c = q/k \quad (4-6a)$$

where  $q = p \times \frac{(1-n-t_f)}{n} \quad (4-6b)$

and

$$k = \frac{t_f E}{h_f - t_f} \quad (4-6c)$$

Flexural stiffness

$$D = \frac{E t_{eq}^3}{12(1-\nu^2)} \quad (4-6d)$$

where  $t_{eq} = t_s + \frac{1}{2} t_f + \frac{1}{2} t_b \quad (4-6e)$

$$\beta = \frac{\lambda}{2} \sqrt{\frac{k}{4D}} \quad (4-6f)$$

TABLE 4-7  
CANDIDATE MATERIALS PHYSICAL AND MECHANICAL PROPERTIES

a. Hastelloy X <sup>⑤</sup>.

Temperature °K	E, MN/m <sup>2</sup> (ref. 4-9)	$\alpha$ , cm/cm-°K (ref. 4-9)	① RA Percent (ref. 4-8)	Yield Stress, MN/m <sup>2</sup>		Ultimate Stress, MN/m <sup>2</sup> (ref. 4-10)	② Stress for 1 Percent Creep in 100 000 Hr, MN/m <sup>2</sup> (ref. 4-10)
				S Basis (ref. 4-9)	Typical (ref. 4-10)		
290	200 × 10 <sup>-6</sup>		34	310	360	790	
370	200			290			
480	190	14.0 × 10 <sup>-6</sup>		260	340	710	
590	180	14.4		250	300	690	
700	170	14.7		240	300	690	
810	170	15.1		220	290	650	230
870							150
920	150	15.5	32 <sup>③</sup>	210	280	570	93
980							59
1030		15.9	40 <sup>④</sup>	180	260	430	37
1090							

NOTES: (1) Minimum tested value, obtained for 0.025 cm sheet.  
 (2) Values are lower than typical values quoted in the reference.  
 (3) Tested at 1000°K.  
 (4) Tested at 1100°K.  
 (5) Density, 8.2 g/cm<sup>3</sup>

b. Type 347 Stainless Steel <sup>①</sup>

Temperature °K	E, MN/m <sup>2</sup> (ref. 4-11)	$\alpha$ , cm/cm-°K (ref. 4-11)	RA Percent (ref. 4-11)	Yield Stress, MN/m <sup>2</sup>		Ultimate Stress MN/m <sup>2</sup> (ref. 4-11)	Stress for 1 Percent Creep in 100 000 Hr, MN/m <sup>2</sup> (ref. 4-11)
				A Basis (ref. 4-12)	Typical (ref. 4-11)		
290	190 × 10 <sup>-6</sup>	16 × 10 <sup>-6</sup>	69	200	230	620	
370	190	16	73	190		560	
420				170	210		
480	180	17	75	160		490	
530				160	190		
590	170	18	73	160		470	
640				150	170		
700	160	18	69				
1000	140	20	70	125	145	269	17.2

NOTES: (1) Density, 8.26 g/cm<sup>3</sup>

TABLE 4-8

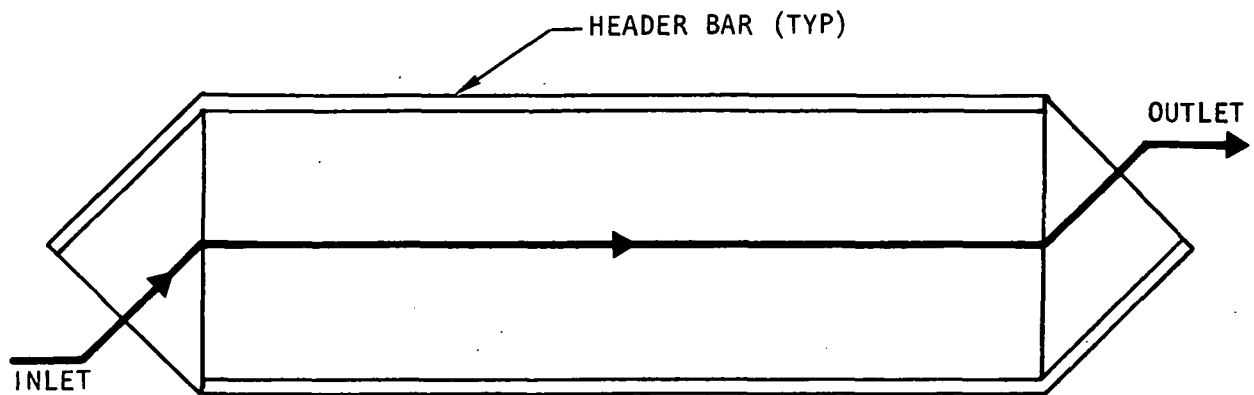
## MATERIAL ALLOWABLE DESIGN STRESSES AT 1000°K

Candidate Material	Allowable Stress for Sustained Operation (100 000 Hr)		Allowable Stress for Short-Time Operation	
	Direct Stress, MN/m <sup>2</sup> (psi)	Bending Stress, MN/m <sup>2</sup> (psi)	Direct Stress, MN/m <sup>2</sup> (psi)	Bending Stress, MN/m <sup>2</sup> (psi)
Hastelloy X	34.4 (5000)	51.6 (7500)	172.0 (25 000)	258.0 (37 500)
Type 347 stainless steel	17.2 (2500)	25.8 (3750)	89.5 (13 000)	114.0 (16 500)

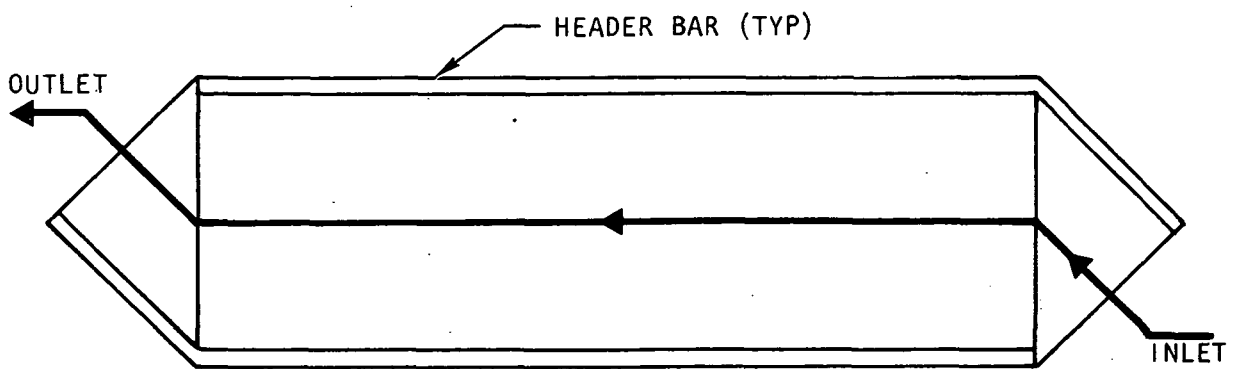
Definitions of symbols used in the preceding equations are as follows:

- $y_c$  central deflection
- $q$  load/fin
- $p$  pressure
- $n$  number of fins/in.
- $k$  spring rate of fins
- $t_f$  thickness of fins
- $t_b$  thickness of brazing alloy
- $t_s$  equivalent thickness
- $h$  height of fins
- $\nu$  Poissons ratio
- $E$  modulus of rigidity
- $l$  length of span

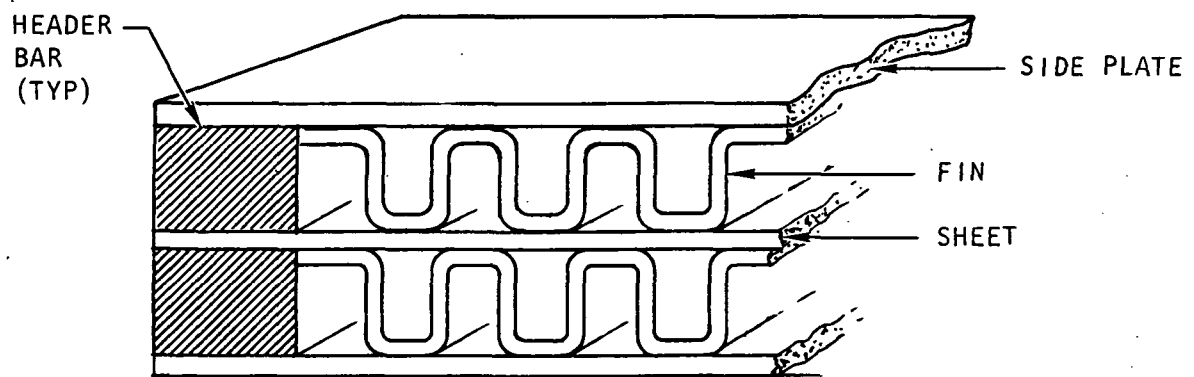
The parameter  $q l^4/64 D\beta^4$  plotted in fig. 4-44 is a modification of the parameter associated with the deflection of a beam on fin elastic foundation per Timoshenko "Plates and Shells." This fin overload factor together with fin imperfection factors due to fabrication are all combined into a fin efficiency factor ( $f$ ) for the fin stress calculation described below.



a. LOW PRESSURE FLUID CIRCUIT



b. HIGH PRESSURE FLUID CIRCUIT



c. PLATE-FIN GEOMETRY

S-77094

Figure 4-43.--Plate-Fin Recuperator with Triangular End Sections.



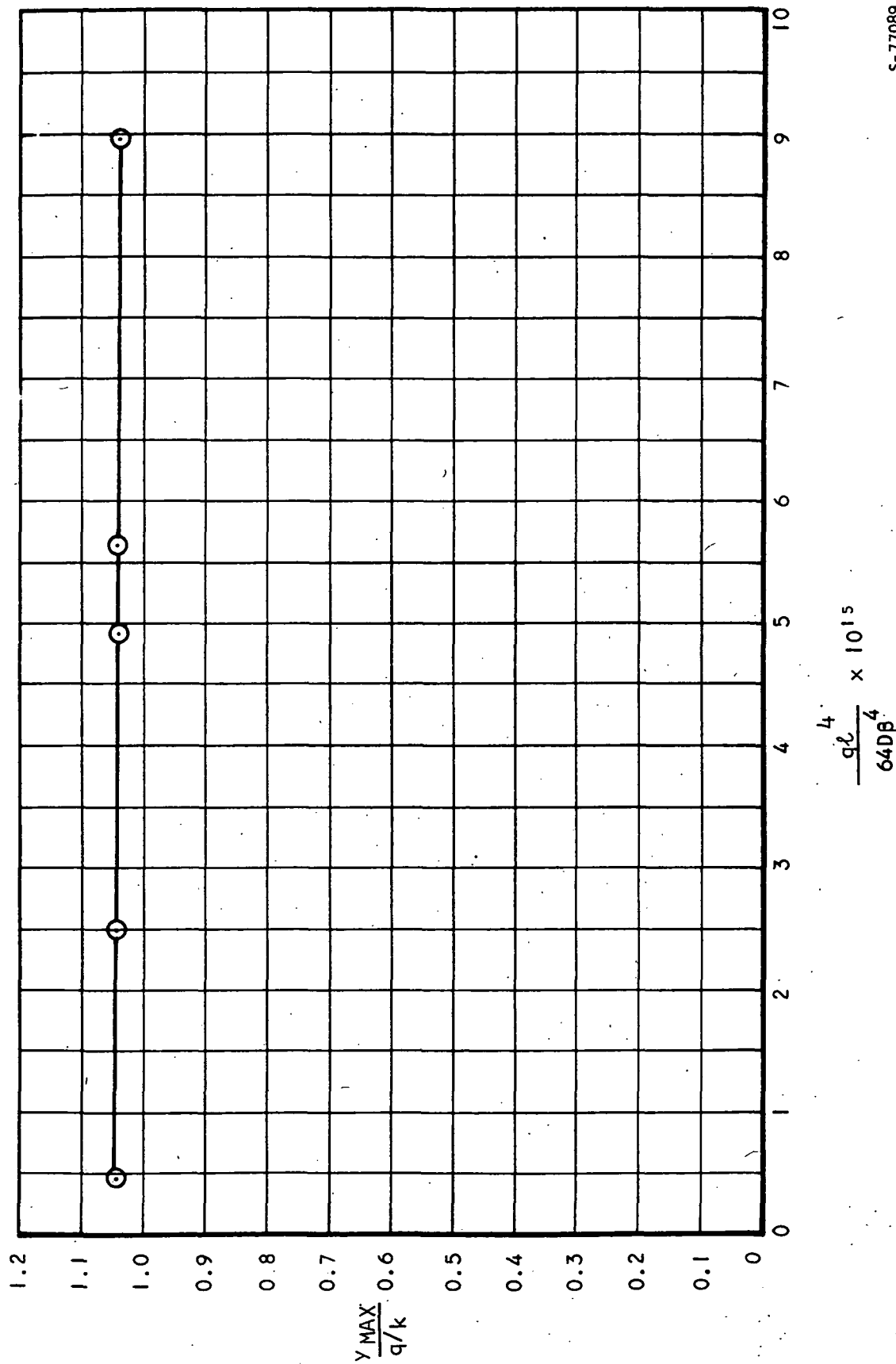
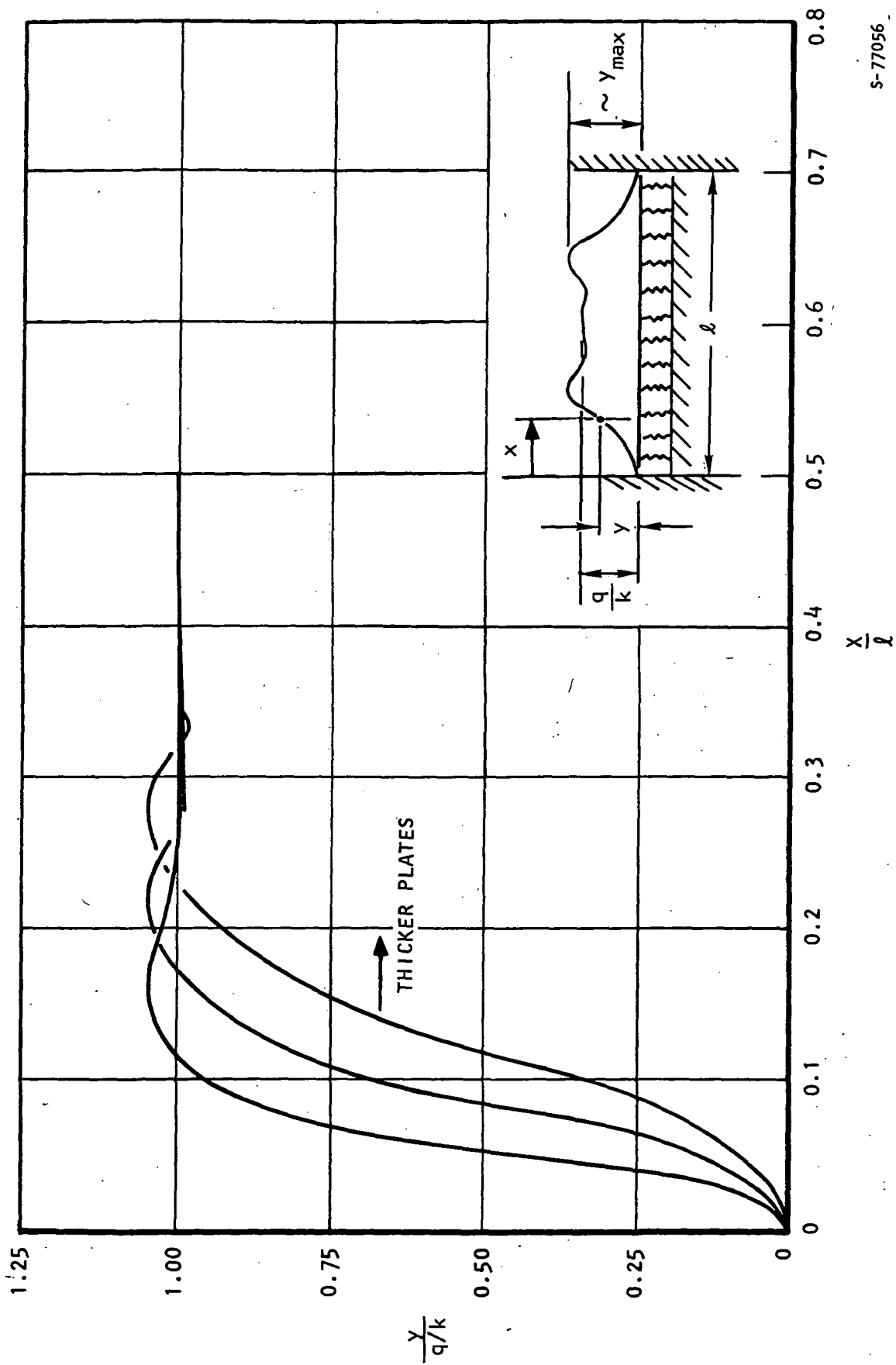
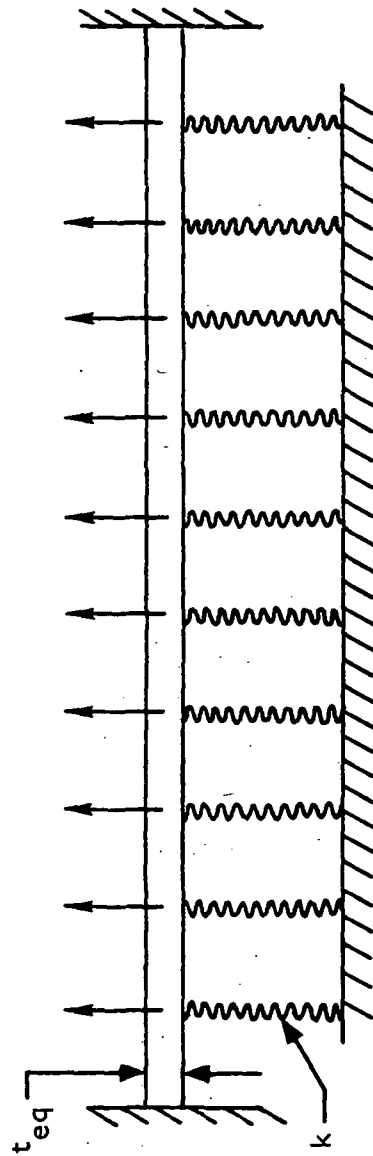
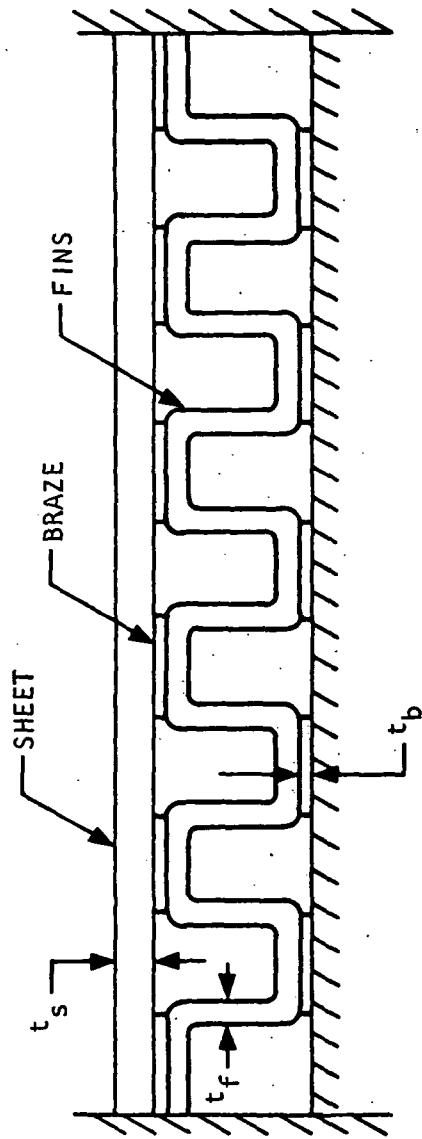


Figure 4-44.--Deflection Overshoot for Various Sheet Thicknesses.



S-77056

Figure 4-45.---Deflection Shape for Several Plate Thicknesses.



S-77091

Figure 4-46.--Model for Determining Deflection Shapes.

Fin tensile stress due to internal pressure is computed from the following formula:

$$\sigma_{fin} = \frac{p}{f} \left( \frac{b_{fin} - t_{fin}}{t_{fin}} \right) \quad (4-7)$$

where  $p$  = internal pressure

$b_{fin}$  = fin spacing

$t_{fin}$  = fin thickness

$f$  = fin strength efficiency factor

Fin strength efficiency factors have been found to range from 0.33 to 0.60 based upon actual test results on a wide variety of plate and fin configurations. The 0.33 factor is used in creep designs and 0.60 is used in short time load situations. The strength efficiency factor is defined as the ratio of actual burst pressure to burst pressure as calculated from ultimate stress properties. The apparent reduction in strength is attributable to non-uniform load distribution across the fins that arises due to inequality in fin height. The taller fins actually buckle during the braze operation and, as a consequence, the shorter fins carry the bulk of the pressure containment forces. Since the fins are never perfectly straight, pressure loads will also cause fin bending stresses. Finally, the fins cannot be formed with perfectly square corners, and stress concentrations will actually occur at the fin-to-plate braze fillet joints. This strength reduction factor is based upon the performance of successfully brazed heat exchangers, i.e., the failure mode at burst is tensile rupture of the fins. For poorly brazed heat exchangers, (incomplete braze joining of the fins and plates), the pressure containment capability of the plate-fin structure is drastically reduced. For this reason, all heat exchangers are subjected to a proof pressure test at 150 percent of working pressure. This proof test is expected to cause a failure in defective cores, and conversely, a unit that passes the proof test is expected to achieve the required pressure capability.

Maximum plate bending stress is given by the following formula for a fixed ended plate under uniform normal pressure:

$$\sigma_{plate} = \frac{p}{2} \left( \frac{b_{fin} - t_{fin}}{t_f} \right)^2 \quad (4-8)$$

where  $t$  = plate thickness

In the core section of the recuperator, a rectangular offset fin was selected with a density of 7.87 fins/cm (20 fins/in.) and a thickness of 0.102 mm (0.004 in.) for both high-pressure and low-pressure fluid circuits. In the triangular end sections, a plain rectangular fin was selected with a density

of 6.30 fins/cm (16 fins/in.) and a thickness of 0.152 mm (0.006 in.) for both high-pressure and low-pressure fluid circuits.

For the selected fin geometry, the maximum stress in the core is

$$\sigma_{fin} = \frac{P}{f} \frac{0.127 (0.050) - 0.0102 (0.004)}{0.0102 (0.004)} = 11.5 \frac{P}{f} \quad (4-9)$$

and the maximum stress in the ends is

$$\sigma_{fin} = \frac{P}{f} \frac{0.159 (0.0625) - 0.0152 (0.006)}{0.0152 (0.006)} = 9.4 \frac{P}{f} \quad (4-10)$$

The recuperator fin-creep stress and the appropriate margin of safety for each candidate material are summarized in table 4-9. Hastelloy X was selected over Type 347 stainless steel material as a result of the fin-creep requirement. Obviously, Hastelloy X is far better suited for the recuperator design considering the additional inertial load requirements.

TABLE 4-9  
FIN-CREEP STRESS SUMMARY

Location	Fluid Circuit	Calculated Creep Stress, MN/m <sup>2</sup> (psi)	Margin of Safety*	
			Type 347	Hastelloy X
Core	High pressure	25.5 (3700)	-0.33	+0.35
	Low pressure	17.2 (2500)	0.00	+1.00
Triangular ends	High pressure	20.9 (3030)	-0.18	+0.65
	Low pressure	14.1 (2050)	+0.22	+1.42

$$\text{*Margin of Safety} = \frac{\text{Allowable stress}}{\text{Calculated stress}} - 1$$

Tube Sheet Thickness Variation--Core thermal stresses are minimized in the design by proper placement of the mounting brackets and by increasing sheet thickness in the passages adjacent to the side plates. Sheet thicknesses of 0.030, 0.041, 0.051, and 0.081 cm (0.012, 0.016, 0.020, and 0.032 in.) are used for transition from the nominal plates in the interior to the thick side plates. This design approach reduces the transient temperature differentials

between the side plates and the adjacent sheets and it improves the area ratios between sheets to give better load distribution. Of the two effects, the improved load distribution gives the largest reduction in sheet thermal strain. For example, when the side plate is significantly stronger in load carrying ability than the adjacent sheet, the weaker sheet is deformed to nearly the full thermal strain potential, i.e.,

$$\epsilon = \alpha \Delta T$$

However, when the balance between the sheets is optimum, the strain level in each sheet will be

$$\epsilon = \alpha \Delta T / 2$$

The plate thickness transition concept is shown schematically in fig. 4-47.

Maximum fin stress for fins between sheets of various thicknesses is shown in fig. 4-48 and tabulated in table 4-10.

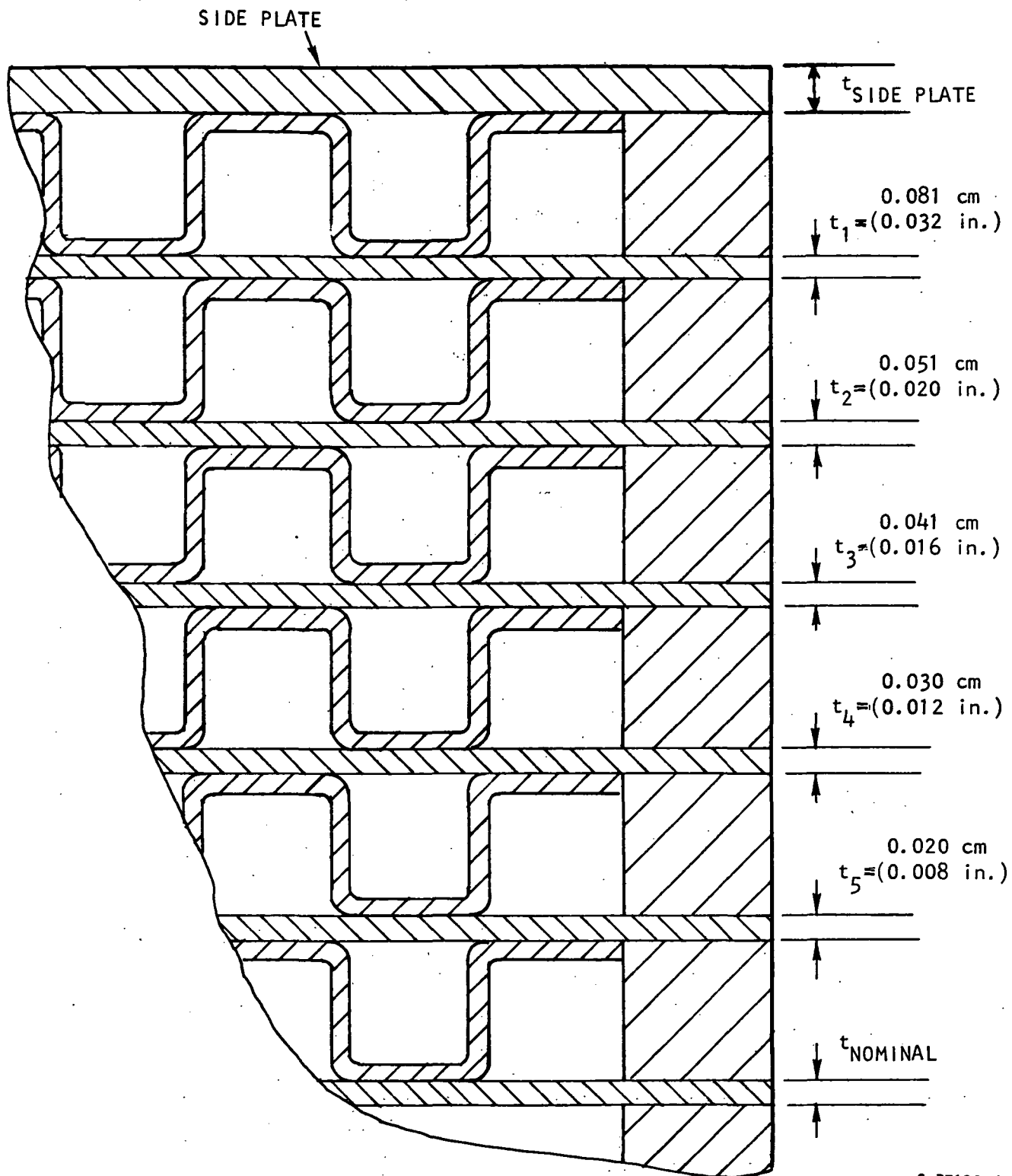
TABLE 4-10  
FIN TENSILE STRESS (PRESSURE LOADED)

Fluid Passage	Tube Sheet Thickness, cm (in.)	Maximum Fully Formed	Stress kN/m psi Conventional	Minimum Fully Formed	Stress kN/m psi Conventional	Average Fully Formed	Stress, kN/m Conventional
Low pressure	0.102 to 0.081 (0.040 to 0.032)	10 710 (1554)	10 270 (1490)	1420 (206)	1407 (204)	5260 (763)	5120 (742)
High pressure	0.081 to 0.051 (0.032 to 0.020)	15 710 (2278)	15 090 (2188)	1400 (203)	441 (64)	7190 (1043)	6570 (953)
Low pressure	0.051 to 0.041 (0.020 to 0.016)	10 290 (1493)	9740 (1413)	1717 (249)	2110 (306)	5240 (706)	5020 (728)
High pressure	0.041 to 0.030 (0.016 to 0.012)	15 600 (2262)	15 010 (2177)	1496 (217)	195 (28)	7160 (1039)	6510 (944)
Low pressure	0.030 to 0.020 (0.012 to 0.008)	9560 (1386)	9720 (1409)	1813 (263)	2289 (332)	5240 (760)	4960 (720)

### Mounting Analysis

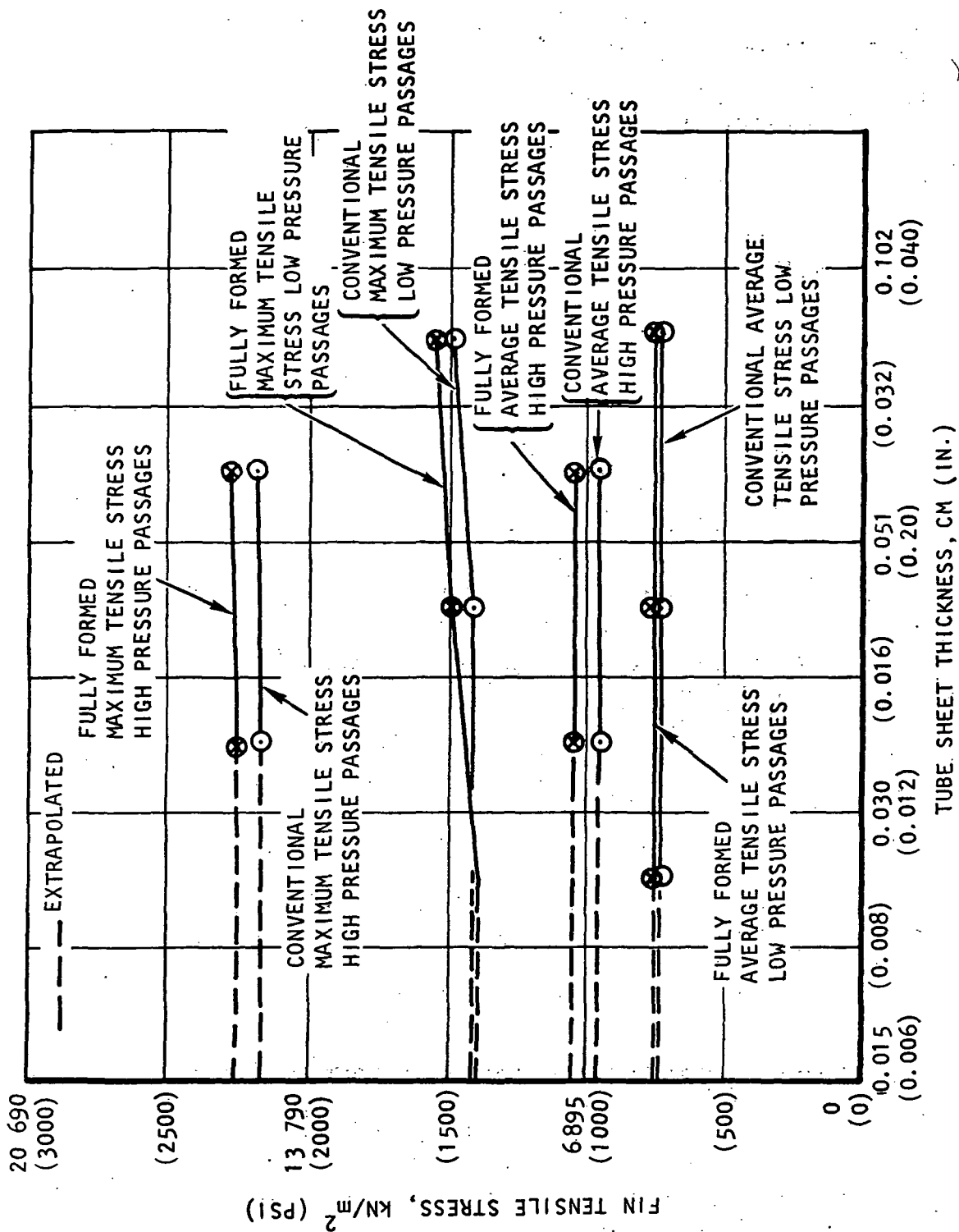
The analysis of the mounting system for the recuperator was based on the inertia and vibration load criteria shown in table 4-11. These criteria were based on information contained in ref. 4-13. The criteria also were based on NASA environmental specification P2241-1 with the recuperator shock mounted on a 15-Hz isolation system.

In the absence of any specified duct loading, the preliminary duct loading listed in table 4-12 was used to design the mounting system. These loads are based on the assumption that flexible couplings will be provided in all ducting connected to the recuperator. The design loads used in the mount analysis are shown in table 4-13.



S-77130-A

Figure 4-47.--Plate Thickness Transition Concept to Minimize Thermal Strains.



S-78266-A

Figure 4-48.--Comparison of Recuperator Fin Pressures.



TABLE 4-11

## PRELIMINARY INERTIA AND VIBRATION LOAD CRITERIA

LOADING CONDITION	DIRECTION OF LOADING	TYPE OF LOADING	LOAD FACTOR	COMBINED LOAD FACTOR
LAUNCH  (NOT OPERATING)	X (LONGITUDINAL)	ACCELERATION	$\pm 20 \text{ g}$	$\pm 20 \text{ g}$
	Y (LATERAL)		$\pm 20 \text{ g}$	$\pm 20 \text{ g}$
	Z (VERTICAL)		$\pm 20 \text{ g}$	$\pm 20 \text{ g}$
CRASH  (NOT OPERATING)	X (LONGITUDINAL)	ACCELERATION	$+ 0$ $- 20 \text{ g}$	$+ 0$ $- 20 \text{ g}$
	Y (LATERAL)		$\pm 6.8 \text{ g}$	$\pm 6.8 \text{ g}$
	Z (VERTICAL)		$+ 0$ $- 10 \text{ g}$	$+ 0$ $- 10 \text{ g}$
OPERATING	X (LONGITUDINAL)	VIBRATION SHOCK ACCELERATION	$\pm 8 \text{ g}$ $\pm 10 \text{ g}$ $\pm 6 \text{ g}$	$\pm 24 \text{ g}$
	Y AND Z (LATERAL AND VERTICAL)	VIBRATION SHOCK ACCELERATION	$\pm 8 \text{ g}$ $\pm 10 \text{ g}$ $\pm 2 \text{ g}$	$\pm 20 \text{ g}$

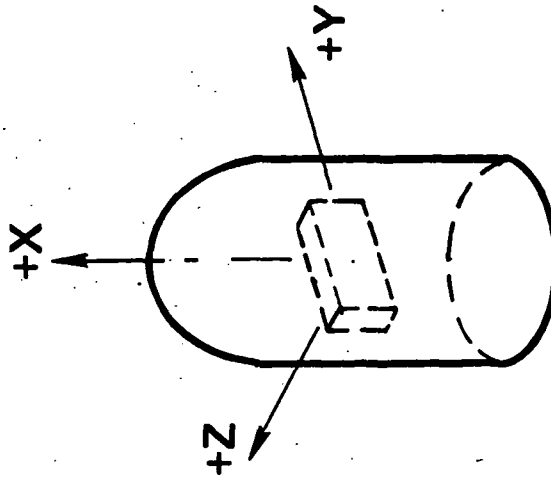
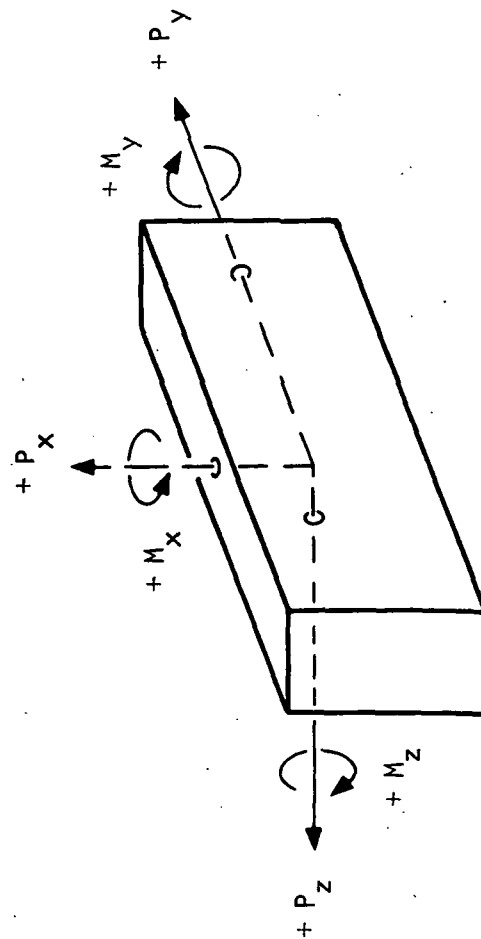


TABLE 4-12

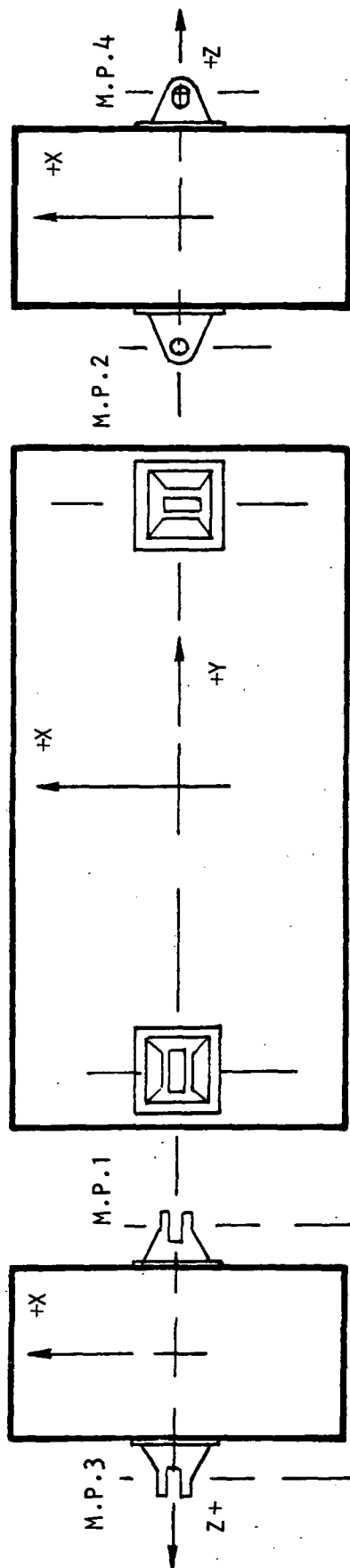
## PRELIMINARY DUCT LOADING CRITERIA APPLIED TO MOUNTS

TYPE OF LOADING	MOMENTS, N-m (IN.-LB)			FORCES, N (LB)		
	$M_x$	$M_y$	$M_z$	$P_x$	$P_y$	$P_z$
LOADING AT RECUPERATOR C.G.	$\pm 136$ ( $\pm 1200$ )	$\pm 362$ ( $\pm 3200$ )	$\pm 136$ ( $\pm 1200$ )	$\pm 2850$ ( $\pm 640$ )	$\pm 2850$ ( $\pm 640$ )	$\pm 2850$ ( $\pm 640$ )



S-7293

TABLE 4-13  
PRELIMINARY MOUNT DESIGN LOADS



MOUNT POINT	DESIGN LOADING, N (LB)		
	X AXIS	Y AXIS	Z AXIS
1	$\pm 5780$ ( $\pm 1300$ )	$\pm 6670$ ( $\pm 1500$ )	$\pm 7120$ ( $\pm 1600$ )
2	$\pm 4890$ ( $\pm 1100$ )	$\pm 1330^{\Delta}$ ( $\pm 300$ )	$\pm 7120$ ( $\pm 1600$ )
3	$\pm 5780$ ( $\pm 1300$ )	$\pm 7120$ ( $\pm 1600$ )	$\pm 980^{\Delta}$ (220)
4	$\pm 5780$ ( $\pm 1300$ )	$\pm 890^{\Delta}$ ( $\pm 200$ )	$\pm 890^{\Delta}$ ( $\pm 200$ )

NOTE:

$\Delta$  FRICTION LOADING ONLY

S-7289

The assumed orientation of the recuperator in the vehicle is shown in the sketch accompanying table 4-11. This orientation was chosen so that the highest inertia forces would be applied along one of the stiffest axes of the recuperator.

The four-point mounting system shown in fig. 4-49 was chosen for the recuperator. The mount brackets are attached to the sides of the unit where the header bars and tube sheets provide excellent backup strength for distributing the localized loading into the structure. The mounting brackets are designed with a sheet metal structure brazed to the recuperator body and welded to a cast or machined portion for attachment to the vehicle support structure. This design minimizes the thermal mass in direct contact with the core and thereby provides increased flexibility during transient conditions. Allowance for relative thermal growth between the recuperator and the vehicle support structure is provided by increasing lug spacing and/or elongating the bolt holes in the lugs as required. Details of the mounting brackets are shown in fig. 4-50. The calculated allowances for the relative thermal growths between the recuperator and the vehicle support structure are included in fig. 4-50.

#### Seal-Plate/Side-Plate Pressure Containment

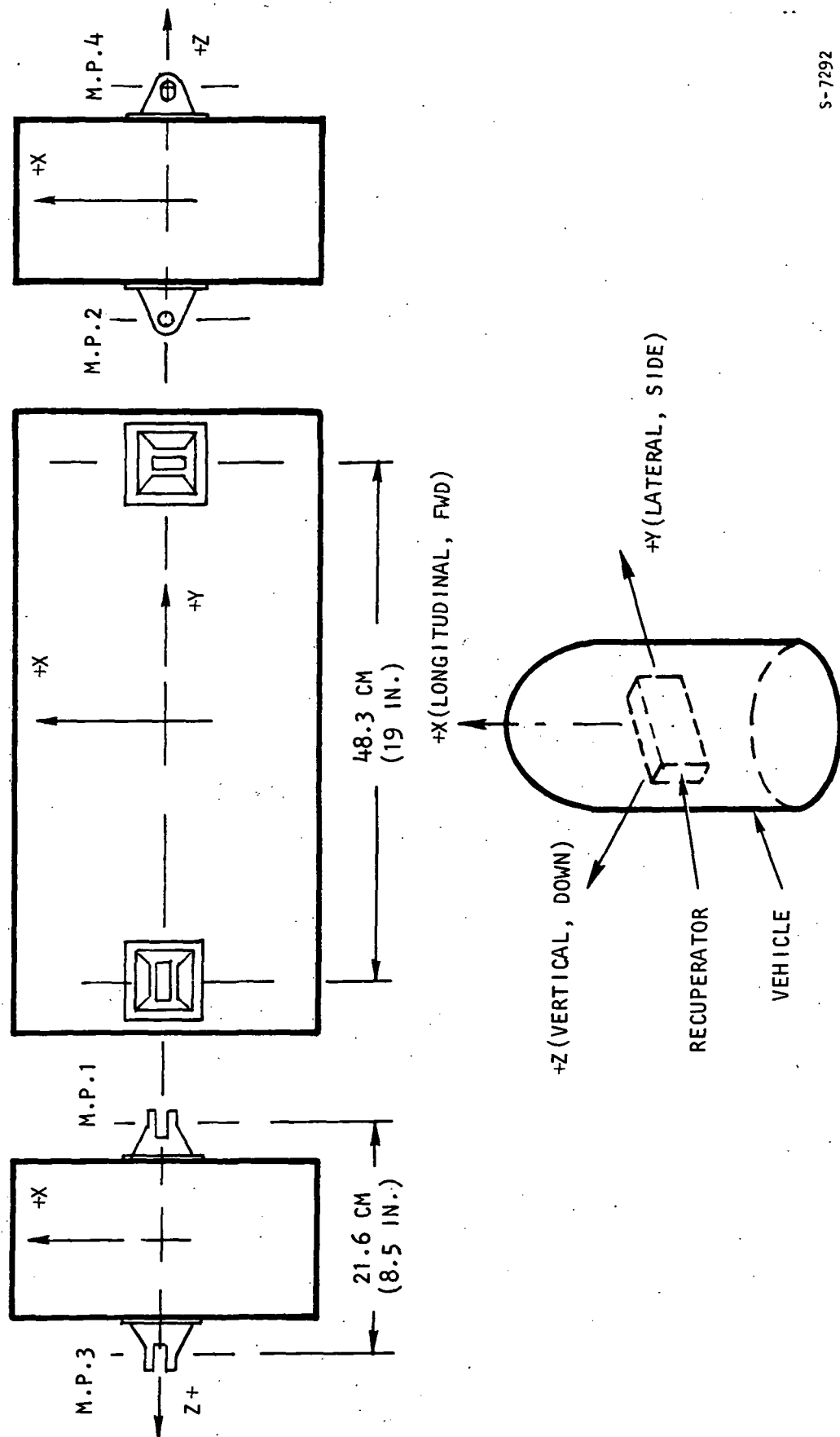
To eliminate the incidence of weld-over braze in the core area, an offset flange was incorporated into the design by extending the side plate 0.635 cm (.250 in.) beyond the header bar. Braze in this region was not permitted to prevent high stress concentration due to possible crack initiation in the braze adjacent to the end weld.

A finite element program was used to determine the stresses that would occur if a leak developed in the header bar/side plate interface. The geometry assumed is shown in fig. 4-51.

Because the pressure is trying to push the radius flat, compressive stresses of  $7030 \text{ kN/m}^2$  (1020 psi) occur throughout the radius. The compressive forces generated by trying to push the radius through are transferred only slightly attenuated to all other elements. The maximum stresses of  $+44\,800 \text{ kN/m}^2$  (+6500 psi) bending plus  $6900 \text{ kN/m}^2$  (1000 psi) compression (51 700 C, 37 900 T) occur in the seal plate/side plate weld. Additional smaller bending stresses occur in the radius. The creep allowable is  $51\,700 \text{ kN/m}^2$  (7500 psi) bending or  $34\,500 \text{ kN/m}^2$  (5000 psi) direct tensile stress. The creep strength in compression is much better than the creep strength in tension; therefore, 51 700  $\text{kN/m}^2$  (7500 psi) C is within the allowable.

#### Tube Sheet/Header Bar Thermal Stresses

During the transient condition, high stresses are generated due to a temperature differential between the header bar and the tube sheet. The stresses induced affect the life of the heat exchanger by causing both plastic and creep damage. It is assumed that these effects may be partitioned, and the sum of the two respective damages accounts for the life of the part. The effects of these two phenomena may be individually studied.



S-7292

Figure 4-49.--Recuperator and Mount Orientation.

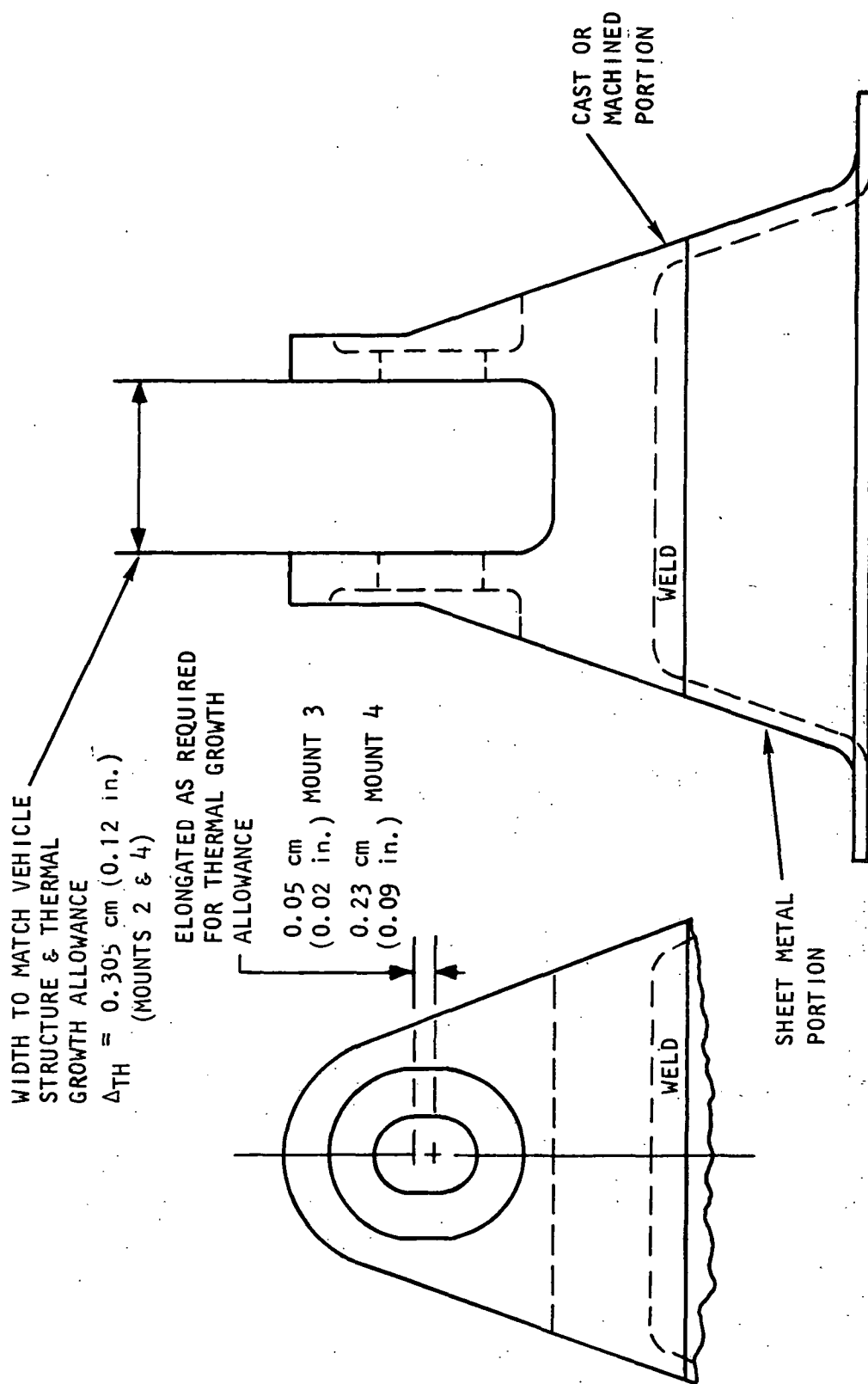


Figure 4-50.--Mounting Bracket Details.

S-78282-A

END WELD SEAL  
PLATE TO SIDE PLATE

SEAL PLATE

END WELD

BRAZE TO  
HEADER BARS

SIDE PLATE

SEAL  
PLATE

BRAZE

HEADER BAR

S-80665

Figure 4-51.--Finite Element Model for Seal Plate/Side Plate  
Interface Analysis.

The number of cycles to crack initiation due to plasticity was computed by the Manson-Halford equation for various levels of stress. This equation was used to establish the upper bound of the failure criteria. The lower bound was established by using the 10 percent rule. After predicting the number of cycles to failure by a theoretical law, the values are multiplied by 10 percent. The theoretical prediction is the upper bound of life expectation and 10 percent of it is the lower bound. Experimental data show that a large number of fatigue failures due to plasticity may be accounted for in this band. A graph of the number of cycles to failure for various levels of stress is shown in fig. 4-52.

If the Norton-Baily steady creep law is assumed to govern in the secondary creep regime, then the damage incurred by the relaxation of induced levels of stress can be computed (see Appendix A). A graph of the damage done per 100 hr is shown in fig. 4-53. In both the plastic and creep calculations, the best data available at the time were used.

A simple conservative computation that is often made when there is an abrupt change in the thickness of a structure and an associated temperature differential, is the shear lag formula. The derivation of the shear lag formula is included in Appendix B.

If the idealized shear lag formula is used, the computed thermal stresses are much too high. This is because only a constant temperature differential is accounted for, not a distribution; and length is not accounted for. In addition, the shear lag model is not fully representative of the introduced stress fields. A finite element model was generated to determine the thermal stresses generated in the core due to the transient temperature distribution. The geometry assumed is shown in fig. 4-54. Using this model, the thermal stresses were computed with an assumed set of conservative boundary conditions. Since the stresses generated are those that determine the cyclic life of the module, a more accurate representation of the boundary conditions was desired and a finite element model of the triangular gas entrance region was generated. The assumed geometry is shown in fig. 4-55. Combination of the two models provides a solution for maximum thermal stresses in a tube sheet during a transient.

Both models account for the large local temperature gradients that occur at the header bar by using a finer grid mesh; however, the shape of the header bar is rectangular in these models. To account for a change in shape from rectangular to channel bars (based on the same temperature profile) the shear lag formula may be utilized to predict an elastic modification in stress magnitude. A typical modification curve and its associated geometry is shown in fig. 4-56.

#### MATERIAL SELECTION

The factors of primary importance in the selection of the recuperator materials are mechanical properties, fabricability, compatibility with brazing filler metals, metallurgical stability, and cost. Materials selected for formed parts, such as fins and pans, must have adequate formability at room temperature and must be amenable to brazing, welding, and all other



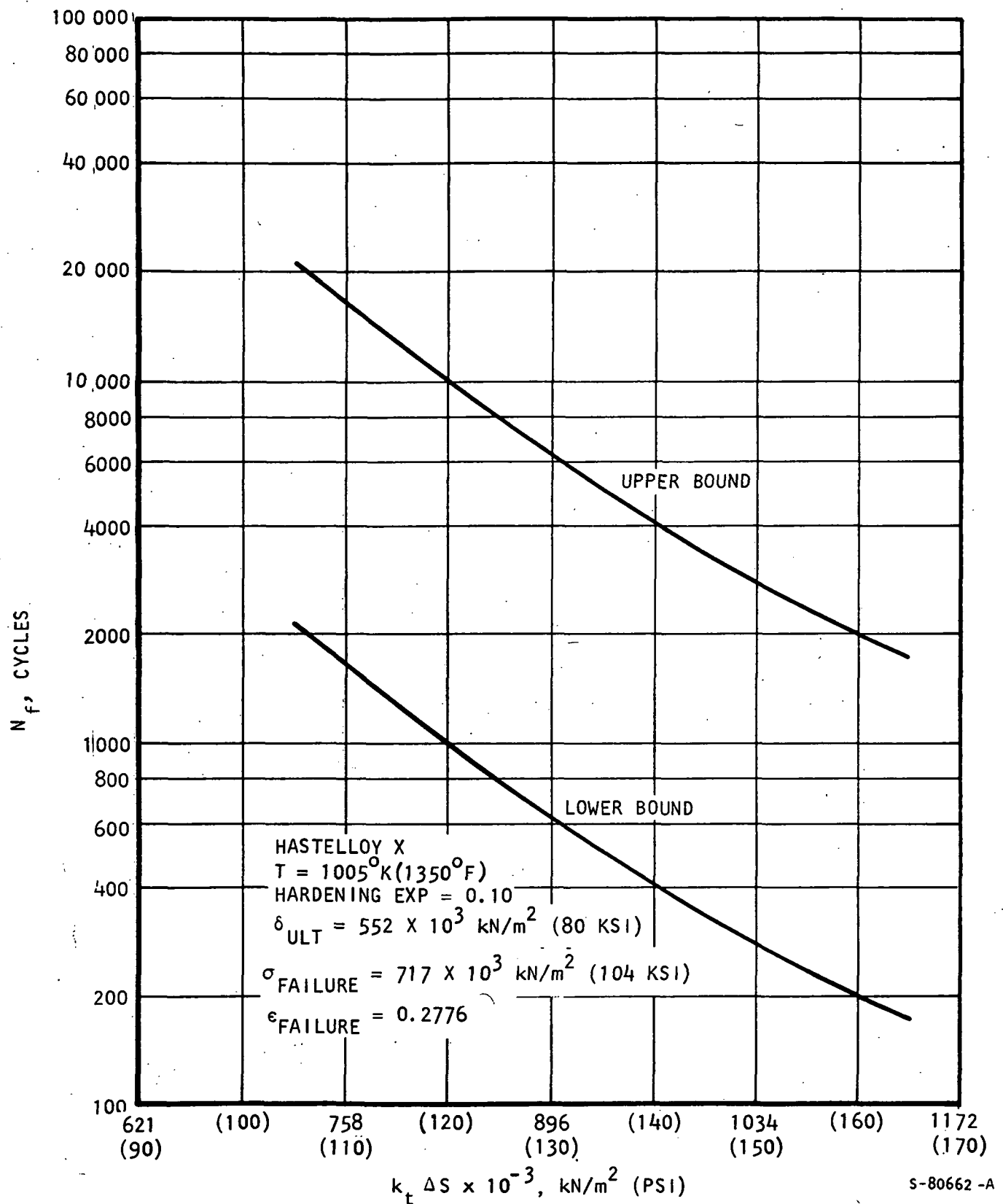


Figure 4-52.--Recuperator Tube Sheet/Header Bar Thermal Stress Versus Number of Cycles to Failure for Various Levels of Stress by the Manson-Halford Equation.

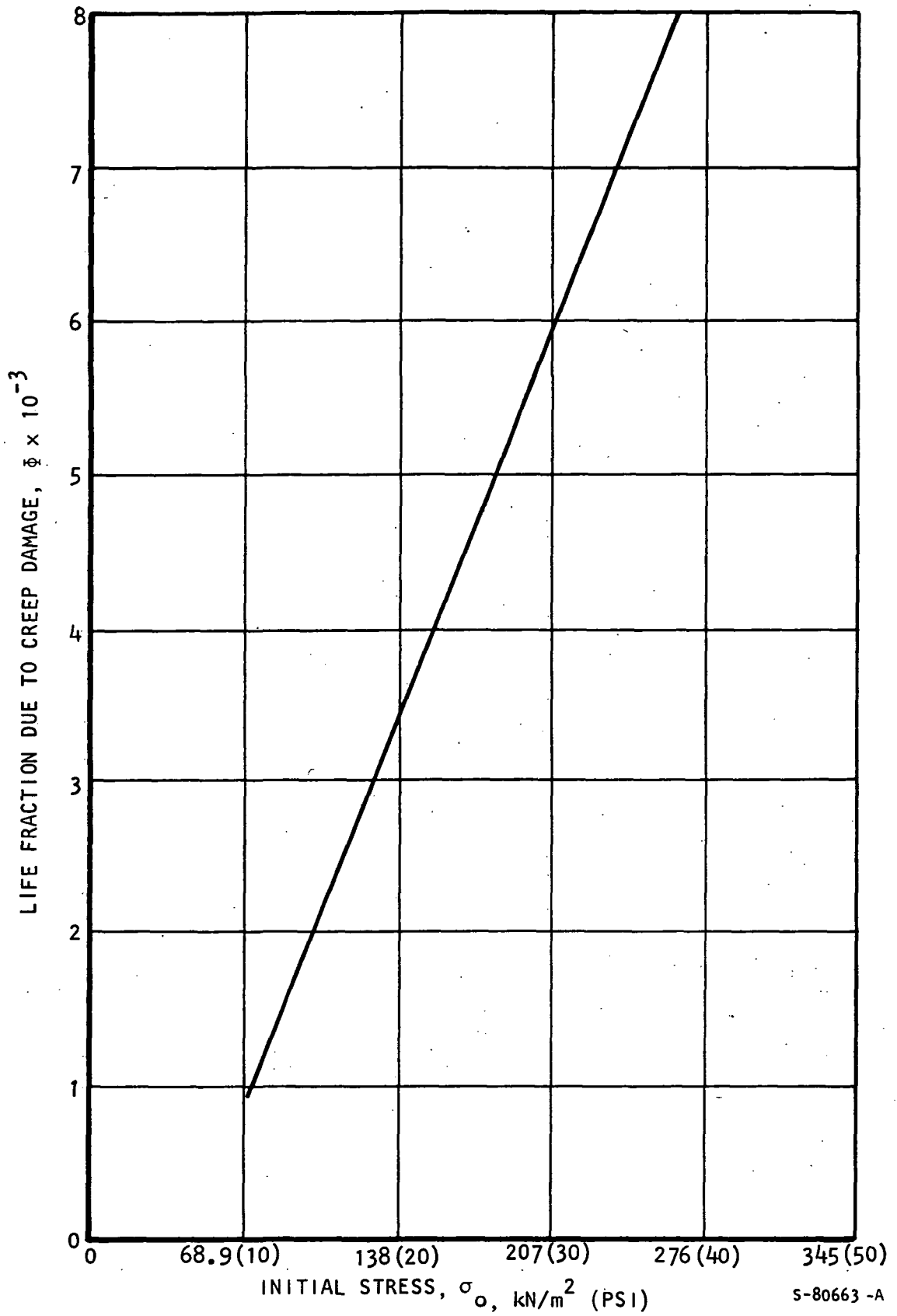
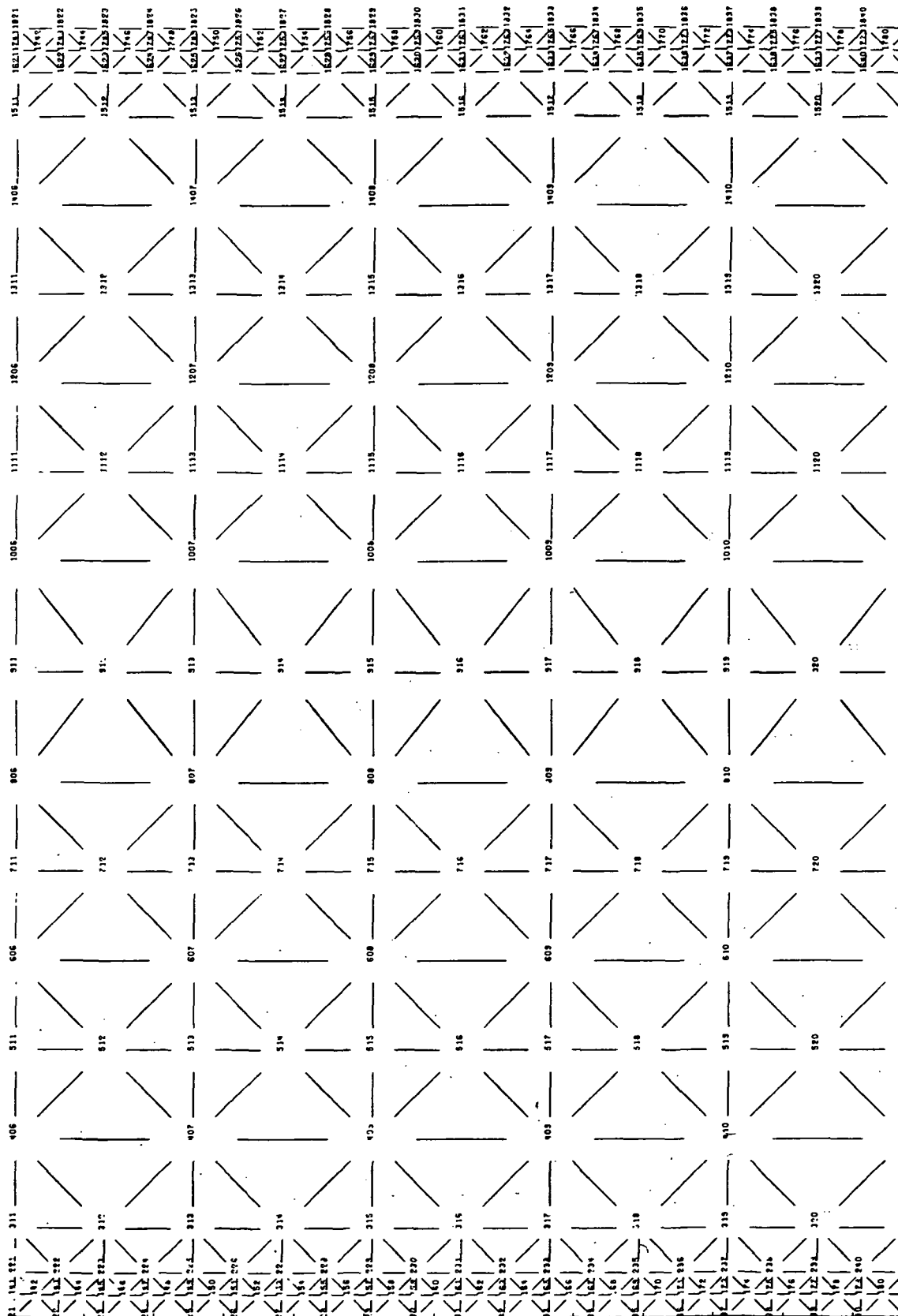


Figure 4-53.--100-Hour Damage Integral for Relaxation of Initial Stress ( $\sigma_o$ ) Due to Secondary Creep Only.

ORIGINAL PAGE IS  
OF POOR QUALITY

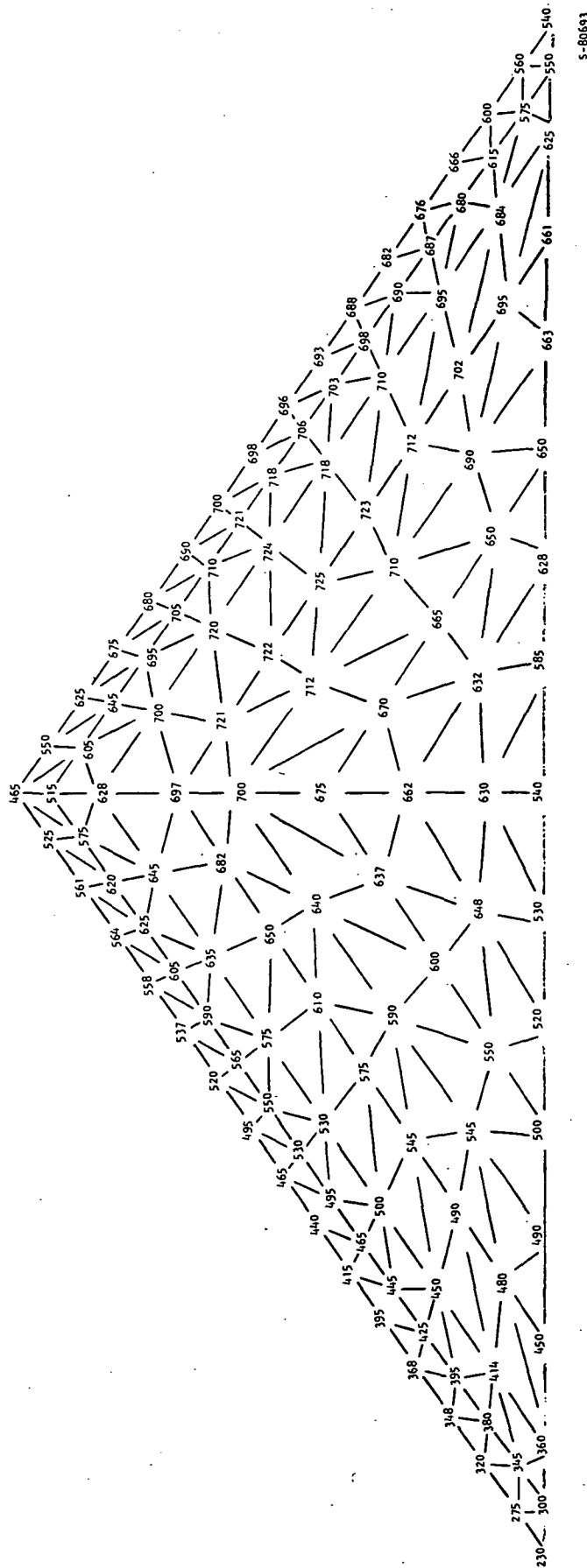


101 BRAYTON RECUPERATOR- TEMPERATURE STRESSES

GEOMETRY ANSYS 1

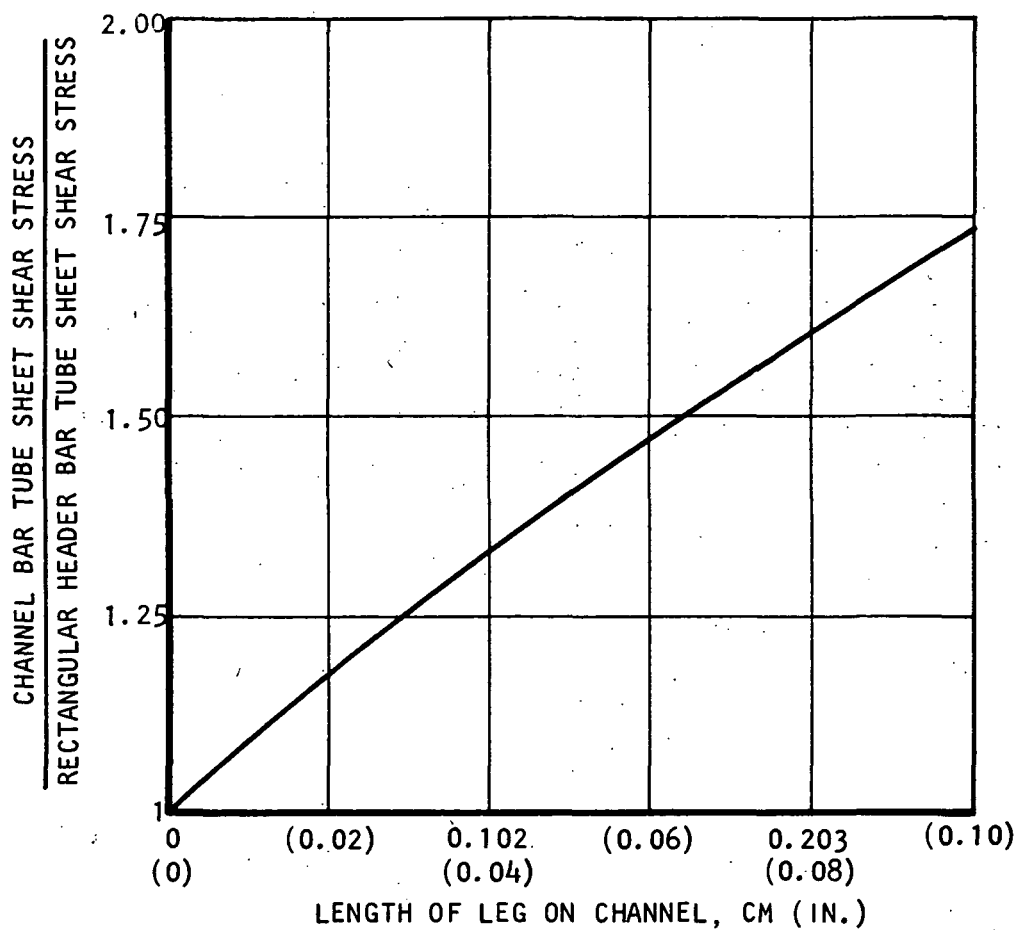
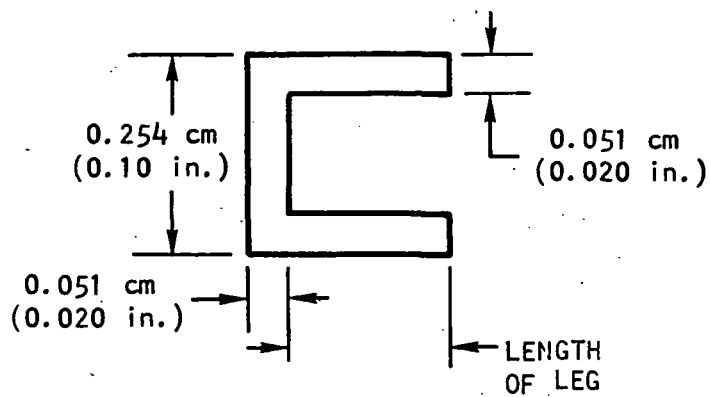
S-80687

Figure 4-54.--Finite Element Model for Analysis of Temperature Stresses.



S-80693

Figure 4-55.--Triangular End Finite Element Model for Analysis of Temperature Stresses.



S-80661-A

Figure 4-56.--Increase in Elastic Stress for a Nonrectangular Header Bar Based on the Shear Lag Approximation.

contemplated manufacturing operations. The strength at time and temperature, or creep properties, must be high enough to prevent deformation and rupture of these thin foil-formed parts, made to the gauges selected for the particular design application.

Since brazing is the most economical means of producing recuperator structures, the compatibility of structural materials with candidate brazing filler metals is of primary importance. The selected base metal/filler metal combinations must satisfy the following general requirements: a compatible brazing temperature must exist to avoid metallurgical changes in the parent material during the braze cycle; there should be minimum erosion and penetration into the base metal, fins, plates, tubes, or headers. The joint should have adequate strength and corrosion resistance, and little or no embrittlement of the parent material due to braze alloy diffusion.

The mechanical properties of the chosen materials must not be detrimentally affected by internal metallurgical changes, such as carbide precipitation, sigma formation, internal oxidation, or diffusion reactions between dissimilar materials, for example, between base metals and filler metals or coatings.

Although there are a number of alloys that fit the general requirements described above as well as the design requirements for the MBR, the best combination of materials properties with proven capabilities is obtained with Hastelloy X. This alloy has been proven in service and is extensively used in gas turbine engines. Hastelloy X was selected as the recuperator material for the Brayton heat exchanger unit (BHXU) alternate design as described in ref. 4-2. Additional tests were conducted to verify the selection of Hastelloy X for this application and are described in the topical report, ref. 4-13.

As a result of these efforts, an extensive data base has been developed on the properties of Hastelloy X including the effects of brazing. In addition to the usual mechanical properties, tests have been run to establish the low-cycle fatigue behavior of Hastelloy X parent material, weldments, and brazed structures.

For fabrication of a Hastelloy X heat exchanger, a brazing alloy should be selected, based on the following requirements:

- (a) A brazing temperature compatible with the annealing or solution heat treatment temperature of the base metal, Hastelloy X.
- (b) Good wettability.
- (c) Minimum penetration into the base metal.
- (d) Good ductility.
- (e) Good joint strength for 996°K (1332°F) operation.
- (f) Good cyclic oxidation resistance for 996°K (1332°F) operation.
- (g) Ability to step-braze by altering alloy composition.

Historically, the alloys selected for this type application have been noble-metal-based. Gold-based alloys such as Nicro (82 Au-18 Ni) have excellent properties in the 750° to 1100°K (900° to 1500°F) temperature range. Additions of palladium and nickel (Palniro 7, 70 Au-8 Pd-22 Ni and Palniro 1, 50 Au-25 Pd-25 Ni) increase the elevated temperature strength of the gold-based alloys. The addition of gold and combinations of gold with palladium are quite expensive, even when used in quantities required for brazing plate-fin heat exchangers. Silver-based alloys, which would be significantly less costly, also require palladium for high-temperature strength, and generally do not have the oxidation resistance associated with the gold-based braze alloys.

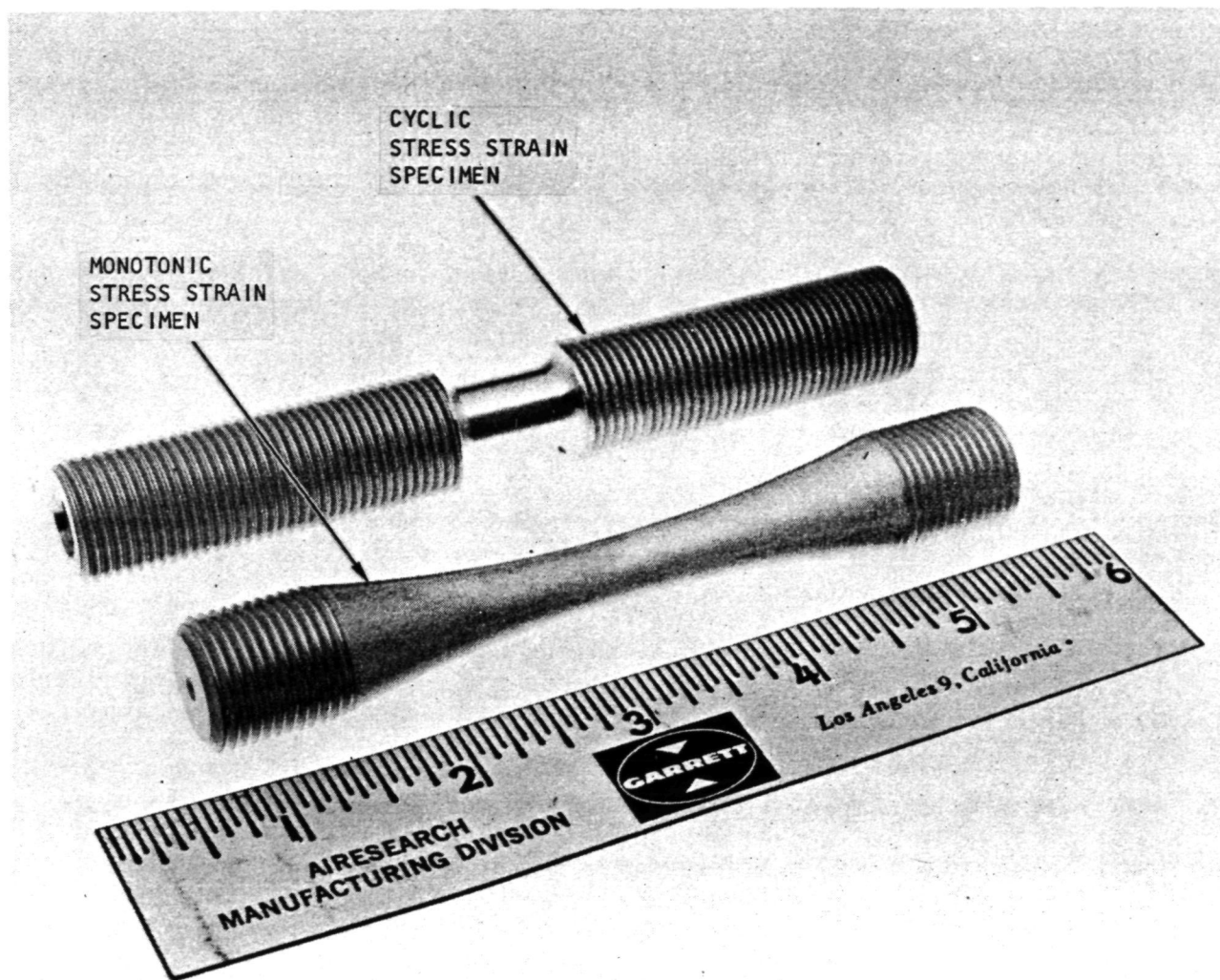
Alternates to noble metal brazing alloys are the brazing alloys containing manganese, copper, and nickel-based alloys. Again, with the exception of a few of the nickel alloys, the alloys containing primarily manganese and copper generally suffer from poor oxidation resistance and/or loss of strength at the 1005°K (1350°F) operating temperature. The problem associated with the use of the nickel-based brazing alloys is that the melting point depressants used are boron, silicon, phosphorous, or a combination of these elements, all of which lead to varying amounts of alloying and/or penetration. Even where these degrading effects are minimized, the braze alloy joints are relatively brittle when compared to the noble metals. Ductility is an important criteria because low-cycle fatigue resistance is directly related to the ability of a material to withstand plastic straining without failure. Finally, there are the cobalt-based alloys, and nickel alloys containing chromium. These brazing alloys generally have brazing temperatures too high for the base metal alloy, Hastelloy X (and stainless steels), because of excessive grain growth in the parent metal during brazing.

Where a high degree of reliability is required, the use of the gold-based brazing alloys is believed justifiable. These filler metals are the only ones that meet all six criteria listed above, particularly with regard to ductility where the ductile surface layer formed by the brazing alloy is known to lead to enhanced resistance to failure due to thermal fatigue. Allowing for step brazing, several of the Palniro alloys and Nicro may be utilized for submodule fabrication.

#### Hastelloy X Parent Metal Tests

To obtain true stress-strain and low-cycle fatigue data, Hastelloy X test specimens were fabricated and tested. A photograph of the two types of specimens used is shown in fig. 4-57. The specimen with variable area over the gauge length was used to obtain the monotonic true stress-strain curve and the other constant area specimen was used to obtain the cyclic true stress strain curve by means of the method described in ref. 4-14.

Three specimens were tested at 645°K (700°F) and 1000°K (1350°F). The monotonic true stress-strain curve test results are plotted and shown in figs. 4-58 and 4-59. The cyclic true stress-strain test results are shown in figs. 4-60 and 4-61. All test specimens were subjected to the psuedo brazing cycle thermal treatment shown in fig. 4-62 prior to testing. The thermal cycle was performed to duplicate the brazing of a Hastelloy X recuperator with AMS 4784 (Palniro 1) brazing alloy.

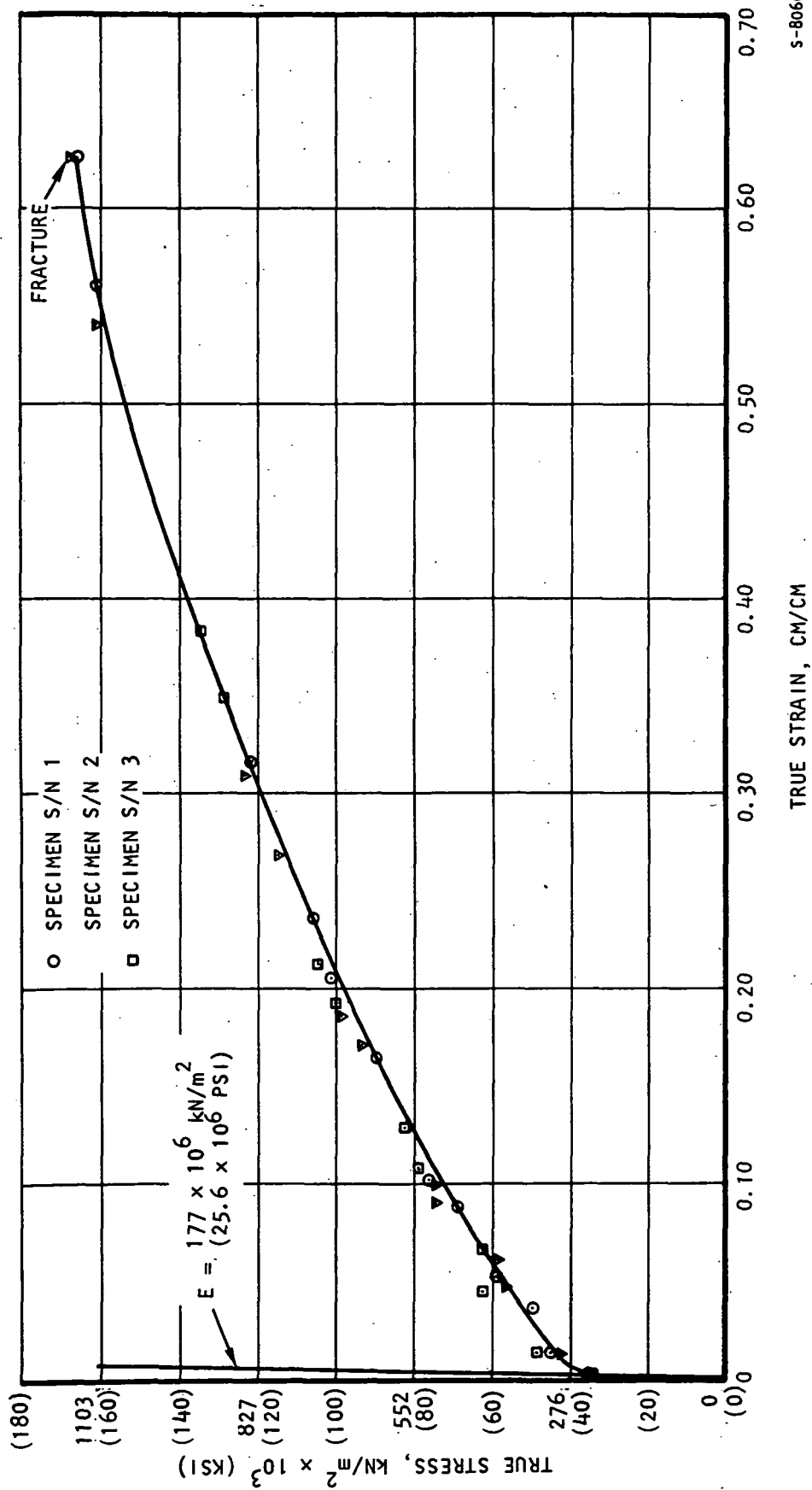


73069

F-18290

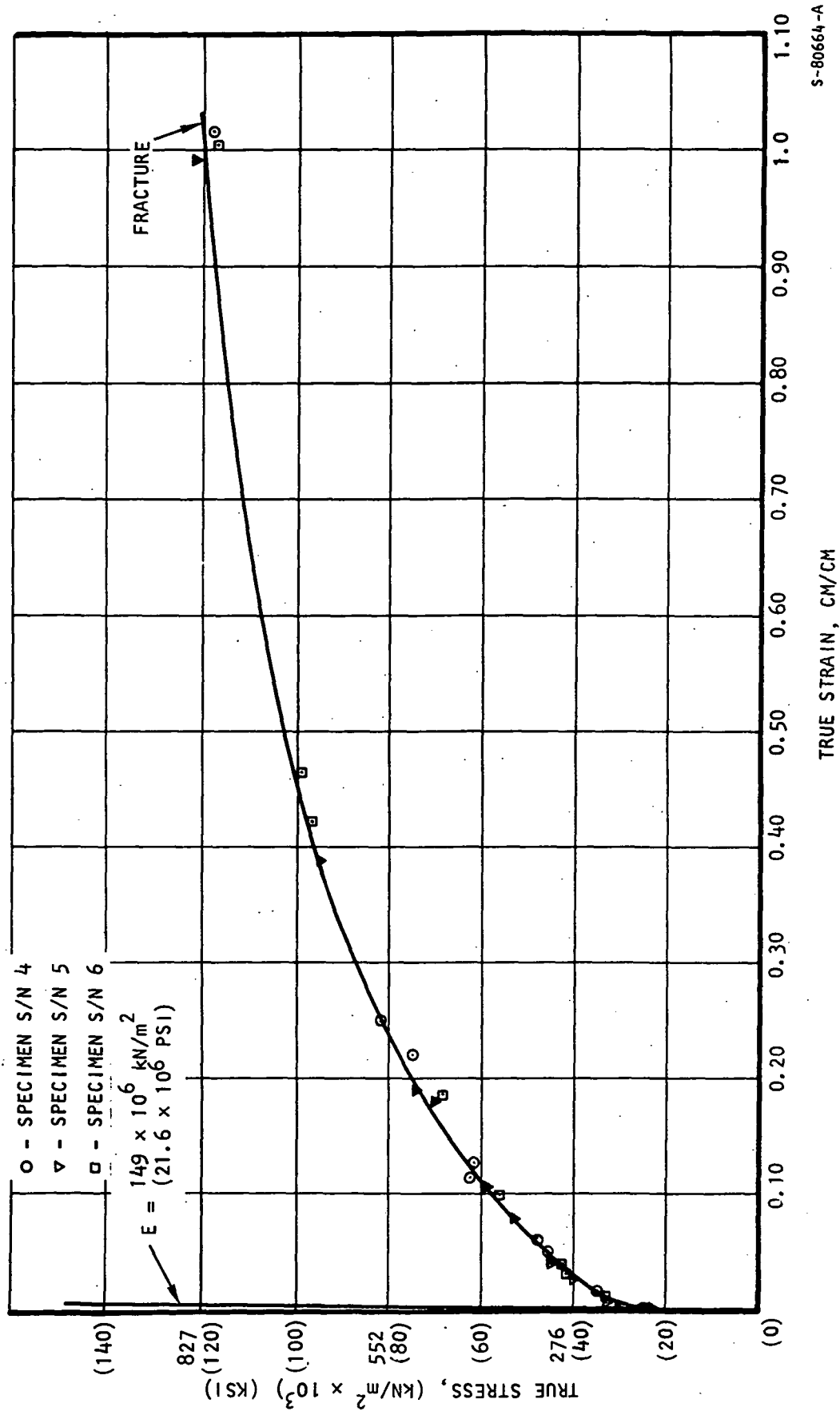
Figure 4-57.--Hastelloy X Material Specimens for Obtaining Stress-Strain Curve.





S-80660 -A

Figure 4-58.---Hastelloy X Material Monotonic Stress-Strain  
 Curve at 644°K (700°F).



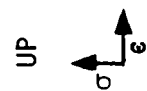
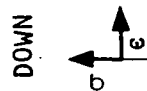
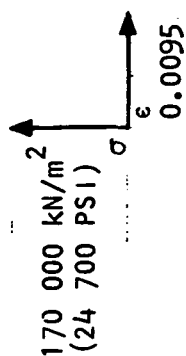
S-80664-A

Figure 4-59.---Hastelloy X Material Monotonic Stress-Strain Curve at 1005°K (1350°F).

ENVELOPE 3

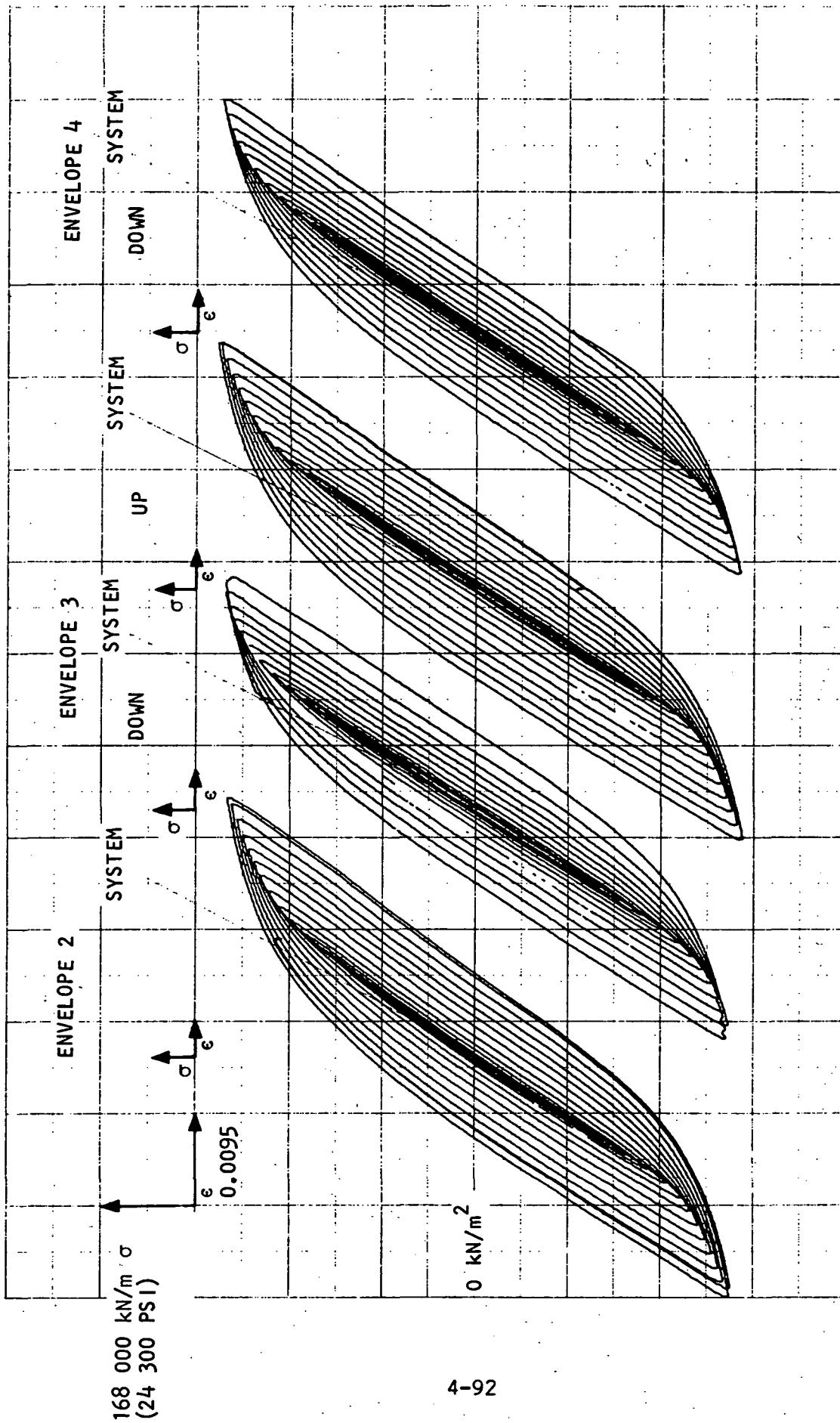
SYSTEM

SYSTEM



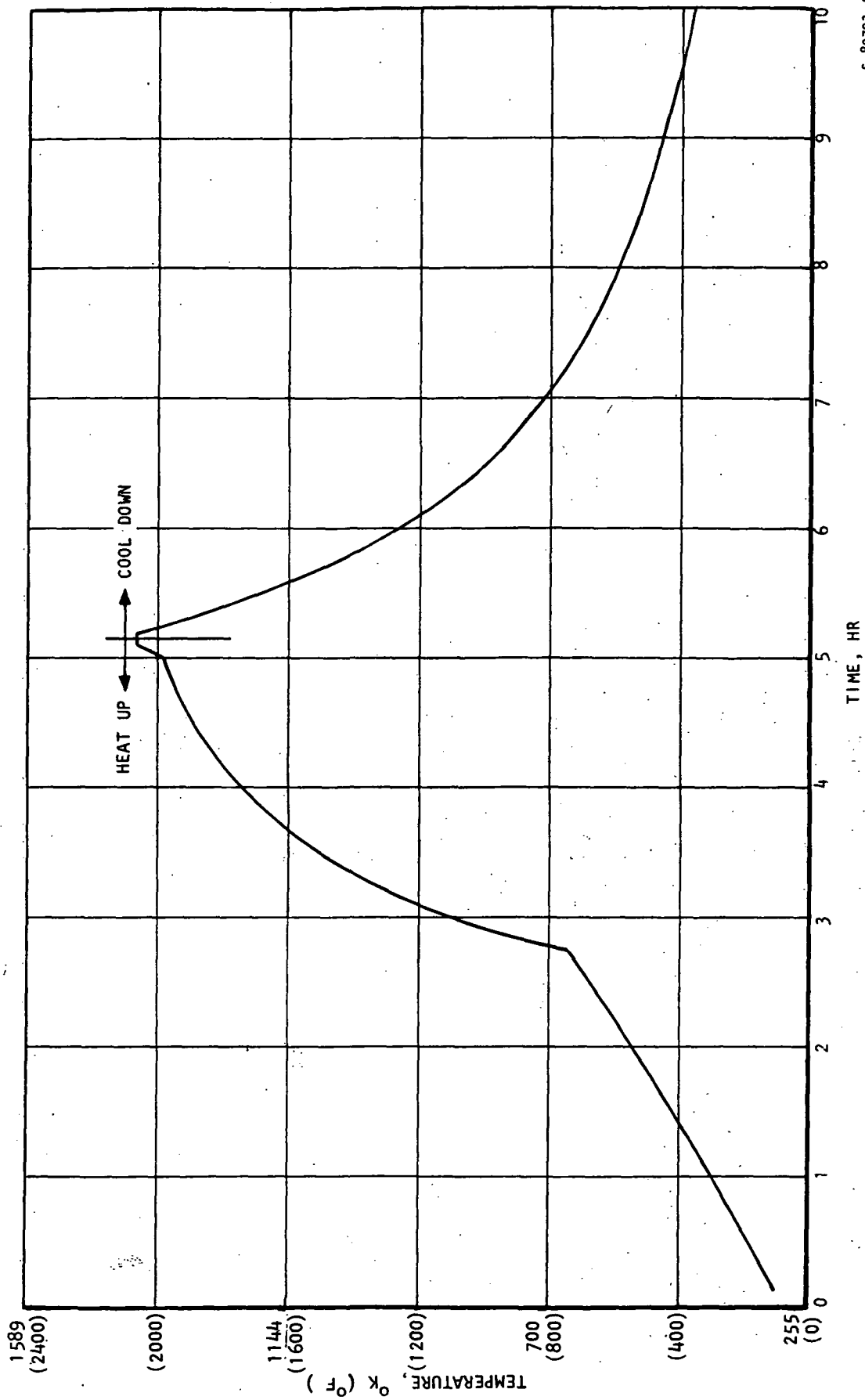
0 kN/m<sup>2</sup>

Figure 4-60. ---Hastelloy X Material Cyclic Stress-Strain Curve at 644°K (700°F).



S-80680-A

Figure 4-61.--Hastelloy X Material Cyclic Stress-Strain Curve at 1005°K (1350°F).



S-80703-A

Figure 4-62.---Hastelloy X Material Pseudobrazing Cycle Pretest Thermal Treatment.

## QUARTER-SIZE MODULES

To verify performance and cyclic life capabilities of the recuperator submodules, it was elected to build and test quarter-size units. That is, a heat exchanger with a counterflow section length and stack height one-half that of the full-size submodule. A reduced-size unit was specified to reduce the cost of the precious metal braze alloy and the energy costs associated with thermal cycle testing. As a guideline it was specified that the quarter-size modules would incorporate all unique design features planned for the submodule.

The submodule cycle life goal is 1000 startup and shutdown cycles. To demonstrate compliance, thermal cycle tests were conducted at off-limit conditions to cause failure in less than 1000 cycles. That is, the severity of the startup temperature transient would be increased to cause higher thermal stresses that would result in failure at less than 1000 cycles of operation, thereby reducing the test costs. Two test units would be used with laboratory test conditions designed to cause failure (low-cycle fatigue cracks) at the 80th and 300th cycle. Results could then be extrapolated to 1000 cycles.

Testing would also afford a check on the recuperator performance. Although the full design point effectiveness could not be achieved because of the reduction in core flow length, an indication of any possible performance deficiencies could be detected.

Quarter-size module design, fabrication, performance testing, and thermal cycle testing are described below.

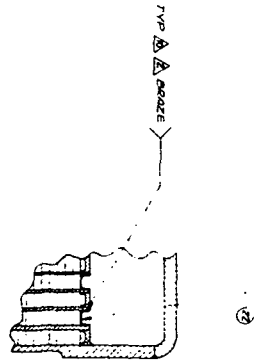
### Design

The core geometry of the quarter-size module was specified to be identical to the full-size unit including material, fin geometry, flow passage width and weight, header bar and tube plate dimensions, and the seal plate design. Based on the analysis of the full-size unit, several design modifications to the original layout, drawing L198773, were accomplished. The final design is shown on drawing SK52160.

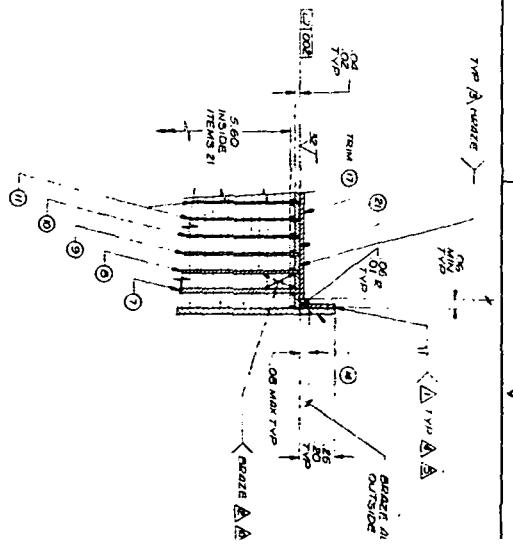
The major design change was attaching the manifolds to the core. Calculations indicated that the stress in the manifold attachment area was excessive because of the flat manifold contour. Moreover, the thermal transient analysis indicated steep temperature gradients and corresponding high thermal stresses at the start of the counter flow section near the outside corners. The solution to the problem was to use manifold attachment flanges. Flat strips with an integral welding lip are brazed to the seal plate several inches away from the critical corner area. In a final assembly operation, the manifolds are welded to the flange lip.

Other design features including channel header bars, graduated tube-plate thickness, and the seal plate are shown in Section BB of drawing SK52160. The outermost tube plate ("side plate") is nominally 0.102 cm (0.040 in.) thick; however, to provide a more optimum weld joint, the side plates are locally increased in thickness to 0.23 cm (0.090 in.) in the area where the 0.23 cm (0.090 in.) thick manifolds are joined to the side plates. The unit is constructed entirely of Hastelloy X using gold-base braze alloys.

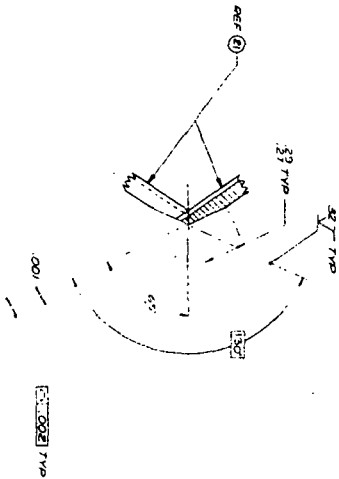
ORIGINAL PAGE IS  
OF POOR QUALITY



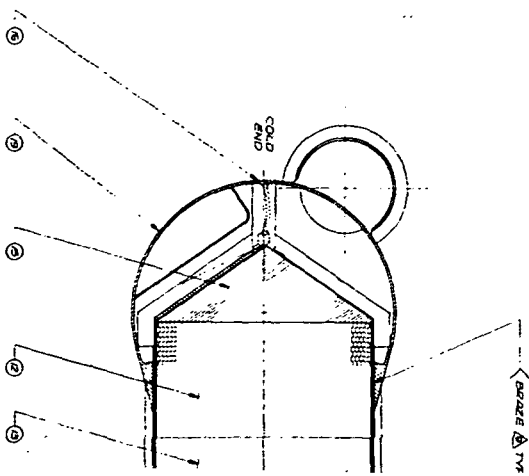
SECTION F-F  
SCALE 1/4"



SECTION B-B  
SCALE 1/4"  
(TYP. DIMENSIONS OF CORNERS)



VIEW B  
SCALE 1/4"  
TYP. 2 PLACES



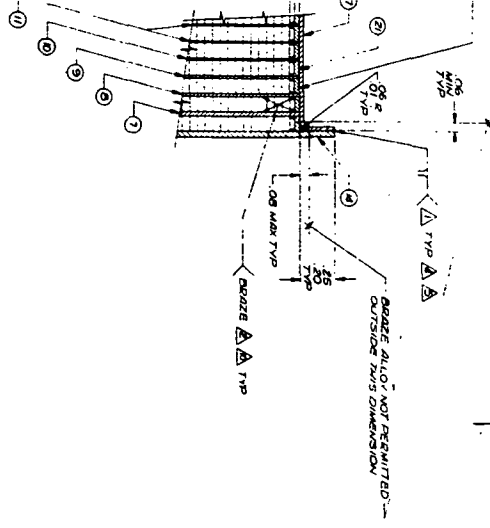
FOLDOUT FRAME 2

SK52160

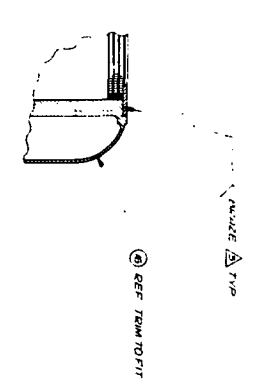
FOLDOUT FRAME 1



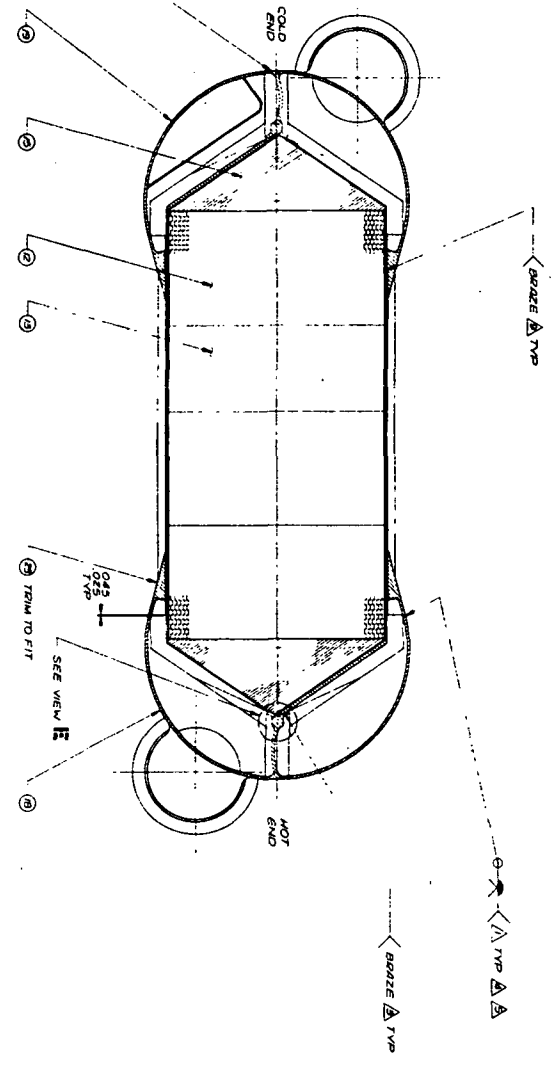




SECTION B-B



SECTION B-B  
SCALE 1/2"  
(BOTH SIDES OF COKE)



SECTION A-A

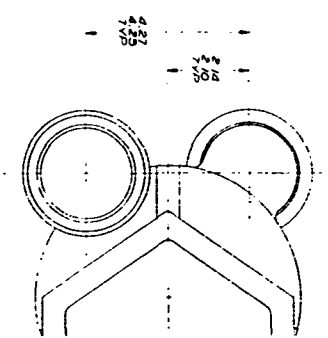
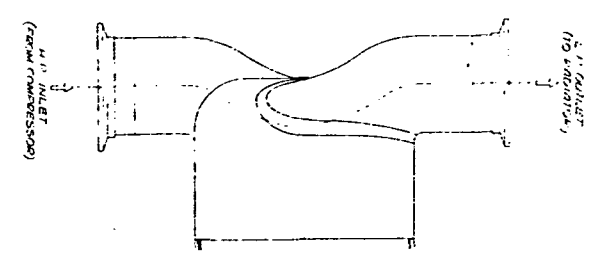
SK52160 E 1

FOLDOUT FRAME

1	2	3	4	5	6	7	8	9	10	11	12	13	14	15	16	17	18	19	20	21	22	23	24	25	26	27	28	29	30	31	32	33	34	35	36	37	38	39	40	41	42	43	44	45	46	47	48	49	50	51	52	53	54	55	56	57	58	59	60	61	62	63	64	65	66	67	68	69	70	71	72	73	74	75	76	77	78	79	80	81	82	83	84	85	86	87	88	89	90	91	92	93	94	95	96	97	98	99	100
---	---	---	---	---	---	---	---	---	----	----	----	----	----	----	----	----	----	----	----	----	----	----	----	----	----	----	----	----	----	----	----	----	----	----	----	----	----	----	----	----	----	----	----	----	----	----	----	----	----	----	----	----	----	----	----	----	----	----	----	----	----	----	----	----	----	----	----	----	----	----	----	----	----	----	----	----	----	----	----	----	----	----	----	----	----	----	----	----	----	----	----	----	----	----	----	----	----	----	-----

FOLDOUT FRAME

SK52160 E 1



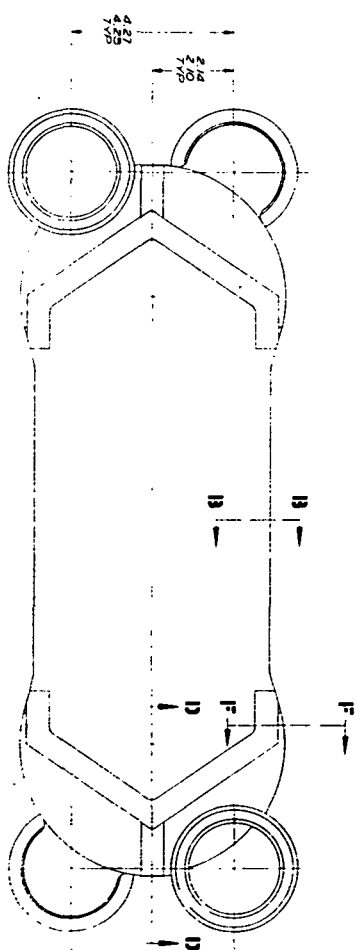
7	6	5	4	3	2	1
---	---	---	---	---	---	---

L.P. INLET  
(FROM TURBINE)

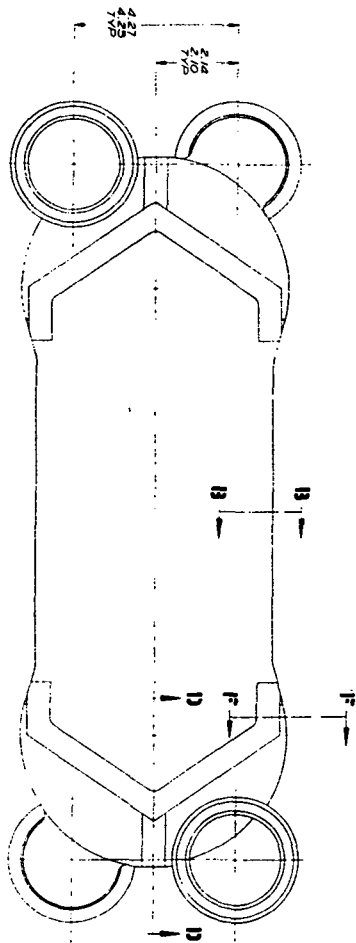
H P INLET  
(FROM COMPRESSOR)

WE OUTLET  
(TO WEAT SOURCE)

FOI, DOUT FRAMIT

[illegible]

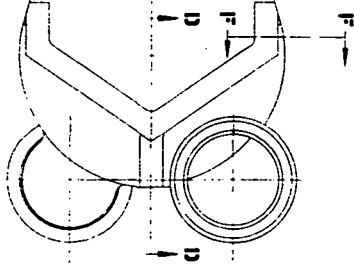
NOTES: 1. 11/10/2010



- 10/10/2014 10:10:10 AM

[illegible]

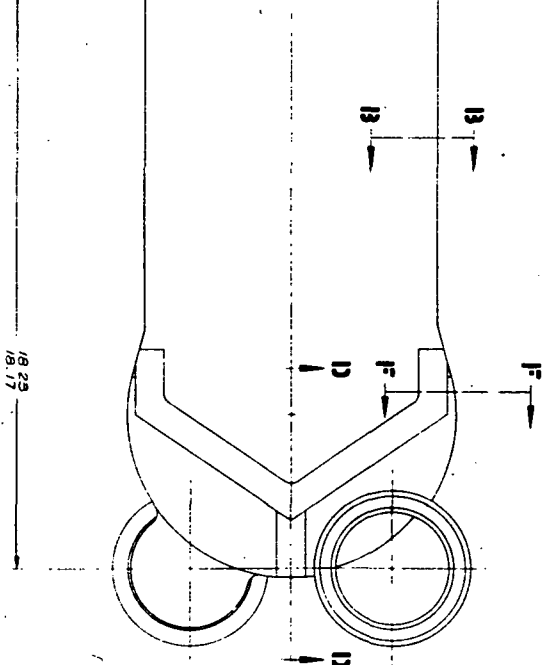
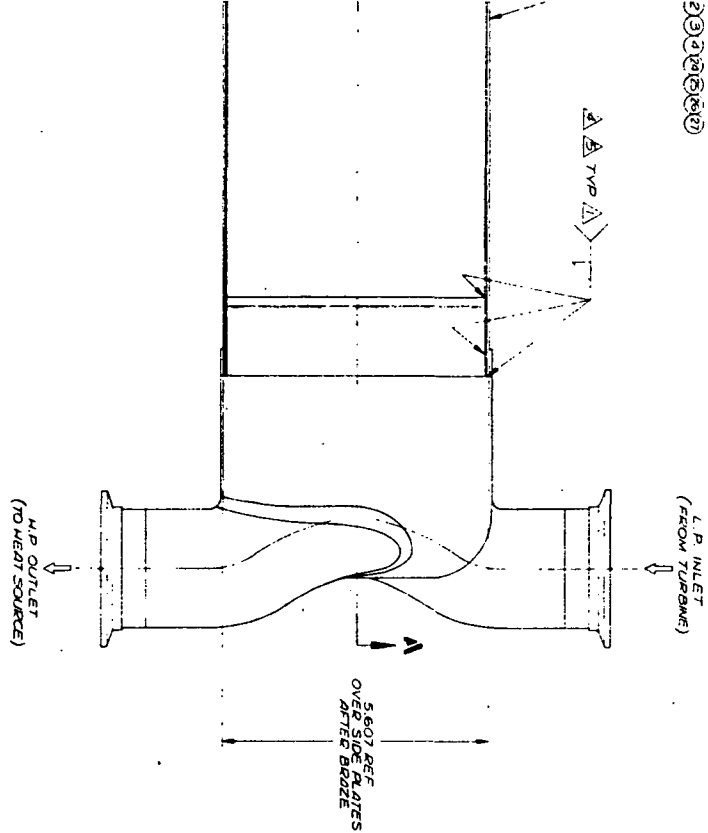
SK 52160



- [illegible]

[illegible]

23222222



- 1. FURNACE BRAZE ITEM 27 PER AIR SPEC WBS-27 USING 75% NB 210 (AWS 4783) & 25% NB 30 (AWS 4782). 32-30 GM/IN<sup>2</sup> (1.325 MESH POWDER) BRAZING ALLOY. BRAZING TEMP 2190°-2140° F.
- 2. FURNACE BRAZE ITEM 2 PER AIR SPEC WBS-27 USING POLYNICO 7 (AWS 4784) BRAZING ALLOY. 0.01 THICK.
- 3. SECTION A-A SHOWS A TYPICAL L.P. PASS. ALTERNATE H.P. PASSES IDENTICAL, EXCEPT THEY ARE COUNTERFLOW.
- 4. MASS SPECTROMETER HELIUM LEAK TEST AS FOLLOWS:
  - a. ITEM 3: 1\*10<sup>-3</sup> SCC/SEC
  - b. FINAL ASSY: 1\*10<sup>-3</sup> SCC/SEC
- 5. PROOF PRESSURE TEST FINAL ASSY AS FOLLOWS:
  - a. HIGH PRESSURE SIDE: 250 PSIG AT 70° F
  - b. LOW PRESSURE SIDE: 169 PSIG AT 70° F(MAX HP FROM HP TO L.P. HP SIDE MUST ALWAYS BE HIGHER IN PRESS. THAN L.P. SIDE)
- 6. FLUORESCENT PENETRANT INSPECT WELD PER MIL-1-6866, TYPE 1, METHOD B
- 7. 100% X-RAYING/GRAPHIC INSPECTION REQUIRED
- 8. FURNACE BRAZE ITEM 3 PER AIR SPEC WBS-27 USING "WE" BEARING ALLOY. 0.01 THICK.
- 9. FURNACE BRAZE ITEM 4 PER AIR SPEC WBS-27 USING POLYNICO 1 (AWS 4784) BRAZING ALLOY. 0.01 THICK.
- 10. WELD PER AIR SPEC WBS-18, EXCEPT EDGE MISMATCH ON BUTT JOINTS TO BE WITHIN 20% OF MATERIAL THICKNESS.

REVISIONS			
NO.	DATE	DESCRIPTION	BY
1	12/11/83	REVISED	SK 52160
2	12/11/83	REVISED	SK 52160
3	12/11/83	REVISED	SK 52160
4	12/11/83	REVISED	SK 52160
5	12/11/83	REVISED	SK 52160
6	12/11/83	REVISED	SK 52160
7	12/11/83	REVISED	SK 52160
8	12/11/83	REVISED	SK 52160
9	12/11/83	REVISED	SK 52160
10	12/11/83	REVISED	SK 52160
11	12/11/83	REVISED	SK 52160
12	12/11/83	REVISED	SK 52160
13	12/11/83	REVISED	SK 52160
14	12/11/83	REVISED	SK 52160
15	12/11/83	REVISED	SK 52160
16	12/11/83	REVISED	SK 52160
17	12/11/83	REVISED	SK 52160
18	12/11/83	REVISED	SK 52160
19	12/11/83	REVISED	SK 52160
20	12/11/83	REVISED	SK 52160
21	12/11/83	REVISED	SK 52160
22	12/11/83	REVISED	SK 52160
23	12/11/83	REVISED	SK 52160
24	12/11/83	REVISED	SK 52160
25	12/11/83	REVISED	SK 52160
26	12/11/83	REVISED	SK 52160
27	12/11/83	REVISED	SK 52160
28	12/11/83	REVISED	SK 52160
29	12/11/83	REVISED	SK 52160
30	12/11/83	REVISED	SK 52160
31	12/11/83	REVISED	SK 52160
32	12/11/83	REVISED	SK 52160
33	12/11/83	REVISED	SK 52160
34	12/11/83	REVISED	SK 52160
35	12/11/83	REVISED	SK 52160
36	12/11/83	REVISED	SK 52160
37	12/11/83	REVISED	SK 52160
38	12/11/83	REVISED	SK 52160
39	12/11/83	REVISED	SK 52160
40	12/11/83	REVISED	SK 52160
41	12/11/83	REVISED	SK 52160
42	12/11/83	REVISED	SK 52160
43	12/11/83	REVISED	SK 52160
44	12/11/83	REVISED	SK 52160
45	12/11/83	REVISED	SK 52160
46	12/11/83	REVISED	SK 52160
47	12/11/83	REVISED	SK 52160
48	12/11/83	REVISED	SK 52160
49	12/11/83	REVISED	SK 52160
50	12/11/83	REVISED	SK 52160
51	12/11/83	REVISED	SK 52160
52	12/11/83	REVISED	SK 52160
53	12/11/83	REVISED	SK 52160
54	12/11/83	REVISED	SK 52160
55	12/11/83	REVISED	SK 52160
56	12/11/83	REVISED	SK 52160
57	12/11/83	REVISED	SK 52160
58	12/11/83	REVISED	SK 52160
59	12/11/83	REVISED	SK 52160
60	12/11/83	REVISED	SK 52160
61	12/11/83	REVISED	SK 52160
62	12/11/83	REVISED	SK 52160
63	12/11/83	REVISED	SK 52160
64	12/11/83	REVISED	SK 52160
65	12/11/83	REVISED	SK 52160
66	12/11/83	REVISED	SK 52160
67	12/11/83	REVISED	SK 52160
68	12/11/83	REVISED	SK 52160
69	12/11/83	REVISED	SK 52160
70	12/11/83	REVISED	SK 52160
71	12/11/83	REVISED	SK 52160
72	12/11/83	REVISED	SK 52160
73	12/11/83	REVISED	SK 52160
74	12/11/83	REVISED	SK 52160
75	12/11/83	REVISED	SK 52160
76	12/11/83	REVISED	SK 52160
77	12/11/83	REVISED	SK 52160
78	12/11/83	REVISED	SK 52160
79	12/11/83	REVISED	SK 52160
80	12/11/83	REVISED	SK 52160
81	12/11/83	REVISED	SK 52160
82	12/11/83	REVISED	SK 52160
83	12/11/83	REVISED	SK 52160
84	12/11/83	REVISED	SK 52160
85	12/11/83	REVISED	SK 52160
86	12/11/83	REVISED	SK 52160
87	12/11/83	REVISED	SK 52160
88	12/11/83	REVISED	SK 52160
89	12/11/83	REVISED	SK 52160
90	12/11/83	REVISED	SK 52160
91	12/11/83	REVISED	SK 52160
92	12/11/83	REVISED	SK 52160
93	12/11/83	REVISED	SK 52160
94	12/11/83	REVISED	SK 52160
95	12/11/83	REVISED	SK 52160
96	12/11/83	REVISED	SK 52160
97	12/11/83	REVISED	SK 52160
98	12/11/83	REVISED	SK 52160
99	12/11/83	REVISED	SK 52160
100	12/11/83	REVISED	SK 52160

## Thermal Analysis of One-Quarter-Size Submodule

A thermal analysis was undertaken to determine the temperature distributions for the one-quarter-size module under steady-state and transient conditions. The objectives of this analysis were: (1) to validate the analytical procedures used to predict temperature distributions with test data, and (2) to determine the required transient to produce fatigue cracks in the unit at a predicted number of cycles.

A thermal model, developed for the one-quarter-size module, is shown in fig. 4-63. This model consists of a three-layer sandwich representing one cold passage and two one-half-size hot sandwiches. Due to the symmetry of the heat exchanger, it was assumed that this would yield accurate temperature distributions throughout the core.

With the thermal model described above, various combinations of airflows and temperature ramps were utilized in an attempt to determine the transient with air for the one-quarter-size module which would roughly approximate the thermal transient experienced by the full-size unit during the prescribed startup sequence. It is not possible to obtain a complete simulation because the performance is different with air compared to the actual application that uses xenon-helium gas. The final results of this survey are shown in figs. 4-64 and 4-65. These figures show the prescribed transient and the resulting transient temperatures at the critical area within the recuperator. In fig. 4-65, the temperature gradients at various times after initiation of the transient are shown for the one-quarter-size module, as well as the maximum temperature gradient for the full-size unit under the prescribed system startup transient. The transient for the one-quarter-size module of fig. 4-64 represents a reasonably close match of the temperature levels and gradients anticipated for the transient for the full-size unit.

From these studies, the critical area within the core (i.e. the highest thermal gradients) was identified and a more detailed thermal model of this area was developed. The critical area of the core was found to be near the hot inlet manifold. The detailed thermal model of this critical area is given in fig. 4-66. In the detailed model, the effects of the header bars, side plate, and manifolds were considered. The results of the detailed thermal model for the imposed transient of fig. 4-64 are shown in fig. 4-67. Based on a maximum temperature differential between tube sheet and seal plate, the case at 90 sec after startup was found to be critical. Fig. 4-68 presents a more elaborate temperature distribution at this critical time. The thermal lag of the manifold pan during transient startup is noted in this figure.

A second transient for the one-quarter-size modules was defined by arbitrarily reducing the time scale of fig. 4-64 by a factor of three. This transient is shown in fig. 4-69. The resulting temperature distributions predicted for this fast transient are shown in figs. 4-70 and 4-71.

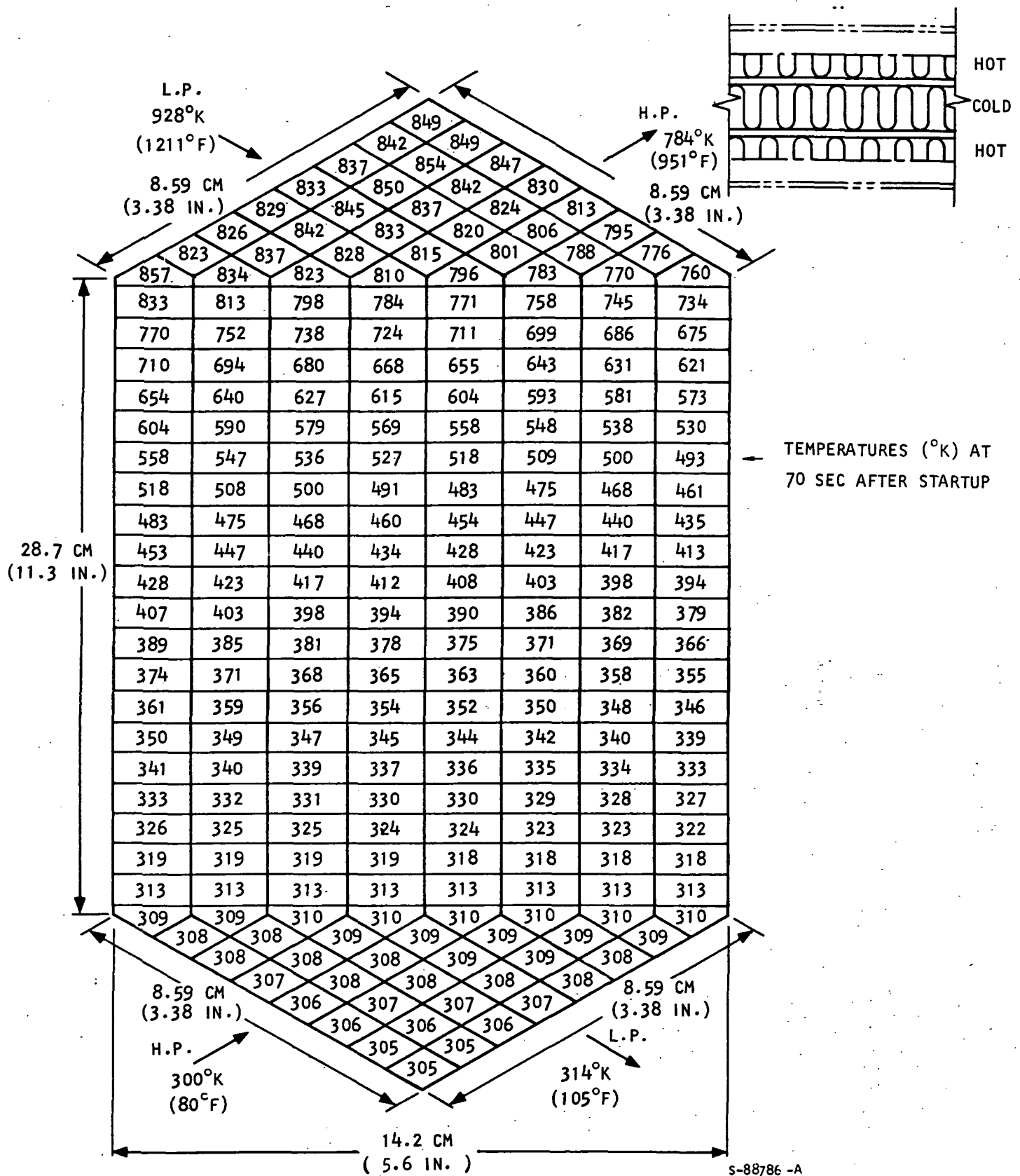
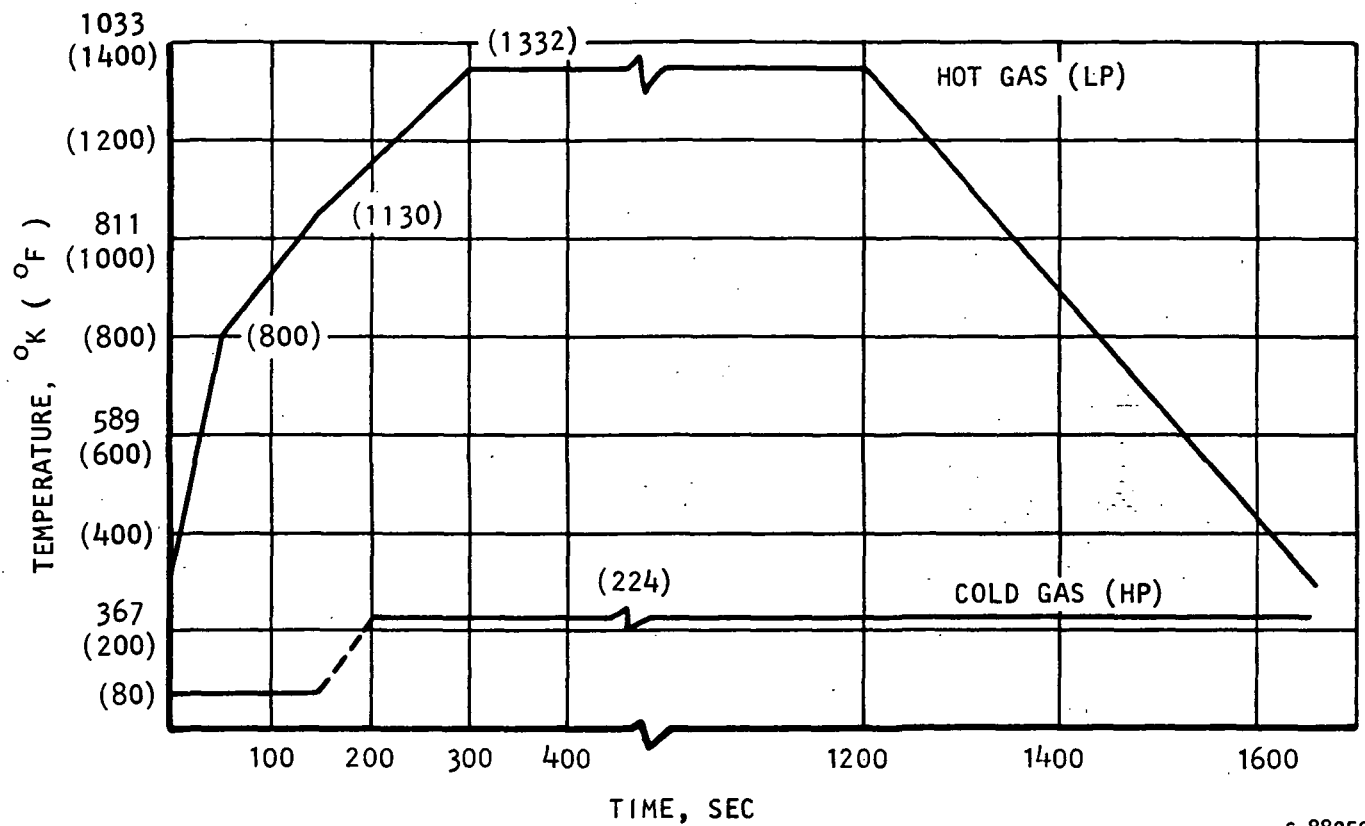


Figure 4-63.--Thermal Model of One-Quarter-Size Recuperator Module.



S-88059 -A

Figure 4-64.--Recuperator Submodule Thermal Transient.



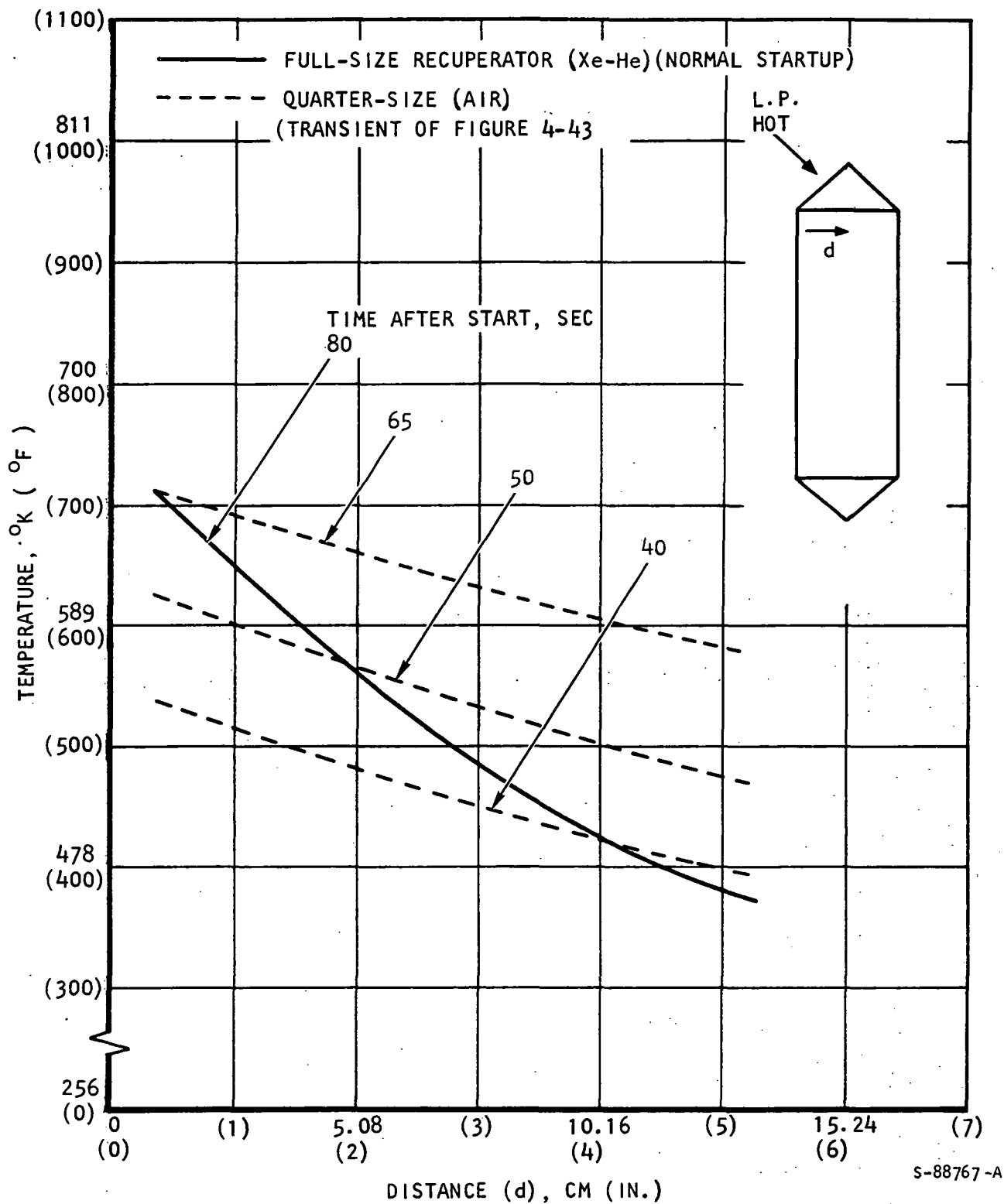


Figure 4-65.--Temperature Gradients after Initiation of Transients.

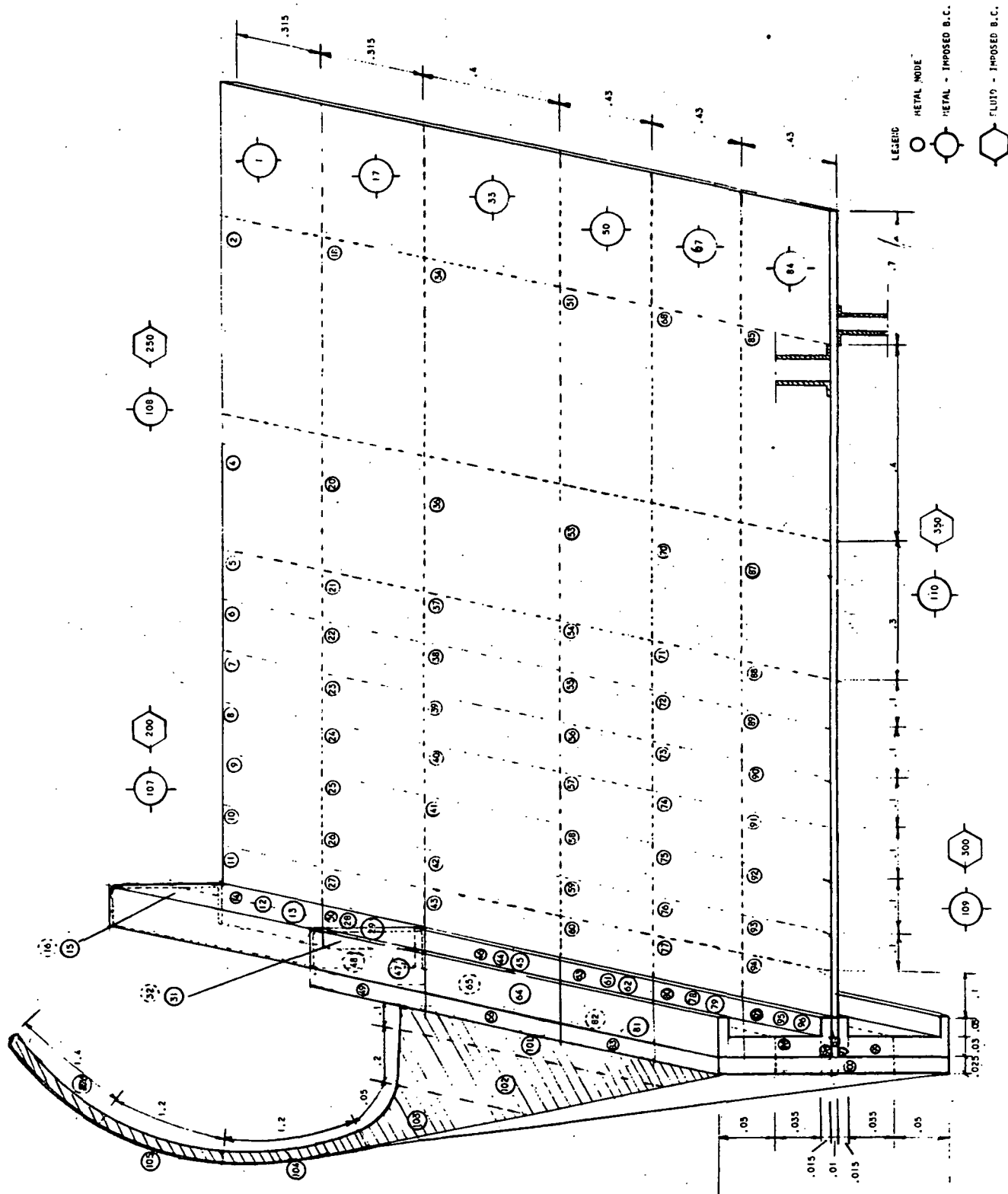


Figure 4-66.--Detailed Thermal Model, One-Quarter-Size Module Critical Area.

S-7853

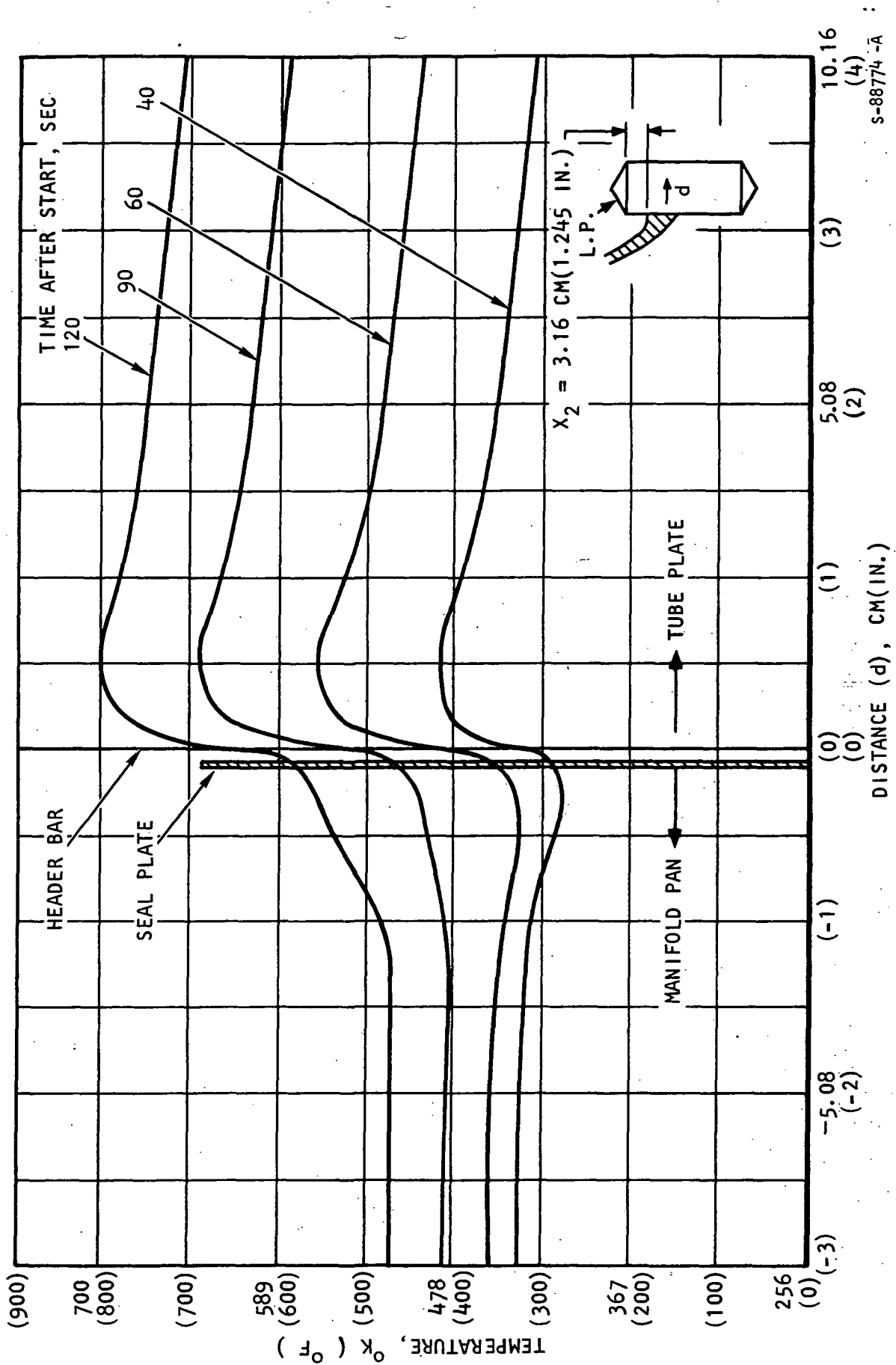
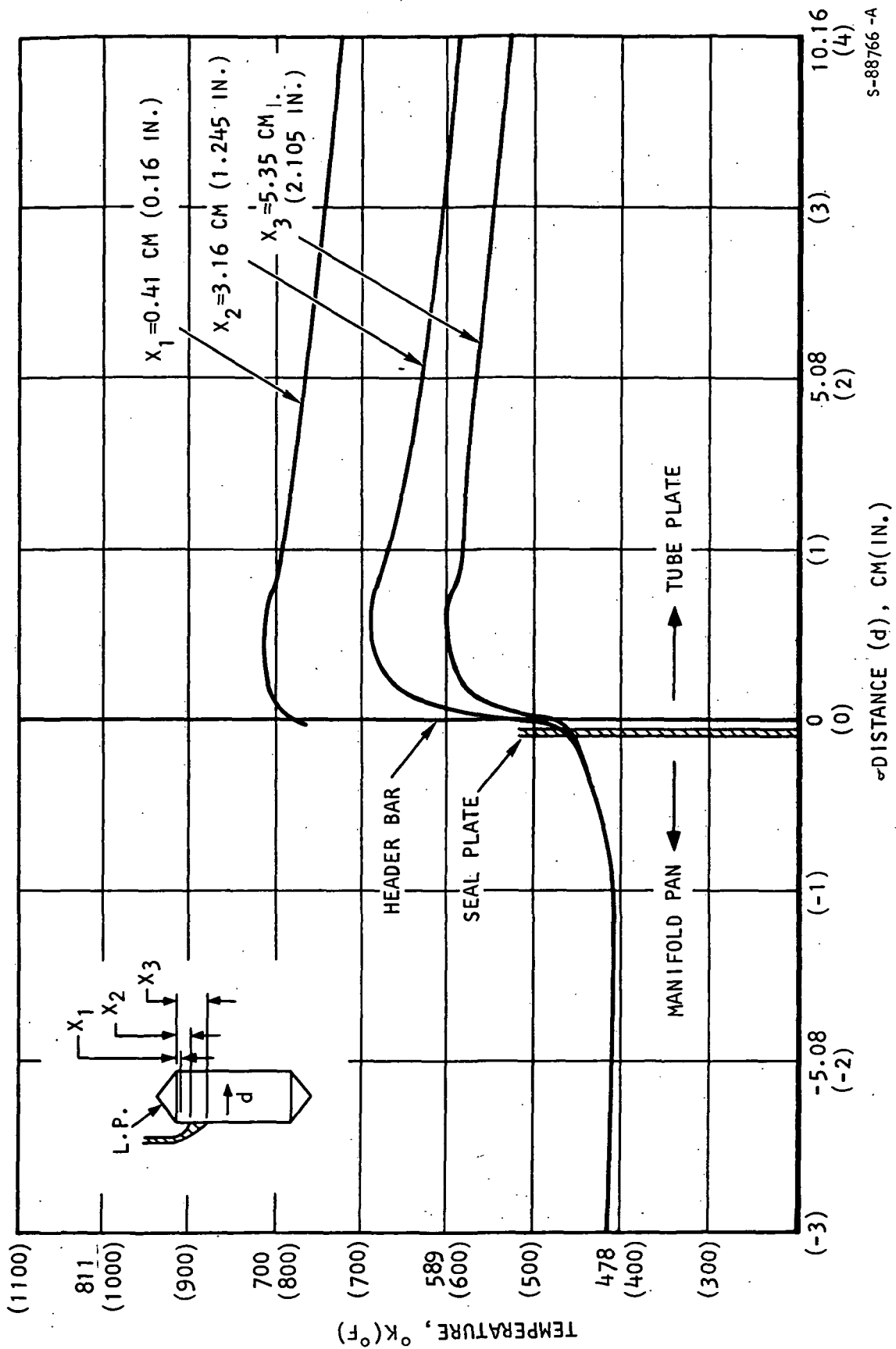


Figure 4-67.--Critical Area Temperature Distribution at Station 3.16 cm.



S-88766 -A

Figure 4-68.--Critical Area Temperature Distribution 90 sec After Startup.

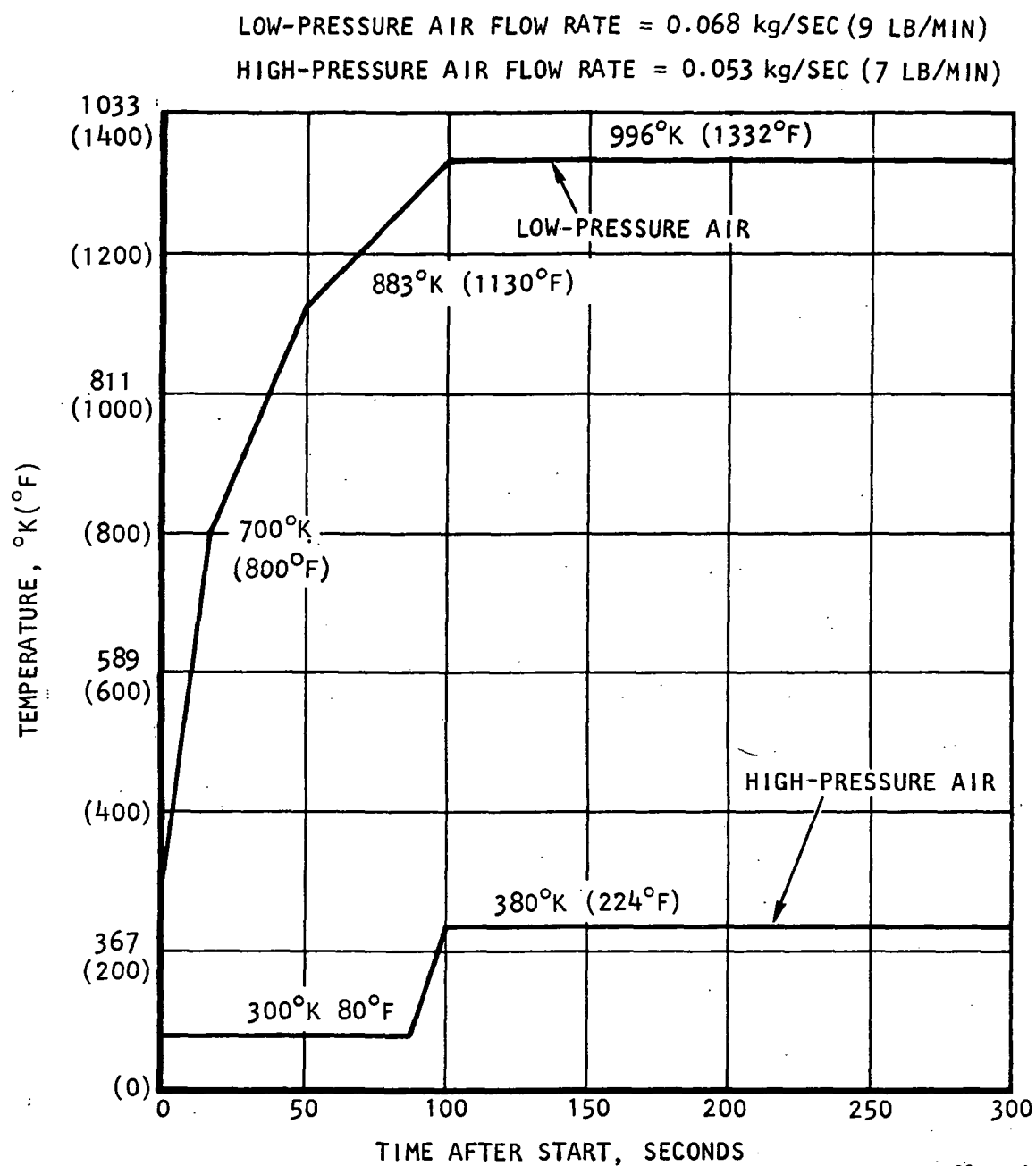
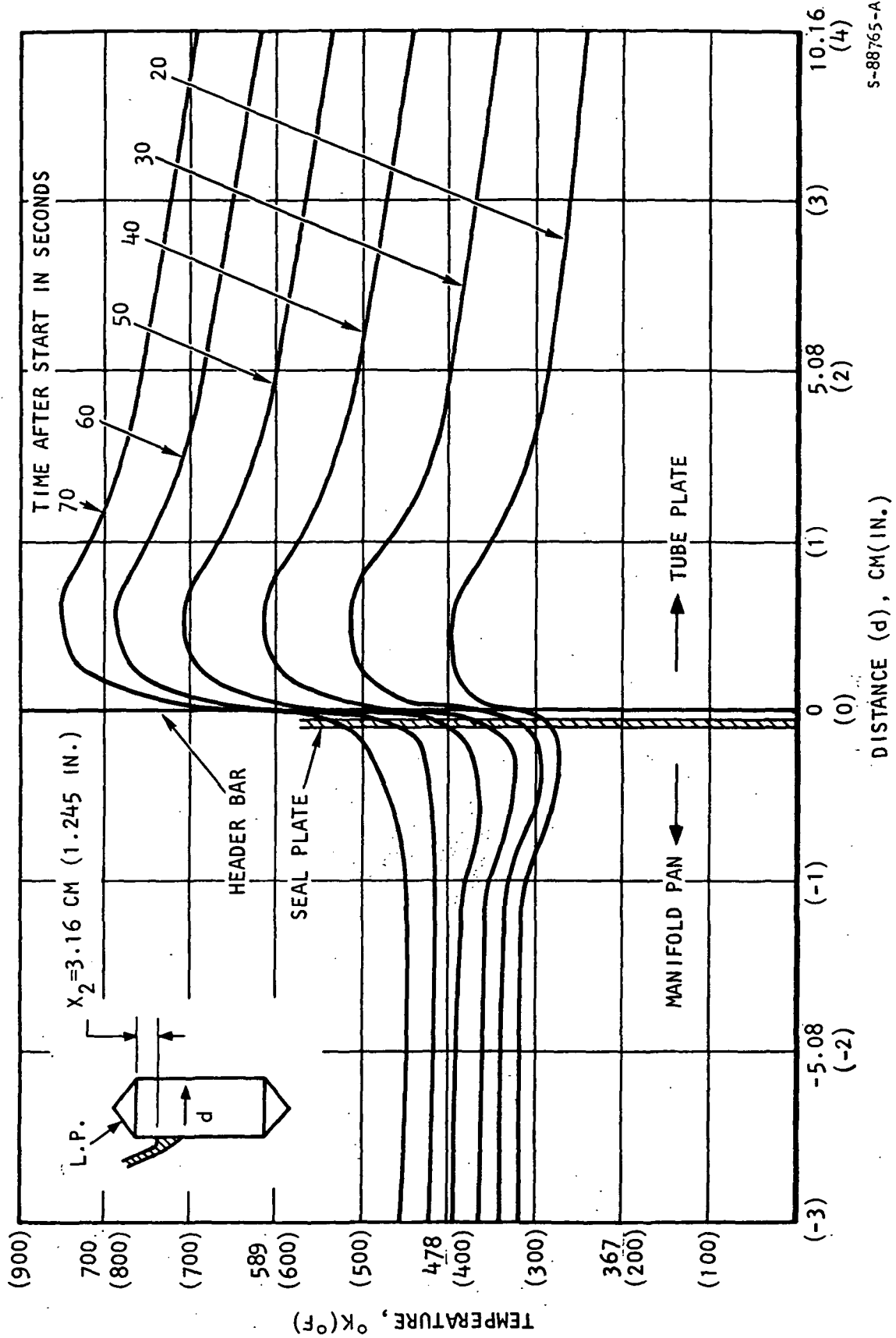
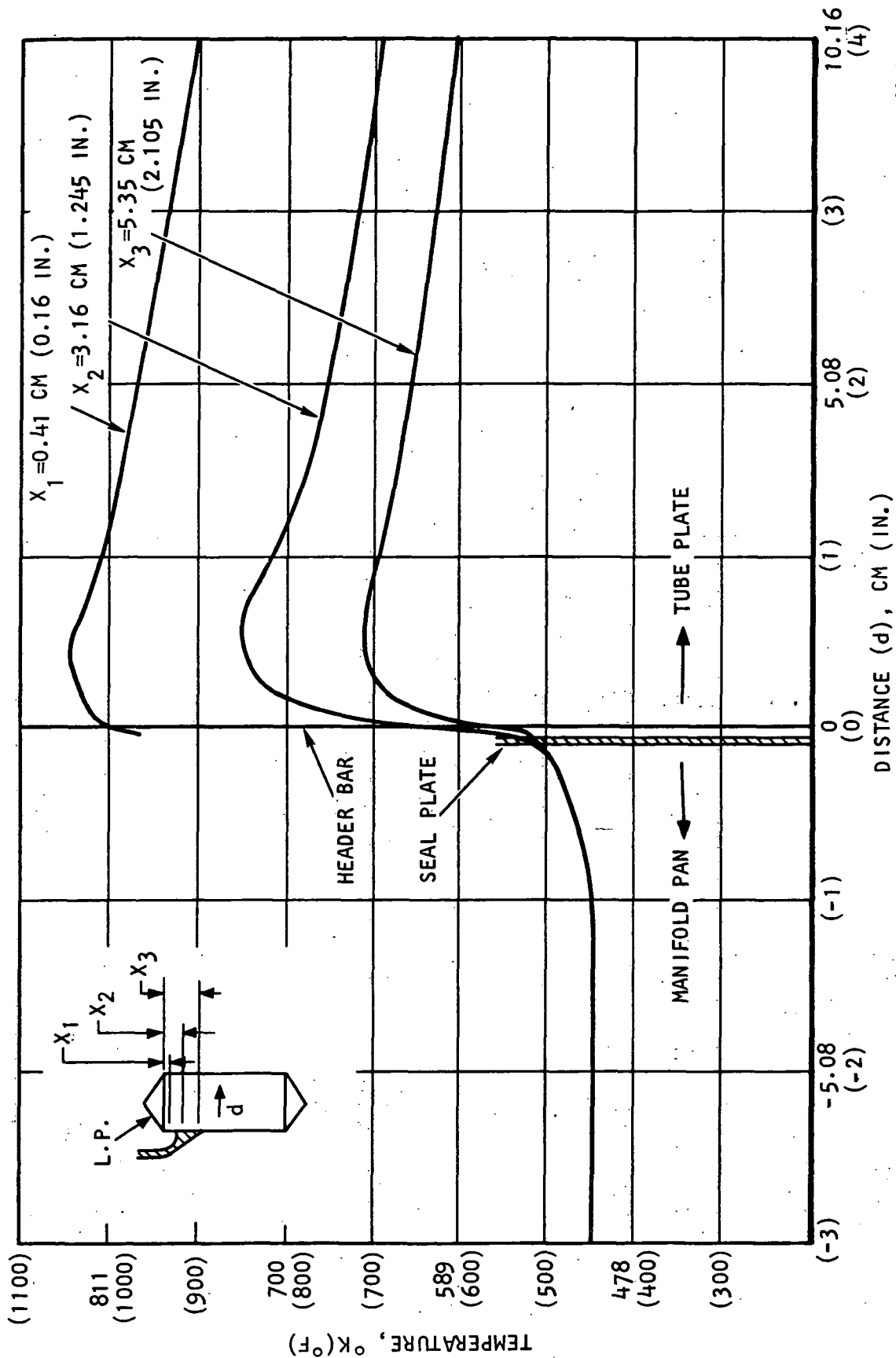


Figure 4-69.--Fast Transient.



S-88765-A :

Figure 4-70.--Critical Area Temperature Distribution, at Station 3.16 for Fast Transient.



S-88787-A

Figure 4-71.--Critical Area Temperature Distribution 70 sec After Startup, Fast Transient.

The resultant temperature distributions for the slow and fast transients were used in a stress analysis to predict the number of cycles before fatigue cracks appeared. With these two points (i.e., the 300- and 100-sec transients), the transient to induce cracking in 80 and 300 cycles could be estimated.

### Low-Cycle Fatigue Analysis

The most critical area in the quarter-size submodule was identified to be in the tube plate adjacent to the header bar in the area next to the manifold attachment flange. More precisely, at  $X_2 = 3.0$  cm and  $d = +1.0$  cm in fig. 4-70. After accumulating sufficient thermal cycles, fatigue cracks would appear in the tube plate resulting in an internal bypass flow of the Xe-He working fluid.

Analyses were completed for both 100- and 300-sec transient conditions. Based on these data, it was predicted that the startup transient would have to be decreased to 60 sec to create a thermal stress sufficient to cause cracks at 80 cycles.

After the initial 60-sec startup transient, a period of time is required for the metal temperatures to stabilize. Portions of the core are at high-stress level and creep will occur, which contributes greatly to the damage incurred during the cycle.

A review of the transient temperature analysis indicated that the hot-gas inlet temperature should be maintained at 996°K (1332°F) for an additional 9 min for the metal temperatures to stabilize. Stress relaxation calculations predicted that a major fraction of the creep damage would occur within 15 min. Thus, a 15-min hold time with the hot-gas inlet maintained at 996°K (1332°F) was specified. A 5-min cooldown ramp was specified to minimize the damage incurred during the shutdown portion of the cycle. A slow cooldown was considered to be more representative of actual operation. An analysis of the 5-min cooldown indicated, however, that a high stress could be developed at the cold end of the core. To avoid any premature failures, in this non-critical area, it was decided to increase the cold-gas inlet temperature from 300°K (80°F) to 380°K (224°F) after completing the first 60 sec of the startup cycle. The reduced temperature differential at the cold end of the core would alleviate the thermal stresses developed during shutdown.

The final set of test conditions for 80-cycle life is shown in fig. 4-72. It was necessary to limit the minimum hot-gas (LP) temperature to 422°K (300°F) because of a limit in the operation of the laboratory in-line combustor. The hot- and cold-gas pressures were set at the design point valves, 494 and 732 kN/m<sup>2</sup> abs, (72 and 106 psia), respectively. The flowrates were established by the transient temperature analysis to approximate performance with Xe-He.



801-4

PRESSURE,  $\text{KN/m}^2$   
(PSIA)

1034 (50)  
689 (100)  
345 (50)  
(0)

COLD GAS HP SIDE

732  $\text{KN/m}^2$  (106 psia)

HOT GAS LP SIDE

494  $\text{KN/m}^2$  (72 psia)

FLOW,  $\text{kg/sec}$  (LB/MIN)

0.0756 (10)  
(8)  
0.0454 (6)  
(4)  
0.0151 (2)  
(0)

HOT GAS (LP SIDE)

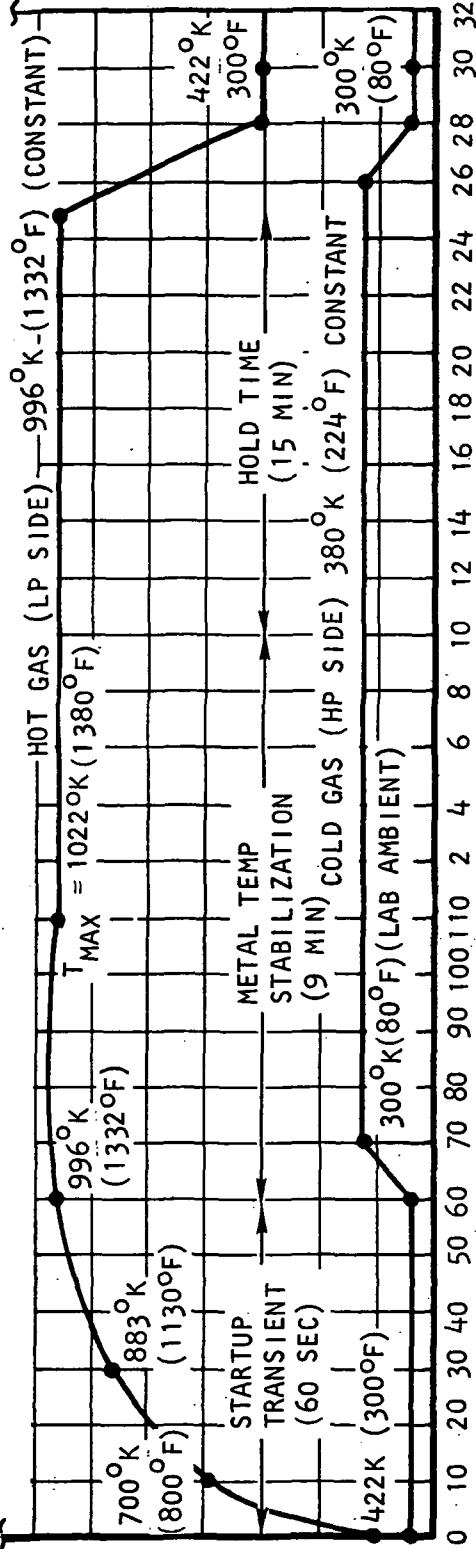
0.068  $\text{kg/sec}$  (9.0 lb/min)

COLD GAS (HP SIDE)

0.053  $\text{kg/sec}$  (7 lb/min)

TEMPERATURE,  $^{\circ}\text{K}$  ( $^{\circ}\text{F}$ )

1033 (1400)  
(1200)  
811 (1000)  
(800)  
589 (600)  
(400)  
367 (200)



TIME, MIN

TIME, SEC

CHANGE OF SCALE

OF SCALE

S-7420-A

Figure 4-72.--Test Conditions for Thermal Cycle Testing, 80-Cycle Life.

## Fabrication

The core was assembled using a 3-step brazing procedure. In the first operation, Palniro 1 braze alloy (50 Au-25 Ni-25 Pd) was procured in 1-mil foil form, cut to size, and tack-welded to the individual tube plates. The header bars were then tacked welded to the foil-coated tube plates using a fixture to maintain the bars within 0.25 mm of true position along their entire length. The fins were then placed into position and the unit was stacked. A picture of the offset heat transfer fins, a header bar, and a side plate is shown on figs. 4-73, 4-74, and 4-75.

During the stacking operation, a series of 20 sheath-type thermocouples, 1.0- mm dia, were installed inside the core assembly. These thermocouples would be monitored during the thermal cycle testing to obtain data that could be used to confirm the transient temperature predictions.

A photograph of the core assembly installed in the carbon braze fixture is shown in fig. 4-76.

Views of the unit after the first braze cycle are shown in fig. 4-77. Visual inspection of the brazing joints with a binocular microscope at a 25X magnification revealed no areas of questionable quality. The header bars were measured for flatness after the brazing cycle and were found to be flat within 0.25 mm (0.010 in.) TIR. Two locations at the high-pressure inlet end had a flatness of 0.4 mm (0.015 in.) TIR.

The sides of the header bars were then machined to provide a smooth surface for braze-attachment of the seal plates. A photograph of the as-machined core assembly is shown in fig. 4-78. No braze joint cracks were observed in the machined surface.

In the second braze operation, the seal plates and the manifold splitters were joined to the core assembly. One-mil Palniro RE (55 Au-37 Ni-8 Pd) foil was used. Additional Palniro RE braze alloy powder also was applied in a slurry form along the splitter-core joint. A photograph of the manifold splitter detail part is shown in fig. 4-79. The apex of the triangular end sections was machined to provide a close fit with the splitter.

In a third braze operation, using Palniro 7 alloy (70 Au-22 Ni-8 Pd), the pan attachment flanges were brazed to the seal plate. The flanges, shown in fig. 4-80, provide pan attachment points that are remote from the core braze joints.

The manifolds, shown in fig. 4-81, were then fitted and welded to the core. The cold, high-pressure inlet manifold incorporates a baffle as required to obtain uniform flow distribution. The completed core assembly with all instrumentation in place is shown in fig. 4-82.

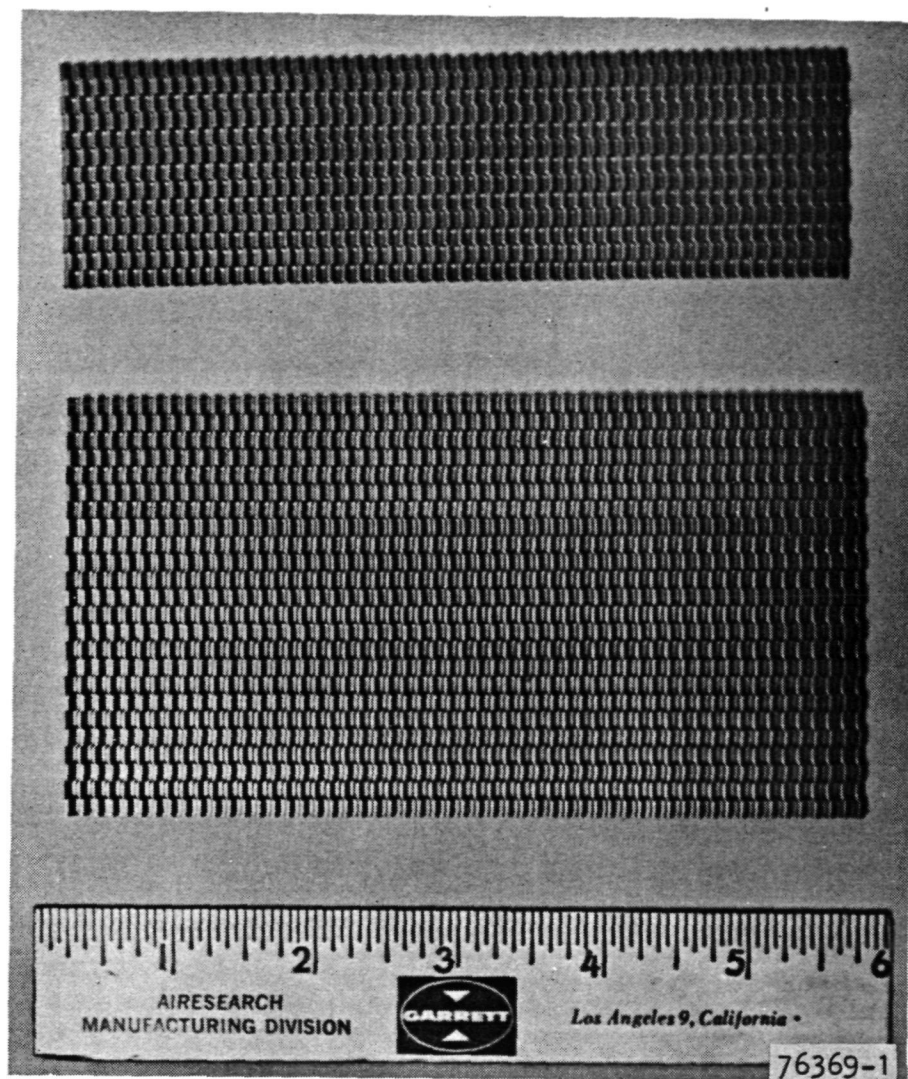


Figure 4-73.--Offset Heat Transfer Fins.

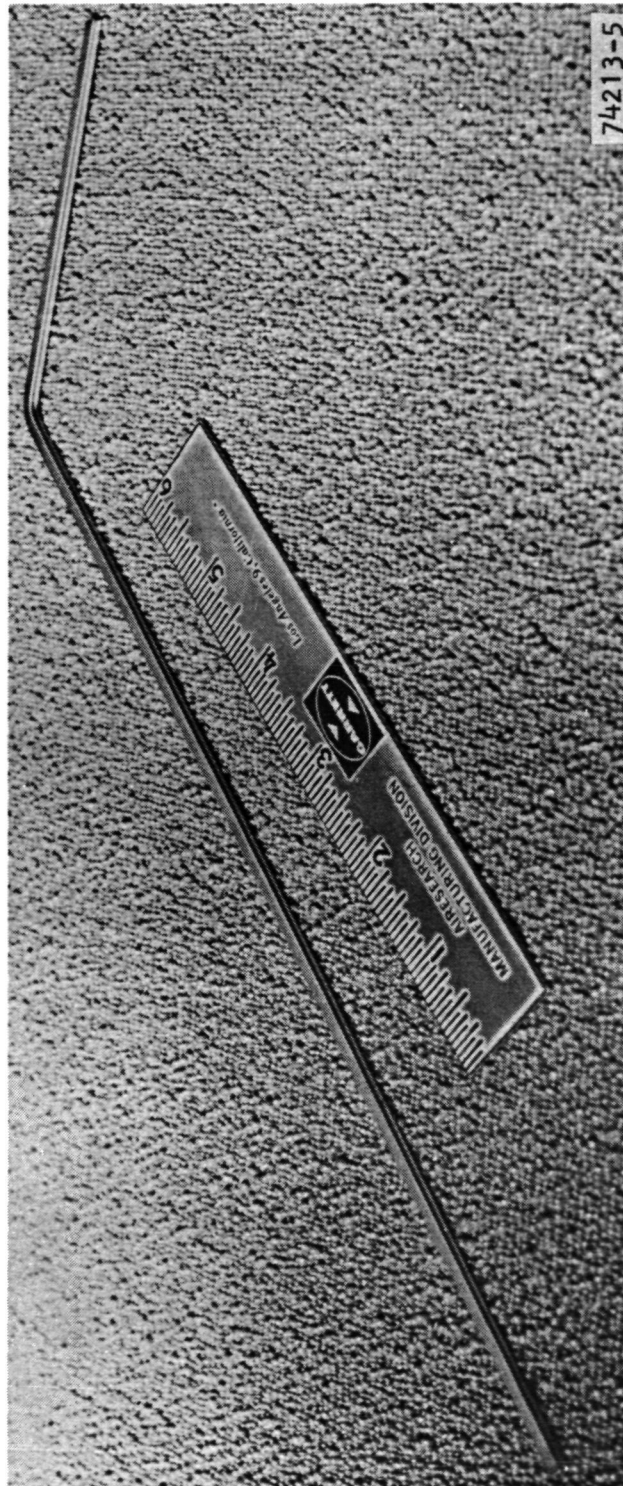


Figure 4-74.--Header Bar.

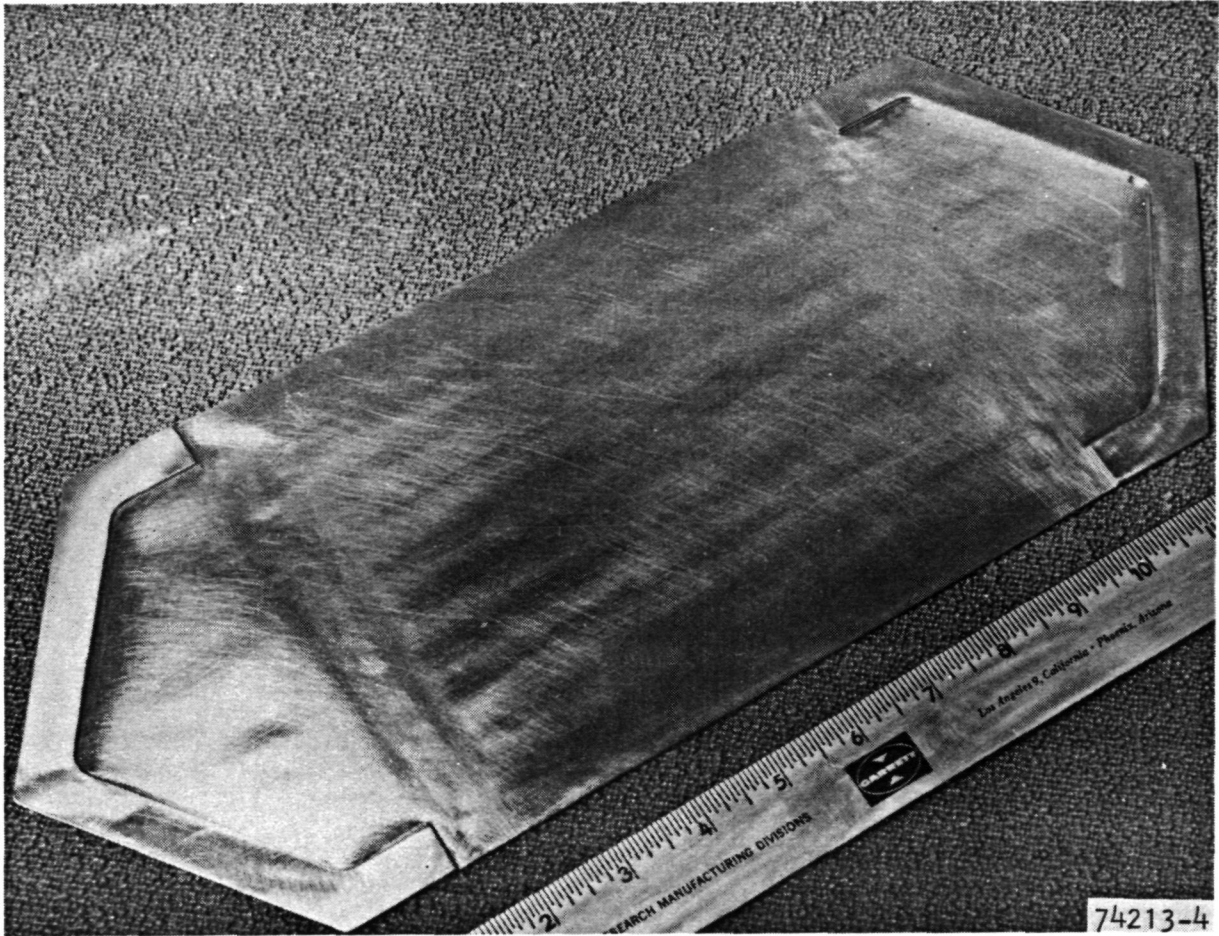


Figure 4-75.--Side Plate.

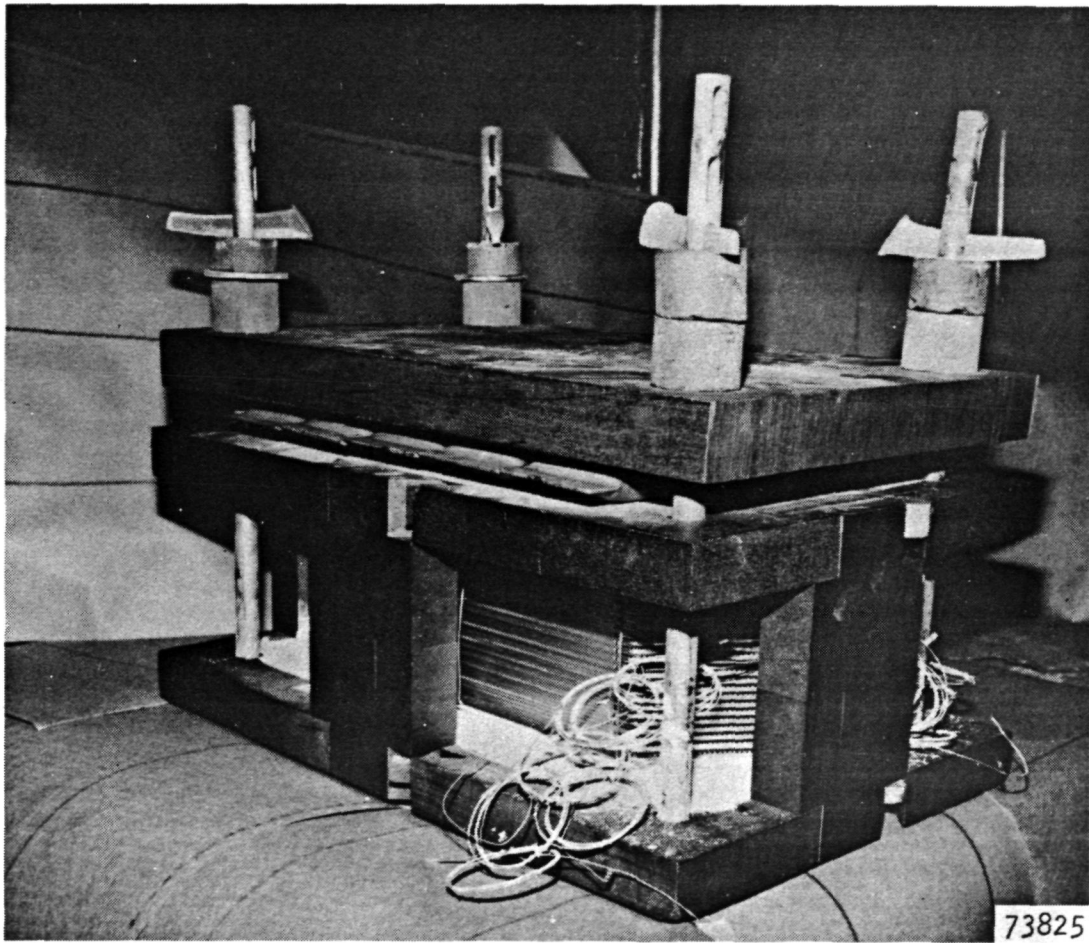
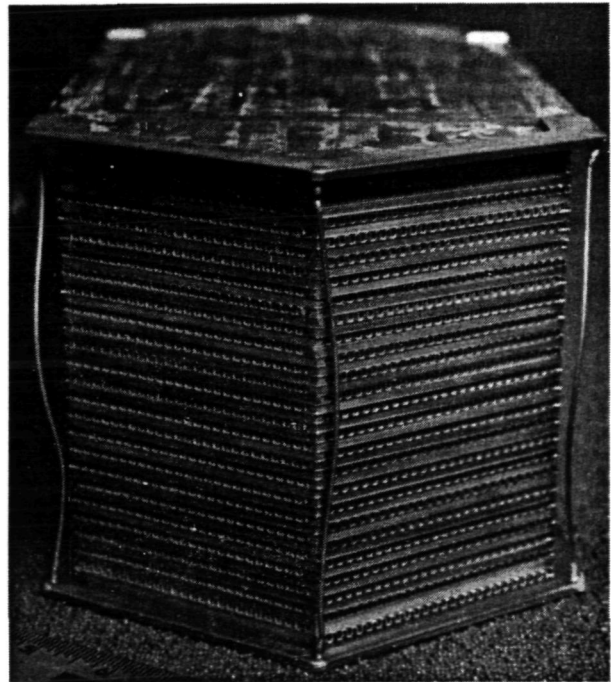
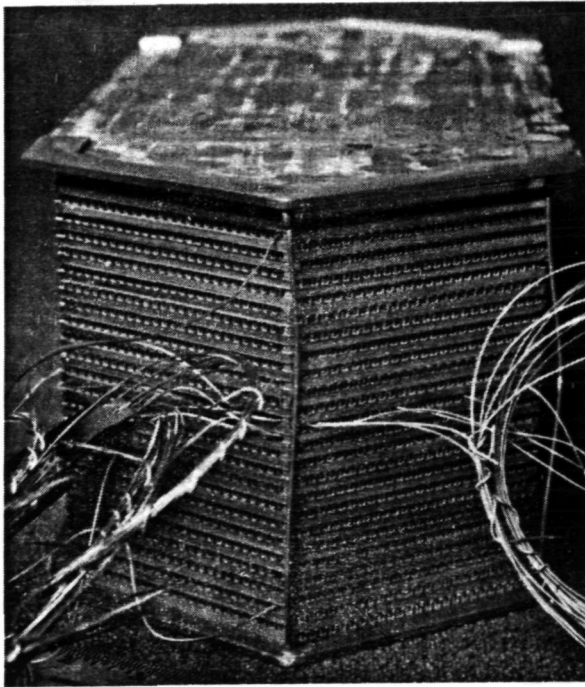
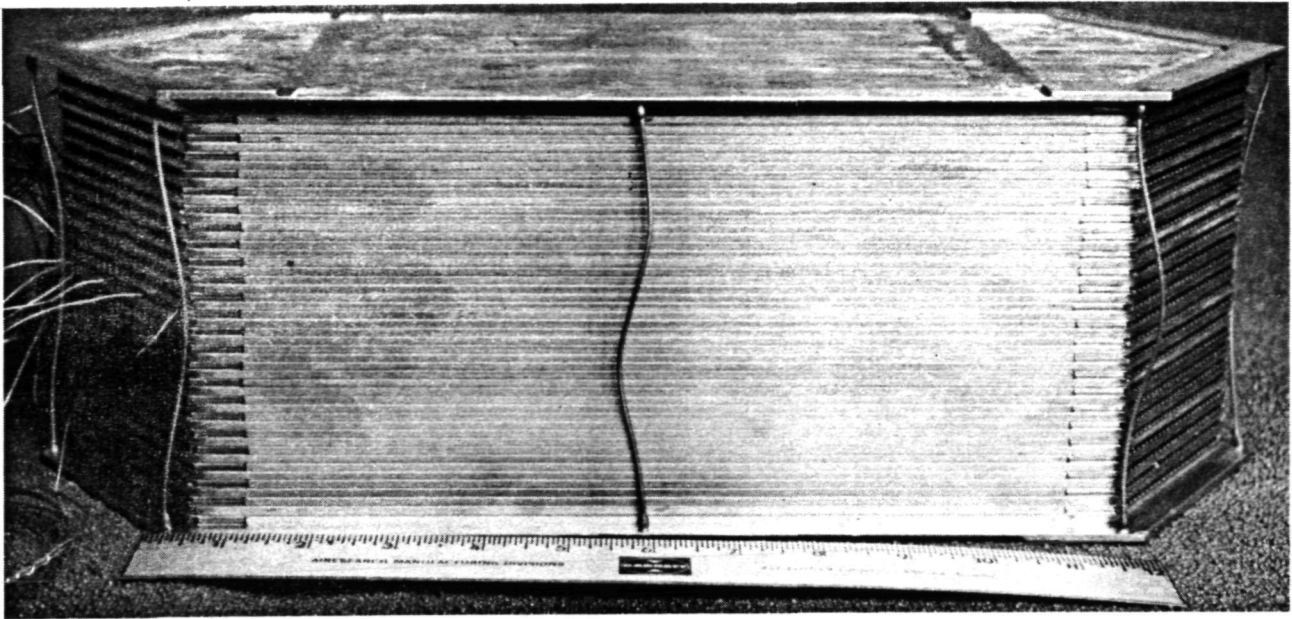


Figure 4-76.--Core Assembly Installed In Carbon Braze Fixture.





F-23931

Figure 4-77.--Core Assembly After First Braze Operation.

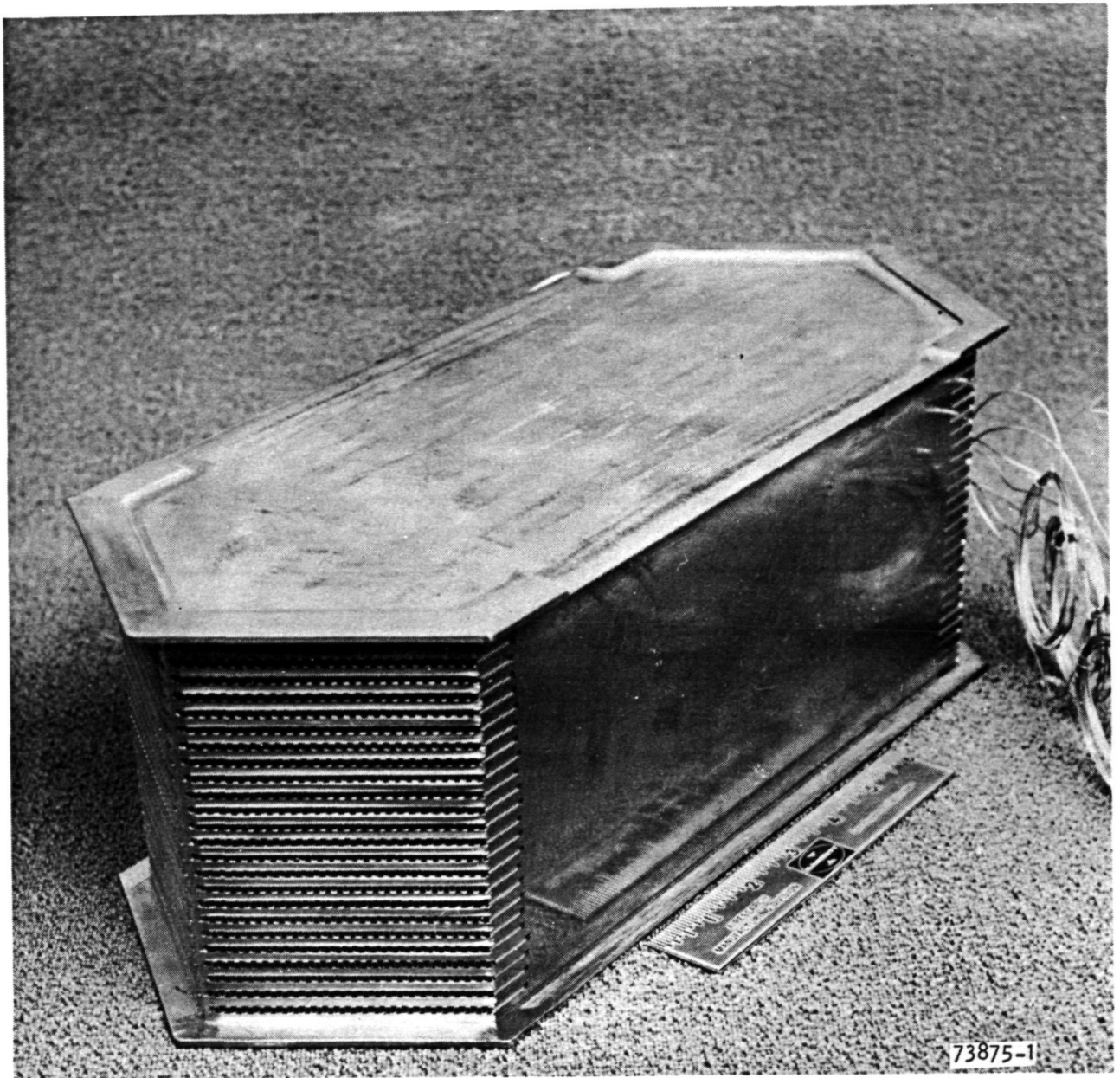


Figure 4-78.--Machined Core Assembly.



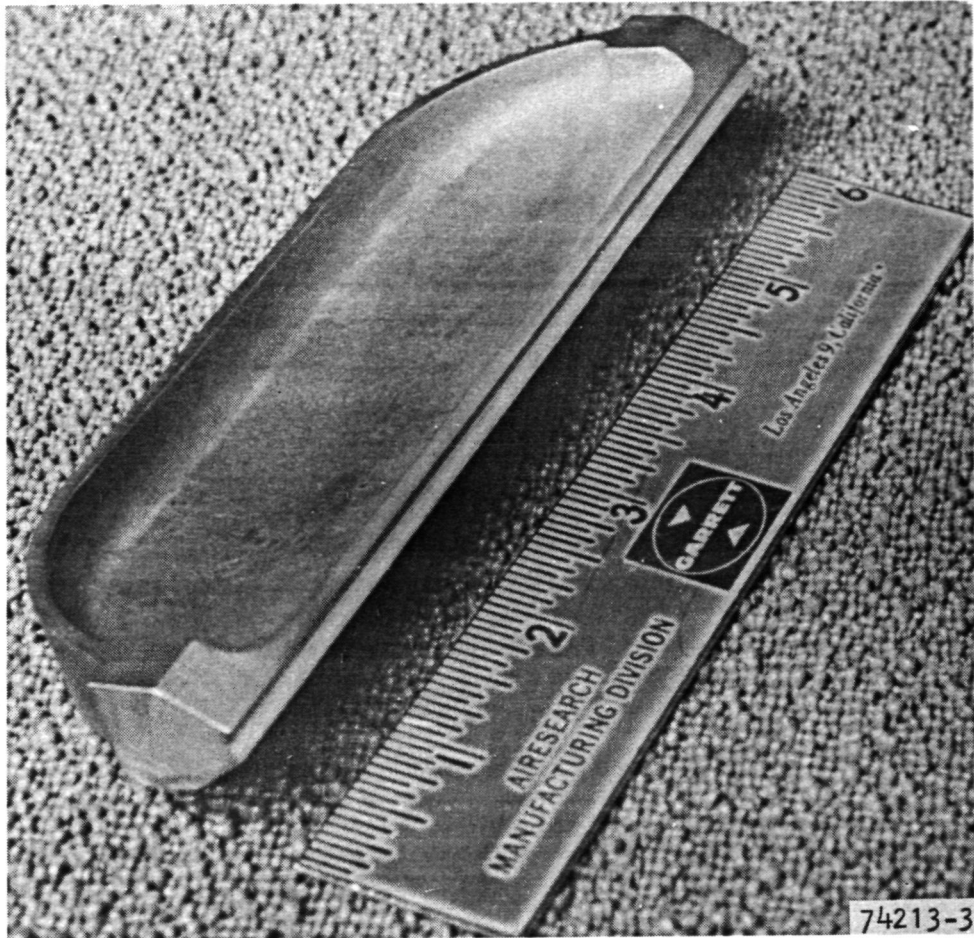


Figure 4-79.--Manifold Splitter.

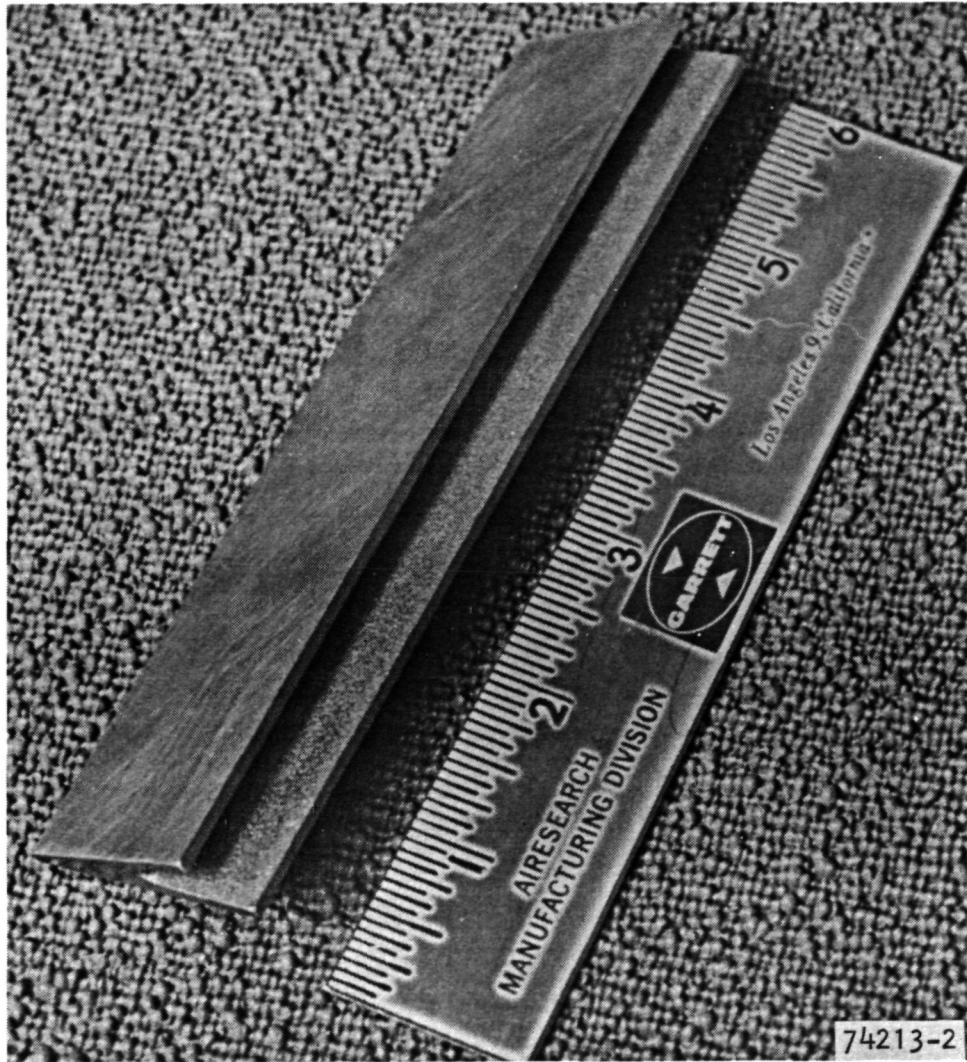


Figure 4-80.--Pan Attachment Flange.

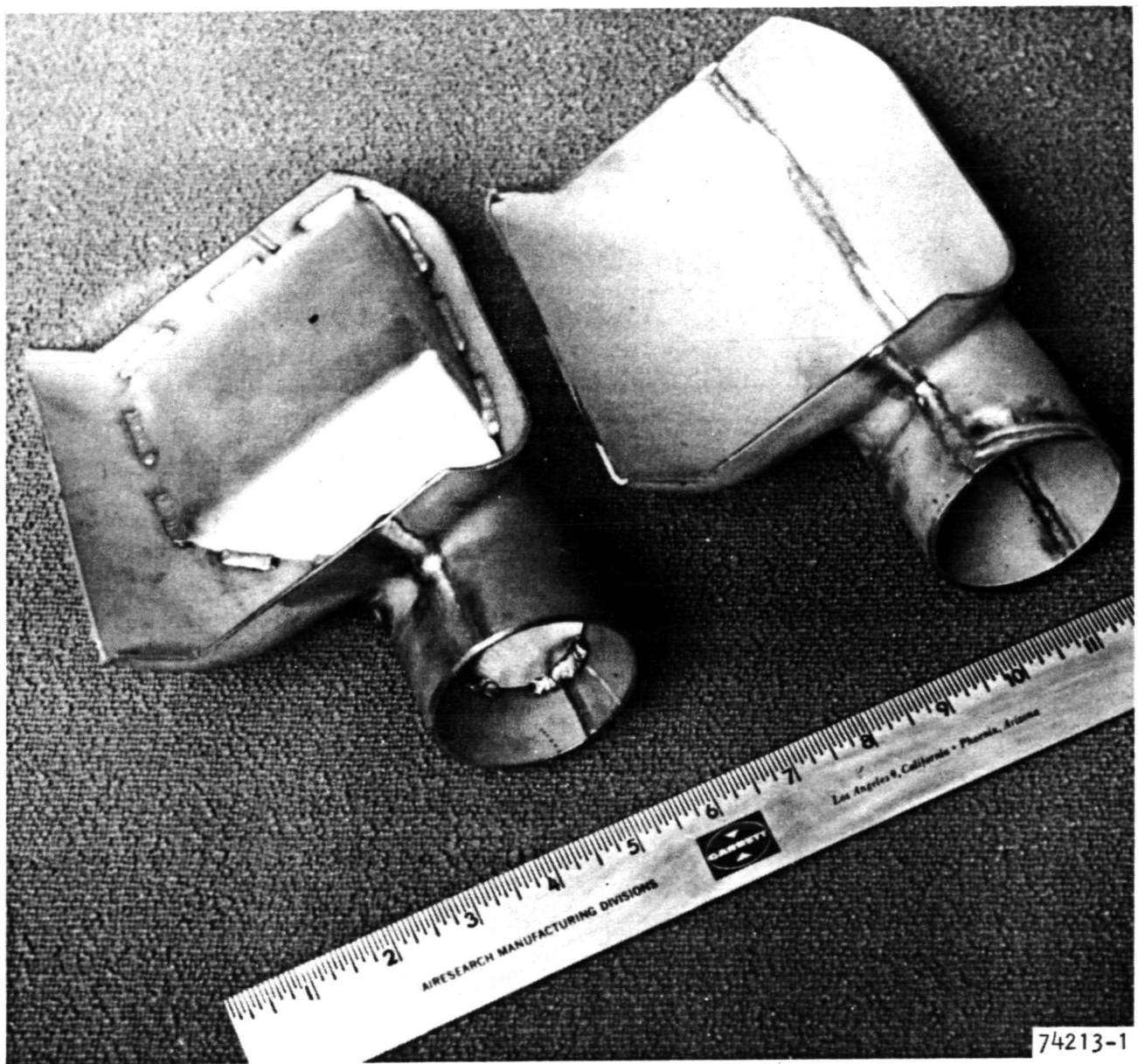


Figure 4-81.--Heat Exchanger Manifolds.

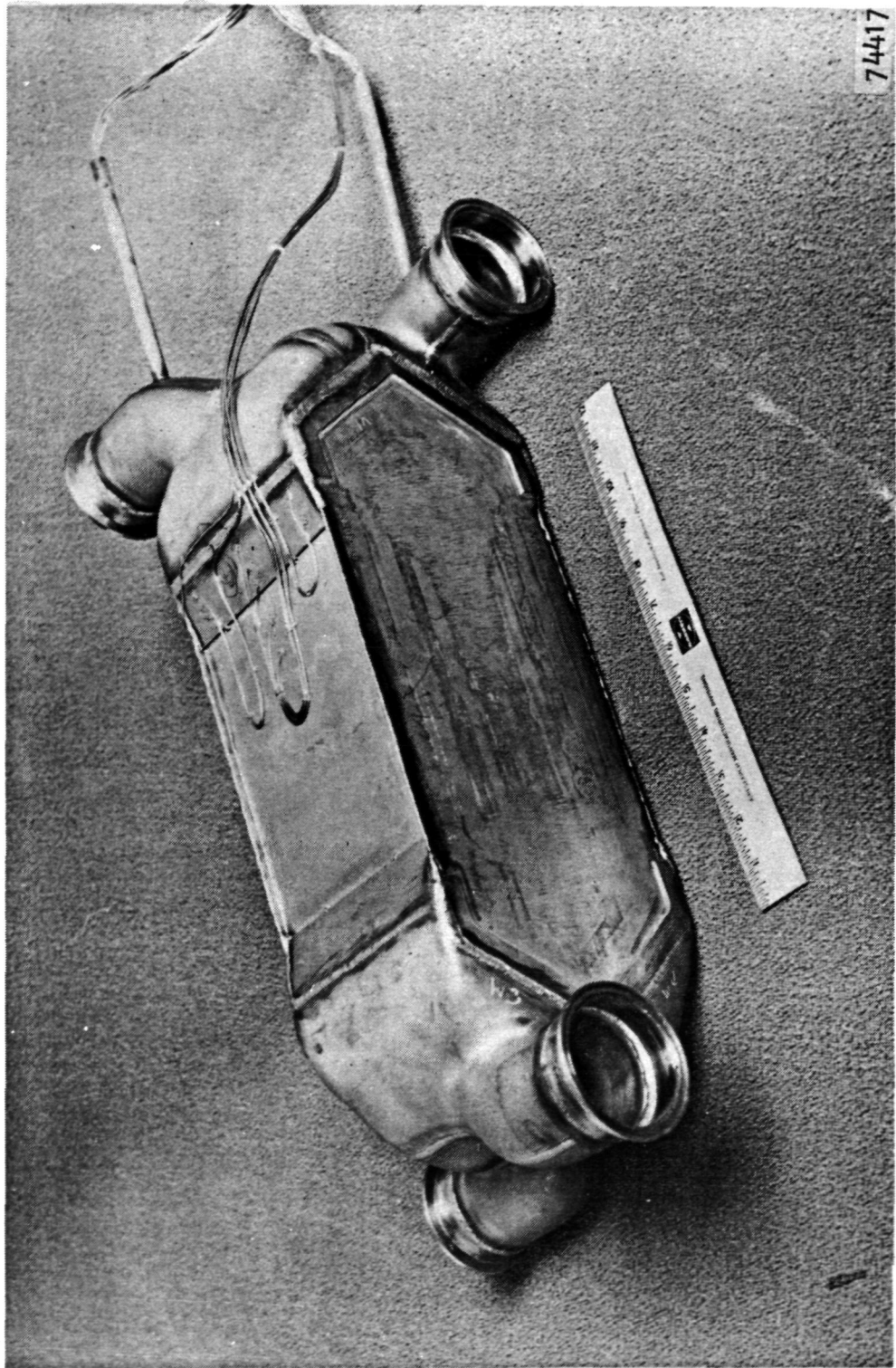


Figure 4-82.--Heat Exchanger Submodule.



Weld joint quality was verified by performing fluorescent penetrant and radiographic inspections (100 percent). The core was pressurized with air to 1723 kN/m<sup>2</sup> (250 psig), the proof pressure. No external leaks, either visible or observed by pressure decay were detected. The core was then checked for interpass leakage and a small leak was detected at the cold end of the core assembly at approximately the turning fin-heat transfer fin interface in the center of the stack height. The high-pressure side was leaking into the eleventh sandwich (low pressure) at a rate of 525 ml in 30 sec (with a pressure differential of 103 kN/m<sup>2</sup> (15 psi)). The resulting interpass leakage at the design conditions was calculated to be less than 0.2 percent. This amount of leakage was considered acceptable and testing of the unit was authorized.

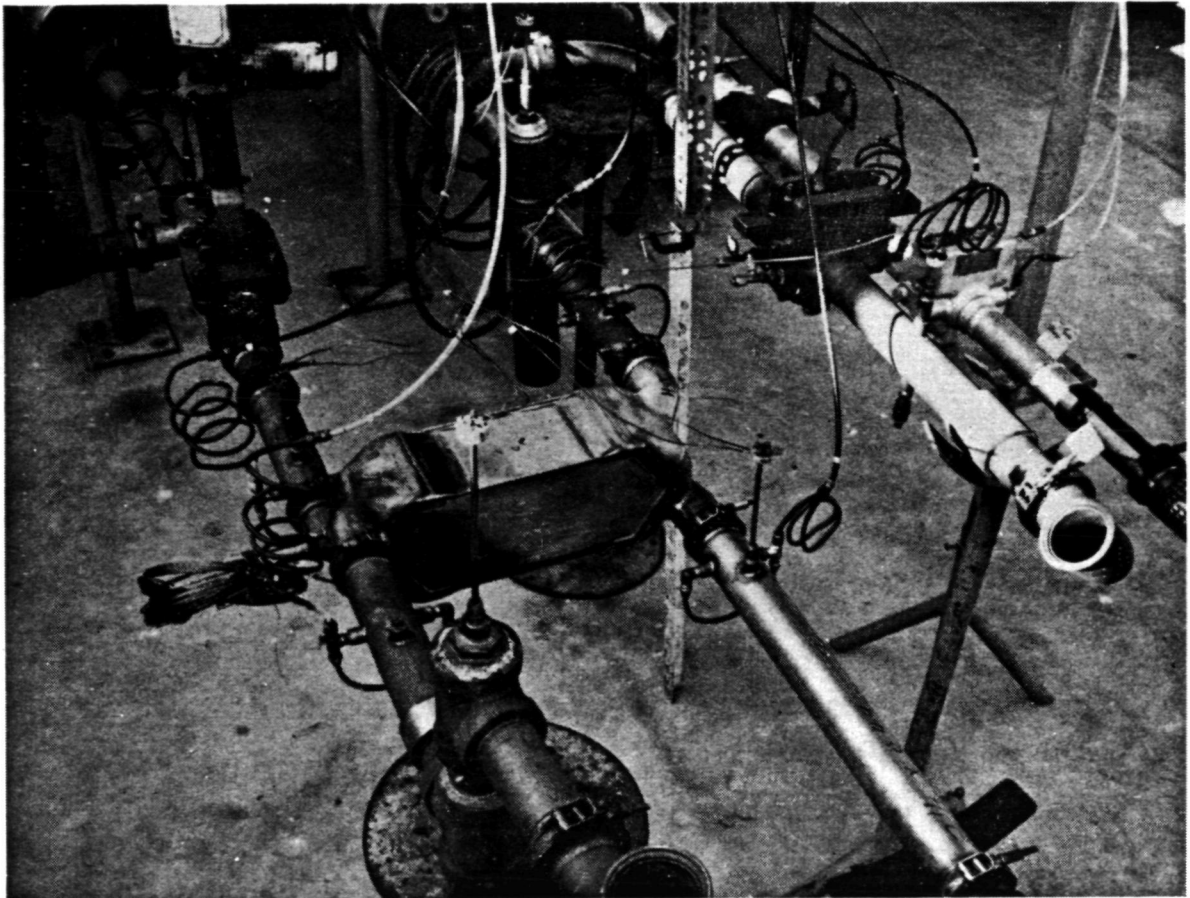
#### Performance Test

The first one-quarter-size submodule fabricated was installed in a test loop (fig. 4-83) and subjected to performance tests. These tests consisted of isothermal pressure drop and heat transfer tests over a range of flow rates at prescribed inlet temperatures. The data from these tests were reduced and plotted as shown in figs. 4-84 through 4-86. Figs. 4-84 and 4-85 give the pressure drop data and fig. 4-86 presents the heat transfer data in terms of temperature effectiveness on the hot and cold sides.

The three highest airflow points, 3.6, 4.5, and 5.4 kg/min (8, 10, and 12 lb/min) of the one-quarter-size test core were used to determine the UA correction factor required to fit the analytical results to the test data. As stated above, the correction factor required for the fit was 27 percent. The three lowest test flows were not used because their hot- and cold-side effectivenesses did not have similar trends. It is believed that this discrepancy is due to excessive heat loss at low flows.

Though the cold-side effectivenesses are predicted to be higher than the hot-side effectivenesses, the test results did not show this difference (probably due to heat losses). As a result, the fit was made by matching the cold-side effectiveness. This is shown in fig. 4-86.

Results of the analysis of these test data are summarized in table 4-14. The major factors degrading recuperator performance are flow maldistribution and heat leak to ambient. A secondary factor is manufacturing tolerances as determined by measuring the actual number of fins in the test unit. The total degradation in performance that can be directly calculated is 28.3 percent equivalent UA, which corresponds closely with the observed decrease of 27.0 percent equivalent UA. Other factors that may have contributed to a decrease in UA, such as instrumentation errors, could amount to as much as 10.1 percent UA degradation. It is concluded, however, that the net effect of instrumentation errors is nil because the observed UA degradation can be directly accounted for. Comparison of the predicted and test values of pressure drop indicates that the predicted pressure drops are slightly conservative.



F-19831

Figure 4-83.--Performance Test Setup (One-Quarter-Size Module).

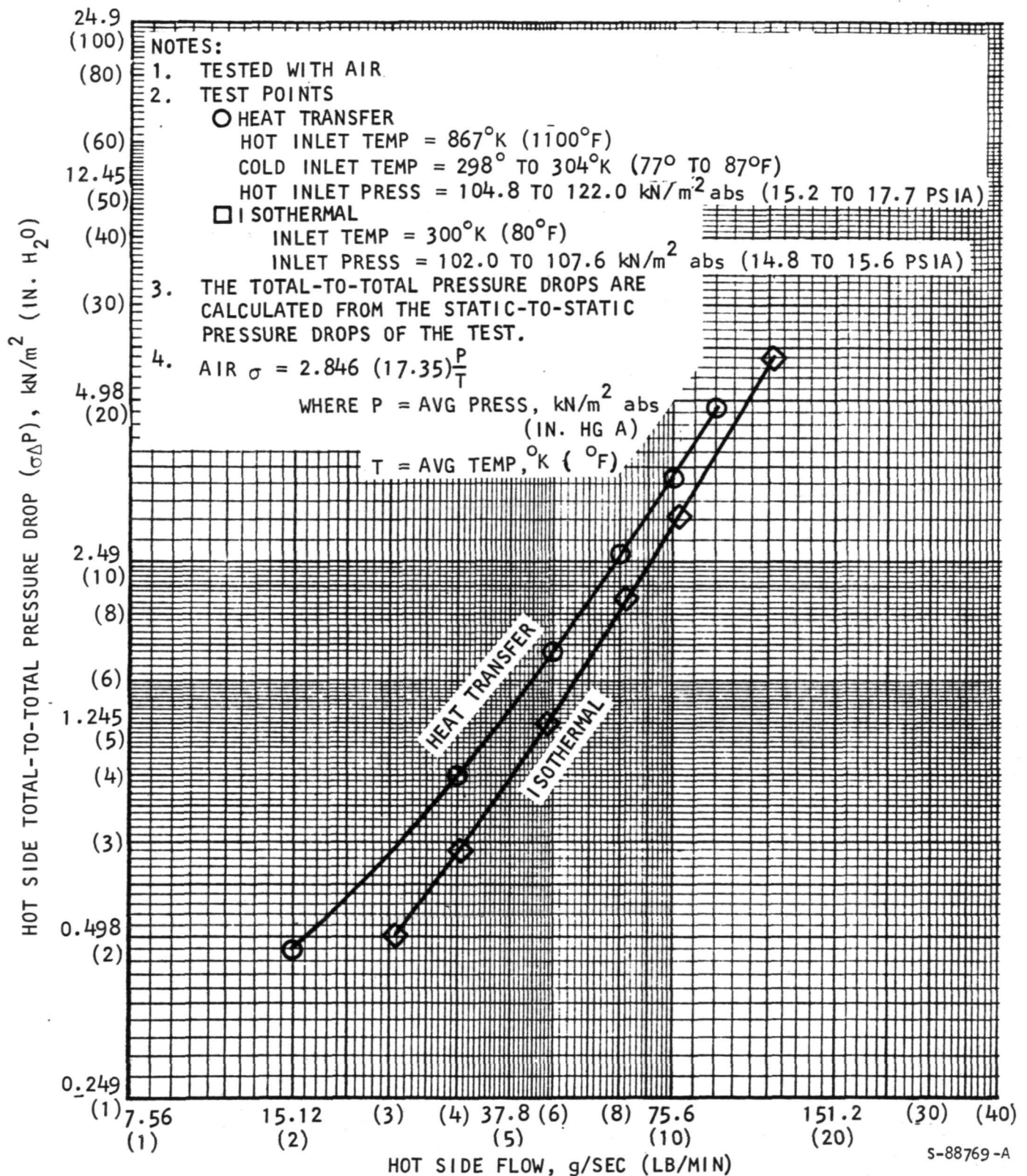


Figure 4-84.--Pressure Drop, One-Quarter-Size Recuperator Submodule.

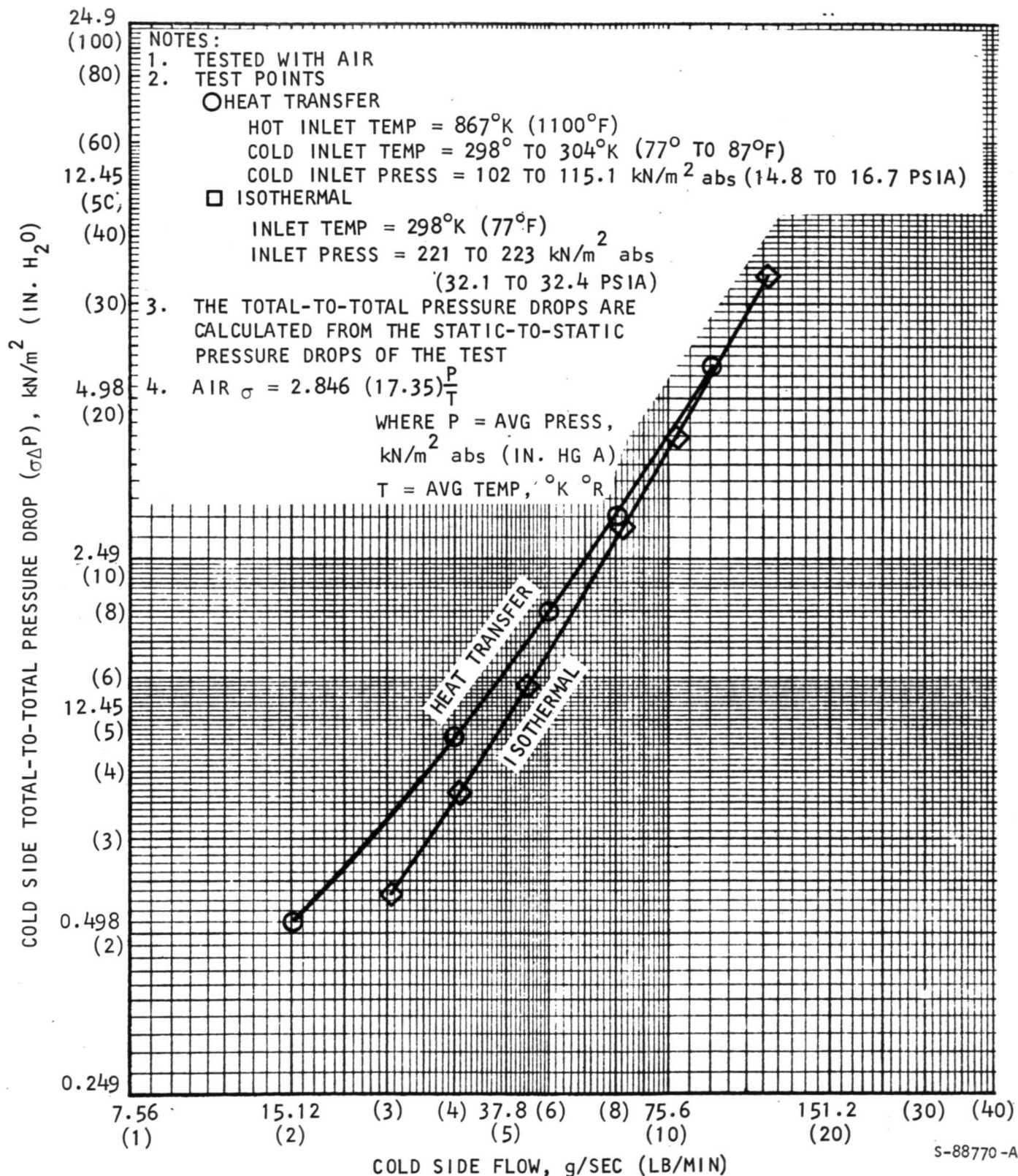


Figure 4-85.--Pressure Drop, One-Quarter-Size Recuperator Submodule.



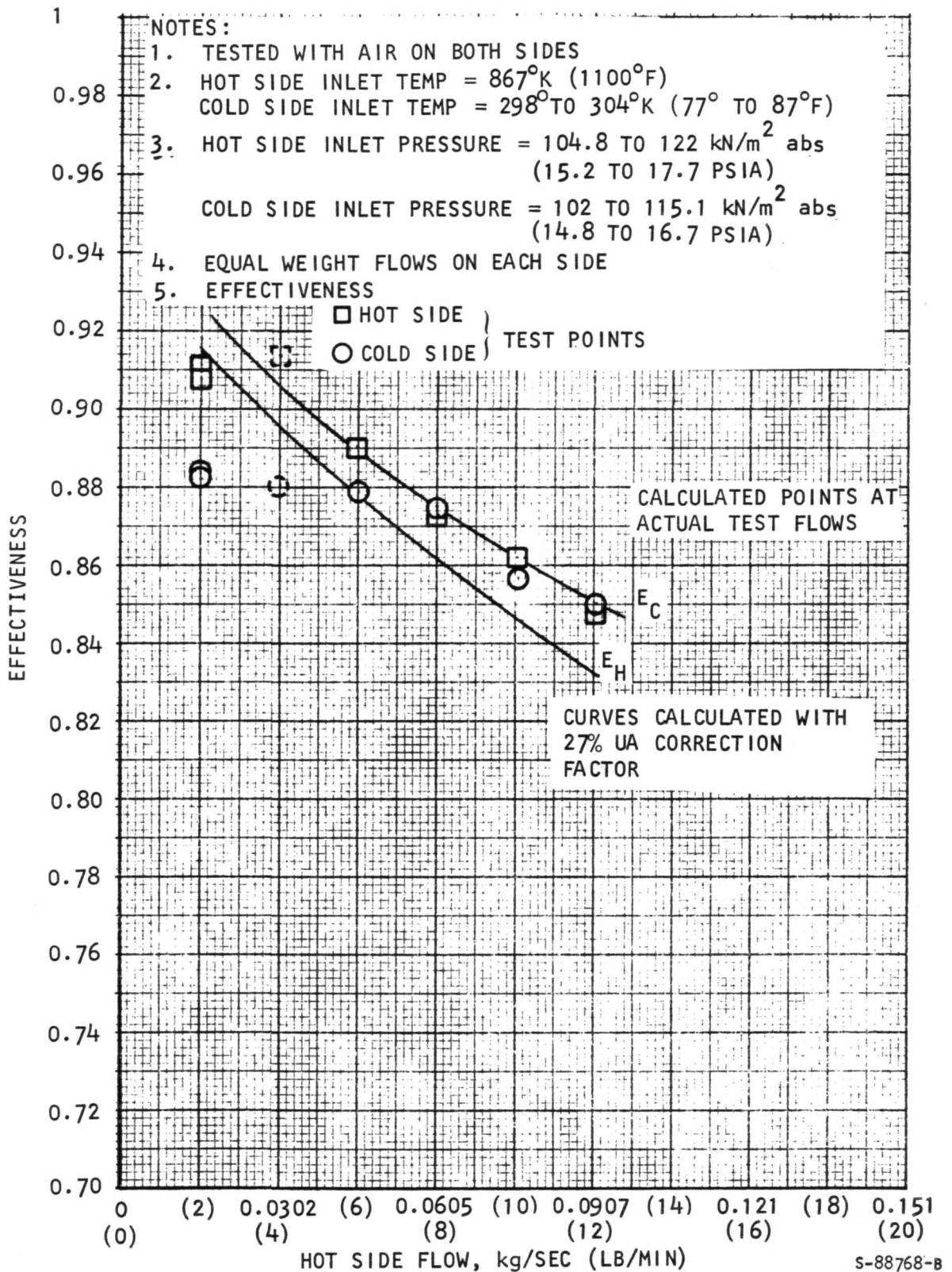


Figure 4-86.--Test and Analytical Heat Transfer Performance.

TABLE 4-14

TEST DATA ANALYSIS SUMMARY  
ONE-QUARTER-SIZE TEST SUBMODULE SK52160-1, SN 1

PERFORMANCE (At 0.0756 kg/sec (10 lb/min) flow both sides)		Predicted (No margin)	Corrected for Test Results	
Cold-side effectiveness Equivalent UA, J/s-K (Btu/min-°F)		0.8957 659 (20.83)	0.863 481 (15.20)	
Decrease in equivalent UA (Predicted-Test) = 27%				
Factors contributing to decrease in equivalent UA:				
Flow maldistribution:		10.0% UA		
Manufacturing tolerance:		3.5% UA		
Heat leak to ambient:		14.8% UA		
Total		28.3% UA		
Other possible factors that may contribute to decrease in equivalent UA (or performance)				
Thermocouple inaccuracy:		4.5% UA		
Flowmeter inaccuracy:		3.6% UA		
Metal thermal conductivity uncertainty:		2.0% UA		
Total		10.1% UA		
PRESSURE DROP				
	Heat Transfer		Isothermal	
	Predicted*	Test	Predicted*	Test
	Hot-side overall $\sigma\Delta P$ , kN/m <sup>2</sup> (in. H <sub>2</sub> O)	3.68 (14.8)	3.66 (14.7)	2.99(12.02)
Cold-side overall $\sigma\Delta P$ , kN/m <sup>2</sup> (in. H <sub>2</sub> O)	4.33 (17.4)	4.23 (17.0)	3.25(13.05)	3.98(16.0)
PRESSURE DROP BREAKDOWN				
Component	Cold Side $\sigma\Delta P^{**}$		Hot Side $\sigma\Delta P^{**}$	
	Heat Transf.	Isothermal	Heat Transfer	Isothermal
Core	2.45 (9.85)	1.93 (7.76)	2.33 (9.38)	1.82 (7.30)
End sections	0.79 (3.16)	0.88 (3.55)	0.85 (3.43)	0.73 (2.93)
Inlet and outlet ducts	0.40 (1.60)	0.43 (1.74)	0.49 (1.97)	0.45 (1.79)
Flow maldistribution induced by manifolds	0.70 (2.80)		0.0	0.0

\* 1.5 Duct Velocity head (6.17 cm (2.43 in.) ID duct

\*\* kN/m<sup>2</sup> (in. H<sub>2</sub>O)

### Thermal Cycle Test, SNI

The thermal cycle test imposed on the recuperator submodule was expected to produce fatigue cracks at approximately 80 cycles by exposing the unit to an accelerated transient condition. Thermal cycling was obtained by varying the low-pressure gas inlet temperature according to the cycle described in fig. 4-72.

A schematic of the test setup is shown in fig. 4-87. Process control equipment was used to vary the air and natural gas flows to obtain the desired transient conditions in a precise, repeatable fashion. A series of calibration runs were performed to adjust the control equipment. During setup calibration and system checkout it was estimated that five 300-sec startups and two 100-sec startup temperature ramps were imposed on the submodule prior to starting the official cycling test. The 100, 300 ramps as well as the 60-sec ramp actually imposed on the test unit are defined in fig. 4-88.

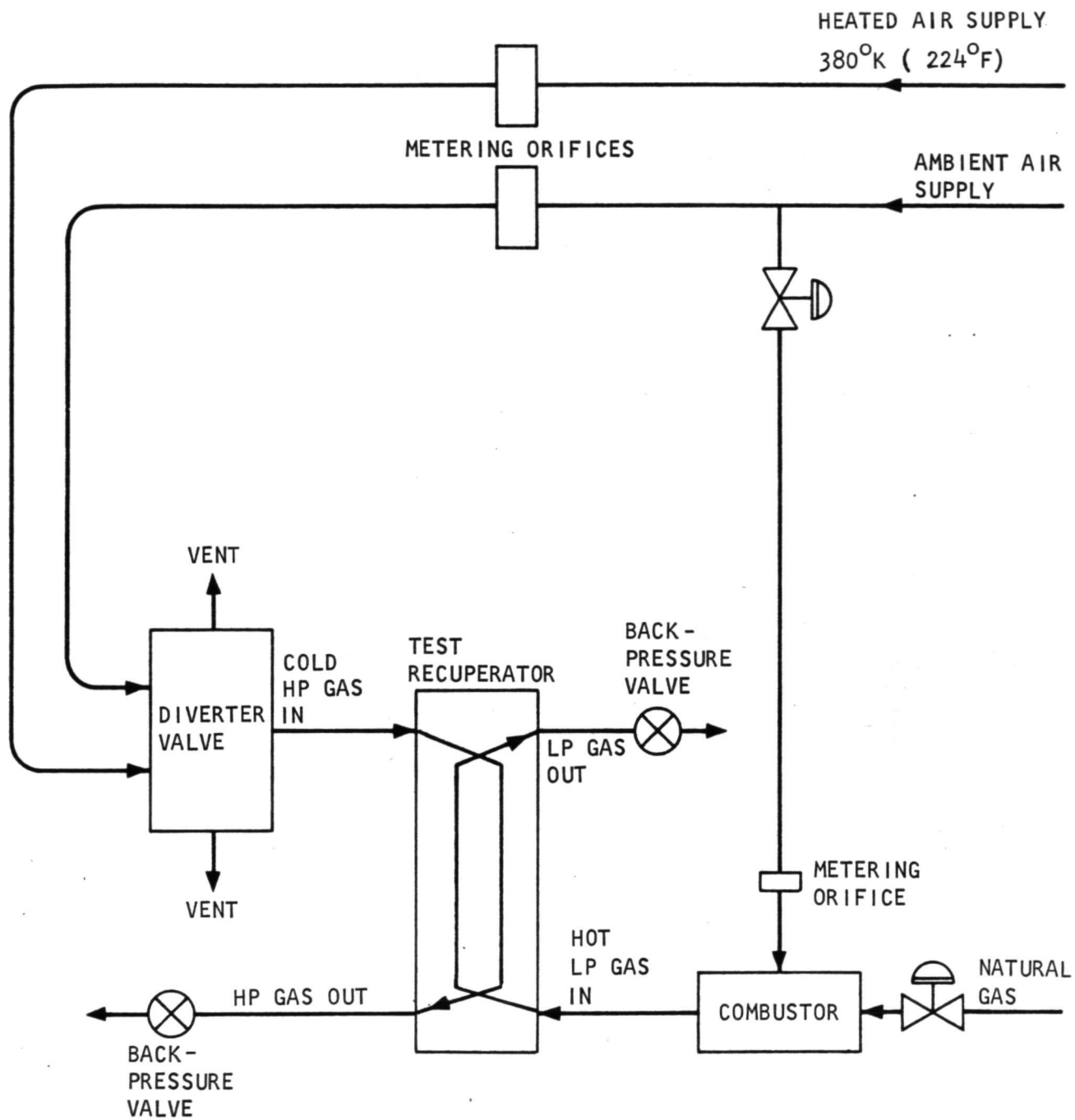
For the first five thermal cycles, a complete set of temperature data was obtained from 38 heat exchanger metal-temperature thermocouples and four fluid-temperature thermocouples. The temperature response at the low-pressure gas inlet was very similar for each run; in fact, the measured temperatures were within a 17°K (30°F) band for all runs.

After completing 10 cycles of operation, the test was stopped and the unit was checked for leakage. No visible external leakage could be detected with the unit pressurized to 241 kN/m<sup>2</sup> (gauge) (35 psig) and coated with a soap solution. An internal leak was noted and was determined to be 1.04 g/sec (0.138 lb/min) at a pressure differential of 241 kN/m<sup>2</sup> (gauge) (35 psig); this rate corresponds to 2.7-percent bypass flow at operating conditions. The leak location was determined to be at the braze joint between the manifold splitter plate and the apex of the triangular end-section on the hot end of the core.

A section of the submodule pan adjacent to the low-pressure inlet (fig. 4-84) was removed to facilitate visual inspection of the suspect area and to determine if other leak paths were contributing to the noted leakage. No other leak paths were discernible due to the magnitude of the core apex/splitter interface leakage.

Because a repair of the defective area might compromise the integrity of adjacent areas, the decision was made to continue the cycling test without an attempt to repair the unit.

The section of pan that had been removed was welded back in place. A leak check was made to provide a baseline for subsequent after-cycle leak checks. The leakage was measured to be 0.238 g/sec (0.0315 lb/min) at 241 kN/m<sup>2</sup> gauge (35 psig). This lower leak rate was attributed to weld shrinkage during the pan replacement, which reduced the leak area by squeezing the parts together.



S-98459 -A

Figure 4-87.--Thermal Cycling Facility Schematic.

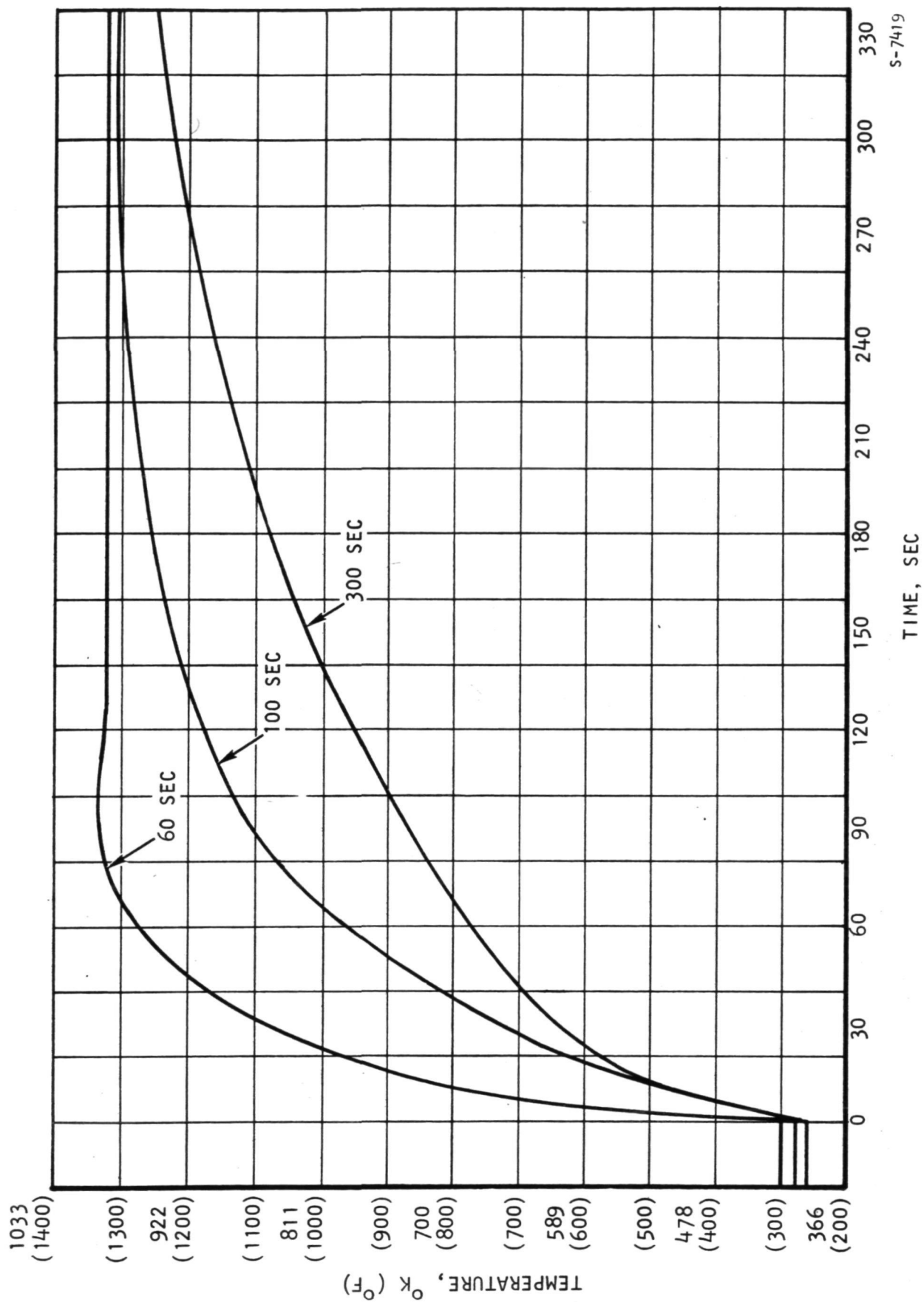


Figure 4-88.--Temperature Transients at Low-Pressure Gas Inlet.

The submodule was returned to the test lab and ten additional cycles completed. After these 20 cycles, the unit was leak-checked and found to be leaking 2.57 g/sec at (0.34 lb/min) 241 kN/m<sup>2</sup> (gauge) (35 psig). The unit was removed from the test rig and additional leak checks were performed in the following manner:

The unit was taken to a quiet area where changes in noise levels caused by changes in leak rates could be heard. Here, with one side of the unit pressurized, it was slowly immersed in water in the direction shown in fig. 4-85. Bubbling was detected at immersion level 1. This was the leak that was seen during the leak check that was made following the completion of fabrication. The unit was then further immersed in water to immersion level 2. It was originally predicted that fatigue cracks in the tube plates would first appear in the area indicated in fig. 4-89. No leakage was detected at level 2. The splitter-core joint at immersion level 3 was the only area where cracks were detected.

Following the immersion leakage checks, the unit was returned to the lab where an additional 20 cycles of thermal testing were completed and a leakage check again conducted. The leakage after 40 thermal cycles was measured and found to have increased to 9.83 g/sec (1.30 lb/min) at 241 kN/m<sup>2</sup> (gauge) (35 psig). The unit was then subjected to the immersion tests described above. During this test, bubbling could be heard when immersion level 2 was reached.

Small amounts of bypass flow can be tolerated; however, in the case described above, the bypass flow amounted to about 20 percent of the total high-pressure flow. This amount of bypass would affect the thermal response of the core assembly. Therefore, to minimize the bypass flow, the high-pressure inlet pressure was reduced to 496 kN/m<sup>2</sup> gauge (72 psig), which was equal to the low-pressure inlet pressure. With approximately equal pressures on both sides of the splitter, the bypass flow was small. This revision to the operating conditions was considered to be acceptable because the stress imposed on the unit due to pressure is small in comparison with the thermal stresses generated at startup. The low- and high-pressure inlet pressures were maintained at 496 kN/m<sup>2</sup> (gauge) (72 psig) for cycles 41 through 80.

Following the second immersion test, the unit was returned to the test lab and the thermal cycling resumed. After completing the 60th thermal cycle, the unit was leak-checked and found to be leaking 12.78 g/sec (1.69 lb/min) at 241 kN/m<sup>2</sup> (gauge) (35 psig).

The unit was again subjected to the immersion leak test as described before. As noted in the previous immersion test, an increase in the bubbling noise could be heard when level 23 was reached.

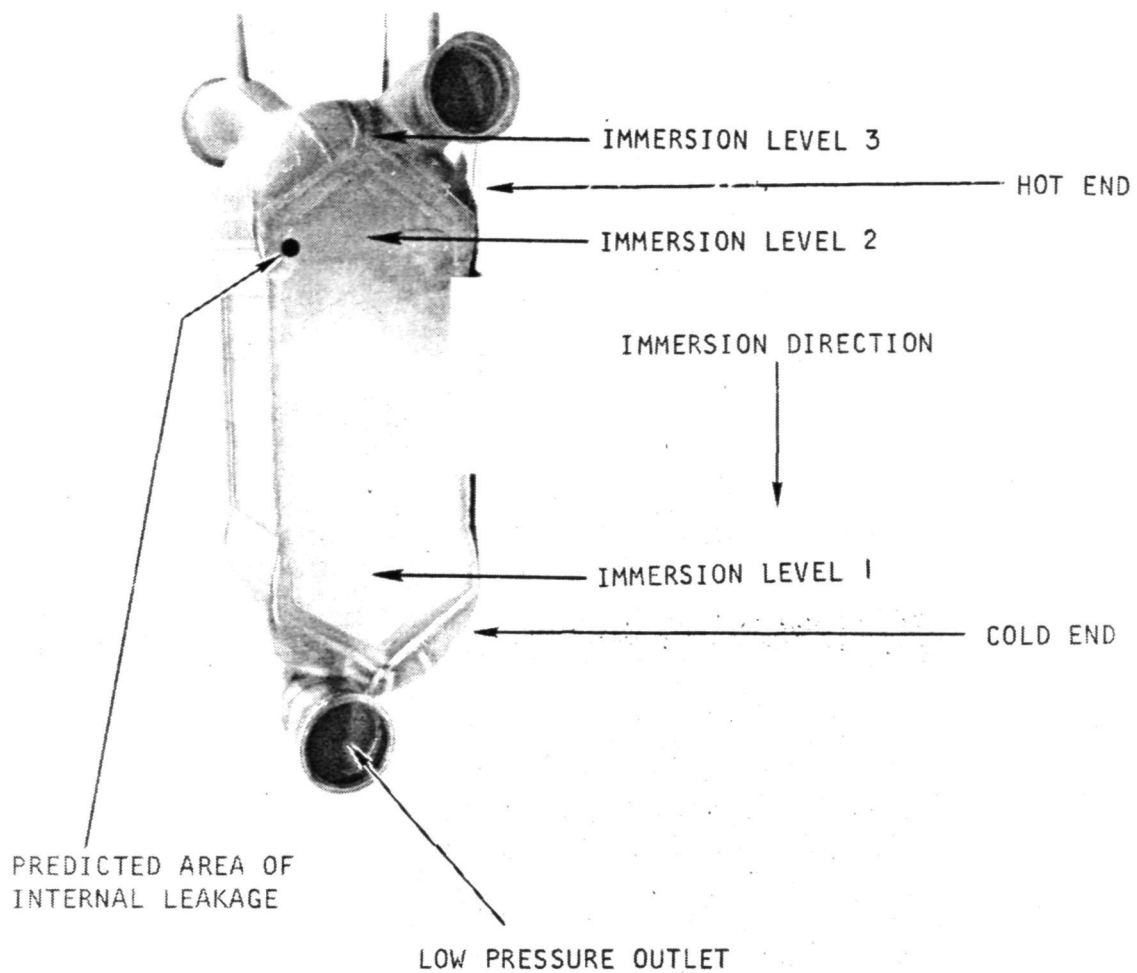


Figure 4-89.--Leak Check Immersion Levels.

F-23960



The unit was returned to the test lab and 20 additional thermal cycles completed. Following completion of the 80th thermal cycle, another leakage test was conducted. The unit was found to leak 12.78 g/sec (1.69 lb/min) at 241 kN/m<sup>2</sup> (gauge) (35 psig), which was the same leakage rate as was measured following the 60th thermal cycle. The unit again was subjected to the previously described immersion tests. Noise level observations were judged to be the same as those noted after the completion of 60 thermal cycles.

The external recuperator leakage was measured using a helium mass spectrometer. The final leak rate was  $9.5 \times 10^{-7}$  scc helium per sec at 1 atmosphere pressure differential compared to  $2.2 \times 10^{-7}$  scc helium per sec at the start of testing. The specification limit was an external leakage of  $1 \times 10^{-6}$  scc per sec; therefore, the unit is considered to have passed the test successfully with regard to external leakage.

Metallographic Examination.--Test observations were that tube plate cracks had developed in the critical area after 40 cycles of operation. To confirm this observation, the unit was sectioned for metallographic examination.

To pinpoint the tube plate cracks, the high-pressure passes on the core sections were sealed on the exposed ends with epoxy resin and fitted with pressurization tubes as shown in fig. 4-90. The sections were pressurized to 140 kN/m<sup>2</sup> (gauge) (20 psig) and submerged in water. No bubbling was observed. This observation was in conflict with the bubbling heard during the water immersion test conducted after the 40th cycle.

To resolve this conflict, the core sections were subjected to extensive micro sampling. Fig. 4-91 defines the location for the micros (arrows show the surface polished).

Photomicrographs, identified by micro number, are shown in figs. 4-92 through 4-101 for each location. Each sample was etched electrolytically in oxalic acid, then photographed at 25X magnification. Except for occasional braze voids in the manifold attachment flange-to-core seal plate joints, the photomicrographs show that the core section is well brazed, and has not suffered thermal damage, i.e., no cracks or distortion of the tube sheets were detected in these areas.

Examination of the splitter-core joint proved more fruitful. A longitudinal section (parallel to the long dimension of the splitter) was taken from the bottom segment as shown in fig. 4-102. Photomicrographs (micro 695) in figs. 4-102 and 4-103 reveal extensive porosity and cracking through the brazing alloy in the splitter-to-core joint, with cracks continuing through the plate-header bar joints into the gas passages. The Palniro 7 and Nioro (used for repair) brazing alloys are fairly heavily oxidized, much more so than observed (or expected) with the Palniro 1 used in core fabrication. The splitter-to-core joint gap is excessively large, measuring as much as 0.064 cm (0.025 in.) in places (fig. 4-104); visual examination shows only about 50 percent joint fill in segments such as pictured in fig. 4-104.



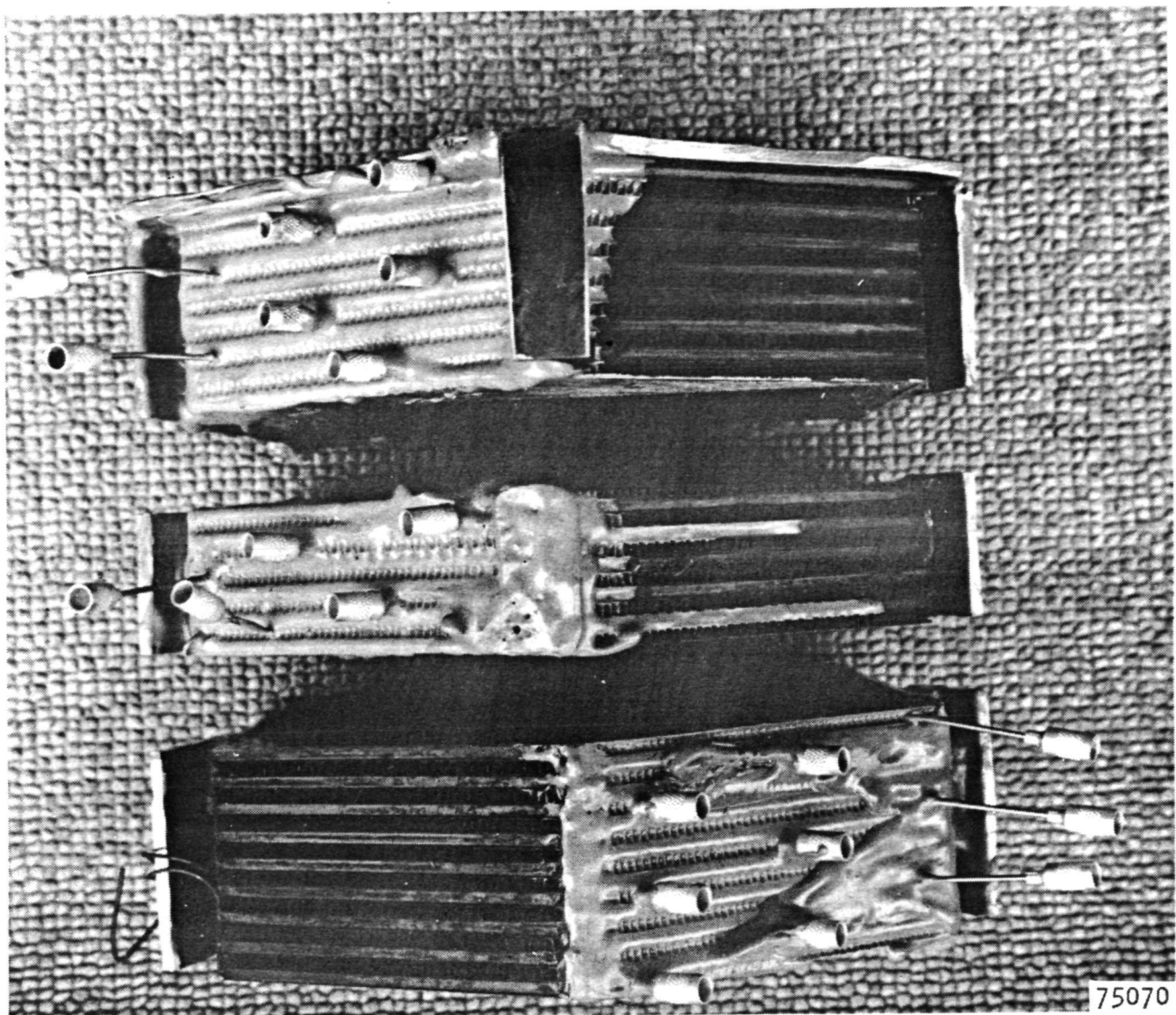
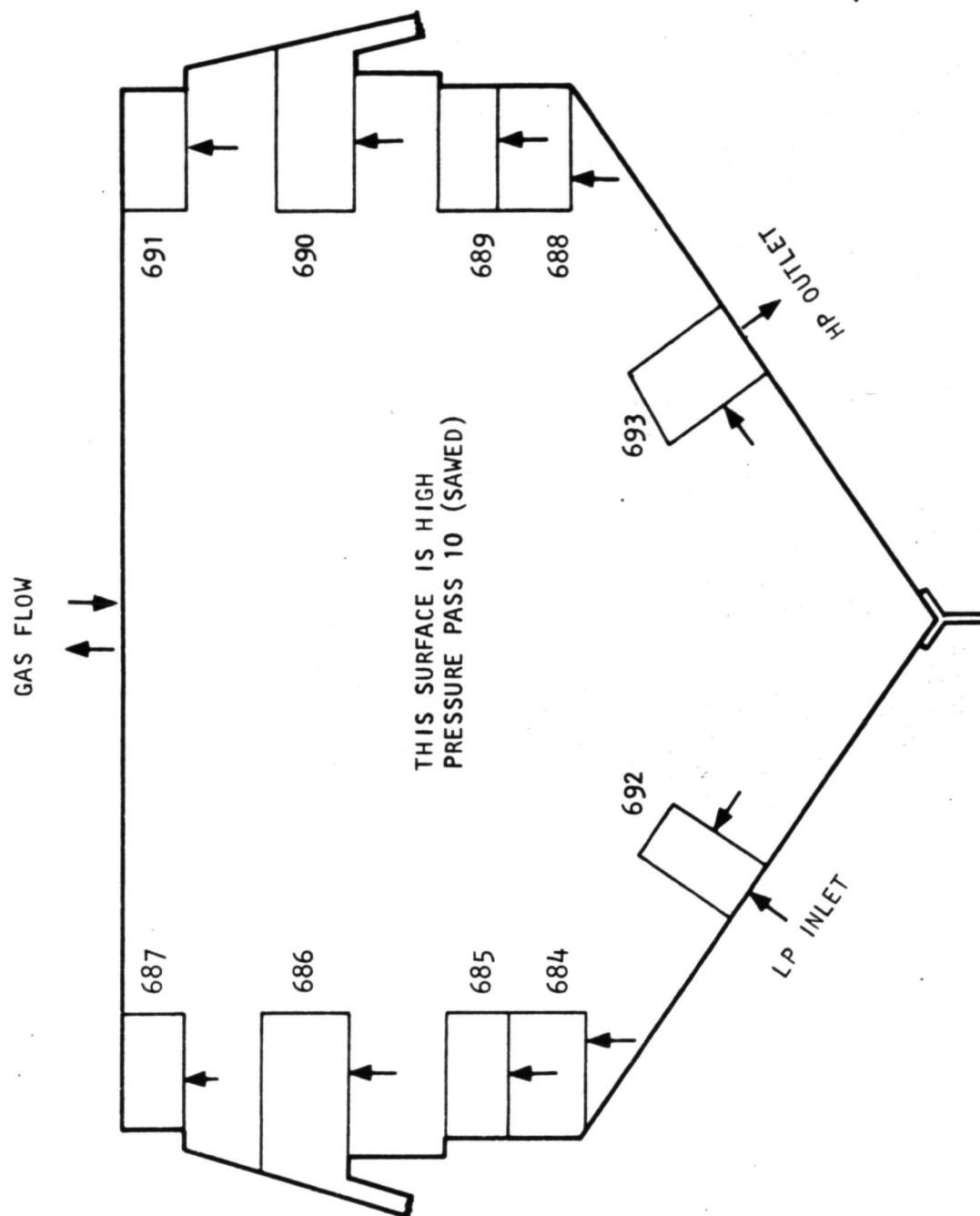
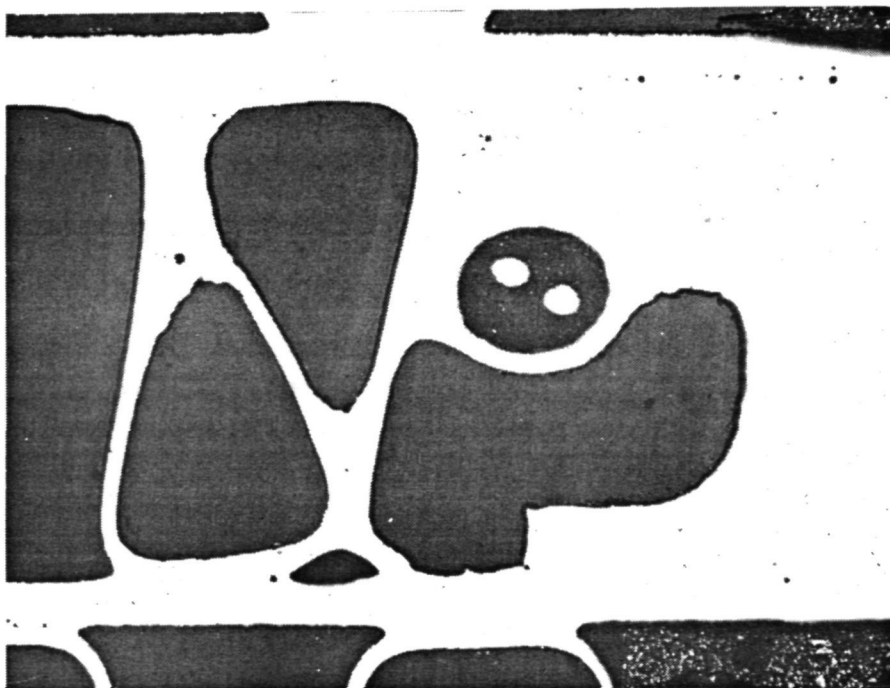
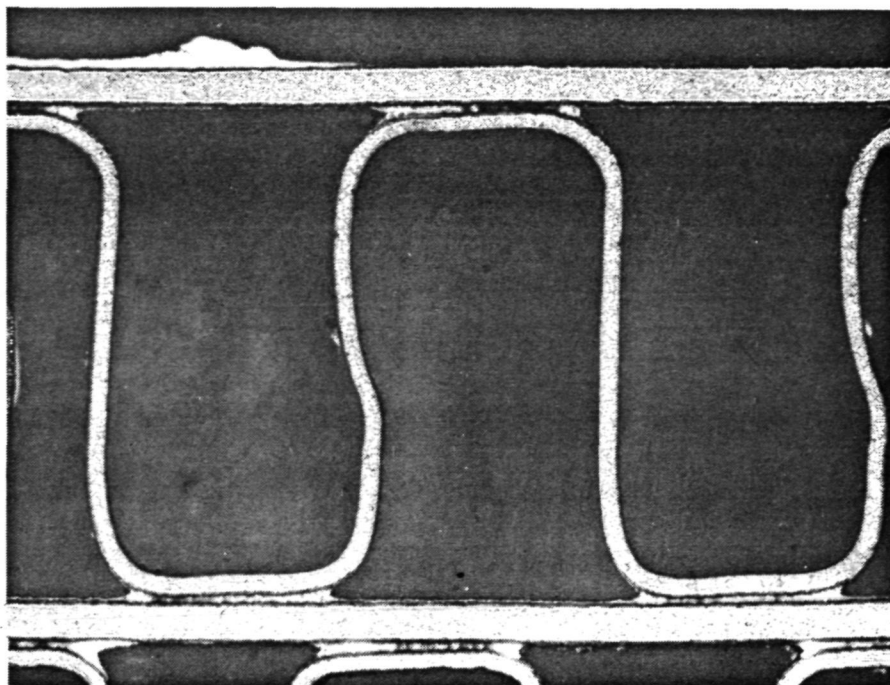


Figure 4-90.--Sectioned Segments of Core with Needles  
Used for Pressurizing Inserted.



S-7268

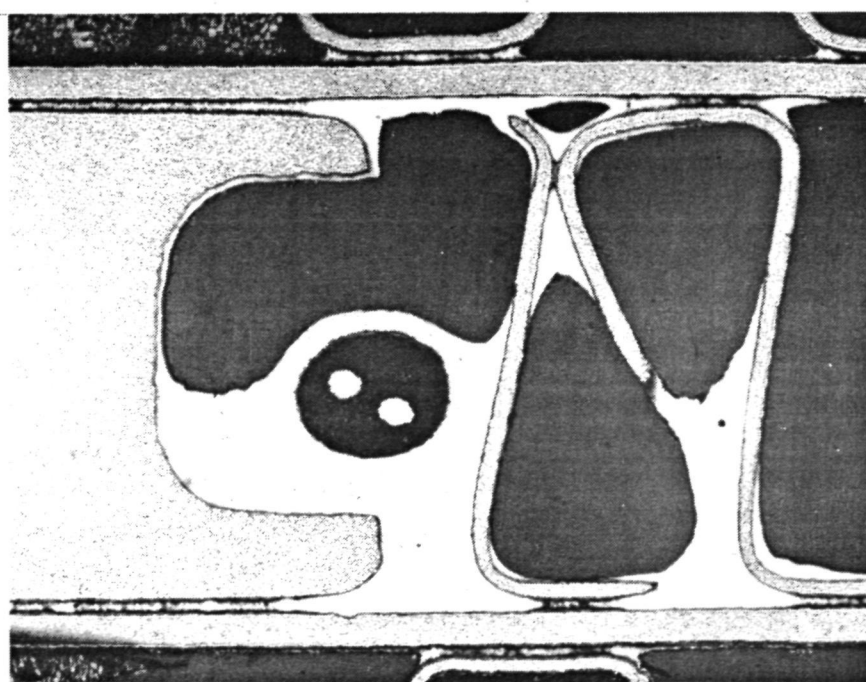
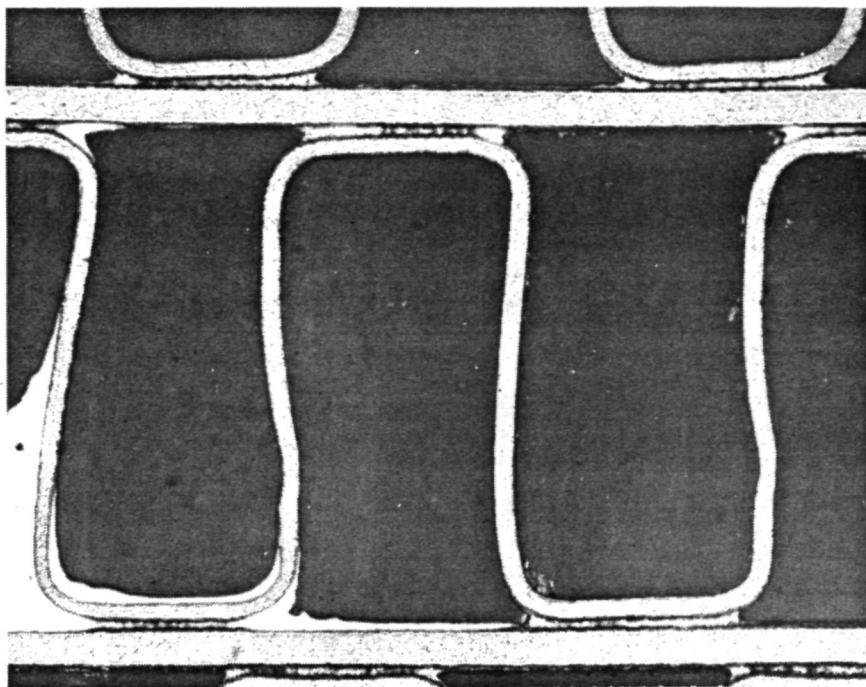
Figure 4-91.--Location of Micros Taken from Section Including Low-Pressure Passes 11 through 13.



F-23940

Figure 4-92.--Micro Sample 684-25X.

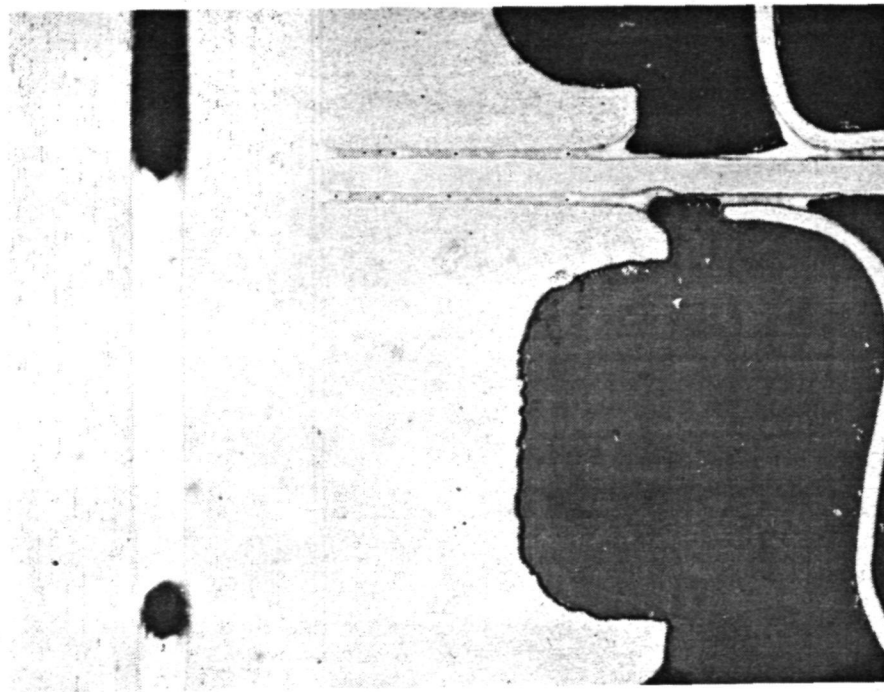
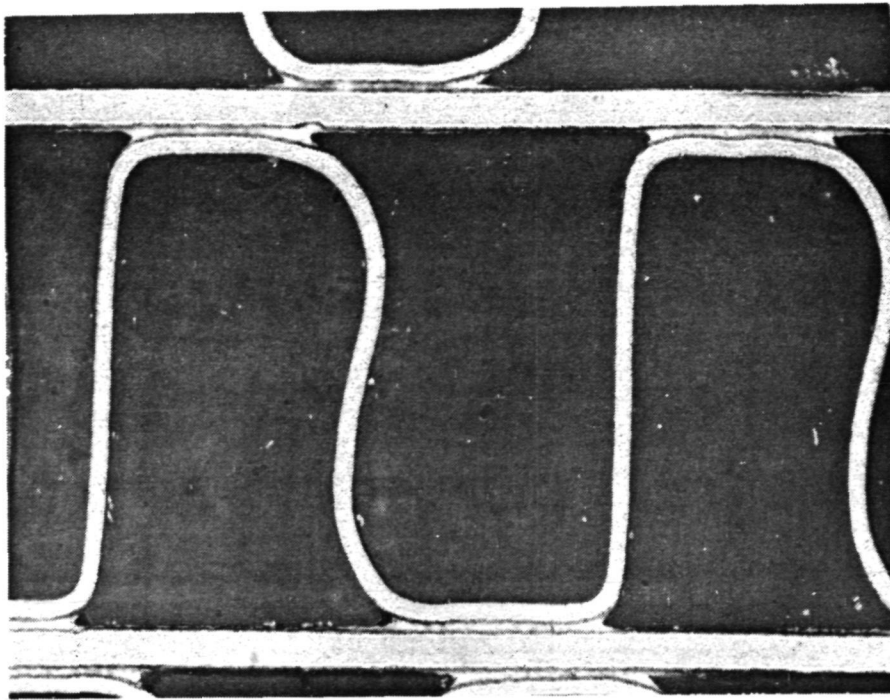
ORIGINAL PAGE IS  
OF POOR QUALITY



F-23939

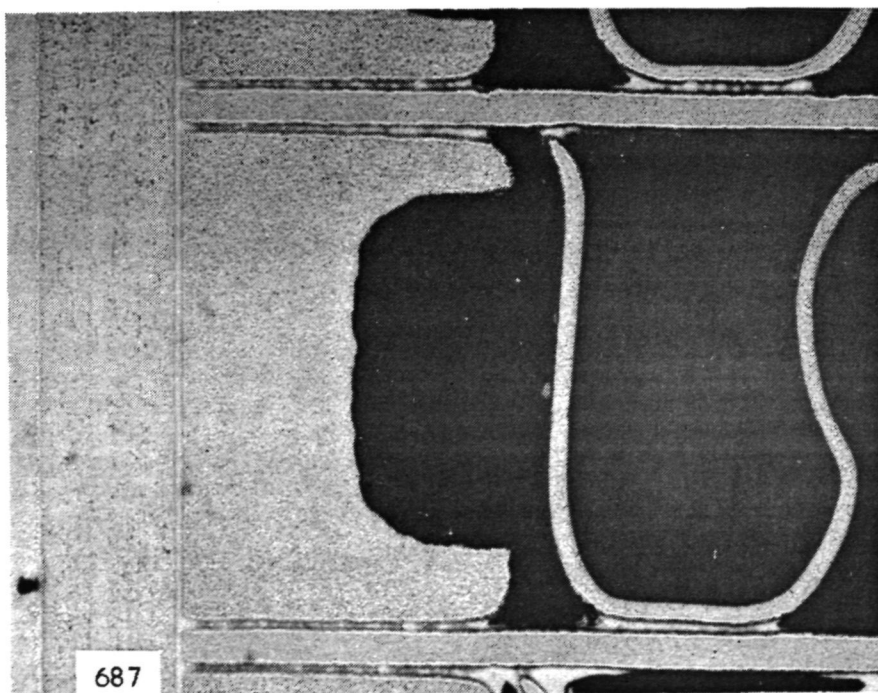
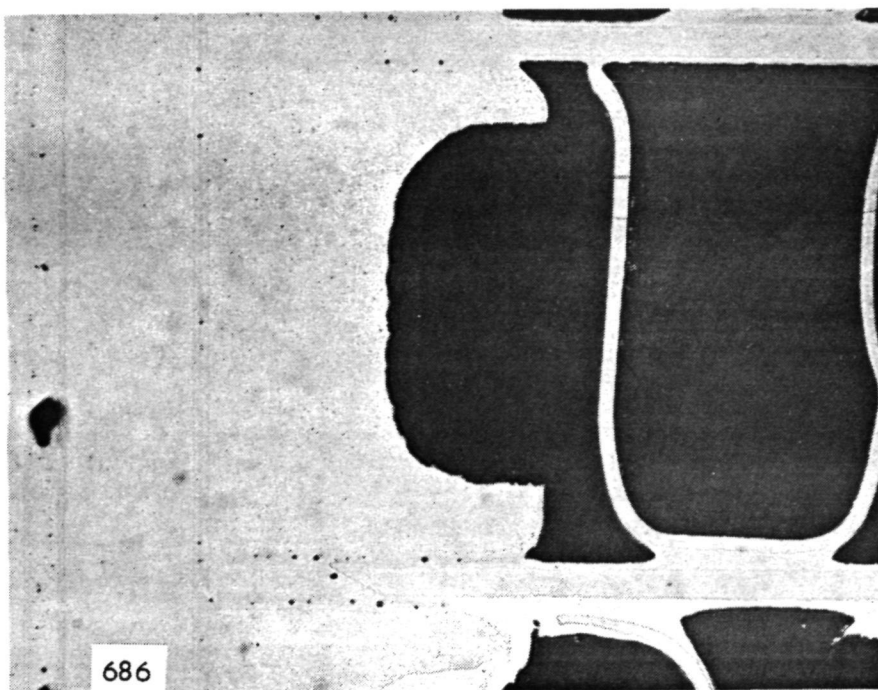
Figure 4-93.--Micro Sample 684-25X.

ORIGINAL PAGE IS  
OF POOR QUALITY



F-23938

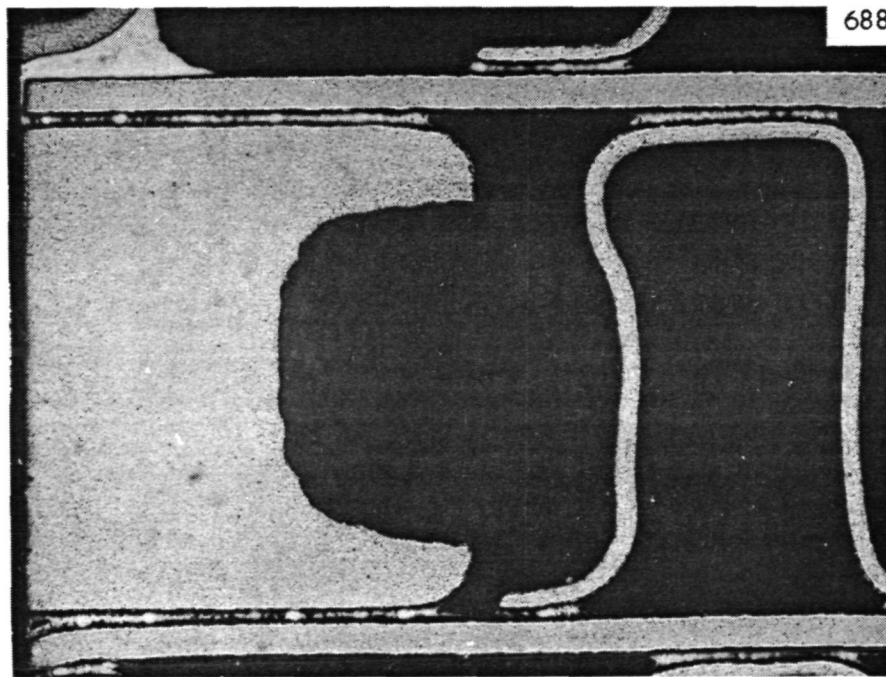
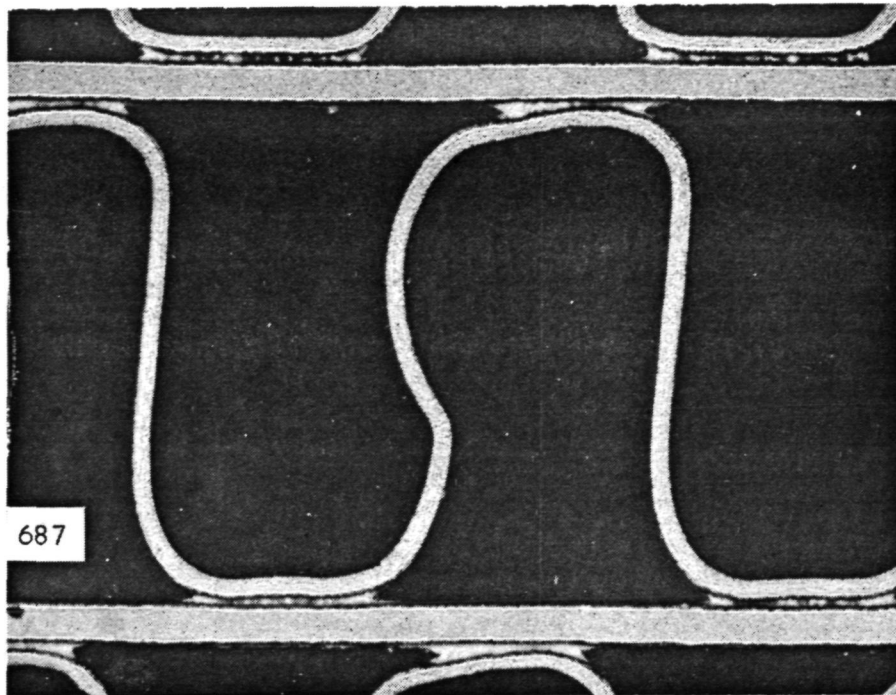
Figure 4-94.--Micro Sample 685-25X.



F-23937

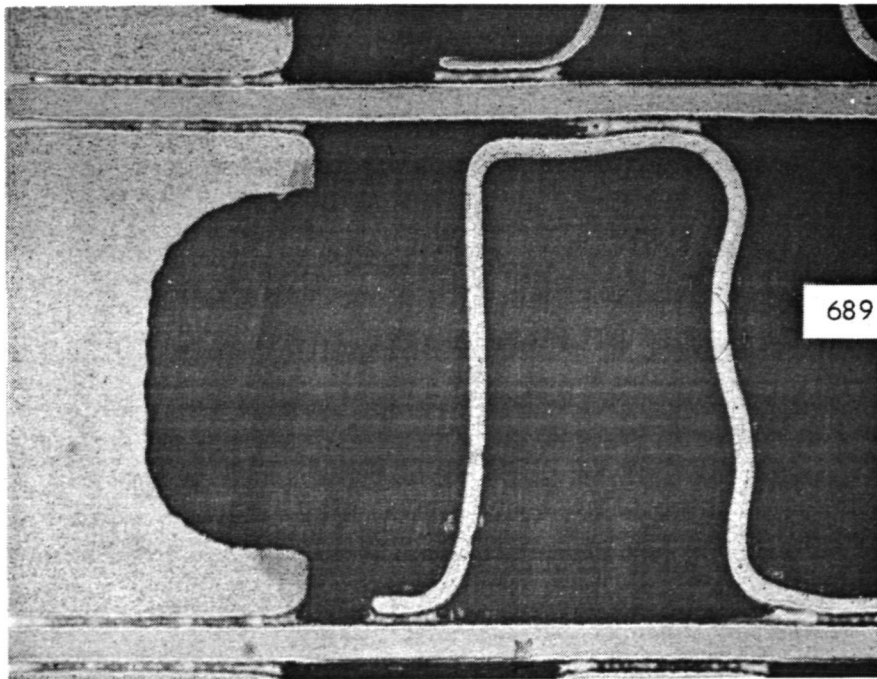
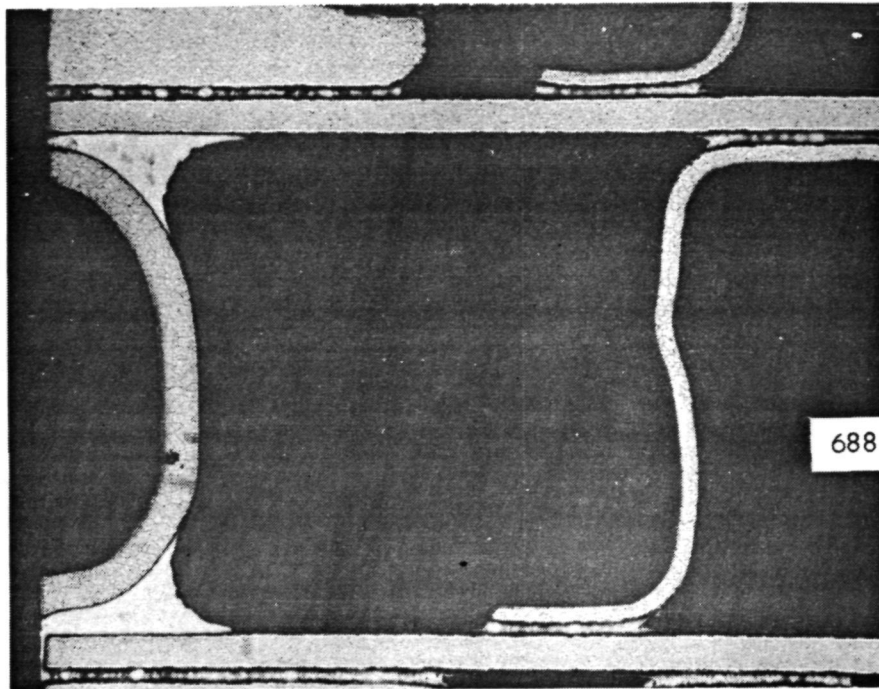
Figure 4-95.--Micro Sample 686 and 687-25X.





F-23936

Figure 4-96.--Micro Sample 687 and 688-25X.

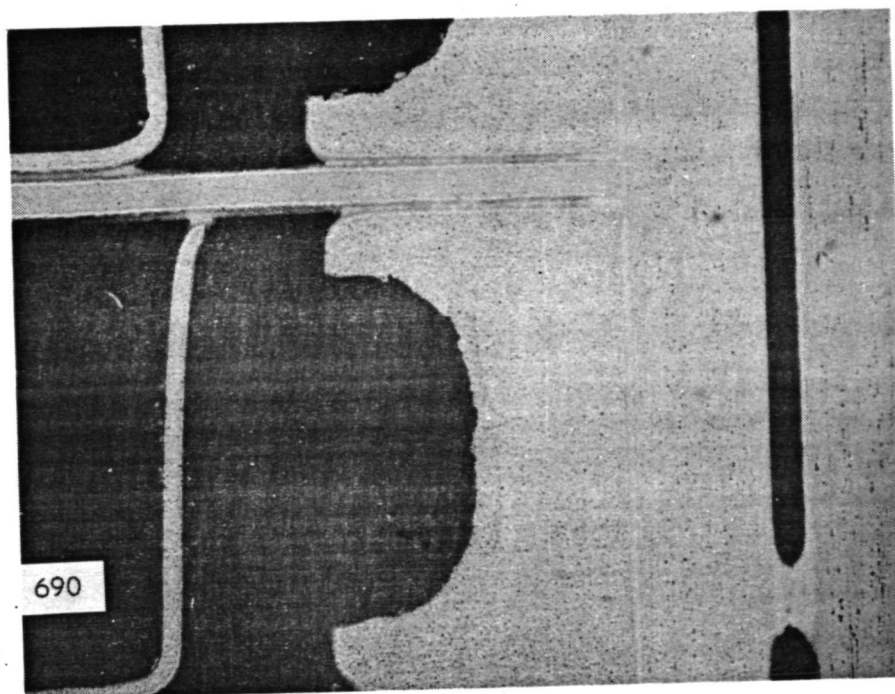
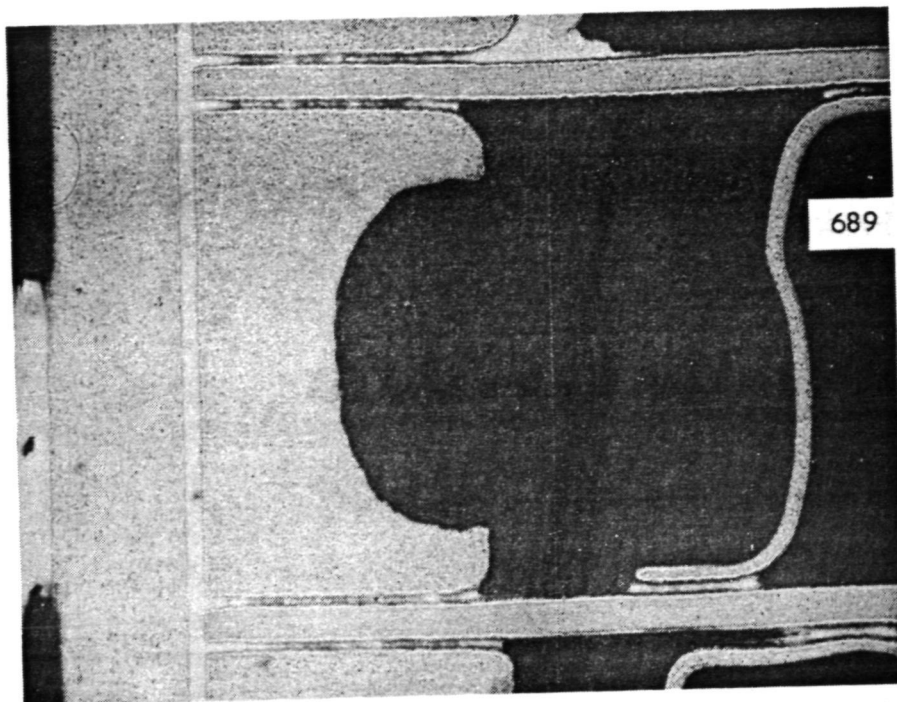


F-23935

Figure 4-97.--Micro Sample 688 and 689-25X.

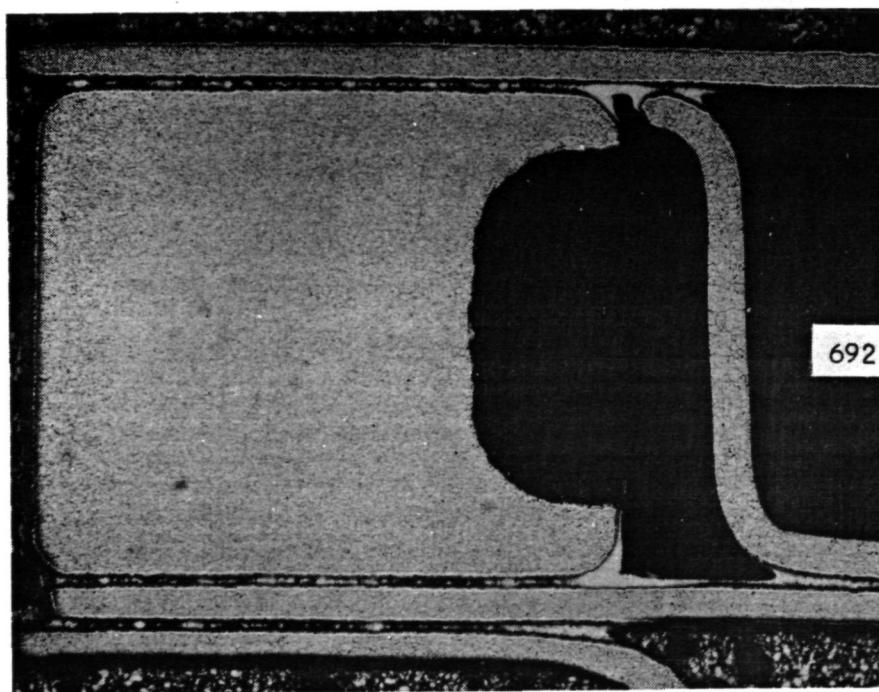
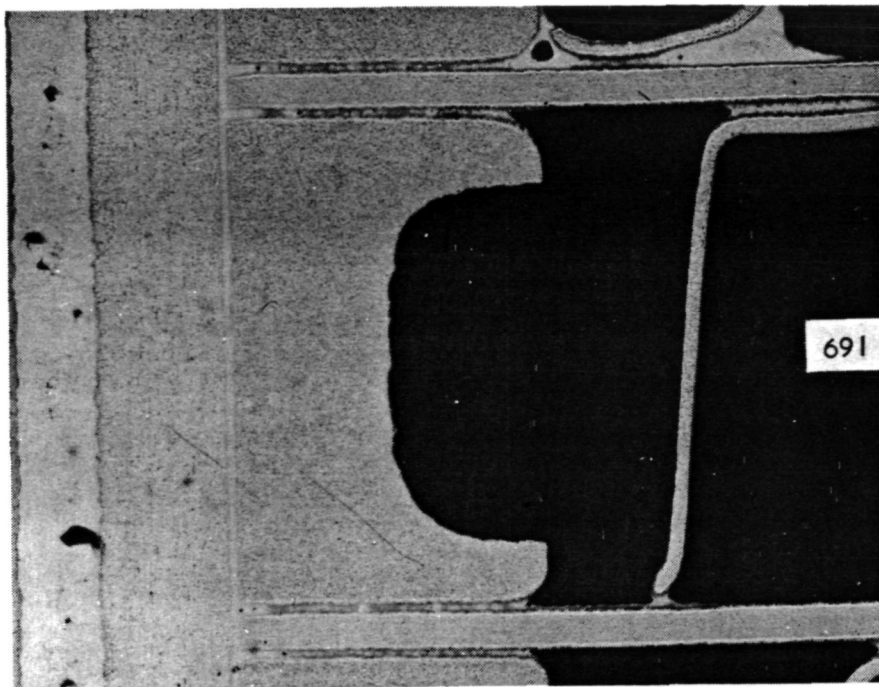
ORIGINAL PAGE IS  
OF POOR QUALITY





F-23934

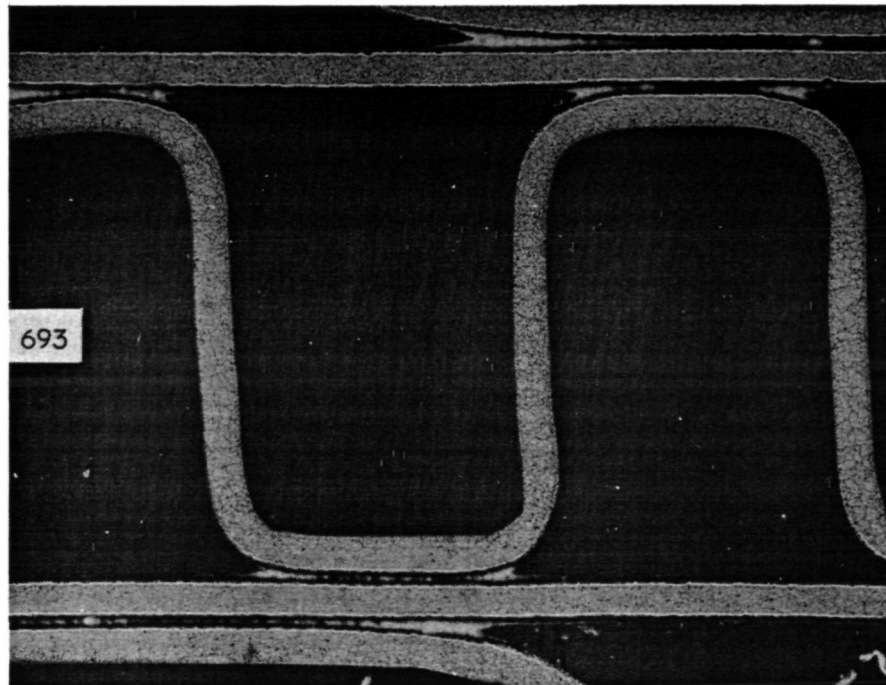
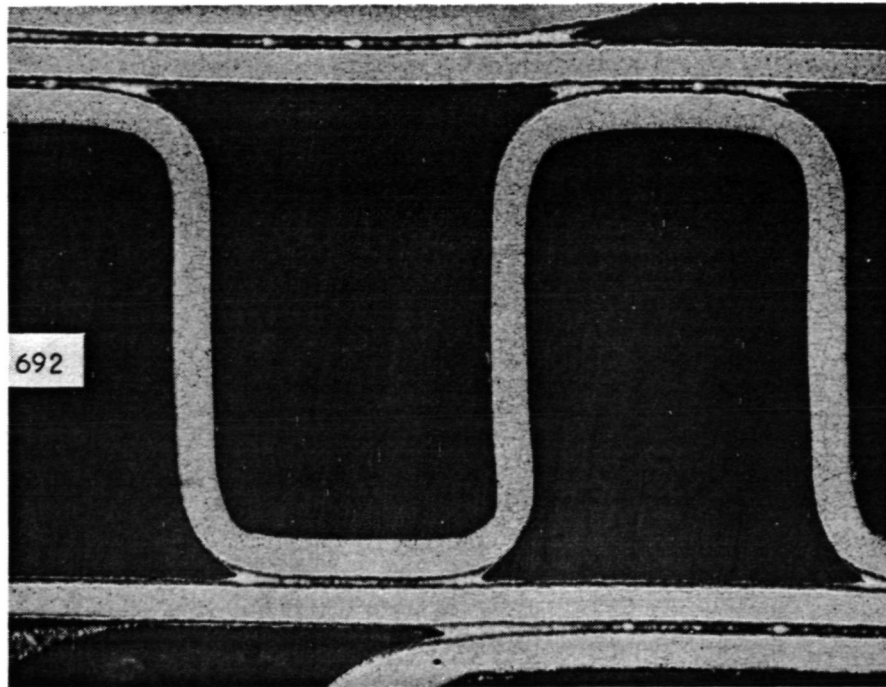
Figure 4-98.--Micro Sample 689 and 690-25X.



F-23933

Figure 4-99.--Micro Sample 691 and 692-25X.

ORIGINAL PAGE IS  
OF POOR QUALITY



F-23932

Figure 4-100.--Micro Sample 692 and 693-25X.

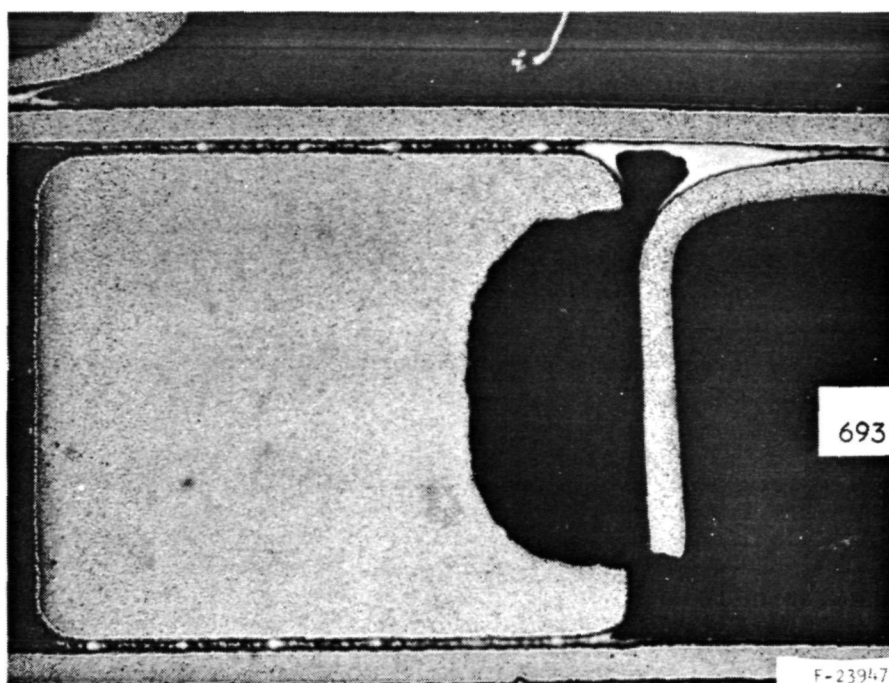
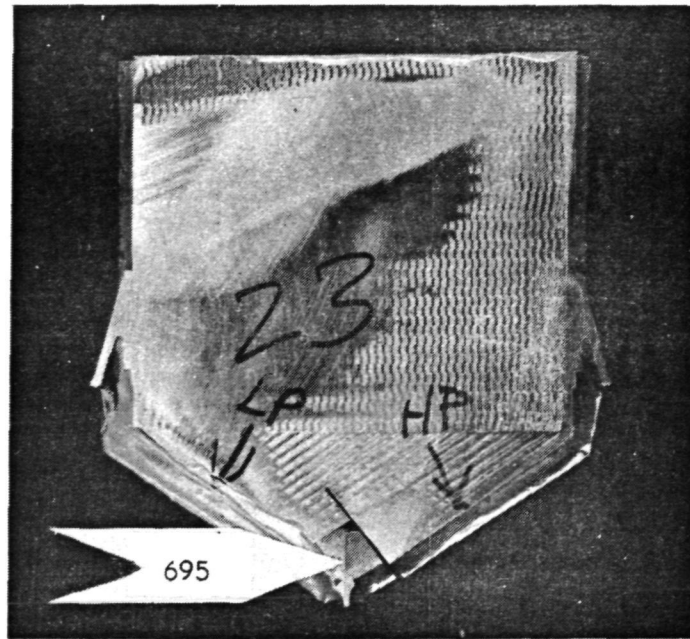


Figure 4-101.--Micro Sample 693-25X.



LOCATION OF MICRO 695 THROUGH NOSE SECTION.

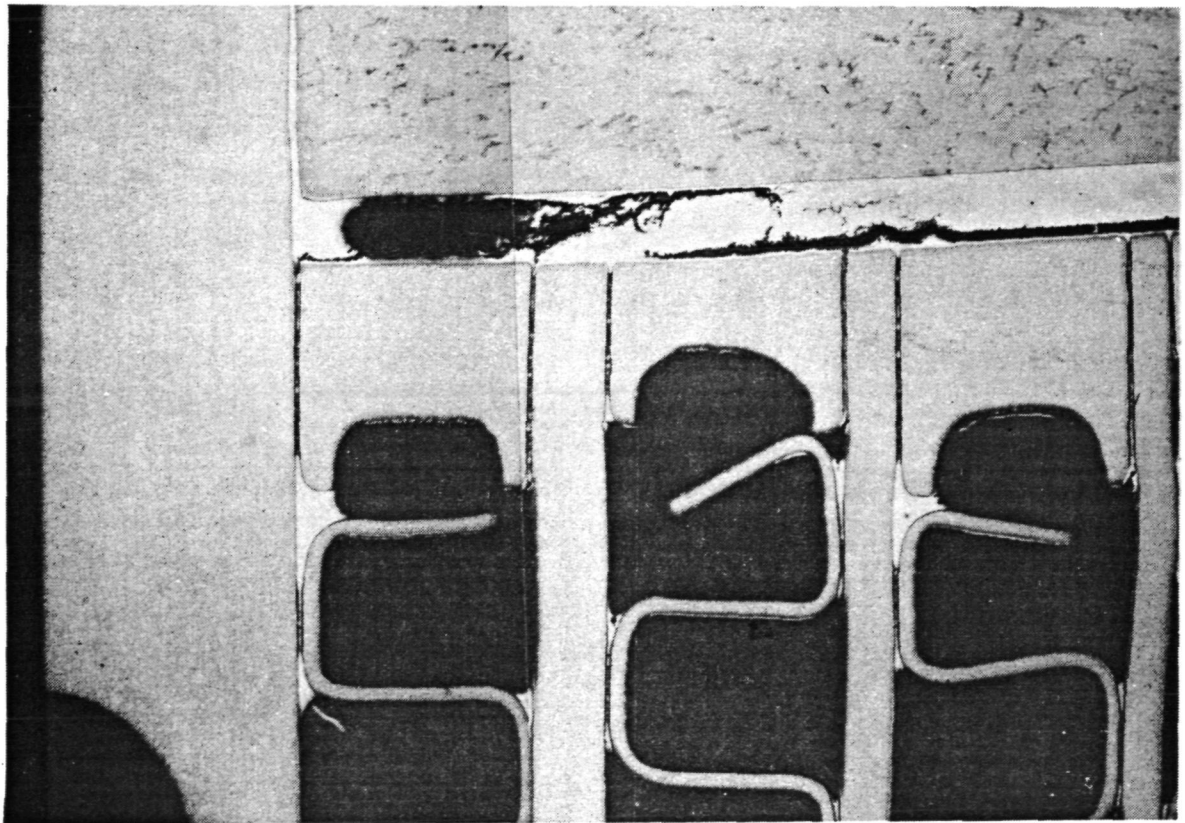
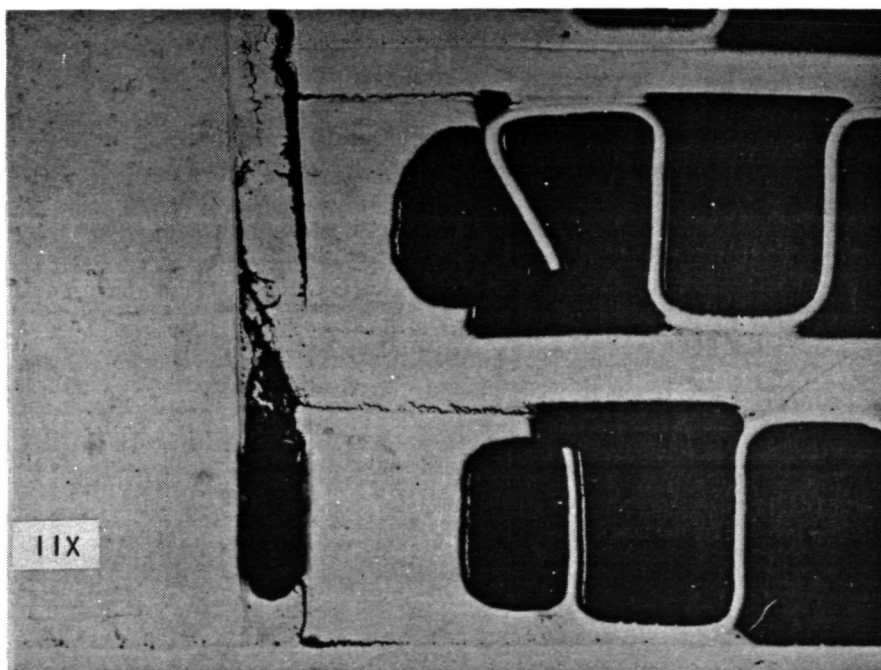
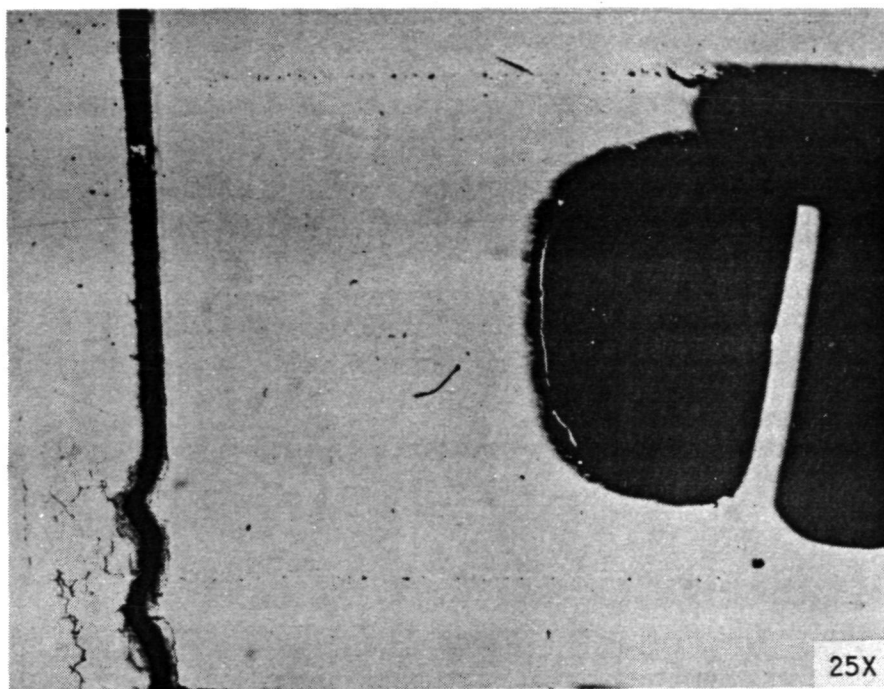


Figure 4-102.--Micro Sample 695-11X.

F-23948





F-23949

Figure 4-103.--Micro Sample 695 Unetched.

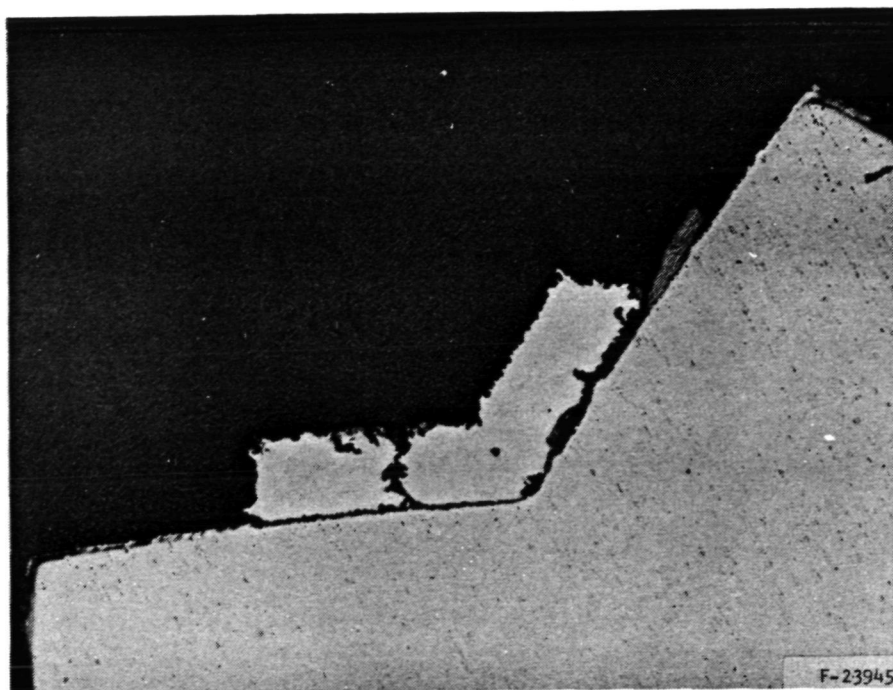


Figure 4-104.--Micro Sample 696-22X.

The first core segment (low-pressure passes 1 to 7) was observed to pass air between low-pressure passes, even after both sides of the splitter were sealed with adhesive. The nose piece from this segment was sectioned both longitudinally and transversely to examine the splitter-to-core joint in detail; photomicrographs from micro samples 752 through 755 are given in figs. 4-105 through 4-107. Fig. 4-105 shows that the brazed joint has separated to within one-half passage height of the top plate, and the plate-header bar joint has failed into the first low-pressure pass. This photo was taken looking toward the low-pressure inlet side of the core. Fig. 4-106 shows a transverse section (at the top) through the joint at about the fifth low-pressure pass, where the joint is observed to have split open and is only partly back-filled with adhesive. The lower portion of fig. 4-106 and fig. 4-107 show the splitter-to-core joint along its length, looking toward the high-pressure outlet side. This joint again is observed to be cracked; the enlarged section at the bottom of fig. 4-107 shows the cracks connecting a series of large and small voids.

Other hot-end sections of the core were examined, but no damage was observed. The low-pressure inlet face (hot-gas inlet) was mounted and polished. No cracks or fin distortions were observed.

The cold end of the core assembly was examined next. The high-pressure inlet pan was removed to facilitate inspection of the core apex/splitter interface braze joint. This visual inspection indicated that the joint was sound on both the high-pressure-in and low-pressure-out sides, as shown in fig. 4-108.

The significant leak noted in pass 11 prior to testing was isolated and found to be due to a hole in the tube plate. The downward bend around the hole as shown in fig. 4-109 suggests mechanical damage to the tube plate before or during fabrication, either creating a hole, or indirectly causing a hole by allowing a heavy local accumulation of brazing alloy.

Examination of the core apex/splitter interface braze joint showed that it was sound and acceptable (fig. 4-110).

Conclusions.--The core section at the hot end was well brazed and essentially undamaged except at the nose area where it was joined to the splitter. It is believed that the cracks that developed in the plate-to-header bar joints at the core apex are the cause of the bubbling and water spurting action that was observed at the conclusion of testing. The air pumping mechanism is illustrated in fig. 4-111. When the high pressure manifold was pressurized, it was possible for air to flow along the crack in the splitter-core joint and pass into a low-pressure passage through the crack in the plate-to header-bar joint. Then airflow proceeded down along the continuous rectangular passage formed by one of the turning fins. Airflow was forced to flow down because the outlet end of the passage was sealed with epoxy. The epoxy was added at the test completion to seal the gross leakage that occurred directly



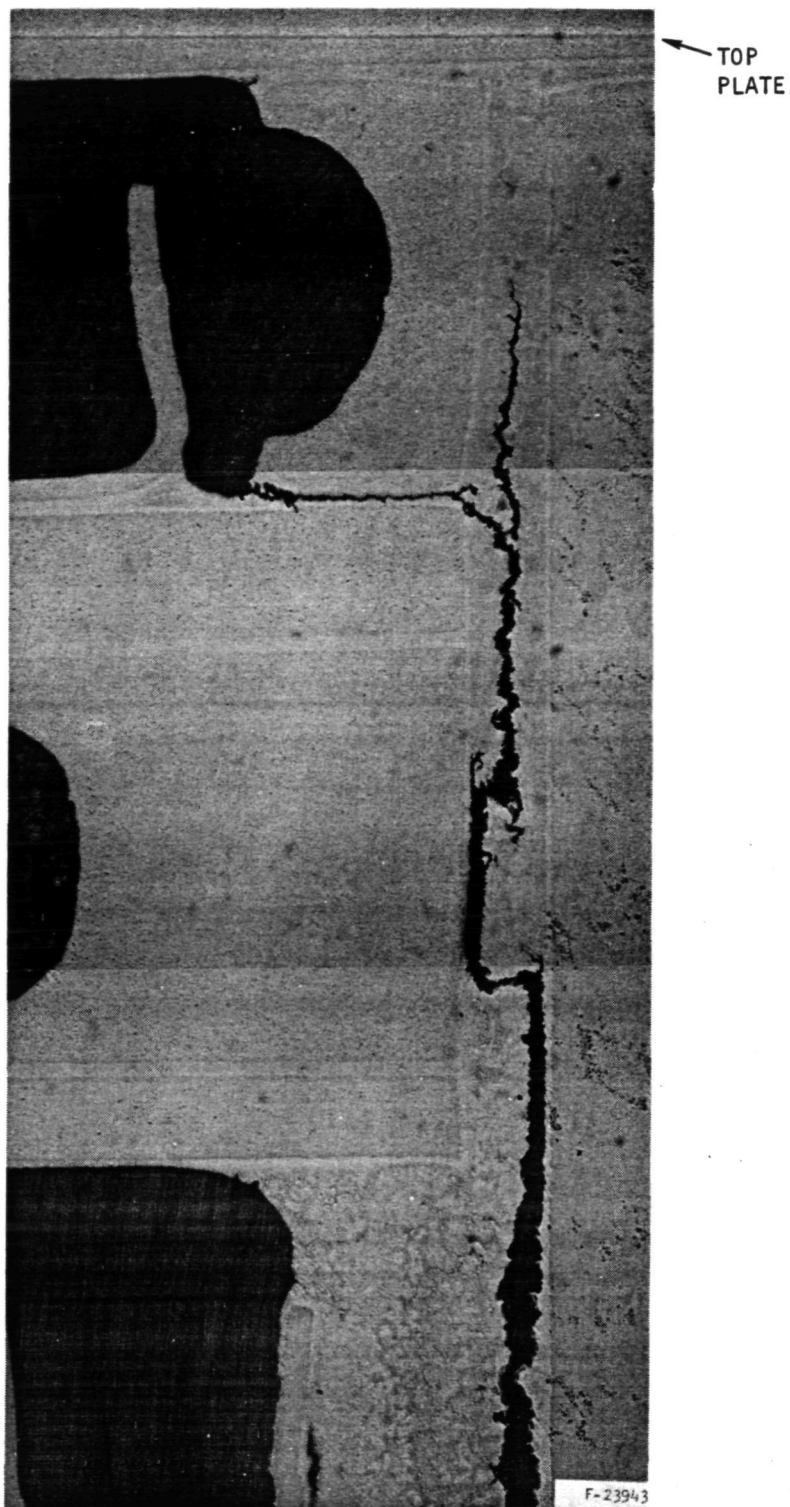
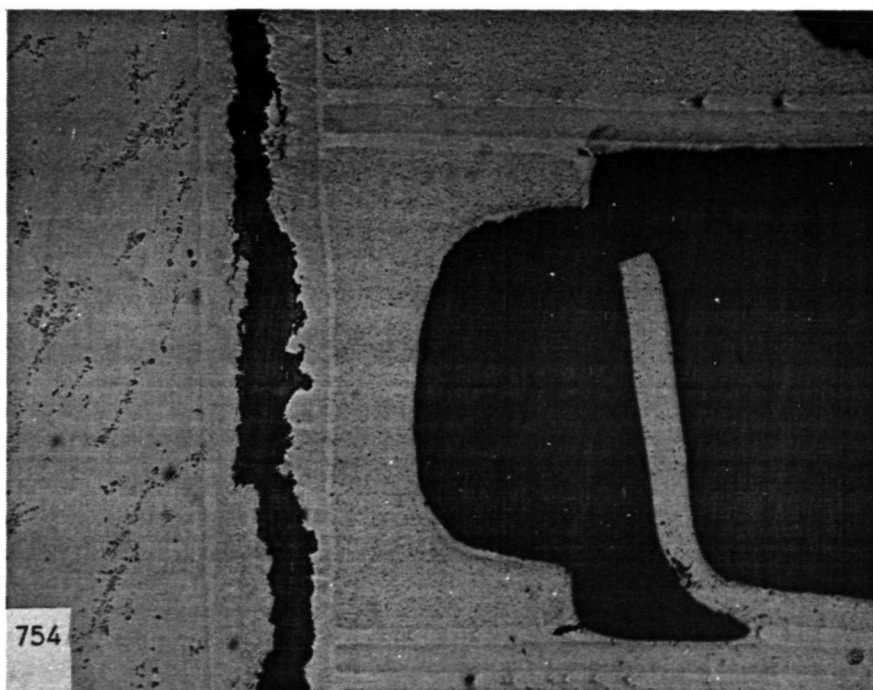
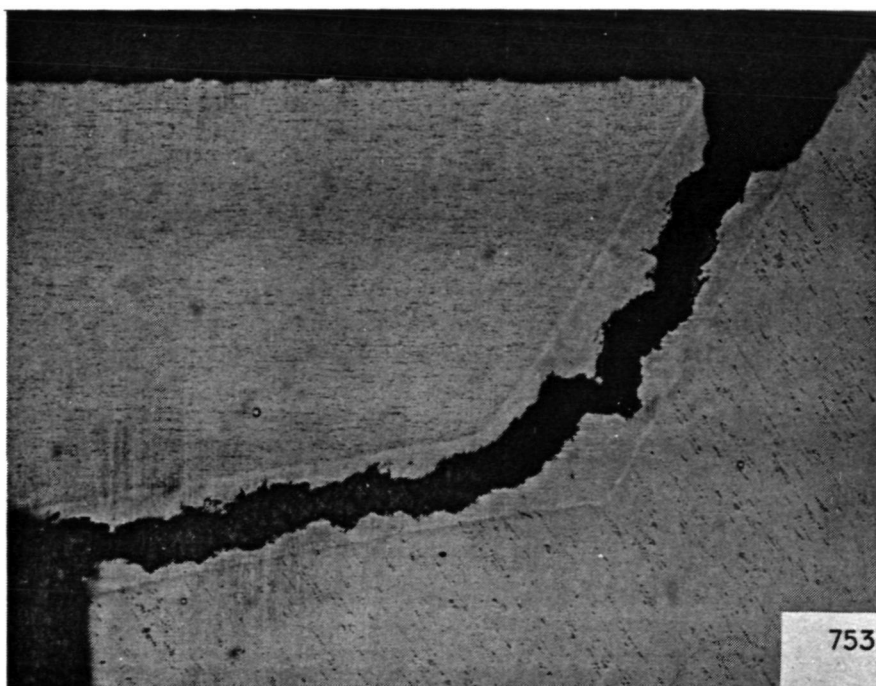


Figure 4-105.--Micro Sample 752 Unetched-25X.



F-23941

Figure 4-106.--Micro Sample 753 and 754 Unetched-25X.

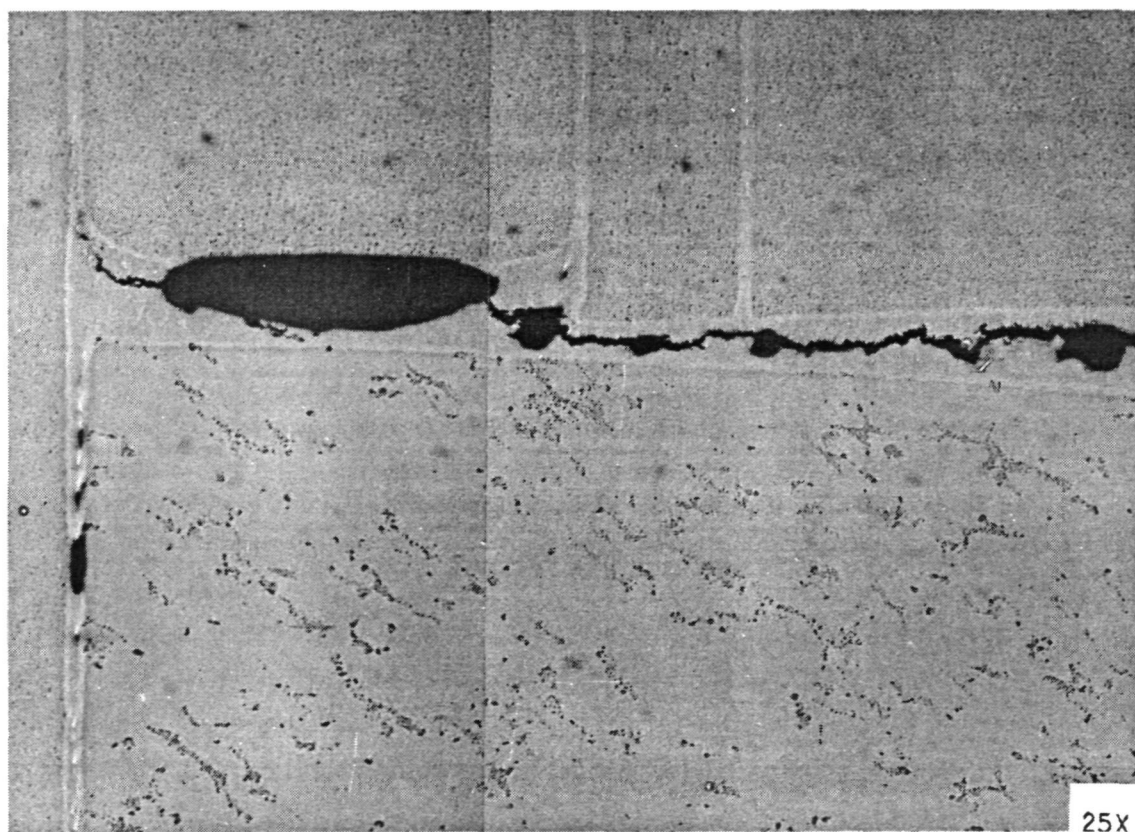
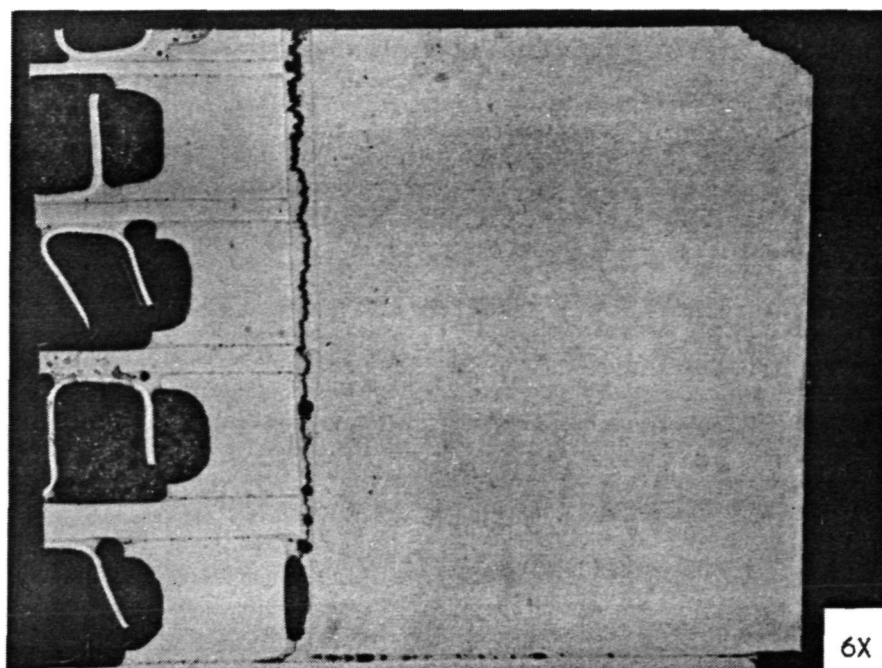
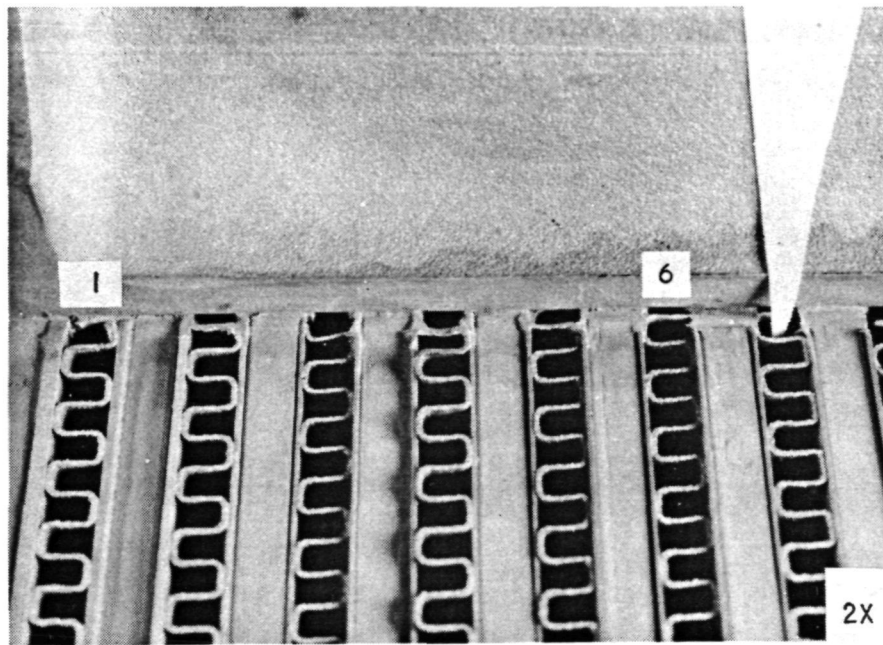
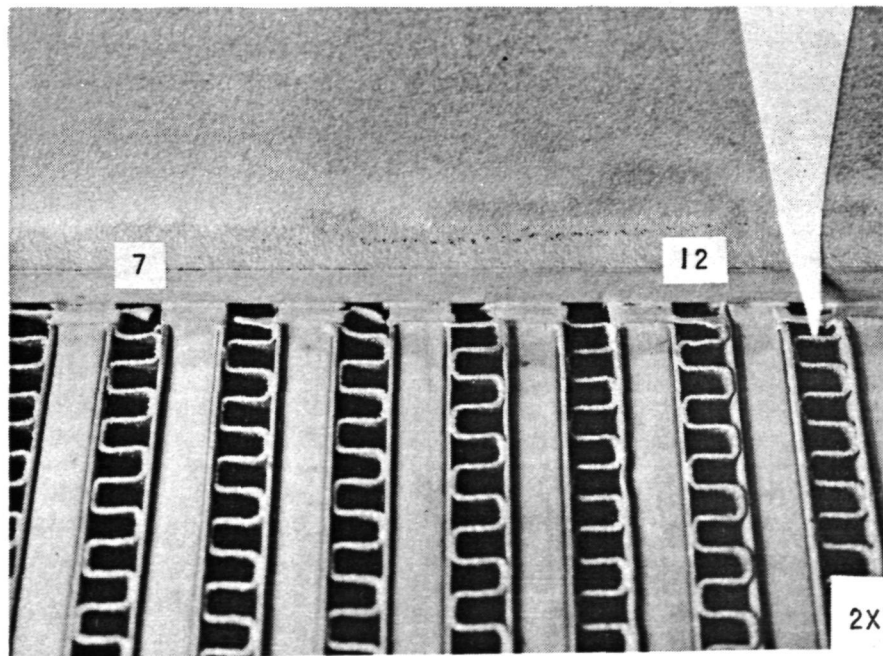


Figure 4-107.--Micro Sample 755 Unetched.

F-23942



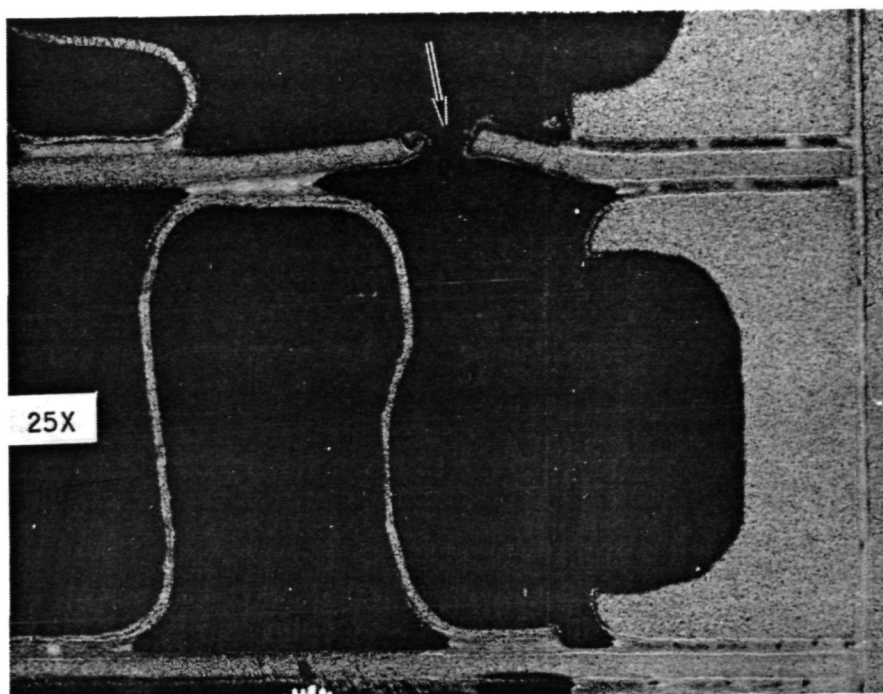
HIGH PRESSURE INLET - PASSES 1 THROUGH 6



HIGH PRESSURE INLET - PASSES 7 THROUGH 12

F-23989

Figure 4-108.--Cold End MBR Passes 1 through 12.



HOLE IN LOW PRESSURE PASS II.

F-23959

Figure 4-109.--Micro Sample 1001.





F-23944

Figure 4-110.--Micro Sample 1021-70X Splitter-to-Core Joint.

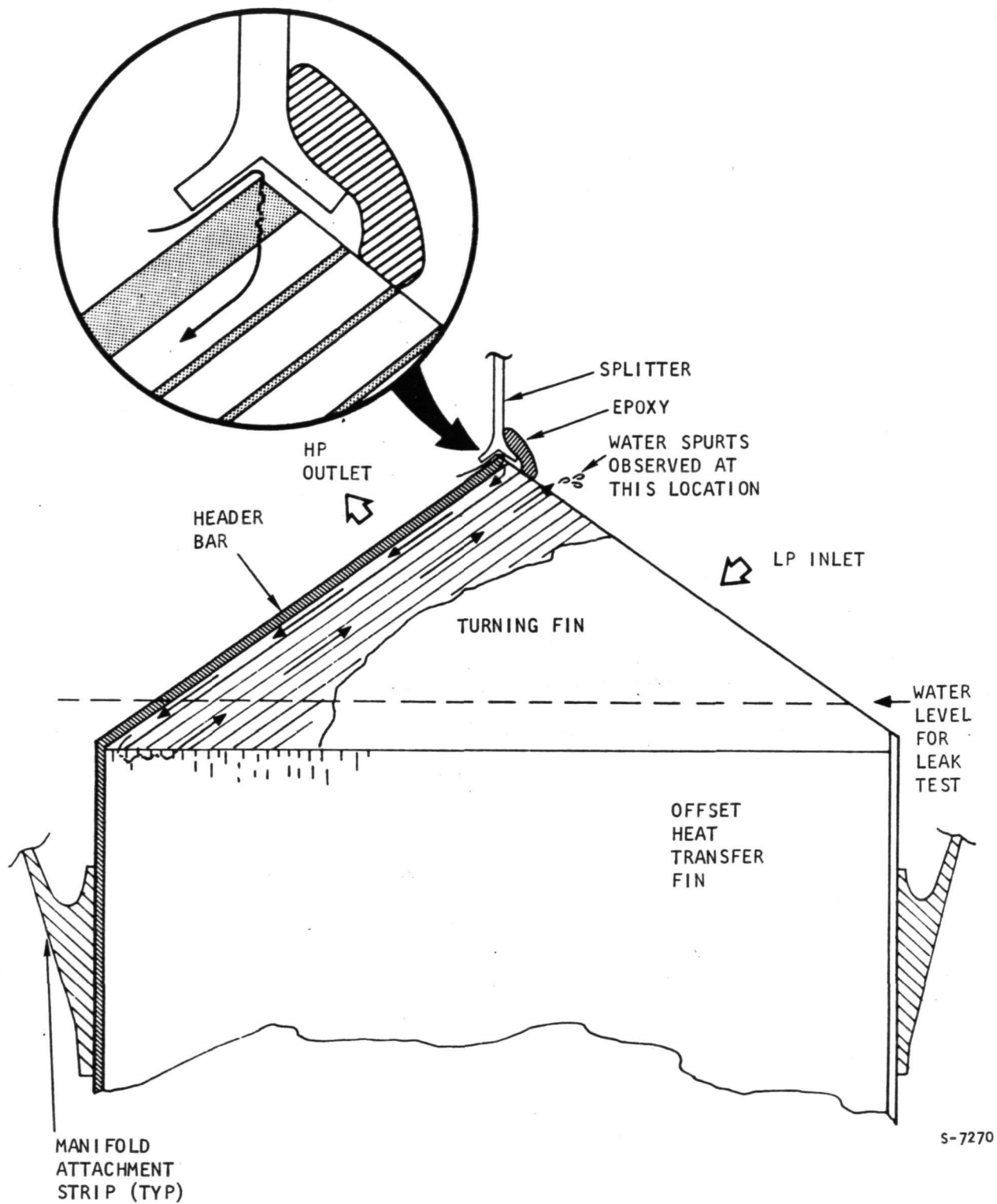


Figure 4-111.--Air Pumping Mechanism.

across the splitter-core joint. At the end of the turning fin passage, which was slightly below water level, the airflow would exit and produce bubbles. These air bubbles could proceed through the openings in the offset fins and enter into another turning fin passage. These bubbles entrapped water pockets and pumped them to the core exit, thus producing the observed water spurts. This mechanism explains why it was possible to hear and see bubbling action even though the defect was above water level.

The splitter-to-core joint was excessively large and not well filled. Rupture occurred through the weaker brazing alloy in this joint, and in some cases was observed to propagate through plate-header bar joints. There was also greater than expected oxidation of the Palniro 7 and Niro brazing alloys in this area, apparently reflecting the lower palladium content by comparison to Palniro 1.

The core section at the cold end was well brazed and would have shown no leakage after the cycle test had it not suffered the mechanical damage previously explained. The fit-up between the core apex and the splitter was very good with no evidence of braze joint voids or cracking.

#### Design Modifications for SN2 Submodule

Fabrication of submodule SN2 had proceeded through the second braze cycle, in which the splitter is attached to the core, when the thermal cycle test on SN1 indicated a deficiency in the basic joint design. It was decided to rework the part to provide an improved splitter-core joint configuration.

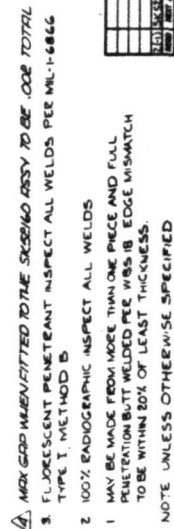
Design of the modified splitter is shown by drawing SK52534, and a photograph of one of the fabricated parts is shown in fig. 4-112. The end (nose piece) of the splitter was machined to an angle of 130 deg to match a corresponding 130-deg angle machined on the apex of the existing core assembly. The braze contact area was maximized by extending the legs to the full width of the part. Slots were machined on the legs to minimize flow blockage.

Fabrication of SN2.--Fabrication procedures for SN2 are identical to those previously described for SN1. Check on the SN1 manifold attachment flange-to-seal plate braze joints indicated several voids. The voids were not large enough to affect short-term test performance, but would be of significance for long duration, greater than 10,000 hr of operation. Thus, the flange base was modified to ensure full braze alloy flow. A stress relief operation on the detail part was specified to prevent warping during the braze cycle.

At the completion of fabrication, two leaks were observed at the manifold splitter-core apex braze joint. The leakage flow was measured and determined to be 1.5 percent of the total high-pressure flow at a design level pressure differential of 240 kN/m<sup>2</sup> (35 psi). Local repairs and an additional furnace braze cycle did not result in any reduction in the leak rate. It was concluded that any further repair operations to eliminate the leak would compromise the structural integrity of the splitter-core joint. The magnitude of the leakage flow was small compared to the total flow. To minimize any effect of leakage



4-156



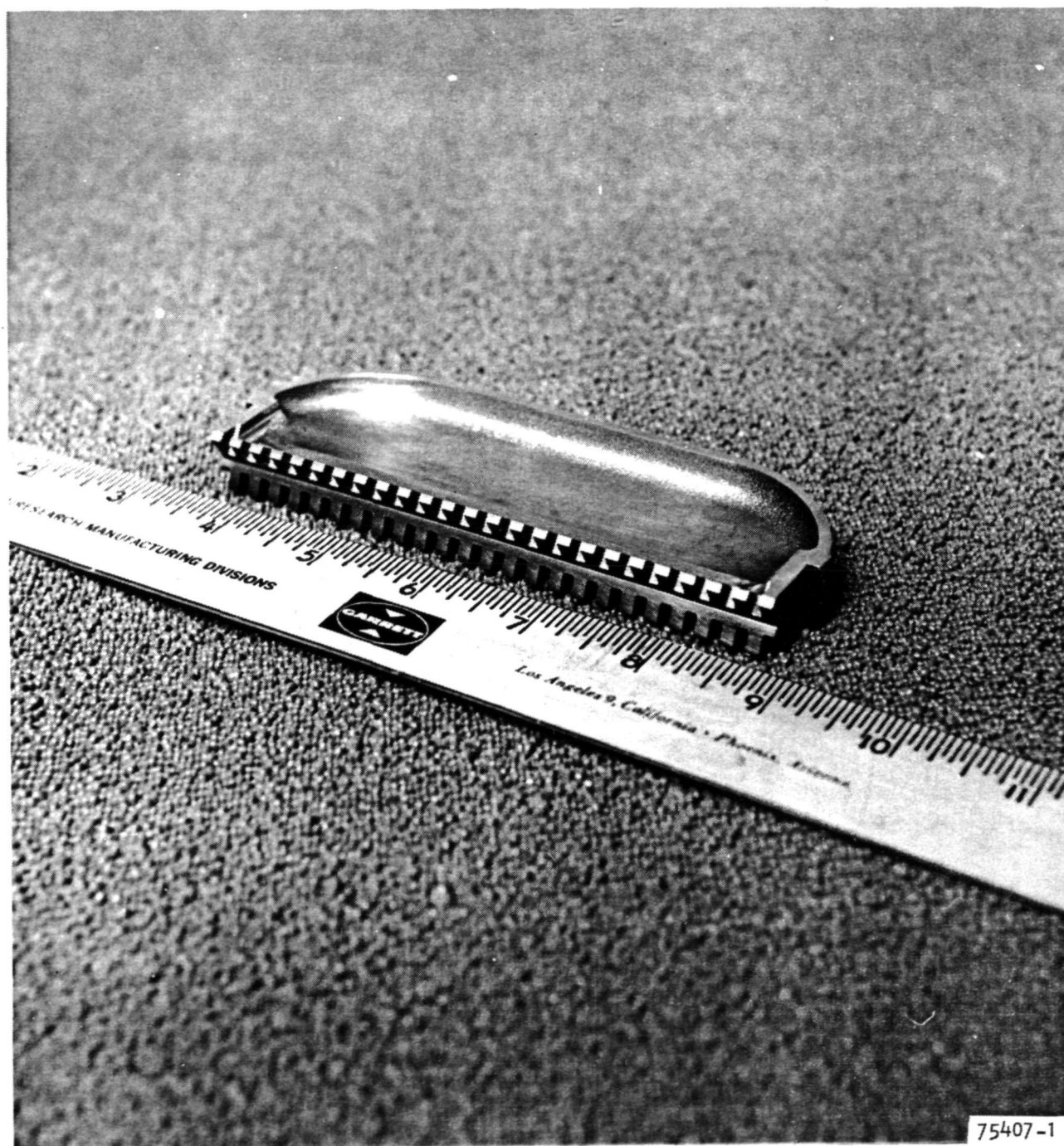


Figure 4-112.--Completed Splitter, Recuperator Submodule No. 2.

on the cycle life, the test procedure was modified to specify that the high-pressure side inlet pressure should be set equal to the low-pressure side inlet pressure  $496 \text{ kN/m}^2$  (gauge) (72 psig) to minimize the bypass flow.

The unit was subjected to the proof-pressure test at ambient temperature by simultaneously pressurizing the high-pressure circuit to  $1724 \text{ kN/m}^2$  (250 psig) (gauge) and the low-pressure circuit to  $1165 \text{ kN/m}^2$  (gauge) (169 psig). The minimal intercircuit leakage across the splitter plate was counteracted by continuous pressure regulation of both circuits.

The mass spectrometer helium leak test indicated a final assembly external leakage rate of  $4 \times 10^{-7}$  standard cubic centimeters per second (scc/sec), which is an acceptable value. (Allowable leakage was  $1 \times 10^{-6}$  scc/sec.)

Thermal Cycle Test.--For the thermal cycle test, equipment similar to that used on the SN1 tests was set up. It was decided to use a thermal cycle identical to that used in the previous test. A slower cycle was originally planned because the second test was designed to produce a failure between 100 and 300 cycles, compared to 80 cycles run in the previous test. The calculated difference in stress level between the two tests was small and the appearance of the first test core was excellent (except for the core/splitter joint); therefore, it was decided to use the same transient to ensure producing the desired failure before 300 cycles. Thermal cycle conditions are defined in fig. 4-72.

The unit was checked for leakage, both internal bypass and external, after completing 5, 10, 20, and 40 cycles of operation. Thereafter, leak checks were performed at about 30-cycle intervals (after completing 70, 100, 130, ... etc cycles). The external leakage check was performed by pressurizing the unit with air to  $241 \text{ kN/m}^2$  (35 psig) and observing for any visible leaks with the aid of a soap solution. A helium leak check for external leakage was performed at the start of testing and at 100-cycle intervals.

Results of the internal leakage flow test conducted after 100 cycles were compared with the initial leakage rate in fig. 4-113. The initial leakage flow was the result of a void in the manifold splitter-to-core braze joint, as discussed previously. The increase in internal leakage indicated by fig. 4-113 is attributed to an enlargement of the original void by thermal stresses occurring at the splitter joint.

Visual examination of the unit following completion of 100 thermal cycles indicated external test damage. This damage consisted of an external leak through the braze joining the pan attachment flange to the seal plate, adjacent to the side plate on the hot end, and through a crack in the seal plate, emanating from the flange corner and continuing through the turned up portion of the seal plate. This leakage area is shown in fig. 4-114. The damaged area, noted as "A" in fig. 4-115, was repaired by TIG brazing using Nicro filler.

Following the repairs, the helium leak check conducted on the test recuperator in accordance with the test plan indicated an external leakage rate of  $1.35 \times 10^{-8}$  scc/sec. The test to determine the internal leakage flow between

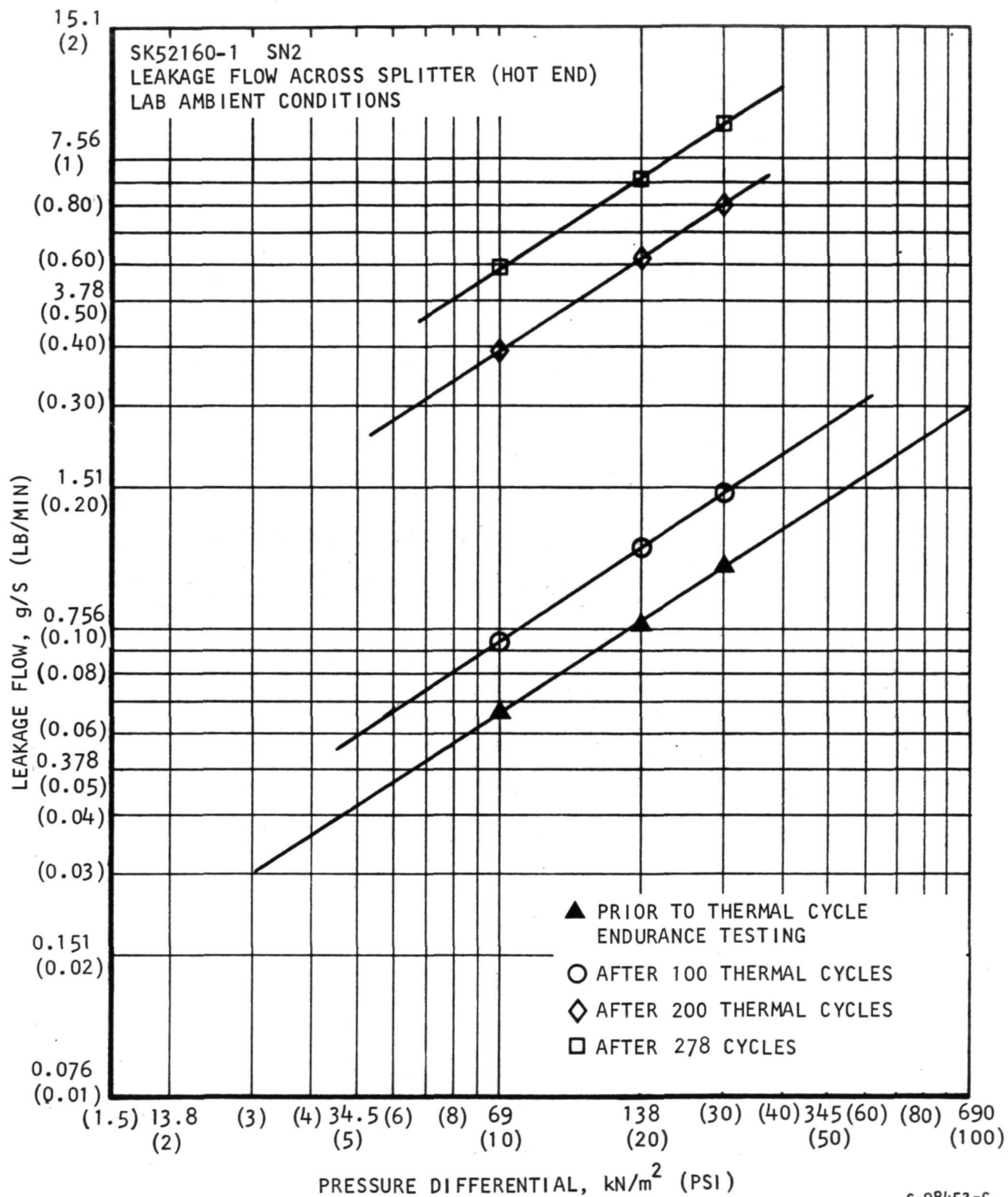


Figure 4-113.--Leakage Flow Across SN2 Splitter (Hot End).

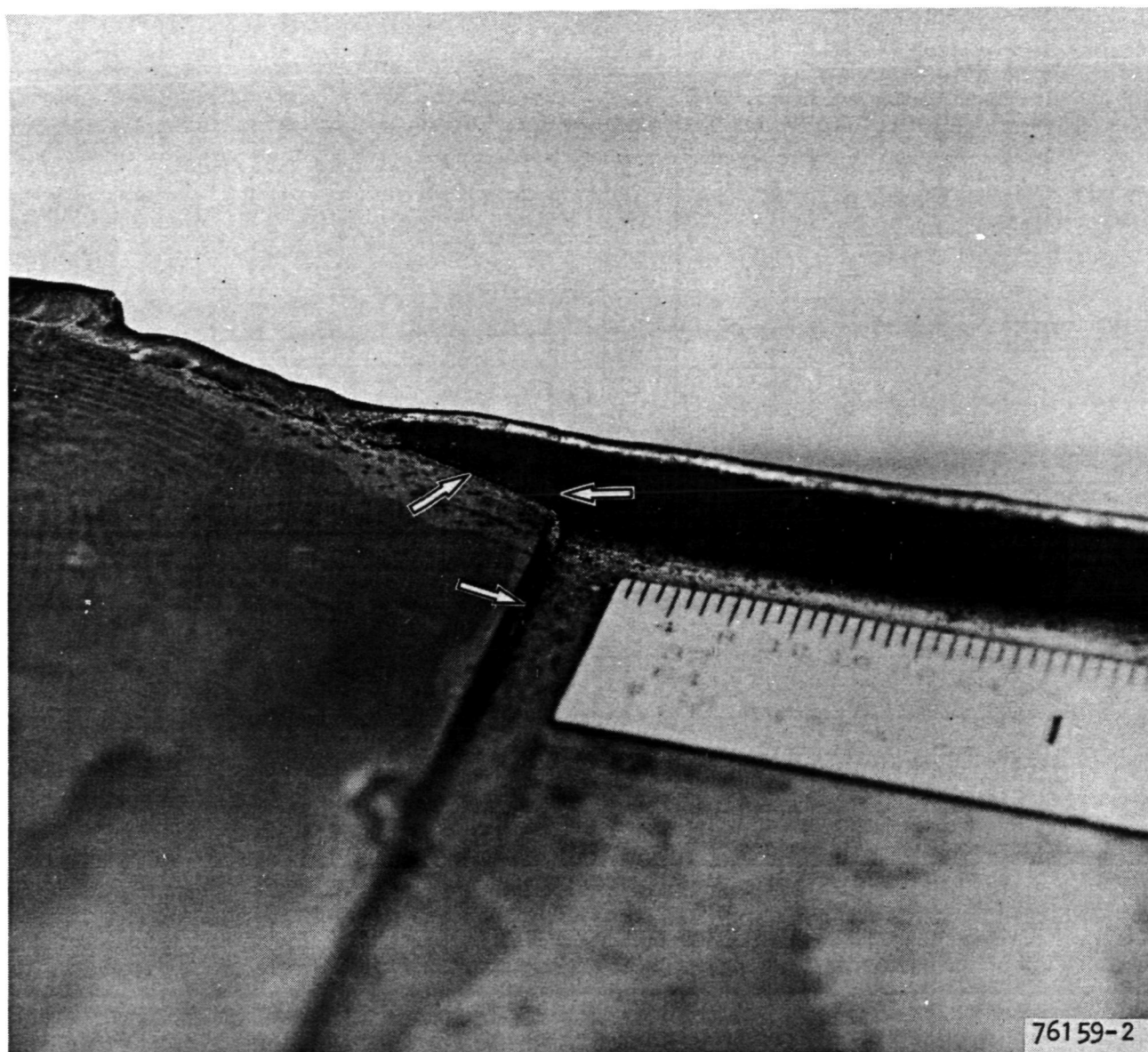
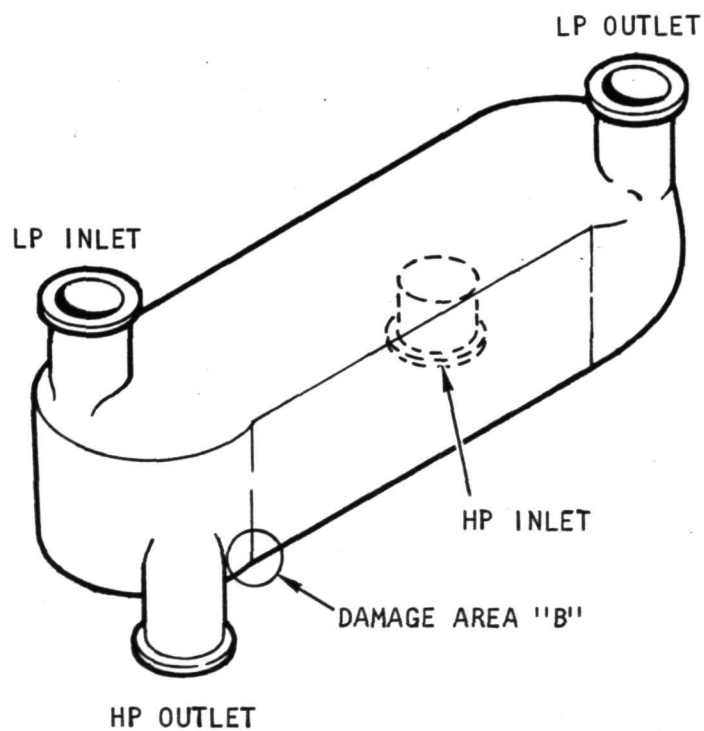
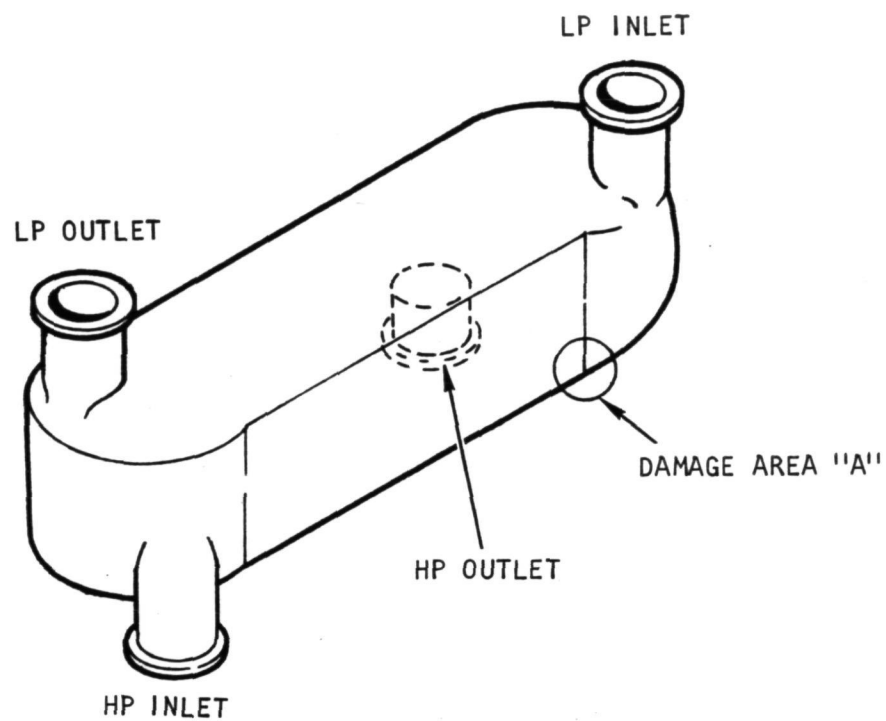


Figure 4-114.--Test Damage after 100 Thermal Cycles,  
Second Recuperator Submodule (SN 2)

F-22106



S-7452

Figure 4-115.--Test Damage Area Identification, Second Recuperator Submodule, (SN 2).



the recuperator high- and low-pressure circuits was repeated to ascertain what, if any, effect the braze repair had on the manifold splitter-to-core braze void. The second test indicated identical flow values to those of the test made prior to the test damage repairs.

The test recuperator was reinstalled in the thermal cycling facility, and testing was resumed. After completing 130 cycles, the unit was removed from the setup and visually examined. External leakage was noted from the repaired area adjacent to the low-pressure inlet manifold (noted as "A" in fig. 4-115) and from a similar area, adjacent to the high-pressure outlet manifold (noted as "B" in fig. 4-115). The measured internal leakage flow increased from 2 to 4 percent of the design point flow at a pressure differential of  $207 \text{ kN/m}^2$  (30 psi).

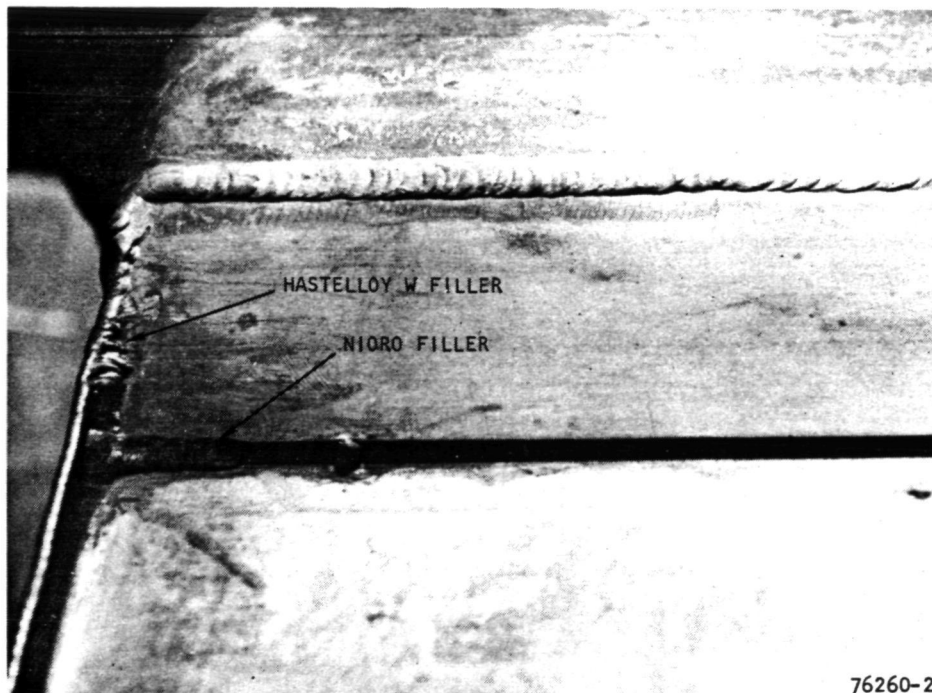
The damaged areas were repaired prior to continuing the thermal cycle testing. The previous repair material in damage area "A" was removed prior to effecting this repair. For that portion of the repair made solely to the side plate and seal plate, Hastelloy W was used as the filler material; for the remainder, the repair was by TIG brazing with Nicro as the filler material. A similar repair procedure was used for area "B". This type of repair is shown in fig. 4-116(a).

The original leak at location "A" was determined to have recurred and was repaired and returned to test after completing cycles 139, 157, and 180.

Following completion of 200 thermal cycles, the recuperator was removed from the thermal cycling facility for visual examination, an internal leakage flow test, and a helium leak check for external leakage as specified in the test plan. The visual examination indicated that the area "A" repair was again exhibiting an external leak. To preclude undue damage to the recuperator core, no further braze or weld repair attempts were made to the immediate leak area. Instead, a triangular patch of Hastelloy X was welded to the pan flange and seal plate to effect a seal. This repair is shown in fig. 4-116(b). The subsequent helium leak check indicated that a satisfactory repair had been made to area A but there was a minor leak in the earlier repair made to area B. The rate of leakage for the recuperator assembly was  $1.0 \times 10^{-6}$  scc/sec; with area B isolated, the leakage rate of the assembly was  $1.5 \times 10^{-8}$  scc/sec.

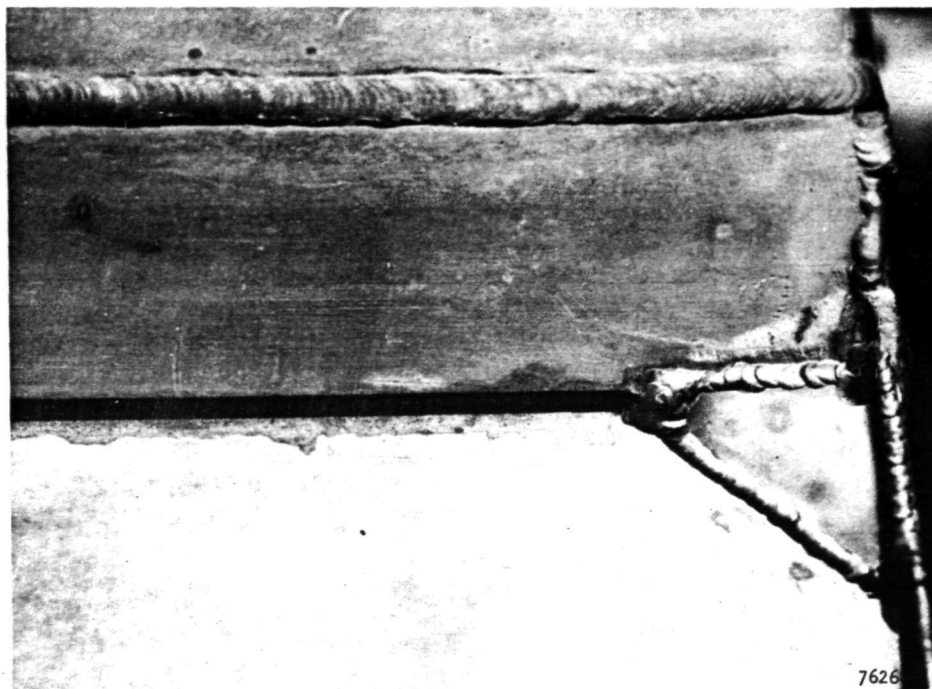
The result of the internal leakage flow test after 200 thermal cycles is compared to the results obtained at 0 and 100 cycles in fig. 4-113. As noted previously, this internal leakage flow was caused by a void in the manifold splitter-to-core braze joint. The continuing change in flow is attributed to the enlargement of the original void by thermal stresses that occurred at the hot end.

After 235 cycles, the test submodule was again removed from the setup, visually examined for external leakage, and subjected to the internal leakage test. No external leakage was evident, but an increase in the internal leakage across the hot end splitter was noted. The test unit was returned to the setup and testing was resumed.



76260-2

a. TEST DAMAGE REPAIR USING HASTELLOY W AND NIORO FILLERS



7626

F-22105

b. TEST DAMAGE REPAIR USING HASTELLOY X PATCH WITH HASTELLOY W FILLER

Figure 4-116.--Test Damage Repair.



A similar examination was made following the completion of 270 thermal cycles. Minimal external leakage was noted from the repaired area adjacent to the high-pressure outlet manifold (area B). Internal leakage across the hot end splitter continued to show an increase. With only minimal external leakage apparent at area B, and no visible structural damage, thermal cycle testing was resumed without any repairs made to the test unit.

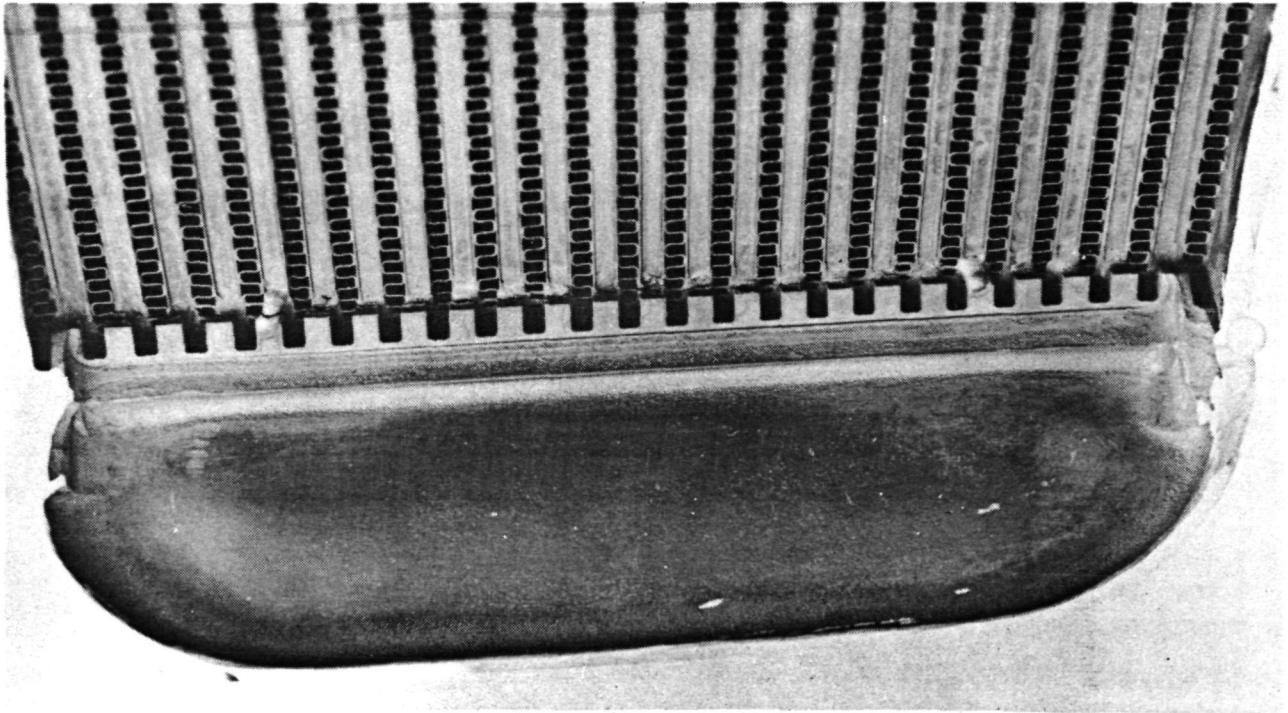
Thermal cycle testing was stopped after completing 278 cycles. It was believed that further testing to meet the program goal of 300 cycles would be of negligible value. An examination for external leakage indicated a crack in the side plate at the end of the increased thickness ledge, adjacent to area A, as well as a crack in area B that was originally noted following completion of 270 thermal cycles. These areas were sealed with epoxy and the unit subjected to a helium leak check. The external leakage for the assembly, with these areas isolated, was  $8.3 \times 10^{-8}$  scc/sec. Internal leakage across the hot end splitter indicated a slight increase over the previous test results. The measured internal leakage at the conclusion of the thermal cycling test (278 cycles) is compared with the results obtained at 0, 100, and 200 cycles in fig. 4-113.

Metallographic Examination.-Subsequent to the nondestructive examinations, the submodule pans were removed from the hot end (low-pressure inlet and high-pressure outlet) to permit direct visual examination of the splitter core apex joint and the core faces. For the splitter-core braze joint, a structural bond was observed for approximately 0.6 cm (1/4 in.). The remaining portion of the joint was cracked. As shown in fig. 4-117 (1/4 in.), examination of the braze joint after removal of the splitter indicated that the joint fitup was adequate and the joint area was originally filled with braze alloy. As noted previously, separation of this joint occurred prior to the thermal cycling test and enlarged as a result of the thermal stresses created during the cycle test.

Some minor damage was observed on the core face at the low-pressure inlet. As shown in fig. 4-118, the leading edges of the fins at the top low-pressure passage were cracked and buckled. Cracks also were observed in some of the sheet metal channel header bars.

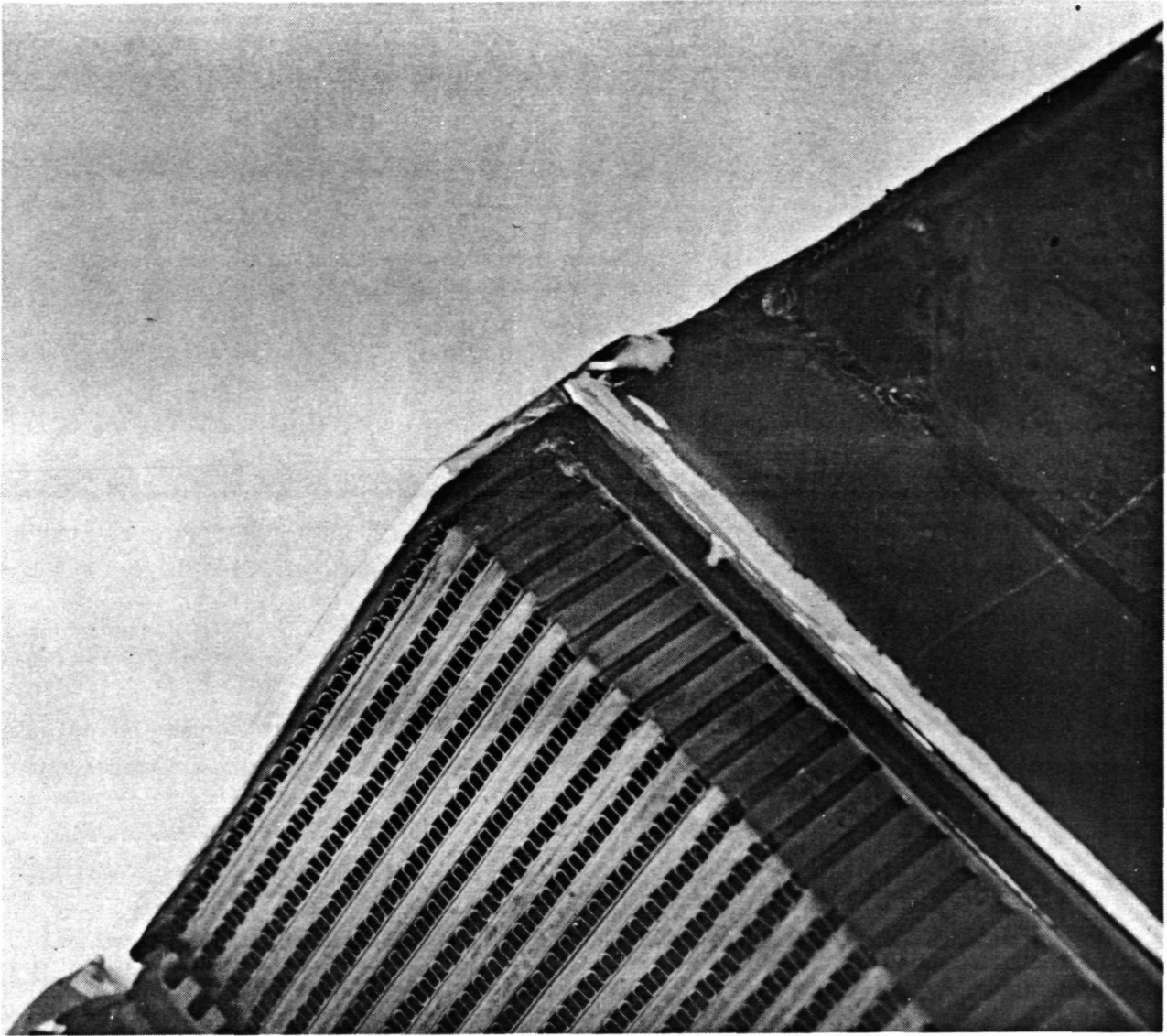
The core in the damaged areas A and B (fig. 4-115), and in similar locations on the opposite side where no external leakage was detected, was sectioned and mounted for structural examination. Micrograph locations are defined in fig. 4-119. Observations are summarized in the following paragraphs.

Micro 3519 (fig. 4-120): Numerous cracks in the fins and the sheet metal header bars are apparent from looking at fig. 4-120. The offset fins in the top low-pressure pass are buckled. There is no damage to the tube plates in the area adjacent to the header bar (this was predicted to be a critical area where low-cycle fatigue cracks would first occur). A gap exists between the channel header bar and the tube plate (second pass from top). This gap is believed to be due to poor fittings for brazing rather than a fatigue failure.



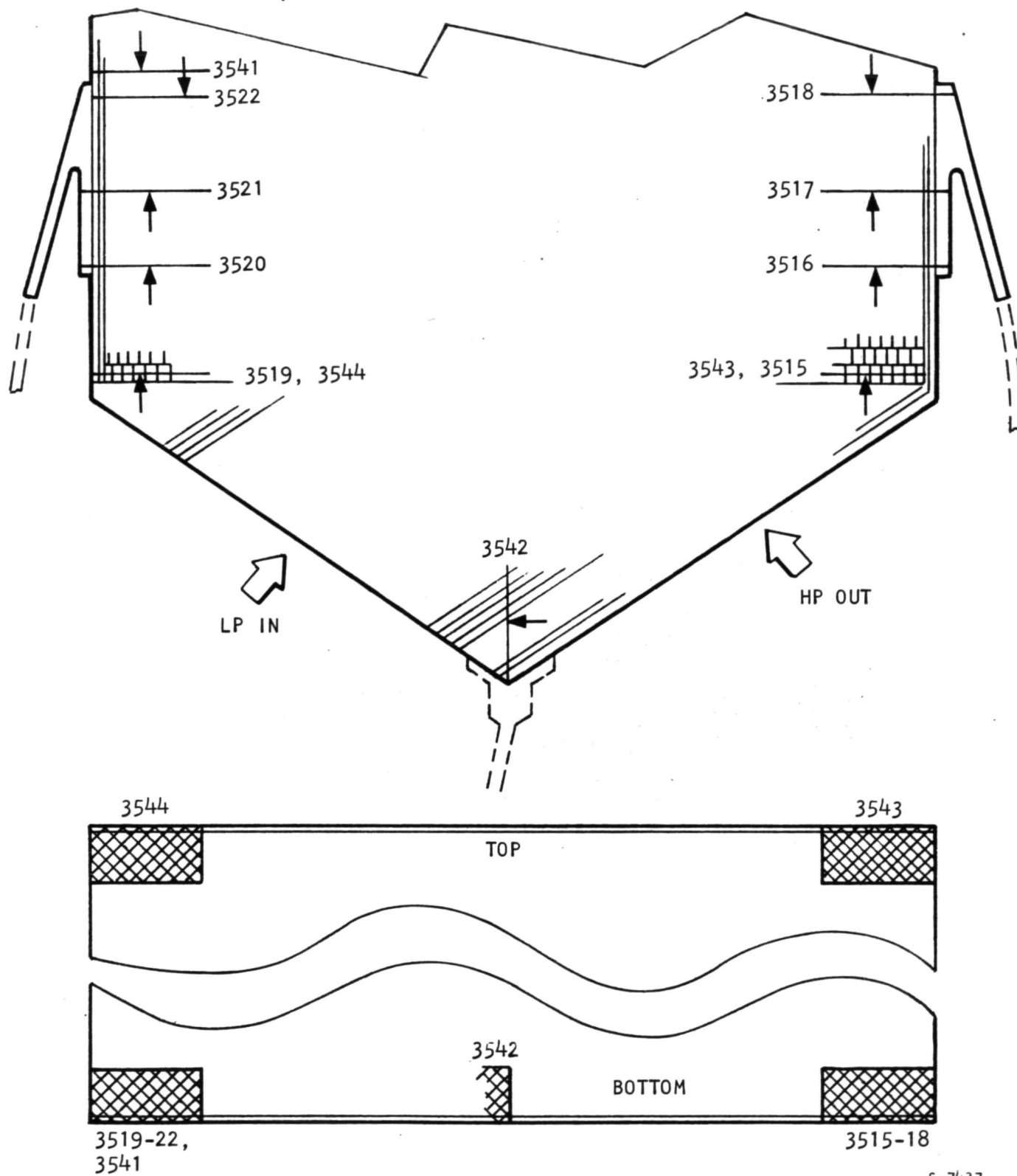
76302-1

Figure 4-117.--Splitter-Core Joint at Low-  
Pressure Inlet (After Test).



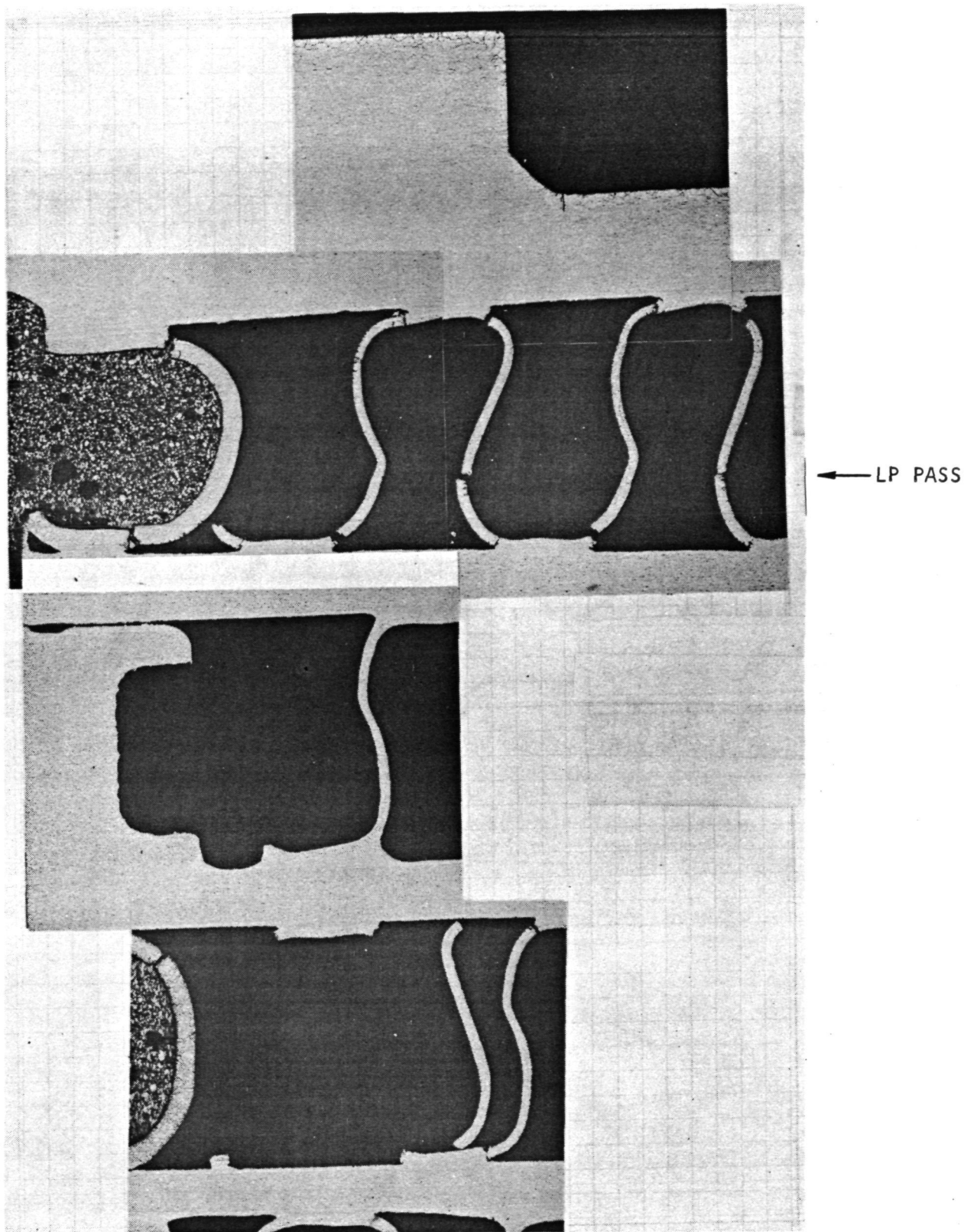
76302-3

Figure 4-118.--Core Face at Low-Pressure  
Inlet After Test.



S-7437

Figure 4-119.--Micrograph Locations, Submodule SN2.



MR 3519  
Figure 4-120.--Metallographic Examination Submodule, SN2, MR3519.



Micro 3520 (fig. 4-121): The following observations were made:

1. A crack occurred in the side plate adjacent to the thickened section. A helium leak was detected at this location at the test conclusion (278 cycles).
2. A tensile failure occurred in the header bar to tube plate joint in the top low-pressure pass.
3. A tube plate crack emanating from the crack in the header bar joint (between first and second passages).
4. A through crack occurred in the seal plate. Oxidation was visible suggesting that the crack occurred during the test rather than as a result of fabrication.
5. The circular section in the gap between the seal plate and machined header bar face is a wire used to aid in closing this gap.
6. Buckled and cracked fins.
7. A separation in the braze joint between the seal plate and the machined header bar face.

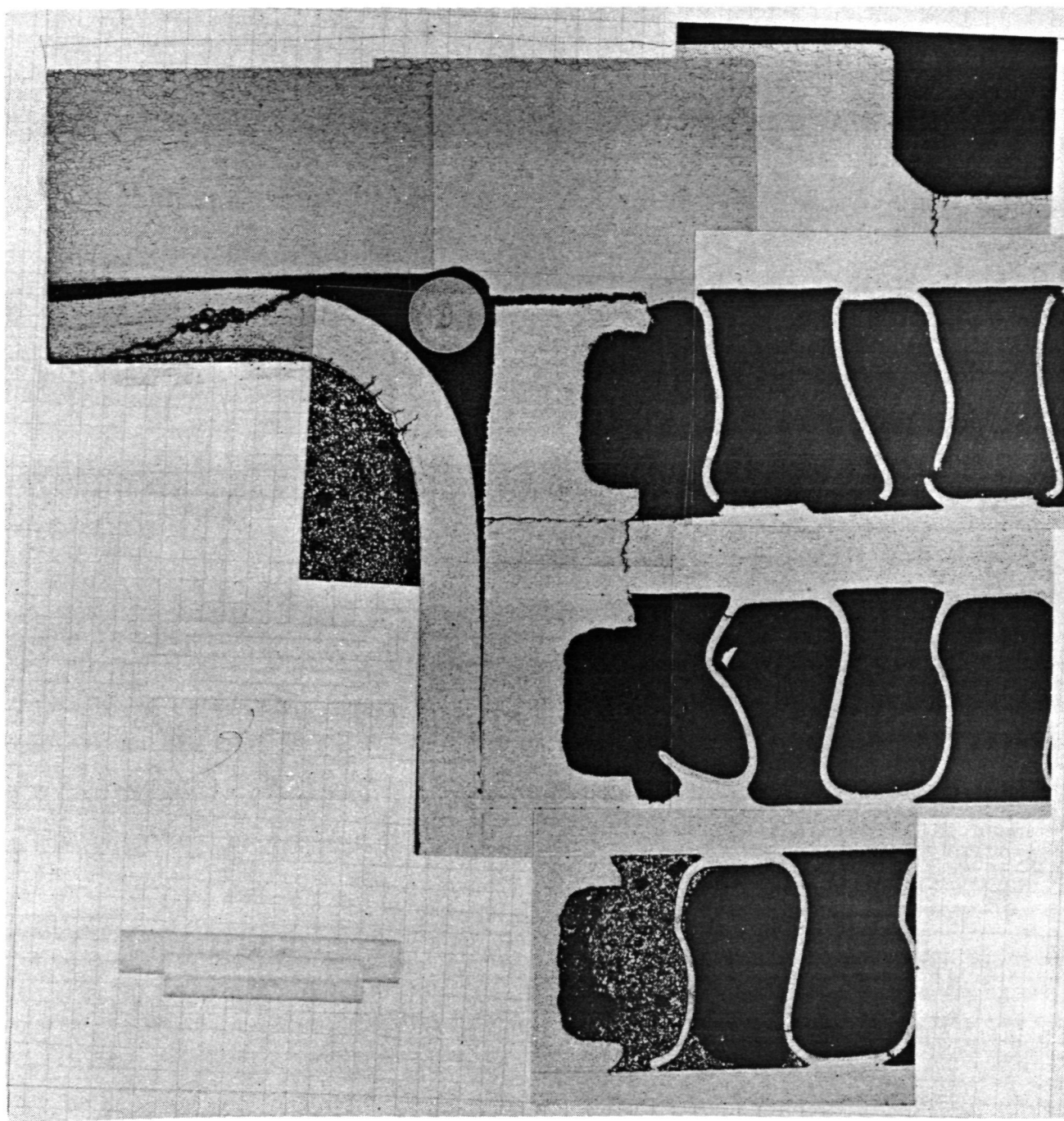
Micro 3516 (fig. 4-122): The appearance of this section was similar to that of micro 3520 including the side plate crack. Note that micros 3516 and 3520 are at the same axial station, but on opposite sides of the core.

Micro 3522 (fig. 4-123): This section was subjected to repeated repairs during the test as evidenced by multiple weld passes along the side-plate/seal-plate joint. The white area in the center of the weld passes was identified as gold-base braze alloy. The large gap between the seal plate and the machined header bar face is attributed to poor fitup during brazing. A tensile failure through the header bar parent material along with fin cracks was evident in the bottom pass of the section.

Micro 3542 (fig. 4-124): The section was taken through the core apex adjacent to the splitter plate. Tensile failures were apparent in several of the tube plate-to-header bar braze joints as well as several cases of fin cracking. This cracking is similar to that observed in the test of the SN1 submodule.

These observations are a complete summary of the various types of damage observed in the metallographic examination. Other portions of the core appeared to be undamaged.

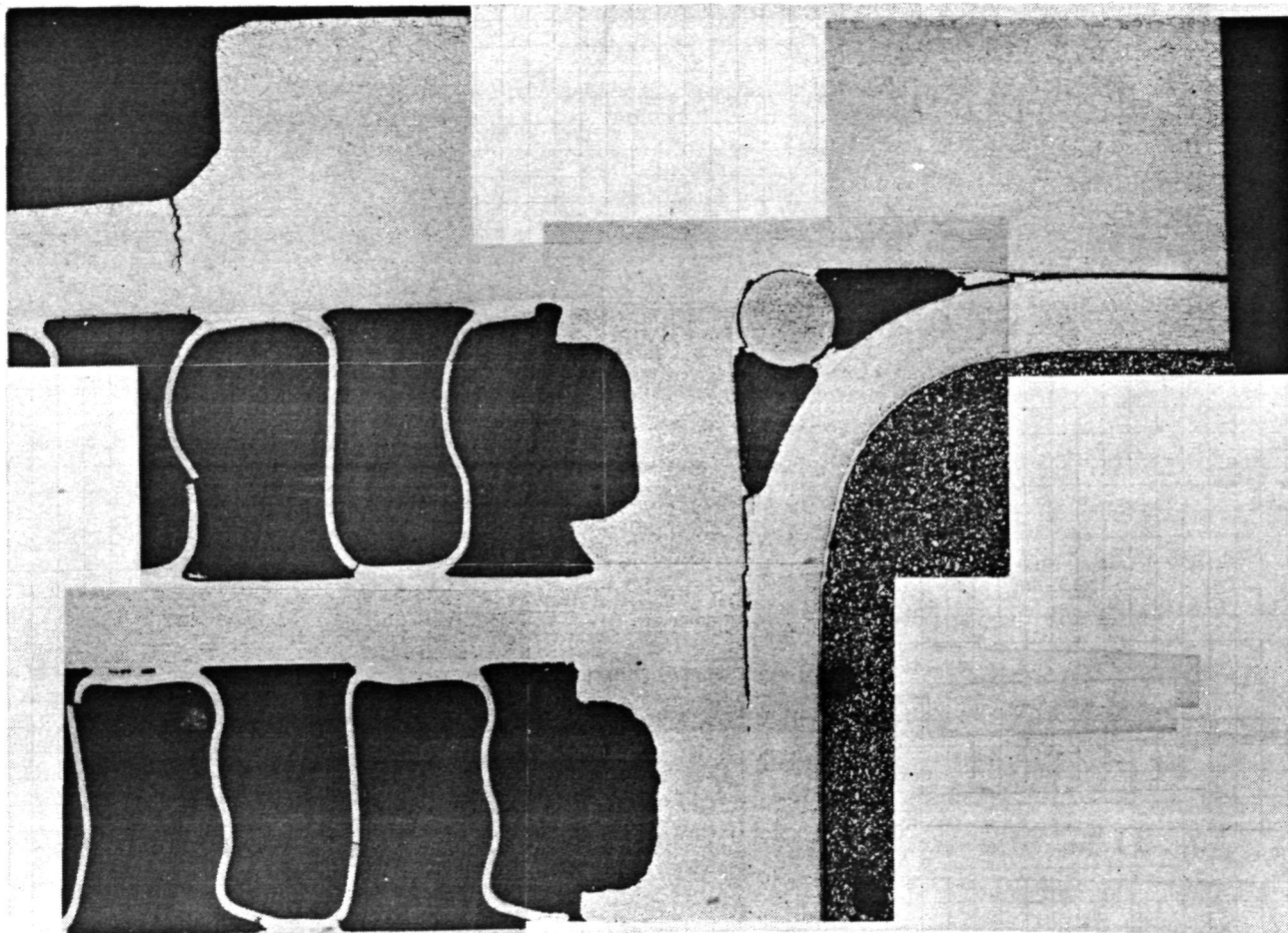
Conclusions.--Since the thermal cycling test was purposely conducted at an accelerated condition, the structural damage to the fins, tube plates, and braze joints apparent in the micrographs was as expected. Most of the damage is



MR 3520

F-23854

Figure 4-121.--Metallographic Examination Submodule, SN2, MR3520.

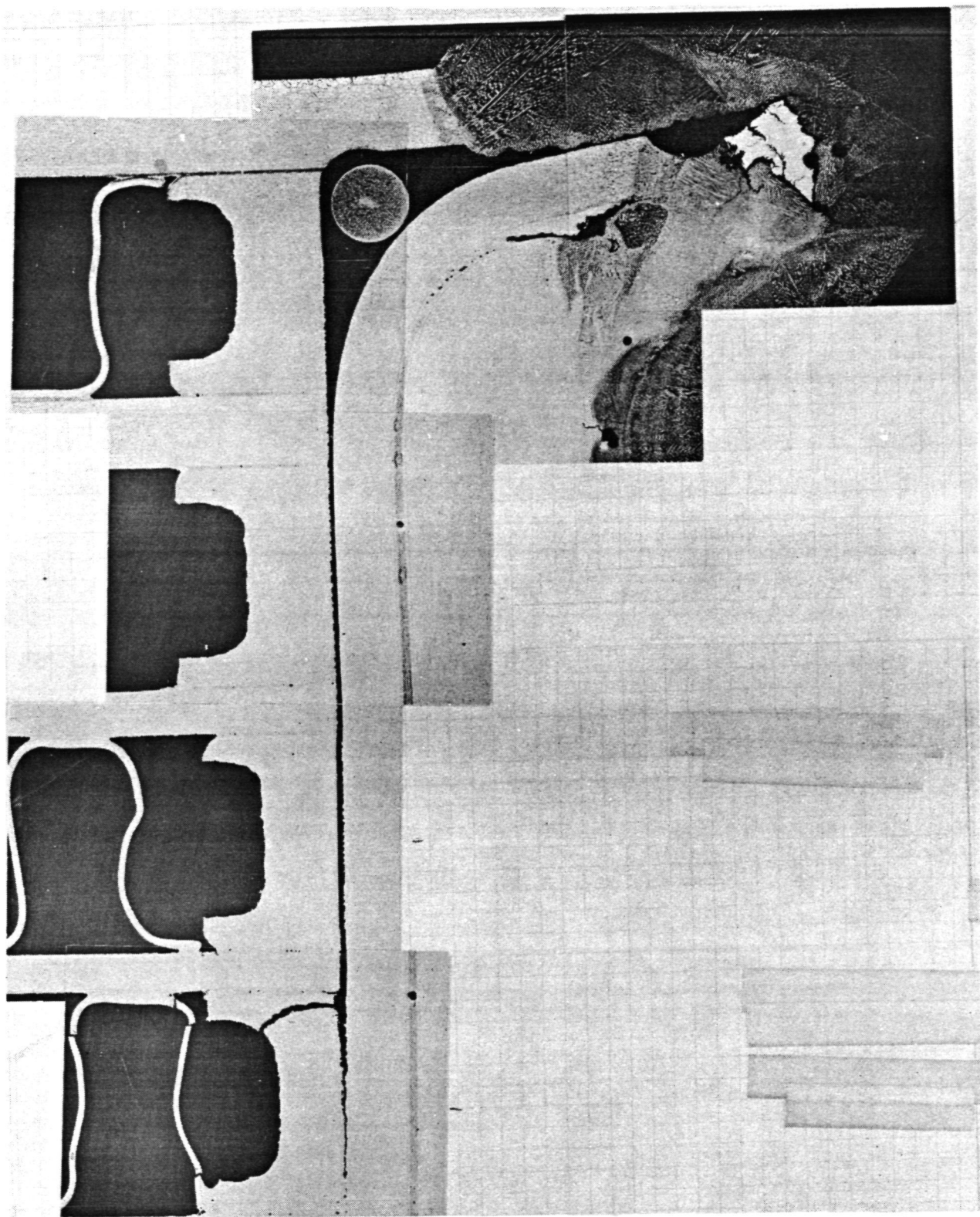


MR 3516

F-23852

Figure 4-122.--Metallographic Examination Submodule, SN2, MR3516.

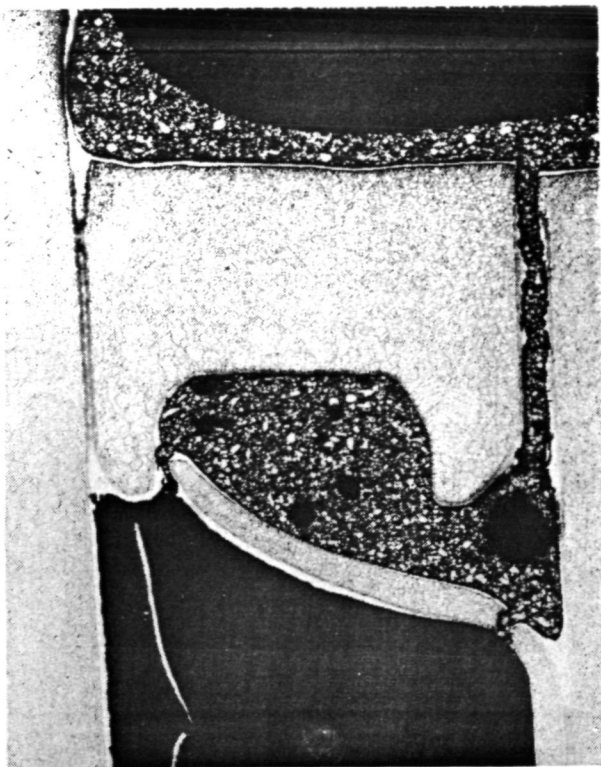




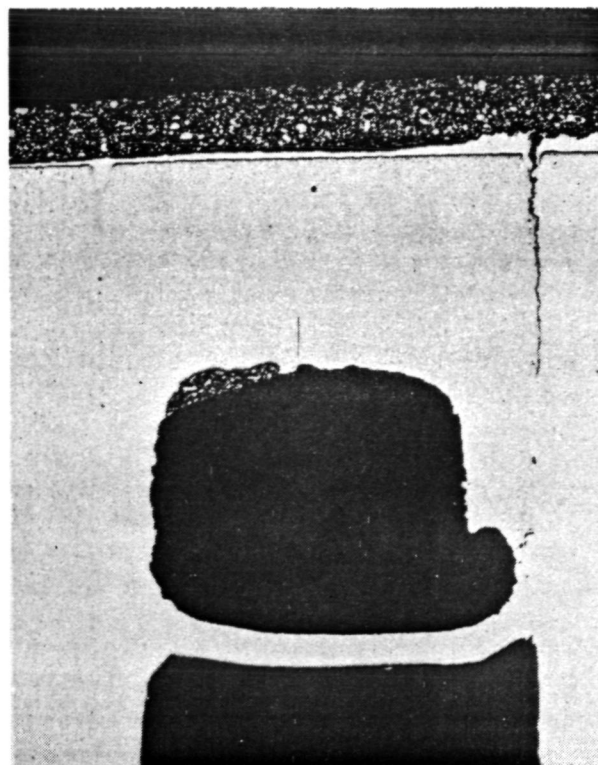
MR 3522

F-23855

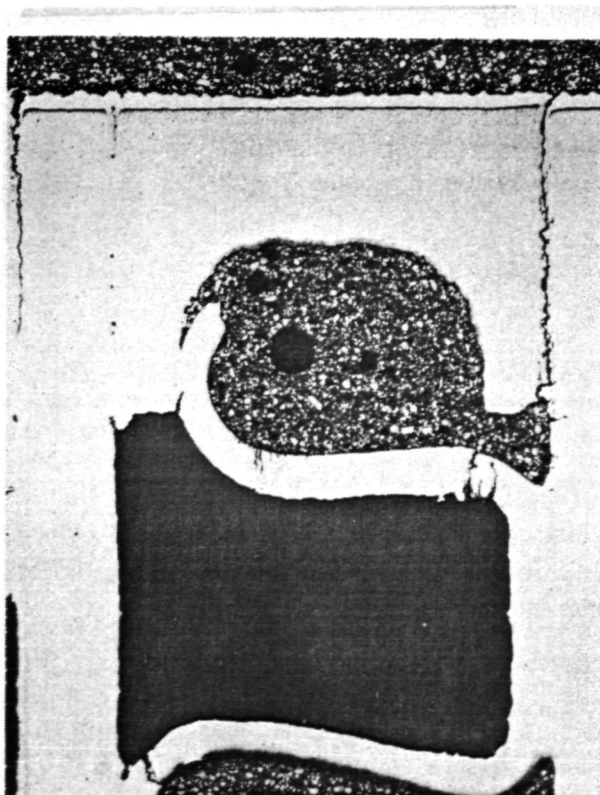
Figure 4-123.--Metallographic Examination Submodule, SN2, MR3522.



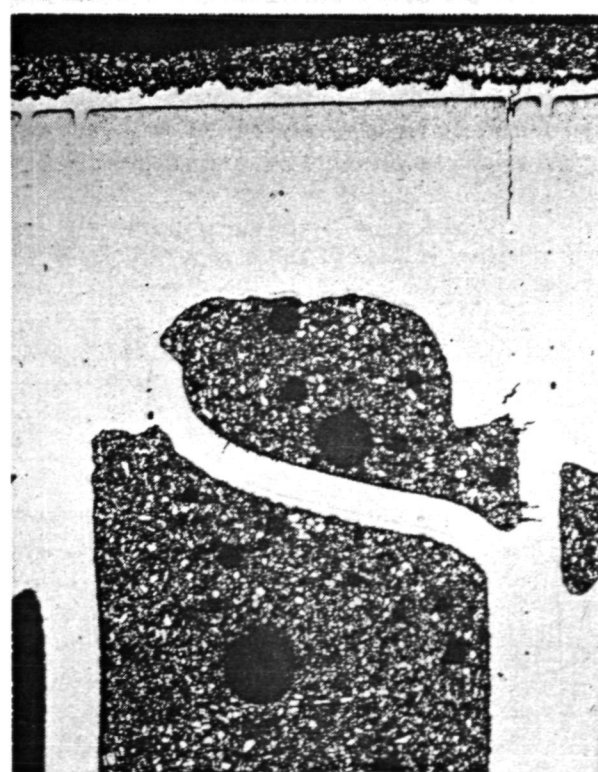
PASS No. 1



PASS No. 2



PASS No. 3



PASS No. 5

F-23851

MR 3542

Figure 4-124.--Metallographic Examination Submodule, SN2,  
Splitter-Core Joint.

caused by a repeated load applied along the stack height direction. The cracks along the side plate, however, are due to a shear lag between the thick and thin sections of the side plate.

The area in which cracking occurred is different from that originally predicted. The basic analysis of the design was conducted using a slow startup transient as specified by NASA (400 sec to reach steady-state). This analysis indicated that the thermal lag between the header bar and tube plate would result in a crack developing in the tube plate adjacent to the header at the hot end of the core. A similar result with a faster 60-sec startup transient was predicted based on an extrapolation of this analysis.

With the fast startup transient used in the thermal cycling test (60 sec to reach steady-state), however, the greatest stress appears to have occurred in the core stack height direction as a result of the thermal lag between the manifold and the heat exchanger core. The core, because of its high rate of heat transfer, rapidly rises in temperature in response to the low-pressure gas inlet temperature transient. The resultant thermal expansion of the core in the stack height direction is resisted, however, by the manifold attachment flanges and the manifold splitter plate. These parts are relatively heavy sections and are in low velocity sections of the core assembly, both of which tend to delay the thermal response.

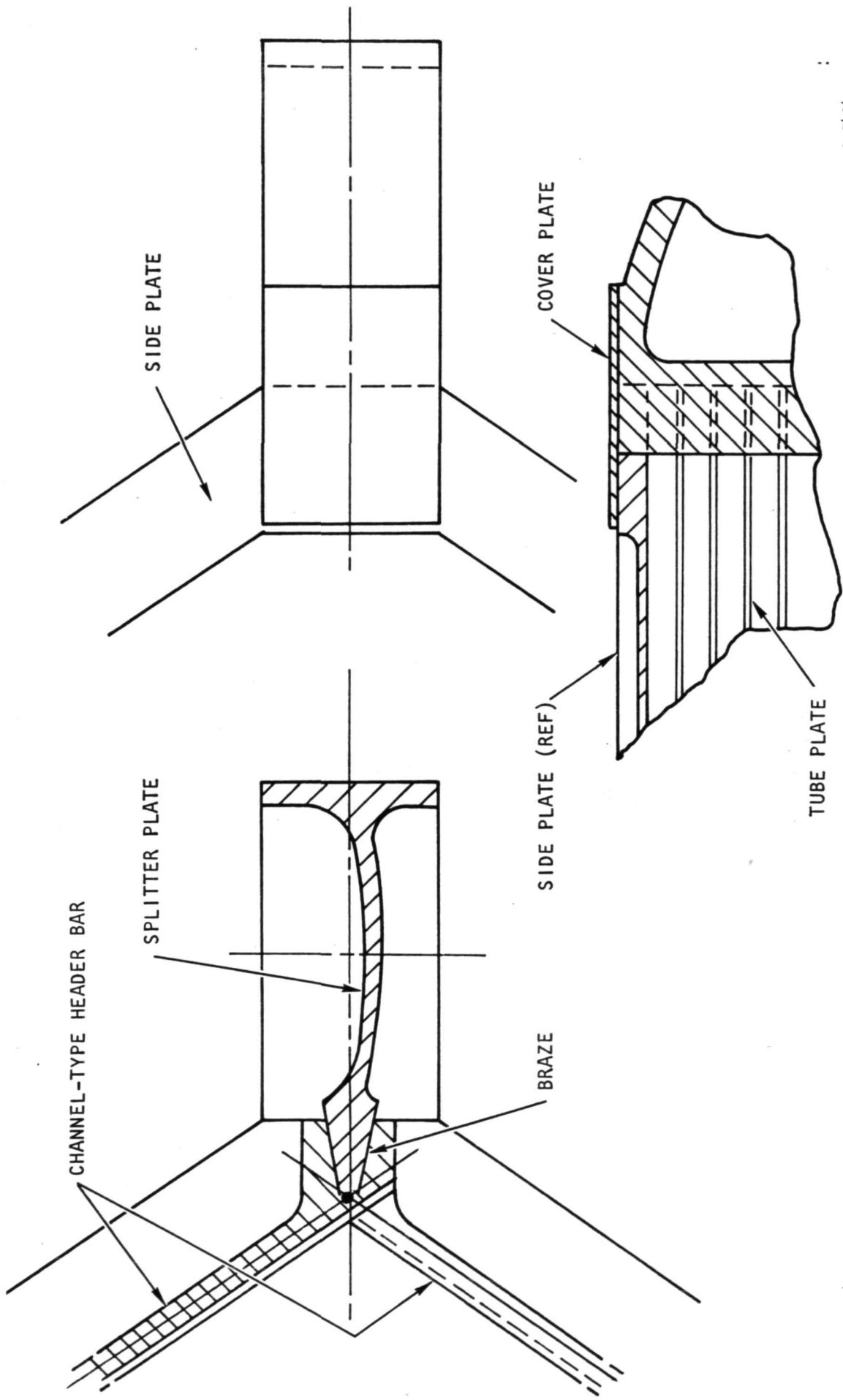
Consequently, during the first portion of the cycle the critical sections of the core, e.g., the tube plate-header bar joints, exceed the elastic limit in compression and a degree of plastic damage is incurred. During the final portion of the cycle, the flanges and the splitter tend to equalize with the core temperature. The critical core sections, which were in compression, are now forced into a high tensile loading and creep damage is incurred. After repeated cycles through this plastic-creep loop a low-cycle fatigue crack results.

The cracks that reappeared in the repaired areas after about every 30 cycles of operation tend to confirm this hypothesis.

It is believed that the extent of fin cracking observed in the test unit will not seriously degrade the long-term structural capability of the unit. A few cracked fins adjacent to the header bars do reduce the pressure load carrying capability, but no serious tube plate deformation or cracking should occur.

The cracks that developed in the side plate are believed to be caused by the difference in thermal response between the thick and thin sections. This is a shear lag type of failure similar to that originally expected to occur.

Overall, the thermal cycling test confirmed the predicted life of the recuperator submodule. The greater severity of the off-limit condition used as the test thermal cycle produced an external leak in the test unit after 100 cycles of operation, which was greater than the predicted life of 80 cycles. On this basis, the design analysis would predict that the unit would achieve the specified life of 1000 cycles with a slow startup transient.



S-7434

Figure 4-125.--Splitter-Core Joint Design.

### Recommended Design Improvements

The splitter-core joint should be modified to provide an additional braze joint shear area to resist the high tensile loads developed at this location. The design recommended for future recuperators is shown in fig. 4-125. The header bars incorporate a paddle-shaped end. When the unit is stacked and brazed, a monolithic structure is formed at the core apex of sufficient size to incorporate a dove-tail joint design. The dovetail will facilitate achieving a close fitup for brazing. A cover plate, either a separate piece or an integral part of the splitter prevents direct exposure of the splitter-core braze joint to space.

The increased section thickness along the ends of the side plate should be extended further down the length of the core and should be blended gradually into the thinner section of the side plate.

The joint between the ends of the manifold attachment flange and the core should be reinforced.

### REFERENCES

- 4-1. Richard, C.E.; Morse, C.J.; and Duncan, J.D.: Topical Report, Design Study, Alternate Brayton Heat Exchanger Unit. AIREsearch Report 69-5194, July 1969.
- 4-2. Duncan, J.D., et al.: Final Design Report, Brayton Heat Exchange Unit, Development Program (Alternate Design). NASA CR-121269, Aug 1973.
- 4-3. Manson, S. S.: Fatigue: A Complex Subject-Some Simple Approximations. Experimental Mechanics, July 1965.
- 4-4. Copper, R. A.: Creep Effects on Elevated Temperature Fatigue. Paper presented at Westec Conference, Los Angeles, California, March 8-11, 1971.
- 4-5. Halford, G. R.: Cyclic Creep-Rupture Behavior of Three High Temperature Alloys. NASA TND-6309, May 1971.
- 4-6. Spera, D. A.: Calculation of Thermal-Fatigue Life Based on Accumulated Creep Damage. NASA TND-5489, October 1969.
- 4-7. Spera, D. A.: The Calculation of Elevated-Temperature Cyclic Life Considering Low-Cycle Fatigue and Creep. NASA TND-5317, July 1969.
- 4-8. Richard, C. E.; Duncan, J. D.; Demogenes, C.; and Flieder, W. C.: Low-Cyclic Fatigue Evaluation for Regeneratively Cooled Panels, To be published by NASA performed under Contract NAS 1-5002.
- 4-9. Anon: Metallic Materials and Elements for Aerospace Vehicle Structures, MIL-HDBK-5A, January 5, 1970 (Change Notice).



- 4-10. Anon: Hastelloy Alloy. Report F30, 037D, Union Carbide Corporation Stellite Division, October 1964.
- 4-11. Anon: Steels for Elevated Temperature Service. ADUSS-1089, United States Steel, January 1966.
- 4-12. Anon: AiResearch Test Data, 1970.
- 4-13. Coombs, M.G., et al.: Topical Report, Brayton Cycle Heat Exchanger and Duct Assembly, (HXDA), Preliminary Design and Technology Tests. NASA CR-121011, Oct 1972.
- 4-14. Landgraf, R. W.; Morrow, J.; Endo, T.: Determination of the Cyclic Stress-Strain Curve. Journal of Materials, vol. 4, No. 1, March 1969, pp 176-188.

## SECTION 5

### 1140°K (1600°F) BELLOWS DEVELOPMENT

Bellows are generally thin elements whose deflection characteristics are utilized to allow relative movement between rigid structures of fluid systems. Commonly, these items are used in fluid-carrying ducts where the need for motion is combined with the need for a hermetic seal.

Bellows are made in many sizes and shapes from a variety of materials. This program will be concerned with the types of metallic bellows that can be used in large diameter ducting 20 cm (8 in.) inside diameter carrying fluids at elevated temperatures 1140°K (1600°F) with extended life requirements of 50 000 hr and 1000 cycles.

Bellows are generally classified according to one of the three primary methods of manufacture, i.e., (1) formed, (2) welded, or (3) machined. Within these classifications, the bellows are categorized according to the shape of the convolution cross section. Table 5-1 illustrates the major bellows classifications and relative characteristics of the various convolution shapes to be considered in this program.

#### BELLOWS TYPES

##### Formed Bellows

Formed bellows are usually made from butt-welded tubing that has been fabricated from closely controlled sheet metal thicknesses. Formed bellows are by far the most common type currently being manufactured and used. They can be produced in many materials and sizes and at a lower cost than the other types. Standard formed bellows can be obtained in sizes up to 92 cm (36 in.) in diameter. Formed bellows are stiffer and require the use of more ductile materials than welded bellows. However, because of the absence of circumferential welds, they are more reliable than welded bellows.









Most formed bellows can be readily manufactured with multiple plies with a four-ply bellow being common. Multiple plies are used to great advantage in providing higher pressure containment capability with lower stiffness than could be obtained using a single ply of equal total material thickness. The various convolution shapes are described below.

Semitoroidal--This shape is attractive for materials with relatively low ductility offering good pressure containment capability and excellent buckling stability. The convolutions may be semicircular, elliptical, sinusoidal, or a combination of various curve forms. A major limitation of this convolution shape is low deflection capability and a resulting high spring rate.

U-Shaped--Flat sections are placed within the semitoroidal sections and a U-shaped or flat plate bellows configuration is formed. This shape is applicable to any of the formed bellows manufacturing methods

TABLE 5-1

## BELLOWS CONVOLUTIONS AND CHARACTERISTICS

	Convolution Shape	Axial Spring Rate	Long Stroke Capability	Resistance to Diff. Pressure
<b>FORMED</b>				
Semitoroidal		Very high	Very poor	Very good
U-shaped		Medium	Fair	Fair
S-shaped		Medium	Fair	Fair
<b>WELDED</b>				
Flat		Medium	Fair	Good
Stepped		Low	Good	Fair
Single sweep		Medium	Good	Good
Nested ripple		Very low	Excellent	Poor
<b>MACHINED</b>				
Rectangular		High	Fair	Excellent

S-7625



and a variety of structural characteristics can be achieved by varying the radii and depth of convolution.

S-Shaped--By slanting the flat portions between the semitoroidal sections or by connecting the semitoroidal sections with curved members, more convolutions can be obtained in a given length and consequently more deflection per unit length is possible. More complex manufacturing processes are required for this shape.

#### Welded Bellows

Approximately one-fifth of the bellows currently being manufactured and utilized are of the welded convolution type. Welded bellows are fabricated from shaped diaphragms that are alternately welded together at the inner and outer diameters. This type of bellows is inherently more expensive than the formed bellows because of the length and difficulty of the weld joints. However, welded bellows offer some significant advantages over formed bellows. Wider choices of material, more deflection per unit length, and a wider choice of structural characteristics are possible with the welded configurations and these will be considered in the choice of bellows that satisfy the four design requirements.

Most welded bellows are of the single-ply configuration; however, a two-ply welded bellows is considered within the capability of present manufacturing techniques. Welded bellows are not currently available in large diameters and bellows exceeding 30 cm (12 in.) in diameter are not considered to be practical.

Various convolution shapes used in welded bellows are shown in table 5-1. with the most common being the nested-ripple type because of its inherent low stiffness and compactness. The other configurations have various characteristics for special applications and must be tailored to the service intended. Welding techniques have been developed to a high degree of sophistication by the manufacturers of welded bellows. The most significant limitation is considered to be the lack of fatigue resistance within the welded joints.

#### Machined Bellows

Machined bellows are turned or ground from bar stock, thick-walled tubing, or forged rings of material used in the other bellows types. Exotic materials that are not available in sheet stock can be utilized in machined bellows with the advantage of higher strength characteristics. Most bellows designs of this type are highly specialized and very costly to manufacture. They are generally much stiffer than the other types and are utilized for applications where ultrahigh pressure containment capabilities are required.

The formed bellows type was chosen as the most likely design to satisfy this program because of the relatively high pressure  $1380 \text{ kN/m}^2$  (200 psi) requirement. The basic formed bellows design is invariably a compromise between the deep U-shaped bellows with large deflection capability and a shallow semitoroidal type convolution with large pressure capability. S-shaped bellows are slightly more flexible than U-shaped bellows, otherwise they are the same.

## DESIGN DATA

### Environment

Bellows under consideration are primarily intended for application in a closed-Brayton power system. For space power application, the cycle working fluid is an inert gas, typically a mixture of xenon and helium gases. The outer surfaces of the bellows are exposed to a space vacuum. For this environment, a refractory alloy bellows material is acceptable because oxidation is not a problem. For terrestrial applications the bellows will be exposed to air either as a cycle working fluid or the outside environment. In this case, the bellows material must be oxidation resistant.

### Candidate Material Properties

The selection of materials for operation in air at 1140°K (1600°F) for extended periods of time involves consideration of creep strength, oxidation resistance, ductility, and weldability. Using these factors, Hastelloy X, Haynes 188, and René 41 have been selected as prime candidate materials. For space applications, a higher strength refractory alloy can be considered. For purposes of comparison, the alloy tantalum-10 tungsten (Ta-10W) is the selected refractory alloy because of its high-temperature strength and ductility. A literature search was performed and the most reliable mechanical properties data were used to provide the basis for a comparative high-temperature bellows design study.

### Typical Mechanical Properties

Published values of the candidate material properties have been compiled for Hastelloy X, Haynes 188, René 41, and Ta-10W, and are shown in table 5-2 for the required operating temperature. Mechanical properties utilized in the design procedure are obtained by applying the established design criteria specified below to the published values.

### Preliminary Design Criteria

The bellows under consideration must operate for a sustained period of time under fluid conditions of high temperature and high pressure; thus short-term elevated temperature properties and material creep behavior will provide a major criterion for the design procedure. The design must also include the capability for proof and burst pressure tests as quality assurance methods; thus room temperature material behavior must be considered. Large thermal movements are generally associated with the application of a typical bellows design, therefore the thermal fatigue behavior also will constitute a major design consideration.

### Service Requirements

The bellows design will be required to operate as a flexible coupling with the capability of handling fluids at a sustained temperature of 1140°K (1600°F) and a sustained pressure of 1380 kN/m<sup>2</sup> (200 psi). The objective service life for the bellows design is:

TABLE 5-2

1140°K (1600°F) MATERIAL PROPERTIES (SHEET METAL)

	Hastelloy X (refs. 5-1, 5-3 and 5-4)	Haynes 188 (refs. 5-2 and 5-5)	Rene 41 (refs. 5-1 and 5-4)	Ta-10W (refs. 5-6 and 5-7)
1. Modulus of Elasticity (E), MN/m <sup>2</sup> (psi)	134 x 10 <sup>3</sup> (19.4 x 10 <sup>6</sup> )	163 x 10 <sup>3</sup> (23.6 x 10 <sup>6</sup> )	159 x 10 <sup>3</sup> (23.0 x 10 <sup>6</sup> )	69 x 10 <sup>3</sup> (10 x 10 <sup>6</sup> )
2. Thermal Expansion Coefficient $\alpha$ , cm/cm/K (in./in./°F)	16.4 x 10 <sup>-6</sup> (9.1 x 10 <sup>-6</sup> )	16.9 x 10 <sup>-6</sup> (9.4 x 10 <sup>-6</sup> )	15.7 x 10 <sup>-6</sup> (8.7 x 10 <sup>-6</sup> )	9 x 10 <sup>-6</sup> (5 x 10 <sup>-6</sup> )
3. Elongation (e), percent	43	73	20	30
4. Reduction of Area (RA), percent	48	-	-	20
5. Yield Stress (0.2 percent), MN/m <sup>2</sup> (psi)	104(15 000)	262(38 000)	550(80 000)	550(80 000)
6. Ultimate Stress, MN/m <sup>2</sup> (psi)	207(30 000)	419(60 700)	620(90 000)	650(95 000)
7. 1000-hr Creep Rupture Stress, MN/m <sup>2</sup> (psi)	39(5600)	67(9700)	128(18 500)	240(35 000)

NOTE: 50 000-hr creep data is extrapolated from the available 1000-hr creep data and is subject to change as more reliable data become available.

50 000 hr at sustained fluid conditions with less than 1 percent creep

1000 operating cycles from ambient to sustained fluid conditions

### Stress Requirements

Allowable stresses for these components must take into account the stresses due to pressure containment. The bellows design criteria will provide for short time proof pressures of 1.5 times the working pressure, and burst pressures of 2.5 times the working pressure. The structure must not yield at proof pressure or rupture at burst pressure. This implies that the proof pressure is the governing design condition if the ratio of yield stress to ultimate stress is less than 1.5/2.5 (0.6), and that the burst pressure will govern if the ratio exceeds 0.6. The allowable stress at working pressure is, therefore, the lesser of the following:

$$\sigma_{all} = f_{tu}/2.5$$

$$\sigma_{all} = f_{ty}/1.5$$

For very ductile materials such as Hastelloy X, the yield condition governs and for the less ductile materials such as René 41 the ultimate condition will apply. Table 5-3 shows the short time pressure containment stress criteria for the candidate materials.

TABLE 5-3

#### SHORT TIME PRESSURE CONTAINMENT DESIGN STRESSES

	Hastelloy X	Haynes 188	René 41	Ta-10w
1. Room temperature				
$F_{ty}/1.5$ , MN/m <sup>2</sup> (psi)	276(40 000)	320(46 400)	550(80 000)	690(100 000)
$F_{tu}/2.5$ , MN/m <sup>2</sup> (psi)	329(48 000)	380(55 500)	475(69 000)	420(60 000)
2. Operating temperature				
$F_{ty}/1.5$ , MN/m <sup>2</sup> (psi)	69(10 000)	175(25 300)	362(53 000)	370(53 000)
$F_{tu}/2.5$ , MN/m <sup>2</sup> (psi)	82(12 000)	167(24 300)	247(36 000)	260(38 000)

When the limiting stress is due to bending, a small amount of yielding can be allowed in the outermost fibers, which leads to a modified stress distribution through the thickness. The ideal plastic bending moment is 1.5 times the computed elastic bending moment for the same peak stress. Accordingly, the allowable indicated elastic stress due to bending loads is taken to be 1.5 times the allowable direct stress.

A second important consideration is the combination of stresses due to pressure and thermal motions. It is known that the sum of stresses due to pressure and thermal motion does not exceed twice the yield stress, plastic strain flow will not occur during repeated cycling of the bellows. When the summation of these stresses exceeds  $2 \times f_{ty}$ , an amount of plastic strain flow equal to the excess stress divided by the elastic modulus will occur. To account for localization of the plastic flow, a strain concentration factor of 2.0 is used to determine plastic strain range during bellows cycling. This numerical result is then used in the formula for low-cycle fatigue:

$$N = \left( \frac{C}{\Delta \epsilon_p} \right)^2$$

where  $N$  = cycles to failure

$\Delta \epsilon_p$  = plastic strain range

$C$  = material ductility constant

The ductility constant is based upon the material reduction of area property, and the formula recommended by S. S. Manson of NASA Lewis Research Center (ref. 5-8) is

$$C = 0.79 \ln \left[ \frac{100}{100-RA} \right]^{3/4}$$

At elevated temperature, all of the above conditions must be satisfied, and in addition, the component must be satisfactory for long-time creep effects. There must be a set of creep criteria that is comparable to that for the short time loading. Accordingly, limitations based upon stress to rupture and stress to one percent creep must be established. The objective design life is 50,000 hr and the hot bellows is designed for sustained pressure operation at maximum operating temperature throughout the entire design life. Allowable stresses at working pressure must be the lesser of the following:

$$\sigma_{all} = (1\text{-percent creep stress})_{50\,000\text{ hr}}$$

$$\sigma_{all} = \left[ (\text{creep-rupture stress})_{50\,000\text{ hr}} \right]^{1/1.2}$$

It will be found that this limitation overrides the short time properties criteria for most materials utilized in the design of bellows.

When the limiting pressure stress is caused by bending, a redistribution of stress occurs both through the thickness and along the length. The steady creep stresses are substantially lower than those indicated by the elastic analysis. By utilizing the plastic moment distribution, an allowable creep stress due to bending can be utilized that is 1.5 times the allowable creep stress due to pure tensile forces. Stated differently, the actual sustained creep stress due to bending is taken to be 0.667 times the indicated elastic stress.

One additional precaution must be taken when designing for cyclic operation in combination with extended sustained operating time at elevated temperature. The stresses due to thermal motions must not produce a plastic loop of any appreciable magnitude during successive cycles. The following rationale is used to explain this requirement. During the first cycle, the bellows may be permitted to yield due to thermal motions during startup. When allowed to hold for an extended time period, creep relaxation will take place and the stresses initially will decay rapidly, and then progressively more slowly until eventually total stress alleviation takes place. Upon cooldown, the stresses will reappear but in the opposite direction (tension where initially compression, etc.). If a great deal of yielding occurs during the cooldown, the original high thermal stress will reappear on the next heatup, and this will be followed by more creep. This creep will add to that due to sustained loading, and will drastically reduce the life of the unit. This condition will not occur at all if the thermal motion stresses do not exceed the yield stress of the material. The problem will be largely eliminated if thermal stresses do not exceed more than 1.5 times the yield stress that has been used in the design criteria.

Table 5-4 summarizes the preliminary high-temperature bellows design stresses. These stresses result from application of the design criteria established to satisfy the long-term life objectives. The extrapolation of short-time creep data was necessary to establish allowable stresses for the 50 000-hr life requirement. Because of the uncertainties associated with the extrapolation of data, the allowable creep stresses must be considered preliminary and hence subject to change as more applicable data become available.

TABLE 5-4  
PRELIMINARY HIGH-TEMPERATURE BELLOWS DESIGN STRESSES

	Hastelloy X	Haynes 188	Rene 41	Ta-10W
1. Direct stress due to pressure loading, MN/m <sup>2</sup> (psi)	17.3(2500)	20.7(3000)	38.0(5500)	138(20 000)
2. Bending stress due to pressure loading, MN/m <sup>2</sup> (psi)	25.5(3700)	31.0(4500)	57.0(8250)	207(30 000)
3. Thermal stress due to transient conditions, MN/m <sup>2</sup> (psi)	155(22 500)	394(57 000)	830(120 000)	620(90 000)
4. Combined stress due to pressure and thermal loading, MN/m <sup>2</sup> (psi)	207(30 000)	525(76 000)	1110(160 000)	827(120 000)



## BELLOWS PARAMETRIC DESIGN STUDIES

A study was performed to evaluate the effects of changes in the convolution shape parameters. Relative convolution height,  $h/r$ , relative convolution width,  $w/h$ , and relative convolution thickness,  $h/t$ , were investigated over the ranges shown in fig. 5-1. The effect of material strength was included in the parametric variations by the use of Hastelloy X, Haynes 188, and Rene 41 superalloy materials, representing low-strength candidates and tantalum-10 tungsten refractor alloy material representing a high-strength candidate. The preliminary bellows designs that evolved from this study cover the complete range of practical formed bellows shapes.

A stress and deflection analysis of nine different convolution shapes with various ply thicknesses was performed with the aid of a proven shell analysis computer program. Results of the shell analysis provide maximum sustained stresses due to internal pressure loading and maximum cyclic stresses due to an imposed axial deflection. These results were used to establish a baseline bellows configuration for each of the nine different convolution shapes and each of the four candidate materials. The formulae used to calculate the various design parameters are given in Appendix C. Fig. 5-2 describes the shell model developed for the parametric study. Dimensional descriptions for each of the nine different convolution shapes are shown in fig. 5-3.

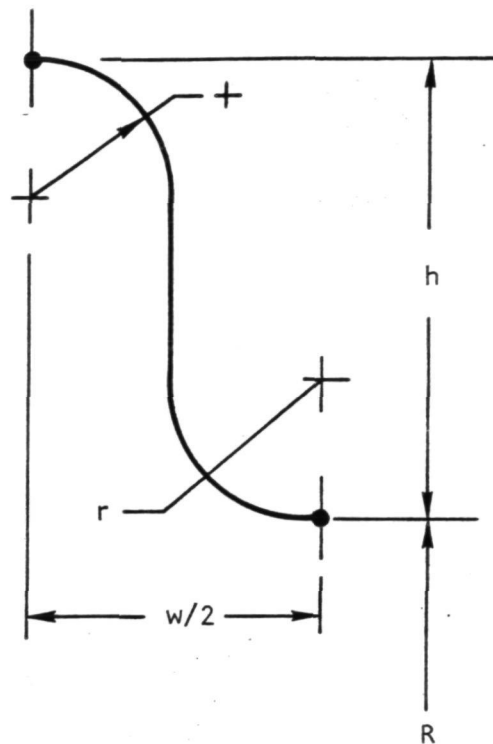
Analytical results for the bellows design parameter variations for each convolution shape and each candidate material are tabulated in figs. 2-4 through fig 2-30 of ref. 5-9. Finally, as a result of the thickness factor,  $h/t$ , variations, a baseline bellows design was selected for each of the convolution shapes and each of the candidate materials. Tables D-1 through D-9 in Appendix D summarize the structural characteristics for each of the nine baseline bellows designs.

## CONCLUSIONS

Bellows designed to operate at 1140°K (1600°F) for a 5-year life in a closed-Brayton power system are feasible. Conventional high-temperature oxidation resistant materials such as Hastelloy X and Haynes Alloy 188 can be used to produce practical designs considering fabrication and installation requirements. Refractory materials, used in a space application, are also feasible and offer performance advantages over the superalloys.

Results of the parametric analysis, summarized in figs. 5-4 and 5-5, lead to the following conclusions:

1. For a given material and convolute height, the active length, extensional and bending stiffnesses increase monotonically with the increase of convolute pitch. The lateral stiffness has a reverse trend.



#### CONVOLUTION SHAPE FACTORS

$$0.125 \leq h/R \leq 0.250$$

$$0.60 \leq w/h \leq 1.4$$

$$12.5 \leq h/t \leq 100$$

#### MATERIALS

HASTELLOX X

HAYNES 188

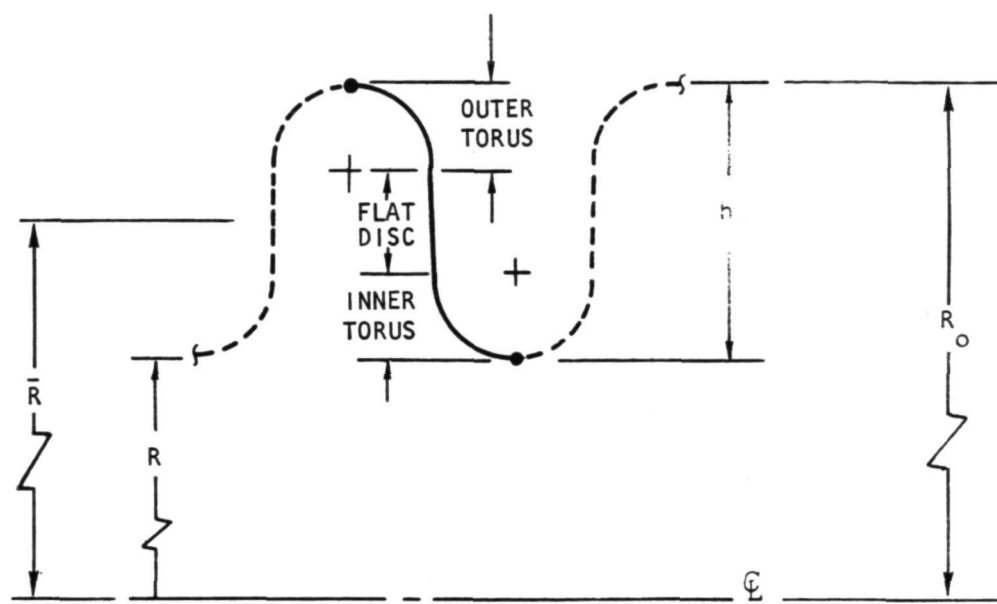
RENE' 41

TA-10W

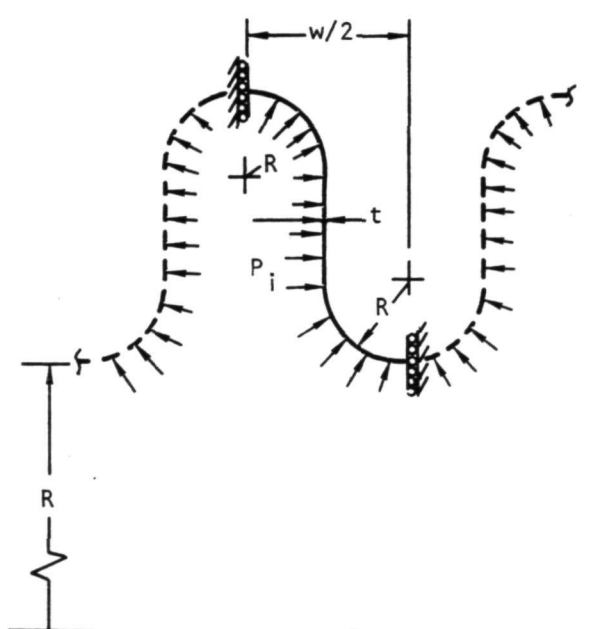
S-87141 A

Figure 5-1.--Range of Convolution Shape Parameters and Materials Investigated

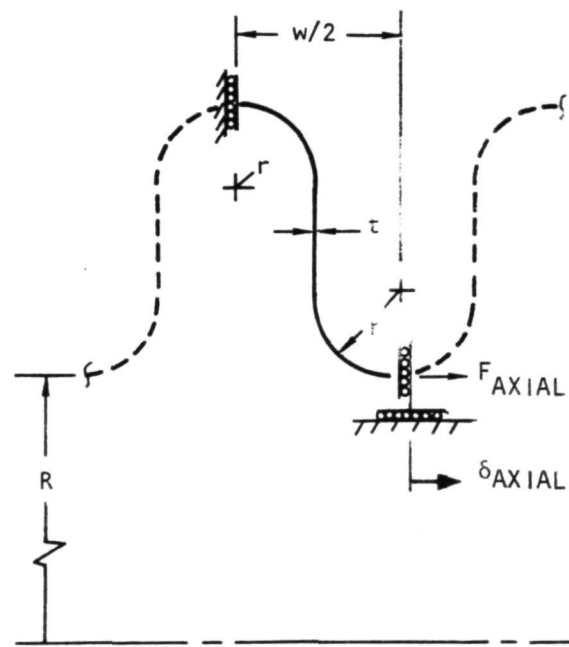




a. ELEMENTS OF SHELL ANALYSIS



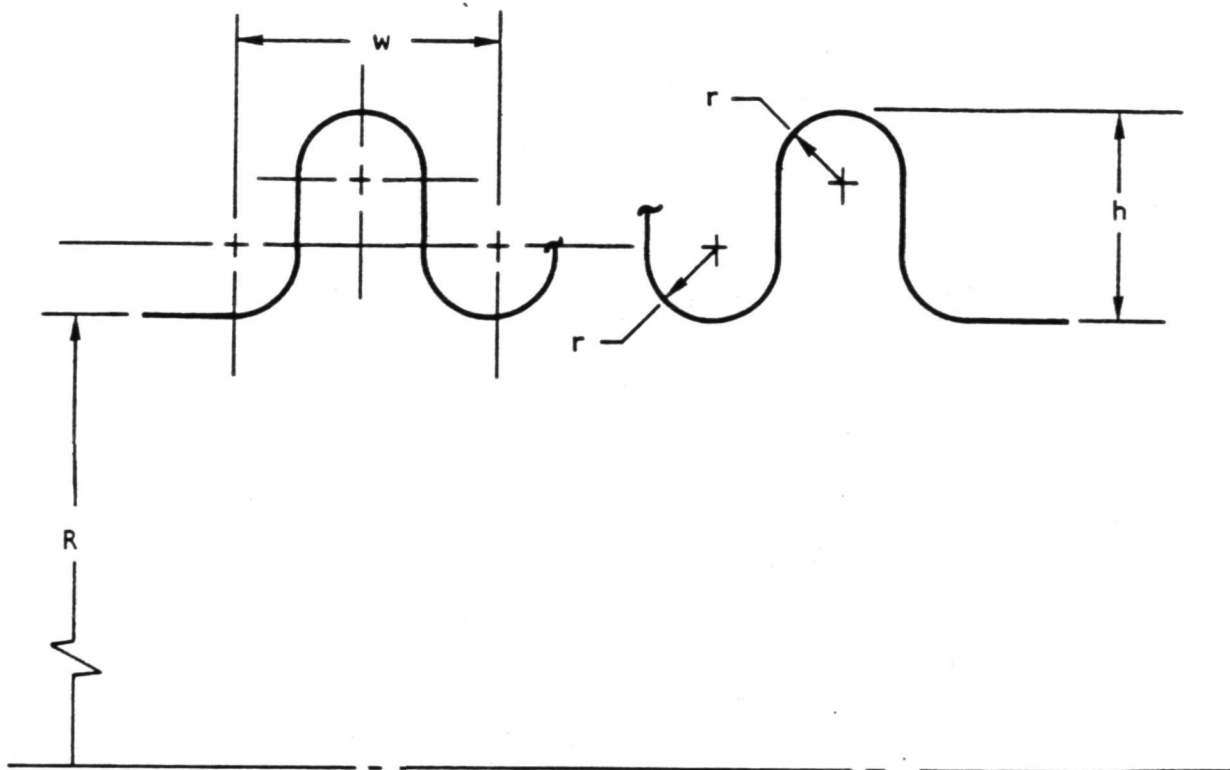
b. INTERNAL PRESSURE LOADING WITH APPROPRIATE BOUNDARY CONDITIONS



c. AXIAL LOADING WITH APPROPRIATE BOUNDARY CONDITION

S-87142-A

Figure 5-2.--Shell Analysis Model for Convolution Parametric Studies.



<b>a. 5.4 BASELINE BELLOWS CONVOLUTION SHAPE</b> INSIDE RADIUS, R, IN. (CM) 4.00 (10.15) HEIGHT, h, IN. (CM) 0.50 (1.27) PITCH, w, IN. (CM) 0.70 (1.78) BEND RADIUS, r, IN. (CM) 0.175 (0.445)	<b>b. 5.5 BASELINE BELLOWS CONVOLUTION SHAPE</b> INSIDE RADIUS, R, IN. (CM) 4.00 (10.15) HEIGHT, h, IN. (CM) 0.50 (1.27) PITCH, w, IN. (CM) 0.60 (1.52) BEND RADIUS, r, IN. (CM) 0.15 (0.381)	<b>c. 5.6 BASELINE BELLOWS CONVOLUTION SHAPE</b> INSIDE RADIUS, R, IN. (CM) 4.00 (10.15) HEIGHT, h, IN. (CM) 0.50 (1.27) PITCH, w, IN. (CM) 0.50 (1.27) BEND RADIUS, r, IN. (CM) 0.125 (0.318)
<b>d. 6.5 BASELINE BELLOWS CONVOLUTION SHAPE</b> INSIDE RADIUS, R, IN. (CM) 4.00 (10.15) HEIGHT, h, IN. (CM) 0.75 (1.905) PITCH, w, IN. (CM) 0.90 (2.286) BEND RADIUS, r, IN. (CM) 0.225 (0.572)	<b>e. 6.6 BASELINE BELLOWS CONVOLUTION SHAPE</b> INSIDE RADIUS, R, IN. (CM) 4.00 (10.15) HEIGHT, h, IN. (CM) 0.75 (1.905) PITCH, w, IN. (CM) 0.75 (1.905) BEND RADIUS, r, IN. (CM) 0.1875 (0.476)	<b>f. 6.7 BASELINE BELLOWS CONVOLUTION SHAPE</b> INSIDE RADIUS, R, IN. (CM) 4.00 (10.15) HEIGHT, h, IN. (CM) 0.75 (1.905) PITCH, w, IN. (CM) 0.60 (1.524) BEND RADIUS, r, IN. (CM) 0.150 (0.381)
<b>g. 7.6 BASELINE BELLOWS CONVOLUTION SHAPE</b> INSIDE RADIUS, R, IN. (CM) 4.00 (10.15) HEIGHT, h, IN. (CM) 1.0 (2.54) PITCH, w, IN. (CM) 1.0 (2.54) BEND RADIUS, r, IN. (CM) 0.250 (0.635)	<b>h. 7.7 BASELINE BELLOWS CONVOLUTION SHAPE</b> INSIDE RADIUS, R, IN. (CM) 4.00 (10.15) HEIGHT, h, IN. (CM) 1.0 (2.54) PITCH, w, IN. (CM) 0.80 (2.03) BEND RADIUS, r, IN. (CM) 0.200 (0.508)	<b>i. 7.8 BASELINE BELLOWS CONVOLUTION SHAPE</b> INSIDE RADIUS, R, IN. (CM) 4.00 (10.15) HEIGHT, h, IN. (CM) 1.0 (2.54) PITCH, w, IN. (CM) 0.60 (1.524) BEND RADIUS, r, IN. (CM) 0.175 (0.445)

S-87147

Figure 5-3.--Dimensional Description of Convolution Shapes Investigated.

NOTE: THICKNESS/PLY AND NUMBER OF PLIES VARIES TO SATISFY PRESSURE CONTAINMENT

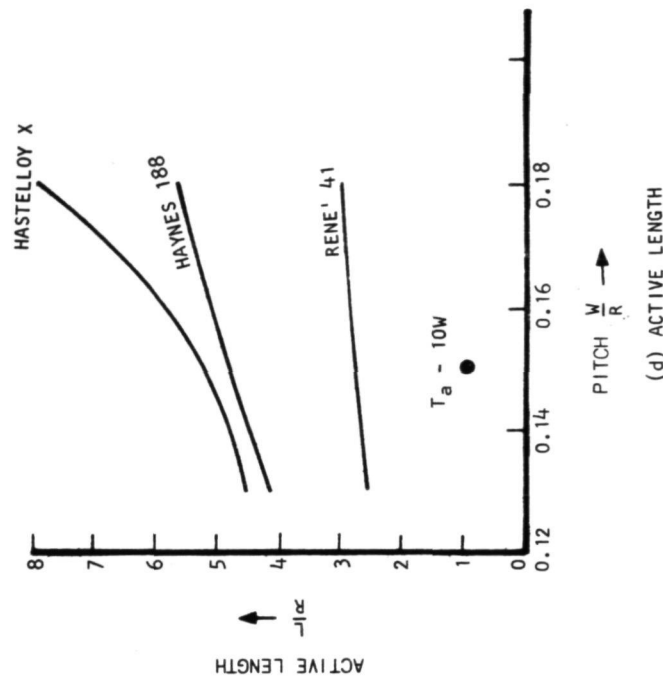
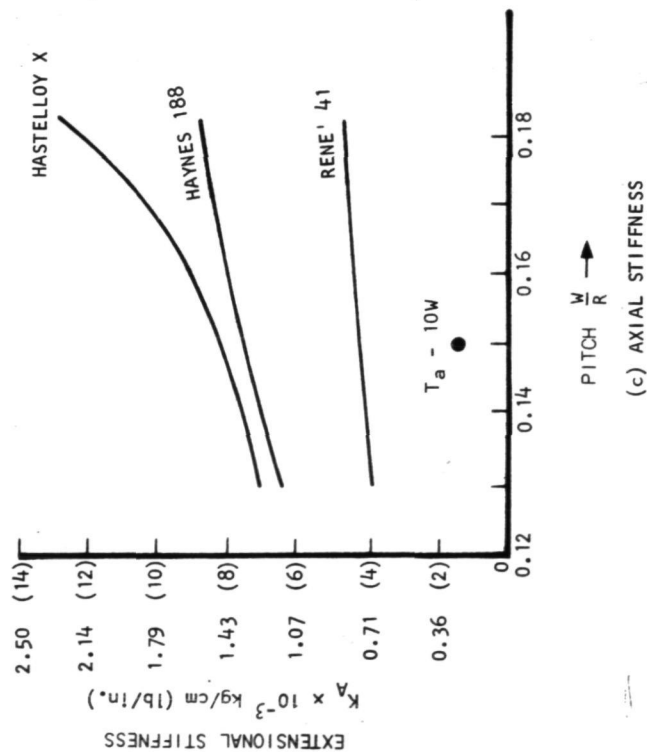
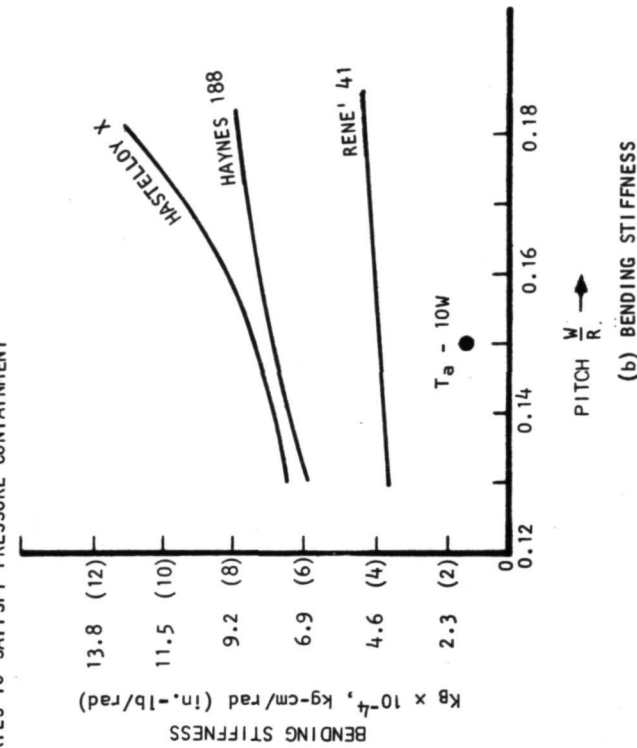
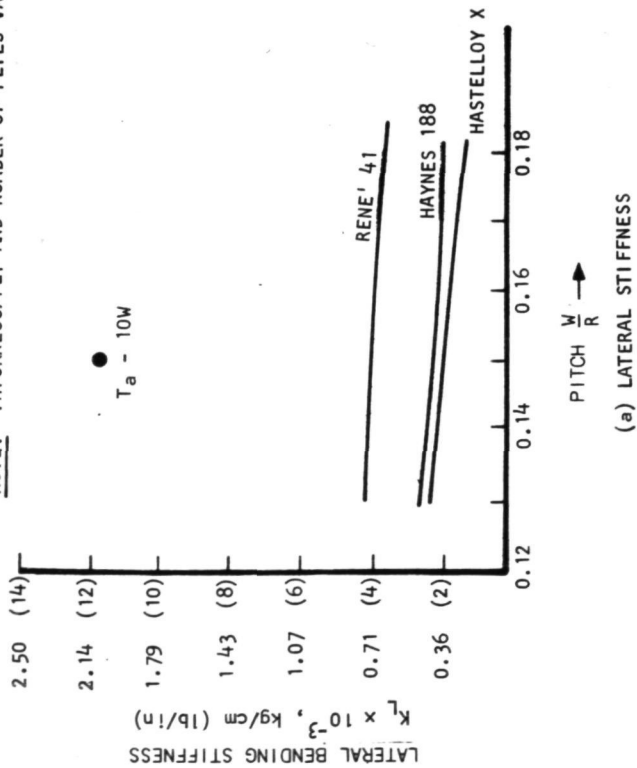


Figure 5-4.--Bellows Design Parameters as a Function of Pitch  
( $h/r = 1/8$ ).

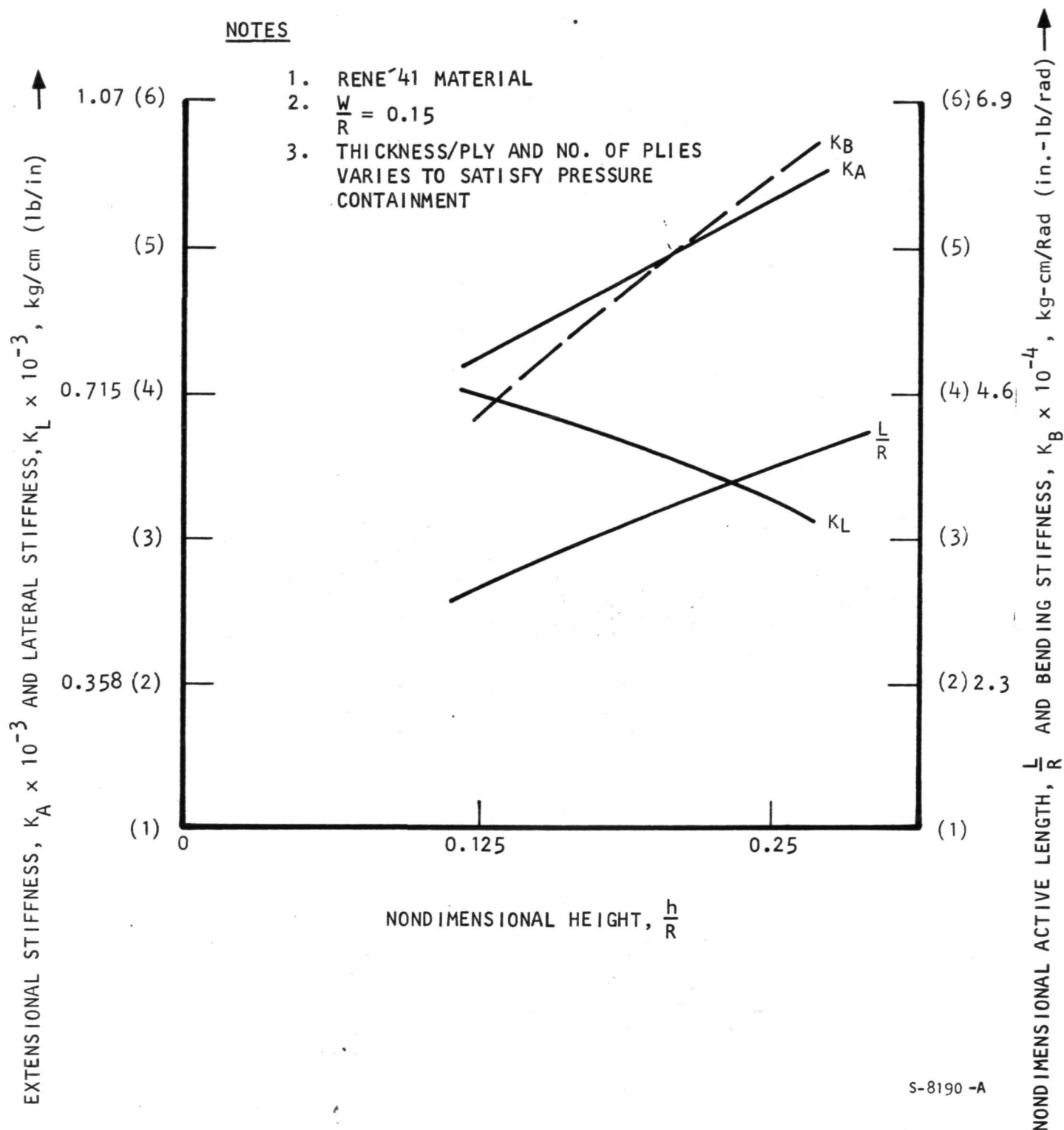


Figure 5-5. Active Length and Stiffness vs. Height.

2. For a given material and a given convolute pitch, the active length, the extensional and bending stiffnesses increase monotonically with the increase in convolute height. Again, the lateral stiffness has the reverse trend.
3. For a given convolute shape, the values of active length, extensional and bending stiffnesses are in a monotonic increasing order corresponding to materials Ta-10W, Rene 41, Haynes 188, and Hastelloy X, respectively. The variation trend is reversed for the case of lateral stiffness.

Hence, for a given set of design parameters, one can optimize the bellows convolution shape for each candidate material. For purpose of optimization, the following factors should be taken into consideration:

- (a) Creep and cyclic life requirements
- (b) Required axial, lateral, and angular movements
- (c) Allowable flange forces and moments
- (d) Axial, lateral, and bending stiffnesses
- (e) Number of plies
- (f) Thickness per ply
- (g) Active length
- (h) Equivalent axial deflection which governs the cyclic life
- (i) Squirr pressure

Lateral stiffness and squirm pressure are important considerations when choosing an optimum bellows shape.

Analyses can be limited to one-half the bellows convolute using a shell of revolution program. This type of small mathematical models saves a considerable amount of computer time and gives all the necessary design parameters described in Appendix D.

Consideration of practical fabrication limits place the following bounds on convolute shape factors:

$$0.04 \leq \frac{h}{R} \leq 0.25$$

The upper limit is based on the maximum elongation of the material (25 percent); below the lower limit, the bellows is too stiff.

$$0.50 \leq \frac{w}{h} \leq 2.0$$

Above  $W/h = 2.0$  the convolute is no longer U-shaped. The lower limit depends on the thickness per ply to meet the  $r_{\min}/t$  criteria.

$$6 \leq \frac{h}{t} \leq 100$$

The upper limit of 100 is arbitrary; the lower limit of 6 is due to fabrication.

$$\frac{r_{\min}}{t} \geq 3; r_{\min} = r - \frac{nt}{2}; r = \frac{w}{4}$$

The lower value is a fabrication limit.

For realistic flange loading a refractory material like Ta-10W or columbium should be used to sustain the combined pressure and temperature loading. Use of refractory materials produced bellows with significantly lower active length and axial stiffness as compared to bellows made from superalloys.

#### REFERENCES

- 5-1. Moon, D.P.; Simon, R.C.; and Favor, R.J.: The Elevated-Temperature Properties of Selected Superalloys, Battelle Memorial Institute, ASTM Data Series DS7-S1, July 1968.
- 5-2. Herchenroeder, R.B.; Mathews, S.J.; Tackett, J.W.; and Wlodek, S.T.: Haynes Alloy No. 188, Cobalt, March 1972.
- 5-3. Richard, C.E.; Duncan, J.D.; Demongenes, C.; and Flieder, W.C.: Low-Cycle Fatigue Evaluation for Regeneratively Cooled Panels; NASA CR-1884, October 1971.
- 5-4. Anon: Metallic Materials and Elements for Aerospace Vehicle Structures, MIL-HDBK-5A, January 1970 (Change Notice).
- 5-5. AiResearch Test Data, 1972.
- 5-6. Sheffler, K.D.: Generation of Long-Time Creep Data on Refractory Alloys at Elevated Temperatures, Final Report, Contract NAS3-13469, NAS CR-72997, TRW ER-7541, TRW Materials Technology Laboratories, May 20, 1971.
- 5-7. Anon, Wah Chang Company Catalog, Albany, January 19, 1971.
- 5-8. Manson, S. S.: Fatigue: A Complex Subject--Some Simple Approximations. William M. Murray Lecture, 1964; Experimental Mechanics, Vol. 5, No. 7, July 1965, pp. 193-226.
- 5-9. Monthly Progress Report "Brayton-Cycle Heat Exchanger Technology Program," AiResearch Manufacturing Company of California, Report 71-7637(34), pp. 2-6 to 2-32.

**Page  
Intentionally  
Left Blank**





## SECTION 6

### LOW-COST, HIGH-TEMPERATURE BRAZE ALLOY DEVELOPMENT

The objective of this task was to select a low-cost, ductile braze alloy suitable for use in Brayton-cycle, plate-fin recuperators operating at 1000°K (1350°F) for up to 10 years. The Brayton-cycle working fluid used in a space power system is typically an inert gas such as a mixture of xenon and helium gases. However, since terrestrial applications and testing could utilize air as the working fluid, oxidation resistance was considered to be a requirement for braze alloy suitability.

Previous recuperator applications utilized Palniro 1, a gold-base braze alloy, because of its excellent flow characteristics, minimum penetration and alloying with the parent metal, high strength, and high ductility. Palniro 1 is an excellent braze alloy in all respects except for its high cost, which is prohibitive for terrestrial applications. The goal of this program was to find an alloy of reasonable cost that could meet or exceed the performance of Palniro 1. The primary factors considered in this evaluation were ductility, erosiveness, oxidation resistance, weldability, creep strength, and low-cycle fatigue resistance. The evaluation was confined to existing alloys.

Special attention was given to ductility. Braze joint cracking, which was observed during tests of Brayton-cycle recuperators, was believed to be a low-cycle fatigue failure caused in part by the low ductility of the Nicrobraz 130 (AMS 4778) braze alloy. This alloy is widely used on steel heat exchangers at AiResearch and has proven to be satisfactory in most applications. It was believed, however, that its use at temperatures above 920°K (1200°F) in a plate-fin heat exchanger was beyond the material capability. Palniro 1 was specified for all succeeding applications because of its high ductility and strength at 1000°K (1350°F).

### CANDIDATE MATERIALS

The task of identifying a low-cost brazing alloy suitable for long-term, high-temperature applications in an oxidizing environment was initiated with an extensive literature search and compilation of vendor experience with available brazing alloys.

Historically, the alloys selected for this type of application have been noble metal based. Gold-based alloys such as Nicro 82 (82 Au-18 Ni) have excellent properties in the 756° to 1090°K (900° to 1500°F) temperature range. Additions of palladium and nickel (Palniro 7 with 70 Au-8 Pd-22 Ni, and Palniro 1 with 50 Au-25 Pd-25 Ni) increase the elevated temperature strength of the gold-based alloys. The alloys of gold and combinations of gold with palladium are quite expensive, even when used in quantities required for brazing plate-fin heat exchangers. Silver-based alloys, which would be significantly less costly, also require palladium for high-temperature strength and generally do not have the oxidation resistance associated with the gold-based braze alloys.

Alternates to noble metal brazing alloys are the brazing alloys containing manganese, copper, and nickel. Again, with the exception of a few of the nickel alloys, the alloys containing primarily manganese and copper generally suffer from poor oxidation resistance and/or loss of strength at the 1000°K (1350°F) operating temperature. The problem associated with using nickel-based brazing alloys is that the melting point depressants used are either boron, silicon, or phosphorous (or a combination of these materials), all of which lead to varying amounts of alloying and/or penetration of the parent metal. Even where these degrading effects are minimized, the braze alloy joints are relatively brittle when compared to joints formed with the noble metals. Finally, there are the cobalt-based alloys and nickel alloys containing chromium. These brazing alloys generally have brazing temperatures too high for the base metal (Hastelloy X or stainless steel) as evidenced by excessive grain growth in the parent metal during brazing.

The selection of a low-cost, 1350°F (1000°K) operating temperature, ductile braze alloy was influenced by a number of metallurgical considerations that required careful evaluation. Therefore, a variety of tests and analyses were conducted to identify the best candidate alloys. Alloys considered included the best of the nickel-based alloys along with the best of the higher-brazing-temperature alloys mentioned above.

Candidate brazing alloys were compared to the Palniro 1 (AMS 4784) and Nicrobraz 130 (AMS 4778) brazing alloys, which were used as reference materials. An initial evaluation was made of all candidate braze alloys on the basis of tee-section brazing tests. Further evaluation was based on accelerated oxidation testing at 1000° to 1090°K (1350 to 1500°F), of plate-fin sections and additional structural tests (hardness, bend, creep-rupture, and tensile tests) on brazed specimens. Welding tests also were conducted to establish braze joint performance under conditions simulating heat exchanger pan attachment.

The alloys considered are shown in table 6-1. These alloys were selected on the basis of experience, a search of available literature, and recommendations from braze filler metal suppliers. In addition, the diffusion sink technique was investigated for the boron-containing alloys. In this approach, base metal powder was mixed with the powdered braze alloy. The base metal powder acted as a sink for the boron to help reduce penetration into fins and tube sheets and thus to minimize parent metal embrittlement. Another brazing alloy dilution approach also was investigated. In this second approach, a lower-melting-temperature alloy was added to brazing alloys that braze above 1450°K (2150°F).

The oxidation resistance of the braze alloys shown in table 6-1 was initially estimated from an accumulation of data from several sources. Unfortunately, the data were obtained under a variety of conditions, making the comparison semiquantitative at best. A study by AiResearch Phoenix, evaluating the behavior of a number of these alloys at 1310°K (1900°F) in a gas turbine atmosphere, indicated that at least 10 percent chromium was needed in the alloy. Tested alloys with this amount of chromium included Nicrobraz 125,

TABLE 6-1

## CANDIDATE BRAZING ALLOYS

Brazing Filler Metal	Nominal Chemical Composition of Brazing Filler Metals												Brazing Temperature		Characteristics and Remarks
	Ni	Cu	Co	Cr	Si	Mn	B	C	Fe	Al	P	Others	°K	°F	
Palniro 1	25	---	---	---	---	---	---	---	---	---	---	50 Au, 25 Pd	1405	2070	Reference material AMS4784
Microbraz 130	Balance	---	---	---	4.5	---	3.0	0.06 (max.)	---	---	---	---	1344	1960	Reference material AMS4778
Microbraz 50	Balance	---	---	13.0	---	---	---	---	---	---	10	---	1340	1950	Variations on Microbraz 50 recommended by the manufacturer
Microbraz 5040	Balance	---	---	5	2.1	---	1.2	---	0.6	---	4	---	1283-1422	1850-2100	
Microbraz 5060	Balance	---	---	8	1.4	---	0.8	---	0.4	---	6	---	1283-1394	1850-2050	
Microbraz 5075	Balance	---	---	10	0.9	---	0.5	---	0.25	---	7.5	---	1256-1367	1800-2000	
Microbraz 150	Balance	---	---	15	---	---	3.5	---	---	---	---	---	1339-1478	1950-2200	High chromium
Microbraz 200	Balance	---	---	7	4.5	---	3.2	---	---	---	---	6 W, 3 Fe	1380	2025	Similar to AMI 400
Microbraz 210	17.0	---	Balance	19	8	---	0.8	---	---	---	---	0.4 C 4W	1458	2150	
Microbraz 220	Balance	---	---	4	---	45	0.8	---	---	---	---	---	1344	1960	
Microbraz 230	Balance	---	---	3.5	2.5	35	0.9	---	1.0	---	---	---	1367-1450	2000-2150	
Microbraz 30 (J-8100)	Balance	---	---	19	10.2	1	---	---	4	---	---	---	1422-1478	2100-2200	Ductile, Low Penetration, service to 1090°K (1500°F), high strength, but high braze temperature
Microbraz LC	Balance	---	---	15	4.5	---	3	0.1 (max.)	3	---	---	---	1450	2150	
AMI 100B	Balance	---	---	30.5	10.2	---	---	---	---	---	---	---	1408	2075	High chromium
AMI 300	Balance	---	---	19.5	9.5	9.5	---	---	---	---	---	---	1381-1436	2025-2125	
AMI 400 (NB 210)	16.4	---	Balance	19.0	8.6	---	0.9	0.4	---	---	---	4.1 W	1450-1478	2150-2200	High elevated temperature strength, low penetration
AMI 792	Balance	---	20	---	3.6	---	1.5	---	---	1.4	---	1.8 La	1450-1478	2150-2200	New experimental filler metals designed for good strength and oxidation resistance. High braze temperature
AMI 793	Balance	---	20	---	4.6	---	0.8	---	---	1.3	---	1.8 La 3.8 Zr	1450-1478	2150-2200	
AMI 794	Balance	---	20	---	4.6	---	0.8	---	---	1.0	---	3.0 Ta 29 W 1.5 La 3.1 Mo	1450-1478	2150-2200	
AMI 791	21	---	Balance	21.8	2.3	---	2.5	---	---	---	---	0.8 La 14.1 W	1450-1478	2150-2200	
AMI 934	9.7	Balance	---	---	---	37.0	---	---	---	---	---	0.15 La 7.0 Pd	1244	1780	Low Pd, Cu Base, La for oxidation resistance
J-8600	Balance	---	---	33	4	---	---	---	---	---	---	25 Pd	1256-1450	1800-2150	High Cr and Pd
BS-1	Balance	---	---	---	1.8	---	1.0	---	---	---	---	41 Au	1283	1850	50% Niore, 50% Microbraz 135 (AMS4779)

ORIGINAL PAGE IS  
OF POOR QUALITY

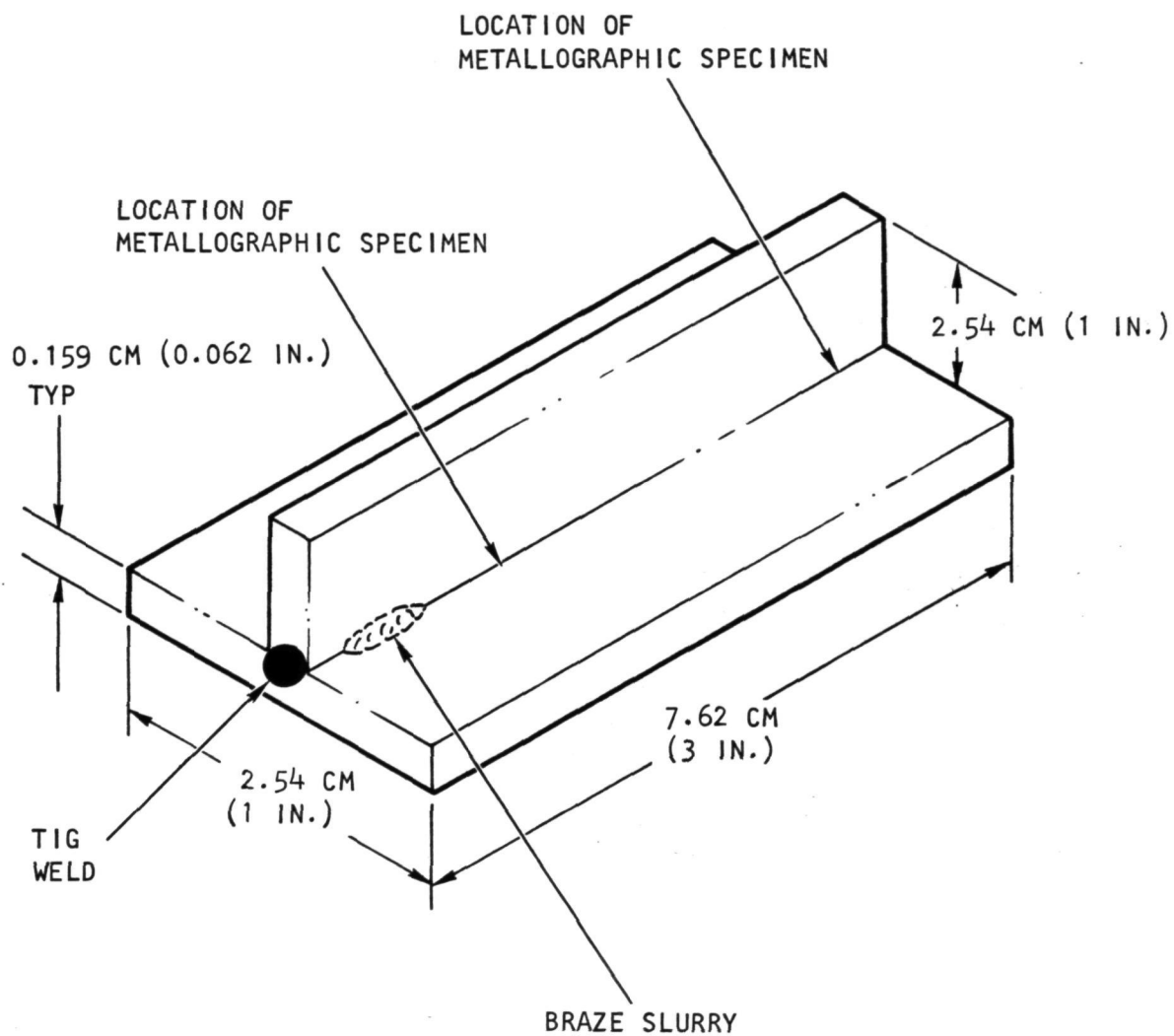
Nicrobraz 20, Nicrobraz 150, Nicrobraz 160, and Coast Metals 60. (A number of these alloys showed considerable penetration, however, and were not acceptable.) Other tests, run by AiResearch, Los Angeles, at 1090°K (1500°F) in air containing sodium sulfate, and by Boeing Aircraft Company at 1030°K (1400°F) in combustion productions, have indicated that a lower chromium content may be acceptable in braze alloys containing an appreciable quantity of silicon. Similarly, the incorporation of rare earth elements such as lanthanum and/or the addition of aluminum or palladium, as found in the Alloy Metals, Incorporated (AMI) alloys, could presumably confer adequate oxidation resistance.

#### PRELIMINARY INVESTIGATION

Tee-sections were fabricated to evaluate the brazing characteristics (i.e., flow, filleting, penetration, erosion, and brazing temperature) of the selected brazing alloys listed in table 6-1. As shown in fig. 6-1, the tee-sections were fabricated from 2.54- by 7.62-cm strips of Hastelloy X (0.159-cm thick) that were TIG tack-welded at both ends. In most instances, Type 347 stainless steel samples were included for comparison. A small amount of the candidate braze alloy was placed on one side of one end of the tee-section, which was then brazed with a 10-min hold at the brazing temperature. The 10-min hold was selected to simulate the brazing cycle of a plate-fin heat exchanger. The test specimens were sectioned and metallographically examined. Metallographic samples were taken adjacent to the area where the braze was applied (the braze reservoir) and at the opposite end of the tee-section. These two locations represent conditions of maximum and minimum metal flow, respectively, and give a measure of the erosiveness of the molten braze alloy. For a plate-fin application, metal flow would be fairly minimal, so that the end section away from the braze reservoir would be more representative of conditions to be expected in a plate-fin assembly.

The results of the work with the tee-sections (vacuum-brazed except as noted) are given in table 6-2, where the effect of each brazing alloy on both Hastelloy X and Type 347 stainless steel material is tabulated. The alloying (erosion) of the brazing alloy and the total penetration (alloying and maximum grain boundary diffusion effects) of the brazing alloy into the parent metal are included. Photomicrographs of the brazed tee-sections are shown in refs. 6-1 and 6-2.

Based on the brazing characteristics given in table 6-2 and on a maximum 1460°K (2165°F) brazing temperature (to minimize grain growth), seven braze alloys were initially selected for additional examination in a plate-fin configuration. The general criterion for selection of a braze alloy was 0.005-cm (2-mil) or less total penetration. In some instances a particular alloy was included because it looked particularly good on one base metal even though it exceeded 0.005-cm (2-mil) penetration on the other base metal. (Nicrobraz 50 is an example of this). The selected alloys are shown in table 6-3, along with the Palniro 1 (AMS 4784) and Nicrobraz 130 (AMS 4778) reference materials. The seven alloys selected for plate-fin panel tests all contained chromium, which probably is essential for oxidation resistance at 1000°K (1350°F). The chromium levels vary from 5 percent in Nicrobraz 5040 to 19 percent in Nicrobraz 30



S-69963-A

Figure 6-1.--Tee-Section for Braze Alloy Screening

TABLE 6-2

## RESULTS OF TEE SECTION SCREENING OF CANDIDATE BRAZE ALLOYS

Brazing Alloy	Brazing Temperature		Flow	Filletting	Alloying		Total Penetration		Remarks
	°K	°F			cm	in.	cm	in.	
HASTELLOY X - Parent Metal									
Palnino 1 0.0025 cm (0.001 in.) thick	1405	2070	G	G	0.003	0.0012	0.003	0.0012	AMS4784
Microbraz 130	1344	1960	G	G	0.0025	0.001	0.010	0.004	AMS4778 0.06°C max.
BS-1	1283	1960	G	G	0.0013	0.0005	0.005-0.0064	0.002-0.025	50' Nioro-50 Microbraz 135 (AMS4779)
Microbraz 50	1297	1875	G	G	0.0056	0.0022	0.0076	0.003	
Microbraz 50	1339	1950	G	G	0.0076	0.003	0.0076	0.003	
Microbraz 50	1255	1800	G	G	0.0041	0.0016	0.0066	0.0026	
Microbraz 5040	1339	1950	G	G	0.0076	0.003	0.013	0.005	
Microbraz 5040	1283	1850	G	G	0.0025	0.001	0.005	0.002	
Microbraz 5060	1297	1875	G	G	0.005	0.002	0.010	0.004	Some porosity
Microbraz 5075	1297	1875	G	G	0.0076	0.003	0.010	0.004	
Microbraz 5075	1255	1000	G	G	0.0025	0.001	0.005	0.002	
Microbraz 150	1450	2150	G	G	0.0064	0.025	0.013	0.005	Filletts irregular
Microbraz 150	1344	1960	G	G	0.0003	0.0012	0.0076	0.003	
Microbraz 200	1380	2025	G	G	nil	nil	0.0076-0.010	0.003-0.004	Irregular and minimal filletts (Run in hydrogen)
Microbraz 220	1344	1960	G	F	0.003	0.0012	0.003	0.0012	Run in hydrogen
Microbraz 230	1344	1960	G	G	0.0036	0.0014	0.0036	0.0014	
Microbraz 30 (J-8100)	1450	2150	G	G	0.005	0.002	0.005	0.002	
Microbraz 30	1422	2100	G	G	0.002	0.008	0.0043	0.0017	
Microbraz LC	1394	2050	G	G	0.0046	0.0018	0.0064	0.0025	
AMI 400	1450	2150	F	P	0.0013	0.0005	0.0025	0.001	Did not fill gap
AMI 400	1478	2200	G	F	0.0056	0.0022	0.0056	0.0022	
AMI 400	1458	2165	G	F-G	0.0013	0.0005	0.0013	0.0005	Porous fillet. Large grain size
Microbraz 210	1458	2156	G	F-G	0.0036	0.0014	0.005	0.002	Large grain size
AMI 792	1478	2200	F	P	0.0025	<0.001	0.0076	0.003	Large grains
AMI 793	1478	2200	F	F	0.0056	0.0022	0.0032	0.0081	Large grains
AMI 794	1478	2200	P	P	Did not flow				

G = Good  
F = Fair  
P = Poor

1 Vacuum Brazed unless otherwise noted.  
2 Total penetration includes alloying and maximum grain boundary diffusion effects.  
3 Measurements recorded at minimum flow area (end opposite braze application area), except as noted.

ORIGINAL PAGE IS  
OF POOR QUALITY

TABLE 6-2. (Continued)

Braze Alloy <sup>1</sup>	Brazing Temperature		Flow	Filletting	Alloying		Total Penetration		Remarks
	°K	°F			cm	in.	cm	in.	
AMI 791	1436	2125	P	P	Did not melt				Heavy skull
AMI 791	1450	2150	P	P	Not eval.				Run in hydrogen, (O <sub>2</sub> contaminated)
AMI 934	1255	1800	F	G	0.0033	0.0013	0.0048	0.0015	Small fillet
J-8600	1450	2150	G	P-F	0.0046	0.0018	0.0046	0.0018	Sample near braze reservoir
J-8600	1366	2000	P	P	0.0038	0.0015	0.0038	0.0015	
J-8600	1394	2050	F	P	0.0025	0.001	0.0025	0.001	
J-8600	1422	2100	G	F	0.0025	0.001	0.0025	0.001	
J-8600	1458	2165	G	F	0.0041	0.0016	0.0041	0.0016	
AMI-1008	1408	2075	G	G	0.002	0.0008	0.002	0.0008	Large grains near braze alloy
<u>347 STAINLESS STEEL - Parent Metal</u>									
Palnir 1	1405	2070	G	G	0.003	0.0012	0.003	0.0012	Near braze reservoir
Nicrobraz 30	1344	1960	G	G	0.002	0.0008	0.0036	0.0014	AMS4784 0.0025 cm (0.001 in.) thick
BS-1	1283	1850	G	G	0.0013	0.0005	0.005	0.002	Overwet (liquefaction)
Nicrobraz 50	1297	1875	G	G	0.005	0.002	0.005	0.002	50% Niore-50% Nicrobraz 135 (AMS4779)
Nicrobraz 50	1339	1950	G	G	0.0041	0.0016	0.0041	0.0016	
Nicrobraz 50	1255	1800	G	G	0.0041	0.0016	0.0041	0.0016	Some skull and porosity
Nicrobraz 5040	1339	1950	G	G	0.005	0.002	0.0076	0.003	
Nicrobraz 5040	1283	1850	G	G	0.0041	0.0016	0.0038	0.0015	
Nicrobraz 5060	1297	1875	G	G	0.0056	0.0022	0.0056	0.0022	
Nicrobraz 5075	1297	1875	G	G	0.0064	0.0025	0.0064	0.0025	
Nicrobraz 5075	1255	1800	G	G	0.0041	0.0016	0.0041	0.0016	
AMI 400	1478	2200	G	G	0.0076	0.003	0.0076	0.003	Some grain growth
AMI 400	1458	2165	G	G	0.0013	0.0005	0.0013	0.0005	
Nicrobraz 210	1458	2165	G	G	0.0041	0.0016	0.0041	0.0016	
AMI 791	1478	2200	G	F-G	nil	nil	0.0013	<0.0005	Some grain growth
AMI 791	1450	2150		Deleted					
AMI 794	1478	2200	F	F	nil	nil	0.0025	0.001	Heavy skull, porous fillet
Nicrobraz 150	1347	1965	G	G	nil	nil	0.0025	0.001	Run in hydrogen

G = Good  
F = Fair  
P = Poor

- 1 Vacuum brazed unless otherwise noted.
- 2 Total penetration includes alloying and maximum grain boundary diffusion effects.
- 3 Measurements recorded at minimum flow area (end opposite braze application area), except as noted

ORIGINAL PAGE IS  
OF POOR QUALITY



TABLE 6-2. (Concluded)

Brazing Alloy	Brazing Temperature		Flow	Filletting	Alloying		Total Penetration		Remarks
	°K	°F			cm	in.	cm	in.	
Nicrobraz 150	1344	1960	G	G	nil	nil	0.0038	0.0015	Run in hydrogen
Nicrobraz 220	1347	1965	G	G	nil	nil	nil	nil	Repeat run - irregular and minimal filletting (Run in hydrogen)
Nicrobraz 220	1344	1960	G	F	nil	nil	nil	nil	Run in hydrogen
Nicrobraz 230	1344	1960	G	G	0.0013	0.0005	0.0046	0.0018	Overwet (liquation)
Nicrobraz 30	1422	2100	G	P	0.002	0.0008	0.0046	0.0008	Cracked
AMI 300	1436	2125	F	P-F	0.0025	0.001	0.0025	0.001	Run in hydrogen (O <sub>2</sub> contaminated)
AMI 934	1255	1800	F	P	nil	nil	nil	nil	Liquation - micro near reservoir
AMI 1008	1408	2075	G	P	nil	nil	nil	nil	

1 Vacuum brazed unless otherwise noted.

2 Total penetration includes alloying and maximum grain boundary diffusion effects.

3 Measurements recorded at minimum flow area (end opposite braze application area), except as noted.

G = Good  
F = Fair  
P = Poor



and Nicrobraz 210 (AMI 400) and 33 percent in J-8600. (It should be noted that J-8600, with 25 percent Palladium, was considered only a backup braze alloy because it cost significantly more than the other alloys.)

TABLE 6-3  
BRAZE ALLOYS SELECTED FOR ADDITIONAL EXAMINATION  
IN A PLATE-FIN CONFIGURATION

Braze Alloy	Braze Temperature		Hold Time at Temp, min.	Braze Atmosphere
	°K	°F		
AMS 4784 (Palniro 1, 0.0025-cm thick foil)	1405	2070	10	Vacuum
AMS 4778	1344	1960	10	Vacuum
NB 30	1422	2100	10	Vacuum
AMI 400 (NB 210)	1458	2165	10	Vacuum
NB 150	1344	1960	10	Vacuum
NB 5075	1255	1800	10	Vacuum
NB 5040	1283	1850	10	Vacuum
NB 50	1255	1800	10	Vacuum
J 8600	1458	2165	10	Vacuum

The plate-fin samples were fabricated and sectioned for metallographic examination. In all cases, the fins and one side plate were Hastelloy X material and the other side plate was Type 347 stainless steel material. Photomicrographs are shown in figs. E-1 through E-12 of Appendix E for both Hastelloy X and Type 347 stainless steel side plates. Included are the selected alloys of Table 6-3 brazed in vacuum and three additional alloys (Nicrobraz 220, Nicrobraz 230, and AMI 934) brazed in hydrogen. The results generally confirm data taken from the tee-sections, with most braze alloys showing relatively low amounts of

alloying and minimal penetration. One exception to this was AMI 400, for which poor filleting was observed on Hastelloy X and complete alloying occurred with the fin (Figs. E-4(a) and (b) of Appendix E). Considerable dissolution of the fins also occurred at the Hastelloy X side plate with the J-8600 braze alloy because of a heavy braze powder buildup within the fin (fig. E-9 of Appendix E). Grain growth does not appear to be a problem except in Hastelloy X when brazed with AMI 400 or J-8600 at 1458°K.

AMI 100B, a modification of Microbraz 30 (J-8100), also was examined. Data from tee-sections are given in Table 6-2. Visual examination showed similar liquation problems as experienced with the Microbraz 30 when used with Type 347 stainless steel. On Hastelloy X, however, this filler metal formed good fillets and had a very low amount of aggression toward the base metal. Microstructurally the intermetallic phase content appears quite high, suggesting possible brittleness problems. Since the brazing temperature for AMI 100B is only 10°K (25°F) lower than the used for Microbraz 30, it does not appear to offer a significant advantage over Microbraz 30. AMI 100B does show less total penetration than Microbraz 30, and for that reason it was not eliminated entirely, but considered to be a backup alloy to Microbraz 30.

#### BRAZE ALLOY HARDNESS

A limited number of microhardness tests were made on the brazing alloy fillets in the plate-fin specimens, both before and after oxidation testing. Hardness data are tabulated in table 6-4. These data indicate the high intermetallic phase content of the Microbraz alloys as compared to Palniro 1. Microbraz 130 (AMS 4778) does soften after exposure to elevated temperatures, but it takes a long time, as softening was not observed after 119 hr at 1000°K (1350°F). Softening was probably due to the outward diffusion of silicon into the surface scale, which certainly is not a desirable feature from the standpoint of oxidation resistance. The variations in hardness of Microbraz 5040 shown after 1000 hr of testing at 1089°K (1500°F) are a function of location of the hardness indentation in the brazing alloy. Although the Microbraz alloys do form considerable amounts of intermetallic phases on solidification, the intermetallic phase generally is surrounded by a fairly ductile phase. The reading of DPH 188, for example, was taken on the brazing alloy where the gap was the smallest and no intermetallic phase was observed. This indicates that joint ductility can be controlled somewhat when using these alloys through careful control of both the amount of filler metal used and the gap to be filled. Further, the introduction of base metal powder to serve as diluent for the brazing alloy can markedly increase ductility. This effect is discussed in a following paragraph. The hardness measurements given in table 6-4 also serve to indicate that the filler metals tested are not undergoing phase changes leading to formation of even more brittle phases as a result of prolonged high-temperature exposure.

TABLE 6-4  
HARDNESS TESTS ON BRAZEMENTS\*

Brazing Alloy	Brazing Temperature,		Material Condition	Diamond Pyramid Hardness (500 grain load)
	°K	°F		
Palniro 1	1405.5	2070	As brazed	272, 216
Palniro 1	1405.5	2070	1000 hr, 1089°K (1500°F)	220
NB 130	1344.4	1960	As brazed	757, 766
NB 130	1344.4	1960	1000 hr, 1089°K (1500°F)	252, 280
NB 130	1344.4	1960	1000 hr, 1000°K (1350°F)	242
NB 130	1344.4	1960	119 hr, 1000°K (1350°F)	784
NB 30	1422.2	2100	As brazed	728, 740
NB 30	1422.2	2100	1000 hr, 1089°K (1500°F)	692
NB 5040	1283.3	1850	As brazed	807, 812, 591
NB 5040**	1283.3	1850	1000 hr, 1089°K (1500°F)	318, 600, 188
NB 5075	1255.6	1800	As brazed	784, 645, 728
NB 5075	1255.6	1800	1000 hr, 1089°K (1500°F)	640

\*See also tables 6-9 and 6-11 for hardness of alloys diluted with Palniro and Hastelloy X powders, respectively.

\*\*Variations in hardness are explained in text.

## OXIDATION TESTING

Oxidation testing was initiated early in the program to determine long-term (3000-hr) results on the candidate brazing alloys. The testing was performed in air atmosphere furnaces at 1005°K (1350°F) and 1089°K (1500°F) using plate-fin test specimens identical to the ones used for the preliminary brazing investigation described above. A typical plate-fin specimen is shown in fig. 6-2 and the configuration is further defined in fig. 6-3. As stated previously, the fins and one side plate were Hastelloy X material and the other side plate was Type 347 stainless steel material.

The braze alloys tested included those listed in table 6-3 plus Microbraz 130, Microbraz 220, Microbraz 230, and AMI 934. The samples exposed at 1005°K (1350°F) gave baseline oxidation rates at normal NASA recuperator design temperatures. The samples exposed at 1089°K (1500°F) gave oxidation rates that were accelerated in an attempt to obtain long-term oxidation data within a reasonable time period. The oxidation rate at 1089°K (1500°F) is nominally 500 times greater than the oxidation rate at 1005°K (1350°F) based on the known effect of temperature on chemical reactions.

Metallographic evaluation of the test samples was made at times of approximately 100, 300, 500, 1000, and 3000 hr, with all samples cooled to room temperature at these times to simulate a mild cyclic condition.

### Results and Discussion

The results of oxidation testing of the plate-fin specimens at 1005°K (1350°F) and 1089°K (1500°F) for times of 119, 311, 502, and 1000 hr are summarized in table 6-5. Measurements made on the depth of oxide penetration into the radius of the filler metal fillet included external scale where present. These data must be treated as semi-quantitative as there is no way to determine if scale was lost in cooling or during preparation.

The first of the oxidation test samples were evaluated after 119 hr of exposure. Very little oxidation occurred on any of the braze alloys except as shown for Microbraz 130 and Microbraz 150 at 1089°K (1500°F). Oxidation was also noted on the Palniro 1 braze joint adjacent to the Type 347 stainless steel, but not on the joints on the Hastelloy X plate. There appeared to be no significant microstructural changes as a result of the exposure to either temperature (i.e., the intergranular penetration neither disappears nor goes deeper into the parent metal during exposure).

After 1000 hours, most brazing alloys showed good oxidation resistance, particularly at 1050°K (1350°F), the exceptions being Microbraz 130, Microbraz 150, and the hydrogen-brazed samples. The 1000-hr, 1005°K (1350°F) oxidation resistances of Microbraz 220, Microbraz 230, and AMI 934 were below acceptable limits and these alloys accordingly were eliminated from the program.

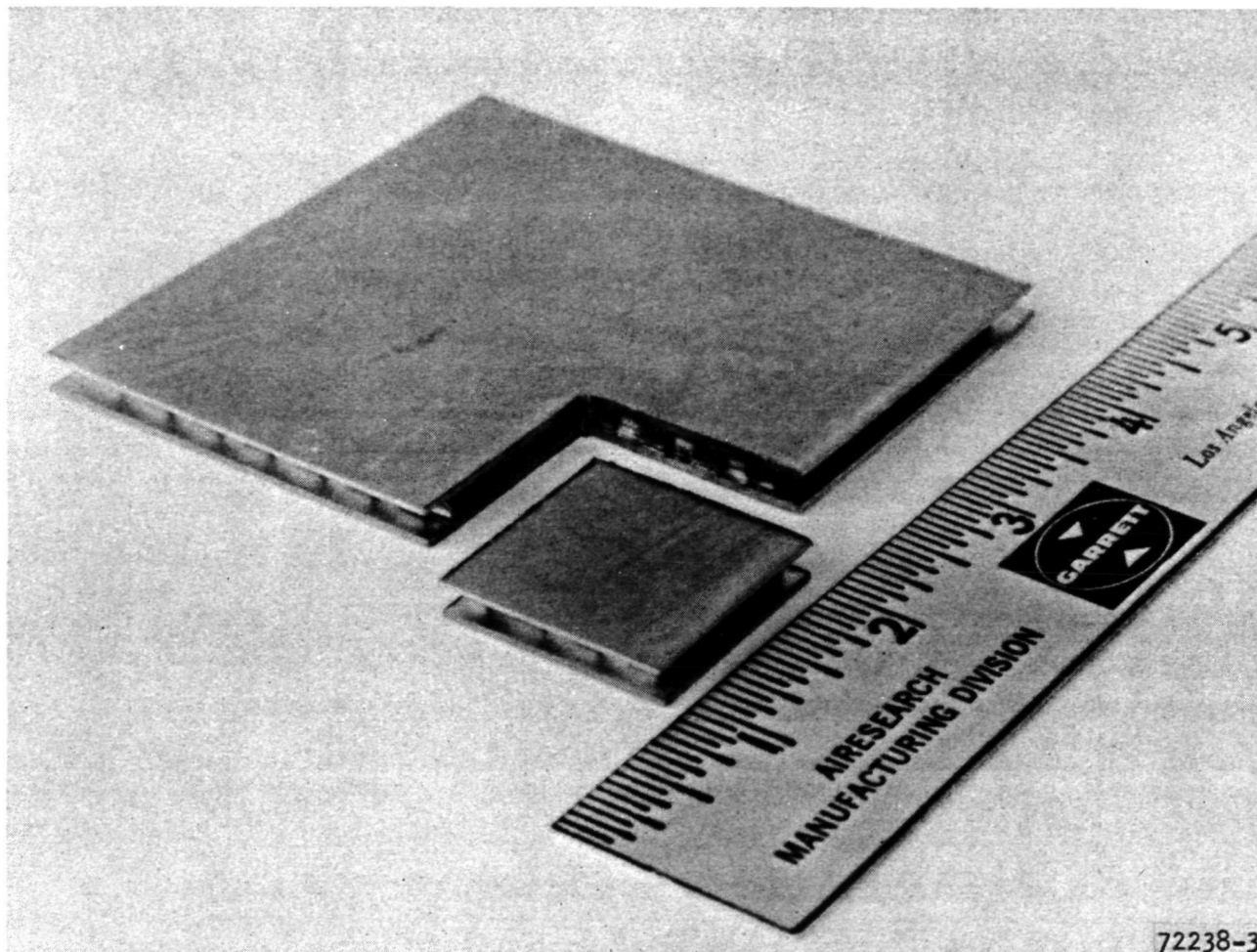


Figure 6-2.--Plate-fin Specimen for Braze Alloy Evaluation and Oxidation Testing (Cut into 2.54 cm (1-in.) squares as shown).

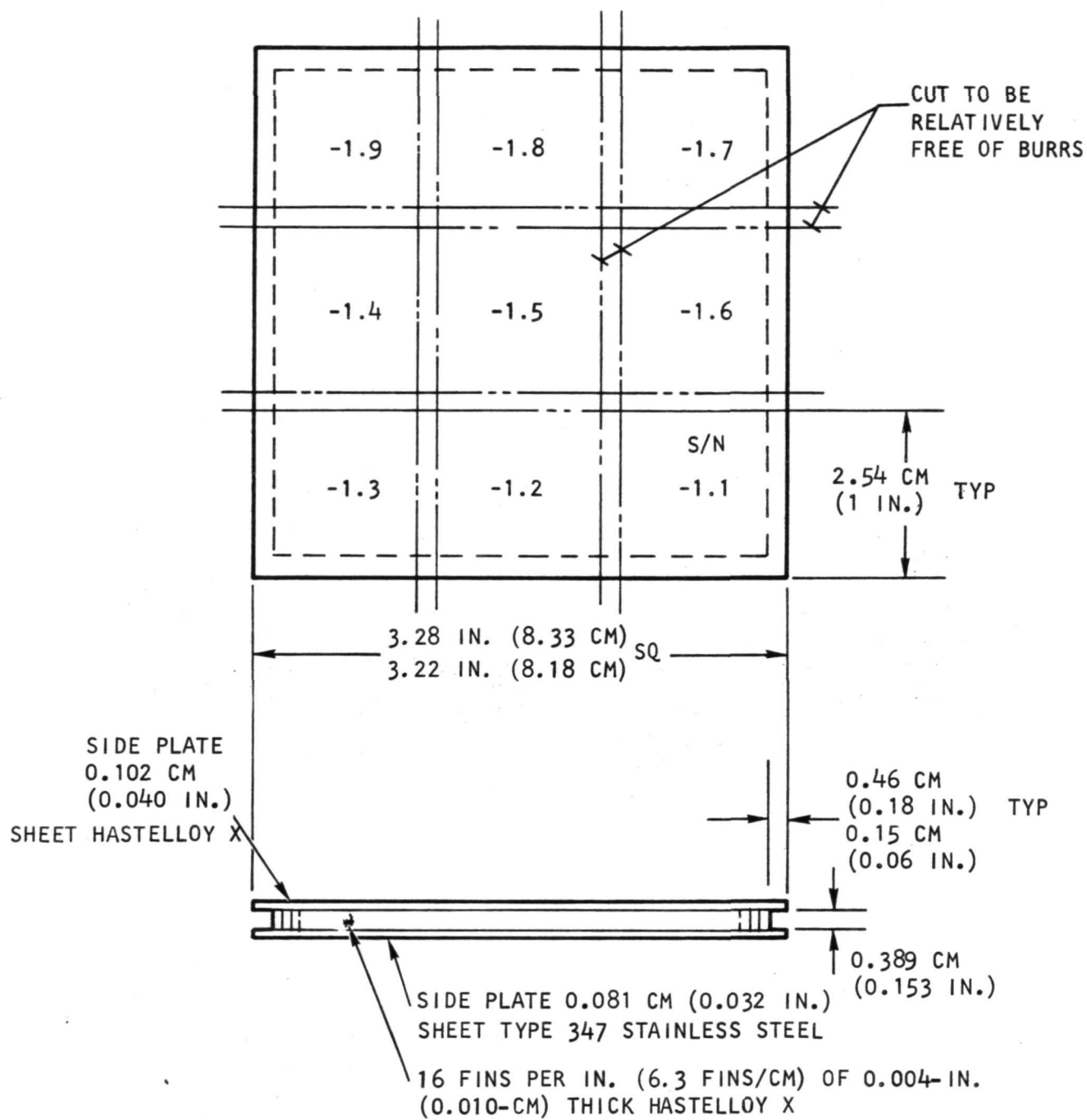


Figure 6-3.--Plate-Fin Oxidation Test Specimens

S-69968-A

TABLE 6-5

## PLATE-F IN SPECIMEN OXIDATION DATA

Brazing Alloy	Test Temp		Oxidation					Remarks
	$^{\circ}\text{K}$	$^{\circ}\text{F}$	Penetration into Fillet Radius, $10^{-3}\text{cm}$ (Mils)		311 hr	502 hr	1000 hr	
Palniro 1 (AMS 4784)	1005	1350	Nil	Nil	Nil	Nil	Nil	Oxidized on type 347 stainless steel Oxidized on type 347 stainless steel
	1089	1500	Nil	Nil	Nil	Nil	Nil	
NB 130 (AMS 4778)	1005	1350	Nil	Nil	Nil	Nil	3.0 (1.2)	External Scale
	1089	1500	1.4 (0.55)	2.0 (0.8)	2.8 (1.1)	4.1 (1.6)	4.1 (1.6)	
NB 30	1005	1350	Nil	Nil	Nil	Nil	Nil	-
	1089	1500	Nil	1.0 (0.4)	0.76 (0.3)	0.51 (0.2)	0.51 (0.2)	
AMI 400	1005	1350	Nil	Nil	Nil	Nil	Nil	-
	1089	1500	0.51 (0.2)	0.76 (0.3)	0.76 (0.3)	1.3 (0.5)	1.3 (0.5)	
NB 150	1005	1350	0.76 (0.3)	Nil	Nil	Nil	3.0 (1.2)	External Scale and Penetration
	1089	1500	1.0 (0.4)	2.0 (0.8)	2.8 (1.1)	4.1 (1.6)	4.1 (1.6)	
NB 5075	1005	1350	Nil	Nil	Nil	Nil	Nil	-
	1089	1500	Nil	1.0 (0.4)	1.3 (0.5)	2.3 (0.9)	2.3 (0.9)	
NB 5040	1005	1350	Nil	Nil	Nil	Nil	0.76 (0.3)	-
	1089	1500	Nil	1.5 (0.6)	1.3 (0.5)	2.0 (0.8)	2.0 (0.8)	
NB 50	1005	1350	Nil	Nil	Nil	Nil	0.76 (0.3)	Oxidized on Type 347 stain- less steel
	1089	1500	Nil	0.51 (0.2)	1.3 (0.5)	1.3 (0.5)	1.3 (0.5)	



Another consequence of elevated temperature is the continued diffusion of elements from the brazing alloy into the parent metal, especially along grain boundaries. This was observed to be much more of a problem at 1090°K (1500°F) than at 1000°K (1350°F) especially with the boron-containing alloys. Even after 1000 hr at 1000°K (1350°F), the total brazing alloy penetration of Nicrobraz 5040 and 5075 into the Hastelloy X fin was only about 0.005 cm (2 mils).

Two alloys, Palniro 1 (AMS 4784) and Nicrobraz 50, showed a low rate of oxidation when used with Hastelloy X but underwent considerable oxidation when the side plate was Type 347 stainless steel. Apparently, interdiffusion reactions led to lower oxidation resistance, pointing out the danger in extrapolating these oxidation test results to parent metal/brazing alloy systems not studied.

The results of the 3000-hr oxidation tests are given in figs. E-13 through E-21 of Appendix E for the Palniro 1, Nicrobraz 30, Nicrobraz 50, Nicrobraz 130, Nicrobraz 150, Nicrobraz 210, Nicrobraz 5040, Nicrobraz 5075 and J-8600 brazing alloys. Both the Nicrobraz 30 and the Nicrobraz 210 (figs. E-15 and E-21, respectively, of Appendix E) have acceptable oxidation resistance in the temperature range of 1005° to 1089°K (1350° to 1500°F).

Oxidation testing also was conducted on three alloys diluted with parent metal powder. An area of concern arising out of powder mixing was the possibility of upsetting the compositional balance of the brazement, primarily as it affects oxidation resistance. Oxidation of panels brazed with 10 percent Hastelloy X dilution was determined after a 500-hr exposure to still air at 1089°K (1500°F). Also included was a panel brazed with Nicrobraz 5075 diluted with 40-percent Hastelloy X powder. In general, no changes in oxidation behavior were noted, as indicated in the representative photomicrographs presented in figs. E-22 through E-24 of Appendix E. Invariably, the outer portion of the fillet was essentially 100 percent brazing alloy, where the oxidation behavior is the same as it is for the undiluted alloy.

### Conclusions

Based on considerations discussed previously, such as flow, filleting, penetration, microstructural stability, and hardness, as well as the oxidation results presented above, the following three alloys were selected for further evaluation testing:

Nicrobraz 30 at 1422°K (2100°F)

Nicrobraz 5040 at 1283°K (1859°F)

Nicrobraz 5075 at 1255°K (1800°F)

These alloys are listed in order of preference for use with Hastelloy X. Because of the temperature separations they are suitable for use in step brazing. A complete list of comments showing the background for selection of these materials is given in table 6-6. It should be noted that Nicrobraz 30 is not suitable for use with Type 347 stainless steel, but, conversely, both AMI 400 and J-8600 are satisfactory. If grain growth can be tolerated, J-8600 also could possibly be used with Hastelloy X.



TABLE 6-6  
SUMMARY OF BRAZING ALLOY TESTING

Brazing Alloy	Brazing* Temperature		Remarks	
	°K	°F	Hastelloy X Parent Metal	Type 347 Stainless Steel Parent Metal
Palniro (AMS 4784)	1405.5	2070	Acceptable	Oxidation
Nicrobraz 130 (AMS 4778)	1344.4	1960	Very aggressive, oxidation	Aggressive, oxidation
Nicrobraz 30 (J-8100)	1422.2	2100	Acceptable	Liquated
AMI 400 (NB 210)	1458.9	2165	Severe grain growth	Acceptable
Nicrobraz 150	1344.4	1960	Aggressive, oxidation	Oxidation
Nicrobraz 5075	1255.6	1800	Mildly aggressive, otherwise acceptable	Mildly aggressive, otherwise acceptable
Nicrobraz 5040	1283.3	1850	Mildly aggressive, otherwise acceptable	Mildly aggressive, otherwise acceptable
Nicrobraz 50	1255.6	1800	Aggressive	Oxidation
J-8600	1458.9	2165	Severe grain growth	Mildly aggressive, otherwise acceptable

\*Vacuum brazed, hold time 10 min at temperature.

## BEND TESTS

Fig. 6-4 shows the results of a simple hammer-over bend test on several of the brazed tee-sections. Palniro 1 was sufficiently strong and ductile to allow essentially a 90-deg bend without cracking in the filler metal joint. Although Microbraz 30 was able to withstand almost as much bending as the Palniro 1 specimen before a crack appeared, the Microbraz 130 (AMS 4778) cracked after only a modest bend. Neither of the latter alloys underwent catastrophic failure in that the cracks were observed to propagate at a finite rate rather than simply running through the filler metal joint with a single hammer blow.

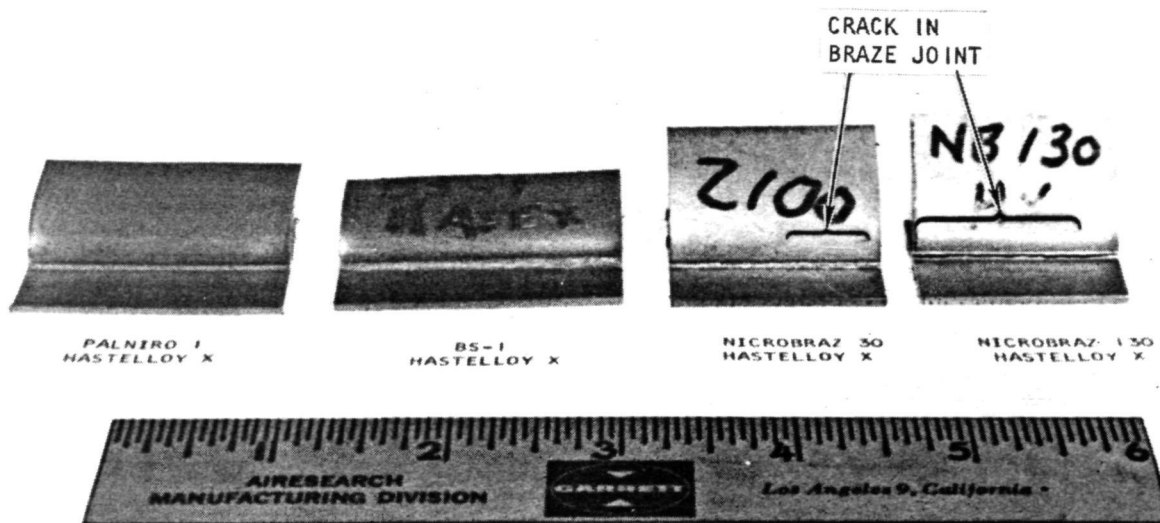
The results with BS-1, a mixture of 50 percent Niore and 50 percent Microbraz 135 (AMS 4779), are indicative of the potential ductility improvement attainable with admixed powders. This filler metal showed only very light cracking on a full 90-deg bend, which is well beyond the capability of Microbraz 135 by itself. The 1283°K brazing temperature used for BS-1 is also below the liquidus of Microbraz 135 (1330°K), and certainly is well below the brazing range of 1338° to 1450°K recommended for this alloy. The flow and filleting of BS-1 were excellent at the 1283°K temperature, suggesting that the melting of Microbraz 135 is enhanced by the presence of the lower melting Niore. The results of this approach warranted further consideration of admixed powders.

## BRAZING ALLOY DILUENT STUDIES

### Noble Metal Diluents

Preliminary tests indicated that small additions of noble metal brazing alloys such as Palniro 1 to Microbraz 30 and Microbraz 210 could both improve ductility and lower the alloy brazing temperatures. A number of brazing alloy combinations were evaluated for melting and flow characteristics, as listed in table 6-7. Microbraz 210 and AMI 400, which are very similar in chemistry, were included to determine if their brazing temperatures could be reduced to 1420°K (2100°F) or below. These alloys had been rejected previously because of the high brazing temperature requirement (1460°K or 2165°F), although they had appeared satisfactory in other characteristics such as erosion, penetration, and oxidation resistance.

Additional tests that were conducted on combinations of Microbraz 30 and AMI 400 with various noble metal brazing alloys are shown in table 6-8. These tests were accomplished utilizing "U" channel sections so that they could be dead weight loaded, i.e., brazed under pressure. This was done to simulate brazing conditions on an actual core, although calculations show that even the heaviest loading, of the order of 414 RN/m (60 psi), is still only 25 percent of the loading obtained in heat exchanger production. A joint thickness of 0.005 cm (2 mils), which is typical in actual practice, would minimize intermetallic phase formation in the joints but still leave the problem in the fillets unresolved. The brazing temperature indicated in table 6-8 does not necessarily correspond to the alloy melting point range shown in table 6-7. Brazing is usually conducted at a temperature level slightly above the point where the alloy is fully melted.



72478-3

F-17362

Figure 6-4.--Bend Tests on Tee Sections.

TABLE 6-7

## STUDIES ON BRAZING ALLOY COMBINATIONS

Brazing Alloy*	Melting				Remarks
	Start		Finish		
	°K	°F	°K	°F	
AMI 400 + 20% Pal I (-140) (-325)	1340	1950	Not complete		Max 1410°K (2075°F)
AMI 400 + 10% Pal I (-140) (-325)	1340	1950	1390	2050	Sluggish
NB 210 + 20% Pal I (-170) (-325)	1340	1950	1380	2025	Sluggish
NB 210 + 20% Pal I (-325) (-325)	1315	1910	1380	2025	Flowed well
NB 210 + 20% Pal I (+325) (-325)	1320	1925	Not complete		Max 1410°K (2075°F)
NB 30 + 20% Pal I (-325) (-325)	1340	1950	1390	2050	Flowed well
NB 30 + 10% Pal I (-325) (-325)	1340	1950	1380	2025	Flowed well
AMI 400 + 20% Pal RE (-140) (-325)	1380	2025	Not complete		Max 1390°K (2050°F)
AMI 400 + 10% Pal RE (-140) (-325)	1370	2000	1380	2025	Very sluggish
NB 210 + 20% Pal RE (-170) (-325)	1370	2000	1380	2025	Sluggish
NB 210 + 20% Pal RE (-325) (-325)	1370	2000	1380	2025	Very sluggish
NB 210 + 20% Pal RE (+325) (-325)	1380	2025	Not complete		Max 1390°K (2050°F)
NB 30 + 20% Pal RE (-325) (-325)	1330	1935	1380	2025	Flowed well
NB 30 + 10% Pal RE (-325) (-325)	1370	2000	1380	2025	Flowed well
AMI 400 + 20% Pal 7 (-140) (-325)	1310	1900	Not complete		Max 1370°K (2000°F)
AMI 400 + 10% Pal 7 (-140) (-325)	1320	1925	Not complete		Max 1370°K (2000°F)
AMI 400 + 20% Pal 7 (-325) (-325)	1310	1900	Not complete		Max 1370°K (2000°F)
AMI 400 + 10% Pal 7 (-325) (-325)	1320	1925	Not complete		Max 1370°K (2000°F)
NB 210 + 20% Pal 7 (+325) (-325)	1320	1925	Not complete		Max 1370°K (2000°F)
NB 210 + 20% Pal 7 (-325) (-325)	1310	1900	1370	2000	Some liquation
NB 30 + 20% Pal 7 (-325) (-325)	1300	1875	1340	1950	Flowed well
NB 30 + 10% Pal 7 (-325) (-325)	1300	1875	1340	1950	Flowed well

\*Numbers in parenthesis denote mesh sizes for the respective powders.

ORIGINAL PAGE IS  
OF POOR QUALITY

TABLE 6-8

RESULTS OF BRAZING ALLOY DILUTION STUDIES UTILIZING  
NOBLE METAL BRAZING ALLOYS\*

SN	Blend	Brazing Alloy Coating g/sq in.	Brazing Temperature		Applied Brazing Pressure		Brazed Joint Gap		Micro-hardness DPH (500 g)	Remarks
			°K	°F	kN/m <sup>2</sup>	PSI	10 <sup>-3</sup> cm	mils		
1	NB 30 + 10 percent Niore	0.25	1250	1800	41	6	Large		NH	Very poor joint filling
2	NB 30 + 20 percent Niore	0.25	1250	1800	41	6	Large		NH	
3	(NB 5075 + 20 percent Hast X) + 10 percent Niore	0.25	1250	1800	41	6	7.6 to 9.1	3.0 to 3.6	NH	Poor joint filling
4	(NB 5075 + 20 percent Hast X) + 20 percent Niore	0.25	1250	1800	41	6	7.6	3.0	477, 481, 597, 362	Skips in joint
5	NB 30 + 10 percent Pal RE	0.25	1380	2025	207	30	7.6 to 9.1	3.0 to 3.6	524, 393, 552, 429	Good joint
6	NB 30 + 20 percent Pal RE	0.25	1380	2025	207	30	6.1 to 7.1	2.4 to 2.8	656, 431, 413, 338	Good joint
7	NB 30 + 20 percent Niore	0.25	1380	2025	207	30	7.6 to 10.2	3.0 to 4.0	560, 362 343	Good joint
8	(NB 5075 + 20 percent Hast X) + 20 percent Niore	NH	1270	1825	207	30	6.4 to 9.1	2.5 to 3.6	365, 394, 368	Excessive flow
9	NB 30	0.25	1420	2100	207	30	7.1	2.8	670, 262, 264	Good joint
10	Pal 1	0.45	1410	2075	207	30	9.1	3.6	NH	Good joint
11	NB 30 + 20 percent Pal 1	0.19	1420	2100	414	60	13.8 to 4.3	1.5 to 1.7	466, 645, 271	Good joint
12	NB 30 + 20 percent Pal 4	0.20	1420	2100	414	60	5.1 to 6.4	2.0 to 2.5	452, 350	Good joint
13	NB 30 + 20 percent Pal 7	0.135	1370	2000	414	60	6.4 to 6.9	2.5 to 2.7	NH	Skimpy fillet
14	NB 30 + 20 percent Pal 7	0.18	1370	2000	414	60	6.4 to 7.1	2.5 to 2.8	516	Skimpy fillet
15	NB 30 + 20 percent Pal 7	0.625	1370	2000	414	60	8.1	3.2	560, 468, 423	Good joint
16	AMI 400 + 20 percent Pal 1	0.315	1420	2100	414	60	10.2 to 12.2	4.0 to 4.8	287, 237	Good joint, small fillet
17	NB 30	0.34	1420	2100	414	60	4.8 to 5.3	1.9 to 2.1	692, 470, 356	Good joint
18	AMI 400 + 20 percent Pal 1	0.195	1420	2100	414	60	6.9 to 8.9	2.7 to 3.5	234	Skimpy joint - voids
19	AMI 400 + 10 percent Pal 1	0.30	1420	2100	414	60	7.6	3.0	262	Skimpy joint

\*All blends were -325 mesh powders except 16 and 19, where the AMI 400 was used as received (essentially -140 mesh)

ORIGINAL PAGE IS  
OF POOR QUALITY

The results from table 6-8, (as pictured in figs. E-25 through E-39, of Appendix E) indicate a fair measure of success with additions of noble metal brazing alloy to either Nicrobraz 30 or AMI 400. The AMI 400 alloys look particularly good from the standpoint of hardness (below DPH 300) and from the standpoint of their microstructures, which show the intermetallic phase present as a distribution of fine particles (figs. E-36, E-38 and E-39 of Appendix E) as opposed to the more massive constituent present with Nicrobraz 30. The reduction in brazing temperature from 1460° to 1420°K for the modified AMI 400 is highly significant in that it allows this alloy to be used in brazing Hastelloy X without grain growth problems. Although the brazed joint fillets were fairly small, they appear adequate. The alloy is quite tough, and cracks propagate slowly, as found in a (hammer) bend test on SN 16 (table 6-8 of Section 6 and fig. E-36 of Appendix E).

The evaluation of alloys containing Nicrobraz 30 was not as straightforward. The distribution of the intermetallic phase in the brazed joint gap is dependent primarily on gap width, generally less the smaller the gap, although other factors such as brazing time, minor temperature variations, and post-brazing cooling rate appear to be influential. The greater problem is in the fillet area where the size of the pool of molten alloy has a direct relation to the amount of intermetallic phase content. This pool size is in turn related to the amount of alloy present, especially as influenced by the wetting and flow characteristics of the brazing alloy. The importance of the intermetallic phase cannot be overemphasized, as is evidenced in figs. E-25, E-26, and E-30 of Appendix E for brazing alloy mixtures based on Nicrobraz 5075, all of which show the brittle component throughout the joint. This condition is undesirable as attested to by the rapid brittle failure of these joints in the (hammer) bend test.

The results of the (hammer) bend test must also be viewed carefully, as even a brittle fillet will withstand the test if it is large enough. Nicrobraz 30 by itself (fig. E-37 of Appendix E) is an example of this. Fracture may occur in a noncritical area such as shown in fig. E-35 of Appendix E. It is not clear whether a similar failure would have occurred in the weld test specimen had it been brazed with this mixture of Nicrobraz 30 and 20 percent Palniro 7, or any of the other blends shown in table 6-8. It is clear from table 6-8 that brazed joint hardness can be reduced by additions of a noble metal brazing alloy. More significantly, such additions lower the brazing temperature of the parent brazing alloy, which allows the use of a series of alloys for step and/or repair brazing, as well as the use of AMI 400 which previously had too high a flow temperature. It is probably necessary to use the powder equivalent of 0.005 cm (0.002 in.) foil for satisfactory brazing. When compared to the 0.0025 cm (0.001 in.) Palniro I foil for which a replacement alloy was sought, the economic savings in using a 10-percent noble metal brazing alloy addition would still be substantial.

The five combination alloys listed in table 6-9 were selected for further investigation. The results are presented in table 6-9. The microhardness readings for the Nicrobraz 30 combination alloys (table 6-9) showed a 10-percent drop in maximum hardness. However, there appeared to be a microstructural change in the distribution of the intermetallic indicated phase within the fillet. Bend test (hammer) results indicated good resistance to fillet cracking in three of the five test samples.

TABLE 6-9

EFFECTS OF NOBLE METAL BRAZING ALLOY ADDITIONS  
ON THE PERFORMANCE OF STANDARD BRAZING ALLOYS

Base Alloy	Diluent	Brazing Temperature		Brazed Joint Gap	Brazed Joint		Microhardness DPH (500 q)	Remarks
		°K	°F		10-3 cm	mils		
Nicrobraz 30	Palniro I	1400	2070	5.1		2.0	625, 479, 255	Took full bend
Nicrobraz 30	Palniro RE	1390	2050	4.1		1.6	610, 501, 260	Failed during bending
Nicrobraz 30	Palniro 7	1370	2000	6.4		2.5	603, 269	Took full bend
Nicrobraz 210	Palniro I	1420	2100	7.6		3.0	297, 249	Took full bend
AMI 400	Palniro I	1420	2100	6.4		2.5	308, 244	Failed during bending

## NOTES:

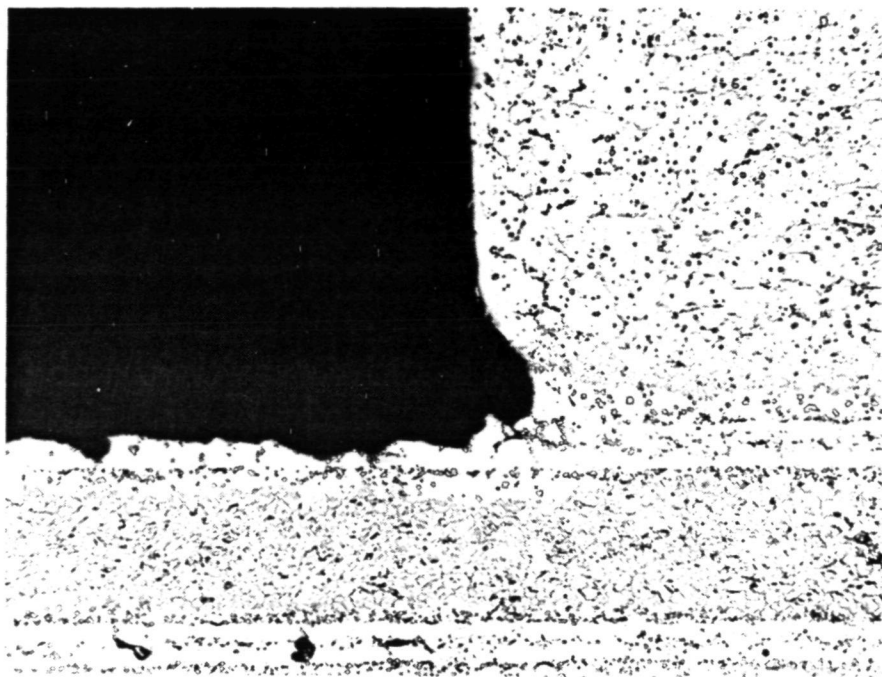
1. All powders were -325 mesh.
2. All samples utilized a power coating of 0.30 grams/in.<sup>2</sup>.
3. All samples were dead weight loaded to about 827 kNm<sup>2</sup> (120 psi) during brazing.
4. The higher microhardness readings were taken on the fillets, whereas the lower readings were obtained within the joint.



The Microbraz 210/Palniro I alloy exhibited marginal flow and filletting. An attempt to improve this was made by brazing a small three pass plate-fin module, fig. 6-5, at 1430°K (2120°F). However, the improvement in brazing characteristics was essentially insignificant. Neither solution, an increase in brazing temperature or an increase in the percentage of Palniro I, is desirable from a cost or a practicality standpoint.

#### Hastelloy X Diluent

The technique of mixing Hastelloy X base metal powder with the brazing alloy powders, in preference to using an expensive noble metal alloy as the diluent, was investigated. Although the Hastelloy X will not melt appreciably, it was believed that it could lead to enhanced ductility by absorbing the brittle intermetallic-phase-forming elements from the filler metal, i.e., boron, phosphorous, and silicon. Further, the softer Hastelloy X particles could arrest cracks that are initiated in the more brittle areas containing brazing alloy. To test this premise, plate-fin samples were fabricated using (1) 10 percent Hastelloy X powder blended with 90 percent brazing alloy, and (2) 40 percent Hastelloy X powder blended with 60 percent brazing alloy.



F-23792

Figure 6-5. Plate-Fin Specimen Brazed at 1433°K with a Mixture of NB210 and 10 Percent Palniro (Micro 26982, Oxalic Acid Etch 100X)



The results of these tests are shown in figs. E-40 through E-43 of Appendix E. In general, the brazed joints were starved of filler metal when 40 percent Hastelloy X powder was used as demonstrated in fig. E-40(b) of Appendix E. This was traced to the use of -170 mesh powders, where the largest particle diameter would be of the order of 0.009 cm (3.5 mils). Since the Hastelloy X particles do not collapse during brazing, they hold the parent metal components apart, and there is insufficient filler metal available to fill such a wide gap. The exception to this was Nicrobraz 5075 (fig. E-41(b) of Appendix E); this alloy apparently flows exceptionally well and is able to fill the joint by drawing from the spaces between the fins. In general, thick brazements are not recommended because of lower joint strength. In particular, filling wide gaps with the Nicrobraz alloys is not recommended because of the greater tendency for formation of brittle intermetallic phases.

Accordingly, these tests were repeated using blends of -325 mesh powder, which has a maximum particle diameter of 0.0043 cm (1.7 mils). A 20-percent addition of Hastelloy X was chosen based on the results of the first series of tests. Photomicrographs of these samples are presented in fig. E-44 through E-46 of Appendix E. Smaller brazed joints were obtained, and microhardness readings were considerably lower than seen previously on the joints using 100 percent brazing alloy. The hardness of the Hastelloy X in the embrittled zone next to the joint was around DPH 300 (compared to DPH 200 in the undamaged material). Hardness readings in the range of 300 to 350 DPH are indicative of Hastelloy X, which has been well penetrated by the brazing alloy. Some cracks were noted around the hardness indentations, particularly in Nicrobraz 5040, apparently as a result of breaking intermetallic phase particles.

Hardness measurements and apparent depths of parent metal damage by the brazing alloy are summarized for both the undiluted and diluted alloys in tables 6-10 and 6-11. The depth numbers are termed "apparent" because they were obtained by measurement from the "apparent" surface of the tube plate, which may be lower than the original surface. Since the tube sheet was completely covered with filler metal, it was impossible to establish the location of the original surface; hence, the measurements must be considered as qualitative. Even so, if one compares the numbers for apparent depth of damage in table 6-10 with those in table 6-11, one must conclude that parent metal damage generally is not reduced by additions of the Hastelloy X powder diluent. The primary effect of the diluent, then, is to reduce joint hardness, i.e., promote ductility. The data suggest, however, that for minimum intergranular penetration a low boron-containing alloy should be used, thus establishing a preference for Nicrobraz 30, followed by Nicrobraz 5075, and finally Nicrobraz 5040.

#### Nickel-Base Alloy Diluents

An approach to lowering the flow temperature of Nicrobraz 210 is to use Nicrobraz 30 as the diluent. Four combinations of the Nicrobraz 210 alloy with up to 50 percent Nicrobraz 30 were made and tested using the weighted-channel Tee-sections. Details and results are given in table 6-12 and figs.

TABLE 6-10  
CANDIDATE ALLOYS FOR BRAZING HASTELLOY X PLATE-FIN  
HEAT EXCHANGERS

Brazing Alloy	Nominal Composition	Brazing Temperature, °K °F		Microhardness DPH (500 g)	Apparent Depth of Parent Metal Damage					
					Type 347 Stainless			Hastelloy X		
					Alloying cm	In. in.	Total cm	Alloying cm	In. in.	Total cm
NB 5040	5 Cr, 2 Si 1 B, 4 P Bal Ni	1283	1850	807, 812, 591	Nil	0.0025	0.001	Nil	0.0064	0.0025
NB 5075	10 Cr, 1 Si 0.5 B, 7.5 P Bal Ni	1255	1800	784, 645, 728	Nil	0.0020	0.0008	Nil	0.0020	0.0008
NB 30 (J-8100)	19 Cr, 10 Si 1 Mn, Bal Ni	1422	2100	728, 740	0.0018	0.0007	0.0007	0.0018	0.0007	0.0011
Palnro 1* (AMS 4784)	50 Au, 25 Pd 25 Ni	1405	2070	272, 216	Nil	Nil	Nil	Nil	Nil	Nil
NB 130* (AMS 4778)	4.5 Si, 3 B Bal Ni	1344	1690	757, 766	Nil	0.0043	0.0017	0.0025	0.001	0.002

\*Included for comparison.

TABLE 6-11

EFFECTS OF DILUTING CANDIDATE BRAZING ALLOYS  
WITH HASTELLOY X POWDER

Hastelloy X Diluent Percent/ Mesh Size	Joint Gap				Microhardness of Joint (DPH)	Apparent Depth of Parent Metal Damage							
	Hastelloy-X					Type 347 Stainless			Hastelloy X				
	Hastelloy-X		347			Alloying, cm (in.)	Total		Alloying		Total		
	cm	in.	cm	in.			cm	in.	cm	in.	cm	in.	
<u>NB 5040</u>													
10/-170	0.011	0.0044	0.011	0.0043	365, 585, 298, 723	Nil	0.0025	0.001	0.0015	0.0006	0.0041	0.0016	
40/-170	0.0091	0.0036	0.010	0.004	---	Nil	0.0025	0.001	0.0020	0.0008	0.0041	0.0016	
20/-325	0.0076	0.003	0.0046	0.0018	349, 309, 336	Nil	0.003	0.0012	0.0025	0.001	0.0036	0.0014	
<u>NB 5075</u>													
10/-170	0.011	0.0044	0.013	0.005	460, 670, 281	Nil	0.0020	0.0008	0.0013	0.0005	0.0038	0.0015	
40/-170	0.010	0.004	0.010	0.004	318, 278, 332	Nil	0.0010	0.0004	0.0013	0.0005	0.003	0.0012	
20/-325	0.0058	0.0023	0.0036	0.0014	336, 322, 324	Nil	0.0015	0.0006	0.0018	0.0007	0.0025	0.0010	
<u>NB 30</u>													
10/-170	0.0084	0.0033	0.0084	0.0033	462, 571, 348, 652	0.0020 (0.0008)	0.0025	0.0010	0.0020	0.0008	0.0020	0.0008	
40/-170	0.011	0.0045	0.010	0.004	---	0.0020 (0.0008)	0.0020	0.0008	0.0020	0.0008	0.0020	0.0008	
<u>NB 130*</u>													
10/-170	0.0097	0.0038	0.010	0.004	757, 497, 774	Nil	0.0041	0.0016	0.0020	0.0008	0.0051	0.002	
40/-170	0.016	0.0063	0.013	0.005	---	Nil	0.0041	0.0016	0.003	0.0012	0.0051	0.002	
20/-325	0.0076	0.003	0.0058	0.0023	438, 458, 334, 391	Nil	0.0051	0.002	0.0023	0.0009	0.0061	0.0024	

\* Included for comparison

ORIGINAL PAGE IS  
OF POOR QUALITY

TABLE 6-12

## NICROBRAZ 210 AND NICROBRAZ 30 COMBINATION BRAZING ALLOYS

Mixture	Powder Mesh Size	Braze Joint Gap		Remarks
		10-3cm	mils	
75% Nicrobraz 210/25% Nicrobraz 30	-140 + 325/-325	6.6	2.6	Not as good a flow as with all -325 mesh powder
50% Nicrobraz 210/50% Nicrobraz 30	-140 + 325/-325	6.1	2.4	Considerable intermetallic phase in fillets
75% Nicrobraz 210/25% Nicrobraz 30	-325/-325	5.6	2.2	DPH 458 hardness in fillet
50% Nicrobraz 210/50% Nicrobraz 30	-325/-325	5.6	2.2	DPH 642 hardness in fillet

## NOTES:

1. All samples utilized a powder coating of about  $0.047 \text{ g/cm}^2$  ( $0.30 \text{ grams/in.}^2$ ).
2. All samples were dead weight loaded to about  $827 \text{ kN/m}^2$  (120 psi) during brazing.
3. Brazing conditions were  $1420^\circ\text{K}$  ( $2100^\circ\text{F}$ ) 10 min, in vacuum.

E-47 through E-50 of Appendix E. Flow conditions at a 1420°K (2100°F) brazing temperature were improved, and, more importantly, the costly noble metal alloy was eliminated. As expected, a comparison of figs. E-47 through E-50 of Appendix E indicates that the amount of Nicrobraz 30 should be minimized since the intermetallic phase was found in abundance with the 50-50 mixtures (figs. E-48 and E-50 of Appendix E). Since visual observation showed that better melting occurred with the -325 mesh powder, a mixture corresponding to that used to braze the sample shown in fig. E-49, i.e., 75 percent Nicrobraz 210 with 25 percent Nicrobraz 30, was used to fabricate a weld test specimen by vacuum brazing at 1420°K (2100°F). The resulting module (shown metallographically in a following paragraph) was free of cracks with acceptable fillets having hardness readings generally below DPH 300.

Hastelloy X tube sheets that were brazed with this combination brazing alloy also have shown good bend ductility.

### Conclusions

Based on the combined test results discussed above, the two candidate brazing alloys selected for creep-rupture testing were Nicrobraz 30 and Nicrobraz 210 combined with Nicrobraz 30 in the ratio of 75:25. Both alloys were -325 mesh powders. Although the latter combination alloy was not necessarily optimized with regard to the ratio of the component alloys, any variations were considered likely to be minor.

### WELD-OVER-BRAZE TESTS

#### Plate/Bar Test Specimen

Plate and bar test specimens using candidate braze alloys were fabricated from Hastelloy X to evaluate the effects of welding over typical heat exchanger braze joints. The "log cabin" test specimen is shown in fig. 6-6. Weld passes simulating pan attachment techniques were made at the corners at the midspan reinforcing bars using two different weld rod materials, Hastelloy W and Inconel 82. Previous observations indicate that such operations result in cracks developing in the weld joint due to metallurgical reactions. The intense local heat off the welding operation also causes a high thermal stress to develop in areas adjacent to the weld zone and, when applied to a brittle braze joint, cracking results.

From these tests, the lack of ductility in Nicrobraz 5040 and 5075 became very apparent, as cracks were found in the unwelded corners. Furthermore, brazing alloy remelting during welding led to serious weld defects. Conversely, the as-brazed test specimen utilizing Nicrobraz 30 was sound. Examination of the welded areas of this latter sample showed exceptionally good resistance to brazing alloy remelting, although a fair number of cracks were observed in the internal plate-header bar fillets. These internal plate-header bar fillets were exceptionally large due to all of the alloy applied to

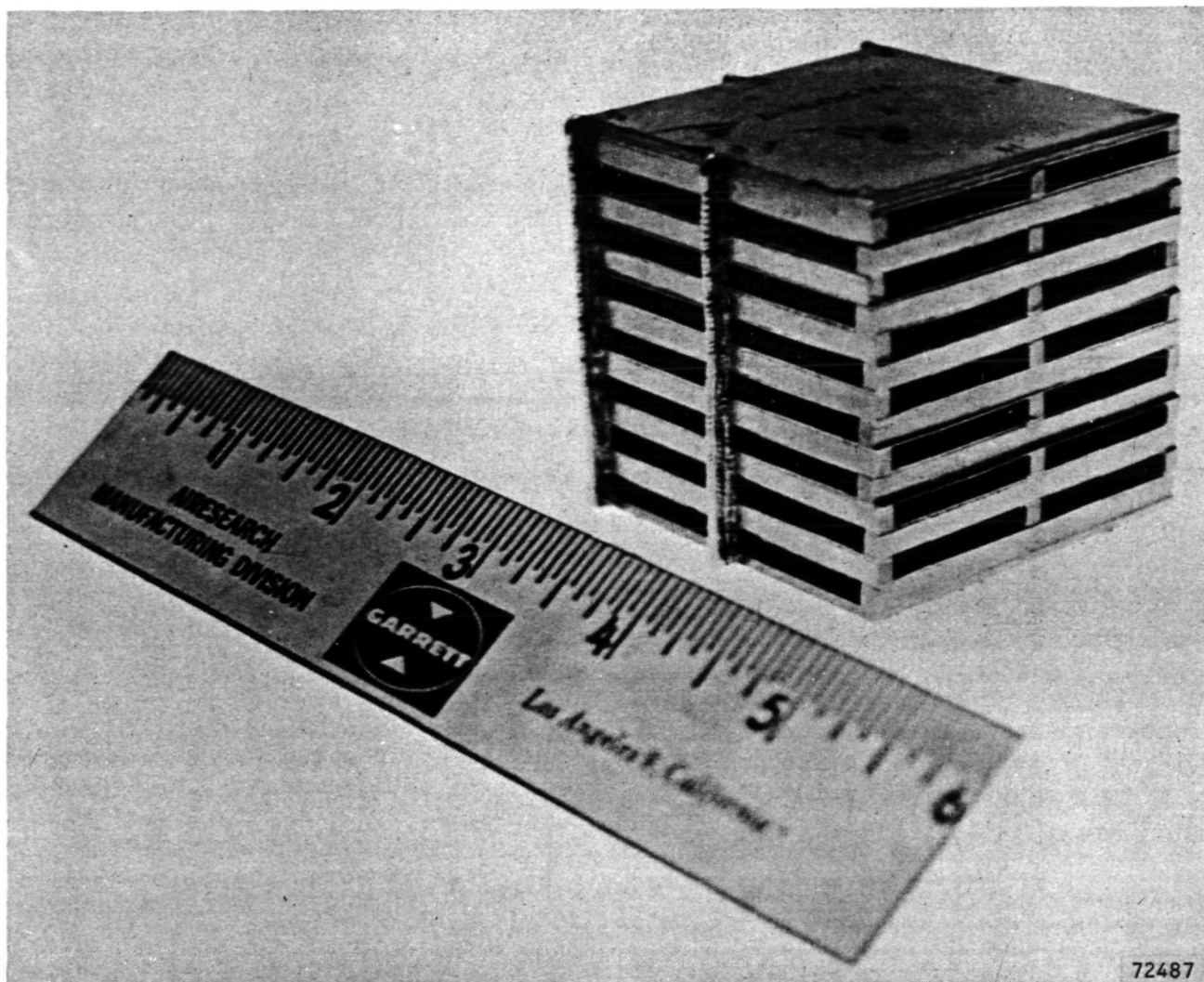


Figure 6-6.--Plate-Header Bar Weld Test Sample



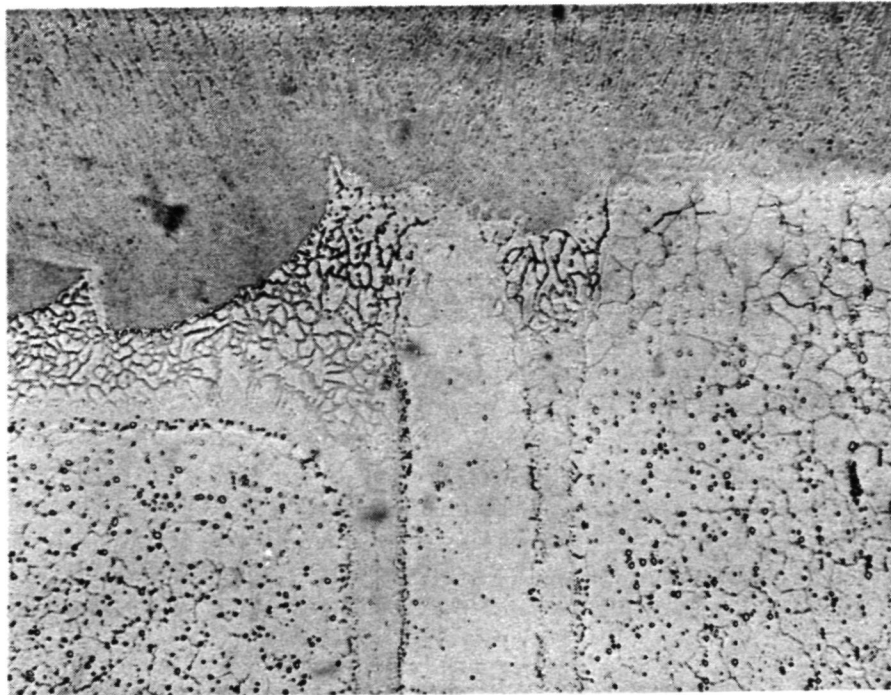
the tube sheet forming this fillet instead of being absorbed in the fin-tube sheet braze joint. Representative photomicrographs are shown in fig. 6-7 for Nicrobraz 30. As a result of these tests, further work with the Nicrobraz 5040 and Nicrobraz 5075 was terminated. The ductility improvement needed for either of these alloys would be very large and the remelting problem during welding not readily solvable.

One distinguishing characteristic of most nickel brazing alloys is the tendency for formation of brittle intermetallic phases during solidification, a feature which is enhanced by wide joint gaps. For example, microhardness readings on the fillets of the plate-header bar test specimen shown in fig. 6-7(b) showed a hardness in excess of DPH 600, whereas readings within the joint were of the order of DPH 260, which is about the hardness of Palniro 1 alloy. This explains why the crack shown in fig. 6-7(b) did not propagate through the joint, i.e., the stresses can be relieved by plastic flow rather than by fracture of the brazing alloy. It is apparent, then, that careful control of the application of this alloy must be exercised to ensure fillet formation just sufficient to prevent notch effects due to undercutting while minimizing the amount of intermetallic phase formed during solidification.

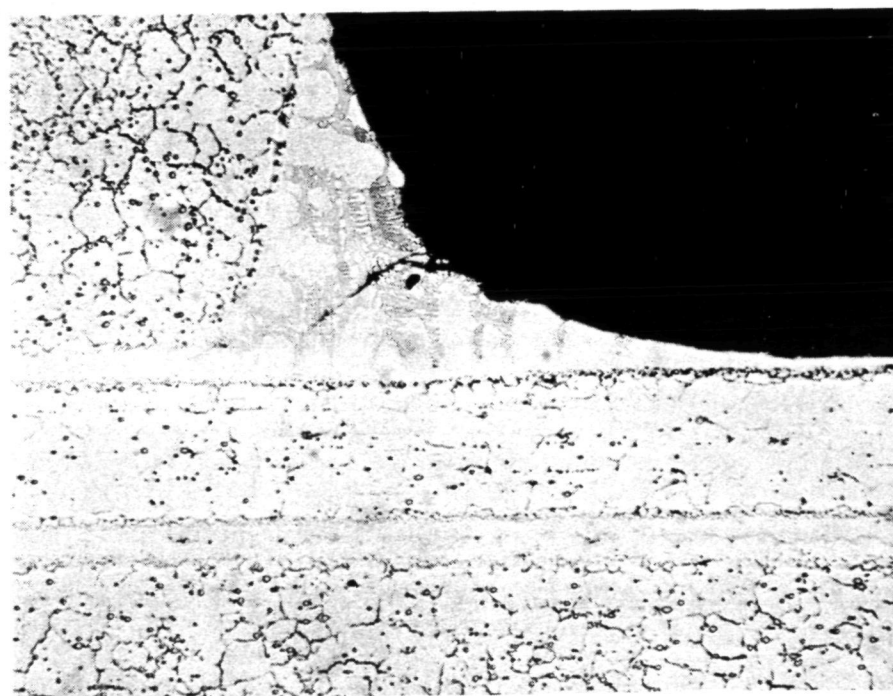
#### Finned Test Specimen

The weld-over-braze tests were repeated using a test specimen similar to the one shown in fig. 6-6 but incorporating Hastelloy X fins brazed between the plates. The fins were used to ensure better distribution of the braze alloy with consequent reduction in fillet size at the tube sheet to header bar joint. This test sample was more representative of actual plate-fin heat exchanger construction than the previous specimen incorporating only bars and tube sheets. The braze alloys used for this second test series were Nicrobraz 30, Nicrobraz 30 with 10 percent Palniro 1, Nicrobraz 210 with 10 percent Palniro 1, and Nicrobraz 210 with 25 percent Nicrobraz 30.

Typical photomicrographs of the plate-fin weld-over-braze test samples are shown in figs. E-51 through E-54 of Appendix E. Examination showed that only the Nicrobraz 210/Palniro 1 and Nicrobraz 210/Nicrobraz 30 did not crack in the interior plate-to-header bar fillets as a result of welding. Cracking in the Nicrobraz 30 occurred in, or adjacent to, the large pools of intermetallic phase formed in the fillets during solidification. As indicated in fig. E-51 of Appendix E, these cracks do not propagate into the softer alloy within the joint. It is therefore essential to control the application of Nicrobraz 30 so that only enough alloy is used to form small fillets, thereby minimizing the amount of intermetallic phase that is formed.



a. WELD OVERLAY



b. BRAZED JOINT

F-17536

Figure 6-7.--Plate-Header Bar Stack Brazed at 1422°K (2100°F) with Microbraz 30 (J-8100).

- a. Weld Overlay on Sandwich of Header Bars and Tube Sheet
- b. Cracked Fillet at Tube Sheet-to-Header Bar Junction Opposite to Weld (Micro 26702 Oxalic Acid Etch, 100X).



### Conclusions

Test results for the two specimen designs and six braze alloys tested are summarized below:

<u>Item Number</u>	<u>Test Specimen Description</u>	<u>Results</u>
1.	NB 30 Bars and plates only	No evidence of braze alloy remelting or weld cracking. No cracks in unwelded corners. Number of cracks in the internal header bar-plate fillets. These fillets were exceptionally large because all the alloy applied to the tube sheet flowed to the header bar because no fins were present.
2.	NB 5040 and 5075 Bars and plates only	Serious weld defects because of braze alloy remelting. Cracks found in unwelded corners.
3.	NB 30 (-325 mesh) Bars, plates, and fins	Cracking in the internal header bar-to-plate fillets. Addition of fins to specimen did not affect degree of cracking.
4.	NB 30 with 10 percent Palniro 1 Bars, plates, and fins	Cracking in the internal header bar-to-plate fillets.
5.	NB 210 with 10 percent Palniro 1 Bars, plates, and fins	Cracking in the internal header bar-to-plate fillets. Marginal flow and filleting.
6.	75 percent NB 210 with 25 percent NB 30 Bar, plates, and fins	No cracks observed. Acceptable fillets with hardness readings less than DPH 600.

Based on these results, it was concluded that the best alloy was the 210/30 combination because of the test specimen freedom from cracking. The cracking observed with NB 30 was believed to be minor and it was concluded that the test evaluation of NB 30 should be continued.

Specific tests to evaluate NB 130 (AMS 4778) and Palniro 1 were not conducted in this series. Previous experience in production heat exchangers indicate that extensive cracking would probably occur with NB 130. During another part of the program (Task 2F, reported in NASA CR-121011), it was attempted to establish the low-cycle fatigue resistance of a typical heat exchanger corner section. A brazement using Palniro 1 was made to simulate

a typical log cabin stack. A weld pass was made directly over the braze joint to simulate a pan attachment. The specimens were then subjected to a reverse bending test to determine their low-cycle fatigue resistance compared to the parent metal. Test results were very erratic with some specimens failing in less than 10 cycles. Photomicrographs of the failed sections indicated that premature failure was induced by cracks in the Palniro 1 braze alloy fillets which developed as a result of the welding operation. It was noted that, due to the specimen design, the braze fillets were excessively large compared to those observed in a typical heat exchanger. These results, however, reinforce the conclusion that the recuperator should be designed to avoid all weld-over-braze operations insofar as possible, regardless of the braze alloy used in the construction.

### CREEP-RUPTURE TESTING

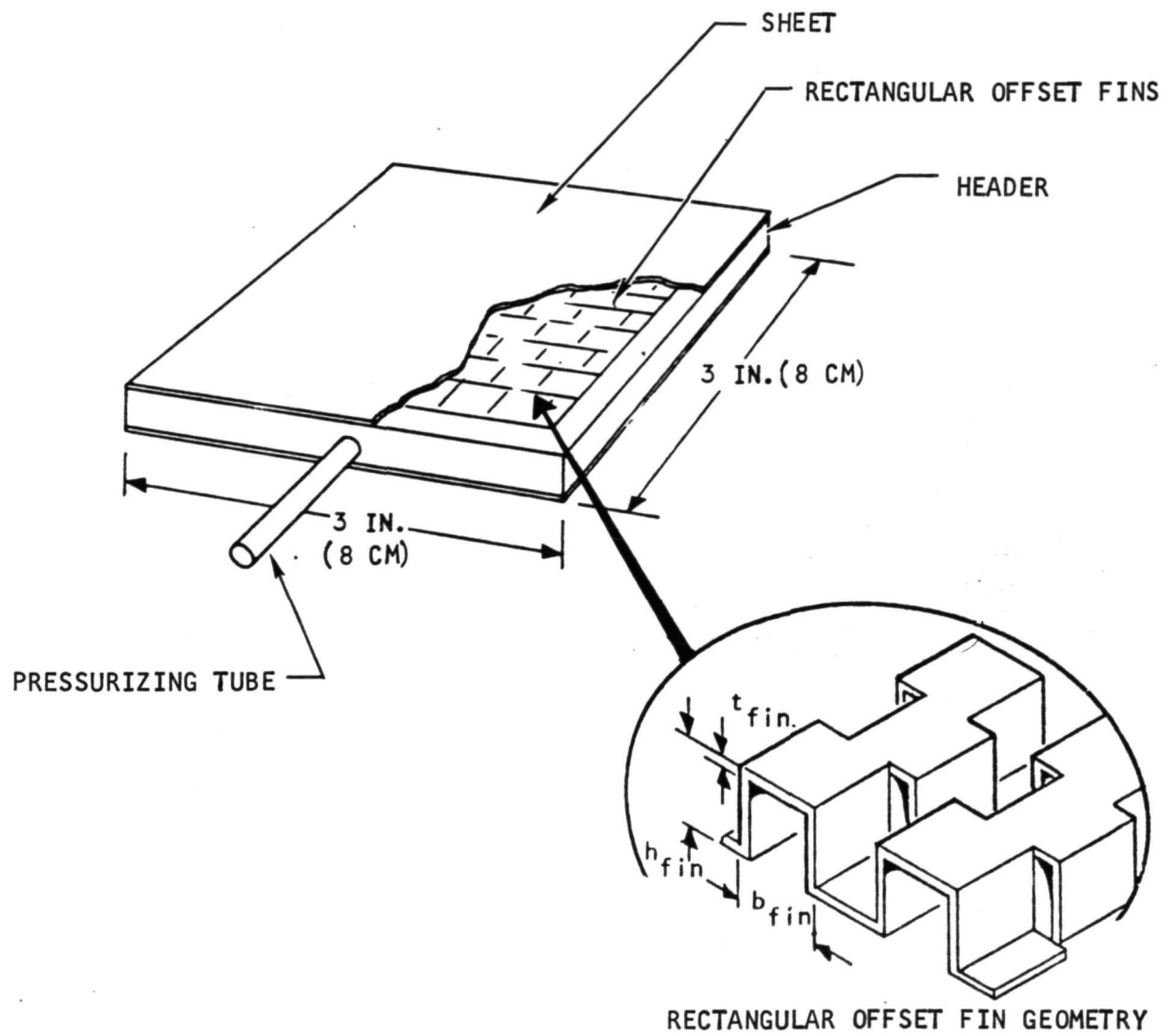
Single-sandwich plate-fin specimens fabricated from Hastelloy X were brazed with the three alloys considered to best meet the specified design criteria. These alloys were Microbraz 30, a mixture of 75 percent Microbraz 210 with 25 percent Microbraz 30, and Palniro 1. Recuperator design requirements specified for the creep-rupture tests included a temperature of 1005°K (1350°F), a pressure of 793 kN/m<sup>2</sup> (115 psi), and a life of 100 000 hr. To accelerate creep rates and obtain useful data within the period of testing, the tests were conducted at a temperature of 1144°K (1600°F). Test pressures ranged from 1700 to 5500 kN/m<sup>2</sup> (250 to 800 psi).

#### Specimen Design

The creep-rupture test specimens were single-sandwich plate-fin assemblies, as shown in fig. 6-8. The basic design incorporated a 7.6- by 7.6-cm (3- by 3-in.) fin sandwich, brazed between tube sheets and closed by header bars, with a pressurizing tube inserted through one of the sides. An exploded view of these components is shown in fig. 6-9. This assembly is representative of the basic pressure containment element in a plate-fin heat exchanger.

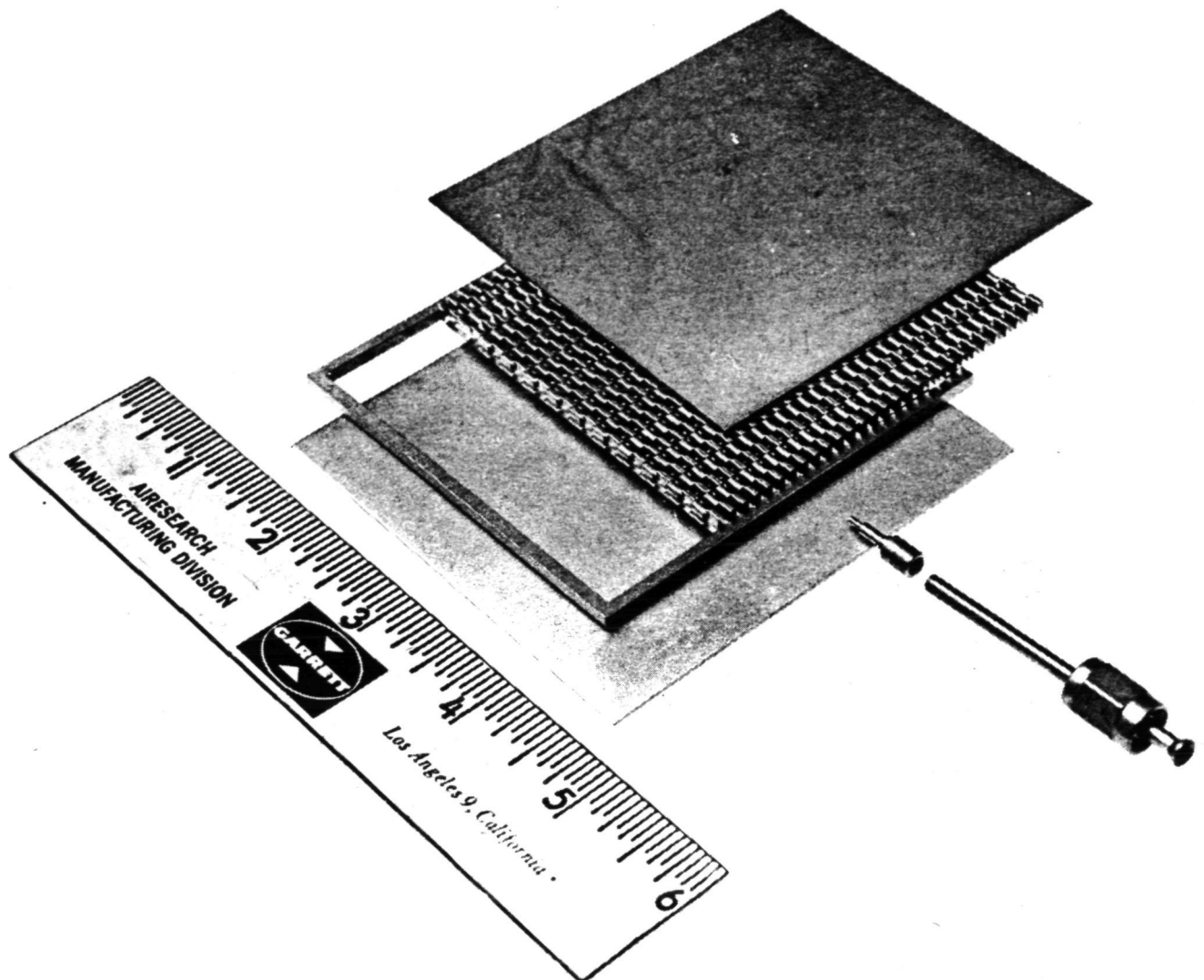
The fin sandwich consisted of 0.010-cm (0.004-in.) thick fins with a fin height (plate spacing) of 0.254 cm (0.100 in.) and a fin count of 51 fins/cm (20 fins/in.). This high-density matrix is typical of fin matrixes selected for high-temperature recuperator applications. Fin height is not an important factor in determining pressure strength since height only affects fin load redistribution capability, primarily in the plastic strain region. The selected height is typical for the design requirements of Brayton-cycle power systems.

A face sheet thickness of 0.064 cm (0.025 in.) was selected to avoid load transfer from the center to the edges of the specimen and to be representative of minimum heat exchanger side-plate thickness. The sheet thickness has only a minor effect on pressure containment capability. Sheet thickness is related to pressure containment capability by its effect on the magnitude of the bending stress due to the unsupported length between fins and due to the



S-61614

Figure 6-8.--Creep-Rupture Test Specimen.



72751

Figure 6-9.--Exploded View of Creep-Rupture Test Panel.

ability of the sheet to transfer a load from the weaker to the stronger fins. It is estimated that fin load reductions at the center of the specimen due to sheet stiffness were less than 10 percent. The face sheet bending stresses were a maximum of about 20 percent of the fin stress, so that the sheets did not influence containment strength.

### Fabrication

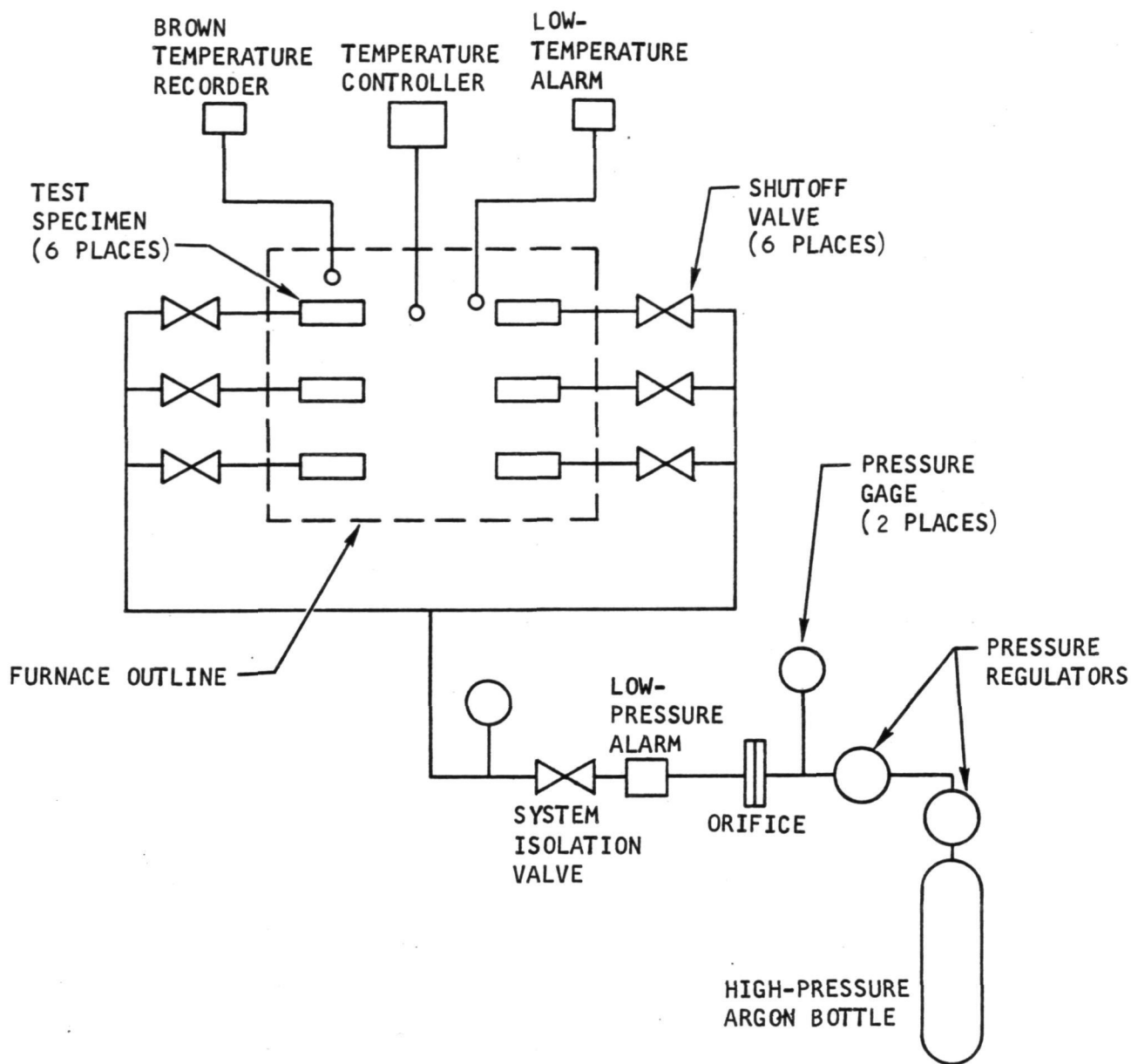
The basic samples were fabricated in single brazing operations with a  $42 \text{ kN/m}^2$  (6 psi) loading applied to the 8 by 8 cm (3 by 3 in.) surface. The alternate brazing alloys were applied on the sheets in powder form to an equivalent foil depth of about 0.005 cm (0.002 in.). A Palniro 1 foil of 0.003-cm (0.001-in.) thickness was used. The time at brazing temperature was specified to be 0.16 hr to simulate the actual brazing cycle on a recuperator. An additional brazing cycle was required for the pressurizing tube and to repair any leaks at the sheet-to-header bar joint. A lower melting point alloy, Nicro (82 Au, 18 Ni), was used for the additional brazing operation, which was performed at  $1260^\circ\text{K}$  ( $1800^\circ\text{F}$ ). The specimens were pressure tested at  $6900 \text{ kN/m}^2$  (1000 psi) at room temperature to verify sample integrity prior to creep-rupture testing.

### Testing

Fig. 6-10 is a schematic representation of one of the two furnaces used for the creep-rupture tests. The two furnaces, with inside dimensions of 25 by 25 by 61 cm (10 by 10 by 24 in.) were each capable of handling six panels and two pressure levels. One furnace had a pressure capability of 13 800 to 20 700  $\text{kN/m}^2$  (2000 to 3000 psi) and the other of 20 700 to 34 400  $\text{kN/m}^2$  (3000 to 5000 psi).

The four groups of three specimens were pressurized from a high-pressure argon bottle through a regulator and an orifice. The orifice permitted sufficient argon flow to maintain pressure if small leaks occurred in the system. On specimen failure, the orifice restricted the argon flow, and the decreased downstream pressure activated the low-pressure alarm. A thermocouple was attached to each specimen and temperatures were recorded periodically. The furnace control temperature was recorded continuously. A separate low-temperature alarm was incorporated for additional system protection. The specimens were placed in a Hastelloy X rack that separated them so that the failure of one panel would not affect the life of an adjoining panel.

The creep-rupture test specimens were instrumented with fiberglass insulated Chromel-alumel thermocouples that were attached to the face sheets of the panels prior to placement in the furnace. Upon temperature stabilization, the panels were pressurized to the selected test pressures. The panel temperatures and pressures were monitored at specific intervals and recorded to ensure that the correct temperatures and pressures were being maintained. Acceptable temperature and pressure variations were  $5.6^\circ\text{K}$  ( $\pm 10^\circ\text{F}$ ) and  $\pm 1$  percent, respectively.



S-61615

Figure 6-10.--Pressure Test System Schematic

## Results and Discussion

The test data are summarized in table 6-13 for the three brazing alloys used in the creep-rupture plate-fin test evaluation. The test results are presented as curves of internal pressure versus time to rupture in figs. 6-11 through 6-14. The predicted pressure capability from average parent metal creep data assuming an ideal fin is also shown as a reference. A least-squares curve fit was used to correlate the test data and is shown on the curve with the correlation factor for each brazing alloy. The correlation factors for Palniro 1, Nicrobraz 30, and the Nicrobraz 210(75 percent)-Nicrobraz 30(25 percent) brazing alloys were 0.965, 0.971, and 0.987, respectively. The high correlation factors give a high degree of confidence in the test data.

The test panel pressure-time curves shown in figs. 6-11, 6-12, and 6-13 are not parallel to the ideal fin curve obtained from the Hastelloy X parent metal creep-rupture data. For Palniro 1 and Nicrobraz 30, this indicates that the creep strength of the two brazing alloys at 1140°K (1600°F) is substantially less than the Hastelloy X parent metal creep strength. The creep strength of Nicrobraz 210(75 percent)-Nicrobraz 30(25 percent) brazing alloy is seen to be more nearly comparable to that of Hastelloy X. It is also noted that the creep strengths of the Palniro 1 samples decrease with decreasing foil thickness in the range of 0.0025 to 0.00076 cm (0.001 to 0.0003 in.).

The plate-fin recuperator testing as related to the recuperator design point is presented in fig. 6-15. Some AiResearch-generated creep data at 1000°K (1350°F) for 0.030-cm (0.012-in.)-thick Hastelloy X material that was pseudo-brazed at the Palniro 1 brazing alloy temperature also is presented in fig. 6-15. The AiResearch data substantiate the parent metal data used from Union Carbide. The parent metal one-percent creep data was reduced by the fin efficiency of the brazing alloy creep-rupture panels (figs. 6-11 through 6-13) in the Larson-Miller region in which the plate-fin creep-rupture testing was performed. The resultant curves (fig. 6-15) show that the Nicrobraz 210(75 percent)-Nicrobraz 30(25 percent) and the Nicrobraz 30 brazing alloys have a creep strength advantage over the Palniro 1 brazing alloy of 1.3 and 1.16, respectively.

Figs. E-55 through E-58 of Appendix E are photomicrographs of the test specimens brazed with Palniro 1 foil thicknesses of 0.0025 cm (0.001 in.), 0.0019 cm (0.00075 in.), 0.0013 cm (0.0005 in.), and 0.00076 cm (0.0003 in.). The photomicrographs are from failed test panels and show the effect of creep damage incurred during the tests. Similar photomicrographs of failed panels brazed with Nicrobraz 30 are shown in fig. E-59.

Figs. E-60 and E-61 show a metallurgical examination of the two panels brazed with Nicrobraz 210(75 percent)-Nicrobraz 30(25 percent). The panel in fig. E-60 ruptured while the panel in fig. E-61 did not. This brazing alloy creeps more than the Hastelloy X, but does exhibit better creep properties than the Palniro 1 or Nicrobraz 30 brazing alloys.



TABLE 6-13

## CREEP TEST RESULTS FOR BRAZING ALLOY EVALUATION

Brazing Alloy	Test Pressure.		Time to Rupture, hr	Strength Ratio*	
	kN/m <sup>2</sup>	psi		Individual	Average
Palniro 1 (AMS 4784)					
0.0008 cm (0.0003 in.)	2200	320	7.4	0.278	0.286
0.0008 cm (0.0003 in.)	2200	320	9.6	0.288	
0.0008 cm (0.0003 in.)	2200	320	11.0	0.294	
0.0013 cm (0.0005 in.)	2200	320	18.2	0.320	0.322
0.0013 cm (0.0005 in.)	2200	320	19.0	0.320	
0.0013 cm (0.0005 in.)	2200	320	21.5	0.328	
0.0019 cm (0.00075 in.)	2200	320	-	-	0.334
0.0019 cm (0.00075 in.)	2200	320	22.2	0.328	
0.0019 cm (0.00075 in.)	2200	320	26.5	0.340	
0.0025 cm (0.001 in.)	2200	320	43.8	0.372	0.391
0.0025 cm (0.001 in.)	2200	320	55.3	0.388	
0.0025 cm (0.001 in.)	2200	320	83.8	0.413	
0.0025 cm (0.001 in.)	3300	480	13.3	0.457	0.466
0.0025 cm (0.001 in.)	3300	480	14.7	0.471	
0.0025 cm (0.001 in.)	3300	480	14.7	0.471	
Microbraz 30, 0.05 gm/cm <sup>2</sup> (0.30 gm/in. <sup>2</sup> )					
	1720	250	243.0	0.384	0.390
	1720	250	252.0	0.384	
	1720	250	342.8	0.403	
	2200	320	116.6	0.438	0.458
	2200	320	148.5	0.457	
	2200	320	197.4	0.478	
	3300	480	38.6	0.552	0.566
	3300	480	49.9	0.565	
	3300	480	57.4	0.582	
Microbraz 210 (75 percent) - Microbraz 30 (25 percent), 0.05 gr/cm <sup>2</sup> (0.30 gm/in. <sup>2</sup> )					
	2200	320	454.0**	0.543	0.541
	2200	320	436.9	0.538	
	3100	450	52.2	0.536	0.566
	3100	450	66.0	0.563	
	3100	450	87.0	0.600	
	4820	700	7.2	0.593	0.601
	4820	700	7.6	0.609	
	5500	800	7.7	0.696	0.696

Note: \* Ratio of test pressure to estimated pressure that would give equal rupture life using parent metal creep rupture properties based on 8 fins/cm (20 fins/in.) and 0.010-cm (0.004-in.) thickness fin geometry.

\*\* Test terminated prior to specimen failure.

ORIGINAL PAGE IS  
OF POOR QUALITY



# CREEP STRENGTH OF PLATE FIN PANELS

MATERIAL: HASTELLOY X

BRAZING ALLOY: AMS 4784 (PALNIRO 1)

0.001-IN. (0.0025 CM)-THICK FOIL

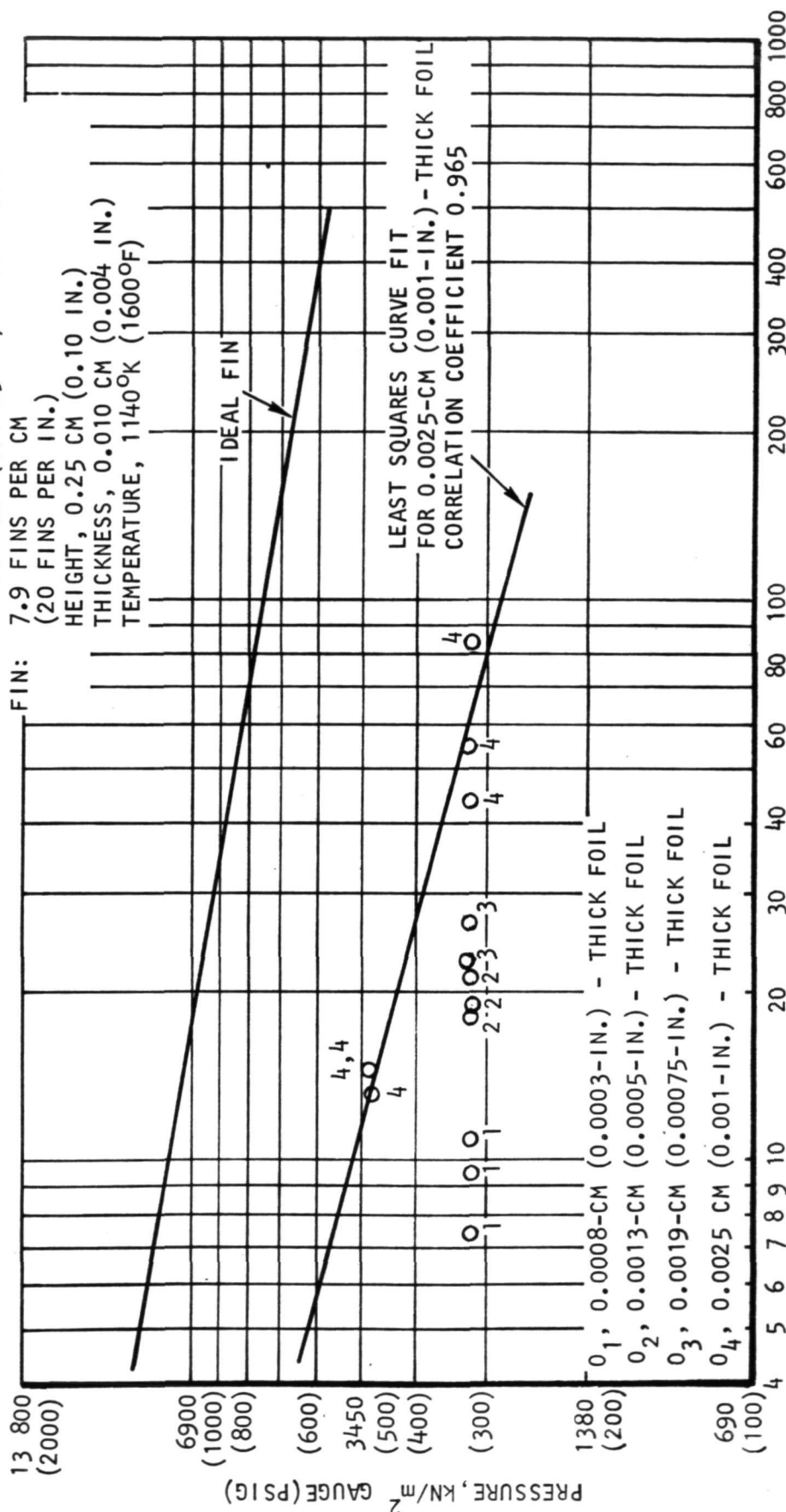
FIN: 7.9 FINS PER CM

(20 FINS PER IN.)

HEIGHT, 0.25 CM (0.10 IN.)

THICKNESS, 0.010 CM (0.004 IN.)

TEMPERATURE, 1140°K (1600°F)



TIME, HR

S-81682-A

Figure 6-11.---Palniro 1 Creep-Rupture Testing.

# CREEP STRENGTH OF PLATE-FIN PANELS

MATERIAL: HASTELLOY X

BRAZING ALLOY: MICROBRAZ 30

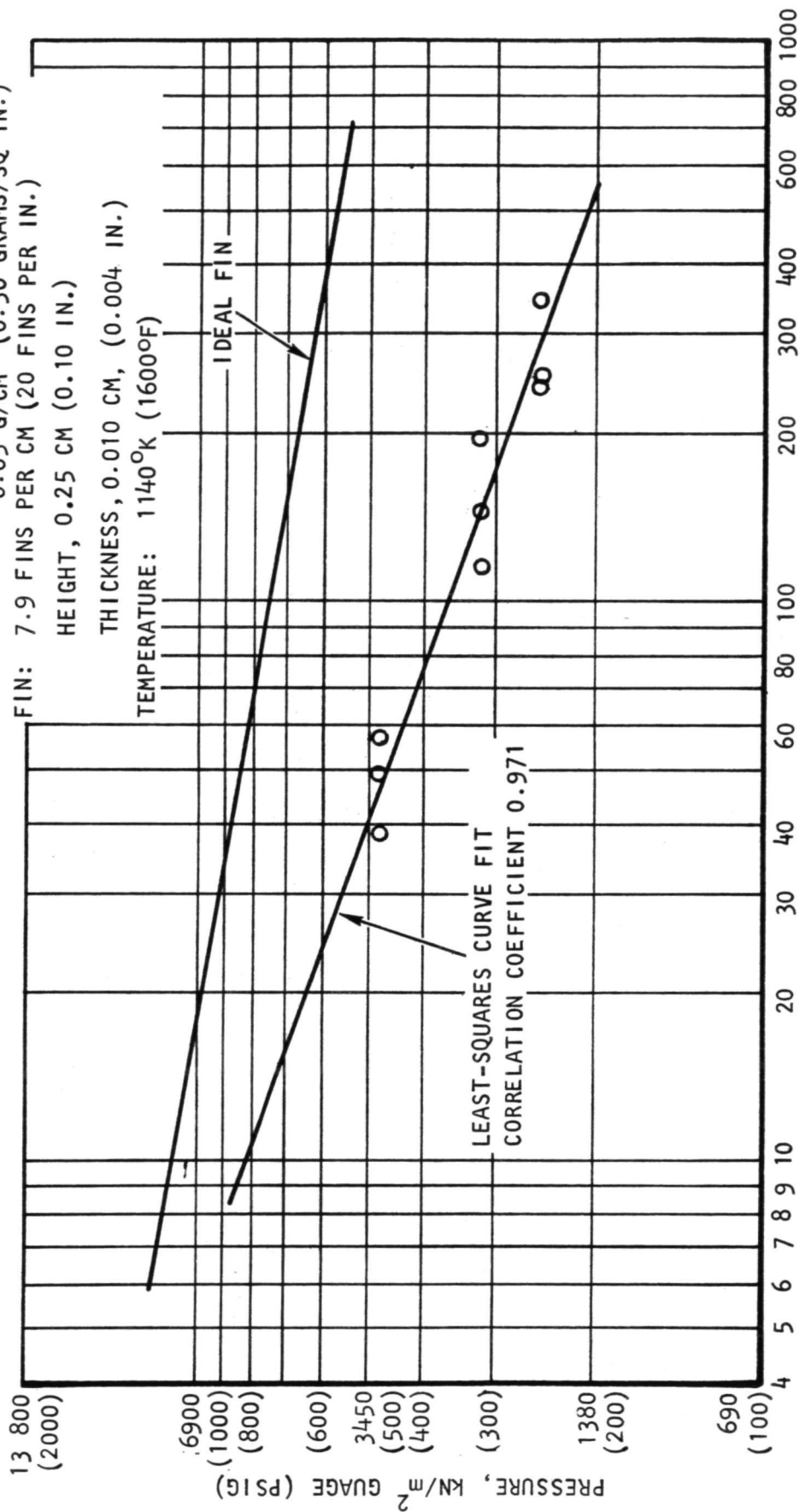
0.05 G/CM<sup>2</sup> (0.30 GRAMS/SQ IN.)

FIN: 7.9 FINS PER CM (20 FINS PER IN.)

HEIGHT, 0.25 CM (0.10 IN.)

THICKNESS, 0.010 CM, (0.004 IN.)

TEMPERATURE: 1140°K (1600°F)



TIME, HR

S-81681-A

Figure 6-12.--Microbraz 30 Creep-Rupture Testing

# CREEP STRENGTH OF PLATE-FIN PANELS

MATERIAL: HASTELLOY X

BRAZING ALLOY: MICROBRAZ 210 (75 PERCENT) - MICROBRAZ 30 (25 PERCENT)  
0.05 CM<sup>2</sup> (0.30 GRAMS/SQ IN.)

FIN: FINS PER IN. 7.9 FINS PER CM, 20 FINS PER IN.

HEIGHT, 0.25 CM (0.10 IN.)

THICKNESS, 0.010 CM (0.004-IN.)

TEMPERATURE: 1140°K (1600°F)

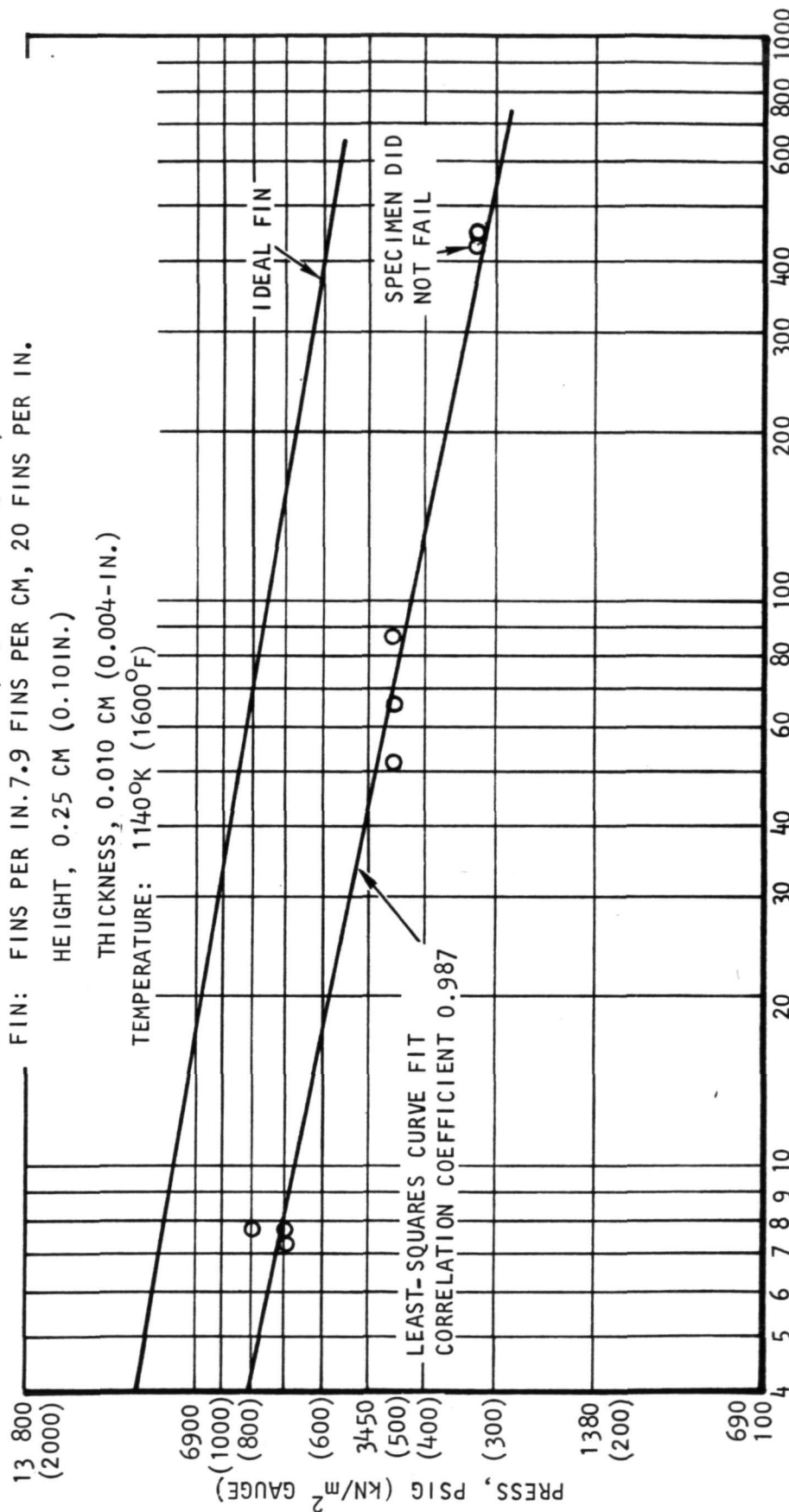


Figure 6-13.---Microbraz 210 (75 percent) - Microbraz 30 (25 percent)  
Creep-Rupture Testing

# CREEP STRENGTH OF PLATE-FIN PANELS

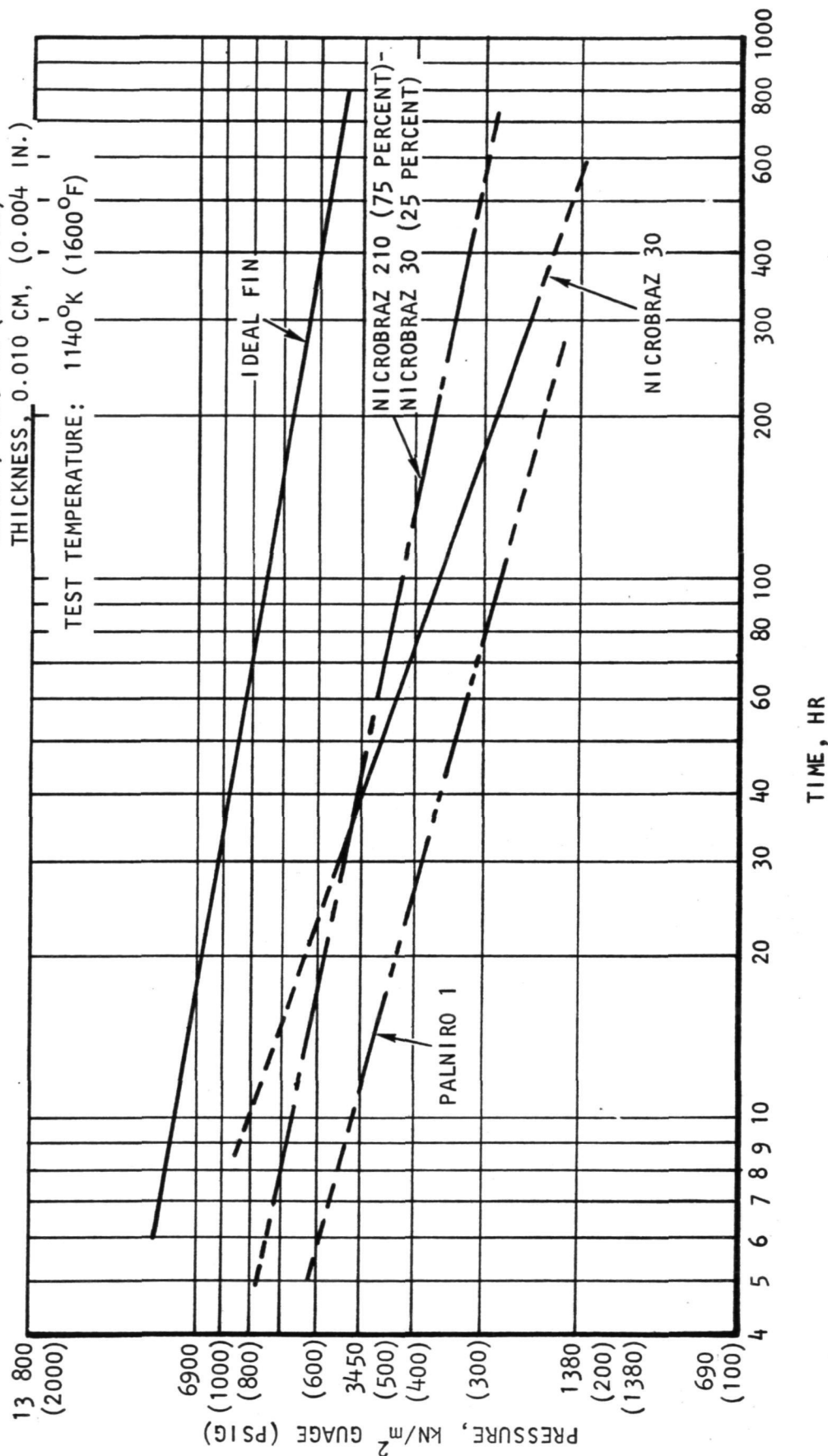
MATERIAL: HASTELLOY X

FIN: 7.9 FINS PER CM, (20 FINS PER IN.)

HEIGHT, 0.25 CM (0.10 IN.)

THICKNESS, 0.010 CM, (0.004 IN.)

TEST TEMPERATURE: 1140°K (1600°F)



S-81680-A

Figure 6-14.--Summary of Brazing Alloy Creep-Rupture Testing

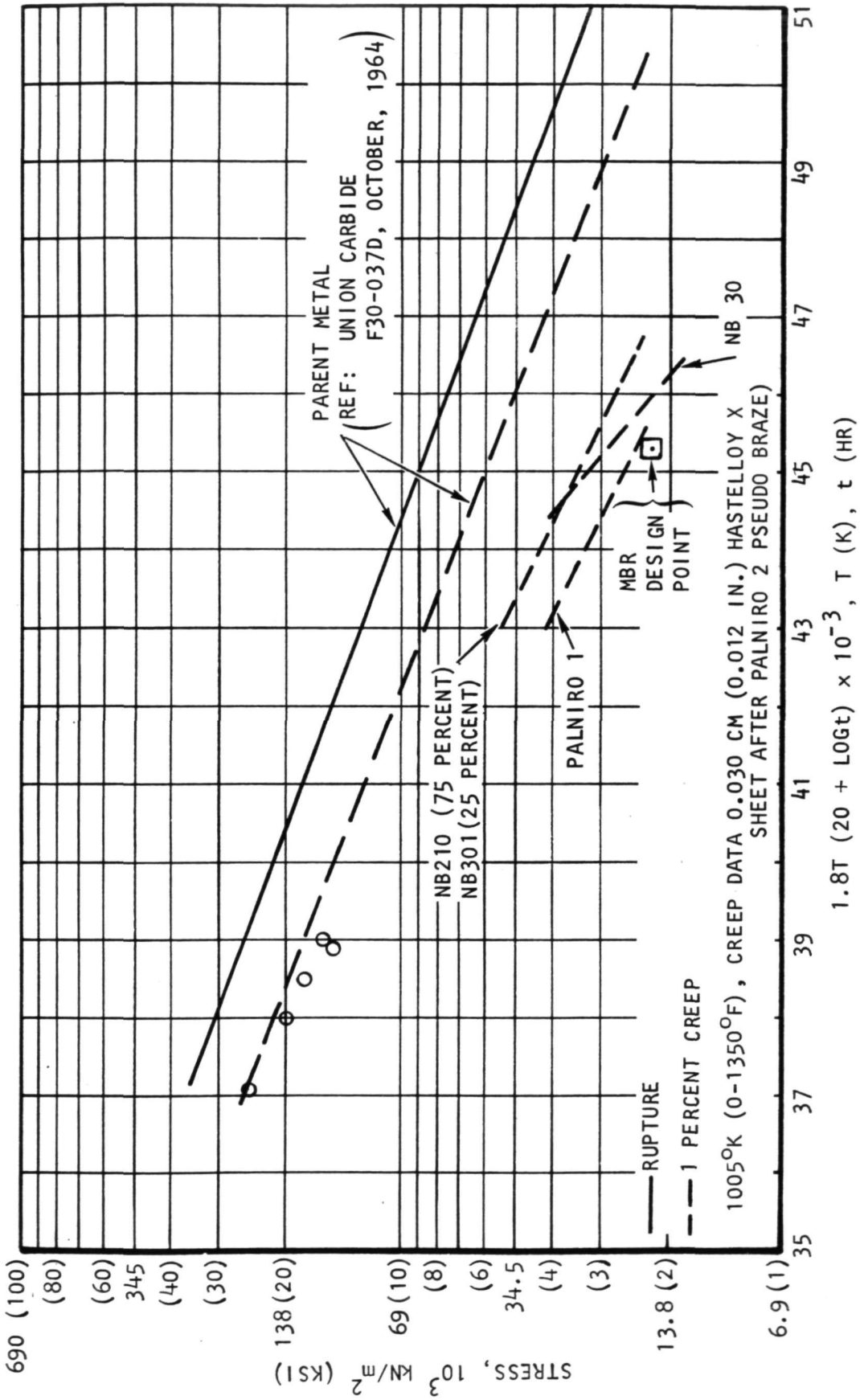


Figure 6-15.--Larson-Miller Curves Showing Plate-Fin Creep-Rupture Testing Related to Mini Brayton-Cycle Recuperator Design Point

### Conclusions

The following comparison of the three braze alloys tested can be made at the recuperator design point:

Larson-Miller parameter	45.3
Design point stress, $10^3$ kN/m <sup>2</sup> (ksi)	15.2 (2.2)
Creep-rupture stress, $10^3$ kN/m <sup>2</sup> (ksi)	
Palniro 1 (0.0025-cm foil)	15.9 (2.3)
NB 30	20.7 (3.0)
NB 210/30	22.8 (3.3)

The higher creep strength exhibited by the low-cost alloys in comparison to Palniro 1 is probably attributable to the larger quantities of these alloys used and the resultant larger fillets formed. Nevertheless, it can be concluded that both Nicrobraz 30 and Nicrobraz 210/30 (75/25) are attractive low-cost alternatives to Palniro 1 on the basis of creep strength.

### TENSILE TESTS

Tensile test data were obtained on 0.025- to 0.30-cm (0.010- to 0.012-in.) thick Hastelloy X material brazed with Palniro 1 and with the combination braze alloy (75 percent Nicrobraz 210/25 percent Nicrobraz 30). The tests were conducted at room temperature and 1005°K (1350°F). The results, shown in table 6-14, indicate that the Nicrobraz 210/30 alloy has ductility comparable to Palniro 1 at 1005°K (1350°F).

TABLE 6-14  
TENSILE DATA FOR HASTELLOY X MATERIAL BRAZED  
WITH 75 PERCENT NICROBRAZ 210, TWENTY-FIVE PERCENT  
NICROBRAZ 30, AND PALNIRO 1

Temperature	Condition	Ultimate Stress, ksi	Yield Stress, ksi	Elongation in 2-in. Sample, Percent
Room Temperature	Pseudo-brazed 1440°K (2135°F)	100	38	40
	NB210 (75 percent) NB30 (25 percent) 1400°K (2135°F)	104	53	16
1005°K (1350°F)	Palniro 1 1405°K (2070°F)	122	58	33

TABLE 6-14 (Concluded)

Temperature	Condition	Ultimate Stress, ksi	Yield Stress, ksi	Elongation in 2-in. Sample, Percent
	NB210 (75 per-cent) and NB30 (25 per-cent 1440°K (2135°F)	80.4	37	31
	Palniro 1* 1405°K (2070°F)	81	35	25

## CONCLUDING REMARKS

A total of twenty-two alloys were originally identified as candidates to replace the gold-base alloys. Tee-section screening tests were performed and based on observations of braze alloy flow, filleting, penetration, and erosion as well as braze temperature a total of seven alloys were selected. Each alloy selected contained chromium, which was believed essential to provide oxidation resistance.

Static oxidation tests were conducted using plate-fin sections. After a total of 3000 hours of exposure the following alloys were considered to have passed: Microbraz 30, 5040, and 5075. Microbraz 210 (AMI 400) also appeared to be acceptable, but the high-braze temperature, 1458°K (2165°F), was known to cause excessive grain growth in Hastelloy X, and this alloy was temporarily dropped.

Mixing of a relatively small percentage (less than 20 percent) of gold-base alloys with low-cost alloys such as NB 30 and NB 210 was found to increase ductility based on microhardness measurements and bend tests.

Additions of Hastelloy X -325 mesh powder to Microbraz 30, 5040, and 5075 was found to reduce braze joint hardness, which should produce increased joint ductility. Parent metal damage was not reduced, however, by the addition of Hastelloy X powder. The data suggest that for minimum intergranular penetration, a low boron-containing alloy such as Microbraz 30 should be used.

Tests with NB 210 using NB 30 as a diluent indicated that the braze alloy flow temperature could be reduced to an acceptable level of 1420°K (2100°F). The most desirable combination of flow with minimum formation of a brittle intermetallic phase was with a mixture of 75 percent NB 210 and 25 percent NB 30.

A final screening test was conducted by using the remaining candidate alloys to braze a small stack of plates, fins, and header bars. After brazing, the corners of the stack were welded to induce a high thermal stress and to check for any adverse metallurgical reactions. Results are listed below.

<u>Braze Alloy</u>	<u>Observation</u>
NB 5040	Extensive braze joint cracking; serious weld joint defects caused by braze alloy remelt.
NB 5075	Same as above.
NB 30 with 10% Palniro 1	Cracks in header bar-to-plate fillets.
NB 210 (75%), NB 30 (25%)	No cracks, good welds.
NB 30	Surface cracks observed in large fillets; good welds.

Based on these results, NB 30 and the combination alloy NB 210/30 were selected for final evaluation. Creep-rupture tests were performed using plate-fin panels at 1144°K (1600°F). Palniro 1 specimens were also tested as a reference material. At the recuperator design point conditions, NB 30 and NB 210/30 were both superior to Palniro 1 in terms of creep-rupture strength. The higher creep strength was attributed to the larger quantity of alloy used which produced larger fillets compared to Palniro 1.

Thus, it was concluded that NB 30 or a combination of NB 210 (75 percent) and NB 30 (25 percent) would be an acceptable low-cost substitute for Palniro 1, the gold-base alloy primarily used in high-temperature Brayton-cycle recuperators. The selected low-cost alloys exhibited acceptable brazing characteristics (flow, filleting and penetration), oxidation resistance, ductility (resistance to cracking), and excellent high-temperature creep strength.

Subsequent evaluation of the NB 210/NB 30 combination alloy in a full-size heat exchanger application indicated a limitation on the application of this alloy. When subjected to a long-duration brazing cycle, that is, more than 3.5 hours above 1250°K (1800°F), the alloy does not fully melt. The mixed alloy exhibits a wide solidus-liquidus range and during a long-duration cycle the NB 210 components do not fully melt. The net result is that the braze joints are too weak to be considered for the recuperator application. All small-scale test specimens were brazed using a cycle that subjected the parts to a total time of 1.5 hours above 1250°K (1800°F) to simulate a full-size heat exchanger cycle. For a cycle of this duration, the combination alloy is believed to be effective.

A long-duration cycle (5 hours above 1250°K (1800°F)) in a vacuum braze furnace is currently used to braze the recuperator submodules described in Section 4. With this long cycle the NB 210/30 combination alloy is not recommended unless the cycle duration is reduced by using a different process, e.g., hydrogen atmosphere brazing.



No adverse effects have been observed using NB 30 in a long-duration braze cycle. The alloy should be effective for the Brayton-cycle recuperator application.

To fully qualify NB 30, small-scale tests should be performed to verify the low-cycle fatigue (LCF) characteristics of typical plate-fin heat exchanger braze joints. Tests would be similar to those described for Palniro 1 alloy in the HXDA Topical Report, NASA CR-121011. Micro hardness measurements and the weld-over-braze tests indicate that NB 30 exhibits adequate ductility and a reasonable LCF life can be expected. LCF testing would establish a data base for NB 30 equivalent to that currently available for Palniro 1.

#### REFERENCES

- 6-1 Monthly Progress Report, "Brayton Cycle Heat Exchanger Technology Program," AiResearch Manufacturing Company of Calif., Report 71-7637(15), Sept 30, 1972.
- 6-2 Ibid, 71-7637(16), Oct 31, 1972.
- 6-3 Ibid, 71-7637(17), Nov 30, 1972.
- 6-4 Ibid, 71-7637(18), Dec 31, 1972.
- 6-5 Richard, C.E.: Low-Cycle Fatigue Evaluation for Regeneratively Cooled Panels. NASA CR-1884. October 1971.



**Page  
Intentionally  
Left Blank**

**Page  
Intentionally  
Left Blank**

Page 1000

1000-1000

1000

Page 1000

1000-1000

1000

## APPENDIX A

### CYCLIC CREEP RELAXATION

The following paragraphs outline a technical approach to be utilized in determining the cyclic damage due to material creep behavior in the thermal fatigue process.

#### NORTON-BAILEY STEADY CREEP LAW

The analytical evaluation of cyclic damage accumulated as a result of material creep behavior must involve the assumption of a basic creep law. If the creep process involves relatively low stresses and large time intervals, primary creep behavior can be neglected and steady creep alone considered. In this case the Norton-Bailey steady creep law (equation A-1) is most widely accepted.

$$\dot{\epsilon} = K (\sigma/\lambda)^n \quad (A-1)$$

where  $K$ ,  $\lambda$ ,  $n$  are constants for a given material at a given temperature

$$\log \dot{\epsilon} = \log K + n \log (\sigma/\lambda) \quad (A-2)$$

From a series of tensile creep tests at the same temperature with variations of applied stress (or load), a plot of strain vs time is obtained resembling the curve in fig. A-1.

The steady strain rate  $\dot{\epsilon}$  is the slope of the straight line portion of the curve (secondary creep regime):

$$\dot{\epsilon} = \frac{\Delta \epsilon}{\Delta t}$$

When the applied stress is divided by an arbitrary constant  $\lambda$ , and the logarithm of the ratio is plotted against the logarithm of the steady creep rate  $\dot{\epsilon}$ , the resulting graph shown in fig. A-2 is a straight line if equation A-2 holds.

From fig. A-1:

$$\log \dot{\epsilon}_2 = \log K + n \log (\sigma_2/\lambda)$$

$$\log \dot{\epsilon}_1 = \log K + n \log (\sigma_1/\lambda)$$

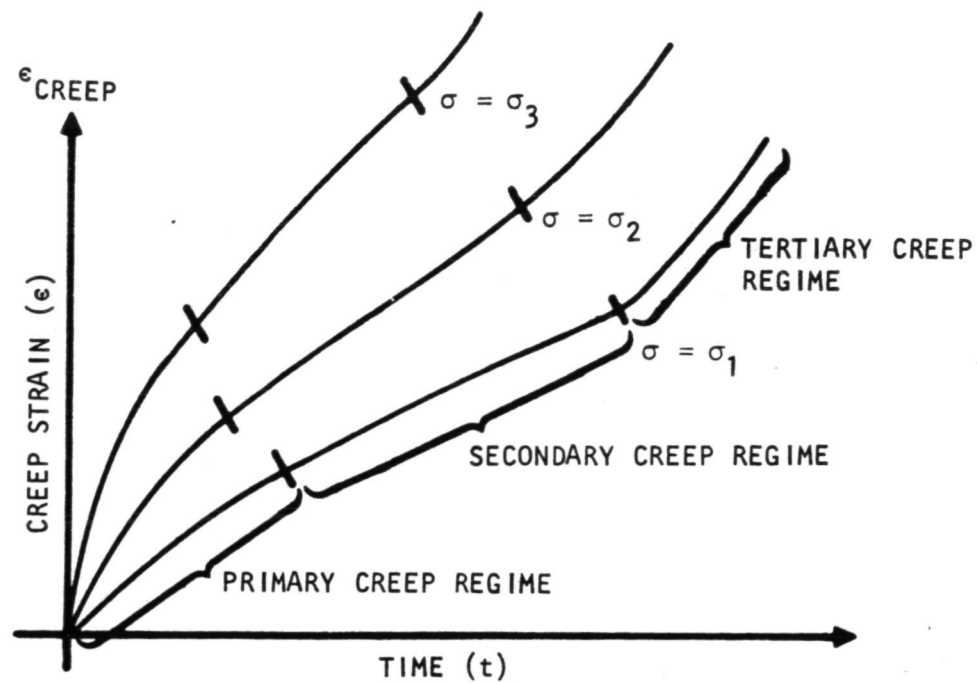


Figure A-1.--Creep Curves for Different Stress Levels.

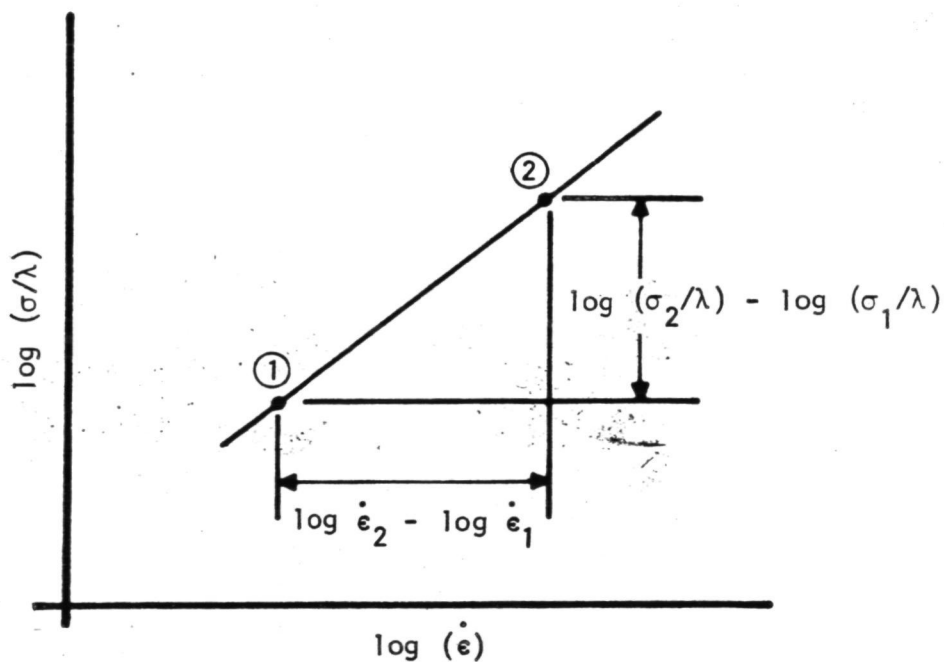


Figure A-2.--Logarithmic Plot for the Determination of the Creep Exponent  $n$ .

$$\text{Thus, } \log \dot{\epsilon}_2 - \log \dot{\epsilon}_1 = n \left[ \log (\sigma_2/\lambda) - \log (\sigma_1/\lambda) \right]$$

$$n = \frac{\log \dot{\epsilon}_2 - \log \dot{\epsilon}_1}{\log (\sigma_2/\lambda) - \log (\sigma_1/\lambda)} \quad (\text{A-3a})$$

or

$$n = \frac{\log (\dot{\epsilon}_2/\dot{\epsilon}_1)}{\log (\sigma_2/\sigma_1)} \quad (\text{A-3b})$$

The plot therefore yields a unique value for  $n$ . The value for  $K$  depends upon the choice of  $\lambda$ . For numerical work it is advantageous to select a value for  $\lambda$  that is slightly larger than the maximum stress ( $\sigma$ ) investigated.

Select:

$$\frac{\sigma}{\lambda} \leq 1$$

#### CREEP RUPTURE

From the mathematical formulation of the Andrades Physical Creep Law, the tensile time to rupture ( $t_{cr}$ ) is defined by:

$$t_{cr} = \int_{\sigma_0}^{\sigma_{ult}} \frac{d[\ln(\sigma)]}{\dot{\epsilon}}$$

where  $\dot{\epsilon} = K (\sigma/\lambda)^n$

and  $d(\ln \sigma) = \frac{d\sigma}{\sigma}$

Thus,

$$t_{cr} = \int_{\sigma_0}^{\sigma_{ult}} \frac{d\sigma}{K(\sigma/\lambda)^n \sigma} = \frac{\lambda^n}{K} \int_{\sigma_0}^{\sigma_{ult}} \frac{d\sigma}{\sigma^{n+1}} = \frac{\lambda^n}{K} \left[ \frac{\sigma^{-n}}{-n} \right]_{\sigma_0}^{\sigma_{ult}}$$

$$= \frac{\lambda^n}{nK} \left[ \sigma^{-n} \right]_{\sigma_{ult}}^{\sigma_0} = \frac{\lambda^n}{nK} \left[ \sigma_0^{-n} - \sigma_{ult}^{-n} \right]$$

$$t_{cr} = \frac{1}{nK} \left[ (\sigma_o/\lambda)^{-n} - (\sigma_{ult}/\lambda)^{-n} \right]$$

$$= \frac{1}{n} \left[ \frac{1}{K(\sigma_o/\lambda)^n} - \frac{1}{K(\sigma_{ult}/\lambda)^n} \right]$$

$$= \frac{1}{n} \left[ \frac{1}{\dot{\epsilon}_o} - \frac{1}{\dot{\epsilon}_{ult}} \right]$$

(A-4)

and since

$$\frac{1}{\dot{\epsilon}_{ult}} \ll \frac{1}{\dot{\epsilon}_o}$$

$$t_{cr} = \frac{1}{n \dot{\epsilon}_o}$$

(A-5)

This assumes failure occurs immediately upon entrance into tertiary creep and primary creep does no damage.

#### STRESS RELAXATION

The initial elastic elongation (strain = constant)

where  $\epsilon_o = \sigma_o/E$

$$\Delta L = \epsilon_o L_o$$

is the initial strain caused by an initial stress. The same elastic elongation should prevail throughout the relaxation process, but creep deformations are developed due to the (initial) applied stress level.

Therefore,

$$\Delta L = L_o (\epsilon_{e1} + \epsilon_{creep}) = L_o \epsilon_o = \text{constant}$$

where  $\sigma$  is the stress at any time and the elastic strain is:

$$\epsilon_{e1} = \sigma/E$$

and the creep strain is

$$\epsilon_{creep} = \epsilon_o - (\sigma/E)$$



Therefore

$$\dot{\epsilon}_{e1} + \dot{\epsilon}_{\text{creep}} = 0$$

For the power law of steady creep:

$$\dot{\epsilon}_{\text{creep}} = K (\sigma/\lambda)^n$$

and

$$(\dot{\sigma}/E) + K (\sigma/\lambda)^n = 0$$

(A-6)

By separation of variables

$$\sigma^{-n} d\sigma = -K \lambda^{-n} E dt$$

and if  $n \neq 1$  the integral becomes

$$\frac{\sigma^{-n+1}}{n-1} = K \lambda^{-n} E t + C$$

and the boundary condition,

$$\sigma = \epsilon_o E = \sigma_o \text{ at } t = 0$$

allows the determination of C

$$C = \frac{\sigma_o^{-n+1}}{n-1}$$

$$\frac{\sigma^{-n+1}}{n-1} - \frac{\sigma_o^{-n+1}}{n-1} = K \lambda^{-n} E t$$

or

$$\frac{\lambda^n}{KE (n-1)} (\sigma^{-n+1} - \sigma_o^{-n+1}) = t$$

(A-7)

#### CREEP STRAIN

When the Norton-Bailey Power Law is applied, the accumulated creep strains attributable to stress relaxation can be determined by substitution of equation A-7 into equation A-1 and performing the integration. From equation A-1:

$$\frac{d\epsilon}{dt} = K (\sigma/\lambda)^n$$

and by rearranging equation A-7

$$\sigma = \left[ \sigma_o^{-n} + 1 + \frac{(n-1)Et}{\lambda^n} \right]^{-\frac{1}{n-1}}$$

the creep strain integral becomes

$$\epsilon_{\text{creep}} = \int_0^{\Delta t} \frac{K}{\lambda^n} \left[ \frac{E K (n-1)}{\lambda^n} t + \sigma_o^{-n+1} \right]^{\frac{-n}{n-1}} dt \quad (\text{A-8})$$

Performing the integration leads to the following expressions for creep strain

$$\epsilon_{\text{creep}} = \frac{1}{E} \left\{ \sigma_o - \left[ \frac{E K (n-1)}{\lambda^n} \Delta t + \sigma_o^{-n+1} \right]^{\frac{1}{1-n}} \right\} \quad (\text{A-9})$$

#### CREEP DAMAGE INTEGRAL

Creep damage during relaxation from the initial prestress ( $\sigma_o$ ) to a stress ( $\sigma$ ) at some later time  $t$  is (as shown in fig. A-3):

$$\Phi_{\text{creep}} = \int_{\text{to}}^t \frac{1}{(t_{\text{cr}})} dt \quad (\text{secondary creep damage})$$

$$t_{\text{cr}} = \frac{1}{n} \left[ \frac{1}{\dot{\epsilon}} - \frac{1}{\dot{\epsilon}_{\text{ult}}} \right]$$

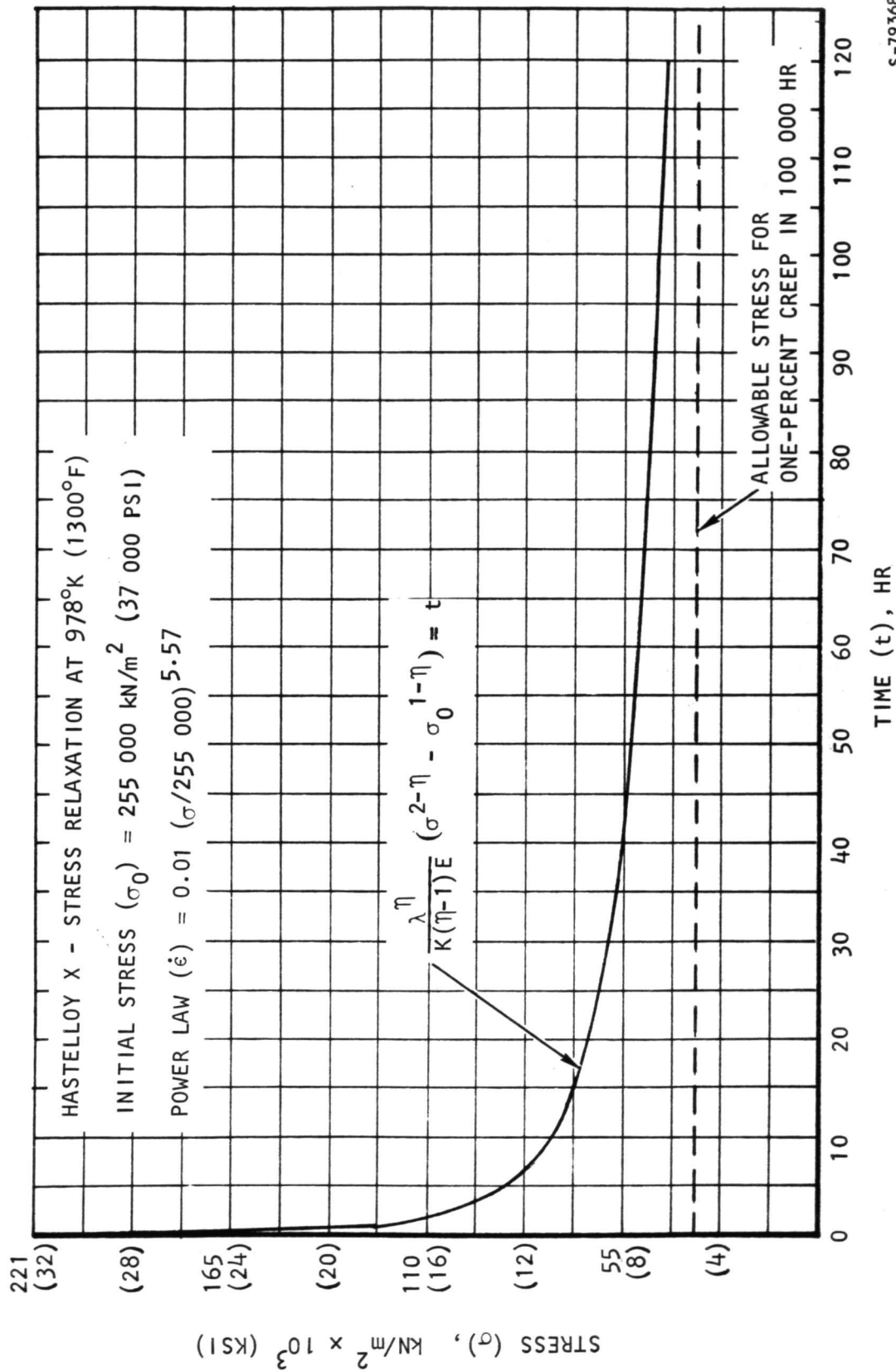
When the creep rate ( $\dot{\epsilon}$ ) is related to stress ( $\sigma$ ) by the Norton-Bailey Power Law, the critical time to cause creep rupture is obtained as follows. The power law is:

$$\dot{\epsilon} = K (\sigma/\lambda)^n$$

And since

$$\frac{1}{\dot{\epsilon}_{\text{ult}}} \ll \frac{1}{\dot{\epsilon}}$$

$$t_{\text{cr}} = \frac{1}{n\dot{\epsilon}} = \frac{1}{nK(\sigma/\lambda)^n} \quad \text{and} \quad \frac{1}{t_{\text{cr}}} = nK (\sigma/\lambda)^n$$



S-79368 -A

Figure A-3. Stress Relaxation of Hastelloy X at 978°K

where

$$\sigma = \left[ \sigma_o^{-n+1} + \frac{K(n-1) Et}{\lambda^n} \right]^{-\frac{1}{n-1}}$$

Thus, the creep damage integral becomes

$$\Phi_{\text{creep}} = \int_0^{\Delta t} \frac{nK}{\lambda^n} \left[ \sigma_o^{-n+1} + \frac{K(n-1)E}{\lambda^n} t \right]^{-\frac{n}{n-1}}$$

Performing the integration leads to the following:

$$\Phi_{\text{creep}} = \frac{n}{E} \left\{ \sigma_o - \left[ \frac{K(n-1)E}{\lambda^n} \Delta t + \sigma_o^{-n-1} \right]^{\frac{1}{n-1}} \right\} \quad (\text{A-10})$$

and by substitution of the expression for accumulated creep strain ( $\epsilon_{\text{creep}}$ ) as defined in Equation A-9, the creep damage life fraction becomes

$$\Phi_{\text{creep}} = n \epsilon_{\text{creep}} \quad (\text{A-11})$$

A typical stress relaxation curve (stress vs time) is depicted in fig. A-3.

To implement the rapid computation of the preceding derivation, a computer program was developed. A plot of the Norton-Bailey Power Law and the stress relaxation curve obtained from the program is shown in figs. A-4 and A-5, respectively.

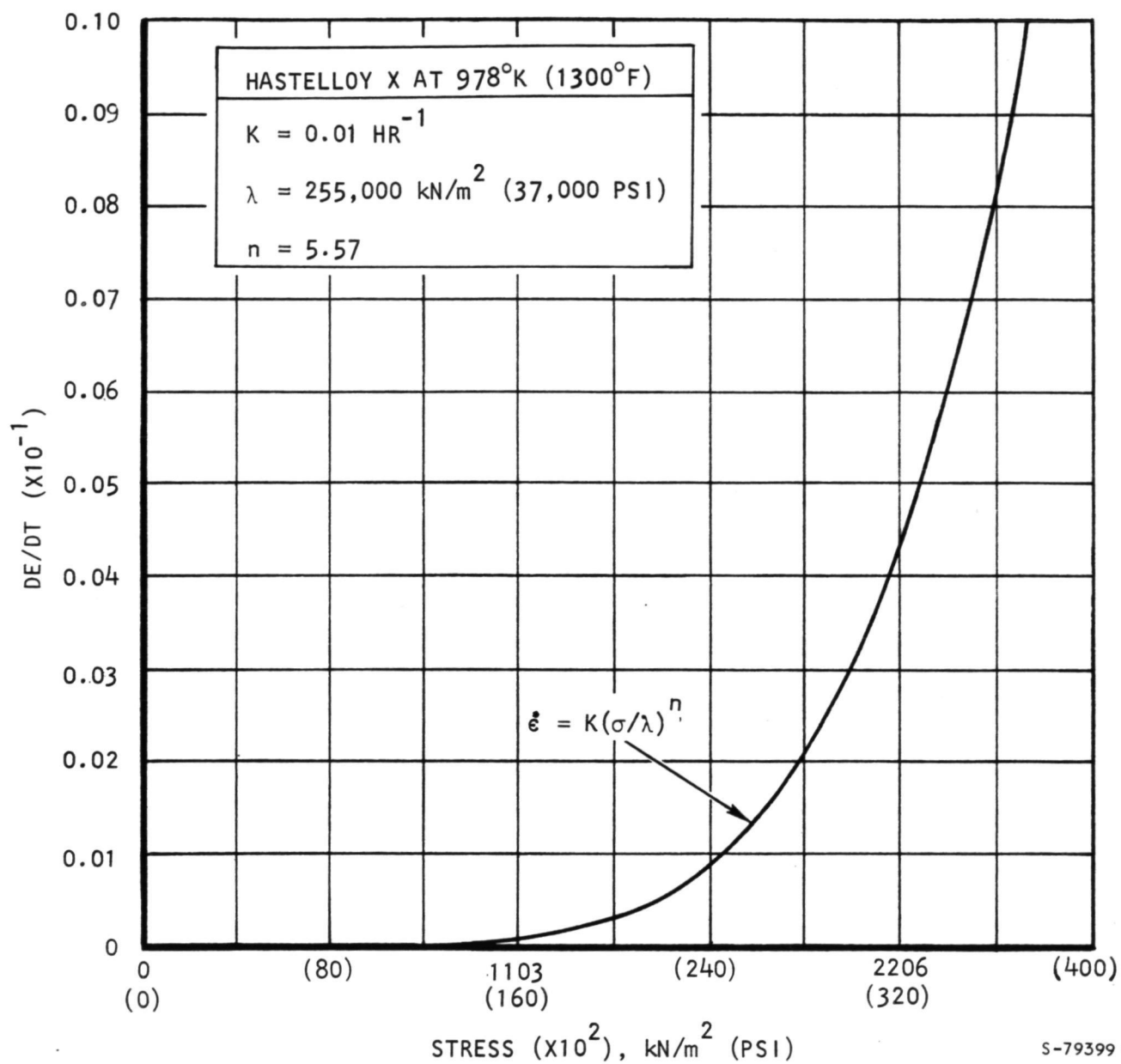
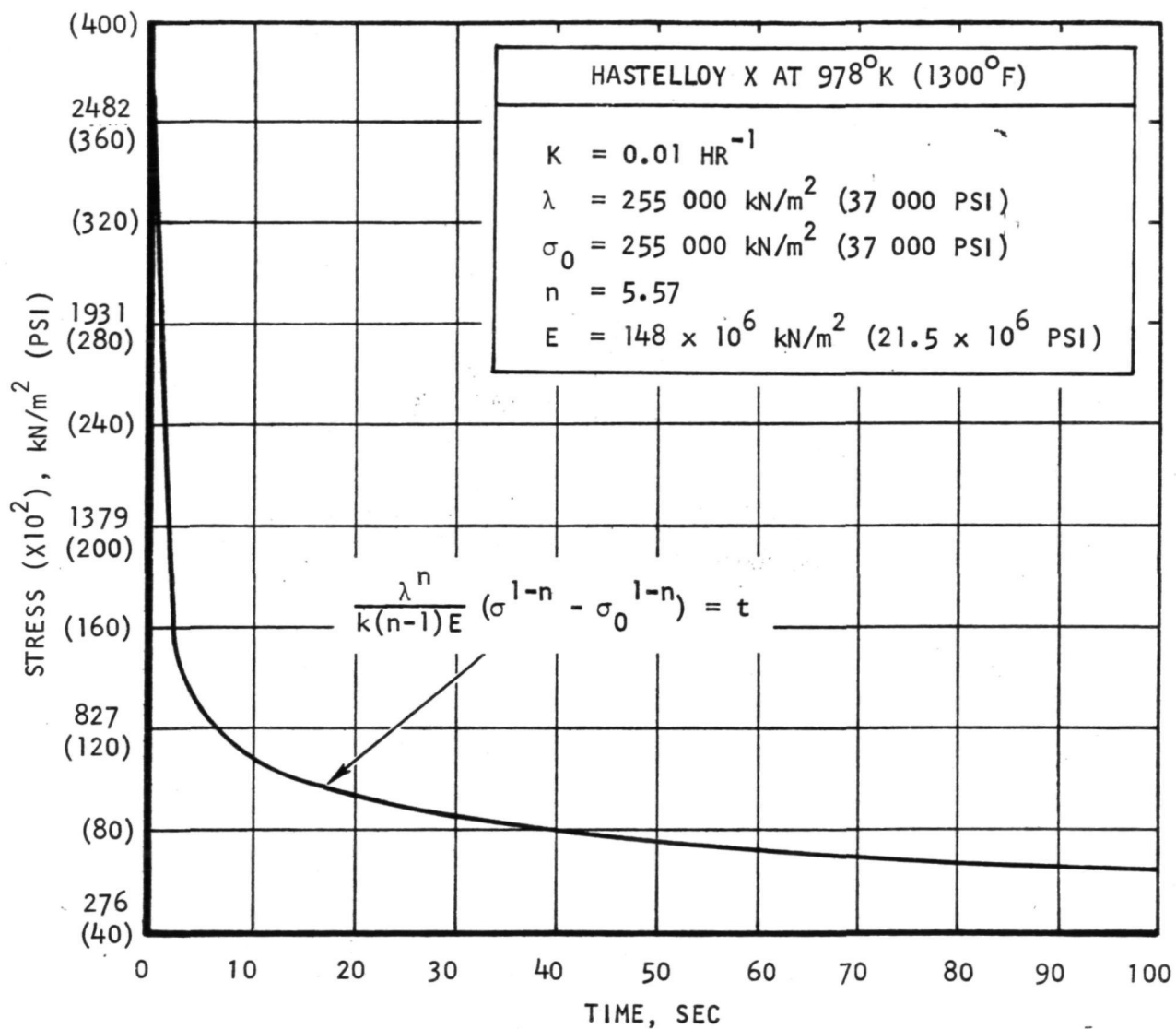


Figure A-4. Norton-Bailey Power Law for Hastelloy X at 978°K (1300°F)



S-79398 -A

Figure A-5. Stress Relaxation of Hastelloy X at 978°K (1300°F)

**Page  
Intentionally  
Left Blank**

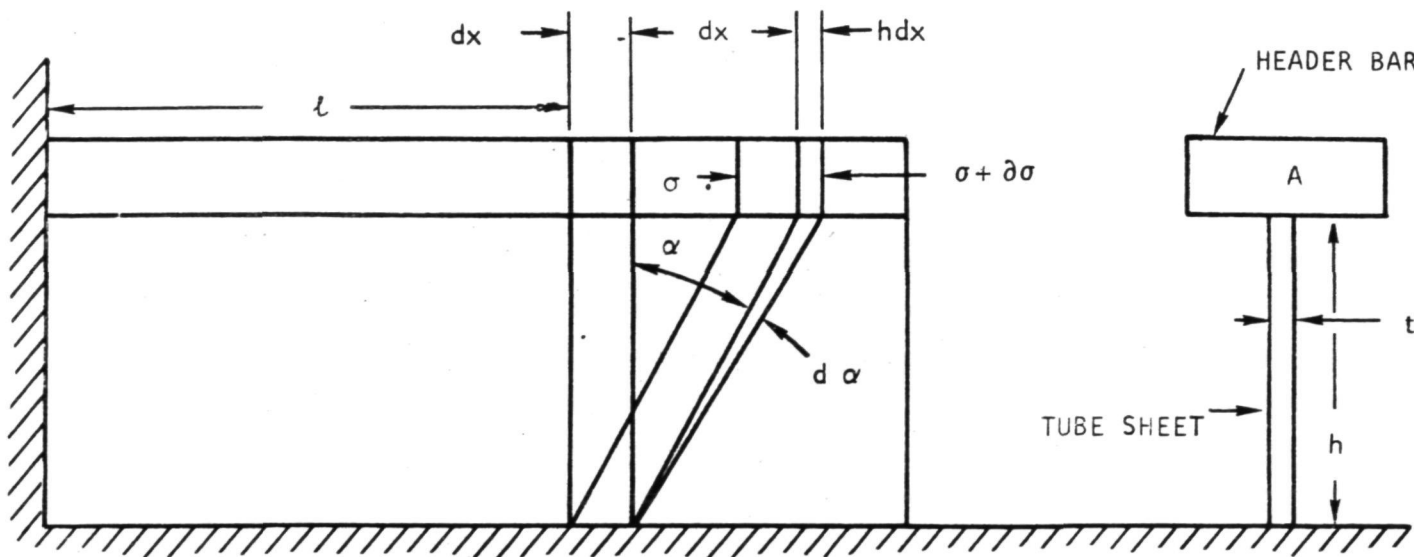




## APPENDIX B

### DERIVATION OF SHEAR LAG FORMULA

Thermal stresses develop in a bar and sheet structure when the bar is very thick compared to the sheet and the thin sheet is subjected to extremely high heat flux. This thermal stress problem arises in the recuperator matrix during a startup transient when the sheet temperature can be as much as 300°F above that of the bar. Derivation of the formulas for tensile stress in the bar and the shear stress in the sheet as a result of this condition are presented below.



S-80666

Analytical Model

Change in length of  $dx$ :

$$1. \quad h \, d\alpha = \mu \Delta T \, dx - \frac{\sigma}{E} \, dx$$

$$2. \quad \frac{d\alpha}{dx} = \frac{1}{h} \left( \mu \Delta T - \frac{\sigma}{E} \right)$$

where  $\Delta T$  = difference in temperature between bar and sheet

$\mu$  = coefficient of expansion

Summing forces on element  $dx$

$$3. \quad A\sigma - \left[ A \left( \sigma + \frac{\partial \sigma}{\partial x} \, dx \right) + G\alpha \, dx \, t \right] = 0$$

$$- \left[ A \frac{\partial \sigma}{\partial x} + Gdt \right] = 0$$

$$4. \quad \frac{\partial \sigma}{\partial x} = - \frac{G\alpha t}{A}$$

$$5. \quad \alpha = \frac{-A}{Gt} \frac{\partial \sigma}{\partial x}$$

$$6. \quad \frac{\partial \alpha}{\partial x} = \frac{-A}{Gt} \frac{\partial^2 \sigma}{\partial x^2} \quad \text{Differentiated equation 5}$$

Equate 2 and 6.

$$7. \quad -\frac{A}{Gt} \frac{\partial^2 \sigma}{\partial x^2} = \frac{1}{h} \left( \mu \Delta T - \frac{\sigma}{E} \right)$$

$$8. \quad -\frac{\partial^2 \sigma}{\partial x^2} = \frac{Gt}{Ah} \left( \mu \Delta T - \frac{\sigma}{E} \right)$$

$$9. \quad \frac{\partial^2 \sigma}{\partial x^2} - \frac{Gt}{AhE} \sigma = -\frac{Gt}{AhE} \cdot \mu \Delta TE$$

$$\text{Let } U^2 = \frac{Gt}{AhE}$$

$$U = \sqrt{\frac{Gt}{AhE}}$$

$$\text{and } V = \mu \Delta TE$$

$$10. \quad \frac{\partial^2 \sigma}{\partial x^2} - U^2 \sigma = -U^2 V$$

Integrating

$$11. \quad \sigma = c \cosh Ux + D \sinh Ux +$$

The boundary conditions are

$$\text{When } x = 0, \sigma = 0, \frac{\partial \sigma}{\partial x} = 0$$

$$\alpha = l, \sigma = 0$$

$$12. \quad \frac{\partial \sigma}{\partial x} = UC \sinh Ux + UD \cosh Ux$$

$$\frac{\partial \sigma(0)}{\partial x} = 0 = UD$$

$$\therefore D = 0$$

$$13. \quad \sigma(l) = 0 = \cosh Ul + V$$

$$\therefore C = -\frac{V}{\cosh Ul}$$

$$14. \quad \sigma = V \left( 1 - \frac{\cosh Ux}{\cosh Ul} \right)$$

$$15. \quad \sigma = \mu \Delta T E \left( 1 - \frac{\cosh Ux}{\cosh U\ell} \right)$$

$$\text{where } U = \sqrt{\frac{Gt}{AhE}}$$

$$16. \quad \text{From 5. } \tau = G\alpha = -\frac{A}{t} \frac{\partial \sigma}{\partial x}$$

$$17. \quad \frac{\partial \sigma}{\partial x} = -\mu \Delta T E U \frac{\sinh Ux}{\cosh U\ell} \quad \text{from 16}$$

Combining 16 and 17.

$$\begin{aligned} 18. \quad \tau &= \frac{\mu \Delta T E U A}{t} \frac{\sinh Ux}{\cosh U\ell} \\ &= \mu \Delta T \frac{EA}{t} \sqrt{\frac{Gt}{AhE}} \frac{\sinh Ux}{\cosh U\ell} \\ &= \mu \Delta T \sqrt{\frac{E^2 A^2 Gt}{t^2 AhE}} \frac{\sinh Ux}{\cosh U\ell} \\ &= \mu \Delta T \sqrt{\frac{EGA}{ht}} \frac{\sinh Ux}{\cosh U\ell} \end{aligned}$$

$$19. \quad \text{At } x = 0 \quad \sigma = \sigma_{\max.}$$

$$\sigma_{\max} = \mu \Delta T E \left( 1 - \frac{1}{\cosh U\ell} \right)$$

$$20. \quad \text{At } x = \ell \quad \tau = \tau_{\max}$$

$$\tau_{\max} = \mu \Delta T \sqrt{\frac{EGA}{ht}} \tanh U\ell$$

**Page  
Intentionally  
Left Blank**



APPENDIX C  
BELLOWS DESIGN

This appendix describes the various formulations used in the parametric study of the bellows design.

EXTENSIONAL, LATERAL, AND BENDING STIFFNESSES

Extensional stiffness,  $K_A$ , is obtained from the shell analysis computer program using the half-convolute model shown in fig. 5-2(c) of Section 5 and its value is given by

$$K_A = \frac{n}{c} \times \frac{F_A}{(2 \times \delta_A)} \quad (C-1)$$

where

$F_A$  = force in axial direction due to axial displacement,  $\delta_A$

$\delta_A$  = axial deflection

$n$  = no. of plies

$c$  = no. of convolutions

The lateral and bending stiffnesses are expressed in terms of extensional stiffness as follows:

$$K_L = 6 \left( \frac{\bar{R}}{L} \right)^2 K_A \quad (C-2)$$

$$K_B = \frac{1}{2} (\bar{R})^2 K_A \quad (C-3)$$

where

$K_L$  = lateral stiffness

$K_B$  = bending stiffness

$\bar{R}$  = mean radius of the bellow (see fig. 5-3(a) of Section 5)

$L$  = length of the bellow

## FLANGE LOADS AND STRESSES DUE TO AXIAL, LATERAL, AND ROTATIONAL MOVEMENTS

Flange loads due to the various movements of the bellows as shown in fig. C-1 are given by

$$F_A = K_A \delta_A \quad (C-4)$$

$$F_L = K_L \delta_L \quad (C-5)$$

$$M_L = \frac{F_L \times L}{2} \quad (C-6)$$

$$M_\theta = K_B \theta \quad (C-7)$$

where

$F_A$  = axial force due to axial displacement,  $\delta_A$

$F_L, M_L$  = lateral force and moment, respectively, due to lateral offset,  $\delta_L$

$M_\theta$  = movement due to the angular rotation,  $\theta$

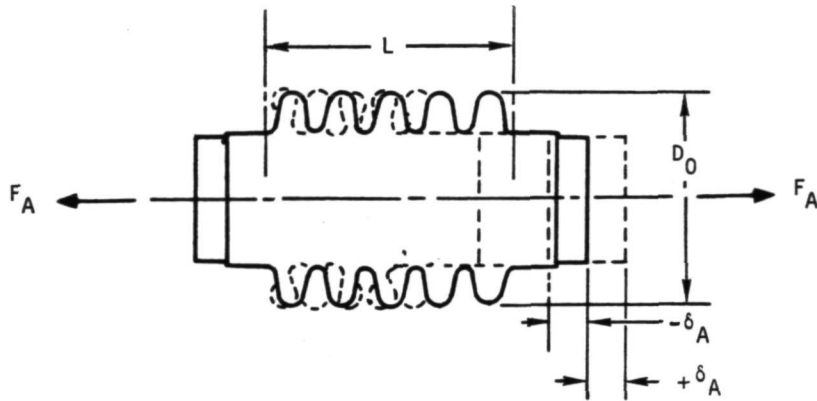
## SQUIRM PRESSURE

The squirm (critical) pressure is calculated using the following formula:\*

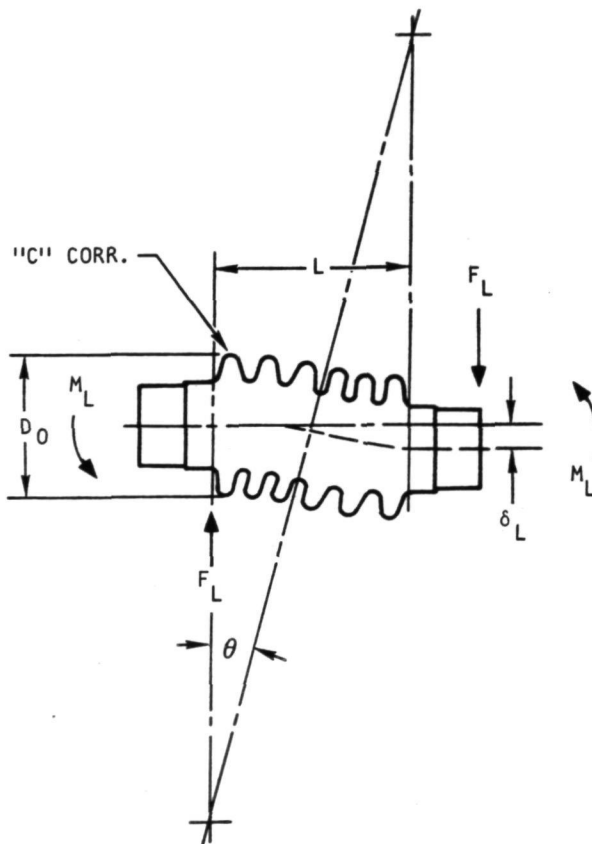
$$P_{cr} = \frac{\pi K_A}{2L} \quad (C-8)$$

\* Graves, R. W., "Analysis of Load Deflections and Buckling Behavior of Metal Bellows", M.S. Thesis, University of California, Los Angeles, December, 1960.

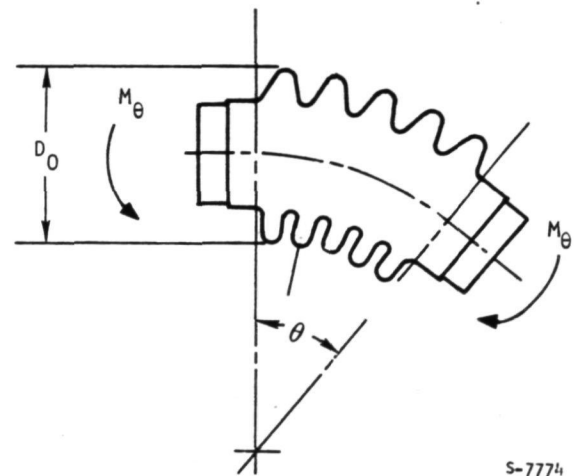




(a) AXIAL MOVEMENT =  $\delta_A$



(b) LATERAL MOVEMENT =  $\delta_L$



(c) ANGULAR ROTATION =  $\theta$

Figure C-1. Axial, Lateral, and Angular Movements of Bellows.



**Page  
Intentionally  
Left Blank**



## APPENDIX D

### BELLOWS DESIGN SUMMARIES

This appendix summarizes the results of the baseline bellows design for each convolution shape and for the following materials:

1. Rene-41
2. Haynes 188
3. Hastelloy X
4. Ta-10W

The bellows convolution shape parameters, inside radius, height, pitch, and bend radius are defined in fig. 5-3 of Section 5.

TABLE D-1

SHAPE 5.4\* HIGH-TEMPERATURE BELLOWS DESIGNS FOR EACH CANDIDATE MATERIAL

Candidate Materials	Rene' 41	Haynes 188	Hastelloy X
Allowable sustained bending stress, MN/m <sup>2</sup> (psi)	57.0 (8250)	31.0 (4500)	25.5 (3700)
Allowable sustained direct stress, MN/m <sup>2</sup> (psi)	38.0 (5500)	20.7 (3000)	17.3 (2500)
Allowable cyclic thermal stress, MN/m <sup>2</sup> (psi)	830.0 (120 000)	394.0 (57 000)	155.0 (22 500)
Thickness per ply, mm (in.)	0.0508 (0.020)	0.0762 (0.030)	0.1016 (0.040)
Active length, cm (in.)	30.23 (11.9)	56.90 (22.4)	80.01 (31.5)
Number of plies	6	7	6
Number of convolutions	17	32	45
Extensional stiffness, kN/m (lb/in.)	816 (4660)	1530 (8750)	2120 (12 090)
Deflection capability, cm (in.)	3.63 (1.43)	2.05 (0.81)	0.80 (0.32)
Bending stiffness, N-m/radian (in.-lb/radian)	4760 (42 100)	8930 (79 000)	12 300 (109 200)
Lateral offset stiffness, kN/m (lb/in.)	630 (3600)	333 (1900)	228 (1300)

\*See fig. 5-3 of Section 5.

TABLE D-2

SHAPE 5.5\* HIGH-TEMPERATURE BELLOWS DESIGNS FOR EACH CANDIDATE MATERIAL

Candidate Materials	Ta-10W	Rene' 41	Haynes 188	Hastelloy X
Allowable sustained bending stress, $\text{MN/m}^2$ (psi)	207 (30 000)	57.0 (8250)	31.0 (4500)	25.5 (3700)
Allowable sustained direct stress, $\text{MN/m}^2$ (psi)	138 (20 000)	38.0 (5500)	20.7 (3000)	17.3 (2500)
Allowable cyclic thermal stress, $\text{MN/m}^2$ (psi)	621 (90 000)	830.0 (120 000)	394.0 (57 000)	155.0 (22 500)
Thickness per ply, mm (in.)	0.02 (0.008)	0.0508 (0.020)	0.0762 (0.030)	0.0762 (0.030)
Active length, cm (in.)	9.14 (3.6)	27.43 (10.8)	48.77 (19.2)	53.34 (21.0)
Number of plies	7	6	6	7
Number of convolutions	6	18	32	35
Extensional stiffness, $\text{kN/m}$ (lb/in.)	385 (1412)	748 (4270)	1340 (7630)	1430 (8140)
Deflection capability, cm (in.)	2.2 (0.866)	3.48 (1.37)	1.90 (0.75)	0.80 (0.32)
Bending stiffness, $\text{N-m/radian}$ (in.-lb/radian)	1445 (12 800)	4360 (38 600)	7780 (68 900)	8300 (73 500)
Lateral offset stiffness, $\text{kN/m}$ (lb/in.)	2065 (11 800)	700 (4000)	385 (2200)	350 (2000)

\*See fig. 5-3 of Section 5.

TABLE D-3

SHAPE 5.6\* HIGH-TEMPERATURE BELLOWS DESIGNS FOR EACH CANDIDATE MATERIAL

Candidate Materials	Rene' 41	Haynes 188	Hastelloy X
Allowable sustained bending stress, $\text{MN/m}^2$ (psi)	57.0 (8250)	31.0 (4500)	25.5 (3700)
Allowable sustained direct stress, $\text{MN/m}^2$ (psi)	38.0 (5500)	20.7 (3000)	17.3 (2500)
Allowable cyclic thermal stress, $\text{MN/m}^2$ (psi)	830.0 (120 000)	394.0 (57 000)	155.0 (22 500)
Thickness per ply, mm (in.)	0.0508 (0.020)	0.0762 (0.030)	0.0762 (0.030)
Active length, cm (in.)	25.40 (10.0)	41.91 (16.5)	45.72 (18.0)
Number of plies	6	5	6
Number of convolutions	20	33	36
Extensional stiffness, $\text{kN/m}$ (lb/in.)	680 (3890)	1130 (6440)	1240 (7080)
Deflection capability, cm (in.)	3.51 (1.38)	1.76 (0.69)	0.78 (0.31)
Bending stiffness, $\text{N-m/radian}$ (in.-lb/radian)	3970 (35 100)	6580 (58 200)	7220 (63 900)
Lateral offset stiffness, $\text{kN/m}$ (lb/in.)	735 (4200)	455 (2600)	420 (2400)

\*See fig. 5-3 of Section 5.



TABLE D-4

SHAPE 6.5\*HIGH-TEMPERATURE BELLOWS DESIGNS FOR EACH CANDIDATE MATERIAL

Candidate Materials	Rene' 41	Haynes 188	Hastelloy X
Allowable sustained bending stress, $\text{MN/m}^2$ (psi)	57.0 (8250)	31.0 (4500)	25.5 (3700)
Allowable sustained direct stress, $\text{MN/m}^2$ (psi)	38.0 (5500)	20.7 (3000)	17.3 (2500)
Allowable cyclic thermal stress, $\text{MN/m}^2$ (psi)	830.0 (120 000)	394.0 (57 000)	155.0 (22 500)
Thickness per ply, mm (in.)	0.0762 (0.030)	0.1016 (0.040)	0.1016 (0.040)
Active length, cm (in.)	32.00 (12.6)	52.58 (20.7)	57.15 (22.5)
Number of plies	5	6	7
Number of convolutions	14	23	25
Extensional stiffness, $\text{kN/m}$ (lb/in.)	919 (5250)	1460 (8320)	1560 (8930)
Deflection capability, cm (in.)	4.32 (1.70)	2.37 (0.93)	1.03 (0.41)
Bending stiffness, $\text{N-m/radian}$ (in.-lb/radian)	5670 (50 200)	8990 (79 600)	9660 (85 500)
Lateral offset stiffness, $\text{kN/m}$ (lb/in.)	665 (3800)	385 (2200)	350 (2000)

\*See fig. 5-3 of Section 5.

TABLE D-5

SHAPE 6.6\* HIGH-TEMPERATURE BELLOWS DESIGNS FOR EACH CANDIDATE MATERIAL

Candidate Materials	Rene' 41	Haynes 188	Hastelloy X
Allowable sustained bending stress, $\text{MN/m}^2$ (psi)	57.0 (8250)	31.0 (4500)	25.5 (3700)
Allowable sustained direct stress, $\text{MN/m}^2$ (psi)	38.0 (5500)	20.7 (3000)	17.3 (2500)
Allowable cyclic thermal stress, $\text{MN/m}^2$ (psi)	830.0 (120 000)	394.0 (57 000)	155.0 (22 500)
Thickness per ply, mm (in.)	0.0762 (0.030)	0.1016 (0.040)	0.1016 (0.040)
Active length, cm (in.)	32.39 (12.75)	47.63 (18.75)	55.25 (2175)
Number of plies	6	6	8
Number of convolutions	17	25	29
Extensional stiffness, $\text{kN/m}$ (lb/in.)	872 (4980)	1340 (7660)	1540 (8800)
Deflection capability, cm (in.)	4.57 (1.80)	2.29 (0.90)	1.05 (0.41)
Bending stiffness, $\text{N-m/radian}$ (in.-lb/radian)	5390 (47 700)	8280 (73 300)	9510 (84 200)
Lateral offset stiffness, $\text{kN/m}$ (lb/in.)	613 (3500)	438 (2500)	368 (2100)

\*See fig. 5-3 of Section 5.

TABLE D-6

SHAPE 6.7<sup>1</sup>HIGH-TEMPERATURE BELLOWS DESIGNS FOR EACH CANDIDATE MATERIAL

Candidate Materials	Rene' 41	Haynes 188	Hastelloy X
Allowable sustained bending stress, $\text{MN/m}^2$ (psi)	57.0 (8250)	31.0 (4500)	25.5 (3700)
Allowable sustained direct stress, $\text{MN/m}^2$ (psi)	38.0 (5500)	20.7 (3000)	17.3 (2500)
Allowable cyclic thermal stress, $\text{MN/m}^2$ (psi)	830.0 (120 000)	394.0 (57 000)	155.0 (22 500)
Thickness per ply, mm (in.)	0.0762 (0.030)	0.1016 (0.040)	0.1016 (0.040)
Active length, cm (in.)	28.96 (11.4)	42.24 (18.6)	51.82 (20.4)
Number of plies	6	7	8
Number of convolutions	19	31	34
Extensional stiffness, $\text{kN/m}$ (lb/in.)	792 (4520)	1320 (7520)	1370 (7840)
Deflection capability, cm (in.)	4.52 (1.78)	2.60 (1.02)	1.14 (0.45)
Bending stiffness, $\text{N-m/radian}$ (in.-lb/radian)	4890 (43 300)	8130 (72 000)	8470 (75 000)
Lateral offset stiffness, $\text{kN/m}$ (lb/in.)	700 (4000)	438 (2500)	385 (2200)

\*See fig. 5-3 of Section 5.

TABLE D-7

SHAPE 7.6\*HIGH-TEMPERATURE BELLOWS DESIGNS FOR EACH CANDIDATE MATERIAL

Candidate Materials	Rene' 41	Haynes 188	Hastelloy X
Allowable sustained bending stress, $\text{MN/m}^2$ (psi)	57.0 (8250)	NO FEASIBLE DESIGN	NO FEASIBLE DESIGN
Allowable sustained direct stress, $\text{MN/m}^2$ (psi)	38.0 (5500)		
Allowable cyclic thermal stress, $\text{MN/m}^2$ (psi)	830.0 (120 000)		
Thickness per ply, mm (in.)	0.1016 (0.040)		
Active length, cm (in.)	38.10 (15.0)		
Number of plies	6		
Number of convolutions	15		
Extensional stiffness, $\text{kN/m}$ (lb/in.)	1080 (6180)		
Deflection capability, cm (in.)	5.64 (2.22)	NO FEASIBLE DESIGN	NO FEASIBLE DESIGN
Bending stiffness, $\text{N-m/radian}$ (in.-lb/radian)	7070 (62 600)		
Lateral offset stiffness, $\text{kN/m}$ (lb/in.)	578 (3300)		

\*See fig. 5-3 of Section 5.

TABLE D-8

SHAPE 7.7\*HIGH-TEMPERATURE BELLOWS DESIGNS FOR EACH CANDIDATE MATERIAL

Candidate Materials	Rene' 41	Haynes 188	Hastelloy X
Allowable sustained bending stress, $\text{MN/m}^2$ (psi)	57.0 (8250)	NO FEASIBLE DESIGN	NO FEASIBLE DESIGN
Allowable sustained direct stress, $\text{MN/m}^2$ (psi)	38.0 (5500)		
Allowable cyclic thermal stress, $\text{MN/m}^2$ (psi)	830.0 (120 000)		
Thickness per ply, mm (in.)	0.1016 (0.040)		
Active length, cm (in.)	38.61 (15.2)		
Number of plies	8		
Number of convolutions	19		
Extensional stiffness, $\text{kN/m}$ (lb/in.)	1120 (6370)		
Deflection capability, cm (in.)	6.34 (2.42)		
Bending stiffness, $\text{N-m/radian}$ (in.-lb/radian)	7290 (64 500)		
Lateral offset stiffness, $\text{kN/m}$ (lb/in.)	578 (3300)		

\*See fig. 5-3 of Section 5.

TABLE D-9

SHAPE 7.8\*HIGH-TEMPERATURE BELLOWS DESIGNS FOR EACH CANDIDATE MATERIAL

Candidate Materials	Rene' 41	Haynes 188	Hastelloy X
Allowable sustained bending stress, $\text{MN/m}^2$ (psi)	57.0 (8250)	NO FEASIBLE DESIGN	NO FEASIBLE DESIGN
Allowable sustained direct stress, $\text{MN/m}^2$ (psi)	38.0 (5500)		
Allowable cyclic thermal stress, $\text{MN/m}^2$ (psi)	830.0 (120 000)		
Thickness per ply, mm (in.)	0.1016 (0.040)		
Active length, cm (in.)	35.56 (14.0)		
Number of plies	7		
Number of convolutions	20		
Extensional stiffness, $\text{kN/m}$ (lb/in.)	942 (5380)		
Deflection capability, cm (in.)	6.01 (2.37)		
Bending stiffness, $\text{N-m/radian}$ (in.-lb/radian)	6160 (54 500)		
Lateral offset stiffness, $\text{kN/m}$ (lb/in.)	578 (3300)		

\*See fig. 5-3 of Section 5.

**Page  
Intentionally  
Left Blank**

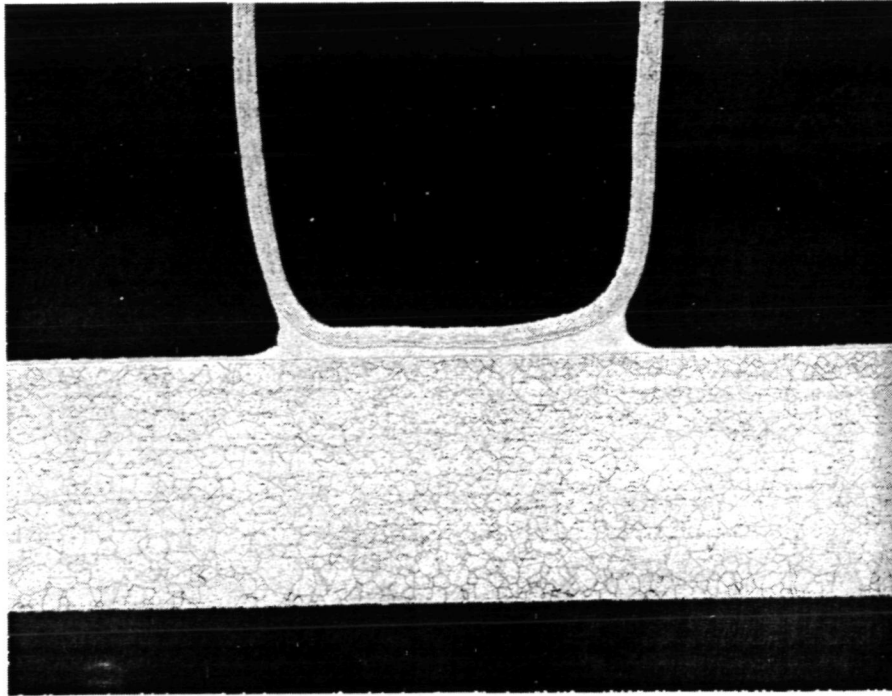




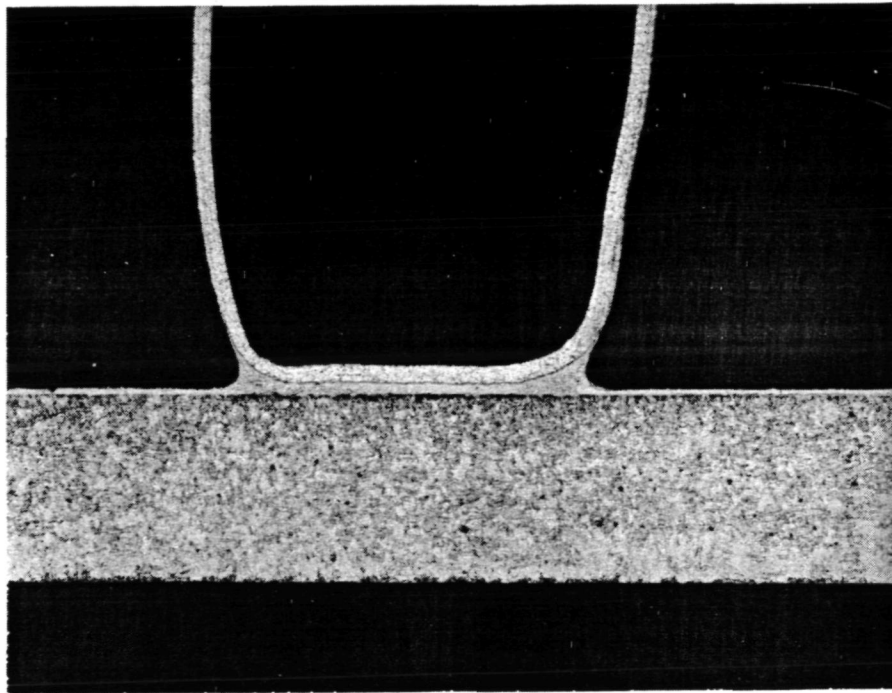
## APPENDIX E

Photomicrographs prepared to examine the behavior of various high-temperature braze alloys are presented in this appendix. The figures document the following data:

<u>Figure Number</u>	<u>Parameter Evaluated</u>
E1-E12	Braze alloy flow and penetration into parent metal on plate-fin specimens.
E13-E21	Oxidation on plate-fin samples after 3000 hr exposure.
E22-E24	Oxidation on plate-fin samples with 10 percent Hastelloy X diluent after 500 hr exposure.
E25-E39	Noble metal braze alloy additions to low-cost alloy.
E40-E46	Effects of Hastelloy X powder additions.
E47-E50	Comparison of flow and filleting and formation of intermetallic phases with varying proportions of Nicrobraz 210 and 30 alloys.
E51-E54	Effects of welding over braze joints on plate-fin specimens.
E55-E61	Post-test examination of creep-rupture test sections.



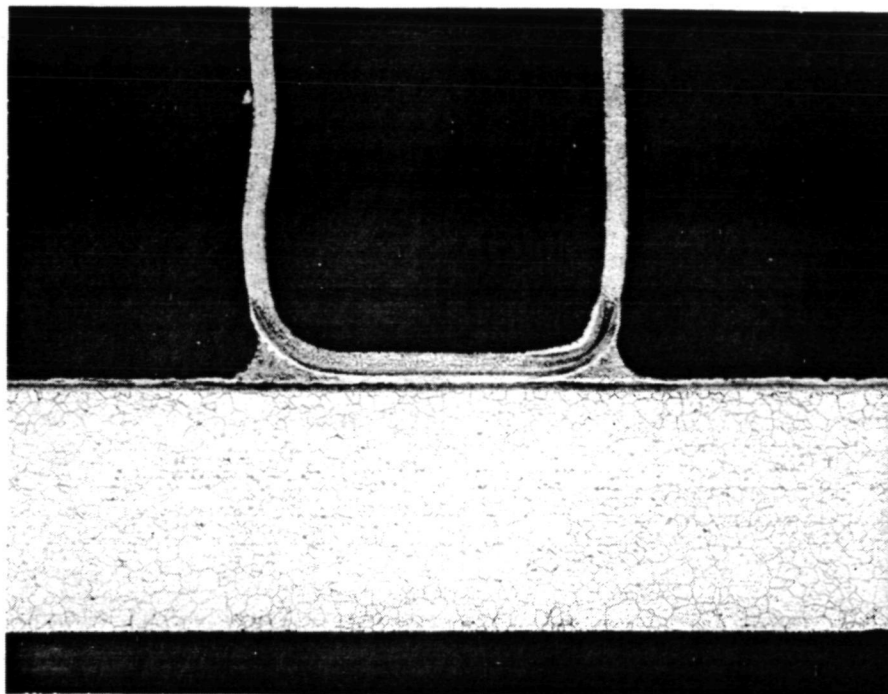
a. HASTELLOY X SIDE PLATE



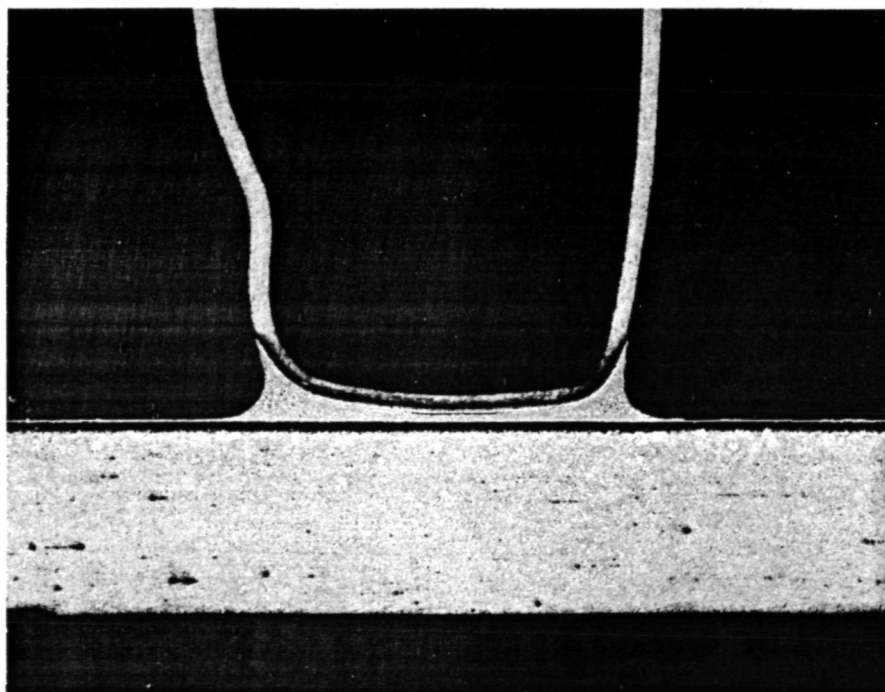
b. 347 CRES SIDE PLATE

F-16999

Figure E-1.--Plate-fin Specimen Vacuum Brazed at 1405°K (2070°F) with  
Palniro 1 (AMS 4784)) (Micro 26121, Oxalic Acid Etch, 30x).



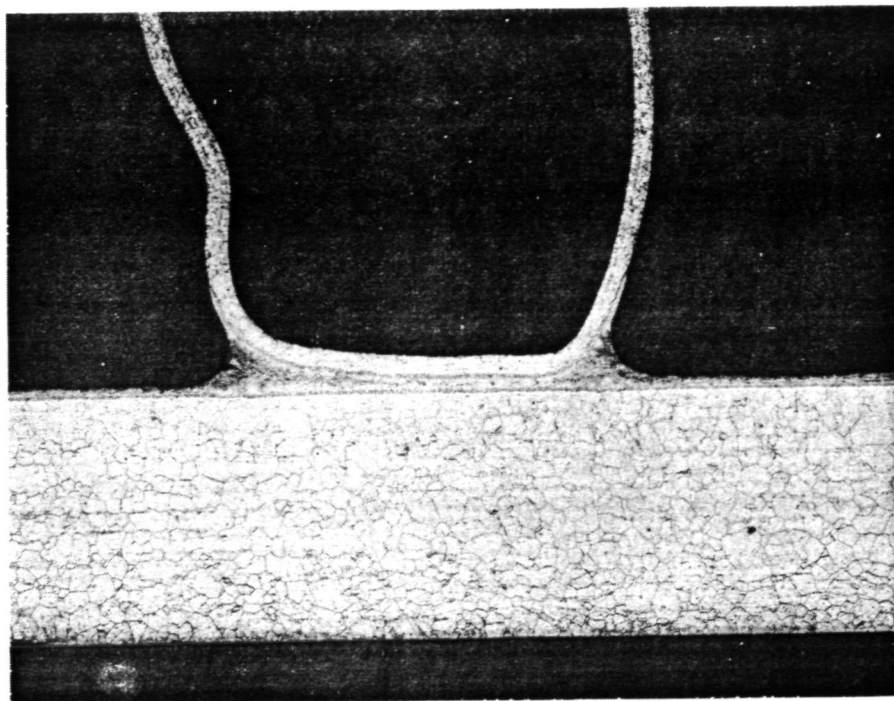
a. HASTELLOY X SIDE PLATE



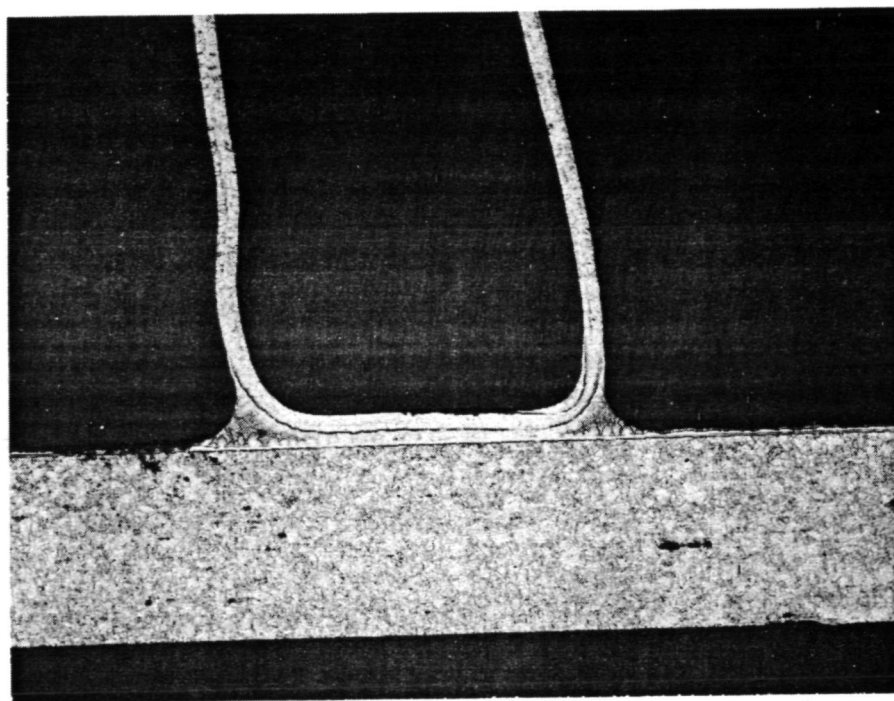
b. 347 CRES SIDE PLATE

F-17000

Figure E-2.--Plate-fin Specimen Vacuum Brazed at 1344°K (1960°F) with Microbraz 130 (AMS 4778) (Micro 26122, Oxalic Acid Etch, 30x).



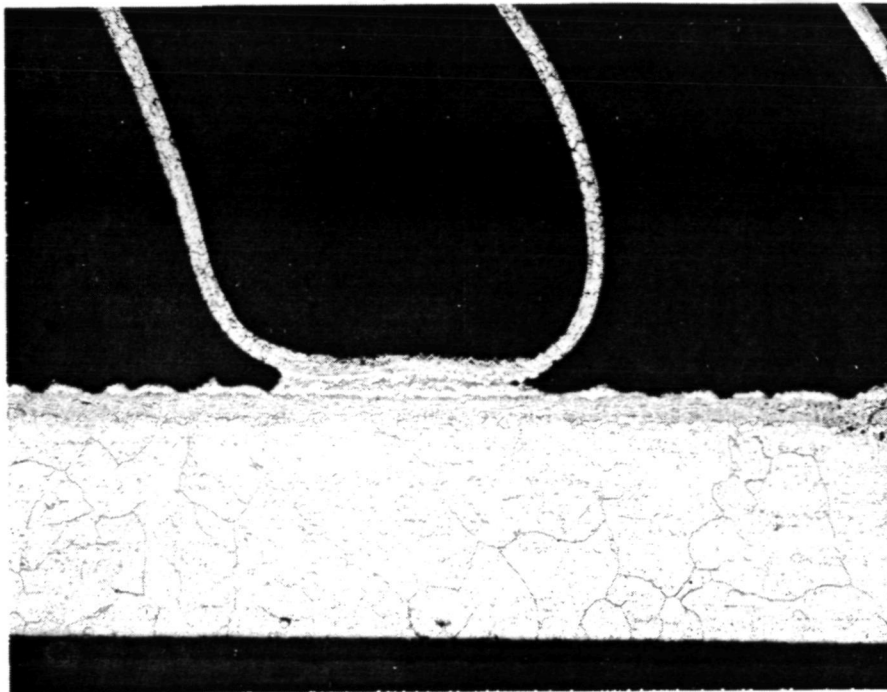
a. HASTELLOY X SIDE PLATE



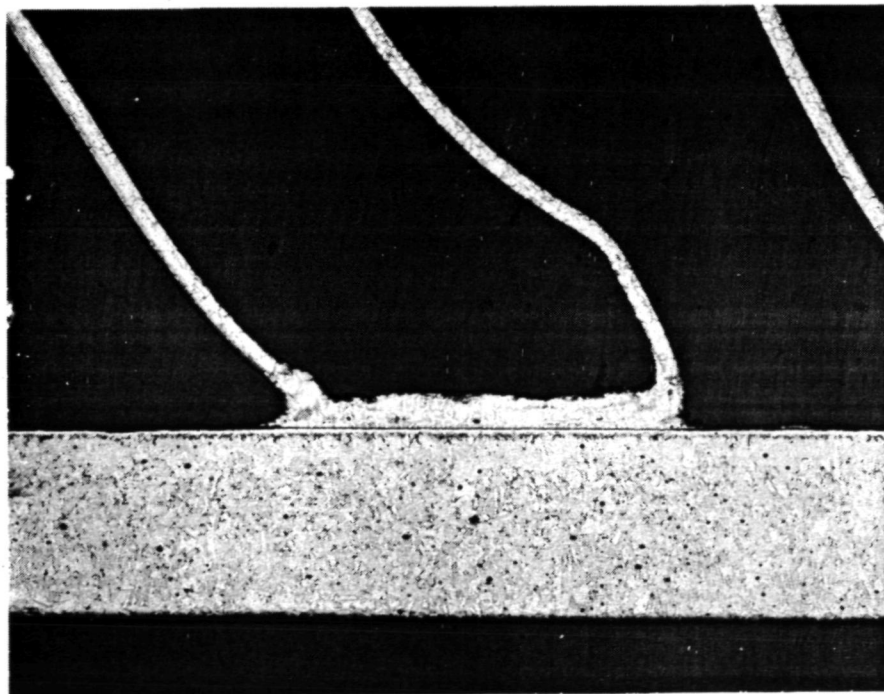
b. 347 CRES SIDE PLATE

F-17001

Figure E-3.--Plate-fin Specimen Vacuum Brazed at 1422°K (2100°F) with Microbraz 30 (J-8100) (Micro 26123, Oxalic Acid Etch, 30x).



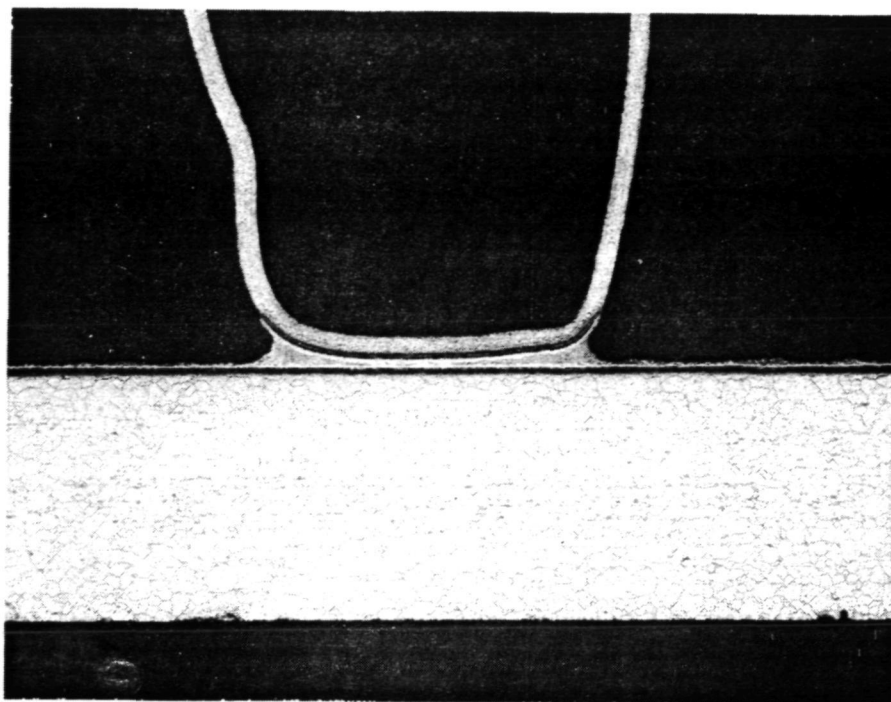
a. HASTELLOY X SIDE PLATE



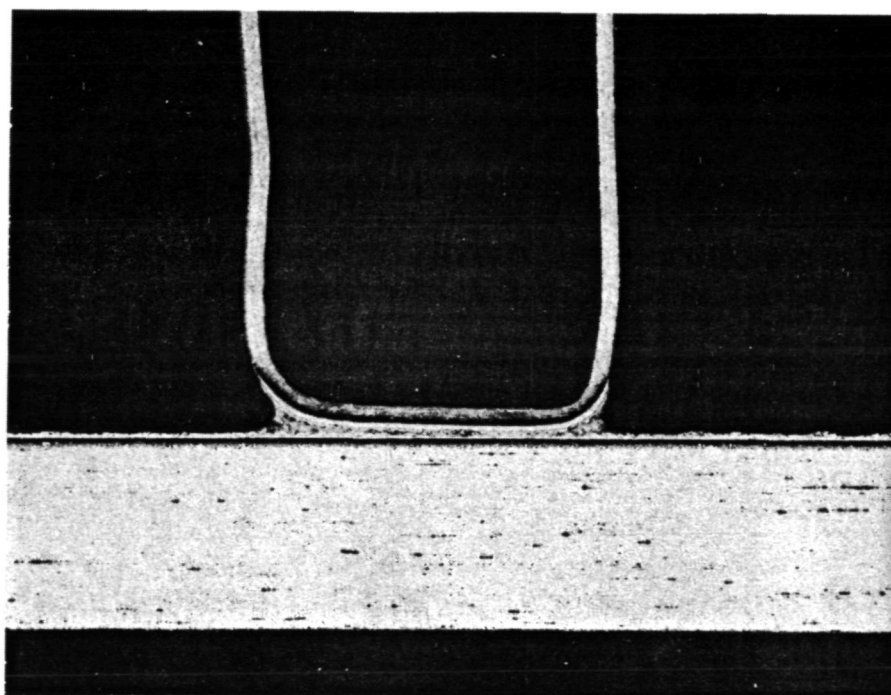
b. 347 CRES SIDE PLATE

F-17006

Figure E-4.--Plate-fin Specimen Vacuum Brazed at 1458°K (2165°F) with AMI 400 (Micro 26125, Oxalic Acid Etch, 30x).



a. HASTELLOY X SIDE PLATE

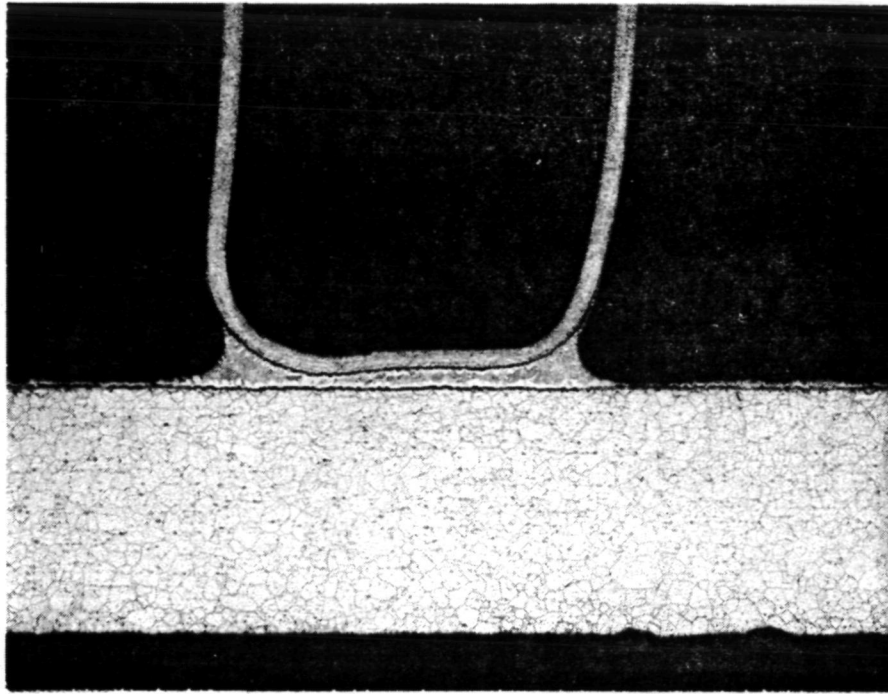


b. 347 CRES SIDE PLATE

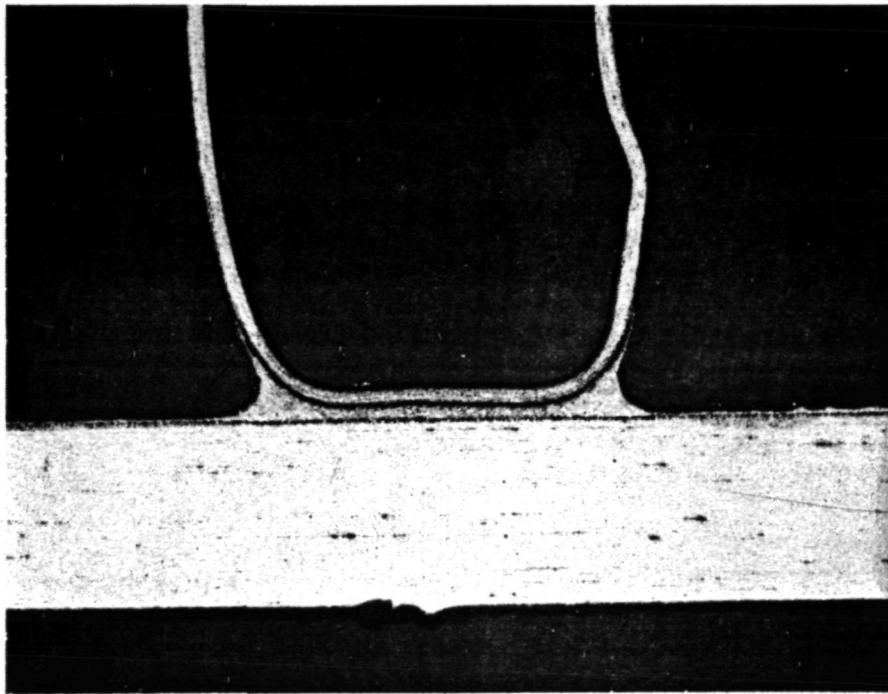
F-17002

Figure E-5.--Plate-fin Specimen Vacuum Brazed at 1344°K (1960°F) with Microbraz 150 (Micro 26126, Oxalic Acid Etch, 30x).





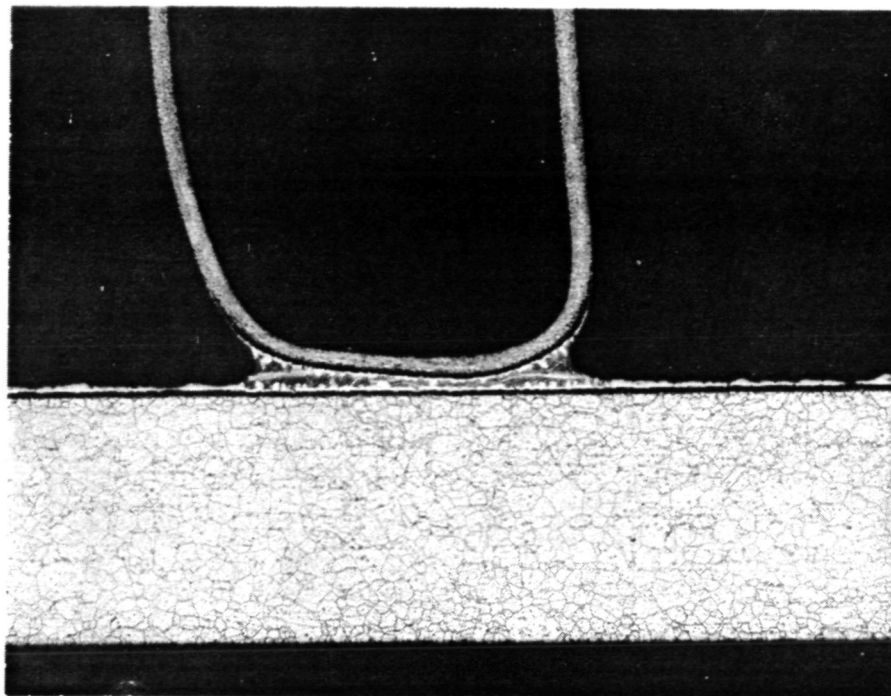
a. HASTELLOY X SIDE PLATE



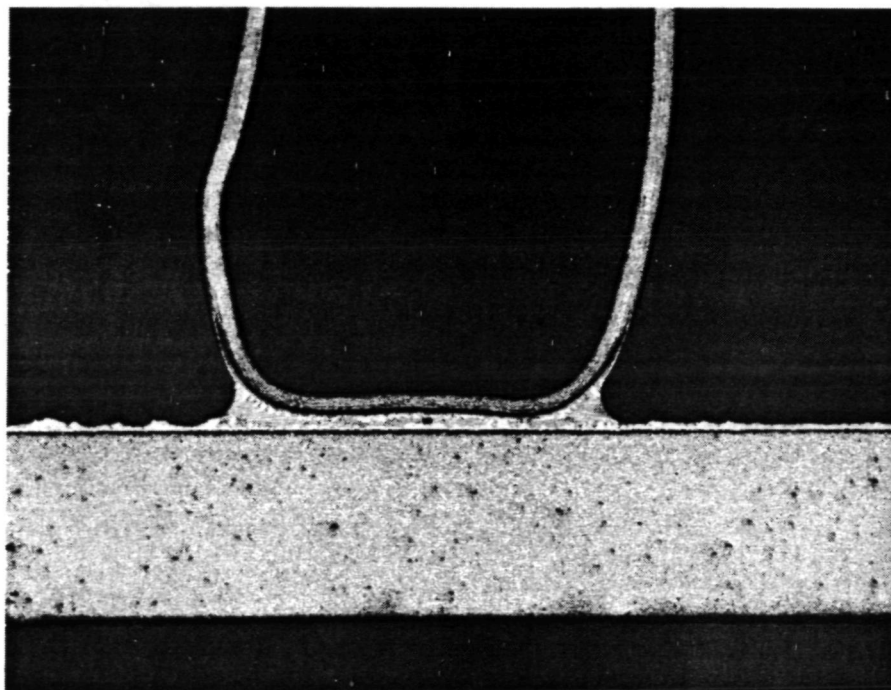
b. 347 CRES SIDE PLATE

F-17003

Figure E-6.--Plate-fin Specimen Vacuum Brazed at 1255°K (1800°F) with Microbraz 5075 (Micro 26124, Oxalic Acid Etch, 30x).



a. HASTELLOY X SIDE PLATE

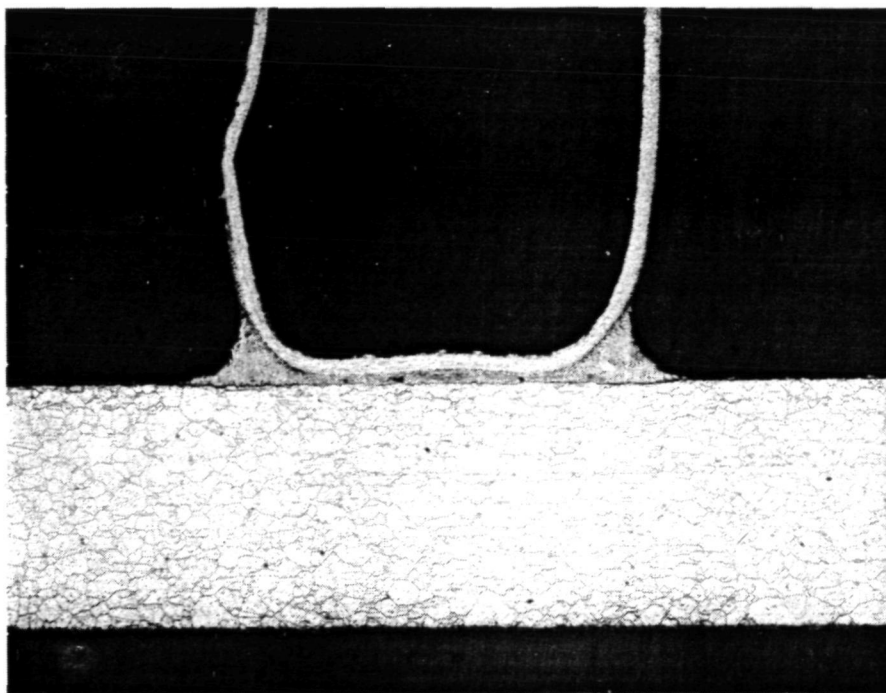


b. 347 CRES SIDE PLATE

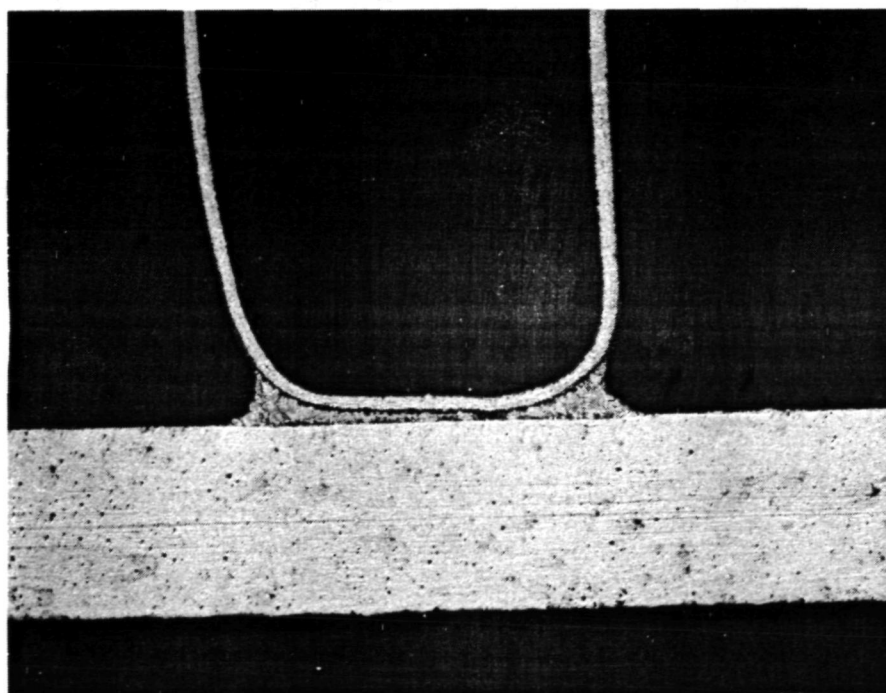
F-17004

Figure E-7.--Plate-fin Specimen Vacuum Brazed at 1283°K (1850°F) with Microbraz 5040 (Micro 26124, Oxalic Acid Etch, 30x).





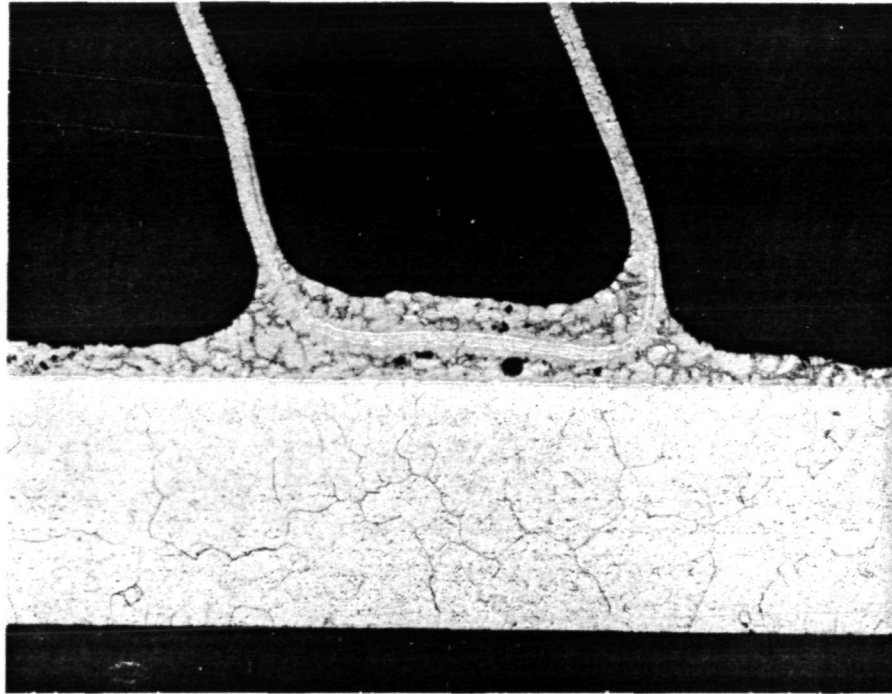
a. HASTELLOY X SIDE PLATE



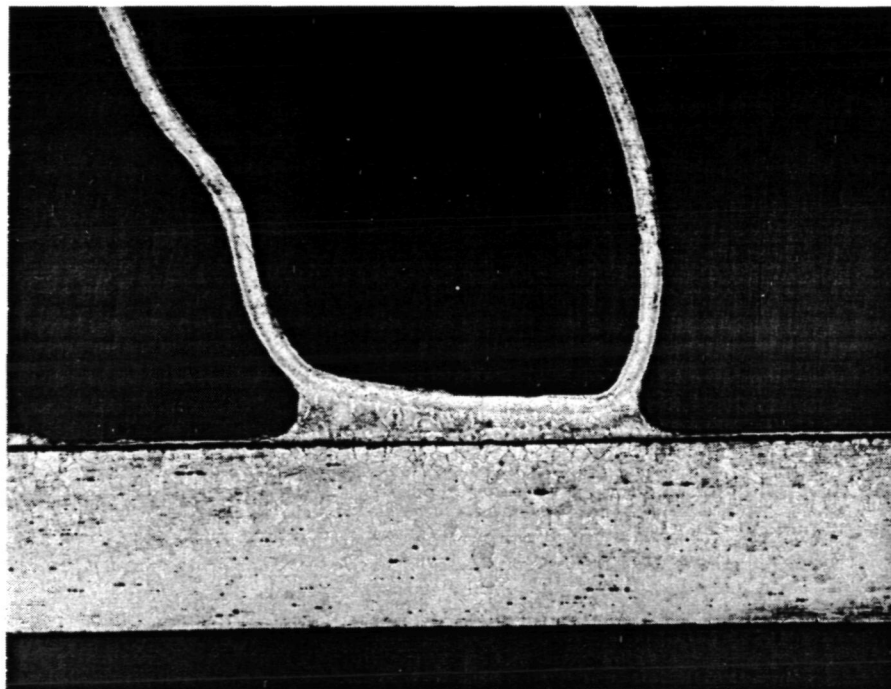
b. 347 CRES SIDE PLATE

F-17005

Figure E-8.--Plate-fin Specimen Vacuum Brazed at 1255°K (1800°F) with Microbraz 50 (Micro 26125, Oxalic Acid Etch, 30x).



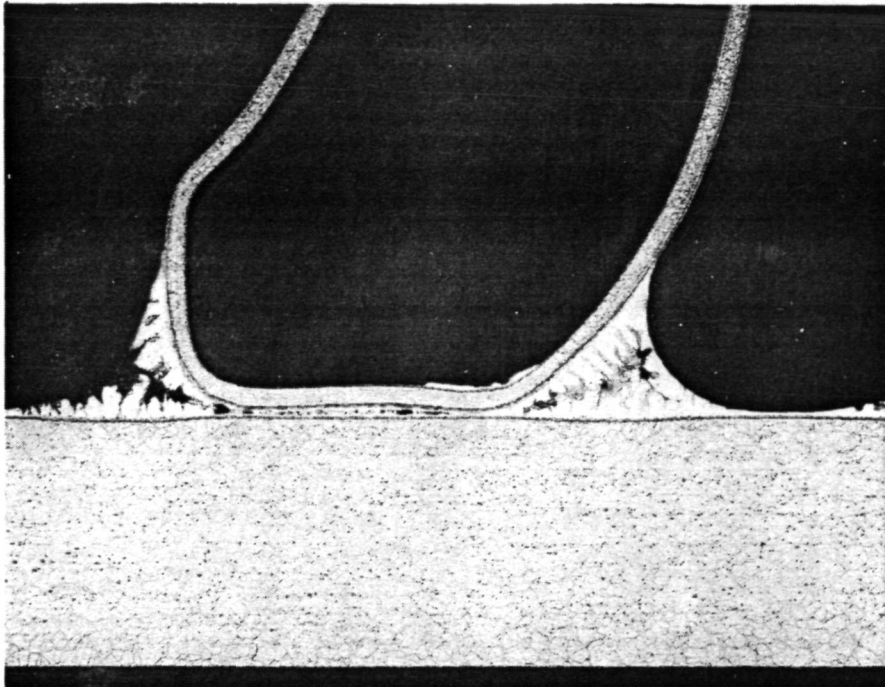
a. HASTELLOY X SIDE PLATE



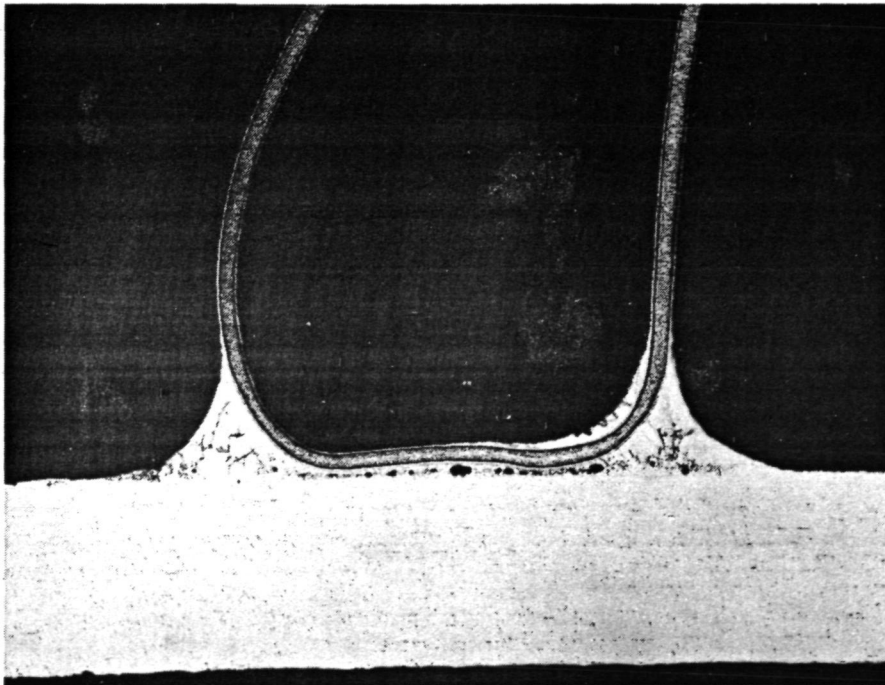
b. 347 CRES SIDE PLATE

F-17007

Figure E-9.--Plate-fin Specimen Vacuum Brazed at 1458°K (2165°F) with J-8600 (Micro 26126, Oxalic Acid Etch, 30x).



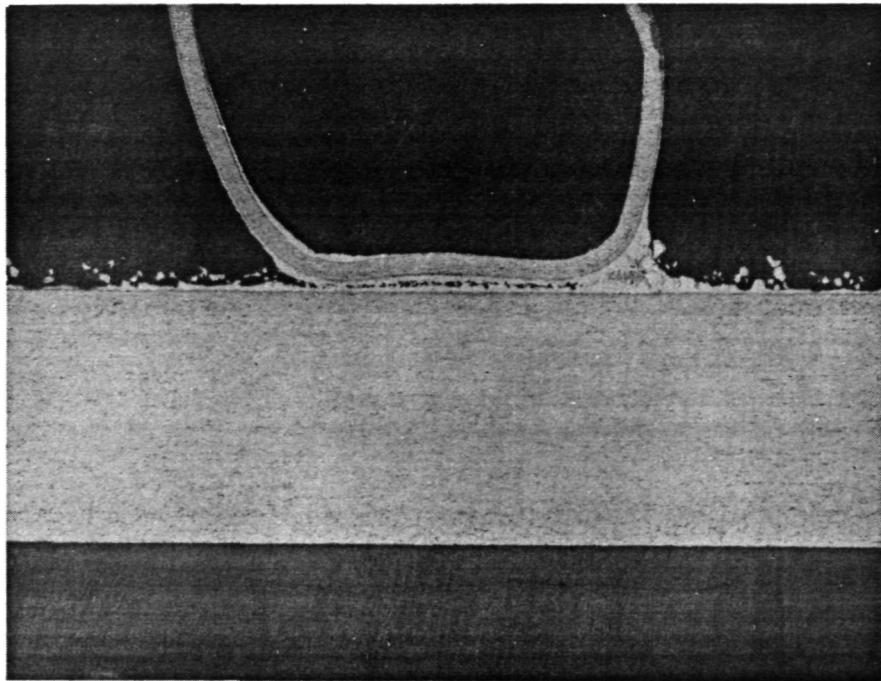
a. HASTELLOY X BASE



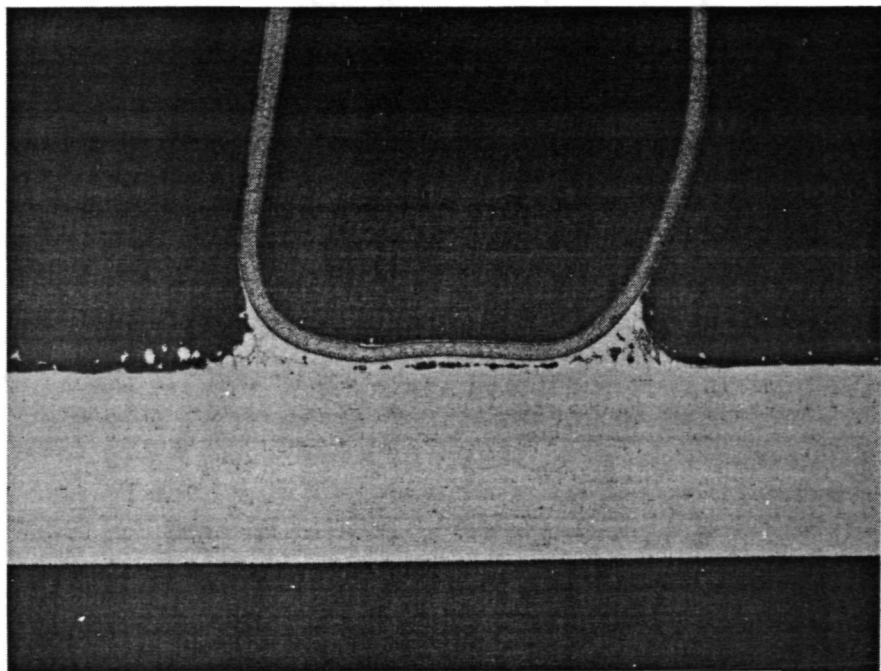
F-17171

b. TYPE 347 STAINLESS STEEL BASE

Figure E-10.--Plate-fin Sample Hydrogen Brazed at 1344.4°K (1960°F) with Microbraz 220. (Oxalic Acid Etch, 30x).



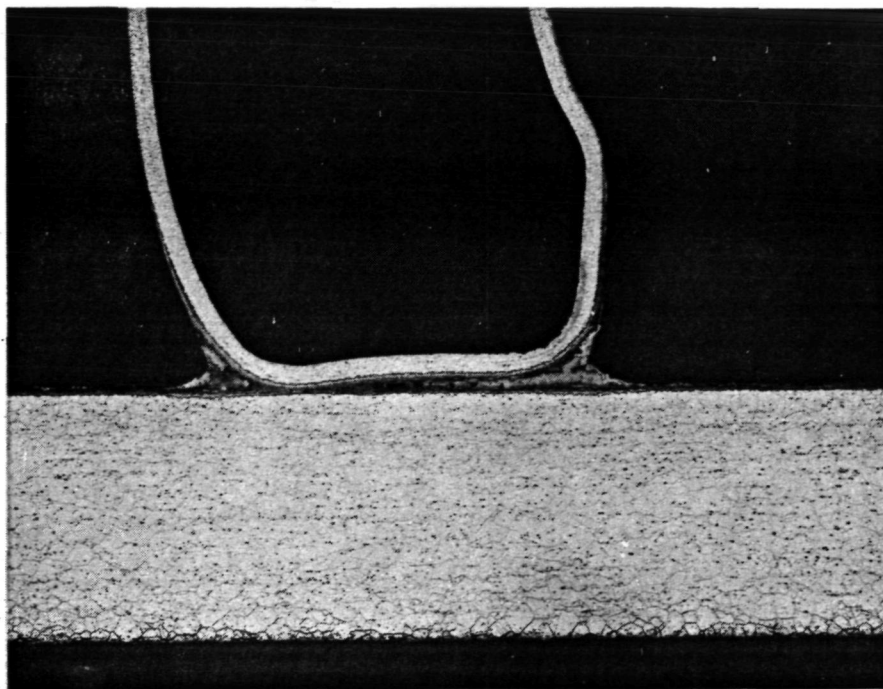
a. HASTELLOY X BASE



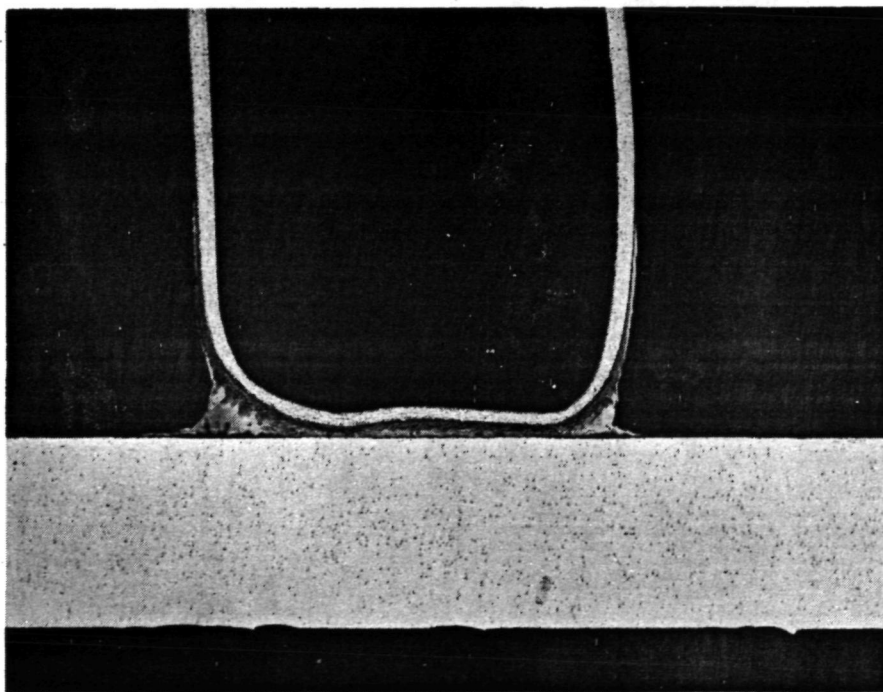
b. TYPE 347 STAINLESS STEEL BASE

F-17170

Figure E-11.--Plate-fin Sample Hydrogen Brazed at 1344.4°K (1960°F) with Microbraz 230 (Oxalic Acid Etch, 30x).



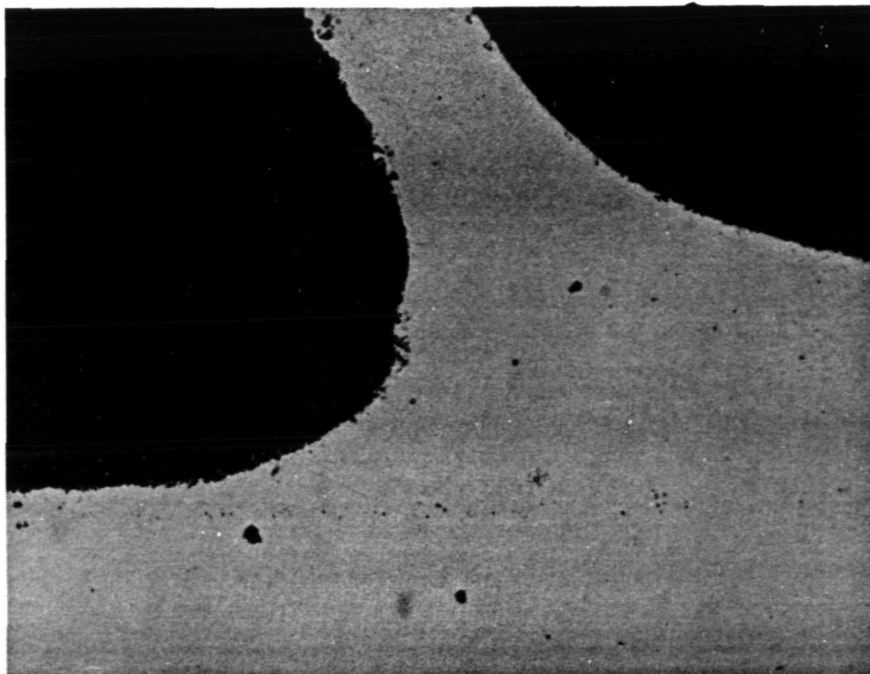
a. HASTELLOY X BASE



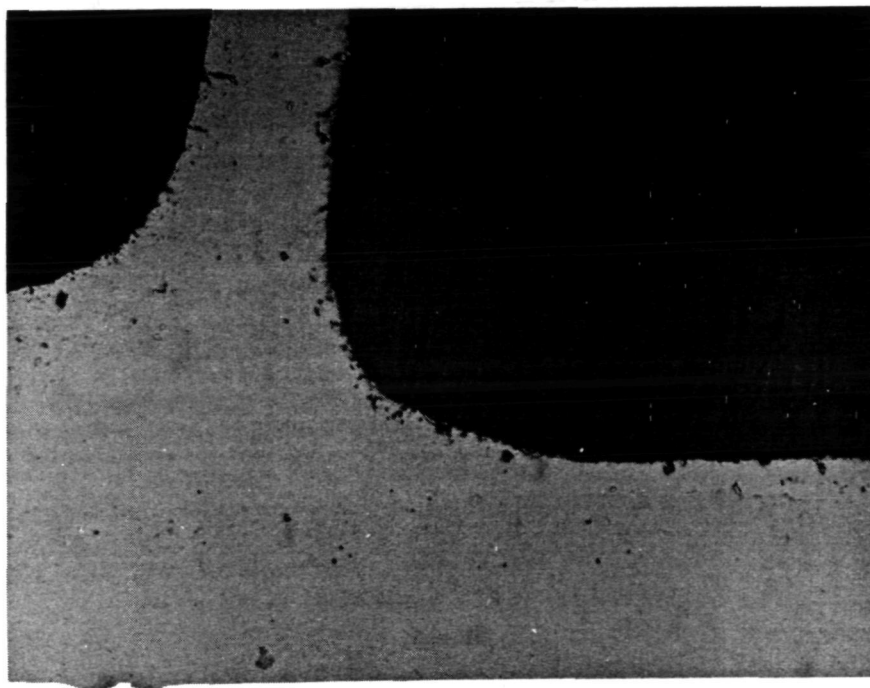
F-17169

b. TYPE 347 STAINLESS STEEL BASE

Figure E-12.--Plate-fin Sample Hydrogen Brazed at 1255.6°K (1800°F) with AMI 934 (Oxalic Acid Etch, 30x).



a. HASTELLOY X PLATE AND FIN  
AT 1005 K (MICRO 27049)

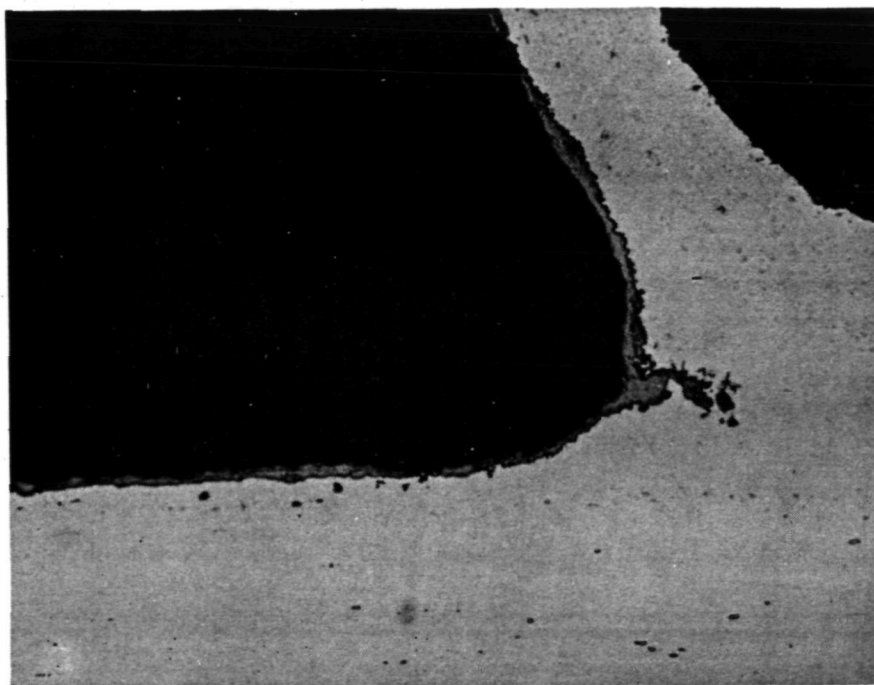


b. HASTELLOY X PLATE AND FIN  
AT 1089 K (MICRO 27040)

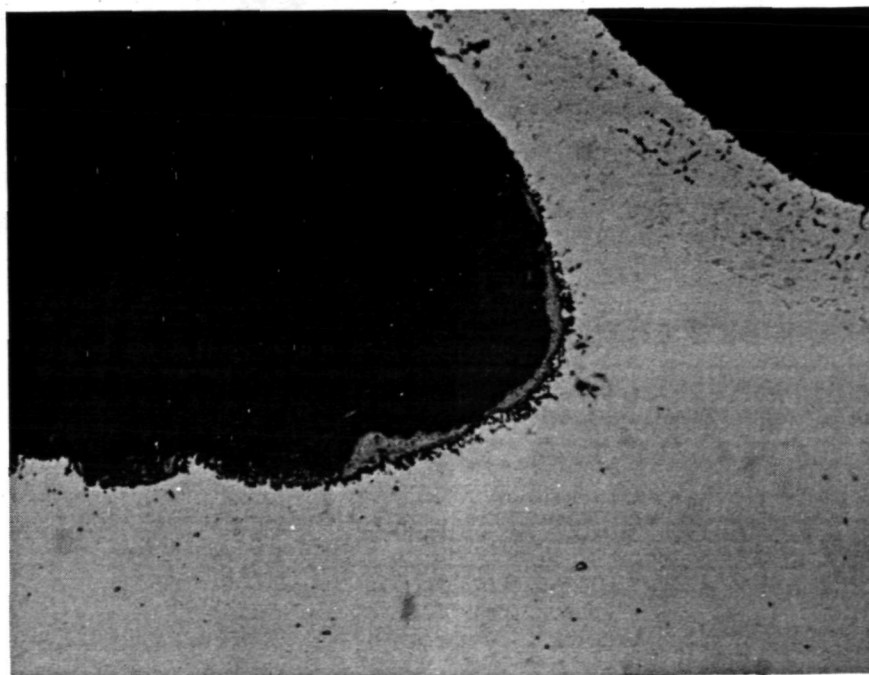
F-17800-A

Figure E-13.--Plate-fin Panel Brazed with Palniro 1 after 3000-hr Exposure to Elevated Temperature Air (Oxalic Acid Etch, 200x).





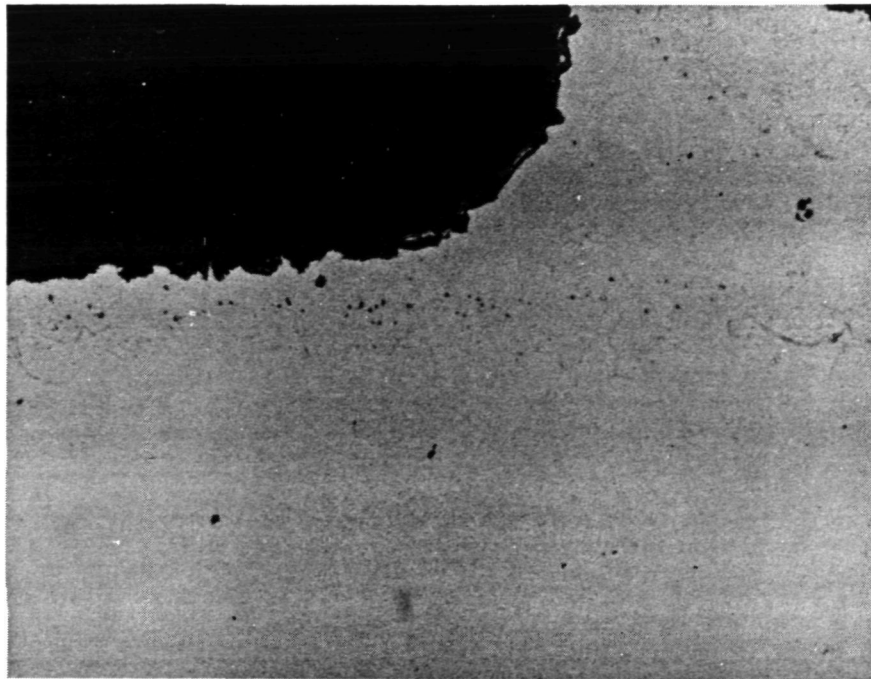
c. CRES 347 PLATE, HASTELLOY X FIN  
AT 1005 K (MICRO 27049)



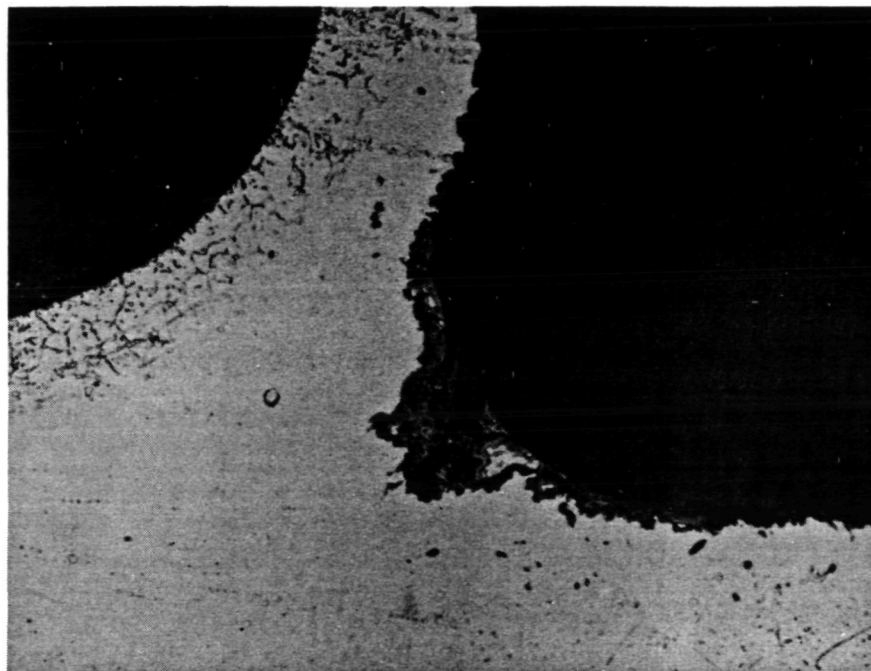
d. CRES 347 PLATE, HASTELLOY X FIN  
AT 1089 K (MICRO 27040)

F-17801-A

Figure E-13.--(Continued).



a. HASTELLOY X PLATE AND FIN  
AT 1005 K (MICRO 27050)

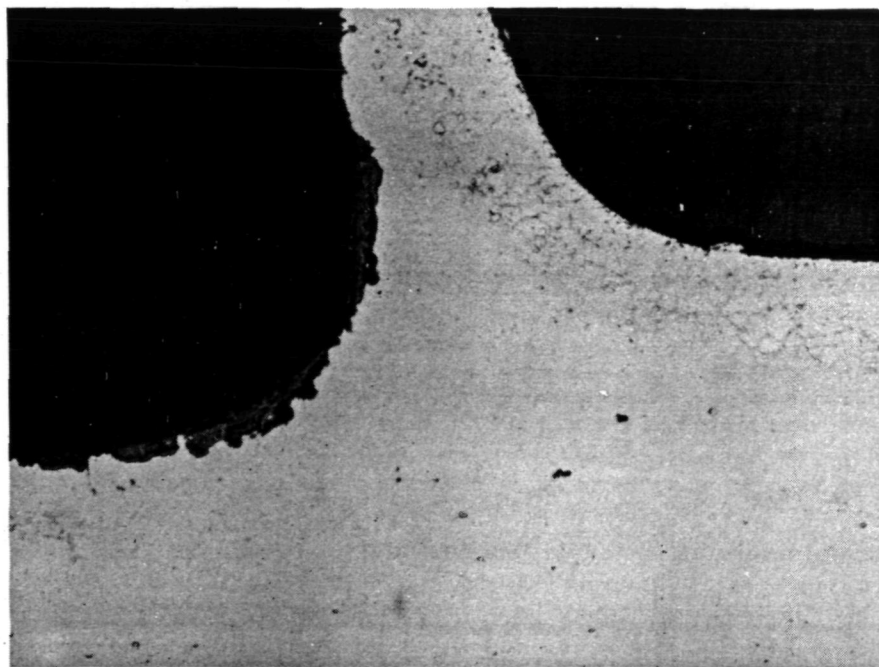


b. HASTELLOY X PLATE AND FIN  
AT 1089 K (MICRO 27041)

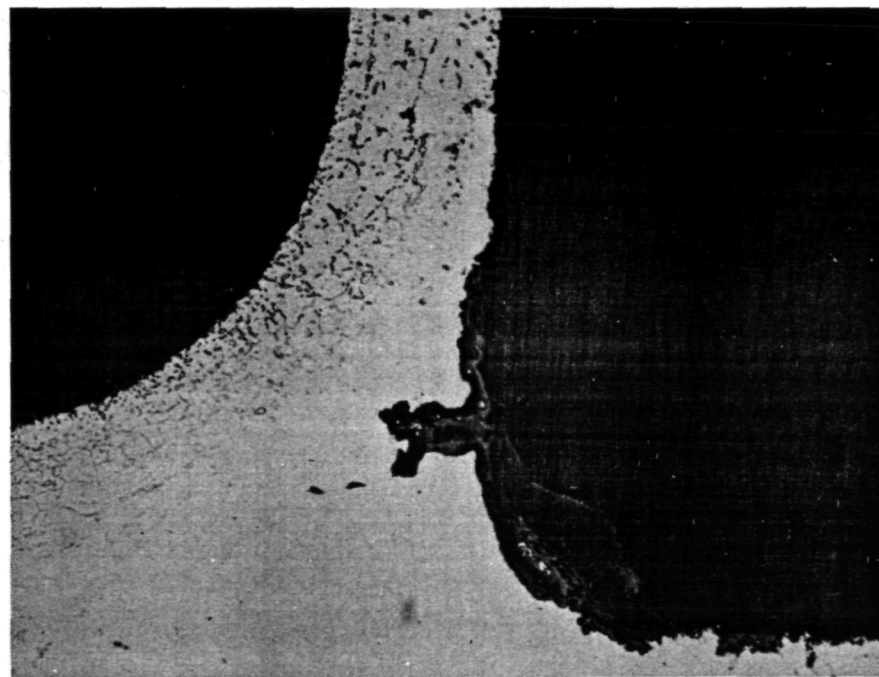
F-17802-A

Figure E-14.--Plate-fin Panel Brazed with Microbraz 130 (AMS4778) after 3000-hr Exposure to Elevated Temperature Air. (Oxalic Acid Etch, 200x).





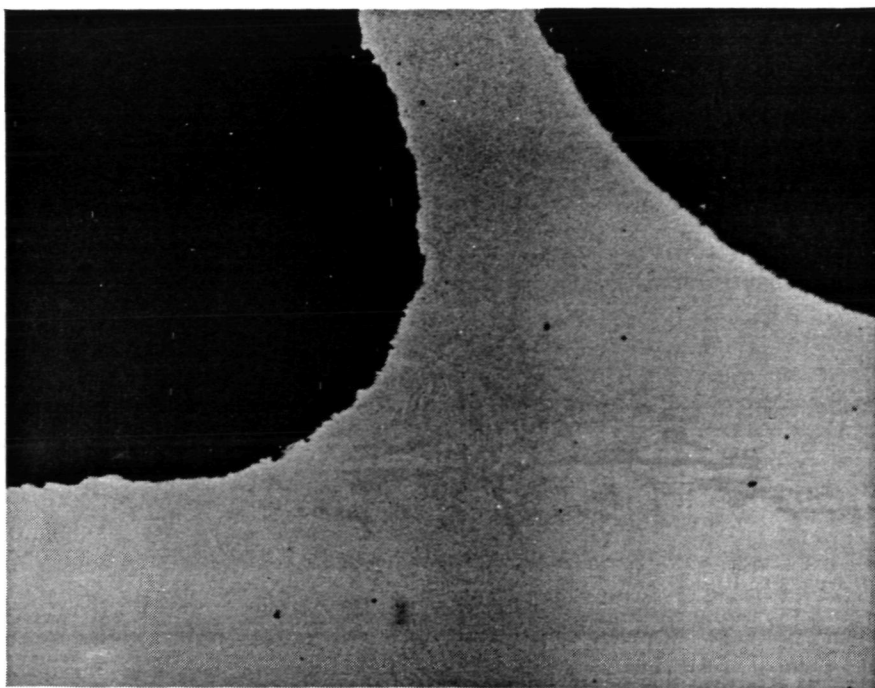
c. CRES 347 PLATE, HASTELLOY X FIN  
AT 1005 K (MICRO 27050)



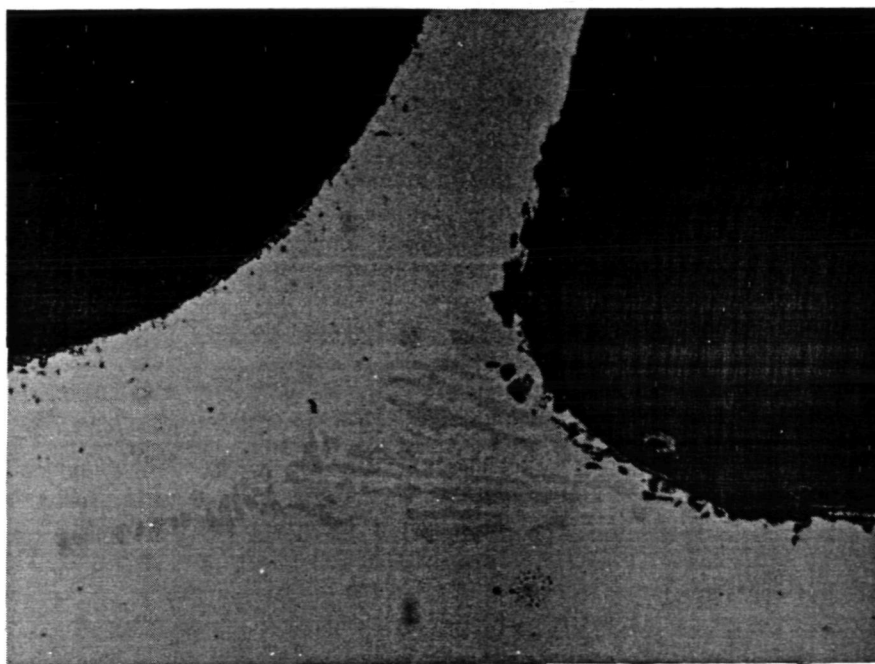
d. CRES 347 PLATE, HASTELLOY X FIN  
AT 1089 K (MICRO 27041)

F-17803-A

Figure E-14.--(Continued).



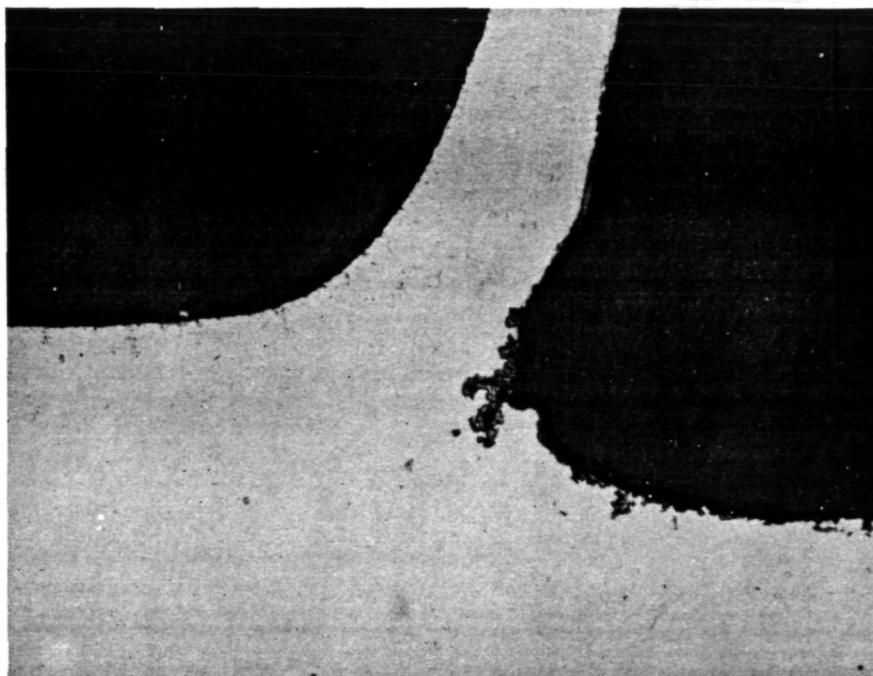
a. 1005 K (MICRO 27051)



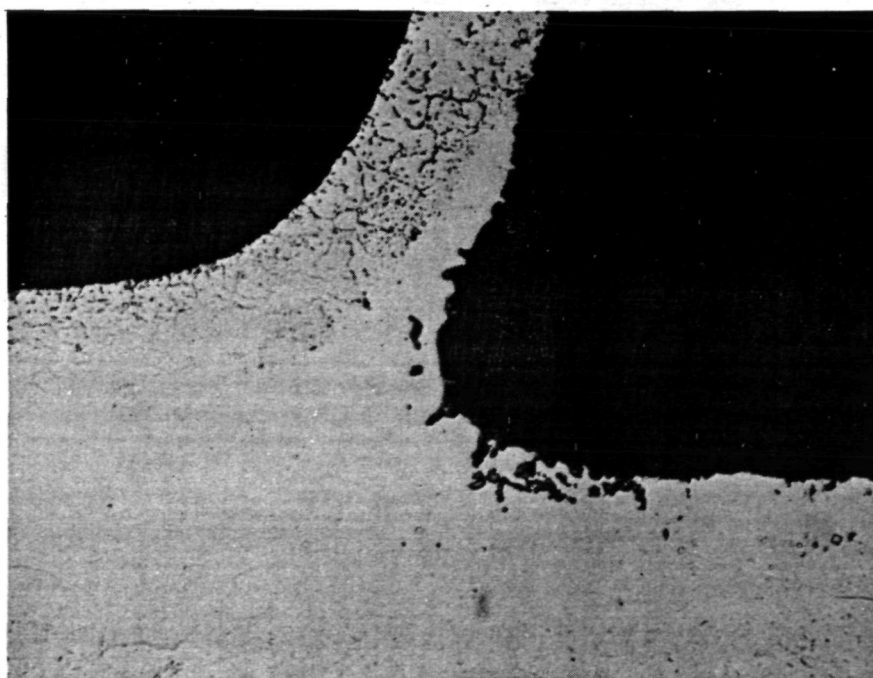
b. 1089 K (MICRO 27042)

F-17804-A

Figure E-15.--Hastelloy X Plate-fin Panel Brazed with Microbraz 30 after 3000-hr Exposure to Elevated Temperature Air. (Oxalic Acid Etch, 200x).



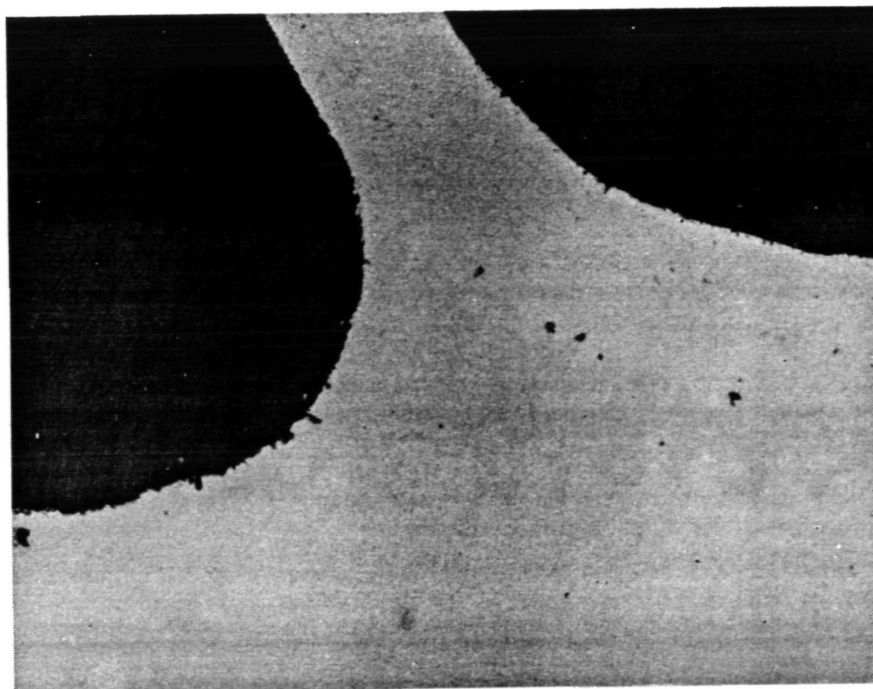
a. 1005 K (MICRO 27052)



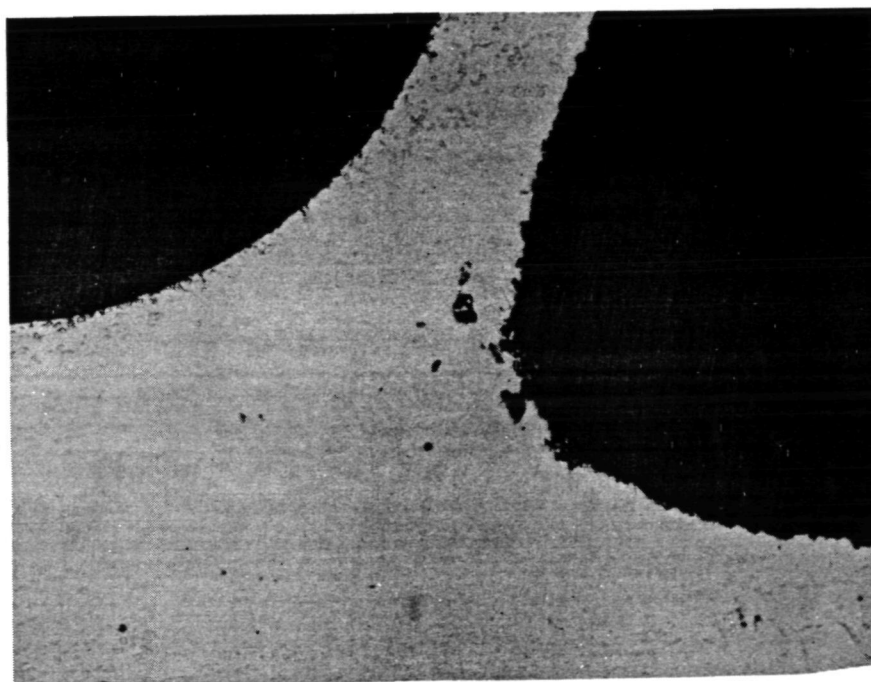
F-17805-A

b. 1089 K (MICRO 27043)

Figure E-16.--Hastelloy X Plate-fin Panel Brazed with Microbraz 150 after 3000-hr Exposure to Elevated Temperature Air. (Oxalic Acid Etch, 200x).



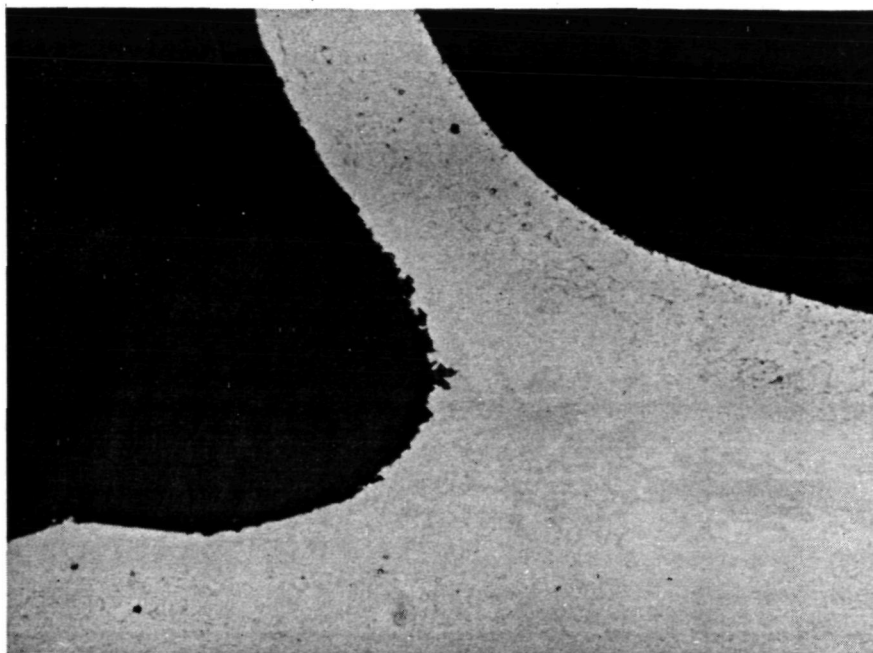
a. 1005 K (MICRO 27053)



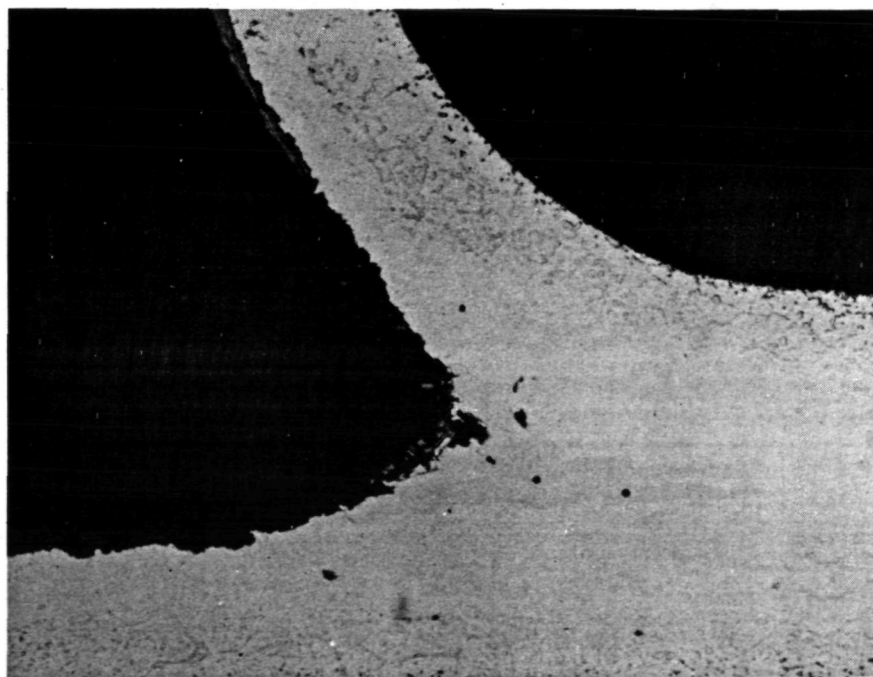
b. 1089 C (MICRO 27044)

F-17806-A

Figure E-17.--Hastelloy X Plate-fin Panel Brazed with Microbraz 5075 after 3000-hr Exposure to Elevated Temperature Air. (Oxalic Acid Etch, 200x).



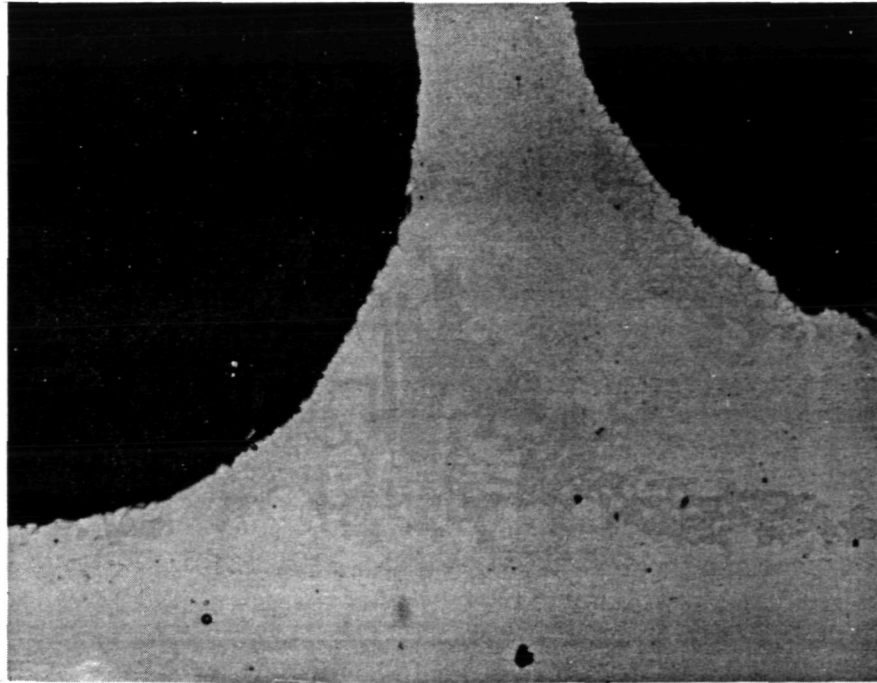
a. 1005 K (MICRO 27054)



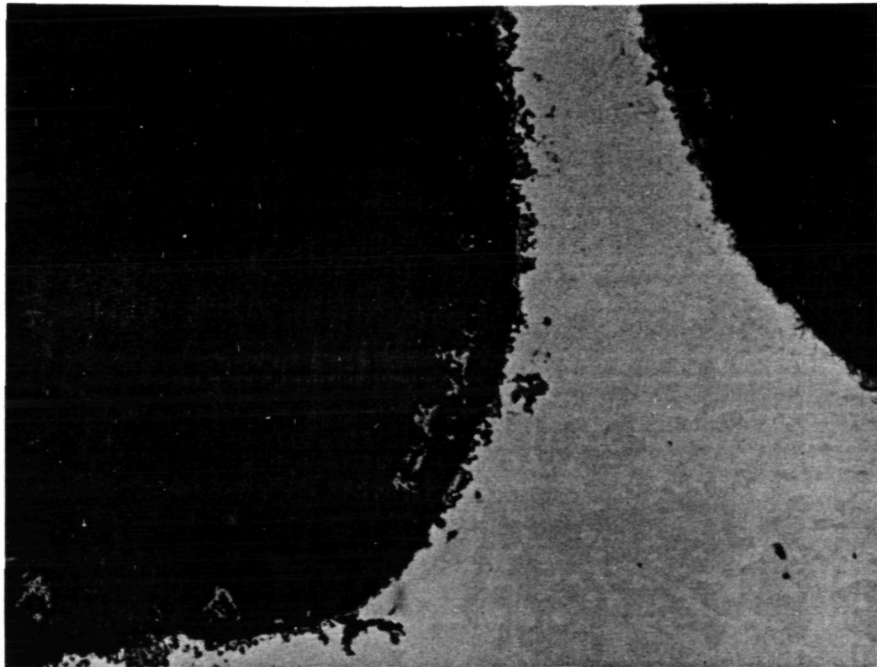
F-17807-A

b. 1089 K (MICRO 27045)

Figure E-18.--Hastelloy X Plate-fin Panel Brazed with Microbraz 5040 after 3000-hr Exposure to Elevated Temperature Air (Oxalic Acid Etch, 200x).



a. 1005 K (MICRO 27055)

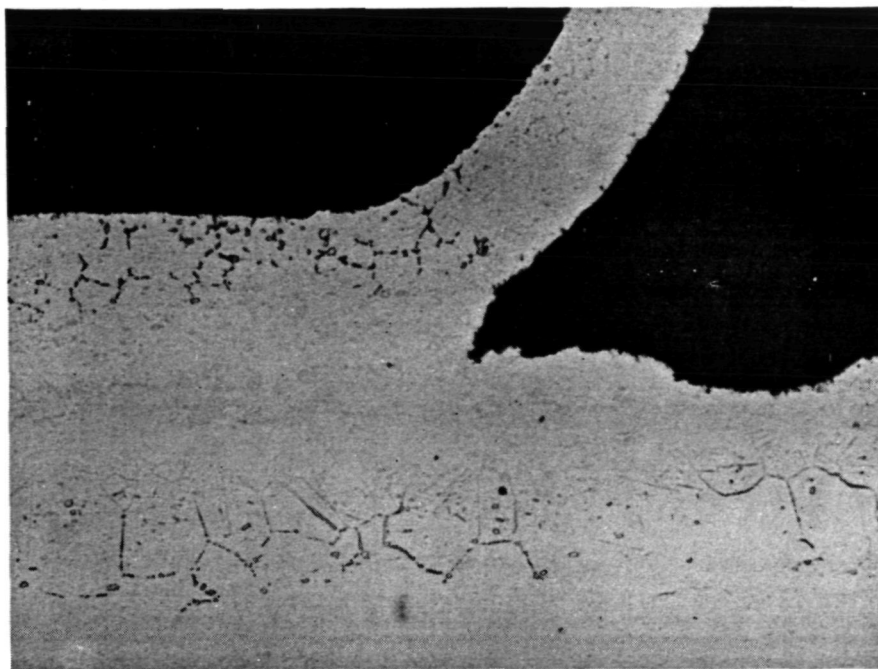


b. 1089 K (MICRO 27046)

F-17808 -A

Figure E-19.--Hastelloy X Plate-fin Panel Brazed with Microbraz 50 after 3000-hr Exposure to Elevated Temperature Air. (Oxalic Acid Etch, 200x).





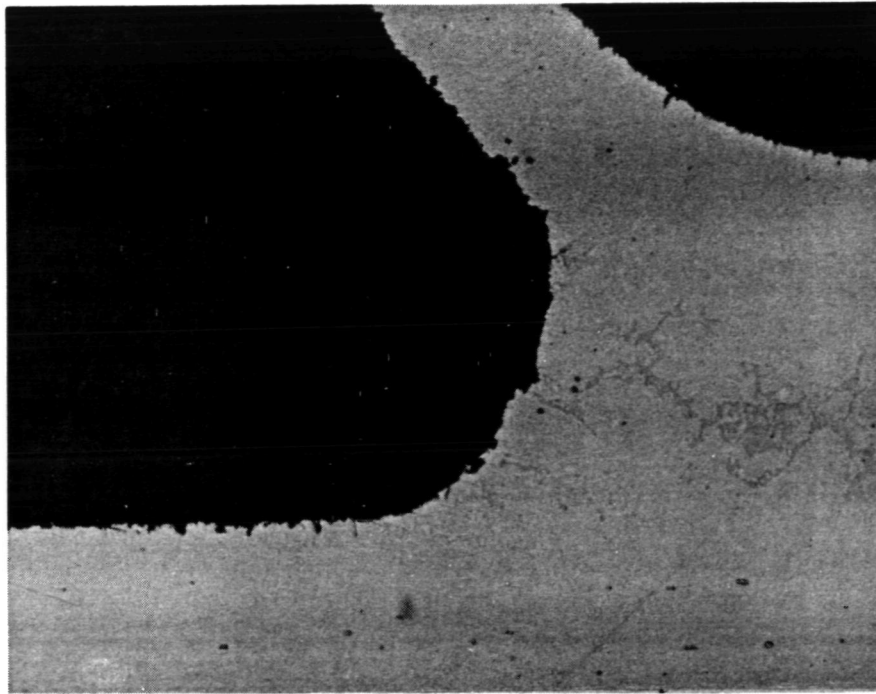
a. 1005 K (MICRO 27056)



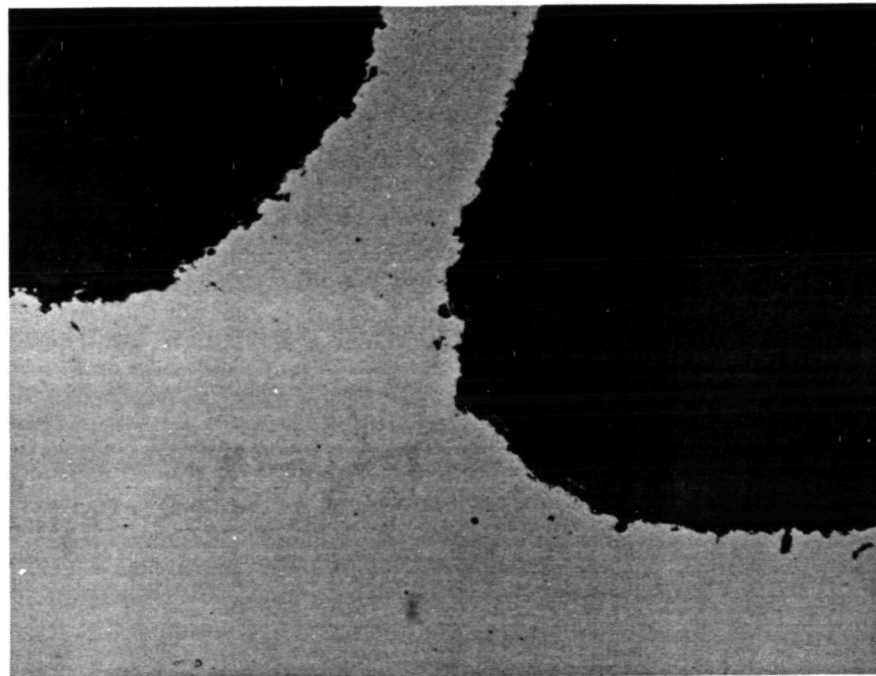
b. 1089 K (MICRO 27047)

F-17809-A

Figure E-20.--Hastelloy X Plate-fin Panel Brazed with Microbraz 210 after 3000-Hr Exposure to Elevated Temperature Air. (Oxalic Acid Etch, 200x).



a. 1005 K (MICRO 17057)



b. 1089 K (MICRO 27048)

F-17810-A

Figure E-21.--Type 347 Stainless Steel Plate, Hastelloy X Fin Panel  
Braze with J-8600 after 3000-hr Exposure to Elevated  
Temperature Air. (Oxalic Acid Etch, 200x).





Figure E-22.--Plate-fin Joint Brazed with a Blend of 10 Percent Hastelloy X in Microbraz 5075 (-170 Mesh Powders) After 500 hr in Air at 1089°K (1500°F) (Micro 26594, Unetched, 200x).



F-17361

Figure E-23.--Plate-fin Joint Brazed with a Blend of 10 Percent Hastelloy X in Microbraz 30 (-170 Mesh Powders) after 500 hr in Air at 1089°K (1500°F) (Micro 26595, Unetched, 200x).



Figure E-24.--Plate-fin Joint Brazed with a Blend of 10 Percent Hastelloy X in Microbraz 130 (AMS 4778) (-170 Mesh Powders) after 500 hr in Air at 1089°K (1500°F) (Micro 26596, Unetched, 200x).

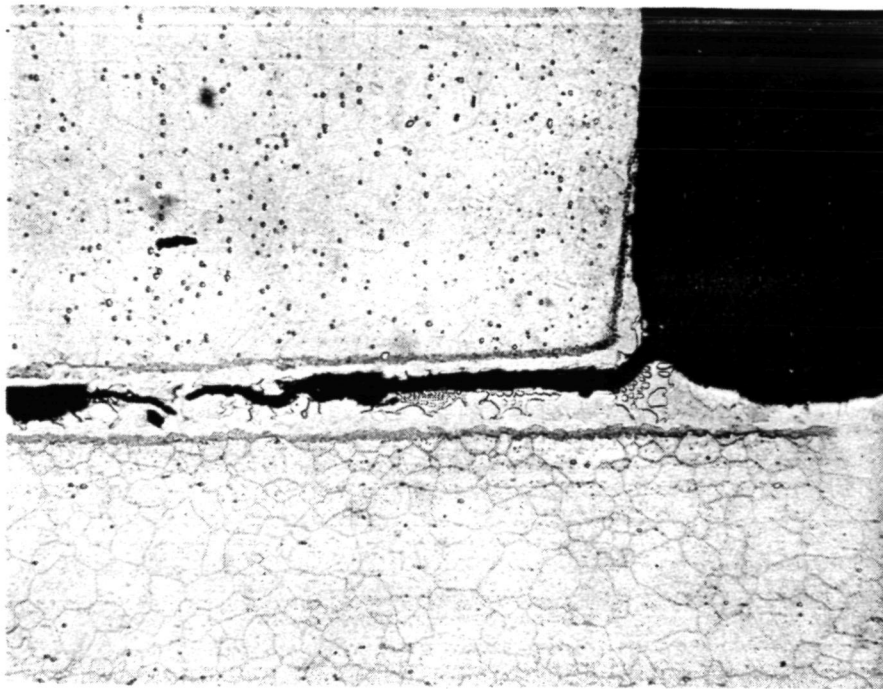
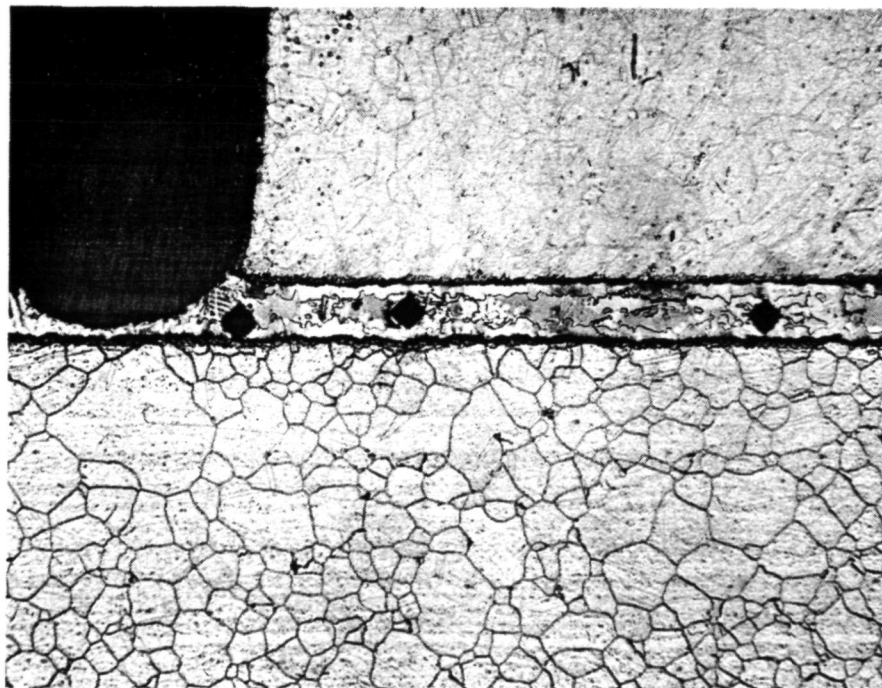


Figure E-25.--Hastelloy X (SN 3) Brazed with (Microbraz 5075 + 20 Percent Hastelloy X) Mixed with 10 Percent Nicro (Micro 26664, Oxalic Acid Etch, 100x).



F-17539

Figure E-26.--Hastelloy X (SN 4) Brazed with (Microbraz 5075 + 20 Percent Hastelloy X) Mixed with 20 Percent Nicro (Micro 26665, Oxalic Acid Etch, 100x).

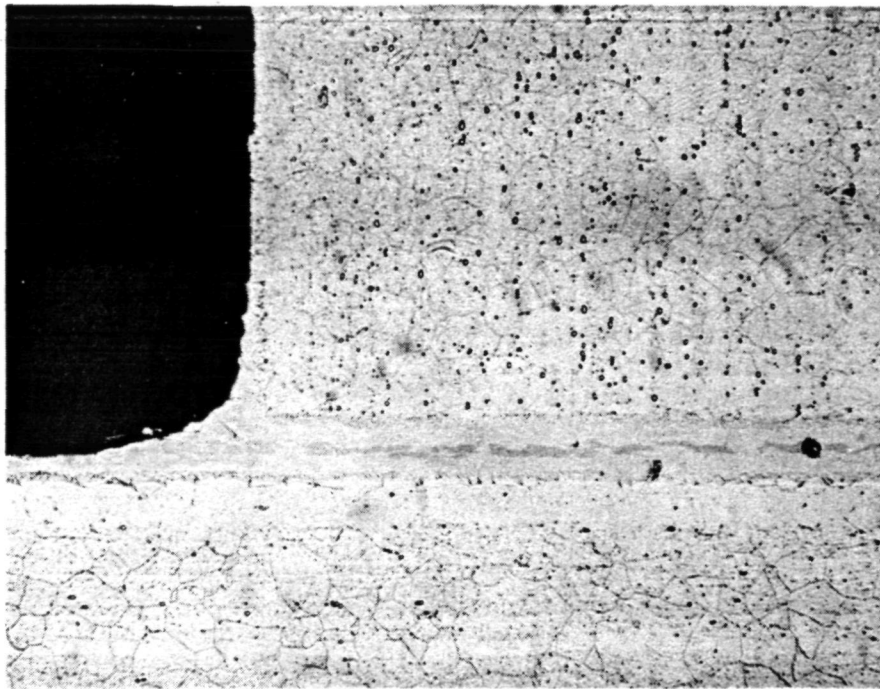
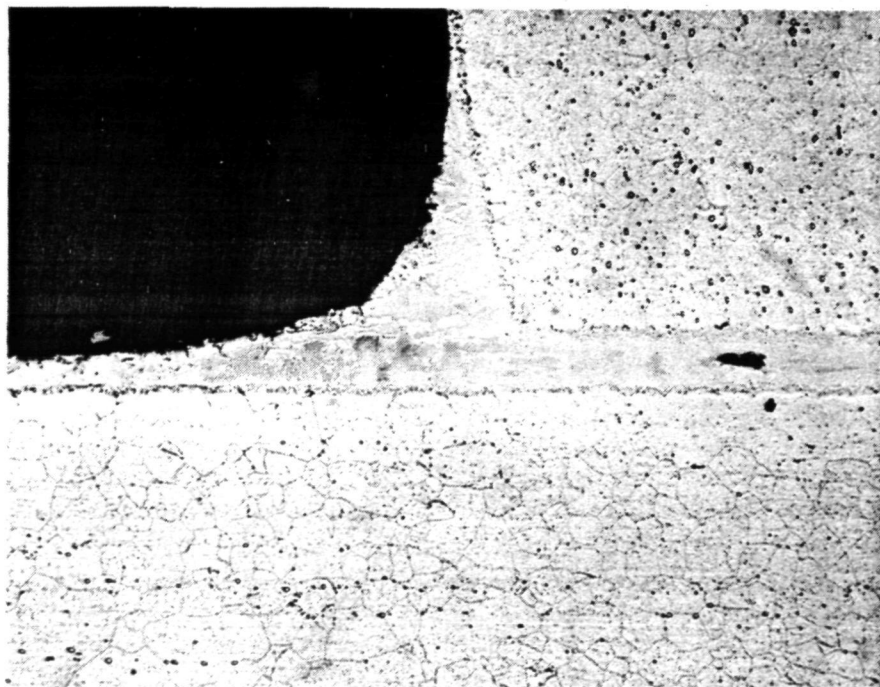


Figure E-27.--Hastelloy X (SN 5) Brazed with Microbraz 30 Mixed with 10 Percent Palniro RE (Micro 26666, Oxalic Acid Etch, 100x).



F-17540

Figure E-28.--Hastelloy X (SN 6) Brazed with Microbraz 30 Mixed with 20 Percent Palniro RE (Micro 26667, Oxalic Acid Etch, 100X).

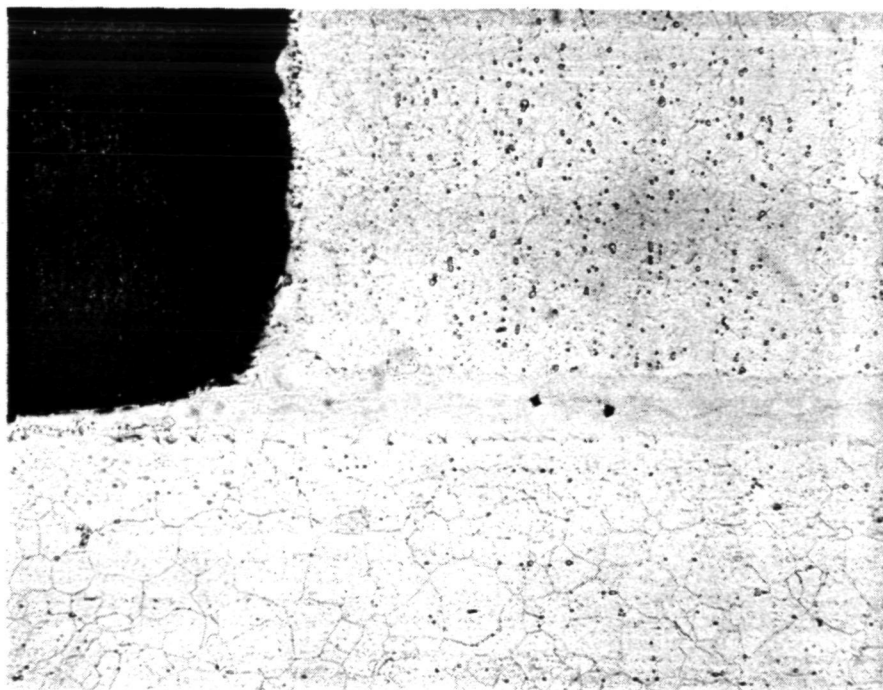
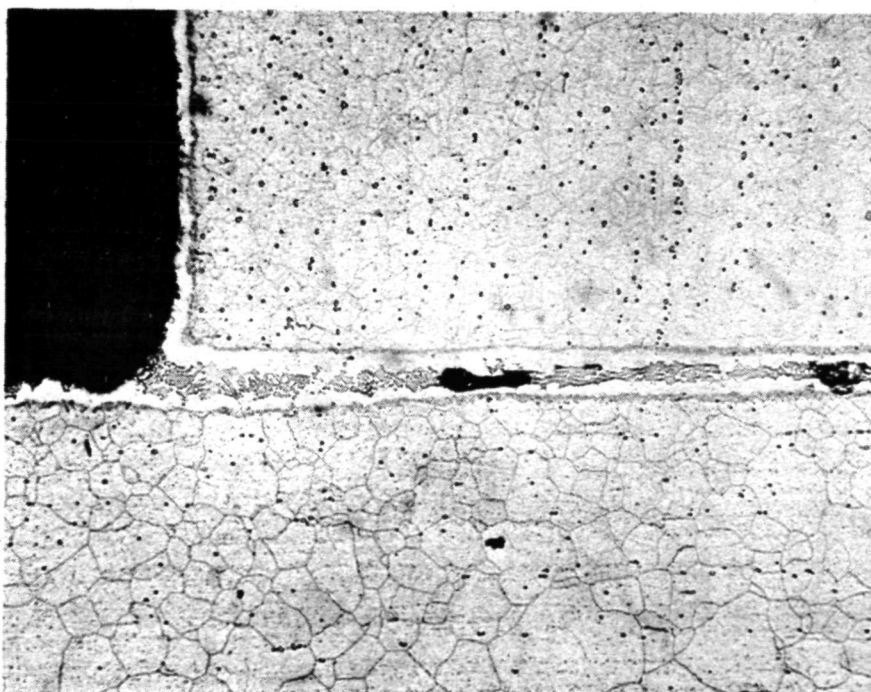


Figure E-29.--Hastelloy X (SN 7) Brazed with Microbraz 30 Mixed with 20 Percent Nicro (Micro 26668, Oxalic Acid Etch, 100x).



F-17541

Figure E-30.--Hastelloy X (SN 8) Brazed with (Microbraz 5075 + 20 Percent Hastelloy X) Mixed with 20 Percent Nicro (Micro 26669, Oxalic Acid Etch, 100x).

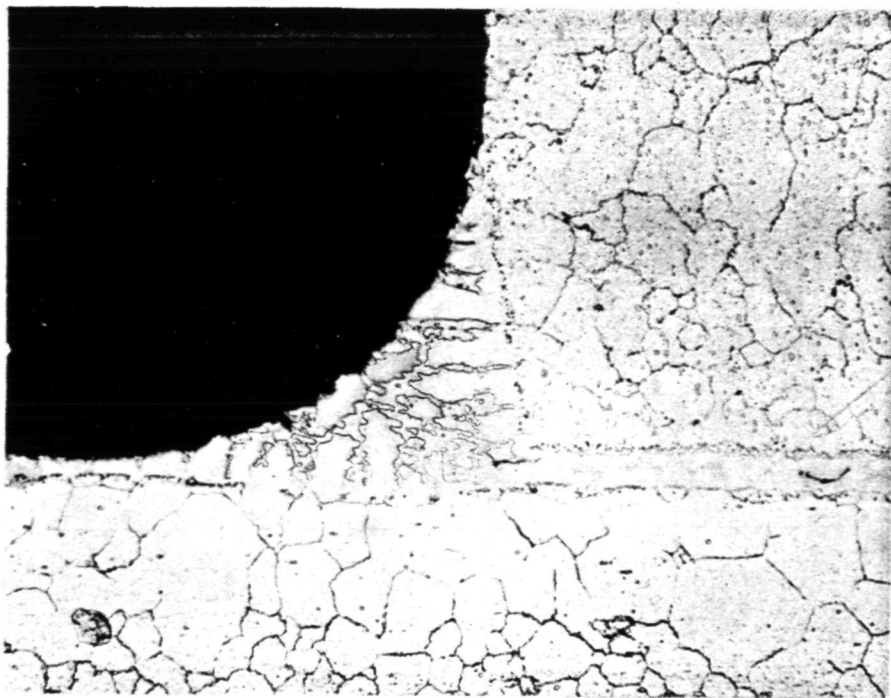


Figure E-31.--Hastelloy X (SN 11) Brazed with Microbraz 30 Mixed With 20 Percent Palniro 1 (Micro 26711, Oxalic Acid Etch, 100X).



F-17542

Figure E-32.--Hastelloy X (SN 12) Brazed with Microbraz 30 Mixed with 20 Percent Palniro 4 (Micro 26712, Oxalic Acid Etch, 100x).



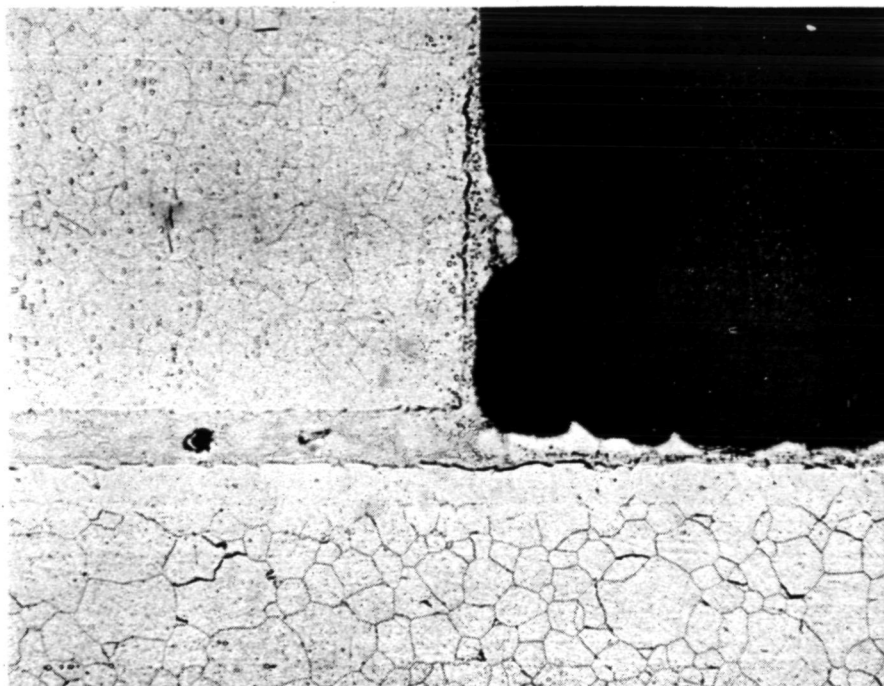
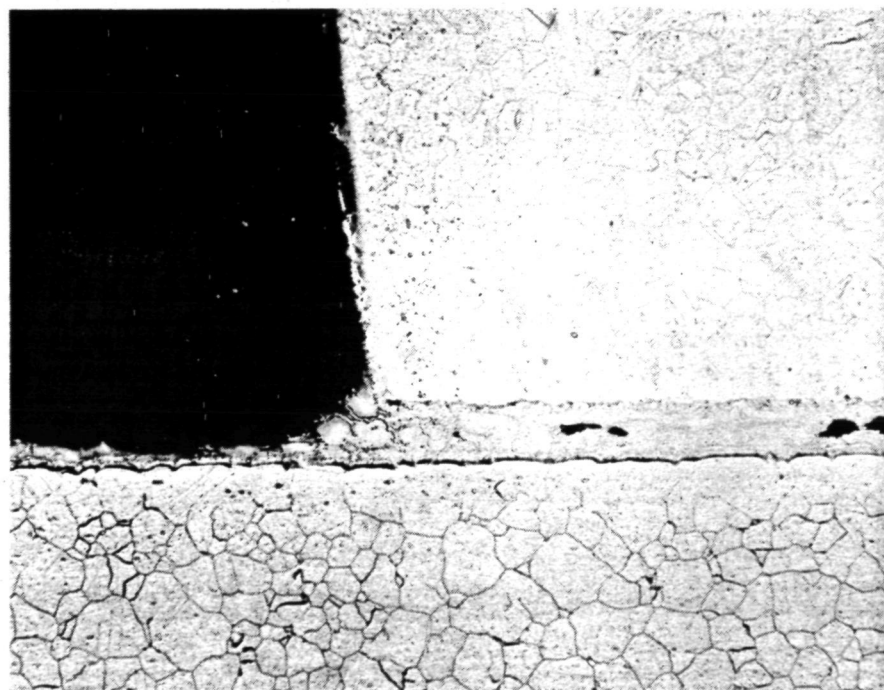


Figure E-33.--Hastelloy X (SN 13) Brazed with Microbraz 30 Mixed with 30 Percent Palniro 7 (Micro 26713, Oxalic Acid Etch, 100x).



F-17543

Figure E-34.--Hastelloy X (SN 14) Brazed with Microbraz 30 Mixed with 20 Percent Palniro 7 (Micro 26714, Oxalic Acid Etch, 100X).

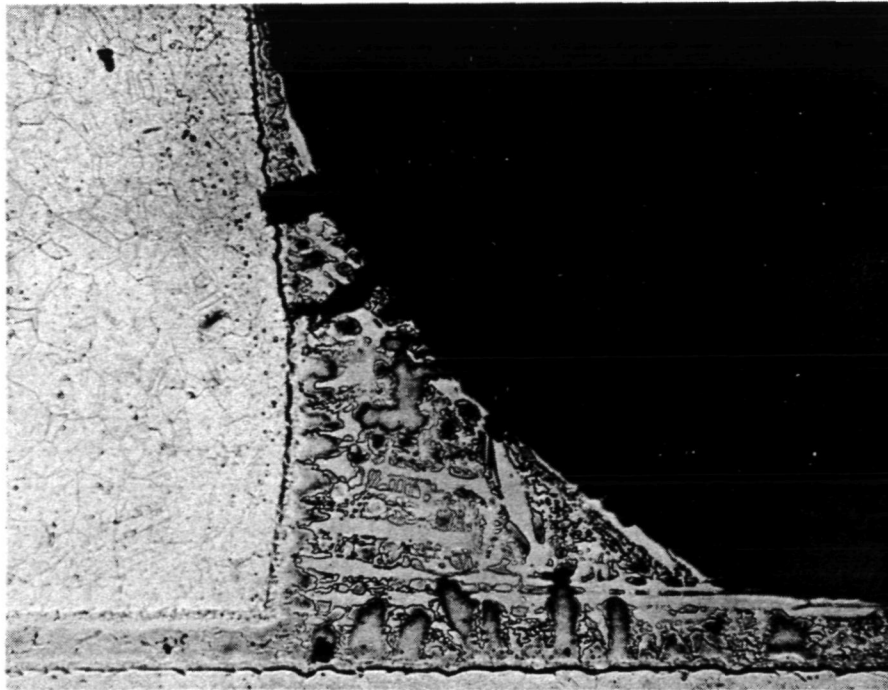
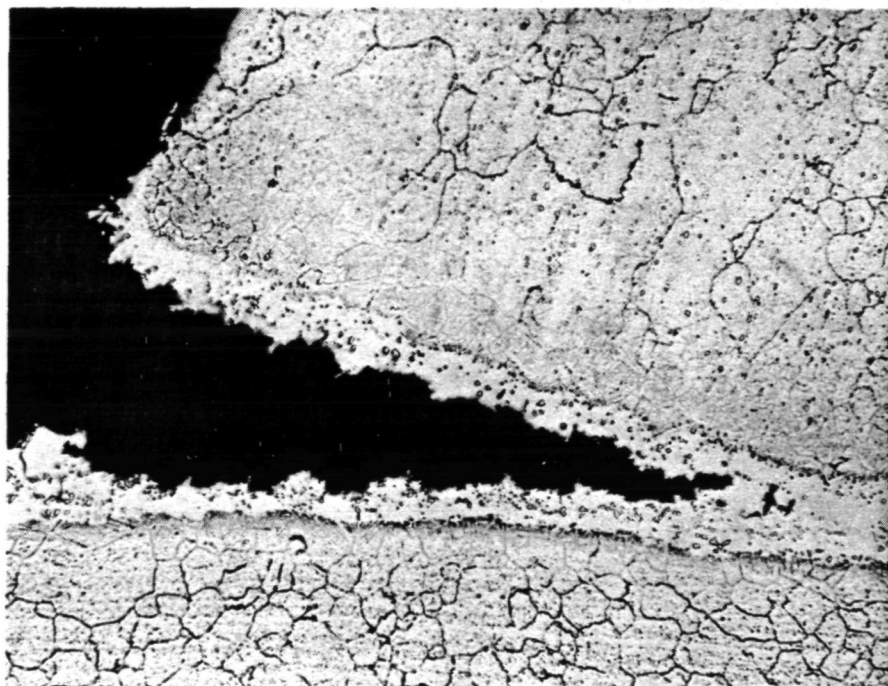


Figure E-35.--Hastelloy X (SN 15) Brazed with Microbraz 30 Mixed with 20 Percent Palniro 7 (Heavy Coat).



F-17544

Figure E-36.--Hastelloy X (SN 16) Brazed with AMI 400 Mixed with 20 Percent Palniro 1 (Micro 26716, Oxalic Acid Etch, 100x).



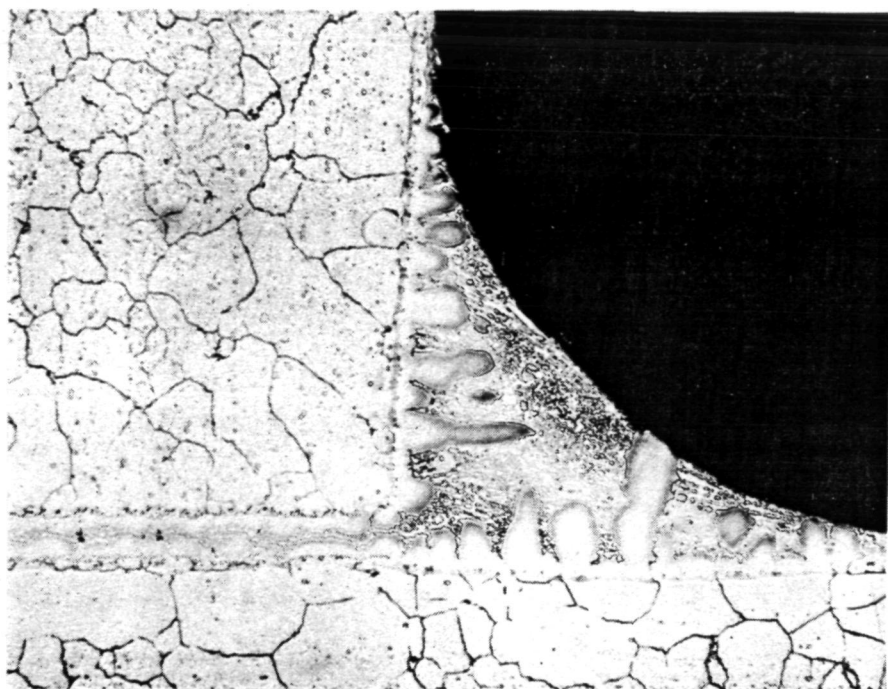
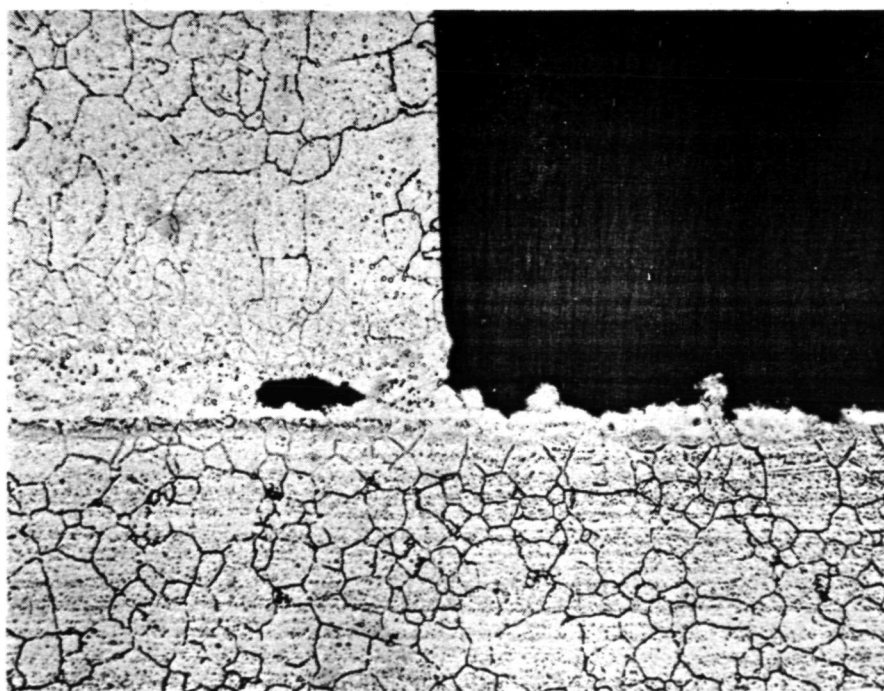
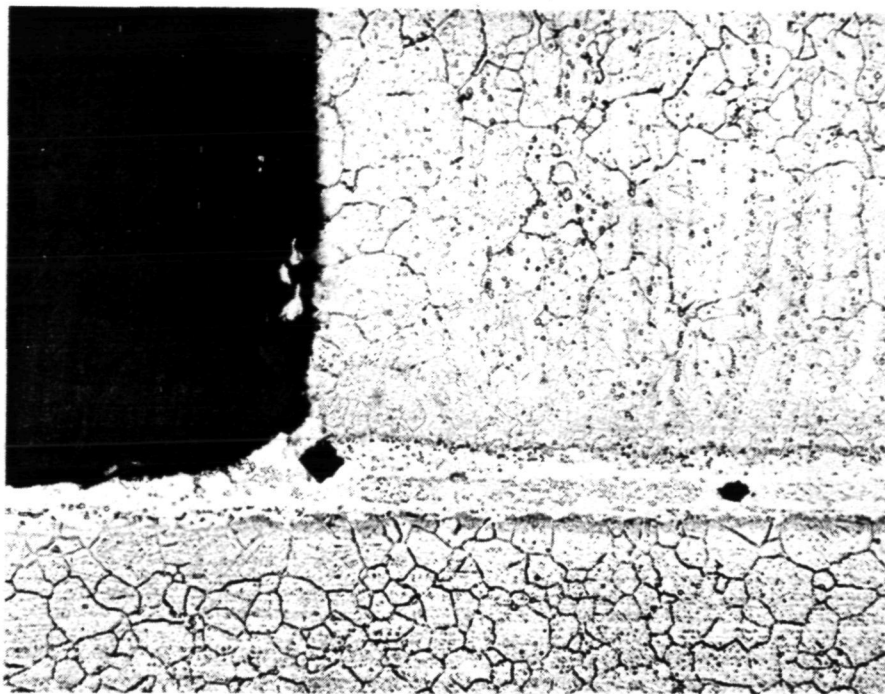


Figure E-37.--Hastelloy X (SN 17) Brazed with Microbraz 30 (Micro 26761, Oxalic Acid Etch, 100x).



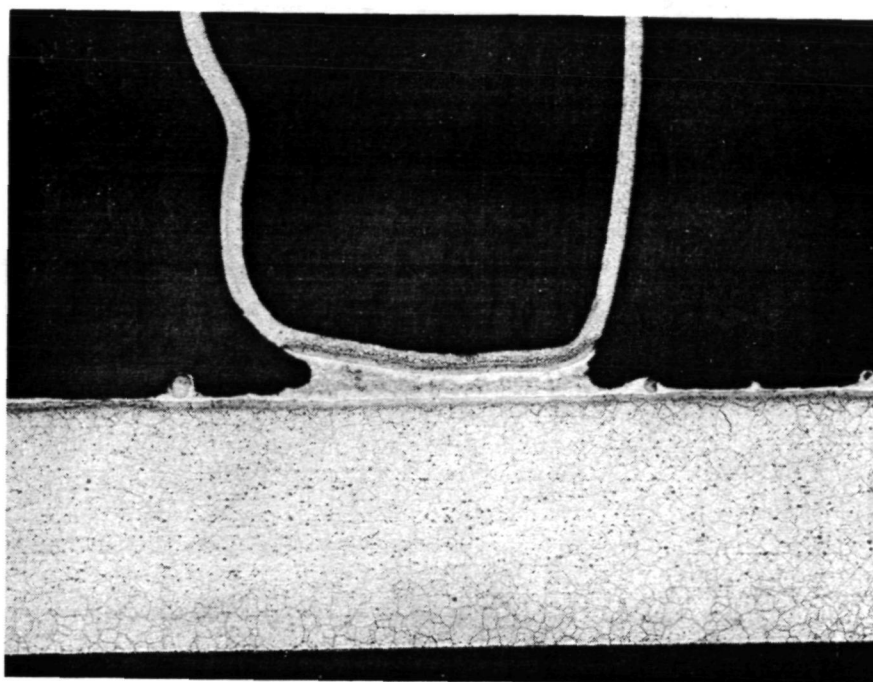
F-17545

Figure E-38.--Hastelloy X (SN 18) Brazed with AMI 400 Mixed with 20 Percent Palniro 1 (Micro 26762, Oxalic Acid Etch, 100,x).

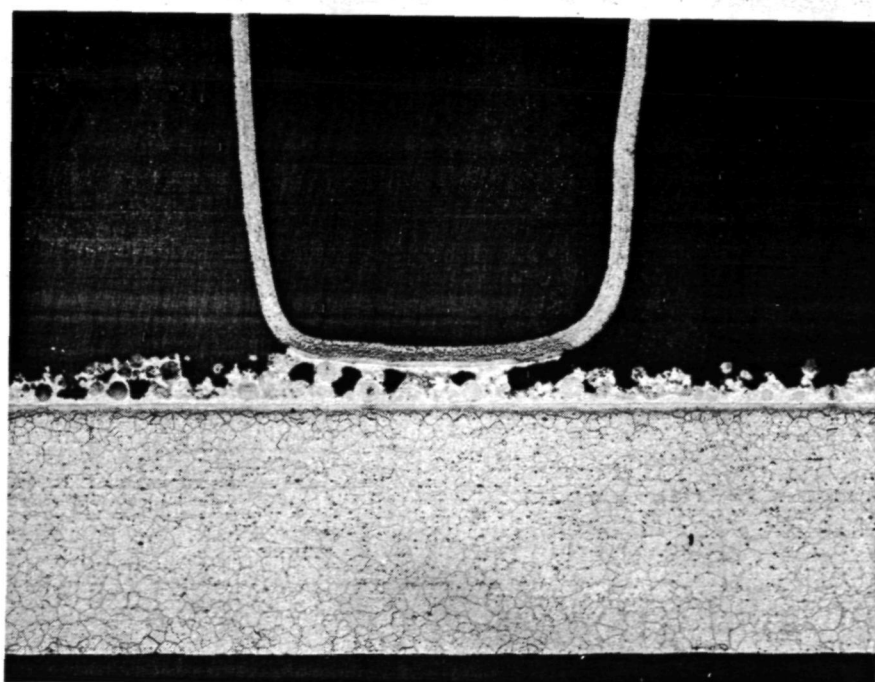


F-17546

Figure E-39.--Hastelloy X (SN 19) Brazed with AMI 400 Mixed with 10 Percent Palniro 1 (Micro 26763, Oxalic Acid Etch, 100x).



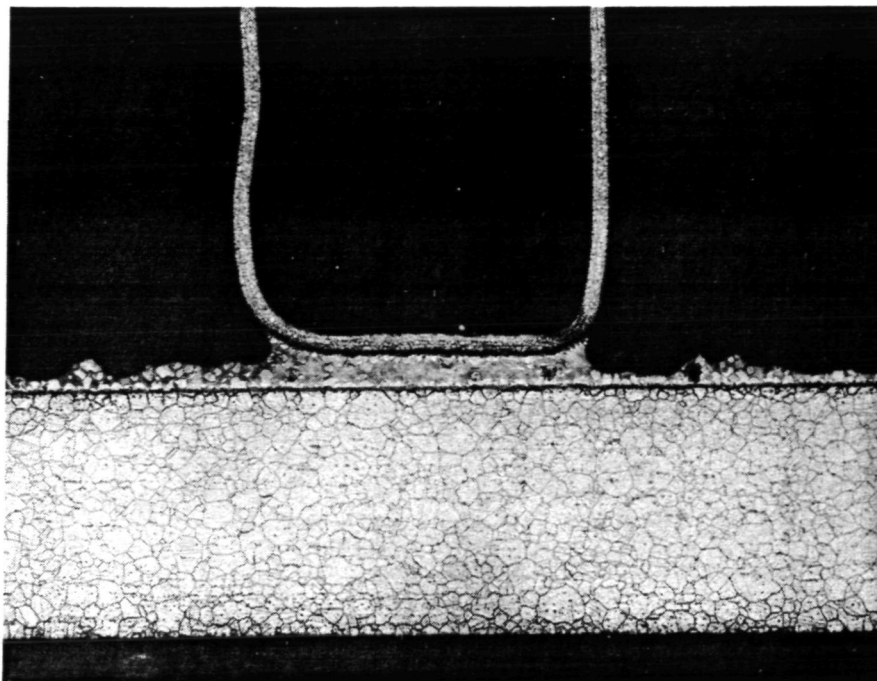
a. 10 PERCENT HASTELLOY X



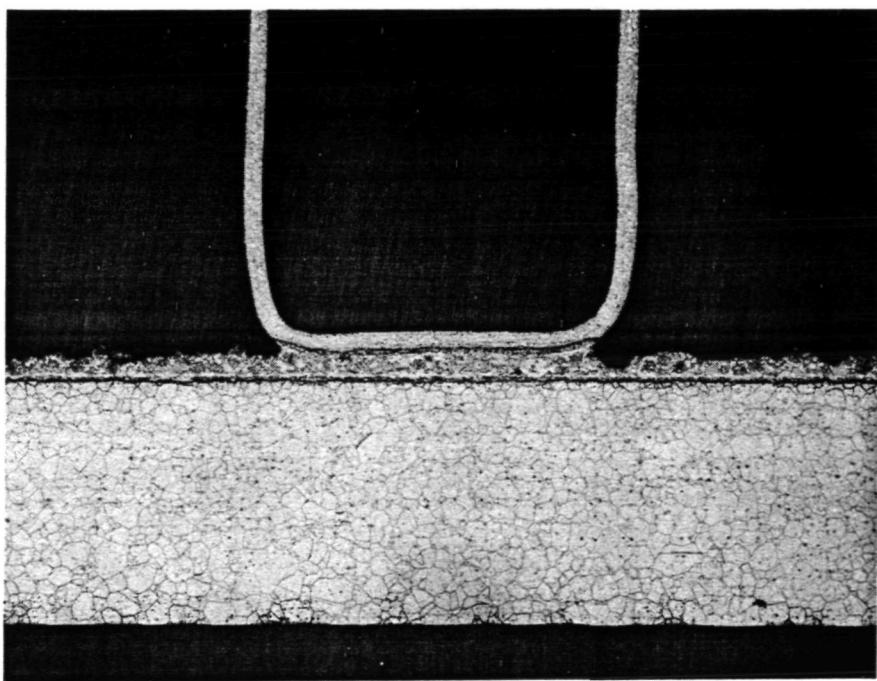
b. 40 PERCENT HASTELLOY X

F-17354

Figure E-40.--Joints Vacuum Brazed at 1344°K (1960°F) with Blends of -170 Mesh Microbraz 130 (AMS 4778) and Hastelloy X Powders (Micro 26503, Oxalic Acid Etch, 30x).



a. 10 PERCENT HASTELLOY X



b. 40 PERCENT HASTELLOY X

F-17355

Figure E-41.--Joints Vacuum Brazed at 1255°K with Blends of -170 Mesh Microbraz 5075 and Hastelloy X Powders (Micro 26502, Oxalic Acid Etch, 30x).

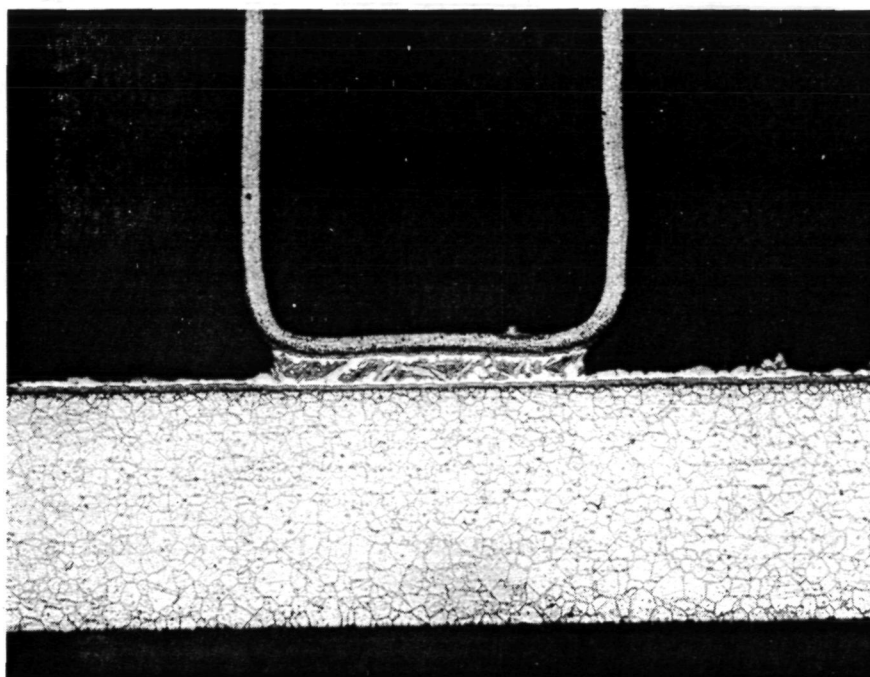
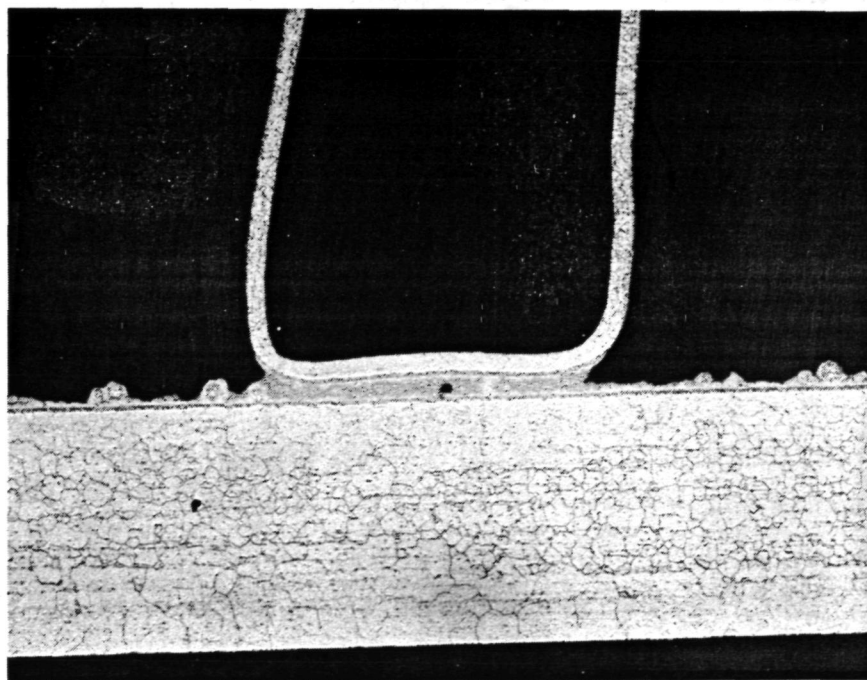
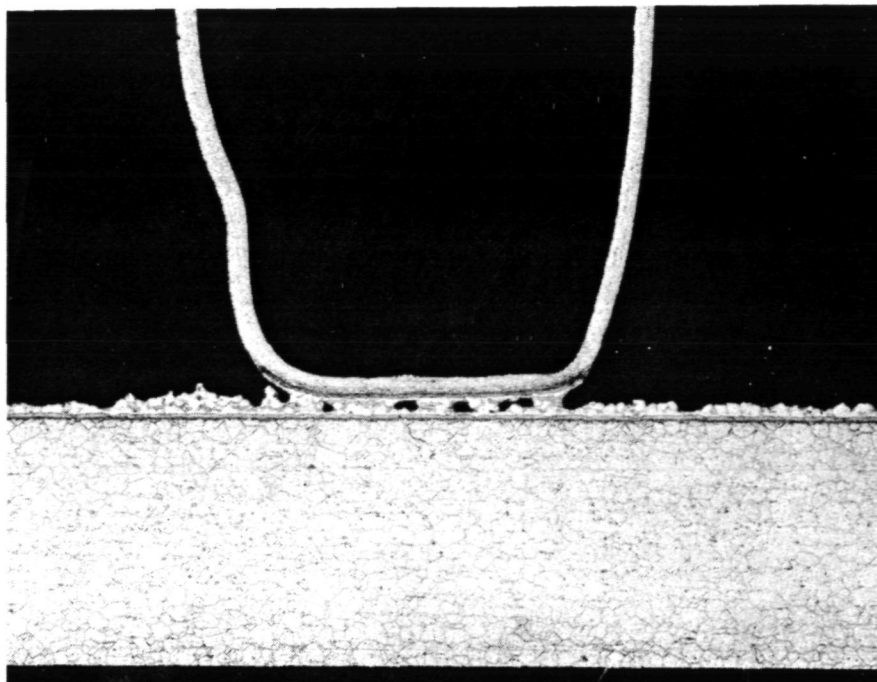


Figure E-42.--Joint Vacuum Brazed at 1283°K (1890°F) with a Blend of 10 Percent Hastelloy X and Nicrobraz 5040 -170 Mesh Powders (Micro 26501, Oxalic Acid Etch, 30x).

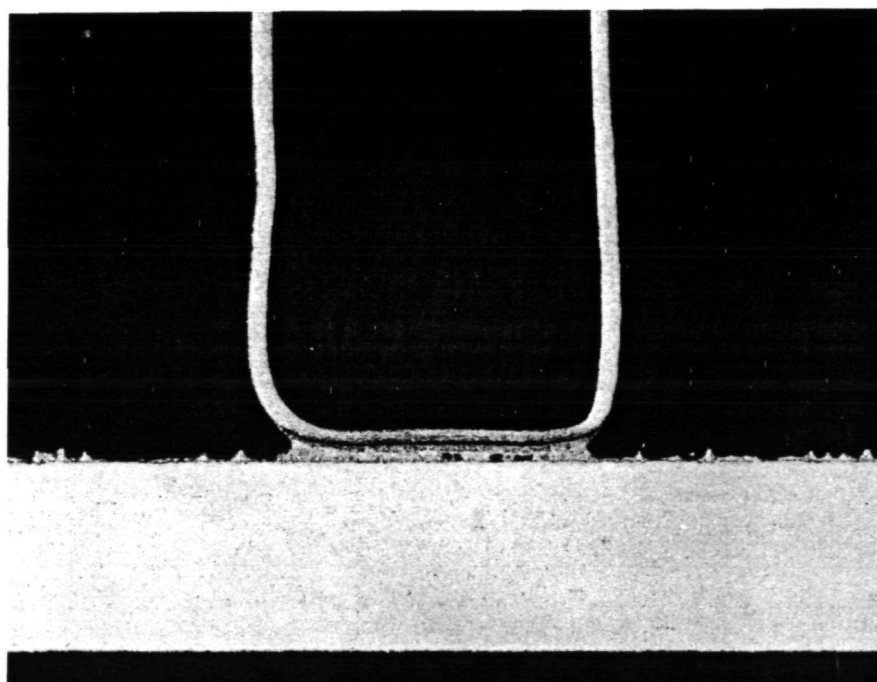


F-17356

Figure E-43.--Joint Vacuum Brazed at 1422°K (2100°F) with a Blend of 10 Percent Hastelloy X and Nicrobraz 30 (J-8100) -170 Mesh Powders (Micro 26504, Oxalic Acid Etch, 30x).



a. HASTELLOY X PLATE

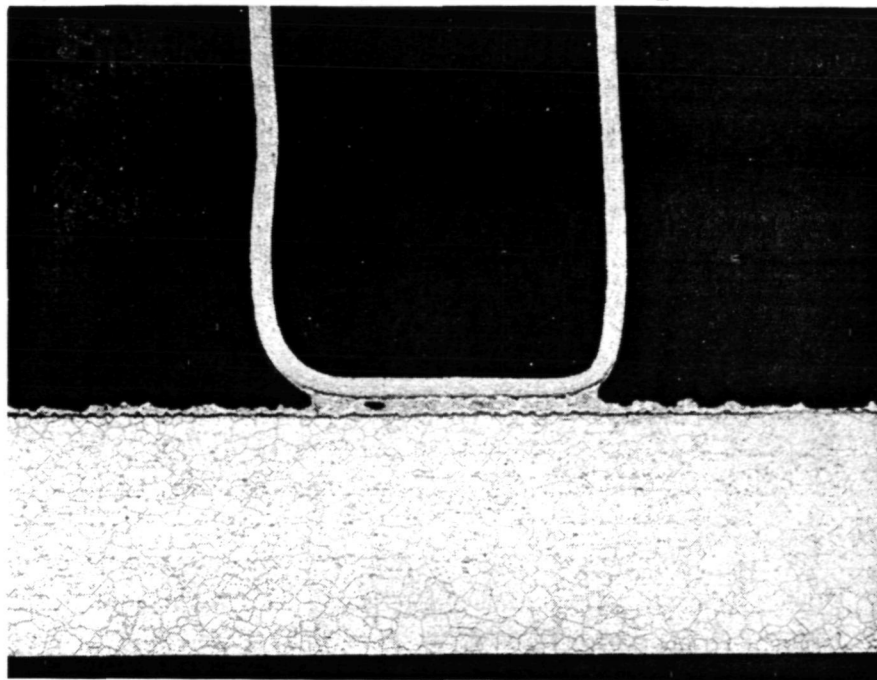


b. 347 CRES PLATE

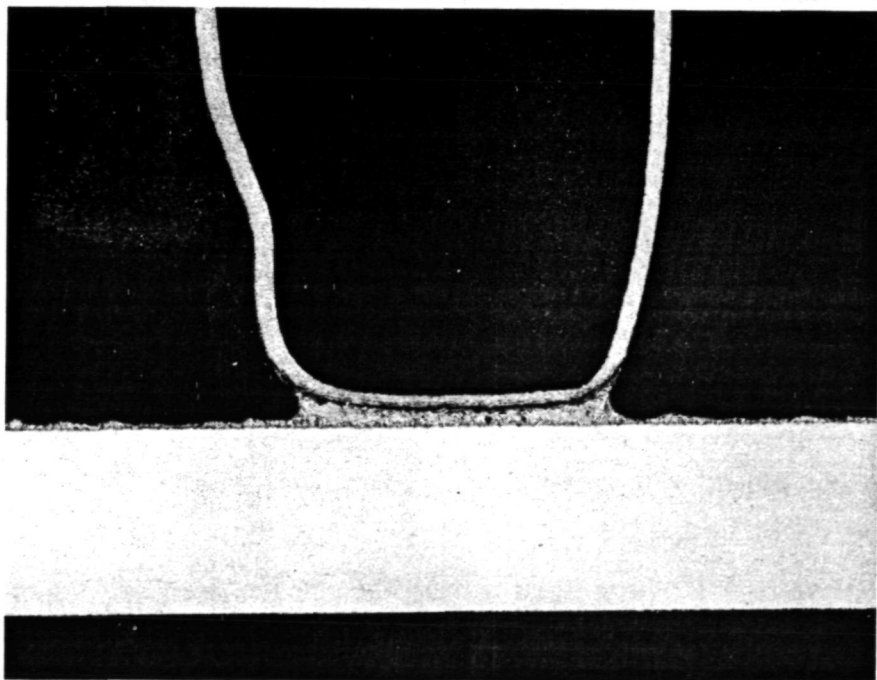
F-17357

Figure E-44.--Plate-fin Joints Vacuum Brazed at 1283°K (1850°F) with a Blend of 20 Percent Hastelloy X in Microbraz 5040 (-325 Mesh Powders) (Micro 26536, Oxalic Acid Etch, 30x).





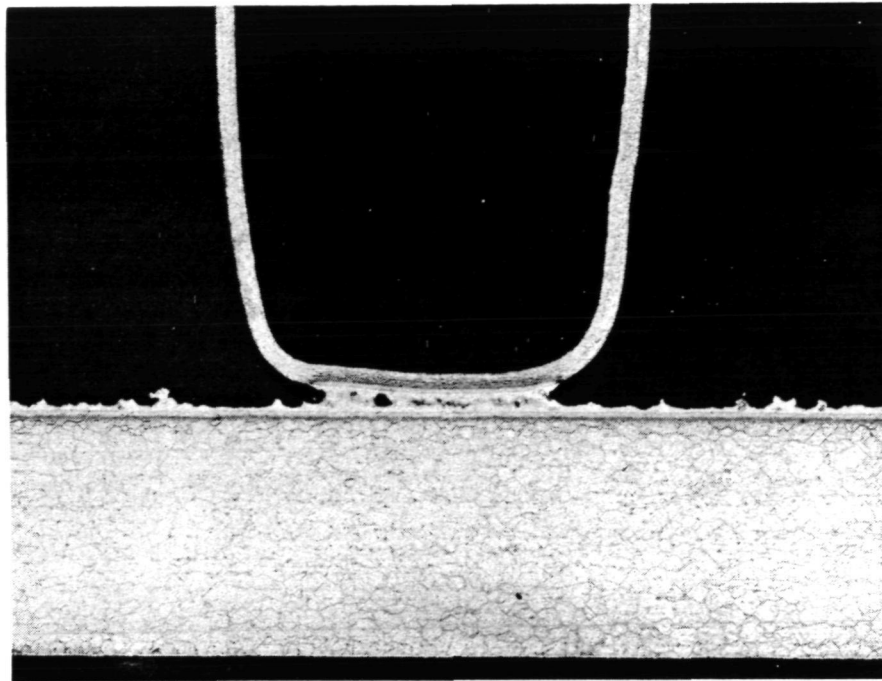
a. HASTELLOY X PLATE



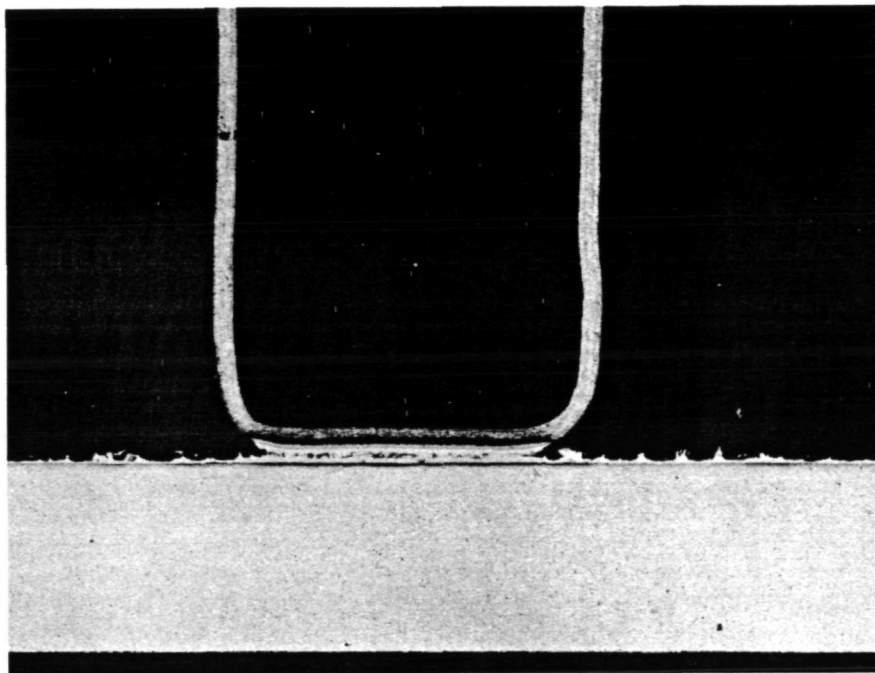
F-17358

b. 347 CRES PLATE

Figure E-45.--Plate-fin Joints Vacuum Brazed at 1255°K (1800°F) with a Blend of 20 Percent Hastelloy X in Microbraz 5075 (-325 Mesh Powder) (Micro 26537, Oxalic Acid Etch, 30x).



a. HASTELLOY X PLATE



b. 347 CRES PLATE

F-17359

Figure E-46.--Plate-fin Joints Vacuum Brazed at 1344°K (1960°F) with a Blend of 20 Percent Hastelloy X in Microbraz 130 (-325 Mesh Powders) (Micro 26538, Oxalic Acid Etch, 30x).



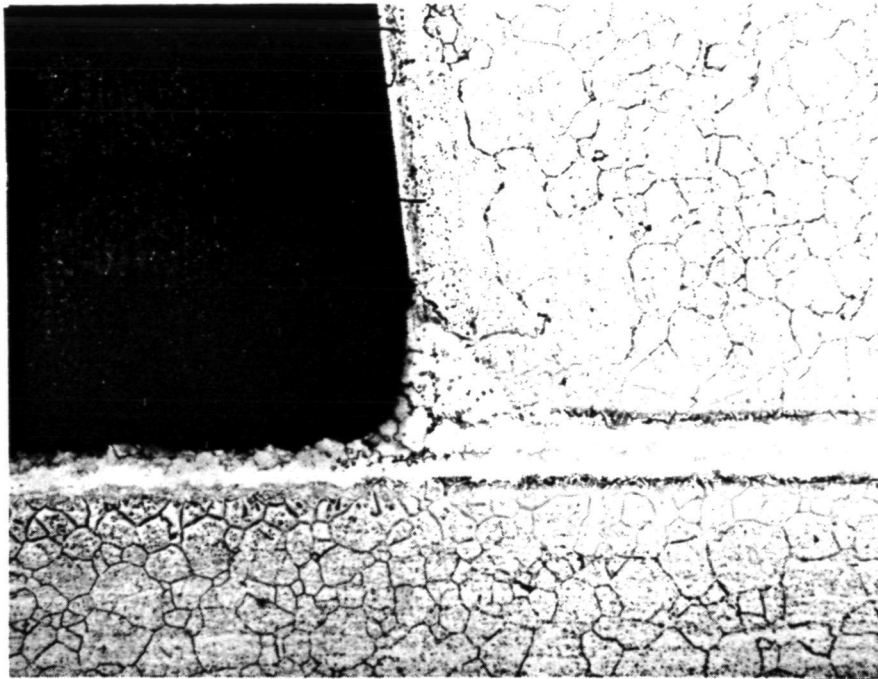


Figure E-47.--Weighted Hastelloy X Channel Section Braze<sup>F-2779h</sup> with a  
75 Percent NB210 (-140 +325) and 25 Percent NB30 (-325)  
Mixture (Micro 27068, Oxalic Acid Etch 100x).

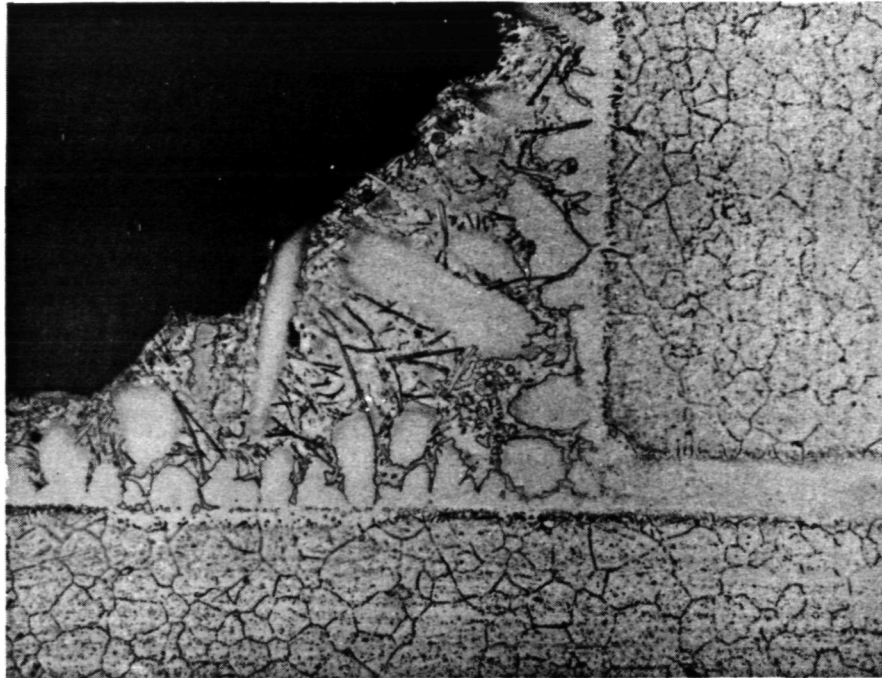
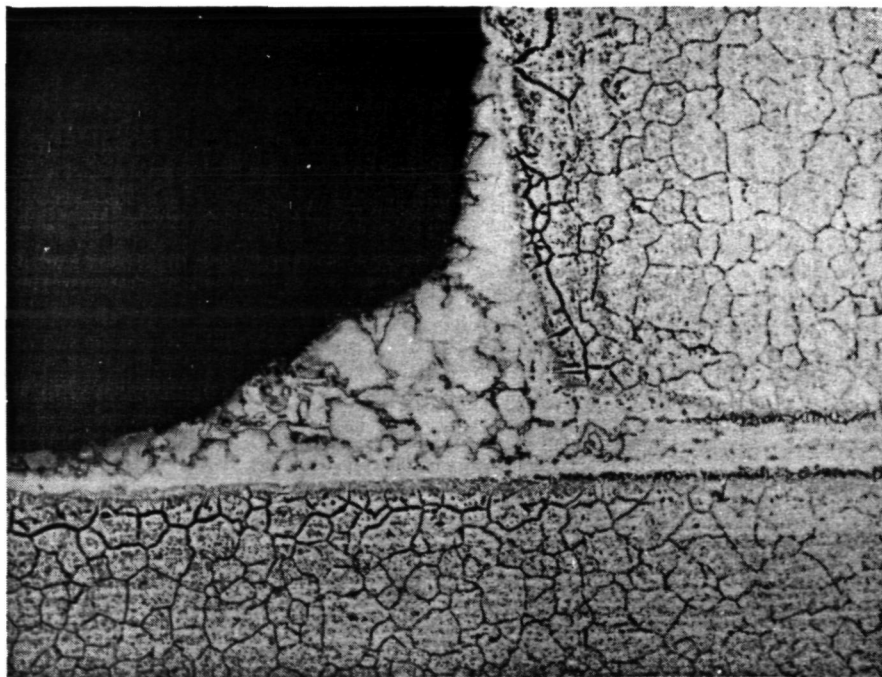
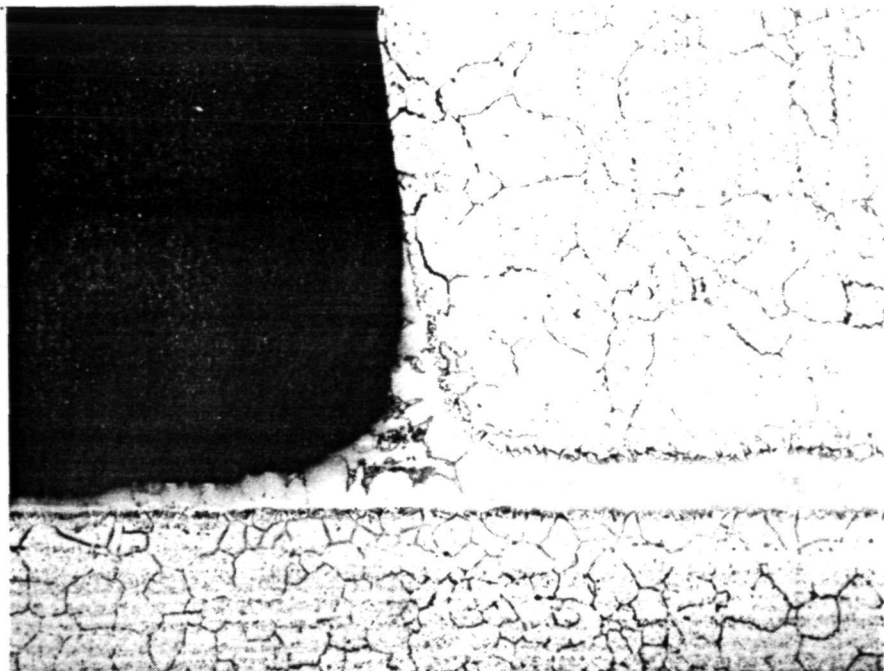


Figure E-48.--Weighted Hastelloy X Channel Brazed with a 50-Percent NB210 (-140 +325) and 50-Percent NB30 (-325) Mixture. (Micro 27071, Oxalic Acid Etch 100x).



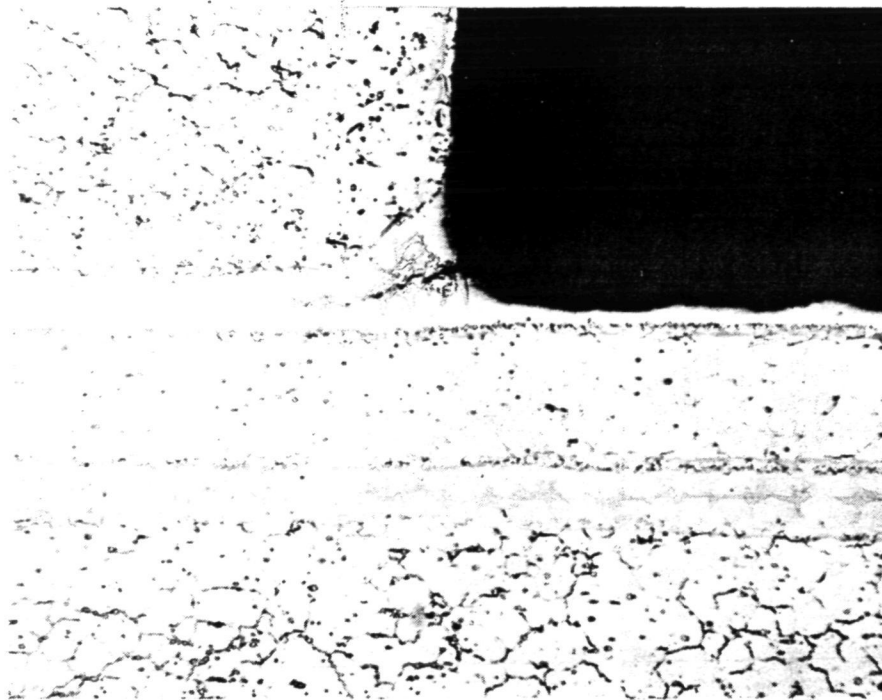
F-17798

Figure E-49.--Weighted Hastelloy X Channel Brazed with a 75-Percent NB210 (-325) and 25-Percent NB30 (-325) Mixture. (Micro 27070, Oxalic Acid Etch 100x).

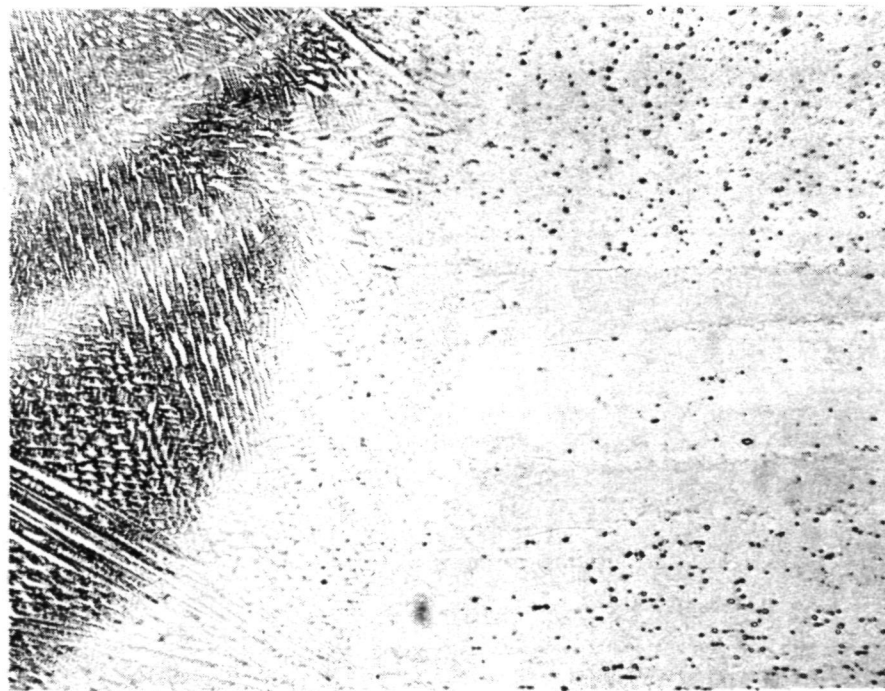


F-23793

Figure E-50.--Weighted Hastelloy X Channel Brazed with a 50-Percent NB210 (-325) and 50-Percent NB30 (-325) Mixture. (Micro 27069, Oxalic Acid Etch 100x).



a. INTERNAL PLATE-HEADER BAR FILLET



F-17795

b. WELD-OVER-BRAZE JOINT

Figure E-51.--Plate-Fin Weld Test Specimen Brazed at 1422°K (2100°F) with Microbraz 30 and Welded with Hastelloy W. (Micro 26922, Oxalic Acid Etch 100x).

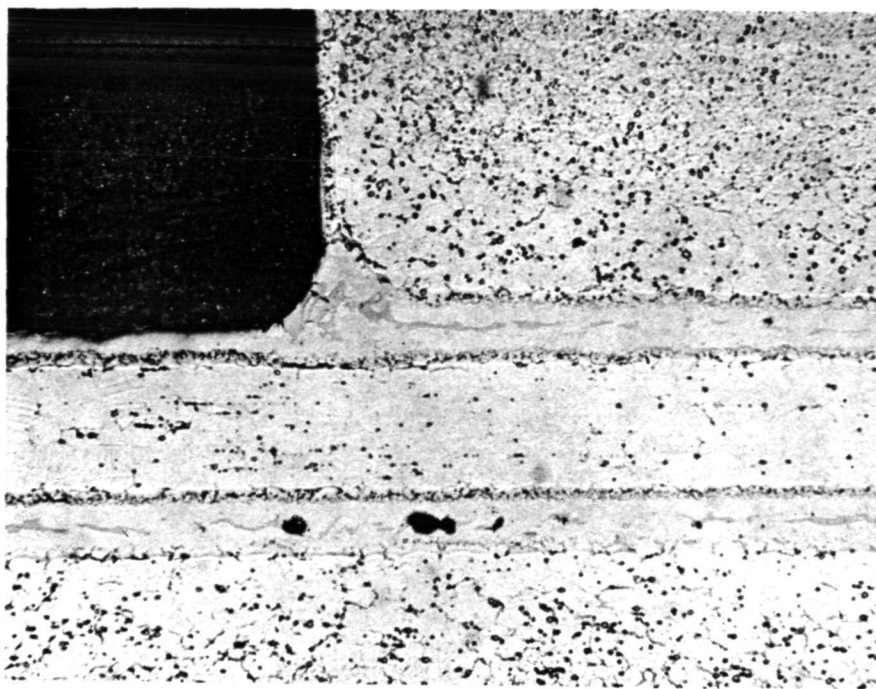
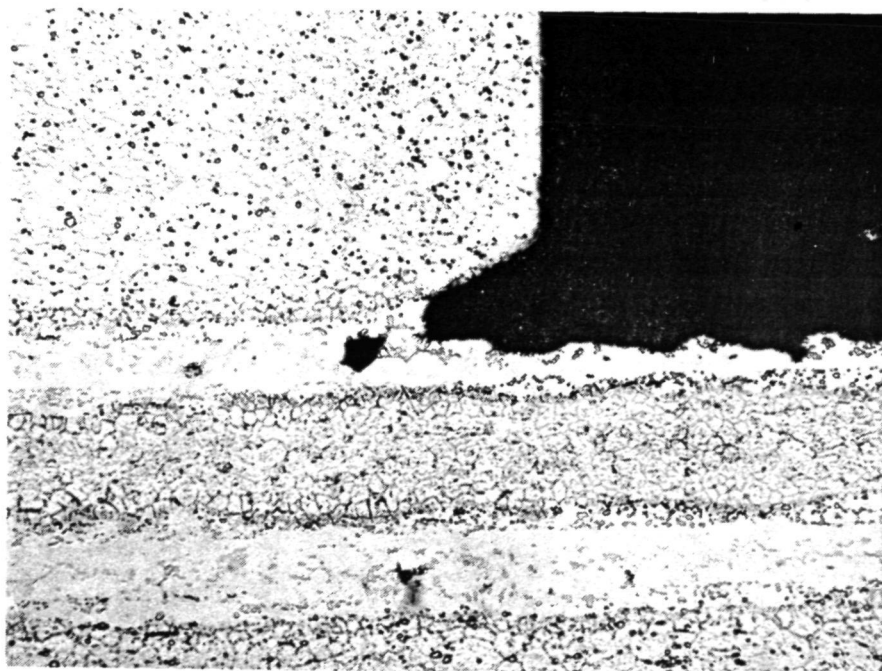
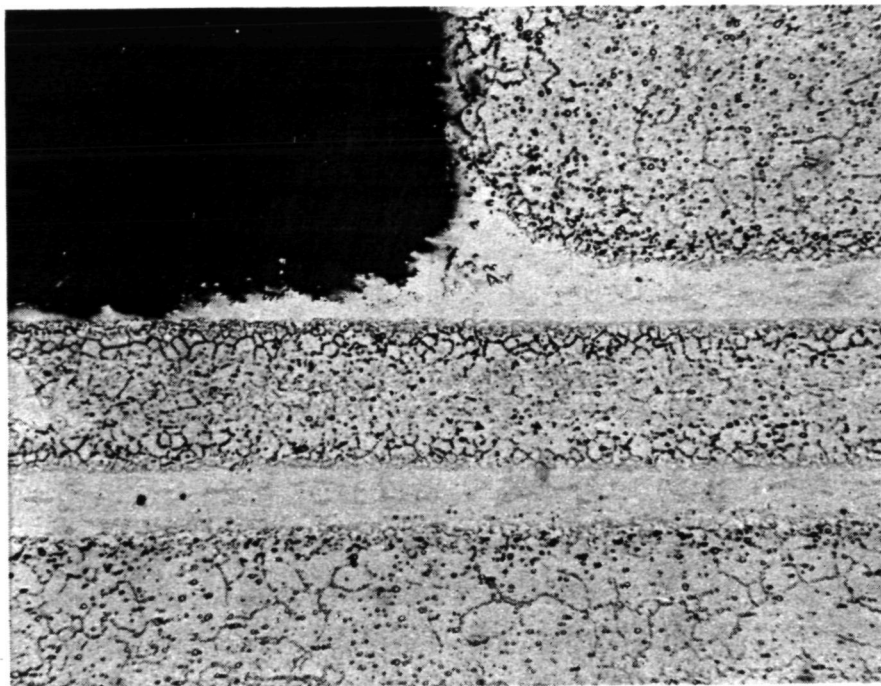


Figure E-52.--Plate-fin Weld Test Specimen Brazed at 1405°K (2070°F) with a Mixture of NB30 and 10 Percent Palniro 1 and Welded with Hastelloy W. (Micro 26926, Oxalic Acid Etch 100x).



F-17796

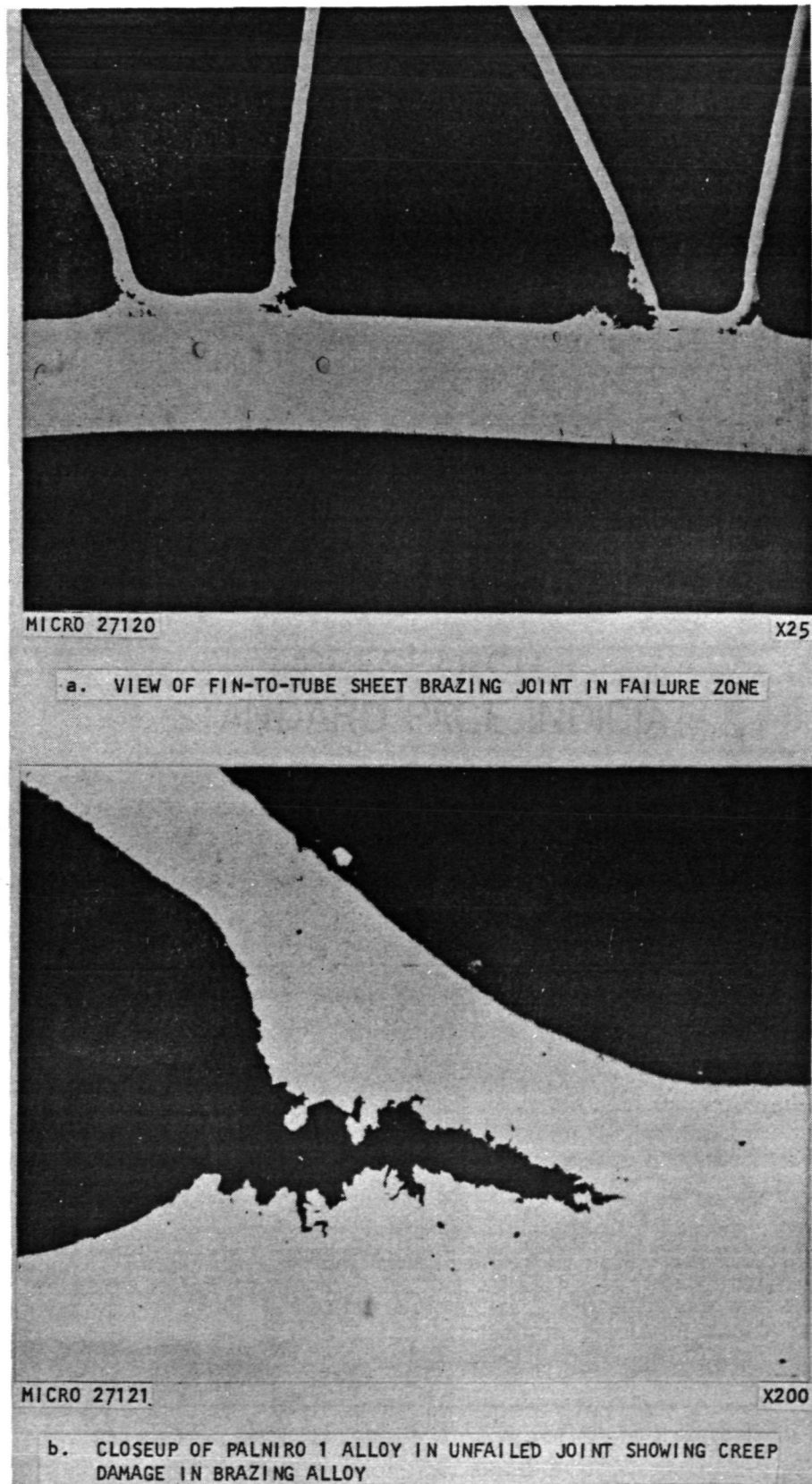
Figure E-53.--Plate-fin Weld Test Specimen Brazed at 1422°K (2100°F) with a Mixture of NB210 and 10 Percent Palniro 1 and Welded with Hastelloy W. (Micro 26924), Oxalic Acid Etch 100x).



F-23794

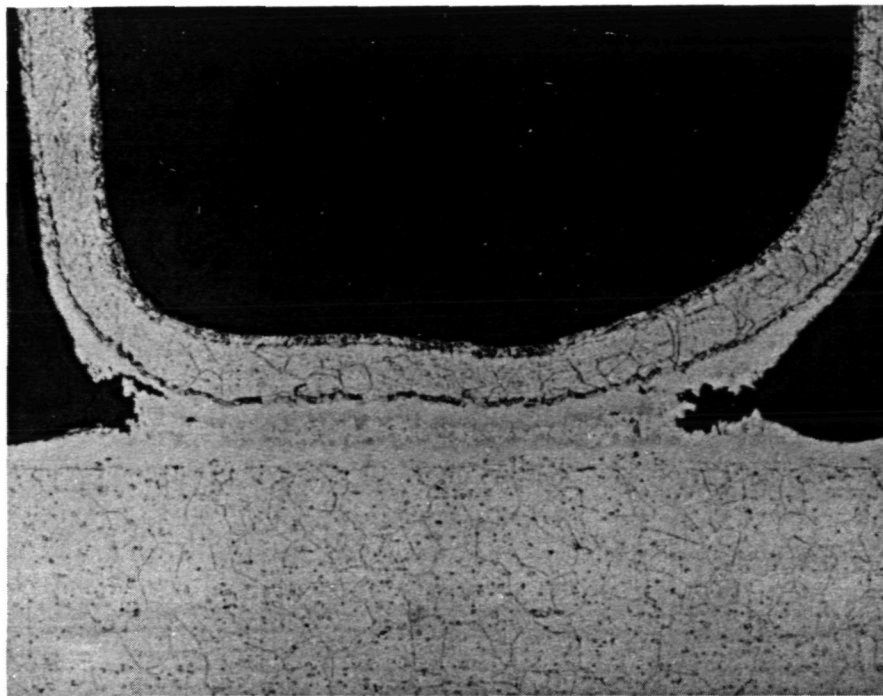
Figure E-54.--Plate-fin Weld Test Specimen Brazed 1422°K (2100°F) with a 75 Percent NB210 - 25 Percent NB30 Mixture of -325 Mesh Powders. Welded with Hastelloy W. (Micro 27061, Oxalic Acid Etch 100x).





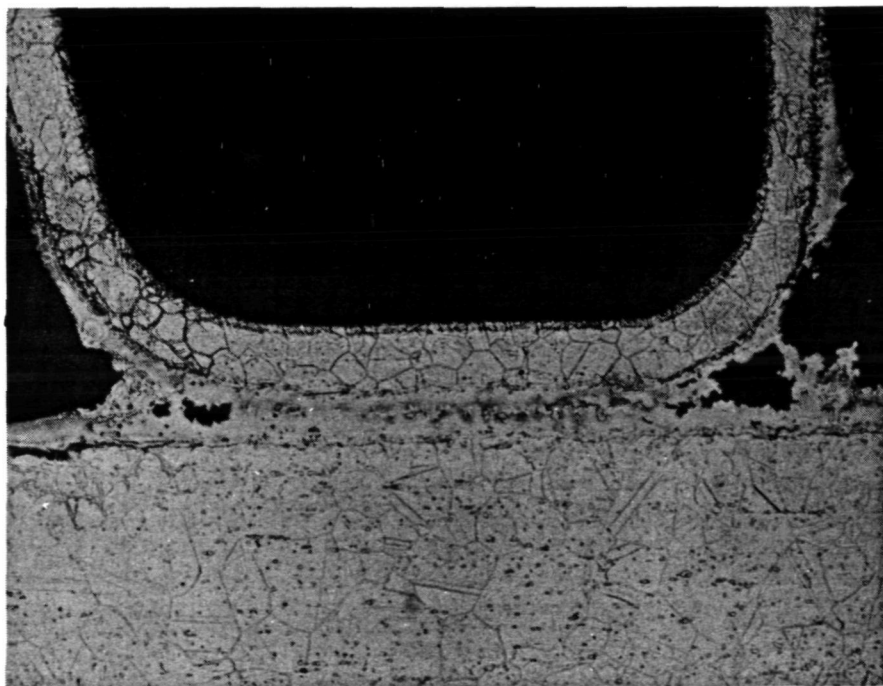
F-18429

Figure E-55.--Failed Creep Rupture Test Panel Brazed with 0.0025-cm (0.001-in.) Thick Palniro 1 Brazing Alloy.



MICRO 27209

X 100



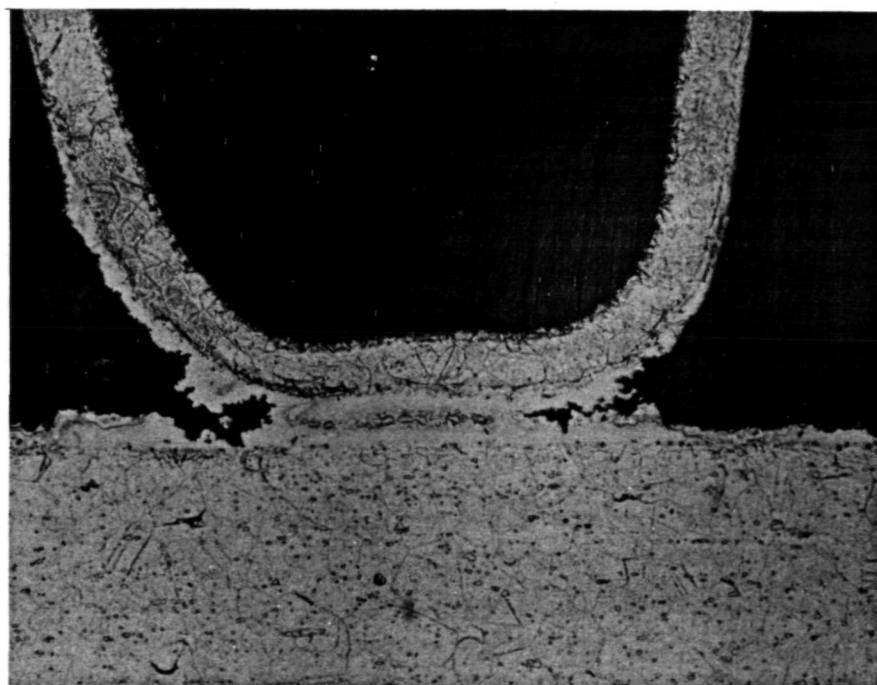
MICRO 27210

X 100

F-23758

Figure E-56.--Creep Damage of Failed Creep-Rupture Test Panels Brazed with 0.0019-cm (0.00075-in.) Thick Palniro 1 Brazing Alloy.



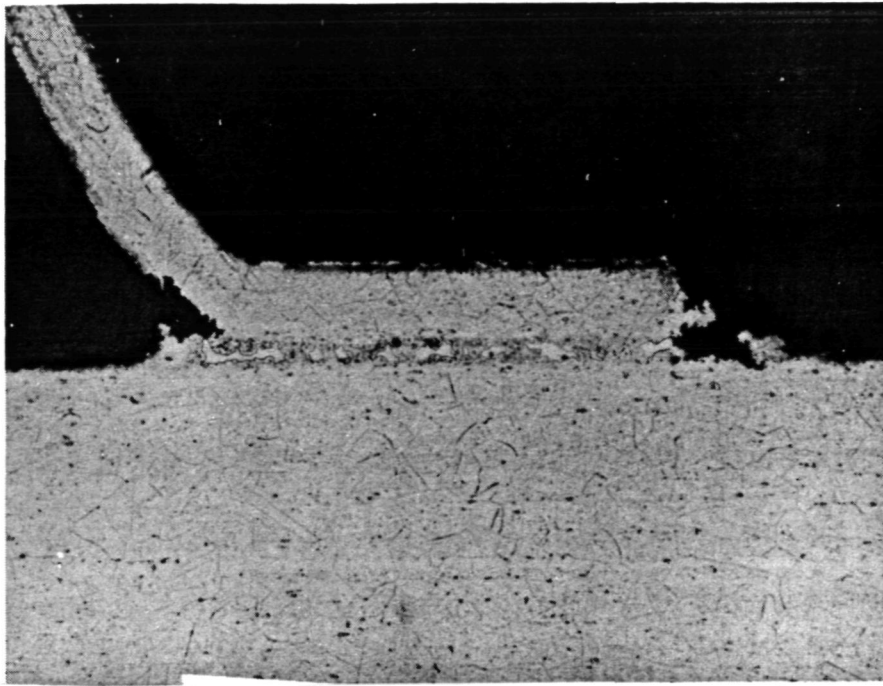


MICRO 27208

X 100

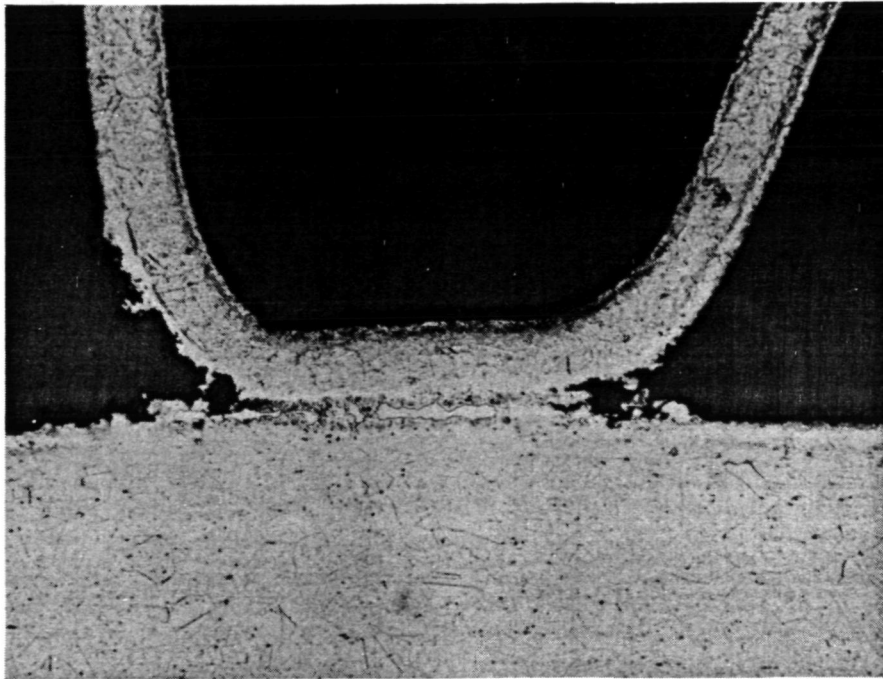
F-23761

Figure E-57.--Creep Damage of Failed Creep-Rupture Test Panel Brazed with 0.0013-cm (0.0005-in.) Thick Palniro 1 Brazing Alloy.



MICRO 27205

X 100

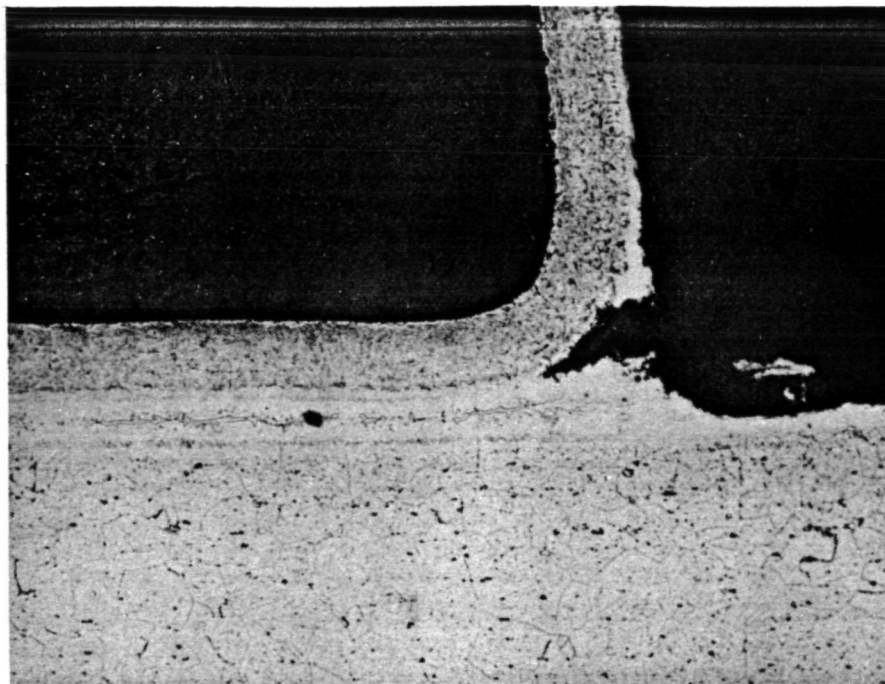


MICRO 27205

X 100

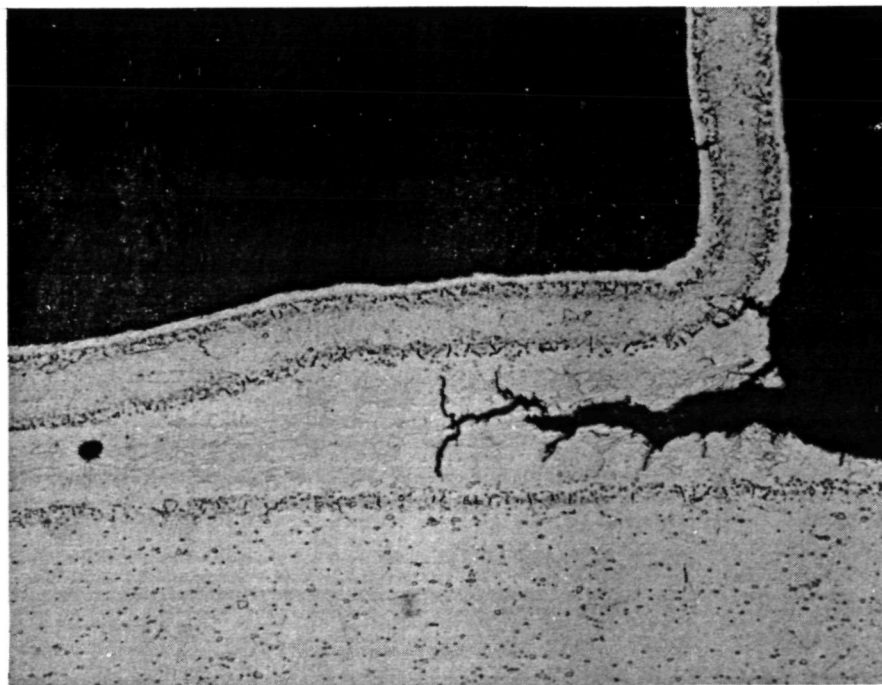
F-23760

Figure E-58.--Creep Damage of Failed Creep-Rupture Test Panel Brazed with 0.00076-cm (0.0003-in.) Thick Palniro 1 Brazing Alloy.



MICRO 27207

X 100

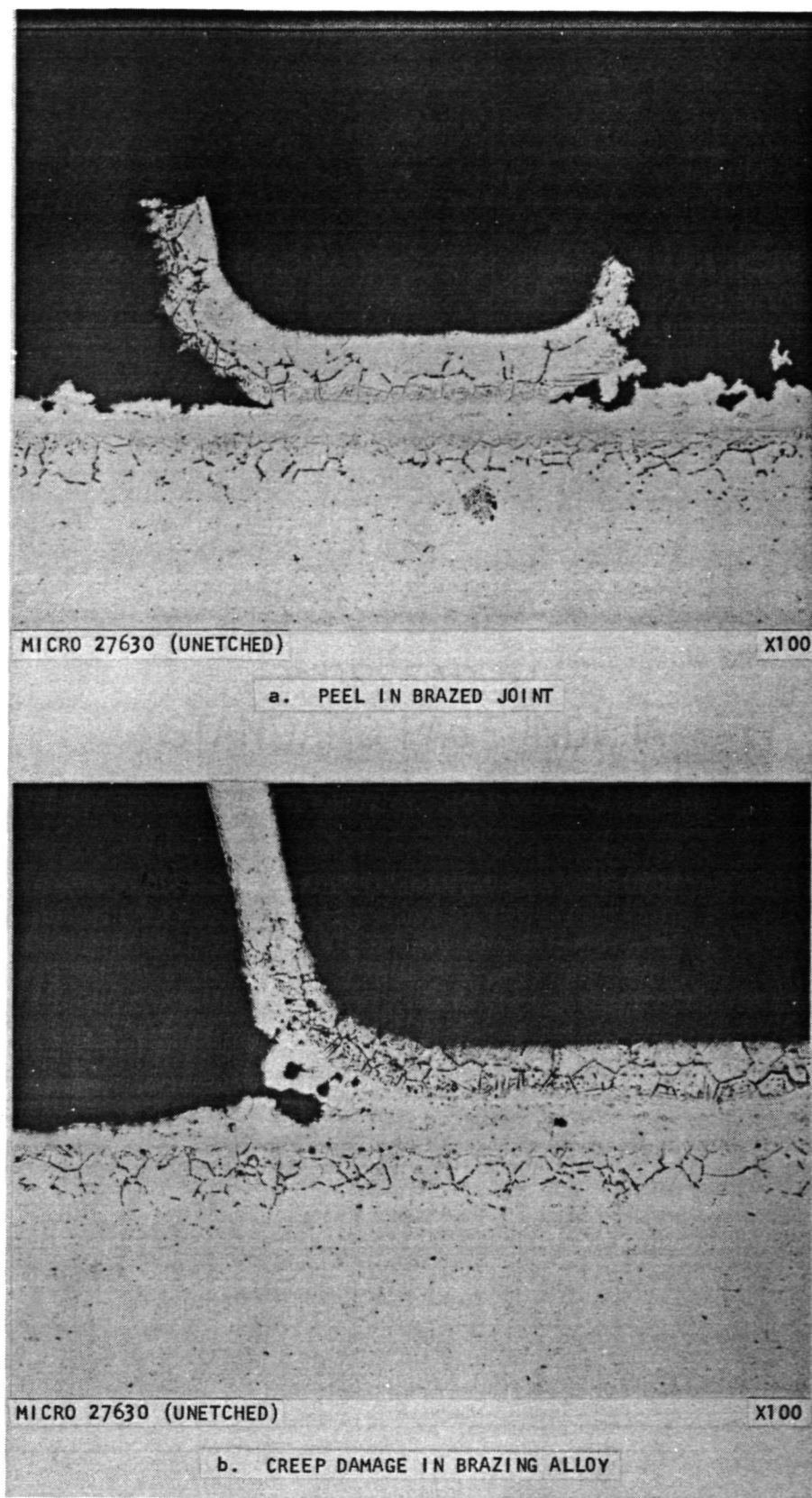


MICRO 27211

X 100

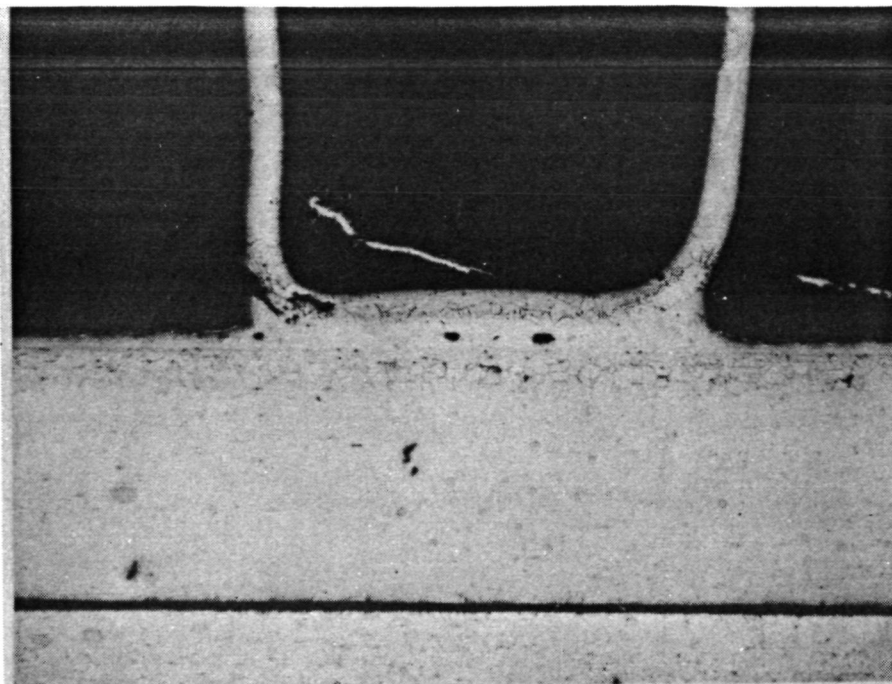
F-23759

Figure E-59.--Creep Damage of Failed Creep-Rupture Test Panel Brazed with Microbraz 30 Brazing Alloy.



F-18430

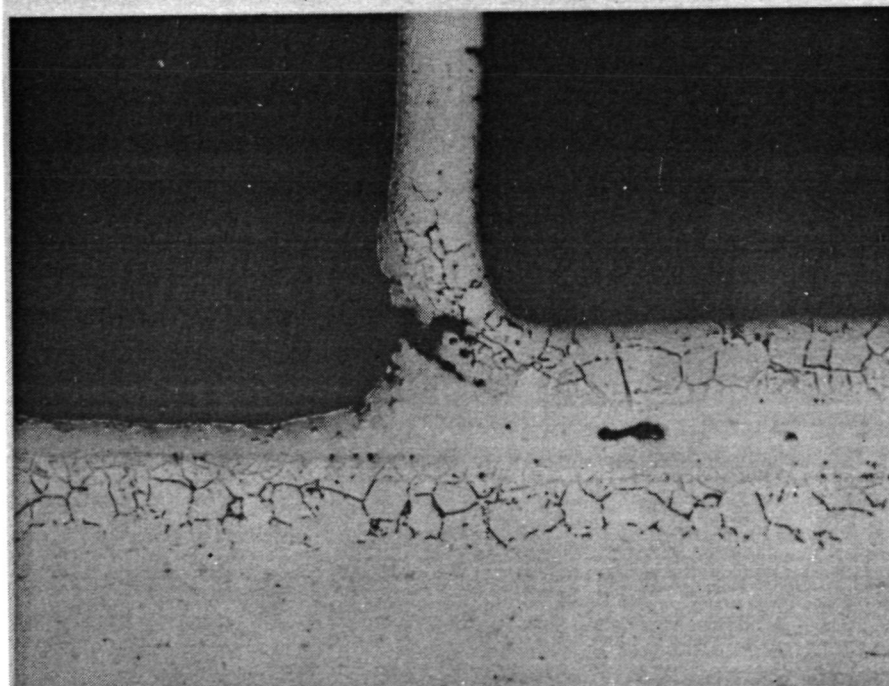
Figure E-60.--Creep Failure in Panel Brazed with Microbraz 210(75 Percent)-Microbraz 30 (25 percent).



MICRO 27926 (UNETCHED)

X50

a. START OF CREEP FAILURE



MICRO 27926 (UNETCHED)

X100

b. START OF CREEP FAILURE

F-18431

Figure E-61.--Start of Creep Failure in Panel Brazed with  
Microbraz 210 (75 Percent)-Microbraz 30 (25 percent).